NAPHTHALIMIDE-BASED MATERIALS FOR ELECTRONIC AND BIOLOGICAL APPLICATIONS

Ph.D. THESIS

by

ANKITA SAINI

DEPARTMENT OF CHEMISTRY
INDIAN INSTITUTE OF TECHNOLOGY ROORKEE
ROORKEE – 247 667 (INDIA)
MARCH, 2018

NAPHTHALIMIDE-BASED MATERIALS FOR ELECTRONIC AND BIOLOGICAL APPLICATIONS

A THESIS

Submitted in partial fulfilment of the requirements for the award of the degree

of

DOCTOR OF PHILOSOPHY

in

CHEMISTRY

by

ANKITA SAINI

DEPARTMENT OF CHEMISTRY
INDIAN INSTITUTE OF TECHNOLOGY ROORKEE
ROORKEE – 247 667 (INDIA)
MARCH, 2018

INDIAN INSTITUTE OF TECHNOLOGY ROORKEE
ROORKEE

CANDIDATE'S DECLARATION

I hereby certify that the work which is being presented in the thesis entitled **"NAPHTHALIMIDE-BASED MATERIALS FOR ELECTRONIC AND BIOLOGICAL APPLICATIONS"** in partial fulfilment of the requirements for the award of the degree of Doctor of Philosophy and submitted in the Department of Chemistry of the Indian Institute of Technology Roorkee, Roorkee is an authentic record of my own work carried out during a period from July, 2013 to March, 2018 under the supervision of Dr. K. R. Justin Thomas, Associate Professor, Department of Chemistry, Indian Institute of Technology Roorkee, Roorkee.

The matter presented in the thesis has not been submitted by me for the award of any other degree of this or any other Institute.

(ANKITA SAINI)

This is to certify that the above statement made by the candidate is correct to the best of my knowledge.

(K. R. Justin Thomas)
Supervisor

Date: **23-03-2018**

Acknowledgments

For me, moving my fingers on the keyboard for jotting what you are reading now is the most emotional task to accomplish. While expressing my thanks to the Almighty and all those including my teachers, parents, brother, friends and colleagues who supported, encouraged and motivated me throughout my tenure at one of the most prestigious institution, I felt like yes, this is the best journey of my life I have travelled till now. A lot more to experience but this one will always be an unforgettable one. I owe my deepest gratitude to each and every one who supported me either directly or indirectly to build this particular dissertation in the way it looks like.

The first and foremost I would like to present special thanks to my supervisor, ***Dr. K. R. Justin Thomas*** *for providing me a pleasant opportunity to pursue Ph.D under his guidance. I am grateful to him for his encouragement, support and fruitful discussions during my PhD tenure. I found myself fortunate enough to have him as an advisor without whom this dissertation would not have been possible. I would like to thank him for always keeping a spirit of enthusiasm alive in me through my ups and downs. I would like to add that he provided sufficient freedom and space to develop myself not only as a chemist but also as an independent individual. When one learns he becomes a star, but when one teaches he becomes a constellation. His valuable comments and suggestions at various stages of my research experience helped me to improve myself not only academically but also personally. I would like to present my special thanks to* ***Mrs. Jeyaseeli Justin*** *who always provided me motherly affection with an experience of home away home feeling with her uncountable blessings, wishes and hugs. I found inadequate words to thank her for providing uncountable delicious lunch and dinner with family,* ***Jones****,* ***Jolin*** *and* ***Judith*** *who made it more enjoyable with their friendly behavior.*

I am grateful to ***Dr. M. R. Maurya*** *as Head, Department of Chemistry, IIT Roorkee and as Chairman of my SRC (Student Research Committee) for providing me the official support and facilities at the department.*

I am extremely thankful to my SRC members, ***Dr. R. K. Peddinti*** *and* ***Dr. B. S. S. Daniel*** *and DRC (Department Research Committee) member,* ***Dr. Anil Kumar*** *for their constant support and encouragement.*

*I sincerely acknowledge Ministry of Human Resource Development (****MHRD****) for providing the financial assistance on time to pursue my doctoral degree comfortably.*

I take this opportunity to owe my gratitude to ***Prof. Kuo-Chuan Ho*** *and* ***co-workers*** *(Department of Chemical Engineering, National Taiwan University, Taipei, Taiwan) for providing the DSSC data of samples. I would like to thank* ***Dr. P. Gopinath*** *and* ***Dr. Partha Roy*** *for showing interest in collaborative work for biological applications with their students,* ***Abhay*** *and* ***Ritu****, respectively. I thank Institute Instrumentation Centre (IIC), IITR for proving instrumentation facilities whenever I need. Also, I acknowledge Department of Science and Technology (DST, FIST) for High Resolution Mass Spectral facility in the department.*

It is said that the best thing you can offer to anyone is the time. My special vote of thanks to seniors, ***Dr. Abhishek Baheti*** *and* ***Dr. Venkateswararao*** *for listening patiently to all my queries. I thank both of them for guiding and teaching me from the very basic to hard core research topics.*

They made the tedious things simple in research and make it unforgettable for me through their constant support and help. When it comes to teaching, I cannot forget my school and college teachers who not only taught the subjects, but also inspire and motivate me to stood by what is right and highlighted a path where creativity and vision matters a lot. Saying thank you is not sufficient enough to what they have taught me.

I am glad to interact with ***Dr. Bhaskar Garg*** *who joined our laboratory as Young Scientist during the last two years of my stay at IITR. I am indebted to him for the help he has provided to me in correction of thesis draft. I respect the support he has offered to me whenever I needed.*

I think that the progress of work is amplified if one has a supportive and lively atmosphere at bench. I believe in I respect, we respect. My thanks go to all of my current and ex-labmates and seniors: ***Joseph****,* ***Sunil****,* ***Tina****,* ***Ambika****,* ***Anupriya****,* ***Abhishek****,* ***Anuj****,* ***Dr. Snehashish, Dr. Karthik****,* ***Dr. Rajendra****,* ***Dr. Govardhana****,* ***Dr. Sushil****,* ***Dr. Balasarvanan****,* ***Rashmi****,* ***Aftaab****,* ***Virender****,* ***Sonu****,* ***Kamesh****,* ***Gopinath****,* ***Hemant*** *and M.Sc interns for their support and valuable discussions.*

When it comes to supportive environment and enjoyment, how can I leave to sincerely thank HEC (Himalayan Explorer Club), IITR team for organizing treks and bringing me closer to mother nature. I would like to extend my list to non-teaching staff including the people at department, hostel, and security who made my stay at IITR more carefree.

How can I forget to mention my friends for providing unconditional support, motivation and accompanying me in the most pleasurable moments at IITR either it be academics or adventure since from the first day I joined IITR till now. I have received special love and affection from ***Surinder****,* ***Iram****,* ***Mandeep****,* ***Varun****,* ***Nishant****,* ***Kiran****,* ***Nitika****,* ***Kavita****,* ***Rajni****,* ***Anuj****,* ***Raj****,* ***Pushpendra****,* ***Sanjay****,* ***Rahul****,* ***Arvin****,* ***Mayank****,* ***Rahul****,* ***Deepa*** *and* ***Arun*** *as well wishers and constant supporters who lighten up my mood through their talks. I am glad to share that we shared a lot that made us laugh aloud together. I would like to thank all my friends and batchmates for tolerating, loving, pampering and understanding me whenever I feel blue or was in seventh heaven during my almost 5 years of Ph.D tenure.*

I would love to share the names of few more people with whom I have shared my ups and downs without any hesitation. I am glad that I have ***Manjul****,* ***Deepika*** *and* ***Kirti*** *to whom I open my heart out unhesitatingly. A token of thanks for my relatives for their patience, pray and blessings they had for me.*

Last but not the least; my genuine respect and admire to a couple I belong , my Father and Mother, ***Sheesh Ram Saini*** *and* ***Raj Dulari*** *for their unconditional love, support and trust they shower on me that keep me strong. My bundle of love and affection for my younger brother and partner in crime,* ***Vishal*** *will never come to an end. When it comes to help me technically, he is the one who stood by me. Special thanks to him for introducing the latest of electronic updates either it be updating my DELL laptop or a mobile phone. Since we consider Lord Ganesha as one of our family member, I am thankful to the foursome who has always shown believe on me, given me strength, encouraged me to be who I am and supported me in all aspects of life.*

Thanks to the God for such a wonderful stay at R-land… ***Ankita Saini***

Abstract

This thesis deals with synthesis and characterization of functional materials derived from 1,8-naphthalimide as potential candidates for electronic and biological applications. The thesis is divided into seven chapters. Chapter 1 presents a review on structure-property relationship highlighting photophysical, electrochemical, electroluminescent, photovoltaic, and biological properties of mono and bis-naphthalimide-based linear and star-shaped molecules. Among the *N*-functionalized and core functionalized dyes, later resulted in elongation of conjugation since the chromophore at imidic position is orthogonal to the conjugating length. Depending upon the behavior of chromophore flanked on naphthalimide, it exhibits either typical charge transfer or π-π* extended conjugation. Bis-naphthalimides are explored for its application particularly in OSCs. The variation in the central chromophore as planar or non-planar PAH or heteroaromatic core resulted in tremendous alternation of photophysical and electrochemical properties. Star-shaped dyes provide a platform to study the effect of chromophore density and molecular symmetry on the optical properties of the dyes. However, effect of strength and variable number of electron withdrawing groups on the properties of naphthalimide is not yet explored. The modulation of aromatic core with different number of electron deficient units is limited. Also, the report on studying the effect of non-conjugated chromophores on the intrinsic properties of naphthalimide unit is narrow. In Chapter 2, the aim, scope and prospect of the work on naphthalimide-based materials is presented.

Chapter 3 demonstrates the synthesis and characterization of bis-naphthalimides-based small molecules and oligomers that helped us to study the effect of different electron withdrawing acceptors and increasing number of benzotriazole unit on the properties. Linear and rigid bis-naphthalimide-based electron deficient dyes were synthesized by Pd-catalyzed Sonogashira cross coupling reaction. The dyes exhibit a red-shifted absorption band and enhanced molar extinction coefficient attributable to the increase in π-conjugation length and enhanced electronic interactions. The narrow structured emission band and small Stokes shifts is reflection of their rigid and planar structure. Solvent polarity has a negligible influence on the optical properties of the dyes. The molecules are prone for self-assembly leading to the formation of nanostructures for the as synthesized samples and those obtained from different solvents. These dyes lead to the formation of controlled morphologies of variable size and shape developed from *J*-aggregated solid state packing. The fluorescence images observed under optical fluorescence microscopy

exhibits multicolor emission under different light source. Electrochemical studies reveal that these dyes acquire LUMO levels in range of -3.2 to - 3.3 eV. The analysis of naphthalimide end-capped benzotriazole-based linear *n*-type small molecular semiconductors show that with increasing number of benzotriazole unit in the oligomer, LUMO is stabilized and HOMO is destabilized, thus leading to narrow band gap. The electronic features and coplanar arrangement of functional entities by density functional theoretical computations ensure close packing arrangement of molecules in the solid state. Furthermore, these dyes show high thermal stability.

Chapter 4 deals with synthesis of pyrene-naphthalimide hybrids by Sonogashira coupling reaction and presents the effects of substitution pattern on optical, electrochemical and thermal properties. The attachment of the naphthalimide moiety is varied at the 1-, 3-, 6-, and 8-positions of the pyrene ring to alter the intrinsic properties. The subtle modifications in the architecture of dyes involving the substituent positioning, molecular symmetries and chromophore density as predicted by theoretical computations greatly influence ground and excited state properties of the functionalized pyrene compounds. The optical properties of these dyes change monotonically from mono, di, tri to tetra substituted core. Among the two isomers 1,6-di-substituted and 1,8-di-substituted, former display more red shifted absorption profile attributed to the extended linear arrangement. The molar extinction coefficient increases from mono to tetra-substituted compound attributed to the increment in chromophore density. Whereas, compared to the parent pyrene molecule, the substituted cores induce a large bathochromic shift in the absorption profile owing to the extension of conjugation. The compounds are green to orange fluorescent and display dependence on solvent polarity confessing an intra molecular charge transfer in excited state. DFT simulation reveals the probability of charge transfer from pyrene donor to naphthalimide acceptor and thus the localization of HOMO/LUMO orbitals on the donor-acceptor moieties except for tetra-substituted dye implying the significant charge transfer occurring during electronic excitation.

Chapter 5 reports carbazole-naphthalimide-based linear donor-acceptor and star-shaped triazine-cored molecules. A series of ethyne-linked compounds were synthesized by a stepwise route involving a Pd/Cu catalyzed Sonogashira coupling reaction. Star-shaped dyes are synthesized in two step initiated by acid catalyzed trimerization of arylnitriles to form triazine core followed by coupling reaction. We highlight structure-property relationship by structural modification of carbazole and/ or naphthalimide. The star-shaped triazine compounds displayed superior optical, thermal and electrochemical properties when compared to linear analogs. These

compounds act as blue to green light-emitting materials. The excited state lifetimes of linear analogs are longer than star-shaped analogs. These fluorescent chromophores are supposed to be potential candidates to acquire a space into organic electronic devices such as OSCs and OLEDs.

Chapter 6 describes the effect of imidic structural variation of naphthalimide-based bipolar materials on photophysics, electrochemistry, morphology and its application in bioimaging. The photophysical and electrochemical studies reveal that these dyes are electronically similar although structurally different from each other. Whereas the structural variations helps to fine tune the morphology of the dyes at microscopic level. They reflect unique and uniform morphology depending on their molecular structure. They show considerably different morphology which is solvent and concentration dependent. Finally, potential biological applications of these dyes are evaluated by investigating their biocompatibilities and cell uptake behaviors.

Chapter 7 presents the conclusion and outlook of the work embodied in the thesis. We present correlation between structural modification and optical properties of the naphthalimide-based dyes. The influence of molecular tuning for determination of the properties and behavior of the naphthalimide functional materials is addressed.

Table of Contents

Candidate's Declaration i

Acknowledgments ii

Abstract iv

Table of Contents viii

List of Figures xii

List of Charts xviii

List of Tables xxii

List of Schemes xxiv

List of Abbreviations xxvi

List of Publications and Conferences xxx

Chapter 1 Electronic and Biological Applications of Naphthalimide Derivatives: A Review

1.1 Introduction 1

1.2 General method for the synthesis of 1,8-naphthalimide 3

1.3 Naphthalimide-based materials for structure property relationships 5

1.3.1 Imide-functionalized naphthalimide derivatives 5

1.3.2 Core-functionalized naphthalimide derivatives 9

1.3.3 Amine-substituted naphthalimide-based dyes 26

1.3.4 Vinyl-linked naphthalimide-based dyes 31

1.3.5 Ethynyl-linked naphthalimide-based dyes 34

1.3.6 Star-shaped naphthalimide-based dyes 39

1.4 Naphthalimide-based materials for electronics 44

1.4.1 Naphthalimide dyes as emitter or electron transporting material in OLEDs 44

1.4.2 Naphthalimide-based materials in OSCs 60

1.4.2.1 Naphthalimide-based directly linked chromophoric materials 60

1.4.2.2 Naphthalimide-based vinyl-linked chromophoric materials 69

1.4.2.3 Naphthalimide-based ethynyl-linked chromophoric materials 73

1.4.2.4 Star-shaped naphthalimide-based materials 76

1.4.3 Naphthalimide-based sensitizers in DSSCs 79

1.5 Naphthalimide-based materials as anticancer and bioimaging agents 81

1.5.1 Mono-naphthalimide-based derivatives 83

1.5.2 Bis-naphthalimide based derivatives 94

1.6. Conclusions and outlook 97

Chapter 2 Naphthalimide-Based Materials for Electronics and Biological Applications: Aim and Scope 98

Chapter 3 Bis-Naphthalimides Bridged by Electron Acceptors

3.1 Introduction 103

3.2 Results and Discussion 107

3.2.1 Synthesis and Characterization 107

3.2.2 Photophysical Properties 112

3.2.3 Self-assembly studies of small molecules 125

3.2.4 Excited State Decay Dynamics 130

3.2.5 Electrochemical Properties 135

3.2.6 Theoretical Studies 137

3.2.7 Morphological Properties 144

3.2.8 Dynamic Light Scattering Analysis 149

3.2.9 Fluorescence Microscopy Analysis 149

3.2.10 Powder X-ray Diffraction Analysis 150

3.2.11 Thermal Properties 151

3.3 Conclusions 153

3.4 Experimental Section 154

3.4.1 General Methods and Instrumentation 154

3.4.2 Sample preparation for THF: H_2O titration studies 155

3.4.3 Sample preparation for optical microscopy morphological studies 155

3.4.4 Synthesis 156

3.4.5 Computational Methods 161

Chapter 4 Pyrene-Naphthalimide Hybrids: Synthesis and Effects of Substitution Pattern on Optical, Electrochemical and Thermal Properties

4.1 Introduction 162

4.2 Results and Discussion 167

4.2.1 Synthesis and Characterization 167

4.2.2 Photophysical Properties 167

4.2.3 Time Resolved Fluorescence Studies 178

4.2.4 Electrochemical Properties 181

4.2.5 Theoretical Studies 182

4.2.6 Thermal Properties 185

4.3 Conclusions 185

4.4 Experimental Section 186

4.4.1 General Methods and Instrumentation 186

4.4.2 Synthesis 186

4.4.3 Computational Methods 188

Chapter 5 Carbazole-Naphthalimide-based Linear D-A and Star-shaped Triazine-cored molecules

5.1 Introduction 189

5.2 Results and Discussion 194

5.2.1 Synthesis and Characterization 194

5.2.2 Photophysical Properties 197

5.2.3 Time Resolved Fluorescence Studies 211

5.2.4 Electrochemical Properties 213

5.2.5 Thermal Properties 216

5.3 Conclusions 217

5.4 Experimental Section 218

5.4.1 General Methods and Instrumentation 218

5.4.2 Synthesis 218

Chapter 6 Effect of Non-conjugated Chromophores on Photophysics, Electrochemistry, Morphology and Bioimaging Applications of Naphthalimide Derivatives

6.1 Introduction 227

6.2 Results and Discussion 229

6.2.1 Synthesis and Characterization 229

6.2.2 Theoretical Studies 232

6.2.3 Photophysical Properties 235

6.2.4 Electrochemical Properties 242

6.2.5 Thermal Properties 243

6.2.6 Morphological Properties 243

6.2.7 Fluorescence Microscopy Analysis 248

6.2.8 Biological Studies 248

6.3 Conclusions 253

6.4 Experimental Section 254

6.4.1 General Methods and Instrumentation 254

6.4.2 Synthesis 254

6.4.3 Computational Methods 258

6.4.4 Microscopy Analyses 258

6.4.5 Fluorescence-based Bioimaging 259

6.4.6 Cell Culture 259

6.4.7 MTT Assay 259

Chapter 7 Conclusions and Outlook

7.1 Conclusions 260

7.2 Future Scope 263

References 265

Supplementary Information S1

List of Figures

Figure 1.1	Pictorial representation of advantages and applications of naphthalimide chromophore.	2
Figure 2.1	Treadmill of mono-imides as *n*-type aromatic core.	99
Figure 2.2	Core numbering and molecular engineering of naphthalimide unit.	99
Figure 2.3	Pictorial representation of aim and scope of naphthalimide-based materials for electronic and biological applications.	101
Figure 3.1	Structures of bis-naphthalimide end-capped dyes.	107
Figure 3.2	(a) Absorption and (b) emission spectra of dyes recorded in DCM.	112
Figure 3.3	Normalized absorption spectra of dyes as drop-casted thin films.	113
Figure 3.4	Emission spectra of the dyes as (a) drop-cast thin films and (b) solid powder.	114
Figure 3.5	Absorption spectra of dyes **3a-3d** recorded in different solutions.	115
Figure 3.6	Normalized emission spectra of dyes **3a-3d** recorded in different solutions.	116
Figure 3.7	(a) Absorption, (b) Normalized emission spectra of the dyes recorded in DCM.	118
Figure 3.8	Absorption and emission spectra of **2**, **5** and **8** recorded in DCM.	119
Figure 3.9	(a) Normalized absorption spectra, (b) Normalized emission spectra of dyes **6**, **8-12** recorded on drop casted thin films. (c) Normalized emission spectra of the solid powder.	121
Figure 3.10	Absorption spectra of dyes **6**, **8-12** recorded in different solutions.	122
Figure 3.11	Normalized emission spectra of dyes **6**, **8-12** recorded in different solvents.	123
Figure 3.12	(a, b) Absorption and emission spectra of **3a** with THF:H_2O titration studies respectively. (c) Normalized absorption and emission spectra of THF solution, thin film and solid state (d) Images of solution (above under normal light, below under UV light) obtained by varying water concentration in THF solvent for **3a** (left to right – increasing water concentration 0-90%).	126
Figure 3.13	(a, b) Absorption and emission spectra of **3b** with THF:H_2O titration studies respectively. (c) Normalized absorption and emission spectra of THF solution, thin film and solid state (d) Images of solution (above under normal light, below under UV light) obtained by varying water concentration in THF solvent for **3b** (left to right – increasing water concentration 0-90%).	127
Figure 3.14	(a, b) Absorption and emission spectra of **3c** with THF:H_2O titration studies, respectively (c) Normalized absorption and emission spectra in THF solution, thin film and solid state (d) Images of solution (above under normal light, below under UV light) obtained by varying water concentration in THF solvent for **3c** (left to right – increasing water concentration 0-90%).	128
Figure 3.15	(a, b) Absorption and emission spectra of **3d** with THF:H_2O titration studies respectively. (c) Normalized absorption and emission spectra of THF solution, thin film and solid state (d) Images of solution (above under normal light, below under UV light) obtained by varying water concentration in THF solvent for **3d** (left to right – increasing water	129

concentration 0-90%).
Figure 3.16 Plot of emission intensity *vs* water fraction in THF solvent for dyes. 130
Figure 3.17 Fluorescence decay profiles of dyes in (a) THF solution, (b) 90% water-THF mixture aggregates for $2x10^{-5}$M solution. 131
Figure 3.18 Fluorescence decay profiles of dyes in DCM ($2x10^{-6}$M). 134
Figure 3.19 (a) CV showing reduction region (b) DPV of the dyes, **3a-3d**. 135
Figure 3.20 (a) CV and (b) DPV of the dyes recorded in DCM. 136
Figure 3.21 Optimized geometries for dyes by DFT calculations using B3-LYP 6-31G(d, p) functionals. 138
Figure 3.22 Electronic distribution in the frontier molecular orbitals of the model compounds **3a-3d**. 140
Figure 3.23 Frontier molecular orbitals of the dyes **8** and **11**. 141
Figure 3.24 Frontier molecular orbitals and major vertical transition of the dyes. 142
Figure 3.25 FESEM images of as synthesized compounds (a-d) **3a-3d** respectively; scale bar: (a) (i) 10 μm, (ii) 1 μm; (b-c) (i) 2 μm, (ii) 1 μm and (iii) DLS-determined size distribution profiles for the aggregates formed from (a-d) **3a-3d** in THF/H_2O (1:9; 2×10^{-5} M), respectively. 143
Figure 3.26 FESEM images (a-d) of compounds **3a-3d** respectively showing formation of ill-defined aggregated cluster owing to poor control over concentration and aggregation, scale bar: 10, 10, 2, 4 μm respectively. 145
Figure 3.27 FESEM images of **3c** (a) long entangled fibres in 50% THF: H_2O; scale bar: (i) 5 μm, (ii) 2 μm; inset showing a long fibrous strand; scale bar 2 μm (b) formation of nanorods in 90% THF: H_2O; scale bar: (i) 5 μm, (ii) 2 μm; inset showing magnified image of nanorods at scale bar 1 μm (c) (i-iv) formation of crystalline 3-D rods, cubes at different scale bar 50, 10, 5, 1 μm respectively from 90% THF: H_2O after 1 week. 145
Figure 3.28 FESEM images of (a) **3d** from 1mM DMF showing spindle shaped nanofibers; scale bar (i) 10 μm, (ii) 2 μm, inset 1 μm (b) (i-iv) **3d** crystalline 3-D structures from 1 wt% DMF (c) **3a** from 1mM DMF; scale bar (i) 10 μm, (ii) 2 μm (d) Precipitates of **3a** from 1 wt% DMF as sheets and flowers; scale bar (i) 100 μm, inset 50 μm, (ii) 50 μm, inset 20 μm. 146
Figure 3.29 FESEM images of drop-casted samples from 1mM DCM solution (a) **3a** scale bar (i) 100 μm; inset 50 μm, (ii) 50 μm; inset 1 μm (b) **3b** showing sieves (i) 20 μm; inset 10 μm, (ii) 5 μm (c) **3c** scale bar (i) 5 μm, (ii) 2 μm; inset 1 μm, (d) **3d** showing sieves (i) 20 μm; inset 10μm, (ii) 5 μm. 147
Figure 3.30 FESEM images of dropcasted **3b** from 1mM DCM solution showing (a) mechanism for formation of sieves, scale bar 10 μm (b) self-rearrangement of nanofibres to form micropores, scale bar 5 μm (c) cross bedded pattern due to multilayer formation, scale bar 10 μm (d) ordered arrangement of nanofibers to form a micropore of diameter ~5 μm, scale bar 2 μm (e) scattered and broken vesicles due to less concentration at edges, scale bar 5 μm (f) collapsed and crowded vesicles due to more concentration at periphery, scale bar 20 μm. 148

Figure 3.31	Fluorescence microscopy images of the dyes (a-d) **3a-3d** respectively obtained from DCM solution (1mM), above row under excitation by blue light (450-490 nm), below row under green light (510-550 nm).	149
Figure 3.32	(a) PXRD and (b) correlation of d-spacing and 2θ of the small molecules.	150
Figure 3.33	(a) TGA and (b) DSC curves of the small molecules.	152
Figure 3.34	TGA curves of the dyes.	152
Figure 4.1	Structures of pyrene derivatives containing naphthalimides peripheries.	166
Figure 4.2	(a) Absorption and (b) emission spectra of the dyes recorded in DCM.	168
Figure 4.3	Normalized absorption spectra of the dyes **14a-14e** recorded in different solvents.	171
Figure 4.4	Normalized emission spectra of the dyes **14a-14e** recorded in different solvents.	172
Figure 4.5	(a) Absorption and (b) Emission spectra of **14a** in TOL-DCM mixture.	174
Figure 4.6	Lippert-Mataga plot for (a) **14a** and **14e** and (b) **14b-14d** dyes.	175
Figure 4.7	Concentration dependent normalized emission spectra of dye (a) **14d** and (b) **14e** recorded in TOL.	175
Figure 4.8	Normalized (a) absorption and (b) emission spectra of the dyes recorded on film prepared by drop cast method.	176
Figure 4.9	FESEM images of as synthesized compounds (i-v) **14a-14e,** respectively; scale bar: 1 μm.	177
Figure 4.10	PXRD spectra of the dyes.	177
Figure 4.11	Normalized solid state emission spectra of the dyes.	178
Figure 4.12	Fluorescence decay data for the dyes in (a) TOL and (b) DCM.	178
Figure 4.13	CV of the dyes (cathodic region) recorded in DCM.	182
Figure 4.14	(a) CV (anodic region) and (b) DPV recorded in DCM.	182
Figure 4.15	Optimized molecular geometries of the modeled dyes.	183
Figure 4.16	FMO of the dyes computed by using TDDFT at the B3LYP level.	184
Figure 4.17	TGA curves of the dyes.	185
Figure 5.1	Structures of target star-shaped dyes and control linear dyes.	193
Figure 5.2	Absorption spectra of the dyes recorded in DCM.	198
Figure 5.3	Normalized emission spectra of the dyes recorded in DCM.	199
Figure 5.4	Absorption spectra of the dyes **17a**, **17c** and **17d** recorded in different solvents.	203
Figure 5.5	Absorption spectra of the dyes **18a-18f** recorded in different solvents.	204
Figure 5.6	Absorption spectra of the dyes **20a-20d** recorded in different solvents.	205
Figure 5.7	Normalized emission spectra of the dyes **17a**, **17c** and **17d** recorded in different solvents.	206
Figure 5.8	Normalized emission spectra of the dyes **18a-18f** recorded in different solvents.	207
Figure 5.9	Normalized emission spectra of the dyes **20a-20d** recorded in different solvents.	208
Figure 5.10	Lippert-Mataga plot for (a) **17a**, **17c** and **17d**, (b) **18a**, **18b**, **18e** and **18f** and (c) **20a** and **20b** dyes.	209
Figure 5.11	Solid state emission spectra of the dyes	210

Figure 5.12	Fluorescence lifetime decay plots of the dyes.	211
Figure 5.13	(a, b) CV and (c) DPV of the dyes **17a**, **17c** and **17d**.	214
Figure 5.14	(a-d) CV and (e) DPV of the dyes **18a-18f**.	215
Figure 5.15	(a, b) CV and (c) DPV of the dyes **20a-20d**.	216
Figure 5.16	TGA curves of the linear and star-shaped dyes	217
Figure 6.1	Structures of the naphthalimide-based D-A small molecules.	229
Figure 6.2	Optimized geometries and interchromic dihedral angles for the compounds.	232
Figure 6.3	Electronic distributions in the frontier molecular orbitals of the dyes **22** and **24a** responsible for prominent absorptions.	233
Figure 6.4	Electronic distributions in the frontier molecular orbitals of the dyes.	234
Figure 6.5	(a) Absorption and (b) emission spectra of dyes recorded in DCM.	235
Figure 6.6	Absorption spectra of the dyes recorded in different solvents.	239
Figure 6.7	Normalized emission spectra of the dyes recorded in different solvents.	240
Figure 6.8	Lippert−Mataga and Stokes shift vs E_T (30) plot for the dyes.	241
Figure 6.9	(a) CV) and (b) DPV of the dyes recorded in DCM.	242
Figure 6.10	TGA curves of the dyes.	243
Figure 6.11	FESEM images of as synthesized dyes. Scale bar: **23a** (10 μm), **23b** (20 μm), **24a** (10 μm), **24b** (5 μm), **24c** (5 μm), **22** (2 μm), respectively.	244
Figure 6.12	FESEM images of dyes obtained from film casted from DMSO solution (2×10^{-3} M). Scale bar = (above row) **23a**, **24a** (100 μm), **23b**, **22** (10 μm); (below row) **23a**, **23b**, **24a** (2 μm), **22** (5 μm).	244
Figure 6.13	Morphology of dyes **24b** and **24c** (A, B) FESEM images obtained from film casted from DMSO solution (2×10^{-3} M). Scale bar = 100 μm, 20 μm respectively, (C) TEM image and (D) SAED image.	246
Figure 6.14	FESEM images of dye **24b** obtained for samples from DMSO solution at different concentrations (A) 2×10^{-3} M, (B) 2×10^{-4} M, (C) 2×10^{-5} M, (D) 2×10^{-6} M, Scale bar = 5 μm).	247
Figure 6.15	FESEM images of dye **24c** obtained for samples from DMSO solution at different concentrations (A) 2×10^{-3} M, (B) 2×10^{-4} M, (C) 2×10^{-5} M, (D) 2×10^{-6} M, Scale bar = 100 μm, 2 μm).	247
Figure 6.16	Fluorescence microscopy images of the dyes **23a, 23b, 24a** and **22**. Images captured under filter excitation (A) UV-2A, (B) B-2A, (C) G-2A. Scale = 100 μm.	248
Figure 6.17	Fluorescence microscopy images of the dyes **24b** and **24c**. Images captured under filter excitation (A) UV-2A, (B) B-2A, (C) G-2A. Scale = 100 μm.	249
Figure 6.18	Microscopy images of A549 cells incubated with 30 μM of dyes **23a**, **23b** and **22** for 12 h. Images captured under (A) bright field, (B) DAPI filter, (C) merge image of A and B, (D) GFP filter, (E) merge image of A and D, (F) merge image of B and D. Scale bar = 100 μm.	251
Figure 6.19	Microscopy images of A549 cells incubated with 30 μM of dyes **24a-24c** for 12 h. Images captured under (A) bright field, (B) GFP filter, (C) merge image of A and B. Scale bar = 100 μm.	252
Figure 6.20	Cell viability of dyes with human lung carcinoma A549 cells incubated with 0 to 50 μM concentrations of dyes for 12 h. The data are presented as mean±SEM values of two individual experiments.	253

Figure 7.1	Pictorial representation of summary of the work accomplished.	261
Figure S1	^{1}H NMR spectrum of **5** recorded in $CDCl_3$.	S1
Figure S2	^{13}C NMR spectrum of **5** recorded in $CDCl_3$.	S1
Figure S3	^{1}H NMR spectrum of **6** recorded in $CDCl_3$.	S2
Figure S4	^{13}C NMR spectrum of **6** recorded in $CDCl_3$.	S2
Figure S5	^{1}H NMR spectrum of **7** recorded in $CDCl_3$.	S3
Figure S6	^{13}C NMR spectrum of **7** recorded in $CDCl_3$.	S3
Figure S7	^{1}H NMR spectrum of **8** recorded in $CDCl_3$.	S4
Figure S8	^{13}C NMR spectrum of **8** recorded in $CDCl_3$.	S4
Figure S9	^{1}H NMR spectrum of **9** recorded in $CDCl_3$.	S5
Figure S10	^{13}C NMR spectrum of **9** recorded in $CDCl_3$.	S5
Figure S11	^{1}H NMR spectrum of **10** recorded in $CDCl_3$.	S6
Figure S12	^{13}C NMR spectrum of **10** recorded in $CDCl_3$.	S6
Figure S13	^{1}H NMR spectrum of **11** recorded in $CDCl_3$.	S7
Figure S14	^{13}C NMR spectrum of **11** recorded in $CDCl_3$.	S7
Figure S15	^{1}H NMR spectrum of **12** recorded in $CDCl_3$.	S8
Figure S16	^{13}C NMR spectrum of **12** recorded in $CDCl_3$.	S8
Figure S17	^{1}H NMR spectrum of **14a** recorded in $CDCl_3$.	S9
Figure S18	^{13}C NMR spectrum of **14a** recorded in $CDCl_3$.	S9
Figure S19	^{1}H NMR spectrum of **14b** recorded in $CDCl_3$.	S10
Figure S20	^{13}C NMR spectrum of **14b** recorded in $CDCl_3$.	S10
Figure S21	^{1}H NMR spectrum of **14c** recorded in $CDCl_3$.	S11
Figure S22	^{13}C NMR spectrum of **14c** recorded in $CDCl_3$.	S11
Figure S23	^{1}H NMR spectrum of **14d** recorded in $CDCl_3$.	S12
Figure S24	^{13}C NMR spectrum of **14d** recorded in $CDCl_3$.	S12
Figure S25	^{1}H NMR spectrum of **14e** recorded in $CDCl_3$.	S13
Figure S26	^{13}C NMR spectrum of **14e** recorded in $CDCl_3$.	S13
Figure S27	^{1}H NMR spectrum of **17a** recorded in $CDCl_3$.	S14
Figure S28	^{13}C NMR spectrum of **17a** recorded in $CDCl_3$.	S14
Figure S29	^{1}H NMR spectrum of **17b** recorded in $CDCl_3$.	S15
Figure S30	^{13}C NMR spectrum of **17b** recorded in $CDCl_3$.	S15
Figure S31	^{1}H NMR spectrum of **17c** recorded in $CDCl_3$.	S16
Figure S32	^{13}C NMR spectrum of **17c** recorded in $CDCl_3$.	S16
Figure S33	^{1}H NMR spectrum of **17bd** recorded in $CDCl_3$.	S17
Figure S34	^{13}C NMR spectrum of **17bd** recorded in $CDCl_3$.	S17
Figure S35	^{1}H NMR spectrum of **17d** recorded in $CDCl_3$.	S18
Figure S36	^{13}C NMR spectrum of **17d** recorded in $CDCl_3$.	S18
Figure S37	^{1}H NMR spectrum of **18a** recorded in $CDCl_3$.	S19
Figure S38	^{13}C NMR spectrum of **18a** recorded in $CDCl_3$.	S19
Figure S39	^{1}H NMR spectrum of **18b** recorded in $CDCl_3$.	S20
Figure S40	^{13}C NMR spectrum of **18b** recorded in $CDCl_3$.	S20
Figure S41	^{1}H NMR spectrum of **18c** recorded in $CDCl_3$.	S21
Figure S42	^{13}C NMR spectrum of **18c** recorded in $CDCl_3$.	S21
Figure S43	^{1}H NMR spectrum of **18d** recorded in $CDCl_3$.	S22

Figure S44 ^{13}C NMR spectrum of **18d** recorded in $CDCl_3$. S22
Figure S45 ^{1}H NMR spectrum of **18e** recorded in $CDCl_3$. S23
Figure S46 ^{13}C NMR spectrum of **18e** recorded in $CDCl_3$. S23
Figure S47 ^{1}H NMR spectrum of **18f** recorded in $CDCl_3$. S24
Figure S48 ^{13}C NMR spectrum of **18f** recorded in $CDCl_3$. S24
Figure S49 ^{1}H NMR spectrum of **20a** recorded in $CDCl_3$. S25
Figure S50 ^{13}C NMR spectrum of **20a** recorded in $CDCl_3$. S25
Figure S51 ^{1}H NMR spectrum of **20aBr$_2$** recorded in $CDCl_3$. S26
Figure S52 ^{1}H NMR spectrum of **20aBr** recorded in $CDCl_3$. S26
Figure S53 ^{1}H NMR spectrum of **20b** recorded in $CDCl_3$ S27
Figure S54 ^{1}H NMR spectrum of **20bBr$_2$** recorded in $CDCl_3$ S27
Figure S55 ^{13}C NMR spectrum of **20bBr$_2$** recorded in $CDCl_3$ S28
Figure S56 ^{1}H NMR spectrum of **20bBr** recorded in $CDCl_3$ S28
Figure S57 ^{1}H NMR spectrum of **20bBr** recorded in $CDCl_3$ S29
Figure S58 ^{1}H NMR spectrum of **20c** recorded in $CDCl_3$ S29
Figure S59 ^{13}C NMR spectrum of **20c** recorded in $CDCl_3$ S30
Figure S60 ^{1}H NMR spectrum of **20d** recorded in $CDCl_3$ S30
Figure S61 ^{1}H NMR spectrum of **20dBr** recorded in $CDCl_3$ S31
Figure S62 ^{13}C NMR spectrum of **20dBr** recorded in $CDCl_3$ S31

List of Charts

Chart 1.1	Retro-synthesis for 1,8-naphthalimide	3
Chart 1.2	A schematic diagram for the synthesis of 1,8-naphthalimide using acenaphthene or naphthalic anhydride as starting materials	3
Chart 1.3	Structures of naphthalimide derivatives with imide functionalization (**S1-S3**)	5
Chart 1.4	Structures of bipolar naphthalimide derivatives (**S4a-S4d**)	6
Chart 1.5	Structures of bipolar naphthalimide derivatives (**S5a-S5c**)	6
Chart 1.6	Structures of naphthalimide-based dyes with different imidic substituents	7
Chart 1.7	Structures of naphthalimide-based AIEgens (**S8a-S8e** and **S9**)	8
Chart 1.8	Structure of bis-naphthalimide-based A-D-A type dye for memory storage (**S10**)	9
Chart 1.9	Structures of *N*-butyl-1,8-naphthalimide derivatives (**S11-S19**)	9
Chart 1.10	Structures of 4-aryl substituted naphthalimide derivatives (**S20a-S20j**)	10
Chart 1.11	Structures of 4-substituted naphthalimide dyads (**S21-S22**)	11
Chart 1.12	Structures of 4-polyaryl substituted naphthalimide derivatives (**S23-S25**)	12
Chart 1.13	Structures of 4-substituted pyridine-functionalized naphthalimide derivatives (**S26a-S26e**)	13
Chart 1.14	Structures of 4-aryloxy substituted naphthalimide derivatives (**S27-S28**)	13
Chart 1.15	Structures of 4-substituted naphthalimide derivatives (**S29-S31**)	14
Chart 1.16	Structures of 4-substituted mono- and bis-naphthalimide derivatives (**S32-S33**)	15
Chart 1.17	Structures of mono- and bis-naphthalimide-fluorene hybrids (**S34-S35**)	16
Chart 1.18	Structures of D-A triphenylamine and naphthalimide-based dyes (**S36-S39**)	17
Chart 1.19	Structures of D-A carbazole and naphthalimide based dyes (**S40-S48**)	18
Chart 1.20	Structures of thienylnaphthalimide dyes (**S49a-S49c**)	19
Chart 1.21	Structures of D-π-A triphenylamine and naphthalimide-based dyes (**S50-S59**)	20
Chart 1.22	Structures of D-π-A triphenylamine and naphthalimide-based dyes (**S60-S61**)	21
Chart 1.23	Structures of carbazole and naphthalimide-based dyes (**S62-S64**)	22
Chart 1.24	Structure of symmetric A-D-A-type bis-naphthalimide carbazole dye (**S65**)	22
Chart 1.25	Structure of D-π-A naphthalimide-based AIEgens (**S66-S69**)	23
Chart 1.26	Structure of bis-naphthalimide derivatives (**S70-S76**)	24
Chart 1.27	Structures of bis-naphthalimide derivatives with different linkers as as A_1-π-A_2-π-A_1 architecture (**S77-S81**)	25
Chart 1.28	Structures of 4-amino substituted naphthalimide derivatives (**S82-S88**)	27
Chart 1.29	Structures of aryl hydrazones of 4-hydrazino-*N*-hexyl-1,8-naphthalimide derivatives (**S89-S90**)	28
Chart 1.30	Structures of hydrazine dyads and triads comprised of naphthalimide and	28

triphenylamine. (**S91-S94**)
Chart 1.31 Structures of naphthalimide-based Schiff base derivatives (**S95-S96**) 29
Chart 1.32 Structures of naphthalimide triads and reference derivatives (**S97-S100**) 30
Chart 1.33 Structures of pyrazoline-naphthalimide hybrids (**S101-S104**) 31
Chart 1.34 Structures of E-Z isomeric 4-styryl-1,8-naphthalimide derivatives (**S105-S107**) 31
Chart 1.35 Structures of D-A conjugated 4-styryl-naphthalimide derivatives (**S108-S109**) 32
Chart 1.36 Structures of D-A triphenylamine and naphthalimide-based dyes (**S110-S114**) 33
Chart 1.37 Structures of monoalkoxynaphthalene–naphthalimide D-A dyes (**S115-S118**) 34
Chart 1.38 Structures of bis-naphthalimide dyes (**S119-S121**) 34
Chart 1.39 Structures of bis-naphthalimide dyes (**S122-S124**) 35
Chart 1.40 Structures of carbazole-naphthalimide hybrids (**S125-S129**) 37
Chart 1.41 Structures of bis-naphthalimide dyes (**S130-S135**) 38
Chart 1.42 Structures of pyrene-naphthalimide-based dyes (**S136-S137**) 39
Chart 1.43 Structures of star-shaped D–π–A type small molecules (**S138-S141**) 40
Chart 1.44 Structures of star-shaped benzene cored naphthalimide derivatives (**S142-S147**) 40
Chart 1.45 Structures of bipolar star-shaped naphthalimide derivatives (**S148-S150**) 41
Chart 1.46 Structures of D–π–A star-shaped triphenylamine and naphthalimide-based derivatives (**S151-S154**) 41
Chart 1.47 Structures of star-shaped donor-acceptor conjugated molecules (**S155-S156**) 43
Chart 1.48 Structures of naphthalimide-based dopants and electron transporting materials in PhOLEDs (**E1-E4**) 45
Chart 1.49 Structures of naphthalimide-based dyes for FOLEDs (**E5-E7**) 45
Chart 1.50 Structures of naphthalimide-based emitters for OLEDs (**E8-E10**) 46
Chart 1.51 Structures of naphthalimide derivatives as emitter materials (**E11-E19**) 48
Chart 1.52 Structures of naphthalimide derivatives with different Schiff bases (**E20-E26**) 49
Chart 1.53 Structures of naphthalimide D-π-A derivatives (**E27-E30**) 50
Chart 1.54 Structures of naphthalimide-based dyes (**E31-E32**) 51
Chart 1.55 Structures of naphthalimide-based dyes as emitting layer in OLEDs 53
Chart 1.56 Structures of linear and star-shaped triphenylamino naphthalimides (**E35-E37**) 53
Chart 1.57 Structures of naphthalimide-based non-fullerene acceptors (**E38-E42**) 61
Chart 1.58 Structures of bis-naphthalimide-based non-fullerene acceptors (**E43-E46**) 62
Chart 1.59 Structures of A-A-A type naphthalimide-based non-fullerene acceptors (**E47-E48**) 63

Chart 1.60	Structures of naphthalimide flanked dyes (**E49-E51**)	64
Chart 1.61	Structures of naphthalimide-based non-fullerene acceptors (**E52-E53**)	65
Chart 1.62	Structures of naphthalimide-based non-fullerene acceptors (**E54-E56**)	66
Chart 1.63	Structures of vinyl-linked bis-naphthalimides as non-fullerene acceptors (**E57-E61**)	69
Chart 1.64	Structures of linear D-A based mono-naphthalimide dyes (**E62-E65**)	73
Chart 1.65	Structures of naphthalimide-based non-fullerene acceptors (**E66-E69**)	74
Chart 1.66	Structures of linear bis-naphthalimide-based non-fullerene acceptors (**E70-E71)**	75
Chart 1.67	Structures of star-shaped naphthalimide triphenylamine derivatives **(E72-E75)**	76
Chart 1.68	Structures of naphthalimide-based sensitizers (**E76-E79**) for DSSCs	80
Chart 1.69	Structures of 3-substituted naphthalimide-based anticancer agents (**B1-B6**)	81
Chart 1.70	3, 6 disubstituted naphthalimide-based anticancer agents (**B7-B12**)	82
Chart 1.71	Structure of first reported bis-naphthalimide **B13** (Elinafide)	83
Chart 1.72	Structures of 3-substituted aryl-naphthalimides (**B14-B20**) as antitumor agents	83
Chart 1.73	Structures of 3-substituted amino naphthalimides (**B21-B24**) as anticancer agents	84
Chart 1.74	Structures of mononaphthalimides **B25a-B25i** with different imidic groups	85
Chart 1.75	Structures of naphthalimide-based anticancer and cell imaging agents (**B26-B27**)	85
Chart 1.76	Structures of naphthalimide-based dyes (**B28-B32**) for cell imaging	86
Chart 1.77	Structures of 4-substituted aminonaphthalimides (**B33-B44**) as antitumor agents	87
Chart 1.78	Structures of 4-substituted amino naphthalimides (**B45-B50**) as anticancer agents	88
Chart 1.79	Structures of naphthalimide derivatives (**B51** and **B52**) possessing leucine side chain as anticancer agents	89
Chart 1.80	Structures of sulfur-substituted naphthalimides (**B53-B59**) as antitumor agents	90
Chart 1.81	Structures of 4-phenyltriazol-naphthalimide derivatives (**B60a-B60e**) as anti-cancer agent	91
Chart 1.82	Structures of C4-benzazole naphthalimide derivatives (**B61-B66**)	91
Chart 1.83	Structures of maleimide-coupled naphthalimide derivatives (**B67–B68**) as cell imaging agent	92
Chart 1.84	Structures of D-π-A naphthalimide-based TICT AIEgens (**B69–B70**) for cell imaging	92
Chart 1.85	Structures of D–π–A naphthalimide derivatives (**B71-B74**) for cell imaging	93
Chart 1.86	Structures of bis-naphthalimide derivatives as anticancer agents (**B75-B80**)	94
Chart 1.87	Structures of bis-naphthalimides **B81** with different imidic groups as	96

anticancer agents.
Chart 1.88 Structures of 3-nitrobisnaphthalimide derivatives (**B82** and **B83**) 96
Chart 3.1 Structures of alkynyl-linked related linear dyes. 105
Chart 4.1 Structures of documented chromophore-substituted pyrene-based organic materials. 186
Chart 4.2 Structures of known pyrene-based rigid organic materials. 187
Chart 5.1 Structures of the related dyes. 190
Chart 6.1 Structures of related naphthalimide-based D-A dyes. 228
Chart 7.1 The proposed naphthalimide-based linear and star-burst functional materials. 263

List of Tables

Table 1.1	Electroluminescent properties of naphthalimide-based materials for PhOLEDs.	55
Table 1.2	Electroluminescent properties of naphthalimide-based materials for FOLEDs.	57
Table 1.3	Optical and photovoltaic properties of dyes (**E38-E56)**.	67
Table 1.4	Optical and photovoltaic properties of dyes (**E57-E61**).	72
Table 1.5	Optical and photovoltaic parameters of dyes (**E62-E75)**.	78
Table 1.6	Optical and photovoltaic parameters of dyes (**E76-E79)**.	80
Table 1.7	In vitro cytotoxicity of dyes **B1-B6** against various cancer cell lines.	81
Table 1.8	In vitro cytotoxicity of dyes **B9-B12** against various colon and lung cancer cell lines.	82
Table 1.9	Cytotoxicity of naphthalimide derivatives **B14-B20** against various cell lines.	83
Table 1.10	Cytotoxicity of dyes **B21-B24** derivatives against various cell lines.	84
Table 1.11	Growth inhibition of dyes **B25g-B25i** against various cancer cell lines.	85
Table 1.12	Cytotoxicity of dyes **B26-27** against HDAC isoforms cell lines.	86
Table 1.13	Cytotoxicity of dyes **B33-B44** derivatives against various cell lines.	87
Table 1.14	Cytotoxicity of dyes **B45-B50** derivatives against lung and breast cancer cell lines.	88
Table 1.15	Cytotoxicity of dyes **B51** and **B52** derivatives against various cell lines.	89
Table 1.16	Cytotoxicity of dyes **B53-B59** derivatives against various cell lines.	90
Table 1.17	Cytotoxicity of dyes **B60a-B60e** derivatives against various tumor cell lines.	91
Table 1.18	In vitro cytotoxicity of polyamine derivatives **B76-B80** against breast cancer cell lines.	95
Table 1.19	In vitro cytotoxicity of dyes **B81a-B81f** against various cancer cell lines.	95
Table 3.1	Optical and electrochemical data of the dyes **3a-3d** recorded in DCM.	109
Table 3.2	Absorption and emission data of the dyes **3a-3d** recorded in different solutions, thin film and solid state.	111
Table 3.3	Optical and electrochemical data of the oligomers, **8-12** recorded in DCM	117
Table 3.4	Absorption data for dyes **6**, **8-12** recorded in different solvents.	124
Table 3.5	Emission data for dyes **6**, **8-12** recorded in different solvents.	125
Table 3.6	Stokes shift data for dyes **6**, **8-12** recorded in different solvents.	125
Table 3.7	Time-resolved fluorescence and photophysical data for the dyes in THF and 90% water-THF mixtures.	132
Table 3.8	Time-resolved fluorescence spectroscopy data of dyes in THF and 90% water -THF mixtures.	132
Table 3.9	Time-resolved fluorescence and photophysical data for the dyes in DCM	134

(2×10^{-6}).

Table 3.10 Time-resolved fluorescence spectroscopy data for the dyes in DCM. 134

Table 3.11 Computed electronic parameters for the compounds by the TDDFT (M06-2x/6-31G(d,p)) method. 139

Table 3.12 Data of DLS-determined size distribution by intensity for the aggregates formed from dyes in THF: H_2O (90%, 2×10^{-5} M). 149

Table 3.13 Calculated interplanar distances, d (Å) using Braggs equation ($n\lambda=2dSin\theta$) from the peaks obtained in powder X-ray diffraction of the small molecules. 151

Table 3.14 Thermal analysis data of the naphthalimide-based small molecules. 151

Table 4.1 Optical data of the dyes **14a-14e**. 169

Table 4.2 Absorption spectral data of dyes **14a-14e** in different solvents. 173

Table 4.3 Emission spectral data for **14a-14e** dyes in different solvents. 173

Table 4.4 Time-resolved fluorescence and photophysical data for the dyes in TOL and DCM (2×10^{-6}). 180

Table 4.5 Time-resolved fluorescence spectroscopy data for the dyes in TOL and DCM, respectively 180

Table 4.6 Electrochemical and Thermal data of the dyes. 181

Table 4.7 Computed electronic parameters for the dyes using M06-2x/6-31G(d,p)) method. 183

Table 5.1 Optical, electrochemical and thermal data of linear control dyes. 200

Table 5.2 Optical, electrochemical and thermal data of star-shaped target dyes. 201

Table 5.3 Photophysical data of the linear dyes. 201

Table 5.4 Photophysical data of the star-shaped dyes. 202

Table 5.5 Stokes shift of the dyes. 202

Table 5.6 Time-resolved fluorescence and photophysical data for the dyes in DCM 212

Table 5.7 Time-resolved fluorescence spectroscopy data for the dyes in DCM 212

Table 6.1 Computed electronic parameters of the dyes in DCM. 234

Table 6.2 Optical, electrochemical and thermal data of the dyes. 237

Table 6.3 Absorption data for dyes recorded in different solvents. 238

Table 6.4 Emission and Stokes shift data for dyes recorded in different solvents. 238

Table 6.5 Cell viability, cytotoxicity and cell proliferation effect of dyes of human lung carcinoma A549 cells estimated from the MTT assay. 253

List of Schemes

Scheme 3.1	Synthesis of the small molecules.	109
Scheme 3.2	Synthetic scheme of the oligomers.	110
Scheme 4.1	Synthetic route to the compounds **14a-14e**.	167
Scheme 5.1	Synthetic protocol for carbazole and naphthalimide-based linear D-A dyes.	195
Scheme 5.2	Synthetic protocol for carbazole and/or naphthalimide-based linear D-A cyano analogs.	195
Scheme 5.3	Synthetic protocol for carbazole or naphthalimide-based star-shaped triazine-cored target dyes.	196
Scheme 6.1	Synthesis of the dyes.	231

List of Abbreviations

1	OSC	Organic Solar Cell
2	OLED	Organic Light-Emitting Diodes
3	OTFT	Organic Thin Film Transistor
4	BHJSC	Bulk Heterojunction Solar Cell
5	DSSC	Dye Sensitized Solar Cell
6	HOMO	Highest Occupied Molecular Orbital
7	LUMO	Lowest Unoccupied Molecular Orbital
8	NHE	Normal Hydrogen Electrode
9	FMO	Frontier Molecular Orbital
10	FOLED	Fluorescence Organic Light-Emitting Diode
11	PHOLED	Phosphorescence Organic Light-Emitting Diode
12	EL	Electroluminescence
13	D-A	Donor-Acceptor
14	OPV	Organic Photovoltaic Voltage
15	TADF	Thermally Activated Delayed Fluorescence
16	TFDF	Triplet Fusion Delayed Fluorescence
17	TTA	Triplet-Triplet Annihilation
18	EQE	External Quantum Efficiency
19	PCE	Power Conversion Efficiency
20	L	Luminance
21	V_{on}	Turn-On Voltage
22	CE	Current Efficiency
23	DIO	Di-iodo octane
24	J_{SC}	Short Circuit Current
25	V_{OC}	Open Circuit Voltage
26	*ff*	Fill Factor
27	η	Efficiency
28	PAH	Polycyclic Aromatic Hydrocarbon
29	IP	Ionization Potential
30	EA	Electron Affinity
31	TOL	Toluene
32	DCM	Dichloromethane
33	DMSO	Dimethylsulphoxide
34	ACN	Acetonitrile
35	THF	Tetrahydrofuran
36	DMF	*N*,*N*-dimethylformamide
37	MeOH	Methanol
38	TFA	Trifluoroacetic acid
39	TEA	Triethylamine
40	EtOH	Ethanol

41	TCE	Trichloroethylene
42	DCB	1,3-Dichlorobenzene
43	SAED	Selected Area Electron Diffraction
44	HRMS	High Resolution Mass Spectroscopy
45	ICT	Intramolecular Charge Transfer
46	Φ_F	Fluorescence Quantum Yield
47	TGA	Thermogravimetric Analysis
48	CV	Cyclic Voltammetry
49	DPV	Differential Pulse Voltammetry
50	HTL	Hole Transporting Layer
51	ETL	Electron Transporting Layer
52	DFT	Density Functional Theory
53	TDDFT	Time-Dependent Density Functional Theory
54	WORM	Write Once Read Memory
55	SRAM	Static Random-Access Memory
56	ISC	Inter System Crossing
57	AIE	Aggregation Induced Emission
58	ACQ	Aggregation Caused Quenching
59	TICT	Twisted Intramolecular Charge Transfer
60	PCT	Photoinduced Charge Transfer
61	PET	Photoinduced Electron Transfer
62	FESEM	Field Emission Scanning Electron Microscopy
63	FWHM	Full Width Half Maximum
64	DLS	Dynamic light scattering
65	NMR	Nuclear Magnetic Resonance
66	FTIR	Frontier Transform Infra-Red
67	LE	Localized Emission
68	DNA	Deoxyribo-Nucleic Acid
69	IC_{50}	Inhibitory Concentration
70	SAR	Structure Activity Relationship
71	*o*-DCB	*o*-dichlorobenzene
72	F_c/F_c^+	Ferrocene/ferrocenoium
73	TGA	Thermal Gravimetric Analysis
74	DSC	Differential Scanning Calorimetry
75	ITO	Indium Tin Oxide
76	NIR	Near-Infra Red
77	Alq_3	Tris(8-hydroxyquinoline)aluminum
78	NPB	1,4-Bis[(1-naphthyl-phenyl)amino]biphenyl
79	$Ir(ppy)_3$	*fac*-Tris(2-phenylpyridine)iridium
80	TCTA	4,4',4″-Tris(*N*-carbazolyl)triphenylamine
81	PEDOT: PSS	Poly(3,4-ethylene-dioxythiophene) poly(styrenesulfonate)

82	CBP	4,4′-Bis(9*H*-carbazol-9-yl)biphenyl
83	mCP	1,3-Di(9*H*-carbazol-9-yl)benzene
84	CIE	Commission International de I'Eclairage
85	CB	Chlorobenzene
86	CN	Chloronaphthalene
87	CF	Fluorocarbon
88	MT	3-methylthiophene
89	NMP	*N*-methyl pyrrolidone
90	DPE	Diphenyl ether
91	TPBi	1,3,5-tris(1-phenyl-1*H*-benzo[*d*]imidazol-2-yl)benzene
92	$Ir(ppy)_2(acac)$	Iridium(III) bis(2-phenylpyridinato-*N*,$C^{2'}$)acetylacetonate
93	FIrpic	Iridium(III) bis[2-(4',6'-difluorophenyl)-pyridinato-*N*,C(2')]-picolinate
94	$(Bt)_2Ir(acac)$	Bis(2-phenyl benzothiozolato-N, $C^{2'}$) iridium (acetylacetonate)
95	Bphen	4,7-Diphenyl-1,10-phenanthroline
96	F4TCNQ	2,3,5,6-Tetrafluoro-7,7,8,8-tetracyanoquinodimethane
97	CuPc	Copper phthalocyanine
98	P3HT	Poly-3-hexylthiophene
99	PCBM	Phenyl-butyric acid methyl ester
100	PPDTBT	(2,5-bis(2-hexyldecyloxy)phenylene)-*alt*-(4,7-di(thiophen-2-yl)-benzo[*c]*[1,2,5]thiadiazole)
101	PTB7-Th	Poly-benzodithiophene–thienothiophene
102	$p\text{-}DTS(FBTTh_2)_2$	7,7′-[4,4-Bis(2-ethylhexyl)-4*H*-silolo[3,2-*b*:4,5-*b*′]dithiophene-2,6-diyl]bis[6-fluoro-4-(5′-hexyl-[2,2′-bithiophen]-5-yl)benzo[*c*][1,2,5]thiadiazole]
103	PPDTFBT	poly[(2,5-bis(2-hexyldecyloxy)phenylene)-*alt*-(5-fluoro-4,7-di(thiophen-2-yl)benzo- [*c*][1,2,5]thiadiazole)]
104	PPDT2FBT	poly[(2,5-bis(2-hexyldecyloxy)phenylene)-*alt*-(5,6-difluoro-4,7-di(thiophen-2-yl)benzo[*c*]-[1,2,5]thiadiazole)]

List of Publications and Conferences

[1] **Saini**, **A**.; Thomas, K. R. J.; Sachdev, A.; Gopinath, P. Photophysics, electrochemistry, morphology and bioimaging applications of new 1,8-naphthalimide derivatives containing different chromophores. *Chem.- Asian J.* **2017**, *12*, 2612–2622.

[2] **Saini**, **A**.; Thomas, K. R. J. Bis-naphthalimides bridged by electron acceptors: Optical and self-assembly characteristics. *RSC Adv.* **2016**, *6*, 71638-71651.

[3] **Saini**, **A**.; Thomas, K. R. J.; Li, C. T.; Ho, K. C. Organic dyes containing fluorenylidene functionalized phenothiazine donors as sensitizers for dye sensitized solar cells. *J. Mater. Sci.: Mater. Electron*. **2016**, *27*, 12392-12404.

[4] **Saini**, **A**.; Thomas, K. R. J.; Huang, Y-J.; Ho, K-C. Effect of π-linker in naphthalimide-based dyes on optical, electrochemical and photovoltaic properties for dye sensitized solar cells. Submitted.

[5] **Saini, A**.; Thomas, K. R. J. Pyrene-naphthalimide hybrids: Synthesis and effects of substitution pattern on optical, electrochemical and thermal properties. To be submitted.

[6] **Saini, A**.; Thomas, K. R. J. Synthesis and analysis of naphthalimide end-capped benzotriazole based *n*- type small molecular semiconductors: Insight into the structure property relationship. To be submitted.

[7] **Saini, A**.; Thomas, K. R. J. Varshney, R; Roy, P. Synthesis, structure property relationship, anticancer activities and cell-imaging of 4-substituted 1,2,3-triazole naphthalimide hybrids. To be submitted.

[8] Poster Presentation at **CFOS** conference held at IITR, Roorkee, Uttarakhand, India on 22nd to 24th Dec, 2017.

[9] Poster Presentation at **20th CRSI-RSC** conference held at Guwahati University, Assam, India on 2nd to 5th Feb, 2017.

[10] The Best Poster Presentation award at the **International Photovoltaic Solar Energy Conference (Solar Asia - 2015)** held at Savitribai Phule Pune University, Pune, India on 30th July to 1st Aug, 2015.

Chapter 1 Electronic and Biological Applications of Naphthalimide Derivatives: A Review

1.1 Introduction

Over the decades, material chemistry has emerged as an immense field of research in science. Innumerable polymers, oligomers, dendrimers and small molecules are documented in the field of material chemistry.[1-5] Tremendous efforts have been devoted to the development of highly efficient dyes through extending the π-conjugated systems and improving the charge mobility in field of optoelectronics.[6,7] To date, pure metal-free organic molecules alternative to metal-complex counterparts have drawn increasing attention due to their low cost without noble metal, easy molecular tailoring and tunable spectral properties.[8,9] Moreover, the small molecules which can be easily solution processed are emerging as a competitive alterative to their polymer counterparts due to several important advantages of small molecules, such as well-defined structures, good solubility, easy purification and facile energy level tuning.[10,11] Several new materials with variable architectures comprising of electron rich (donor) and/or electron deficient (acceptor) molecules have led to the origin of a variety of semiconductors possessing unique physicochemical properties. Tremendous efforts have been devoted to the synthesis of highly efficient dyes through extending conjugation with different linkers to study the structure property relationships and to improve the charge carrier mobilities. To date, several comprehensive reviews and research have covered the design and synthesis of small molecules including *p*-type semiconductors with hole-transporting properties for vacuum or solution processed electronic devices.[12-37] However, studies on electron-deficient materials possessing good electron-transporting properties are inadequate. In comparison, *n*-type conjugated chromophores with low-lying energy levels and high electron affinity are scarce, irrespective of their applications as electron acceptor materials in OSCs,[38-42] electron transport materials in OLEDs[43-44] or *n*-type materials in OTFTs.[45-46] Despite this, practical devices based on organic semiconductors possessing air-stable electron-transporting properties are limited due to the lack of ambient stability of charge carriers. Till date, numerous electron acceptors are reported based on benzothiadiazole,[47-48] fluorenone,[49-51] diketopyrrolo[3,4-*c*]-pyrrole-1,4-dione,[52-54] quinoxaline,[55-56] benzotriazole[57-58]and imides derivatives[59-63].

Among various organic optoelectronic materials, aromatic imides have emerged as versatile *n*-type semiconductors.[64] However, the extended polyhydrocarbon planar core and poor solubility of larger imides are some of the prominent issues that limit their practical applications. To mitigate these issues, various functionalization strategies have been developed to synthesize

relatively stable and soluble derivatives of high order rylene diimides such as naphthalene diimides and perylene diimides. Nevertheless, these bulky materials could not be extended effectively for the synthesis of small molecules. The introduction of an imide group with polycyclic aromatic hydrocarbons can lower their LUMO levels to meet the basic requirement of *n*-type organic semiconductor materials. The urge to fulfill the quest of an alternative possessing facile and stable imide is resolved by using 1,8-naphthalimide chromophore.[65-68] Over the past decade, numerous derivatives of naphthalimide have been investigated to explore their possible applications in optoelectronics, sensing, biological imaging, and medicinal chemistry.[69-74] Naphthalimide derivatives exhibit good charge transporting and fluorescence properties and exhibit an easy and facile functionalization with appropriate experimental conditions useful to vary the π-conjugation to enhance its electron-accepting ability.

In this review, we will focus on molecules exclusively employing naphthalimide as the building block for the electronic devices such as OLEDs, OSCs (BHJSCs) and DSSCs, structure property relationship studies and biological applications (Figure 1.1).

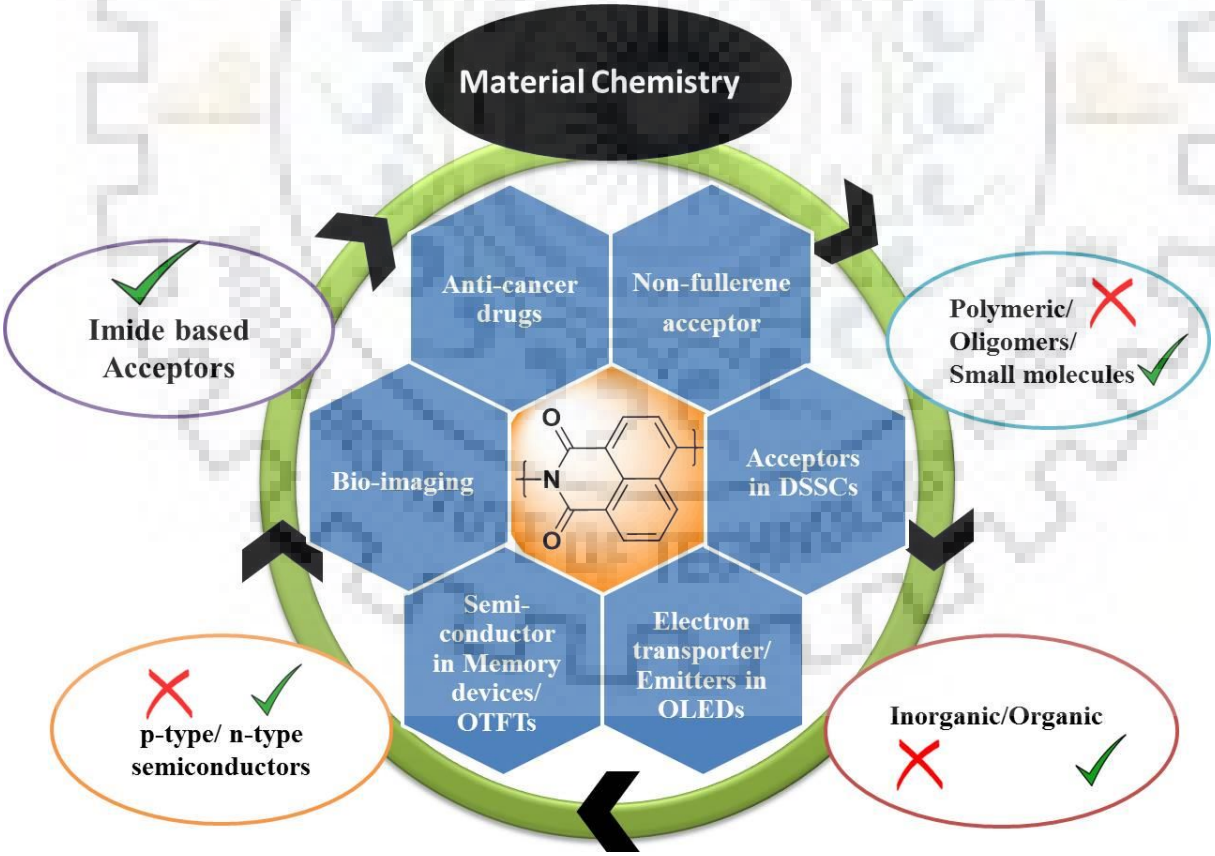

Figure 1.1 Pictorial representation of advantages and applications of naphthalimide chromophore.

To appreciate the role of chromophoric skeleton for diversified applications, it would be worthwhile to shed light on the basic structure and synthetic strategy of the chromophore. 1,8-naphthalimide represents a heterocyclic ring system containing a fused naphthalene ring to an imide unit. In general, imide functional group is derived from an acid anhydride by replacing oxygen atom with the (-*N*H) group (Chart 1.1). Thus, the core is named as 1*H*-benzo[*de*]isoquinoline-1,3(2*H*)-dione. Being highly polar in nature, imide based cores show good to moderate solubility in polar solvents. The imidic *N*-atom, generally derived from ammonia/ alkyl or aryl amines is acidic in nature and resists molecular hydrolysis unlike the structurally similar acid anhydrides.

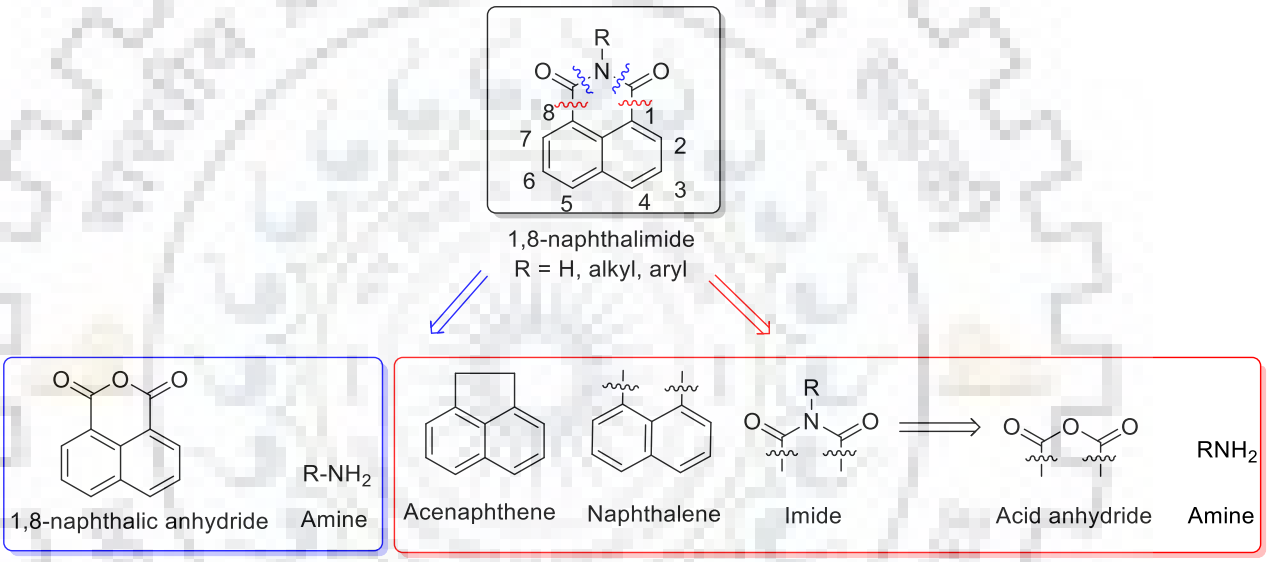

Chart 1.1 Retro-synthesis for 1,8-naphthalimide.

1.2 General method for the synthesis of 1,8-naphthalimide

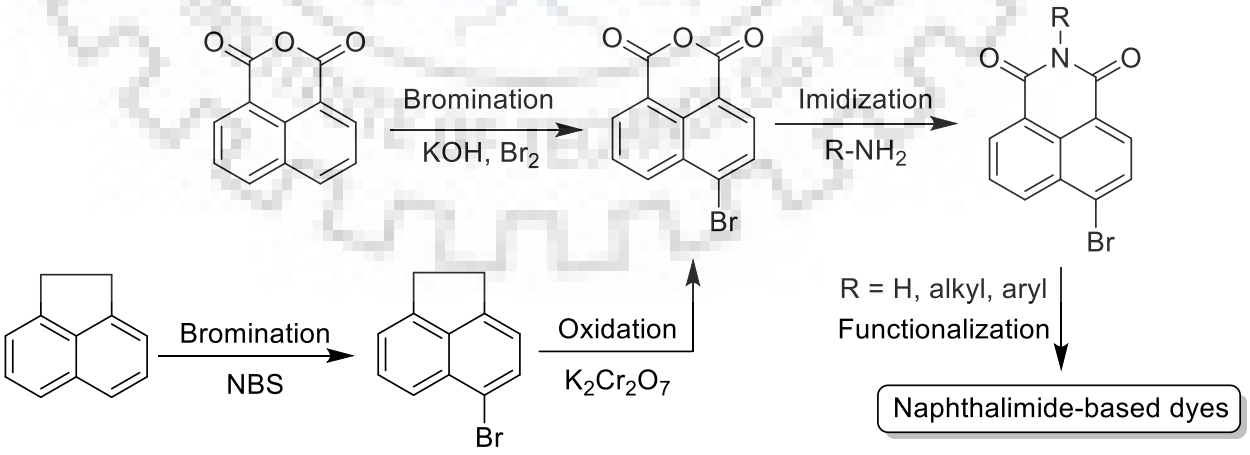

Chart 1.2 A schematic diagram for the synthesis of 1,8-naphthalimide using acenaphthene or naphthalic anhydride as starting materials.

A schematic representation for the synthesis of 1,8-naphthalimide is depicted in Chart 1.2. The most facile and an easy one-step method for the synthesis of 1,8-naphthalimides relies on the dehydrative condensation of naphthalic anhydrides with respective alkyl or aryl amines at high temperature. Both anhydrides and amines are heated or refluxed in a high boiling polar solvent or a mixture of solvents at high temperature. The reaction can be carried out in the absence or presence of zinc acetate ($Zn(OAc)_2$) as promotor/catalyst depending upon the reactivity of amine to yield desired naphthalimides in good to excellent yields. The second most accessed and documented synthetic procedure embarks on the use of acenaphthene as starting material which can be brominated and later undergo steps of reactions to yield naphthalimide. Specifically, the intermediate 5-bromoacenaphtene is oxidized to yield 6-bromo naphthalic anhydride using potassium dichromate ($K_2Cr_2O_7$) followed by imidization to yield 4-bromo 1,8-naphthalimide. This core provides an appropriate platform for functionalization using different substitution and C-X coupling reactions.

In this chapter we have outlined a detailed literature survey on the naphthalimide derivatives. For clarity, naphthalimide-based materials are classified into three major categories on basis of application which is sub-classified based on their molecular substitution and framework. In the first part (1.3), naphthalimide-based materials for structure property relationship studies possessing comparative physiochemical properties are discussed, followed by discussion of naphthalimide-based dyes as either non-fullerene acceptors, electron transporting materials/ emitters in OLEDs or acceptors for DSSCs in the second part (1.4). In the third part (1.5), naphthalimide-based molecules for bioimaging and medicinal applications particularly as anticancer agents will be discussed. At the end we will conclude the survey in section 1.6 as conclusions and outlook.

1.3 Naphthalimide-based materials for structure property relationships

Naphthalimide as a chromophore provides a wide possibility of dual functionalization on imide moiety and/or aromatic core by different substituents affecting photophysical and electronic properties of the derivatives. The structure-property relationship and effect of linkers and donor/ acceptor strength allow one to tune molecular design, resulting in a variety of functionalized naphthalimides. These derivatives tend to exhibit unique structural, morphological and electronic properties rendering them to behave as potential candidates to explore their properties for practical applications.

1.3.1 Imide-functionalized naphthalimide derivatives

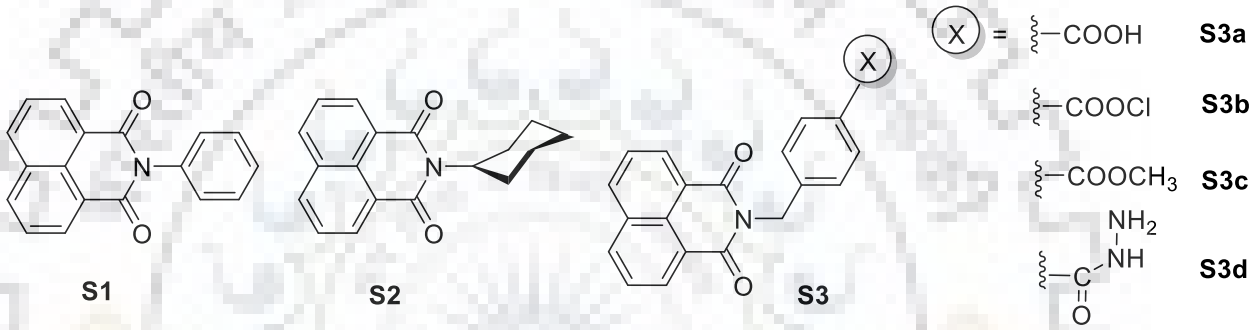

Chart 1.3 Structures of naphthalimide derivatives with imide functionalization (**S1-S3**)

Ge *et al.*[75] synthesized two naphthalimide AIEgens **S1-S2** differing at imidic position (Chart 1.3). Both dyes exhibited an absorption band at λ = 330 nm featured to naphthalimide unit. **S1** displayed polymorphism since it displayed two emission peaks at λ = 400 and 470 nm. Both dyes exhibited enhancement in emission in their aggregated state due to AIE effect. Although, **S2** displayed a strong AIE due to the more non-planar substituent, **S1** displayed multichromism under different external stimulus, attributable to the intermolecular π-π stacking.

Srivastava *et al.*[76] synthesized and characterized four compounds **S3a-S3d** as nanoaggregates with aggregation-enhanced emission in DMF-water system (Chart 1.3). They emit enhanced emission in both aggregated and in the solid states. The SEM images displayed uniform formation of cubic-shaped nanoaggregates for **S1a** and **S2b,** and spherical and flower-shaped morphology for **S3c** and **S3d**, respectively. The photophysical properties of the dyes were correlated with the nature of benzoic acid derivatives ascribed to combinatorial effect of π–π stacking, intermolecular and intramolecular interactions, and was also evident in crystal arrangement. The biexponential lifetimes of dyes in solid state displayed occurrence of a short lived and a long lived species due to the solution and aggregates formation. The energy levels

calculated using DFT resulted in high lying LUMO at 2.5 eV and stabilized HOMO level at 6.6 eV.

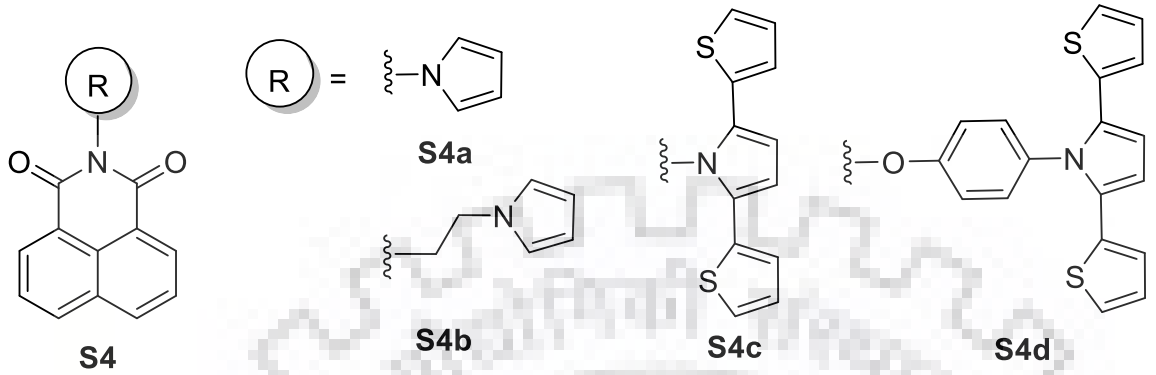

Chart 1.4 Structures of bipolar naphthalimide derivatives (**S4a-S4d**)

Ledwon *et al.*[77] synthesized D-A-conjugated bipolar small molecules **S4** based on pyrrole and 1,8-naphthalimide (Chart 1.4). Strong emission was observed for **S4a-c** while **S4d** display quenched emission due to the non-planarity of the chromophores. The dyes exhibited a reversible reduction wave due to the reduction of naphthalimide, and an irreversible oxidation peak. It was observed that the introduction of thiophene units enhanced the oxidation propensity by lowering the oxidation potential from 1.29 V (**S4a)** to 0.52 V (**S4c)**. Also, **S4b** exhibited a potential of 0.91 V which was shifted by 380 mV, compared to the parent dye **S4a**. The reduction potential shifted anodically from -1.57 V to -1.79 V for **S4a** and **S4c** attributable to the enhanced electron-donating strength of the later. It was realized in uplifting of HOMO energy level from -5.95 eV to -5.18 eV for **S4a** and **S4c**, respectively. For all the derivatives, LUMO and HOMO-2 was localized on naphthalimide and HOMO was composed of pyrrole and its conjugated moiety.

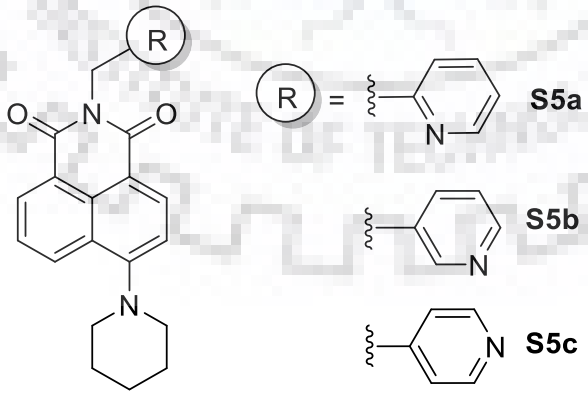

Chart 1.5 Structures of bipolar naphthalimide derivatives (**S5a-S5c**)

Grepioni *et al.*[78] reported three 4-piperidinyl-1,8-naphthalimide-based crystalline materials **S5a-S5c** possessing different linkage at *n*-methylpyridine moiety (Chart 1.5). These dyes were

found to develop co-crystals with 1,4-diiodotetrafluorobenzene due to the different arrangement of the molecules in the lattice. **S5a** displayed a red-shifted absorption and emission respectively at λ_{abs} = 413 and λ_{em} = 534 nm relative to that of **S5c** centered at 393 and 520 nm. However, **S5c** displayed strong quantum yield (0.33) compared to **S5a** (0.11). It was observed that the absorption and emission properties of the dyes were highly solvent-dependent. The dyes exhibited a positive solvatochromism in both ground and excited state by 20 nm and 50 nm, respectively attributable to the presence of ICT transitions. This was supported by subsequent quenching of quantum yield on moving from non-polar to polar solvents. This was further correlated with the enhanced non-radiative rate constants for polar solvents where the molecules exhibited specific interactions with solvent. However, the fluorescence was found to be dependent on the different arrangement of scaffold in the solid state, ascribed to the isomeric difference in pyridine linkage.

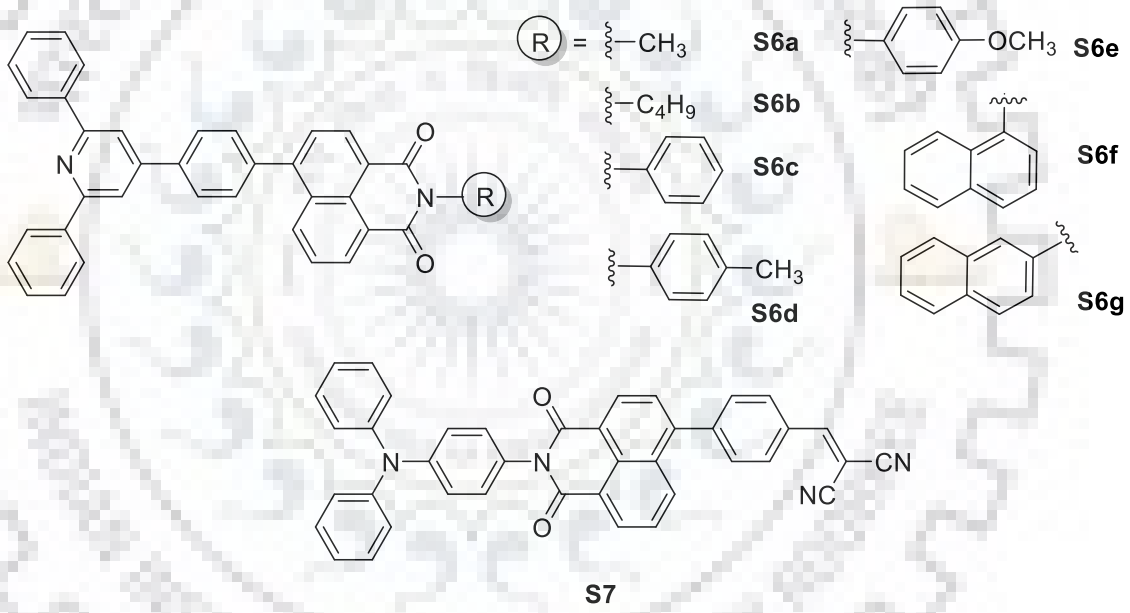

Chart 1.6 Structures of naphthalimide-based dyes with different imidic substituents

Liu *et al.*[79] reported a set of fluorescence compounds **S6a-S6g** bearing 2,4,6-triphenylpyridine and 1,8-naphthalimide units coupled by Suzuki cross coupling reaction (Chart 1.6). The photophysical properties of the dyes revealed that the alteration of groups on naphthalimide core had negligible role in the absorption profile, but the emission properties of the compounds were dependent on the position of substituents, and exhibited solvatochromism. Most of the dyes exhibited high quantum yields and thermal stability making them potential candidates for optoelectronic applications. All the dyes possessed reversible oxidation peak and resulted

HOMO level lying between 5.13 to 5.36 eV. Further, these dyes had high lying LUMO levels (1.56 to 1.62 eV) which could facilitate the electron injection.

Dong *et al.*[80] reported asymmetric bipolar D-A-A type dye **S7** where triphenylamine was linked to dicyanovinylene *via* naphthalimide unit for memory storage as irreversible non-volatile WORM behavior (Chart 1.6). The dye resulted in ICT from triphenylamine to naphthalimide and dicyanovinyl acceptor, which was somewhat weaker and blue shifted in comparison to triphenylamine analog **S109** due to orthogonal position. It displayed a red shift of ca. 10 nm with a broad shoulder due to the molecular interaction. **S7** exhibited a quasi-reversible oxidation with a high lying HOMO at -5.27 eV and LUMO at -2.39 eV. The device, silicon wafer/Al/**S7**/Al, displayed a good current retention and did not degrade with a stable CT state. This promoted the charge delocalization in the molecule and resulted in charge storage.

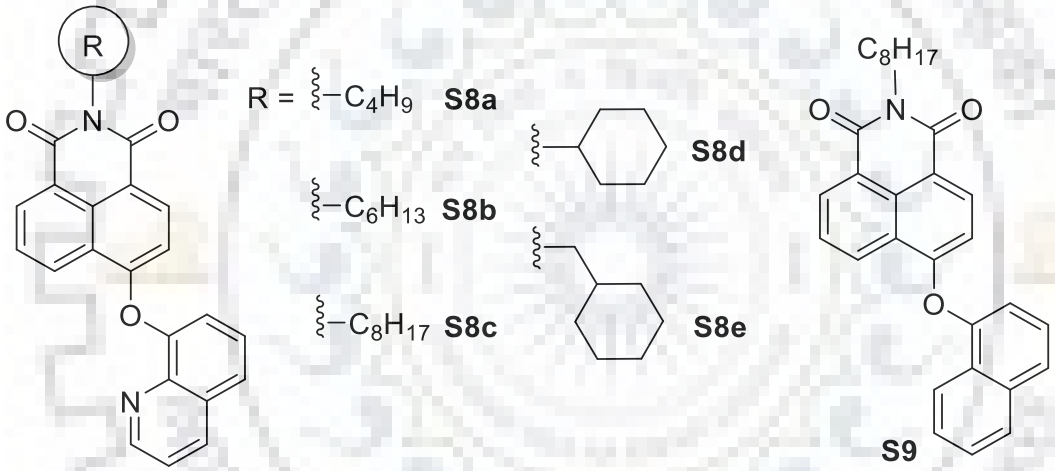

Chart 1.7 Structures of naphthalimide-based AIEgens (**S8a-S8e** and **S9**)

Naphthalimide-based V-shaped angular organic dyes **S8a-S8e** and **S9** were reported by Mehar *et al.*[81] as AIEgens to understand the effect of substituents at imidic and 4th position of naphthalimide core (Chart 1.7). Depending upon the imidic substituent, different nanomorphologies of these dyes were obtained due to intermolecular π–π interactions. Furthermore, the *J*-aggregates were found highly fluorescent and used as sensors for phenylnitro explosive detection in aqueous medium.

Zhuang *et al.*[82] synthesized A-D-A type naphthalimide and carbazole triad **S10** for memory device (Chart 1.8). Dye displayed two absorption bands attributed to the ICT at λ = 373 nm and below 360 nm arising from π–π* transition of the conjugated backbone. **S10** exhibited irreversible oxidation and reduction at 1.1 V and -1.2 V respectively. The high lying LUMO level at -1.88 eV

acted as charge trap, a requirement for exhibiting SRAM memory behavior. The fabricated devices, ITO/**S10**/Al, exhibited volatile memory status.

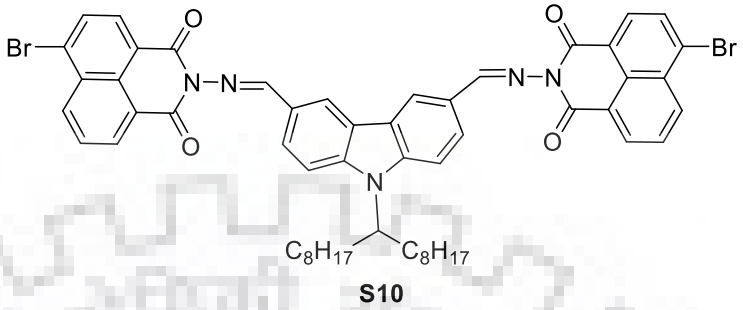

S10

Chart 1.8 Structure of bis-naphthalimide-based A-D-A type dye for memory storage (**S10**)

1.3.2 Core-functionalized naphthalimide derivatives

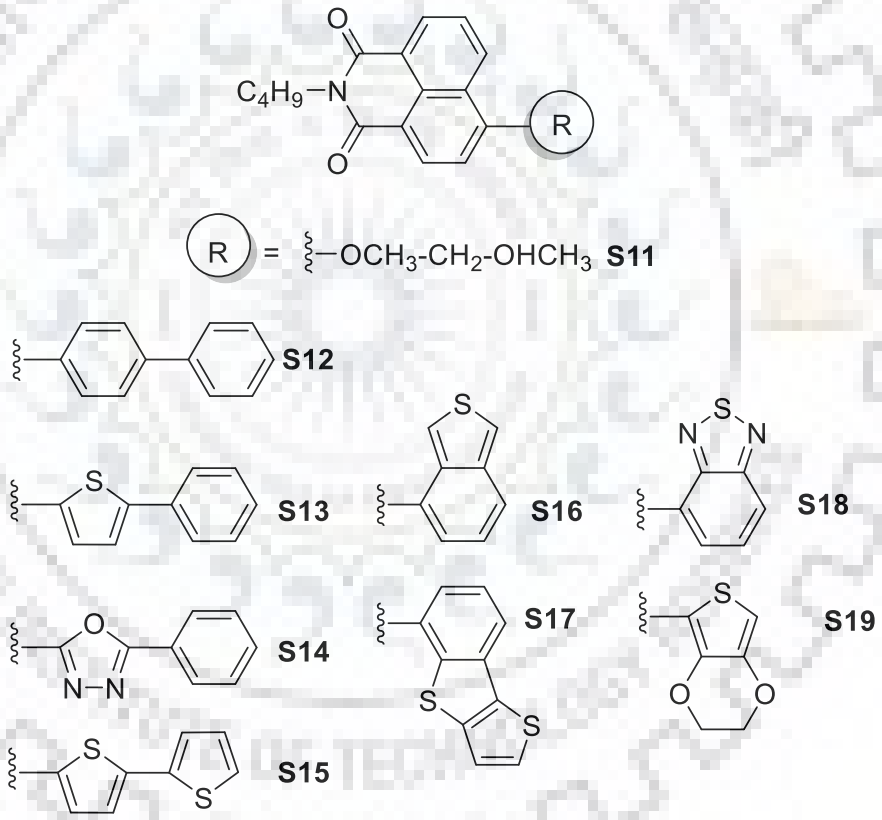

Chart 1.9 Structures of *N*-butyl-1,8-naphthalimide derivatives (**S11-S19**)

Sun *et al.*[83] computed a series of linear *N*-butyl-1, 8-naphthalimide derivatives **S11-S19** to explore their optical properties (Chart 1.9). The FMO analysis of these structures revealed that the observed vertical electronic transitions were due to ICT depending on the substituent groups at 4th position of naphthalimide. The maximum absorption and emission wavelength of **S12-S19** dyes is shifted bathochromically when compared to **S11** (326 nm) due to extended conjugating system.

The LUMO was found to be localized on naphthalimide units with major contributions except for **S18** where benzothiadiazole acted as a strong acceptor. The HOMO was found to be distributed on substituent group and naphthalene unit of naphthalimide. The HOMO contribution of naphthalimide in **S12-S18** is less than 90.1% as in **S11** while contribution from substituent group increased from 9.9% to 83.75 for **S17** due to enhanced electronic richness of substituent group. The HOMO energy values was raised for **S13**, **S15-S17** and **S19** while that for **S12**, **S14** and **S18** it was stabilized to -7.379, -7.613 and -7.535 eV respectively compared to **S11** lying at -7.354 eV. However, LUMO level for all the dyes lowered down compared to **S11**. The excitation transitions observed in absorption spectra for **S12-S19** corresponded to HOMO-LUMO and HOMO-1 to LUMO.

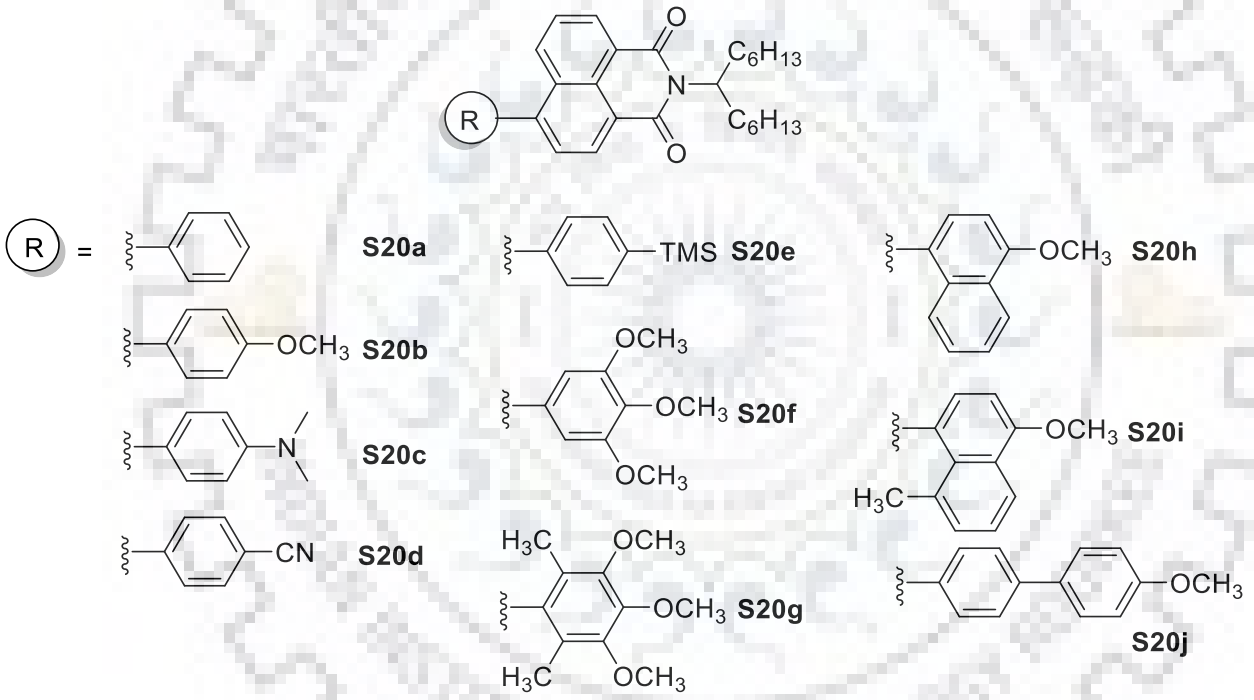

Chart 1.10 Structures of 4-aryl substituted naphthalimide derivatives (**S20a**-**S20j**)

Greiner *et al.*[84] synthesized and studied a set of 4-aryl substituted naphthalimides **S20a**-**S20j** (Chart 1.10). The dyes exhibited a typical D-A architecture with a positive solvatochromism as inferred by theoretical studies. The optical properties were found to be dependent on the molecular geometry and thus a non-planarity between the push-pull chromophores enhanced the ICT. The orthogonalization of the set of two chromophoric units resulted in quenched fluorescence. Among the series of chromophores, dyes **S20b** and **S20h** displayed a tremendous effect of polarity of medium on the optical properties, presumably due to the strong D-A interaction as well as

molecular geometry. This work exemplifies that an adjustable fluorescence and efficient quantum yield can be obtained with certain dyes by fine-tuning of the molecular geometry.

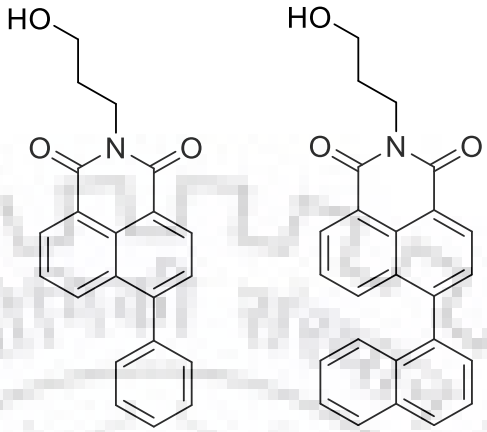

S21 **S22**

Chart 1.11 Structures of 4-substituted naphthalimide dyads (**S21-S22**)

Mallia *et al.*[85] reported a non-parallel stacked arrangement of D-A pairs **S21-S22** for prolonging the lifetime of photoinduced charge separated states (Chart 1.11). The steric repulsion in naphthalimide naphthalene dyad **S22** destabilized the planar geometry which helped in the non-parallel arrangement of the D-A stacks in the crystalline state. The absorption spectra of both the dyes exhibited two distinct bands in ACN, one centered at λ = 270−280 nm and other at λ = 350−353 nm. The low energy region band originated from $\pi-\pi^*$ transitions arising from HOMO to LUMO electronic transitions. Whereas, the shorter wavelength absorption band was attributed to $n-\pi^*$ transitions due to HOMO-1 to LUMO transitions. Both the dyads possessed a structureless emission band at 570 and 430 nm, respectively. Upon photoexcitation of the **S22** dyad, using femtosecond transient absorption spectroscopy it was seen that the electron transfer from naphthalene to the singlet excited state of naphthalimide moiety resulted in radical ion pair intermediates, which survived >10000-fold longer in the aggregated state as compared to that of monomeric dyad. The dyes showed a positive solvatochromism in emission spectra depicting a polarized excited state. The lifetime of the excited state species was enhanced on increasing the solvent polarity. **S21** and **S22** exhibited both oxidation and reduction peaks at 1.54 and 2.48 V, and -1.33 and -1.30 V, respectively. The oxidation potential of the dyes exhibited an easy removal of electrons compared to unsubstituted naphthalimide at 4^{th} position. The DFT computed structures of **S21** and **S22** revealed that the electron density of HOMO was distributed over

naphthalimide and substituent unit while electron density of LUMO was localized on naphthalimide unit only.

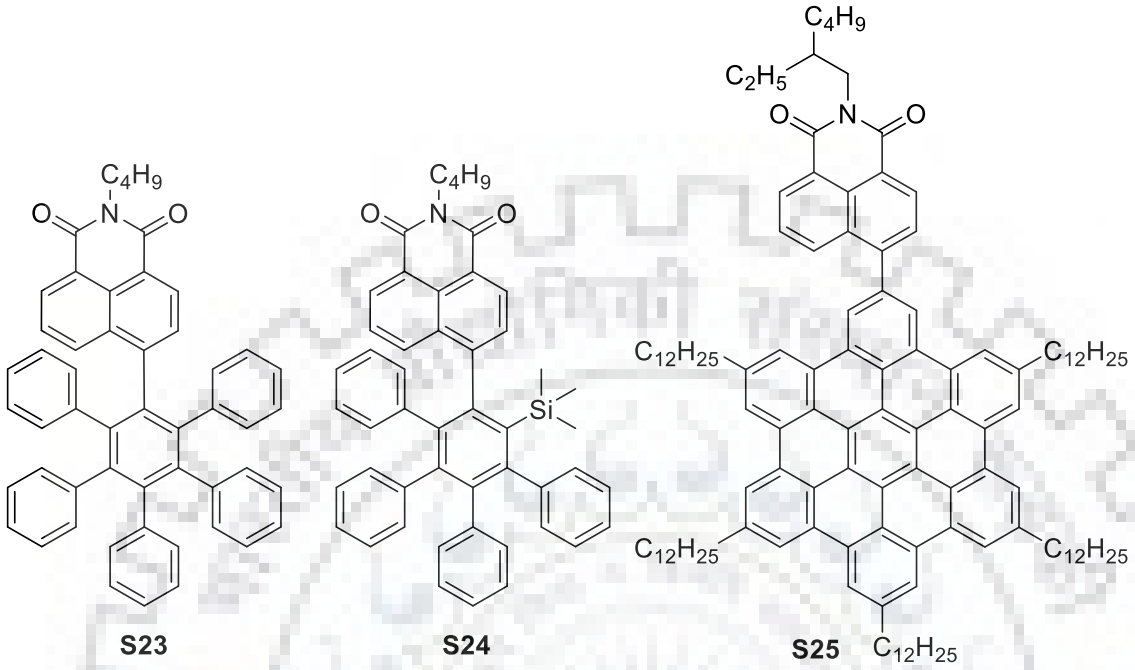

Chart 1.12 Structures of 4-polyaryl substituted naphthalimide derivatives (**S23-S25**)

Two new AIEgens **S23** and **S24** based on naphthalimide and dendritic polyphenyl were synthesized by Wang *et al.*[86] shown in Chart 1.12. The work highlighted utilization of naphthalimide chromophore otherwise an ACQ due to its facile π-π stacking as AIE molecules by coupling to polyphenyl. The dyes exhibited unique AIE properties in MeOH/H_2O mixtures. Both the dyes were used for detection of nitroaromatics. Unlike **S23**, $SiMe_3$-containing **S24** exhibited remarkably enhanced optical properties and displayed more sensitivity in the fluorescence detection of nitroaromatic explosives.

Keerthi *et al.*[87] synthesized a hexa-peri-hexabenzocoronene-based D-A dyad **S25** having with naphthalimide unit (Chart 1.12). The dyad demonstrated ICT interactions as a broad absorption band in the range of 400-600 nm. The dyad displayed a solvent dependent emission spectra attributable to facile CT from PAH to naphthalimide. A narrow band gap of 2.70 eV with a stabilized HOMO at -6.01 eV and LUMO at -3.31 eV were found suitable for **S25** to be used as the n-type semiconductor.

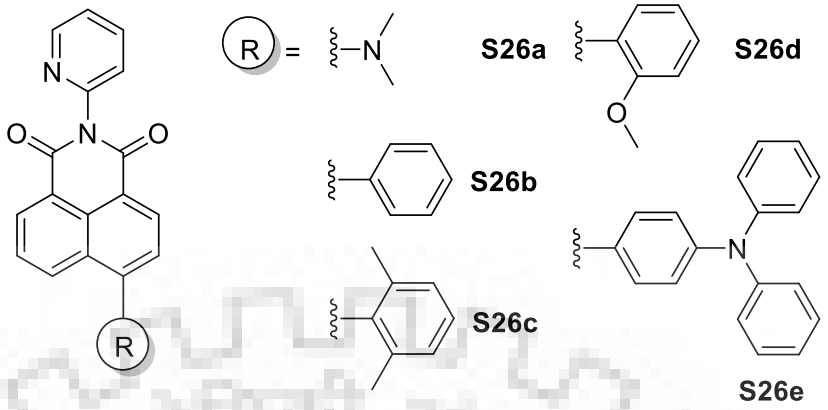

Chart 1.13 Structures of 4-substituted pyridine-functionalized naphthalimide derivatives (**S26a-S26e**)

A set of core-substituted pyridine-functionalized naphthalimide derivatives **S26a-S26e** were synthesized using Suzuki coupling reaction by Qu *et al.*[88] (Chart 1.13). The reported dyes were found AIE active and favoured self-assembly to form uniform nanoparticles. **S26a-S26e** dyes could be divided into two sets of dyes; **S26b-S26d**, and D-π-A dyes **S26a** and **S26e**. **S26b-S26d** displayed similar absorption profile at λ = 350 nm. While **S26a** and **S26e** exhibited a red-shifted absorption band at 430 nm corresponding to CT interactions. The set-2 dyes displayed poor emission than set-1 due to the pronounced CT in former. Moreover, **S26e** exhibited two emission peaks at λ = 370 nm (solvent dependent) and 430 nm (solvent dependent). This was due to TICT present in dye attributed to its non-planar and propeller structure. The time resolved analysis revealed that in aqueous medium, **S26b** and **S26e** possessed longer lifetime of 4.5 ns and 6.3 ns, respectively. This implies that excited state of aggregates is more stable than in solution, and favour AIE.

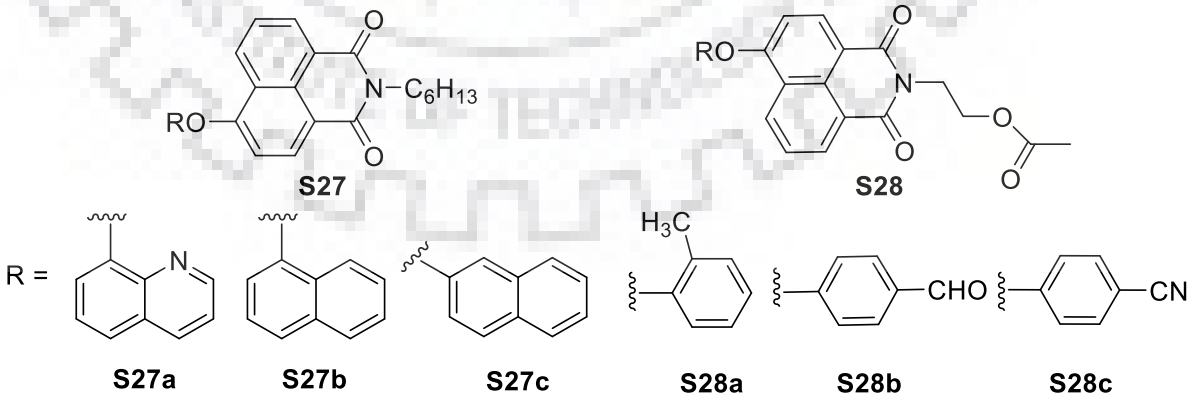

Chart 1.14 Structures of 4-aryloxy substituted naphthalimide derivatives (**S27-S28**)

Meher *et al.*[89] synthesized a series of V-shaped naphthalimide AIEgens **S27a-S27c** and studied their self-assembly properties (Chart 1.14). **S27a** formed a highly fluorescent nanoribbon like structure (<100 nm diameter) having hundreds of microns length in aqueous media. This may be attributed to the presence of N-atom promoting the head-to-tail π—π interactions as was also revealed by single crystal analysis. The other two molecules **S27b** and **S27c** were found to be typical AIEgens and self-assembled into unsymmetrical nanoparticles due to the absence of strong head-to-tail π—π interactions. Under physiological conditions, the self-assembled **S27a** nanoribbons were found to be highly sensitive and selective towards the multi-functional non-heme protein, ferritin. The work provides a direction to tune the self-assembly of the naphthalimide derivatives by facile and easy variation at the 4th position of the chromophore.

Ulla *et al.*[90] reported naphthalimide-based blue organic light emitting materials **S28a-S28c** having electron-donating phenoxy unit at the 4th position of the core (Chart 1.14). All the dyes displayed a CT absorption band at λ = 350 nm, which was bathochromically shifted by 15 nm in the film state. However, the emission spectra of **S28** dyes exhibited a broad and featureless band centered at λ = 415 nm. Irreversible oxidation and reduction peaks were observed for set of dyes with a low-lying LUMO level at 3.31–3.43 eV, making them suitable as n-type semiconductors.

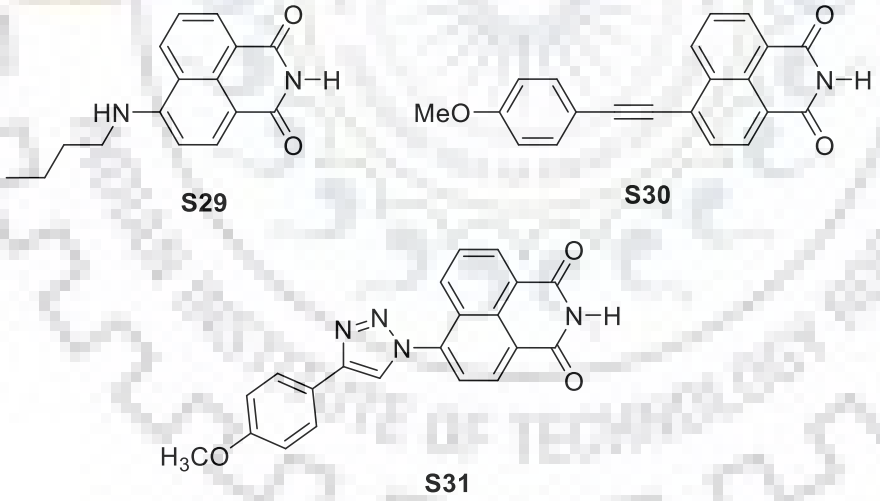

Chart 1.15 Structures of 4-substituted naphthalimide derivatives (**S29-S31**)

Rémy *et al.*[91] synthesized a series of π conjugated naphthalimide derivatives **S29-S31** having a methoxy arylethynyl or a methoxyphenyl triazole as a donor unit (Chart 1.15). Because of the lower donating character of the methoxy group, the absorption band of **S30** is blue shifted (λ = 402 nm) compared to **S29** (λ = 430 nm). Unlike **S30**, **S31** displayed a less intensified CT band due to the high non-planarity of the molecule. Both, **S29** and **S30** showed an intense emission

band in the visible region. However, a much higher Stokes shift was observed for **S30** due to the extended conjugation. Whereas **S30** had a high fluorescence quantum yield (0.57) and displayed efficient PCT in solution as well as in the powder state, **S31** was found weakly fluorescent (0.03). Being highly non-planar, **S31** exhibited a large Stokes shift (11201 cm^{-1}), which was ascribed due to strongly polar character of its emissive excited-state. Further, **S31** gave a higher value of non-radiative rate constant than other compounds, indicating that the triazole linker induce additional non-radiative deactivation pathways.

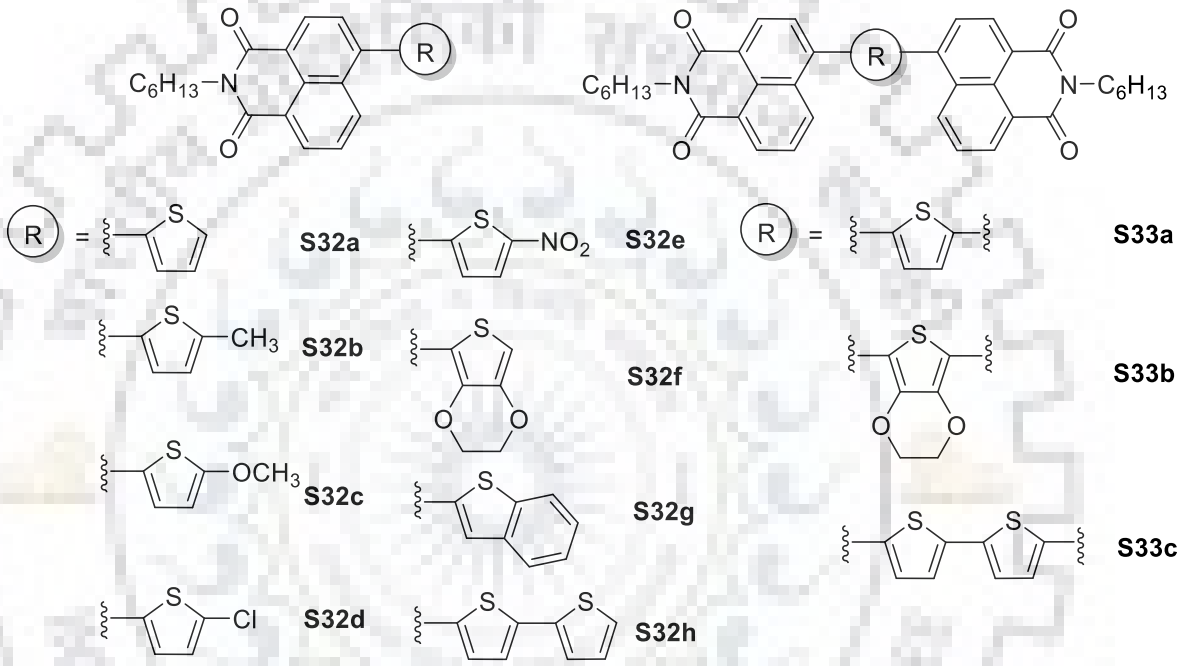

Chart 1.16 Structures of 4-substituted mono- and bis-naphthalimide derivatives (**S32-S33**)

Zhengneng *et al.*[92] utilized Pd-catalyzed direct C-H bond arylation to synthesize mono- and bis-naphthalimide derivatives **S32-S33** coupled to thiophene at C-4 position (Chart 1.16). Specifically, the bis-naphthalimides **S33a-S33c** displayed a 10-30 nm red shift absorption profile compared to their mono-naphthalimide analogs. Also, extension in conjugation as in **S32f**, **S32g** and **S32h** resulted in bathochromic shift of 19 nm, 7 nm and 69 nm respectively compared to **S32a**. Unlike **S32a**, all the dyes displayed a bathochromic emission band, which was centered at λ = 465 nm with blue fluorescence. Also, **S32b** and **S32c** having 2-substituted thiophene displayed blue and green fluorescence with emission band at 482 and 503 nm, respectively. However, **S32e** exhibited no fluorescence due to the presence of nitro substitution. The shifts in the absorption and emission spectra were found to be dependent on the nature of electron-donating or withdrawing capability of the substitutes on thiophene ring.

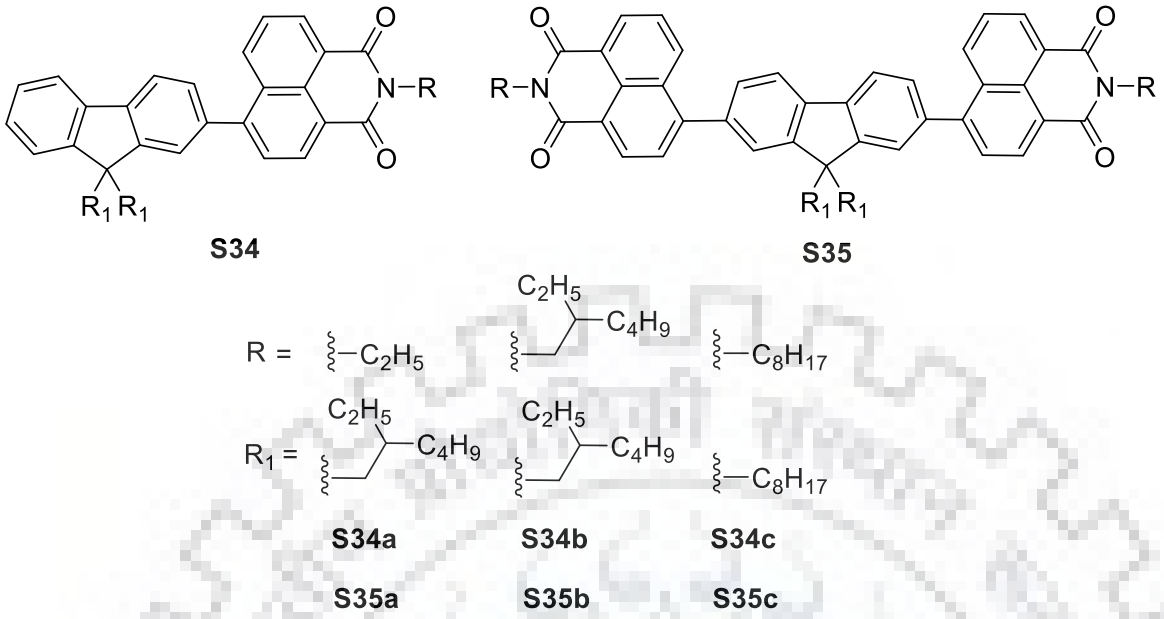

Chart 1.17 Structures of mono- and bis-naphthalimide-fluorene hybrids (**S34-S35**)

Gudeika *et al.*[93] synthesized a series of D-A structured electron-transporting naphthalimide-substituted derivatives of fluorene **S34-S35** by Suzuki coupling reactions (Chart 1.17). The dyes displayed 15-20 nm red shift compared to naphthalimide at 340 nm. The π-π* transition band at 306 nm corresponded to fluorene unit. The molar extinction coefficient of disubstituted fluorene derivatives was twice than mono-substituted derivatives, attributable to the more pronounced electronic transitions in the former. The dyes **S34a-S34c** displayed more intense emission band at 435 nm than dyes **S35a-S35c.** The dyes displayed a solvent dependent emission profile due to the charge transfer characteristics. All dyes exhibited a reversible reduction wave in the range of -1.55 to -1.80 eV due to the reduction of naphthalimide, indicating high electron deficiency of the molecules. The LUMO of the dyes were found low lying located at -3.29 to -3.52 eV that further demonstrated the high electron deficient nature of these derivatives. The influence of alkyl chain substituents on the electron mobility of the dye was also studied. In particular, the electron mobility of the **S35c** having long and linear alkyl chains displayed higher mobility than **S35b** with branched and short chains. This was attributed to the influence of alkyl chains on the intermolecular packing of the dyes.

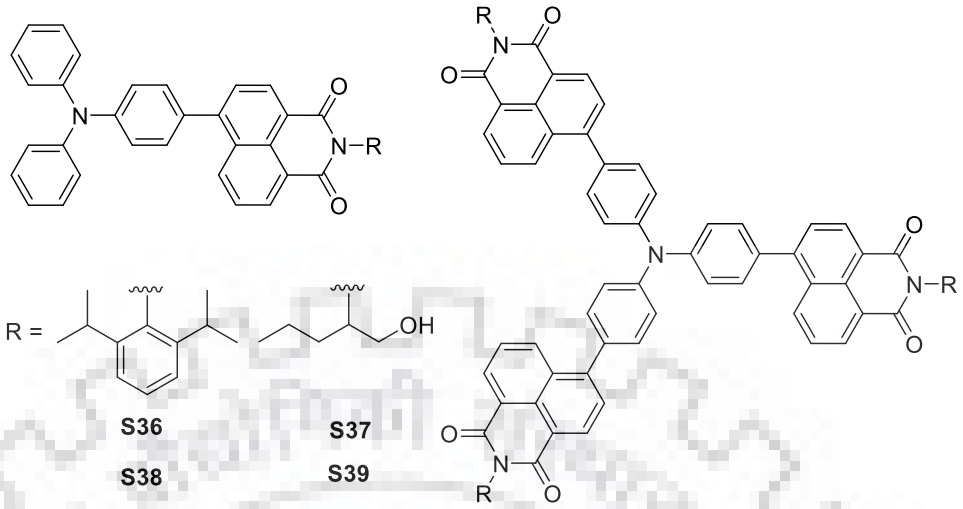

Chart 1.18 Structures of D-A triphenylamine and naphthalimide-based dyes (**S36-S39**)

Mallia *et al.*[94] focused on the self-assembling property of twisted D-A dyads comprising triphenylamine and naphthalimide **S36-S39** (Chart 1.18). The dyads underwent self-assembly in THF, forming spherical/vesicular aggregates dictated by weak co-operative intermolecular interactions (π−π and H-bonding). In contrast to their monomeric counterparts, the dyads underwent self-assembly. All the dyes displayed two absorption bands at λ = 310 nm and 410−420 nm due to the π-π* transition and CT interactions. Further, the dyes displayed solvatochromism in the excited state. The lifetime measurements for the dyes exhibited both a monoexponential decay profile in non-polar solvents, and a biexponential decay in polar solvents. This explains that in polar solvent, a long-lived radiative decay occurred from local excited state and shorter component due to CT state. Further, a long-lived CT was observed for intermediates in the aggregated state of triphenylamine-naphthalimide-based conjugates, attributable to the delocalization of charge carriers through D−A aggregates. In the aggregated state, the dyads showed ca. 10^4−fold enhancement in the lifetime compared to their monomeric counterparts. This may be attributed to the favorable arrangement of the D−A system thereby stabilizing the charge carriers in the self-assembled skeleton. The electrochemical studies revealed that the linear dyes were difficult to both oxidize and reduce compared to those of star-shaped dyes. It is interesting to infer that **S36** and **S38** were easy to oxidize and reduce compared to **S37** and **S39** since later possessed a high redox potentials. Whereas, **S36** exhibited an oxidation (1.17 V) and two reduction peaks (-1.81 and -1.22 V), **S38** displayed a positively shifted oxidation potential (0.89 V) and reduction at -1.72 and -1.17 V. Similar, trend was observed for **S37** and **S39** The concentration-dependent absorption, emission and excitation spectroscopic studies along with

morphological analysis in THF demonstrated the existence of spherical/ vesicular aggregates for these dyes.

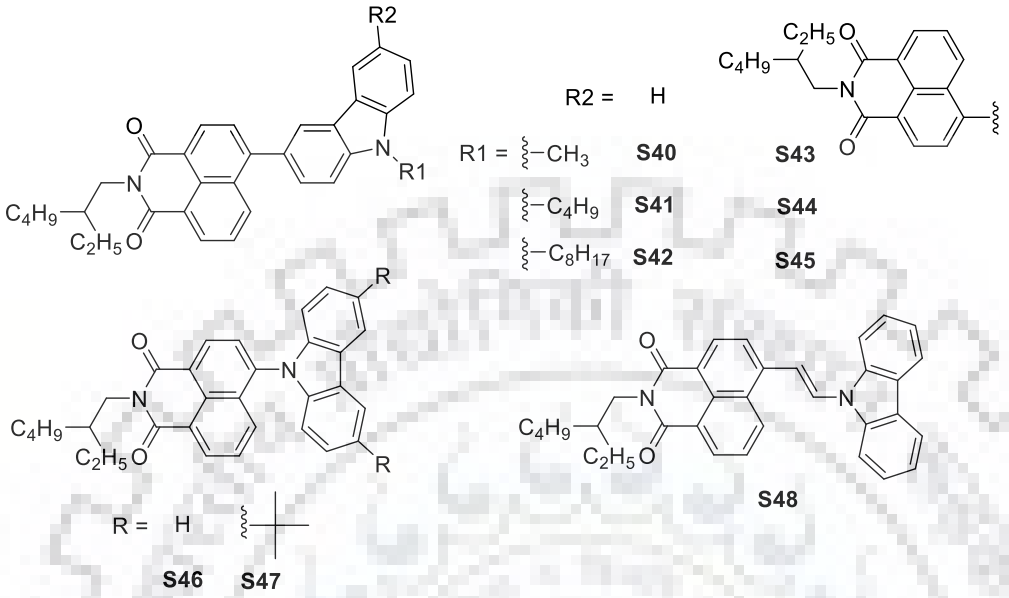

Chart 1.19 Structures of D-A carbazole and naphthalimide based dyes (**S40-S48**)

Gudeika *et al.*[95] synthesized a series of D-π-A linear dyes **E40-E48** to study the structure property relationship of substitution and the linking topology on the optical properties of the dyes (Chart 1.19). The dyes exhibited a significant molecular conformational change due to the different linkage of carbazole (C-3, C-6 and N-9) on the 4th position of naphthalimide core. The dyes possessed a high thermal stability and glass transition temperature upto 87 ˚C. The 3-substituted (**S40-S42**) and 3, 6-disubstituted carbazole (**S43-S45**) flanked on naphthalimide exhibited two broad absorption bands at λ = 344 nm and 398 nm, which were attributed to the naphthalimide and CT state. The molar extinction coefficients of the disubstituted carbazole **S43-45** were found to be doubled than those of mono-substituted dyes **S40-S42** resulting from the extended π-conjugation. The dyes **S46-S48** exhibited a more red-shifted absorption at 420-430 nm with an intense CT band. The dyes **S40-S45** displayed broad and structureless emission band in THF at λ = 520 nm indicative of ICT character of the excited state. However, the dyes **S46-S48** with N-9 substitution exhibited a red shift emission band at 540-580 nm. It is interesting to note that the quantum yield for **S46-S48** dyes was quenched and lowered ten times than those of **S40-S45**. The HOMO electron density was localized majorly on carbazole and naphthalene unit and LUMO was centered on naphthalimide unit for all the dyes. The dye **S45** possessing naphthalimide at 3, 6 position of carbazole displayed distribution of electron density extended

over both the units. All the dyes exhibited an irreversible oxidation potential in the range of 0.66-0.96 V, attributable to the removal of electron from the carbazole unit and quasi-reversible high reduction potential in range of -1.76 to -1.88 V. However, the C-3 and C-3, 6- linked dyes displayed a more positive oxidation potential in the range of 0.85-0.96 eV than those of N-9 linked dyes.

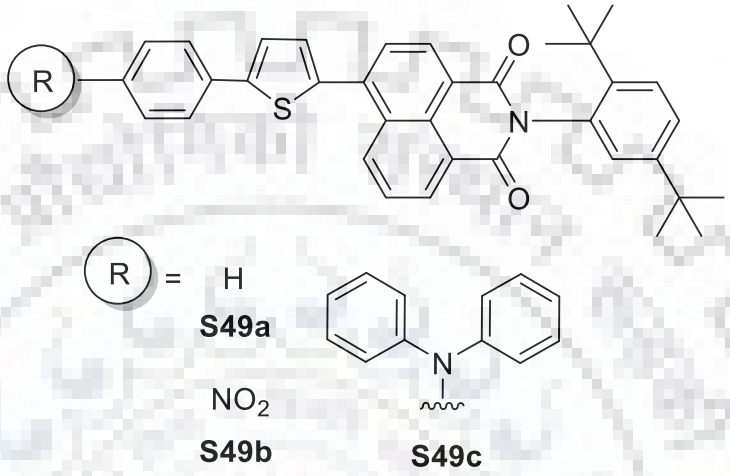

Chart 1.20 Structures of thienylnaphthalimide dyes (**S49a-S49c**)

Inari *et al.*[96] synthesized thienylnaphthalimide dyes **S49a-S49c** having phenyl, 4-nitrophenyl and triphenylamine units, and substituted by 2,5-dibutylphenyl at imidic position (Chart 1.20). Compared to the parent naphthalimide, these dyes exhibited a red shift in absorption by 60-100 nm. Incorporation of phenylthienyl in **S49a** bathochromically shifted absorption profile ($\Delta\lambda$ = 65 nm) to 398 nm. The introduction of diphenylamine on phenylthienyl unit bathochromically shifted absorption profile from 398 to 440 nm, attributable to the strong D-A interactions. In emission profile, the dyes **S49a-S49c** displayed a broad and structureless band at 493, 479 and 575 nm, respectively. On increasing the solvent polarity, the fluorescence quantum yield of **S49a** was also increased, however, **S49c** displayed fluorescence quenching due to the stabilized CT excited state. Further, the presence of single component exponential decays revealed the occurrence of single excited species. The long-lived lifetime of 2.6 ns for **S49c** facilitated the non-radiative decays compared to short-lived lifetime for dyes **S49a** and **S49b**. All the dyes exhibited two oxidation peaks. However, **S49b** exhibited more positive potentials than **S49a** due to the electron-withdrawing nature of the substituent. Further, the oxidation waves for **S49c** appeared at less positive potentials than **S49a** due to the ease in oxidation of the species. Nevertheless, the reduction potentials of all the dyes displayed minor alterations in the peak

positions. Thus, the HOMO energy level was influenced more than LUMO, which was ascribed to the difference in the electron donating capacity at core position of naphthalimide.

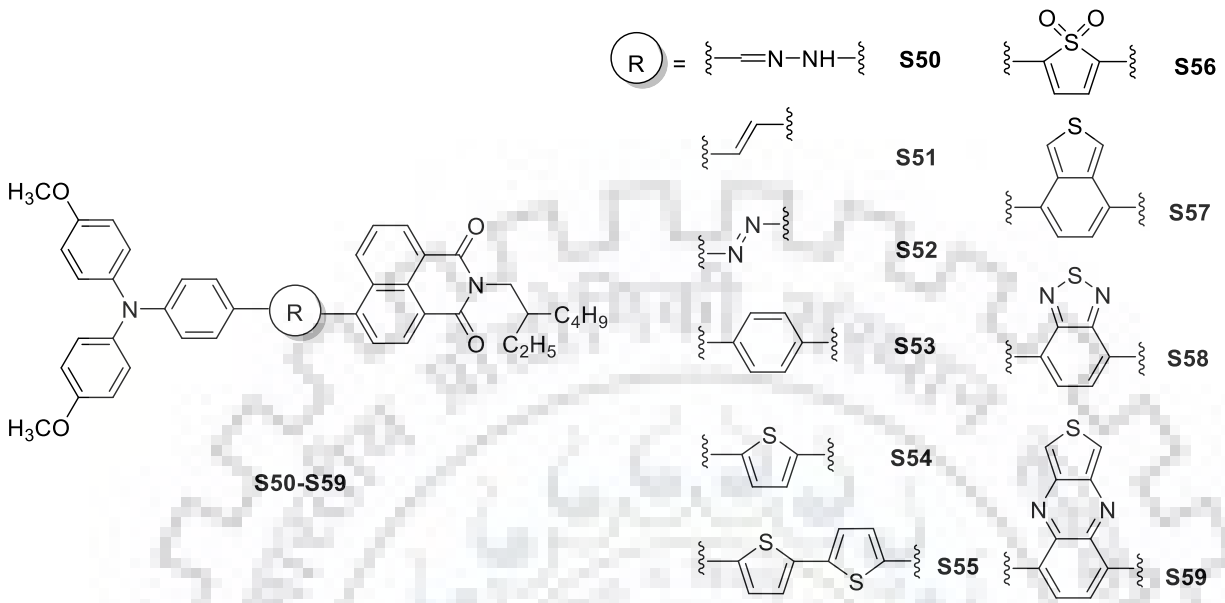

Chart 1.21 Structures of D-π-A triphenylamine and naphthalimide-based dyes (**S50**-**S59**)

Jin *et al.*[97] reported a series of D-π-A type triphenylamine and naphthalimide based dyes **S50-S59** with different linkers to explore the structure property relationship of these dyes as charge transporting material and emitter for OLEDs (Chart 1.21). For all the modeled dyes, HOMO was composed of larger than 87% contributions from donor and bridge with little contribution from naphthalimide unit. However, LUMO was comprised of naphthalimide except for **S56**, **S58** and **S59**. The strength of CT from donor to acceptor decreased in order of **S55**> **S52**> **S53**> **S54**> **S57**> **S51**> **S50** and **S59**> **S58**> **S56**. The photophysical properties were found to be CT dependent due to the variations in the strength of donor and acceptor units. The absorption profile of **S51–S59** displayed a strong red-shift in comparison to **S50**. Specifically, the dye **S54** displayed a 20 nm red shifted absorption and emission spectra compared to **S53** due to an enhanced electronic communication in the former. Among **S50-S59**, **S55** exhibited ca. 202 nm bathochromic shift due to the pronounced CT. However, **S59** exhibited an emission band at λ = 949 nm, which was red shifted by ca. λ = 312 nm than **S57**, presumably, being the strong electron-acceptor that could facilitate stronger CT.

Mallia *et al.*[98] explored the self-assembly properties of a twisted non-symmetrical D-D-A type naphthalimide-based material **S61** and compared it to D-A type **S60** (Chart 1.22). **S61** triad was composed of triphenylamine, anthracene and naphthalimide units to achieve a long-lived charge separation *via* aggregation. The small molecule possessed a steric hindrance imposed by

diisopropyl groups of naphthalimide and the propeller-shaped triphenylamine unit, inducing a non-planarity in the molecule. Further insight towards the non-planar geometry of the triad was presented by a unique antiparallel arrangement between the adjacent units. The D-A dye **S60** exhibited absorption profile centered at λ = 260 and 350−395 nm with a shoulder band around 400 nm, attributable to n → π* and π → π* electronic transitions. However, dye **S61** displayed a 20 nm red-shifted absorption due to an extended conjugation. Both the dyes displayed a dual fluorescence character due to the LE and CT emission state. In particular, **S60** displayed a shoulder band at λ = 500 nm and a red-shifted intense broad band at 620 nm due to CT. In contrast, **S61** exhibited ca. 80 nm red shift in CT band, which was shifted ca. λ = 280 nm compared to anthracene and naphthalimide emission peaks. The solvent polarity-dependent absorption and emission analysis highlighted the presence of ground state CT interactions. **S60** exhibited two reduction potentials at -1.17 V and -1.25 V which were cathodically shifted by 20 mV in respect to **S61**. However, the oxidation potential of **S60** at 1.42 V was at higher potential than **S61** attributed to the enhanced electronic richness of **S61**. **S61** displayed two oxidation potentials at 1.02 and 1.32 V, arising from the oxidation of triphenylamine and anthracene, respectively.

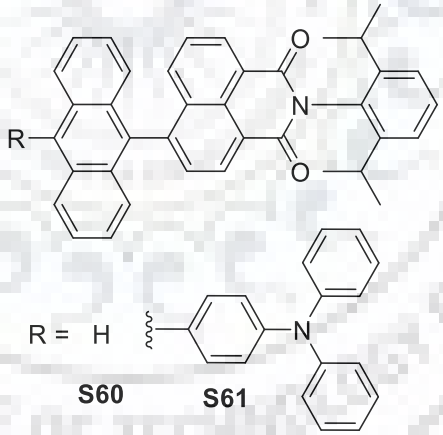

Chart 1.22 Structures of D-π-A triphenylamine and naphthalimide-based dyes (**S60**-**S61**)

Li *et al.*[99] synthesized three D–A molecules **S62-S64** with varying number of thiophene moieties in the π-bridge (Chart 1.23). It was found that insertion of thienyl linkers gradually enhanced the film crystallinity and also improved stacking and orientation in the film state. The dyes displayed a poor quantum yield due to the strong D-A interactions within the molecules. The introduction of thienyl group in the backbone resulted in lowering the oxidation potential and thus destabilizing HOMO level from -5.89 eV to -5.58 eV, to -5.52 eV for **S62-S64**, respectively.

Theoretical calculations revealed that the introduction of thiophene π-bridges increased the planarity of the molecules. As a result, the fabricated memory devices showed an enhanced multilevel performance. All of the fabricated devices were characterized as WORM-type memory materials with improved device repeatability. Furthermore, all devices exhibited lower threshold voltages, with narrow distribution and low energy consumption.

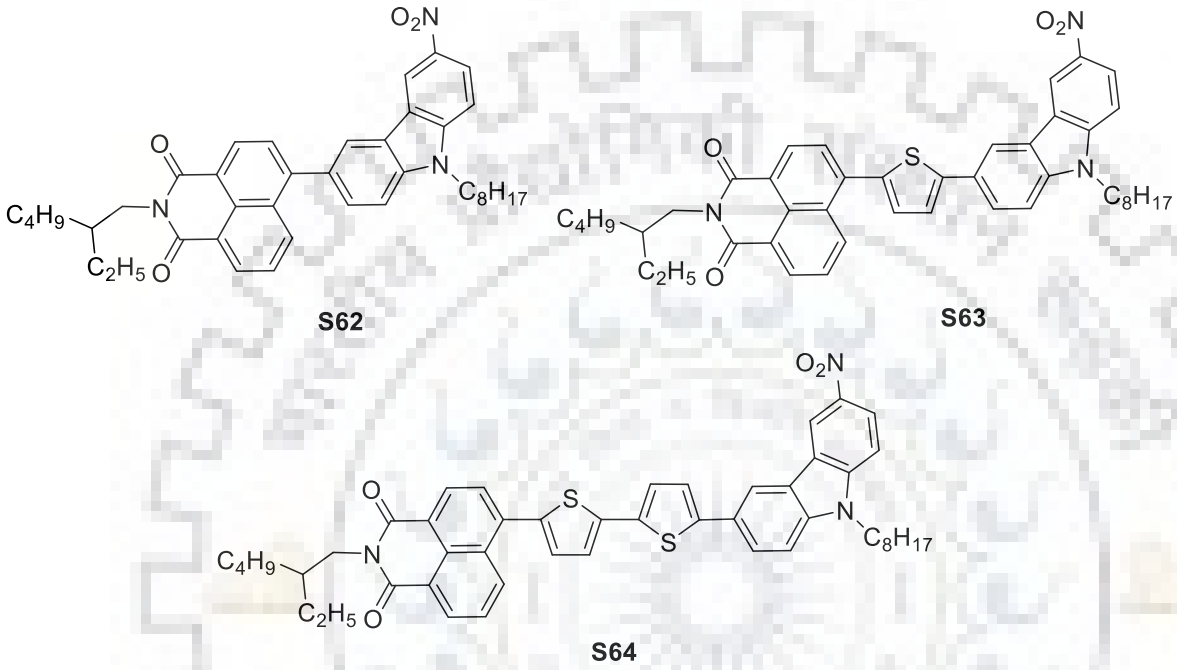

Chart 1.23 Structures of carbazole and naphthalimide-based dyes (**S62-S64**)

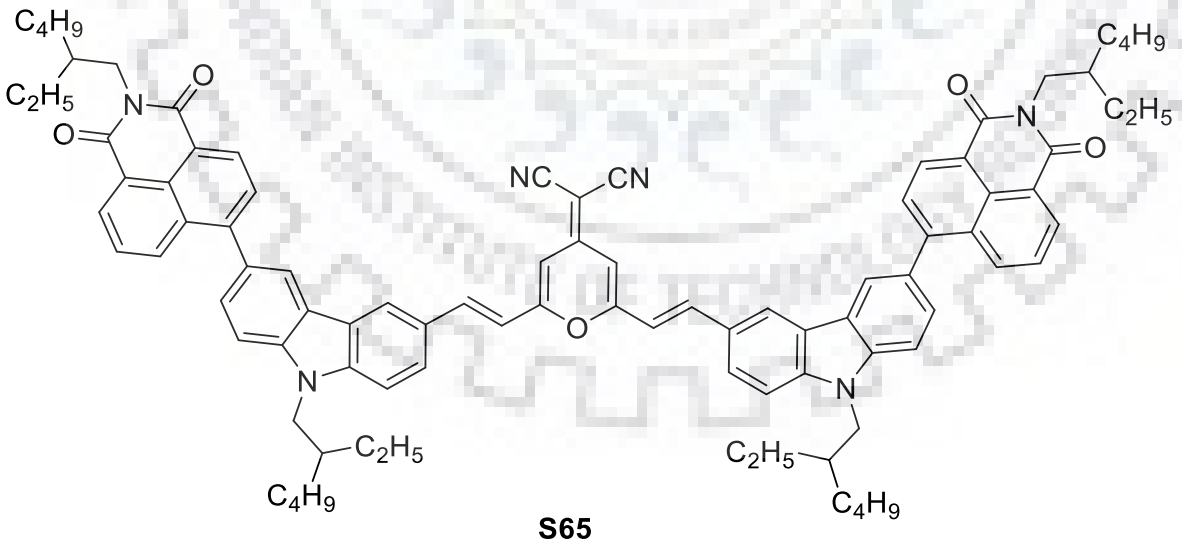

Chart 1.24 Structure of symmetric A-D-A-type bis-naphthalimide carbazole dye (**S65**)

Zhang *et al.*[100] synthesized a symmetric A-D-A-type bis-naphthalimide-based small molecule **S65** as a p-type semiconductor (Chart 1.24). In **S65**, naphthalimide and central

(dicyanomethylene)-4*H*-pyran units (acceptor) linked to carbazole units (donor) resulted in a strong ICT band at λ = 452 nm. In thin film, the absorption profile resulted in ca. 100 nm bathochromic shift. The energy levels of **S65** were analyzed to be -5.51 and -3.26 eV as HOMO and LUMO energy level, respectively. A memory storage device with a configuration of ITO/**S65**/Al exhibited ternary non-volatile memory behavior.

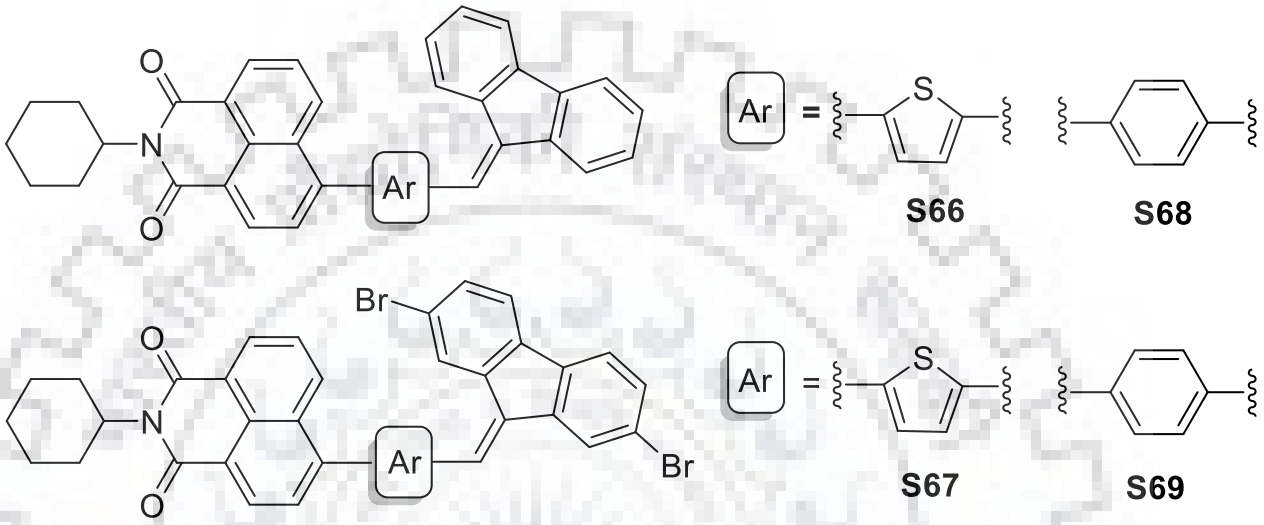

Chart 1.25 Structure of D-π-A naphthalimide-based AIEgens (**S66-S69**)

Gopikrishna *et al.*[101] reported typical D-π-A AIEgens **S66-S69** having mono-substituted dibenzofulvene and naphthalimide system with different linkers (Chart 1.25). In the excited state, the thiophene substituted dyes, **S66** and **S67**, displayed AIE with positive solvatochromism of 50 and 74 nm in excited state with red and orange emission due to ICT, respectively. Both the dyes displayed a high quantum yield in the condensed state due to formation of *J*-aggregates. However, the aryl-substituted dyes **S68** and **S69** either showed a poor blue emission (**S68**) or was found to be AIE inactive (**S69**) due to heavy metal effect.

Xia *et al.*[102] synthezised a fluorescent bis-naphthalimide **S70** (Chart 1.26) in which the presence of two naphthalimide planes allowed the molecule to act as a double-channel rotor. Specifically, **S70** exhibited a blue-shifted emission in the twisted state and longer emission in the planar state while aggregated. In the excited state, **S70** showed strong ICT properties with a positive solvatochromism of 50 nm. **S70** displayed a red-shifted emission band centered at λ = 473 nm and 500 nm in aggregated and powder form, respectively. Owing to the restriction of intramolecular rotation effect, the dye resulted in strong emission character in condensed state.

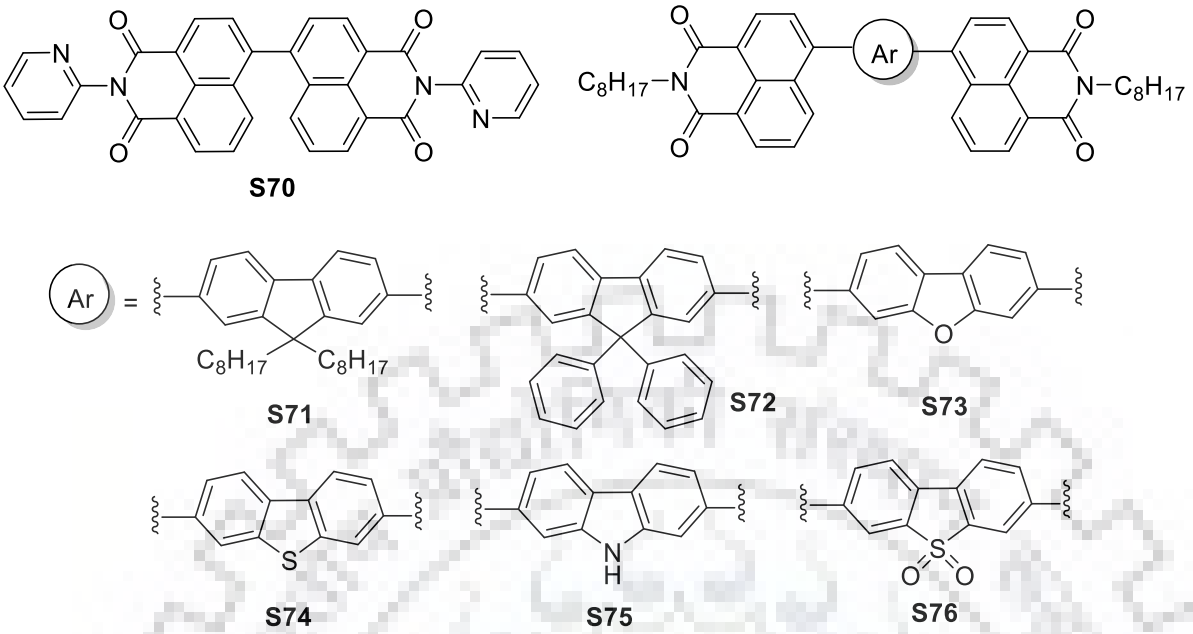

Chart 1.26 Structure of bis-naphthalimide derivatives (**S70-S76**)

Chai *et al.*[103] studied the model structures of a series of D-A naphthalimide-substituted fluorene derivatives **S71-S76** (Chart 1.26). The group explored the optical, electronic, and charge transport properties of **S71-S76** to use them as charge transport and/or luminescent materials for OLEDs. The FMO analysis revealed out that the vertical electronic transitions of absorption and emission were of ICT in nature, arising from center to the periphery. The D-A bipolar molecules displayed large bathochromic shifts in their optical spectra depending upon the strength of donors. The theoretical results indicated that the optical and electronic properties of **S71-S76** were affected by the substituent groups at fluorene moieties, depending upon the electronic richness of the central core.

Zhang *et al.*[104] demonstrated a WORM memory device using A_2–π–A_1–π–A_2-structured **S77** comprising benzothiadiazole as central acceptor and peripheral naphthalimides bridged by hexyl-thiophene (Chart 1.27). The dye displayed a CT absorption band at 474 nm while a π-π* transition at λ = 333 nm was assigned to the naphthalimide unit. The film absorption spectrum of **S77** bathochromically shifted by 16 nm, depicting formation of molecular aggregates. The dye displayed two reversible oxidation and reduction potentials, with a narrow optical band gap of 2.21 eV, and a deep seated LUMO at -3.25 eV. The fabricated device with ITO/**S77**/Al configuration exhibited a non-volatile and rewritable property.

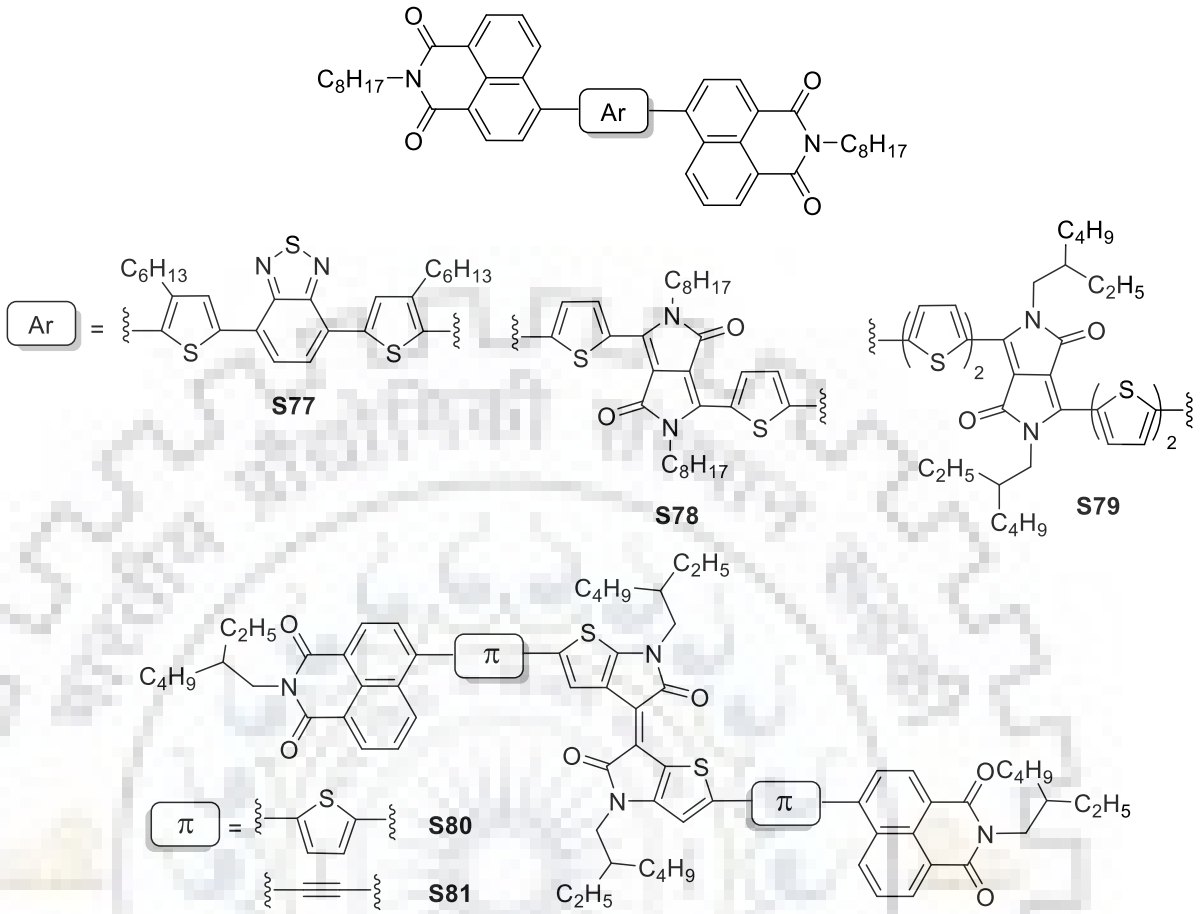

Chart 1.27 Structures of bis-naphthalimide derivatives with different linkers as as A_1-π-A_2-π-A_1 architecture (**S77-S81**)

Hendsbee *et al.*[105] synthesized A_1-π-A_2-π-A_1 architecture based small molecule **S78** where diketopyrrolopyrrole was used as a central acceptor and flanked by thiophene end capped naphthalimide units on both the sides (Chart 1.27). The choice of naphthalimide was made to stabilize both HOMO and LUMO energy level, and to direct self-assembly. The dye displayed two distinct absorption bands at λ = 400 nm and 600 nm, originating from localized π-π* transitions and CT respectively. **S78** displayed a red shifted profile compared to **S77** due to enhanced electron deficiency and extended conjugation. However, the molecular framework of **S78** was twisted out of plane from central core due to the large naphthalimide end-capping. The dye displayed two reversible oxidations and reduction waves, attributable to the oxidation of thiophene units and reduction of both naphthalimide and diketopyrrolopyrrole units. The molecule possessed a deep seated HOMO at -5.4 eV and a LUMO at -3.5 eV. However, the charge carrier mobility of the dye was found to be low as a result of non-planarity of the conjugating backbone.

Li *et al.*[106] synthesized A_1-D-A_2-D-A_1 type naphthalimide endcapped diketopyrrolopyrrole-based **S79** for organic multilevel memory device (Chart 1.27). The dye exhibited two absorption bands, one below 450 nm and other above 500 nm attributed to the π-π* transitions and ICT, respectively. The absorption profile was bathochromically shifted by 100 nm in thin film due to the facilitated intermolecular interactions. **S79** displayed the irreversible oxidation and reduction waves at potentials of 0.67 V and -1.32 V, respectively. The HOMO and LUMO were calculated to be -5.03 eV and -3.52 V, and were found suitable for hole-injection CT from the HOMO to the ITO of the device. The HOMO energy level of **S79** was lifted by 370 mV as compared to **S78** due to an increased electronic richness. Thus, the hole injection was easier than electron injection. The DFT analysis revealed that HOMO and LUMO were unevenly distributed, resulting in charge delocalization all over the molecular backbone. The fabricated memory device with configuration of ITO/**S79**/Al displayed current–voltage curve for sandwich memory storage. Even after switching off voltage, the device remained in ON state i.e. non-volatile WORM memory.

McAfee *et al.*[107] synthesized two thienoisoindigo and naphthalimide-based π-conjugated materials **S80** and **S81** utilizing either C−H bond activation cross-coupling protocol or Sonogashira cross-coupling reactions (Chart 1.27). Both the dyes were studied for their optical, electrochemical and thermal properties, and offered a comparison of the structure-property relationships as a result of the two different π-bridging units. Both the dyes extended their absorption to NIR where **S80** showed a 30 nm red shift due to increase in the conjugation length and D-A character. The use of thiophene bridging units displayed a red-shift in absorption whereas the acetylene bridge offered a stabilization of the electrochemical energy levels, leading to relatively more electron-deficient material. The dyes exhibited reversible multi-electron reduction and two oxidation waves. The reduction potential of **S80** was negatively shifted to -1.23 V than that for **S81 (**-1.16 V). **S80** displayed a 140 mV lower oxidation potential due to enhanced electronic richness of the core. Thus, the energy levels of **S81** were stabilized due to enhanced electron deficiency of the backbone.

1.3.3 Amine-substituted naphthalimide-based dyes

Xu *et al.*[108] synthesized 4-substituted 1,8-naphthalimide and 1,8-naphthalic anhydride iminophosphoranes **S82** and **S83** from the reduction of the corresponding azides using different phosphine ligands (Chart 1.28). In this way, a convenient and highly efficient method for the reduction of 4-azidonaphthalimide to 4-aminonaphthalimide **S82** was developed using PMe_3. The structure of **S83** was confirmed by single crystal X-ray diffraction analysis where the N-P bond

length was found to be shorter indicating presence of double bond. The molecule exhibited a twisted conformation with a P-N-C bond angle of 129.1°. Compared to the parent dye **S82**, introduction of iminophosphoranes at the 4-position of the core (**S83**) resulted in a red-shift, similar to other 4-amidonaphthalimide documented in literature. The low energy region absorption band at ~430 nm for the dyes was originated from the facile CT. When compared to 4-amino-1,8-naphthalimide, the fluorescence spectrum of the iminophosphoranes displayed a weak solvatochromism. Thus, the investigated optoelectronic properties of **S83** indicated that the introduction of phosphine substituents had a direct influence on the optical properties, making it as a potential organic luminescent material.

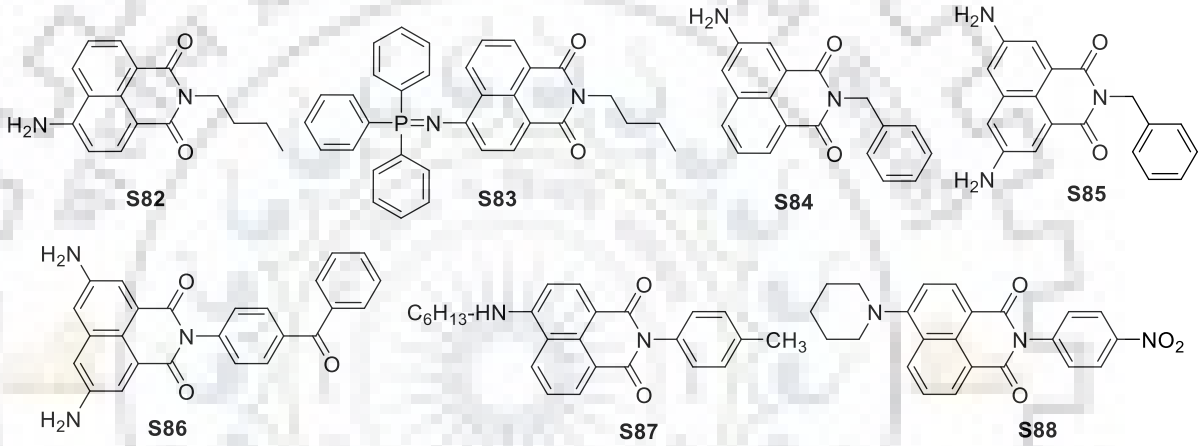

Chart 1.28 Structures of 4-amino substituted naphthalimide derivatives (**S82-S88**)

Zhang *et al.*[109] synthesized a variety of naphthalimide derivatives **S84-S88** by dual functionalization of the core (Chart 1.28). All the synthesized derivatives were used as photoinitiators in combination with some selected salts or amines to enhance the rate of cationic polymerization of epoxides. The photophysical properties of **S84-S88** varied greatly depending upon the substitution at imidic and core. The dyes bearing amino group or derivatives displayed red shifted absorption band at ca. 430 nm, which was attributed to the CT from amine to naphthalimide. The enhanced light absorption properties of the dyes were attributed to the electronic transitions from the HOMO to LUMO.

Ivanov *et al.*[110] reported a series of aryl hydrazones of 4-hydrazino-*N*-hexyl-1,8-naphthalimide **S89a**-**S89f** and **S90** to evaluate their solution and solid state fluorescent properties (Chart 1.29). In particular, **S89c** exhibited a ca. 7 nm blue shift in comparison to **S89a** with a strong emission at λ = 567 nm. The solid-state fluorescence spectra of hydrazones were red-shifted by 33-76 nm than those in solution, indicating the presence of intermolecular interactions. Unlike

S89a, **S89f-S89g** displayed the most bathochromically shifted emission band in both solution and solid state. The dyes with electron-donating substituents derivatives **S89e**, **S89f, S89g** and **S90** display more influenced fluorescence spectra relative to those of compared to unsubstituted and electron withdrawing substituents such as **S89a**, **S89c** and **S89d**.

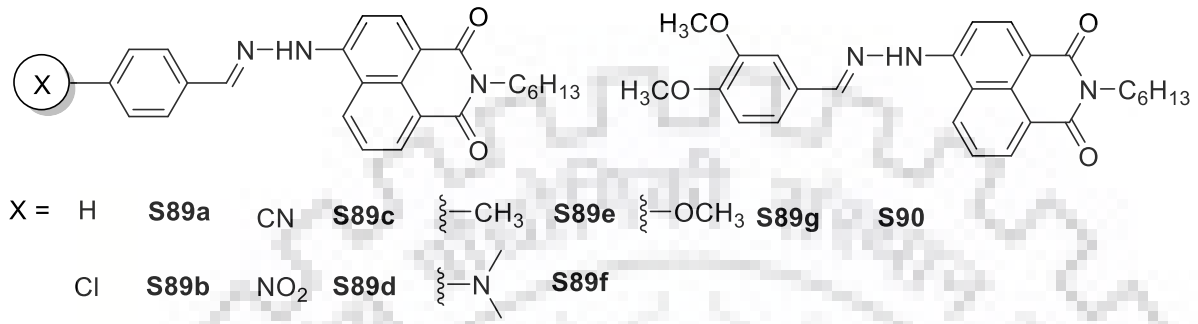

Chart 1.29 Structures of aryl hydrazones of 4-hydrazino-*N*-hexyl-1,8-naphthalimide derivatives (**S89-S90**)

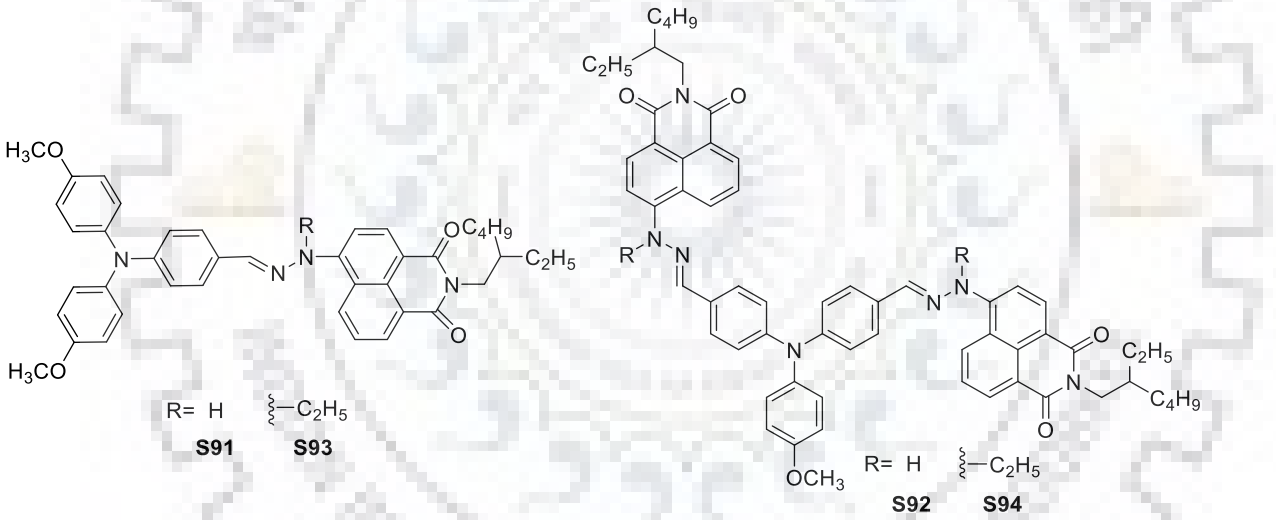

Chart 1.30 Structures of hydrazine dyads and triads comprised of naphthalimide and triphenylamine. (**S91-S94**)

Gudeika *et al.*[111] synthesized hydrazine-based dyads and triads **S91-S94** comprised of naphthalimide and triphenylamine units (Chart 1.30). It was observed that the absorption profiles of mono-hydrazones **S91** and **S93** were red shifted compared to dihydrazones **S92** and **S94** due to the strong electron-donating strength of the core in former set of dyes. It was also realized that the dyes **S91** and **S92** displayed a pronounced bathochromic absorption spectra compared to dyes **S93** and **S94** due to facilitated intermolecular hydrogen bonding in the former dyes. In terms of energy levels, **S94** displayed a positive oxidation potential (50 mV) compared to **S93** at 0.30 V. Further,

the reduction potentials for the substituted dyes was shifted towards more positive potential at -1.86 and -1.84 V compared to its analogs **S91** and **S93** (-1.97 V and -1.99 V).

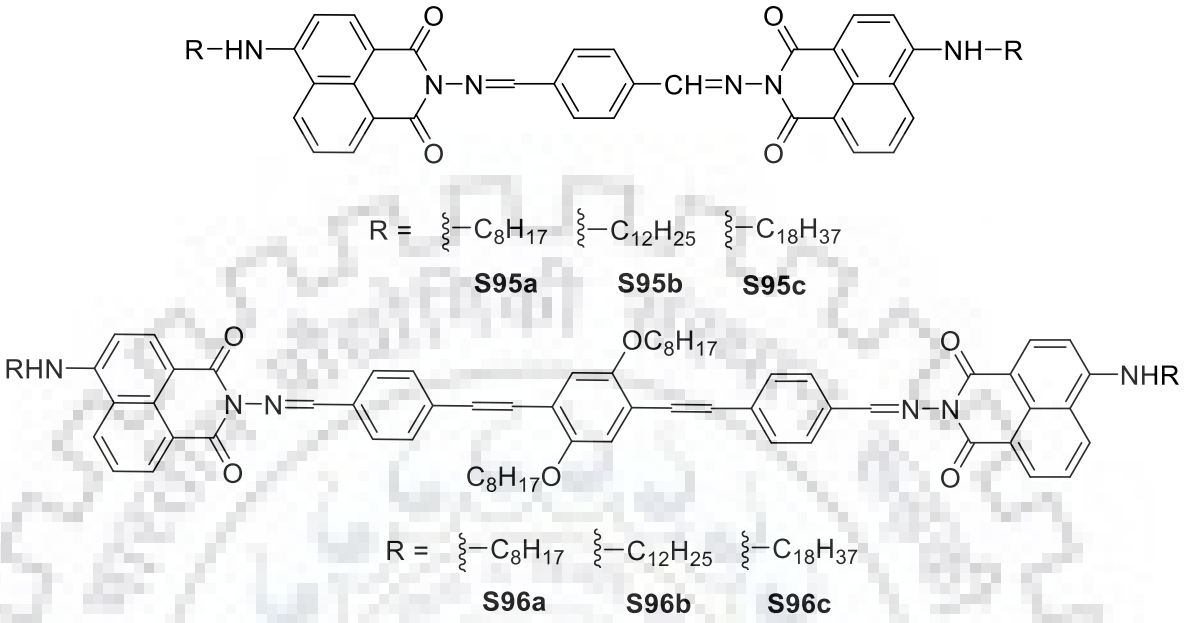

Chart 1.31 Structures of naphthalimide-based Schiff base derivatives (**S95-S96**)

Zhang *et al.*[112] reported a set of naphthalimide based-Schiff base derivatives **S95-S96** (Chart 1.31). Specifically, **S96** displayed a new red-shifted absorption band at λ = 348 nm in comparison to **S95** series, which was attributed to enhanced conjugation by phenylenevinylene in the former. Within the series, the different of substituents had negligible effect on both absorption and emission profile. All the dyes exhibited good to excellent fluorescence quantum yield in the range of 0.70-0.95.

The synthesis and excited state dynamics of a series of light-harvesting antenna molecules **S97-S100** were reported by Dubey *et al.*[113] (Chart 1.32). Notably, an efficient covalent attachment of two identical naphthalimide chromophores to the 1,7-bay positions of perylene-3,4,9,10-tetracarboxy derivatives *via* phenoxy attachment was performed. All derivatives were found highly stable having rigid structure with negligible electronic communication between the donor and acceptor components. However, for the reference dyes, **S98a** and **S100a** exhibited red shift absorption profile due to stronger donor strength compared to **S97a**. In contrast to **S97**, **S98** exhibited a bathochromic shift ($\Delta\lambda$ = 39 nm) due to enhanced electronic richness. The dyes **S97-S100** displayed a linear trend within the series and profile was found to be sum of the two chromophoric units (naphthalimide and perylene core) due to the non-chromophoric interactions in the ground state. Further, it was revealed that the donor and acceptor configuration results in an

efficient overlap of optical properties by the FET. The electrochemical studies further supported the lack of conjugation within the series of dyes as the oxidation potential for these dyes were quite similar to those of the reference dyes **S97a** and **S98a**. However, the reduction potential of **S100** was shifted towards positive potential (-1.09 eV) suggesting more electron deficiency of the core than other analogs **S97-S99**.

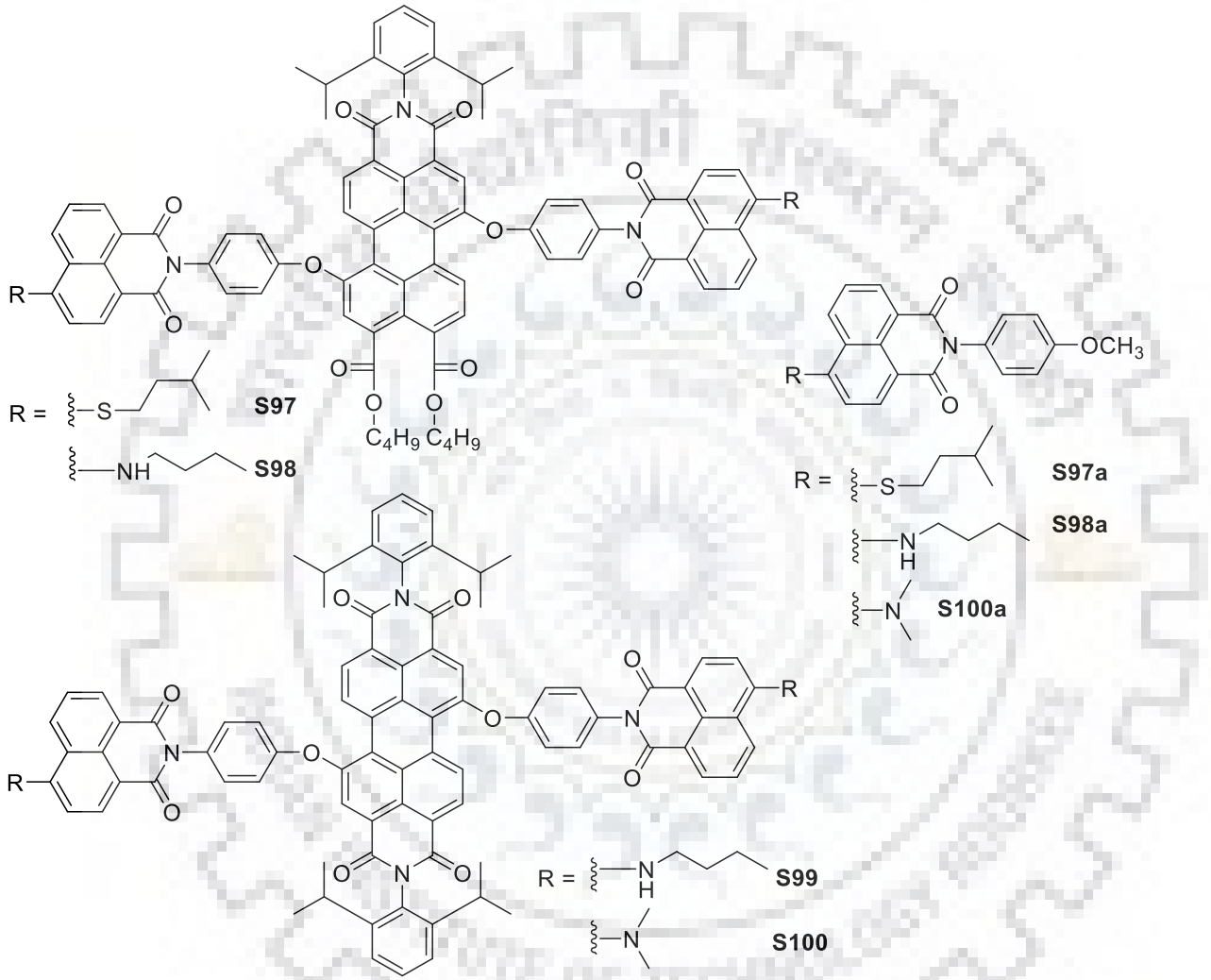

Chart 1.32 Structures of naphthalimide triads and reference derivatives (**S97-S100**)

Wang *et al.*[114] reported a series of pyrazoline-naphthalimide hybrids **S101-S104** and explored their photophysical properties as potential hole-transporting materials in OLEDs (Chart 1.33). In contrast to **S101**, the introduction of substituents on phenyl group resulted in ca. 10 nm red shift in the absorption spectrum. Similarly, the dye **S104** exhibited a red-shifted absorption band at 476 nm, attributable to an increased electron delocalization which was also reflected in the emission spectra. **S104** displayed emission at 548 nm which experienced a bathochromic shift (43 nm) relative to that of compared to **S101** due to enhanced pronounced electronic delocalization.

This was in contrast to the photophysical properties of **S103**. Both **S102** and **S103** displayed emission at 516 and 513 nm which was hypsochromically shifted than **S104**. All the dyes exhibited a reversible oxidation wave which was shifted positively from 1.48 (**S102**) to 1.39 V (**S104**) due to ease in oxidation. The dyes possessed HOMO and LUMO energy levels in the range of 5.79-5.88 eV and 2.41-2.65 eV, respectively which was found similar to that of hole transporting material, 4,4'-bis(1-naphthylphenylamino)biphenyl.

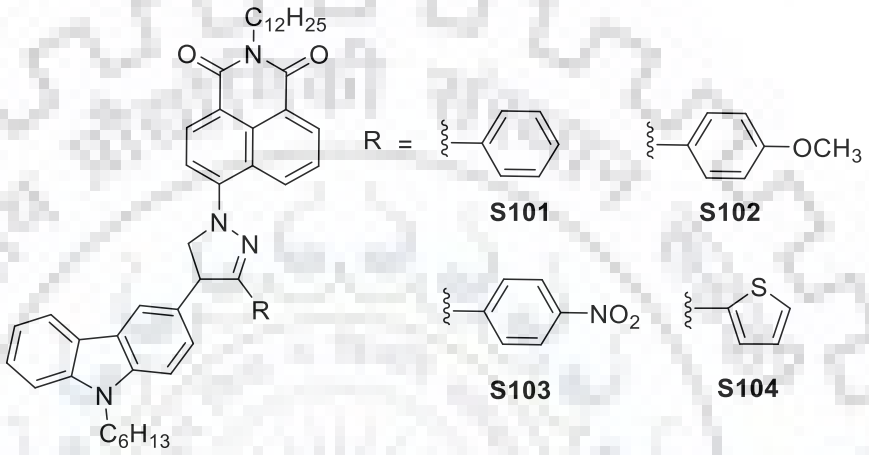

Chart 1.33 Structures of pyrazoline-naphthalimide hybrids (**S101-S104**)

1.3.4 Vinyl-linked naphthalimide-based dyes

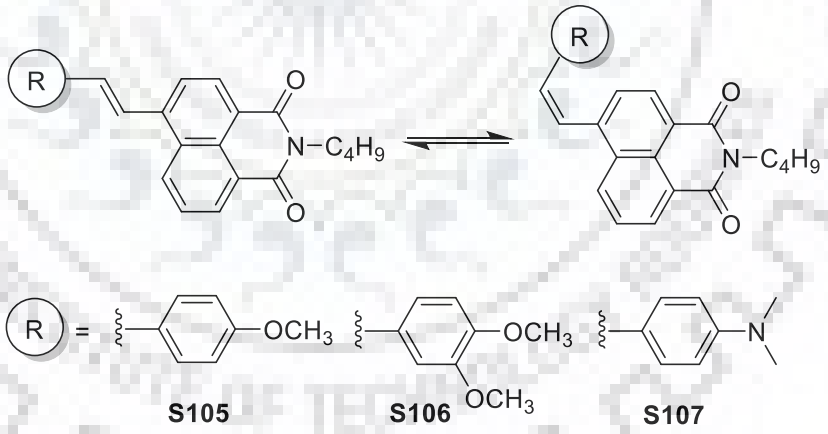

Chart 1.34 Structures of *E-Z* isomeric 4-styryl-1,8-naphthalimide derivatives (**S105-S107**)

Arkhipov *et al.*[115] reported a set of *E-Z* isomeric 4-styryl-1,8-naphthalimide derivatives (**S105-S107**) to study their photochromic and fluorescence properties (Chart 1.34). The dyes displayed a molecular geometry change from *E* to *Z* isomer without altering conjugation accompanied by a transition of the structure into a non-planar state. **S105-S107** displayed a broad CT absorption band which was in agreement with increasing donor strength. Thus, **S107** exhibited a 90 nm bathochromic shift compared to **S105**. Similar trend was followed in emission spectra.

S105 and **S106** displayed emission band at λ = 405 and 412 nm which are blue shifted compared to emission band of **S107** observed at 460 nm. It is interesting to note that **S107** did not show any change in the fluorescence quantum yield either in pure *E*-form or *Z*-form. However, unlike **S107**, the methoxy substituted dyes, **S105** and **S106**, exhibited a decrease in the quantum yield by 1.2-fold, which could be ascribed to the tremendous change in the molecular geometry relative to **S107**.

Panchenko *et al.*[116] studied the effects of solvent and molecular structure on the photophysical properties of styrylnaphthalimides-based dyes **S105-S107** (Chart 1.34). The dyes were capable to penetrate cell membranes, demonstrated AIE properties and used as cell imaging agents. Due to an increase in electron-donating character of styryl fragment from **S105** to **S107** caused a red shift in both the absorption and emission spectra. All the dyes demonstrated a positive solvatochromism while an analysis of the Stokes shifts on the polarity of the solvent using Lippert-Mataga equation allowed determining the change in the dipole moment upon excitation. Based on the transient absorption spectra and time-resolved fluorescence measurements, the presence of two different emissive states was proved. Further, the primarily formed planar local excited state dominated in the non-polar solvents like cyclohexane and toluene where it relaxed mostly through fluorescence and *E,Z*-isomerisation pathways. Thus, the main relaxation pathways of the local excited singlet state of **S105-S107** were radiative decay, TICT state and *E,Z* photoisomerization.

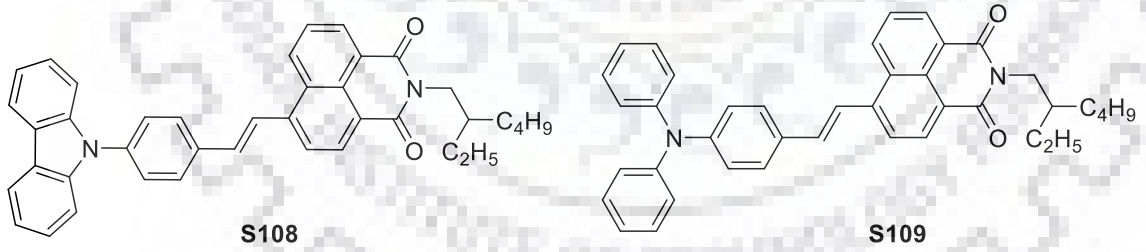

Chart 1.35 Structures of D-A conjugated 4-styryl-naphthalimide derivatives (**S108-S109**)

Ren *et al.*[117] demonstrated the effect of coplanarity of donor unit on the flash memory storage using typical D-A conjugated molecules **S108** and **S109** (Chart 1.35). The dye **S109** displayed ca. 55 nm red-shifted absorption profile at 457 nm due to strong D-A interactions. Both the dyes exhibited a 10 nm bathochromic shift in the film state. Moreover, **S108** displayed more broadening in the absorption spectra than **S109,** attributable to its molecular locking. Both **S108** and **S109** displayed one irreversible oxidation at 1.42 and 0.98 V corresponding to the oxidation of carbazole and triphenylamine unit, respectively. Compared to **S108** (-5.66 eV), **S109** exhibited

a lifted HOMO level at -5.22 eV due to an enhanced electron richness. Further, the LUMO level of **S109** was found high lying at -3.03 eV than a deep seated LUMO of **S108** at -3.15 eV. Device fabricated using **S108** was tested to have a turn-on voltage between -2.2 V to -2.6 V, and turn-off voltage between 2.6 V-3.0 V. However, **S109** was found to have a low turn on voltage and high turn-off voltage. In terms of device stability, **S108**-based device displayed a better stability as well as reproducibility than that of **S109**, attributable to its coplanar structure and ease in the film formation.

Gudeika *et al.*[118] synthesized D-A dyes **S110-S112** comprising triphenylamine and naphthalimide linked by vinyl group (Chart 1.36). The dyes displayed bathochromic and hyperchromic absorption bands by increasing the number of 1,8- naphthalimide unit. The most red shifted broad absorption band was ascribed to the CT within the molecule. All derivatives exhibited a broad structureless emission band due to an excited ICT state. The thereotical calculations suggested that the HOMO was localized on triphenylamine while LUMO was delocalized unevenly on naphthalimide unit. The HOMO energy level of the dye **S110** was high lying at -5.18 eV compared to dye **S112** at -5.25 eV, depending upon the increase in the number of naphthalimide moiety. However, the electron affinity of the dyes remained intact ~-3.06 eV, and were stabilized with respect to hydrazine dyad (**S111**) and triad (**S112**) analogs.

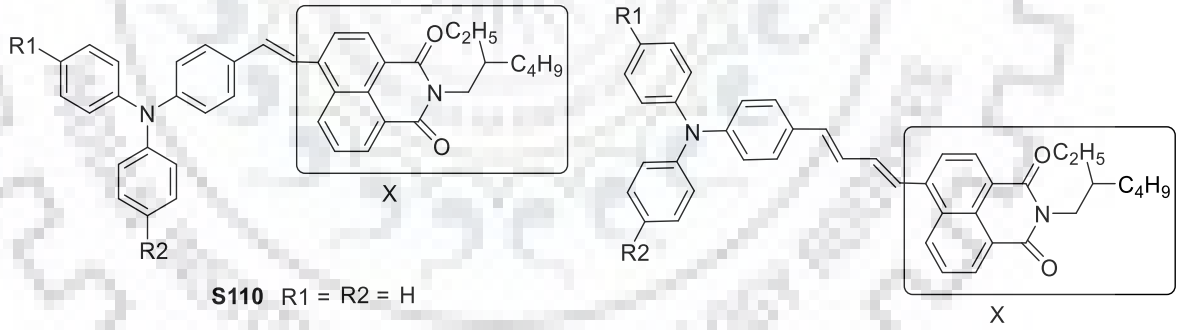

S110 R1 = R2 = H

S111 R1 = H R2 = X

S112 R1 = R2 = X

S113 R1 = R2 = H

S114 R1 = H R2 = X

Chart 1.36 Structures of D-A triphenylamine and naphthalimide-based dyes (**S110-S114**)

In successive work, the solution processable D-A-based small molecules **S113** and **S114** comprising triphenylamine and naphthalimide were synthesized using heck coupling reaction by Gudeika *et al.*[119] (Chart 1.36). Due to pronounced D-A character, the compounds showed positive solvatochromic fluorescence with significant reduction of the emission yield. The HOMO values of the compounds as measured by the CV were calculated to be -5.22 and -5.27 eV while LUMO as -3.20 and -3.18 eV. On the other hand, the theoretical computed HOMO and LUMO

were found to be contributed from the triphenylamine-olefinic linkages and naphthalimide moieties, respectively confirming the ICT in both compounds.

1.3.5 Ethynyl-linked naphthalimide-based dyes

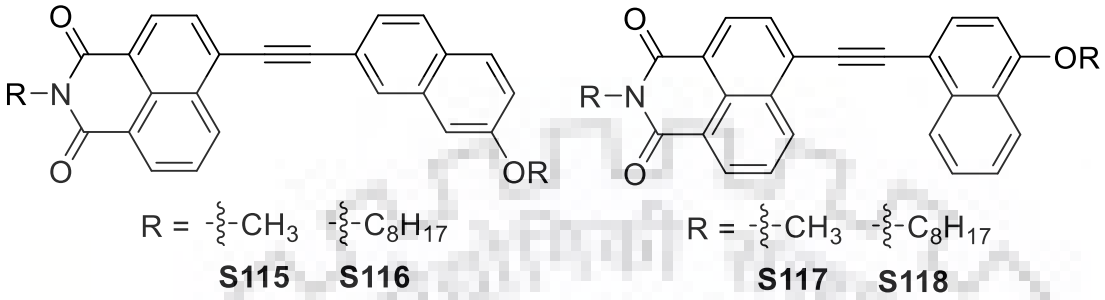

Chart 1.37 Structures of monoalkoxynaphthalene–naphthalimide D-A dyes (**S115-S118**)

Peebles *et al.*[120] studied and illustrated the stimuli-responsive properties of a set of aromatic conjugated monoalkoxynaphthalene–naphthalimide D-A dyes **S115-S118** (Chart 1.37). Among the set of dyes, **S115** and **S118**, showed a difference in solid-state emission attributed to rate of solvent evaporation. However, the other dyads, **S116** and **S117** showed only one color for both evaporation rates. It is interesting to mention that the dyad **S118** displayed mechanochromic, thermochromic and vapochromic stimuli-responsive behavior in the solid-state. This reversible anonymous behavior of **S118** was evaluated as a consequence of free molecular rotation, configuring orange crystalline solid in thermodynamically stable head-to-head fashion relative to that of yellow crystalline head-to-tail packing in **S116**.

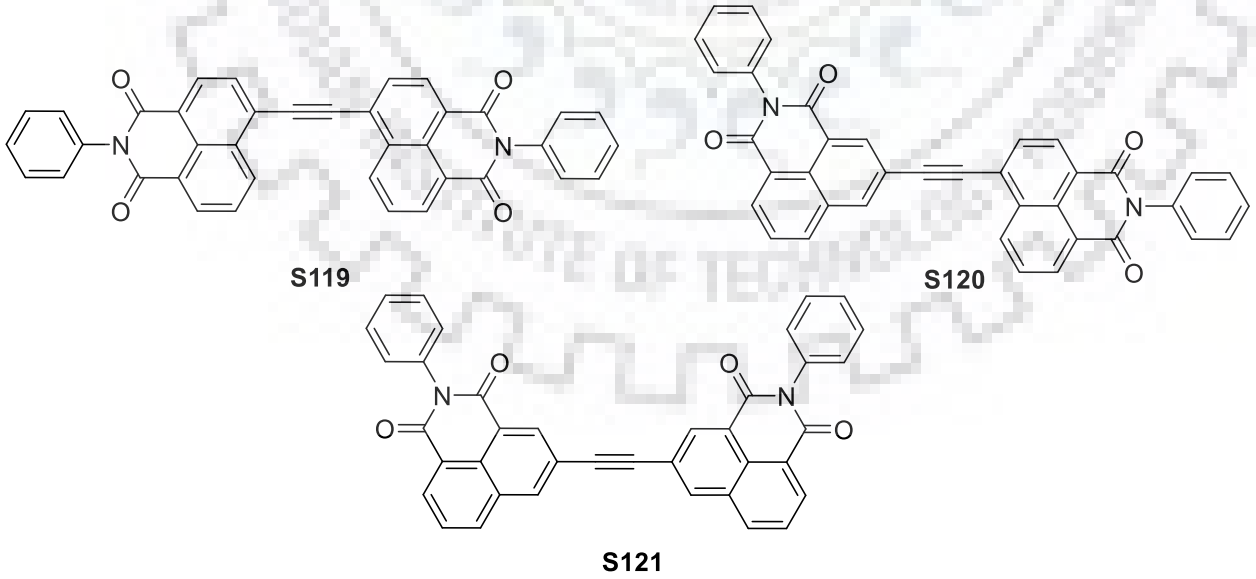

Chart 1.38 Structures of bis-naphthalimide dyes (**S119-S121**)

Kim *et al.*[121] reported three blue-emitting bisnaphthalimide dyes **S119-S121** differing in linking mode (Chart 1.38). **S121** displayed a 15 nm blue shifted absorption profile compared to **S119** and **S120** due to non-conjugating skeleton which was ambiguous to interpretation of data by the researchers. However, the dyes exhibited an emission at the same wavelength. The electron density was localized at the HOMO level and delocalized at LUMO energy level. The HOMO energy level was altered from -6.22 to -6.26 and -6.18 eV for **S119**, **S120**, and **S121**, respectively. The LUMO level was raised to -2.80 eV for **S121** compared to -3.14eV for **S119**. It was inferred that para-linked bis-naphthalimides were quite effective for extending π-conjugation than those of meta-linked dyes.

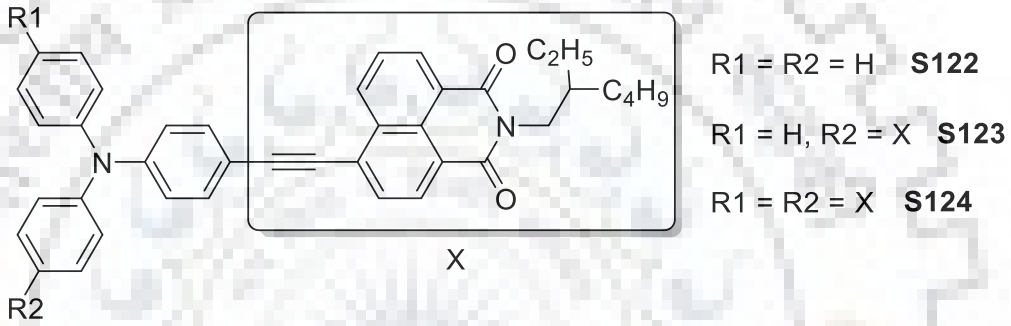

Chart 1.39 Structures of bis-naphthalimide dyes (**S122-S124**)

In yet another work, Gudeika *et al.*[122] investigated the influence of ethynyl linkages on the photophysical, electrochemical and charge-transporting properties of the triphenylamine and naphthalimide-based materials **S122-S124** (Chart 1.39). The photophysical and charge transporting properties were influenced by the ethynyl bridging since it facilitated planarization of the molecules and induced effective charge separation. Similar to the previously reported dyes, **S36-S39**, the ICT band in **S122-S124** also appeared at 450-470 nm and red-shifted by 20-40 nm relative to those of single bond linked derivatives. The intensity of ICT band is independent of number of terminal groups indicative of lack of inefficient delocalization. This was supported by the uneven electron density spread over electronically different naphthalimide in terms of LUMO molecular orbital of **S124**. The emission spectra of **S122-S124** were centered and displayed a positive solvatochromism of Δ80-90 nm indicative of polar excited state. However, the fluorescence quantum yield of **S124** droped drastically due to the pronounced ICT. The DFT computed MOs revealed that the HOMO was localized entirely on the triphenylamine core and linkers while LUMO was contributed by naphthalimide core with some extension to linkers. Thus, both HOMO and LUMO electron density was spread on the ethynyl linkage which resulted in

efficient CT and charge transportation. The energy levels of synthesized dyes were found to be stabilized with an increase in the naphthalimide units. In comparison to **S122** (0.68 V), the oxidation potential of **S124** was cathodically shifted by 50 mV, displaying the poor electronic richness of triphenylamine. A shift in the reduction potential to -1.51 V for **S124** (110 mV less than that of **S122**) was attributed to an increase in the electron deficiency of the molecule. The dyes exhibited excellent thermal stabilities upto 470 °C which were found greater than those of directly linked (**S36-S39**) or vinyl-linked dyes (**S110-S112**). Further, the thermal stability increased with increase in number of naphthalimide units. The influence on the hole mobilities was clearly observed with mobilities higher than ca. 10^{-3} $cm^2 \cdot V^{-1} \cdot s^{-1}$ for dye **S122** and 10^{-2} $cm^2 \cdot V^{-1} \cdot s^{-1}$ for **S123** which is graeter than derivatives with the single-bond and double bond-linkages between the two core. Thus, the high fluorescence quantum yields, high thermal stability and good hole mobilities of **S122-S124** make them suitable candidates for hole transporting and emitting materials for OLED applications.

Liu *et al.*[123] synthesized a series of carbazole-naphthalimide hybrids **S125-S129** to understand the structure property relationship (Chart 1.40). The dyes were designed to improve the fluorescence yields and charge transport properties. The dyes absorbed in range of 400-450 nm due to π–π^* transitions within the skeleton. Among the set of dyes, **S125b** displayed blue shifted absorption ($\Delta\lambda$ = 36 nm) compared to the dyes with C-3 linked carbazole unit, presumably, due to the pronounced CT in the later attributable to the facile electronic communication. However, dyes **S129a** and **S129b** displayed a structured absorption band due to the molecular rigidity and lack of CT. All hybrids displayed green emission with a centered emission band at 540-560 nm. It is worth to mention that all the dyes except **S125a** and **S125b** exhibited red shift emission profile attributed to the facile intermolecular interactions forming aggregates. **S126a** and **S126b** restricted formation of aggregates due to N-9 substitution of carbazole. The dyes could be suitably used as hole-transporting materials in OLEDs as they displayed HOMO energy level in the range of -5.13 to -5.66 eV, similar to typically used hole transporting NPB.

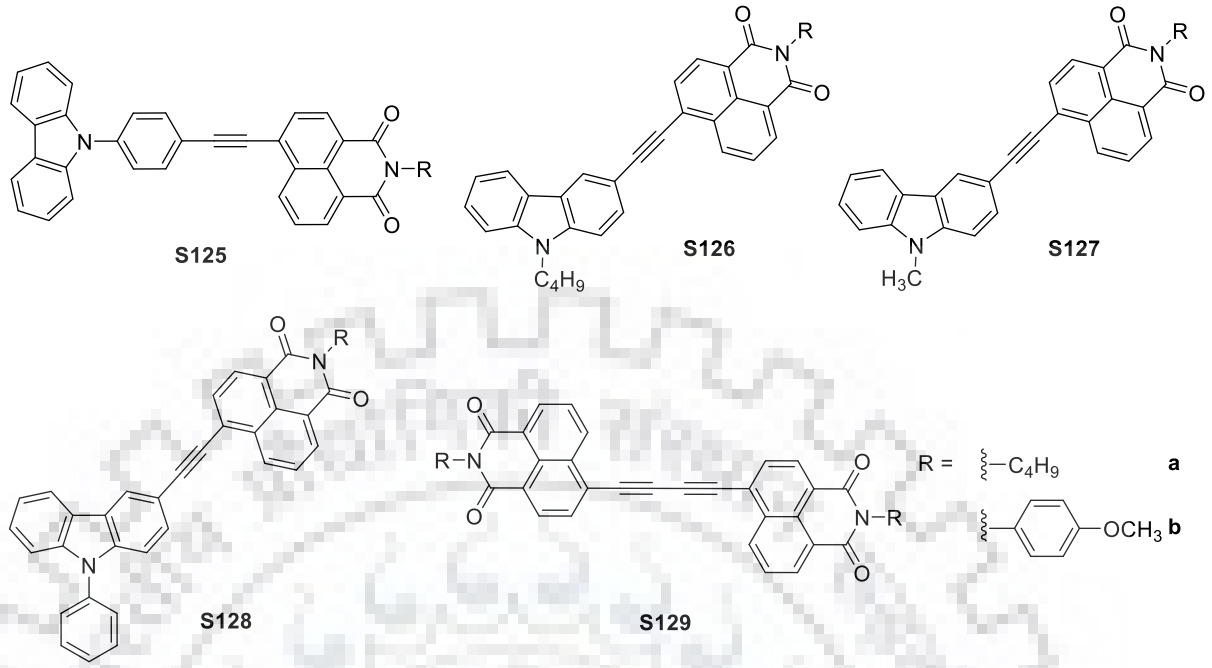

Chart 1.40 Structures of carbazole-naphthalimide hybrids (**S125-S129**)

Cao *et al.*[124] reported highly planar molecule **S130** and **S131** based on 4-ethynyl-1,8-naphthalimide having different alkyl chain length and possessing gelation properties (Chart 1.41). The planarity of the conjugated backbone facilitated intermolecular interactions, which were responsible in the formation of organogels. The structured absorption bands at 390 nm and 423 nm were observed for the dyes, arising from the naphthalimide core, while appearance of a new band at 360 nm in the gel state indicated H-type aggregation due to π−π intermolecular stacking. In solution, the dyes displayed a strong emission at 470 nm with quantum yield of ~50%. However, the gelators exhibited ca. 80 nm red-shifted fluorescence bands along with a new shoulder in high energy region. Interestingly, a switchable drastic fluorescent change from blue to yellow was observed between solution and gel state. Furthermore, the excited state lifetime of gelators was ten times greater than that in the solution due to the formation of aggregates.

Thompson *et al.*[125] reported two D-A bridged dyes **S132** and **S133** having meta- and para-substituted π-spacer between the carbazole and naphthalimide moiety (Chart 1.41). It was observed that the para- substitution in **S133** was beneficial over meta- conjugation in **S132** and resulted in a better CT interaction in the ground state. Though dyes were found to be independent of solvent polarity in the ground state yet displayed a positive solvatochromism in the excited state. The meta- linked dye resulted in electronic coupling in the excited state facilitating a facile electron transfer.

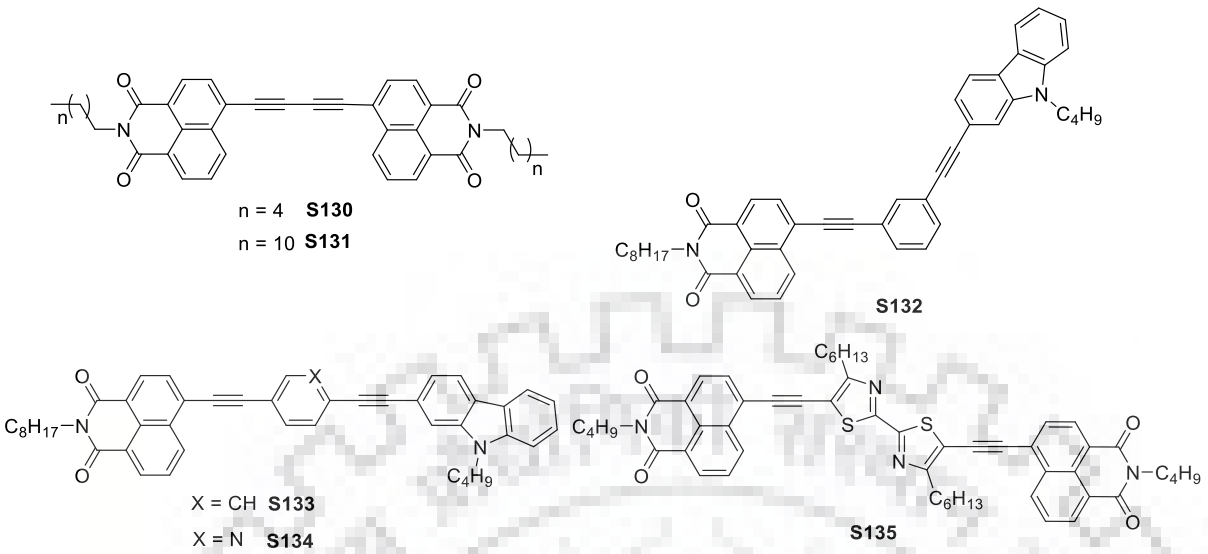

Chart 1.41 Structures of bis-naphthalimide dyes (**S130-S135**)

In yet another work, Wang *et al.*[126] synthesized an analogous dye **S134** by replacing the phenyl linker (**S133**) with a pyridyl linker, and used it in a memory device (Chart 1.41). Interestingly, the linker replacement shifted the electron density from carbazole to the naphthalimide moiety, highlighting the role of spacer in distribution of electron density as well as stabilizing the HOMO and LUMO energy levels. In the film state, **S134** exhibited a red shift in absorption profile by 15 nm in comparison to broad π-π* transition at 398 nm in solution. This clearly indicated that the dye underwent molecular rearrangement. Further, the pyridyl acetylene-linkage facilitated molecule assembly into one-dimensional molecular tapes *via* hydrogen-bonding and afforded well-ordered crystal structures due to the molecular planarity. The fabricated memory device with configuration of ITO/**S134**/Al displayed non-volatile WORM memory behavior.

Maragani *et al.*[127] reported a typical A-A-A conjugated planar systems **S135** comprising of bis-thiazole and naphthalimide as acceptors (Chart 1.41). The dye displayed a strong absorption band at 450 nm corresponding to π-π* electronic transitions. Two reversible reduction waves at -1.08 and -1.65 V were attributed to reduction of bisthiazole and naphthalimide. The HOMO of the dye was stabilized to -5.85 V due to electron-deficiency of the core while LUMO was located at -3.24 V. The major contribution of absorption band observed at 428 nm was supposed to arise from HOMO-1 to LUMO+1 corresponding to π-π* electronic transitions.

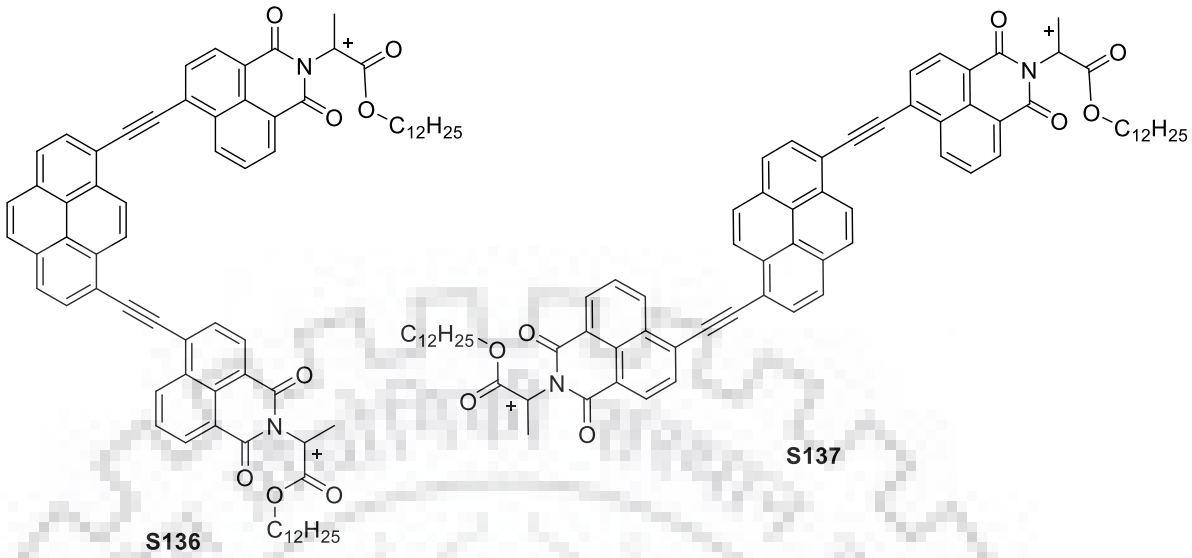

Chart 1.42 Structures of pyrene-naphthalimide-based dyes (**S136-S137**)

Liu *et al.*[128] synthesized two chiral 1,8-naphthalimide-based pyrene enantiomers **S136** and **S137**, displaying circularly polarized luminescence induced by self-assembly (Chart 1.42). In binary solvent system both dyes displayed an emergence of new red-shifted band on aggregation. However, in solution the emission band at 541 nm was quenched, and bathochromically shifted by 70 nm attributable to the *J*-aggregation. The strong π-π* interactions between pyrene and 1,8-naphthalimide achieved a rigid self-assembly structure in aggregated state and exhibited a higher circularly polarized luminescence signals.

1.3.6 Star-shaped naphthalimide-based dyes

Jin *et al.*[129] designed and computed a set of star-shaped D–π–A type small molecules **S138-S141** comprising of 1,8-naphthalimide as central core flanked by different aromatic heterocyclic donors (Chart 1.43). These modeled structures were investigated as emitters and solar cell materials to study their photophysical and charge transport properties. From the computed absorption spectra, it was revealed that molecules having different electron-rich aromatic heterocyclic end groups and spacers tend to red shift the absorption bands, narrowing the band gap. From the data, it was depicted that the HOMO-2 → LUMO transitions was responsible for the origin of major absorption band. These transitions were assigned to the CT from electron-rich moieties to naphthalimide unit. The computed dyes showed a significant solvent-dependent absorption and emission spectra attributable to the bipolar nature of the dyes. The introduction of the electron-deficient end groups such as benzothiadiazole and others helped to stabilize CT.

Further, the ethyne π-bridge and benzothiazole/ benzothiadazole as end groups increased the hole transfer due to the enhanced molecular planarity.

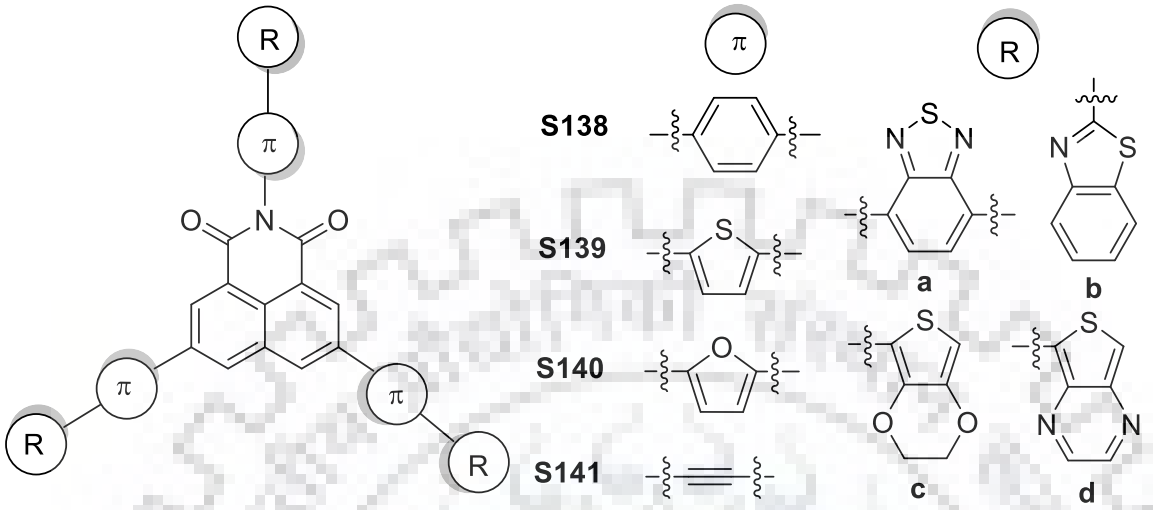

Chart 1.43 Structures of star-shaped D–π–A type small molecules (**S138-S141**)

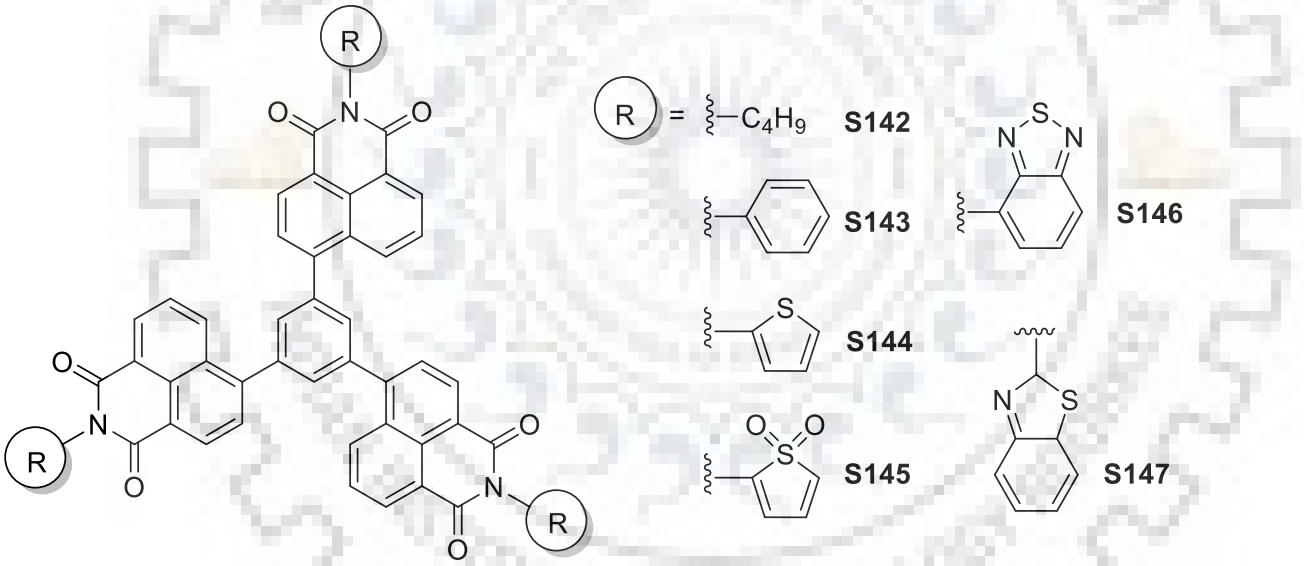

Chart 1.44 Structures of star-shaped benzene cored naphthalimide derivatives (**S142-S147**)

Jin[130] performed theoretical investigation of star shaped benzene-cored naphthalimide derivatives **S142-S147** having different substituents at imidic position (Chart 1.44). They reported their optical, electronic, and charge transport properties as potent emitters in OLEDs. For all the dyes LUMO was composed of naphthalimide with major contribution of 92.6% while the distribution of HOMO depended on the type of imidic chromophore. For **S142**, **S143** and **S146** HOMO was spread over naphthalimide and central benzene core with minor contributions from imidic cores. In contrast, the HOMO electron densities of **S144** and **S146** were localized over

substituent groups with contribution of >95%. However, for **S145** HOMO was found diffused to naphthalimide and substituent group. Depending on the distribution of energy levels, the absorption band corresponded to HOMO-1 to LUMO for **S142** while for **S143-S147** it was from HOMO to LUMO and HOMO to LUMO+1 along with or without HOMO to LUMO+2. Further, the absorption spectra remain unaltered and observed at 365 nm since imidic substitution was orthogonal in nature and did not contribute to conjugation enhancement. However, **S144-S147** displayed bathochromic shift of 5, 27, 8 and 53 nm respectively compared to emission spectra of **S142-S143**. These dyes displayed electron reorganization energy (λ_e = 0.110 – 0.180 eV) larger than Alq_3 (λ_e = 0.276 eV) which means that they are suitable candidates as electron transporting layer. Further, **S143-S147** exhibited a larger value of hole reorganization energy (λ_h = 0.292 – 0.328 eV) compared to *N*,*N*'-diphenyl-*N*,*N*'-bis(3- methylphenyl)-(1,1'-biphenyl)-4,4'- diamine which is typical hole transport material (λ_h = 0.29 eV). Thus, dyes were proved as promising charge transport materials in OLEDs.

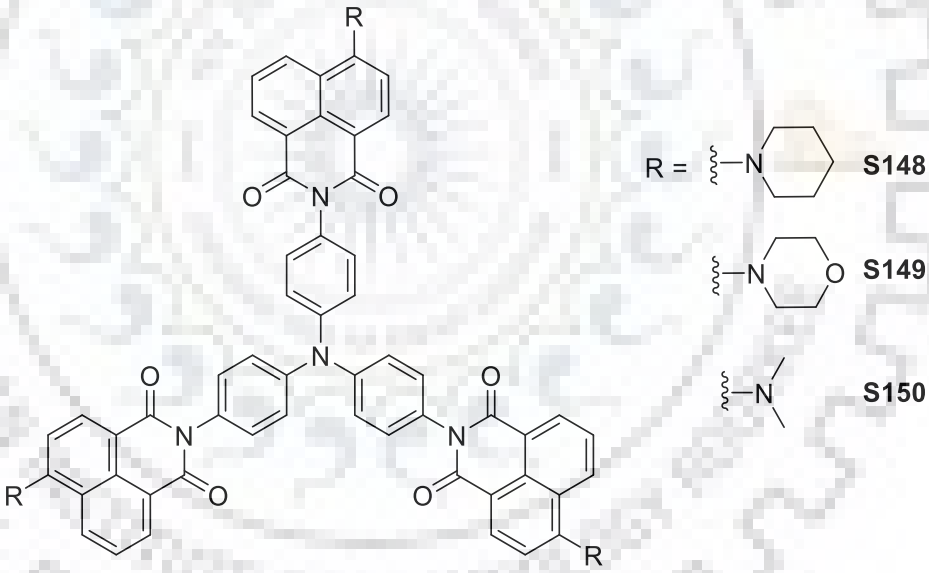

Chart 1.45 Structures of bipolar star-shaped naphthalimide derivatives (**S148-S150**)

Zhu *et al.*[131] synthesized and studied bipolar star-shaped naphthalimide derivatives **S148-S150** comprising triphenylamine as a central core and naphthalimide functionalized at imidic position (Chart 1.45). The dyes were suitably characterized and exhibited absorption bands at 310 nm and at 400 nm originating from triphenylamine and naphthalimide units, respectively. Due to the more electron donating nature of the substituent at 4th position of naphthalimide, **S148** and **S149** displayed red shift spectra. The existence of strong fluorescence quenching for the naphthalimide moiety bonded to triphenylamine unit was observed due to the PET progress. The

dyes exhibited a trend in reversible oxidation peaks, which was attributed to the ease in oxidation of triphenylamine influenced by substituent on naphthalimide. Among the set of dyes, **S150** possessed a high lying HOMO at -5.36 eV due to the anodically shifted oxidation at 1.08 V compared to **S148** and **S149** (1.15 and 1.19 V).

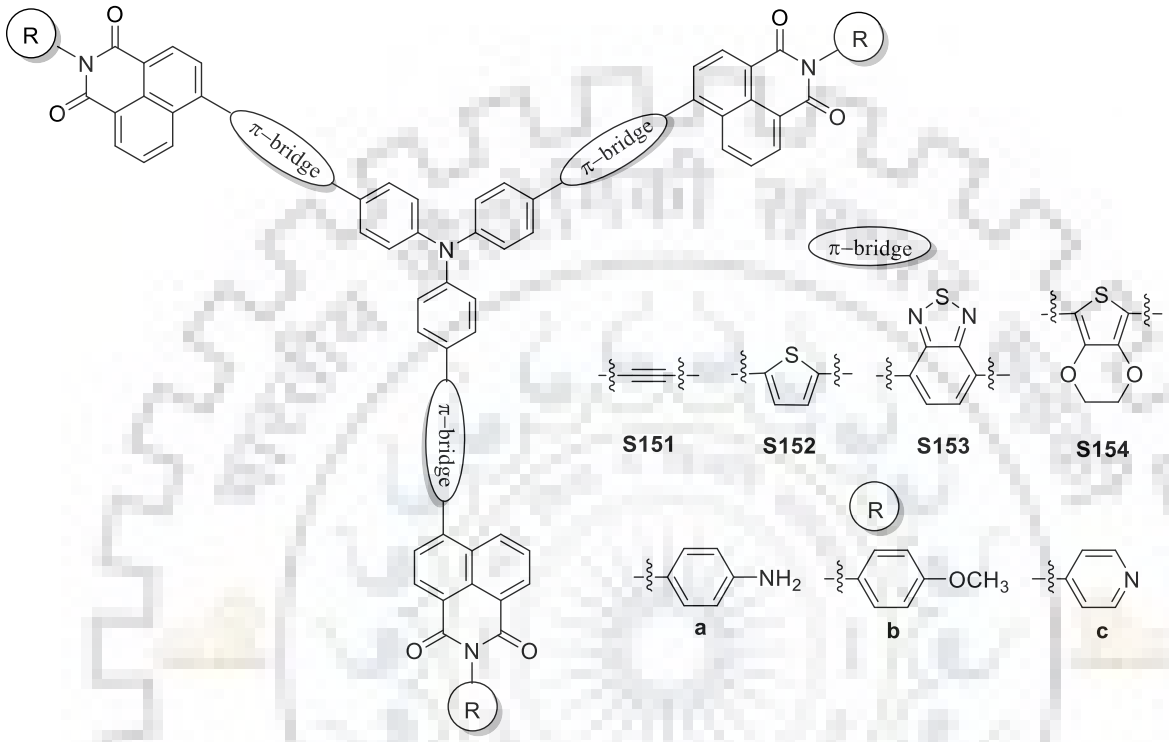

Chart 1.46 Structures of D–π–A star-shaped triphenylamine and naphthalimide-based derivatives (**S151-S154**)

Jin *et al.*[132] modeled a set of D–π–A star-shaped triphenylamine and naphthalimide based derivatives **S151-S154** with different π-bridges to explore their optical, electronic, and charge transport properties as potential OSC materials (Chart 1.46). The computational data revealed that these materials can act as ambipolar materials. In all the dyes, the HOMOs were localized on the triphenylamine and conjugating bridges with little contribution (ca. 23%) from naphthalimide. However, the LUMO resided mainly on naphthalimide with 77% contributions for dyes **S151**, **S152** and **S154** dyes. In **S153**, the LUMO was also spread over benzothiadiazole as conjugating bridge. The MO analysis indicated that for dyes **S151**, **S152**, **S154** the electronic transitions occurred from HOMO to LUMO i.e. triphenylamine and conjugating bridges to terminal naphthalimides. However, for set of three dyes **S153** the CT was from triphenylamine to linker (benzothiadiazole) and naphthalimide. Further, these computed structures were considered as good electron transfer agents since they displayed a smaller λ_e than that of typically used Alq_3

(0.276 eV). Notably, the introduction of ethynyl bridge in **S151** set of dyes resulted in an improved charge transportation.

It is well documented that star-shaped materials inherent facile solution processibility and high solubility compared to linear D-A materials. Wu *et al.*[133] explored two star-shaped donor-acceptor conjugated molecules **S155** and **S156** based on triphenylamine (D), thiophenes (spacer) and 1,8-naphthalimide (A) as storage materials (Chart 1.47). The studies revealed that the difference in the length of the spacer influenced the switching on-off properties of the storage devices by controlling extend of CT. The dyes displayed efficient CT from D to A. Both of the dyes exhibited a non-volatile WORM memory characteristic and excellent thermal stability of upto 450 ˚C. The DFT calculations showed that HOMO was localized on triphenylamine and thiophene while LUMO was localized to naphthalimide. In contrast to dye **S155**, **S156** exhibited an irreversible WORM memory storage due to the deep trapping barrier of electron delocalized on naphthalimide unit, and stabilized CT. An irreversible WORM memory could also be contributed due to the highly twisted conformation of molecule which favors spatial charge localization.

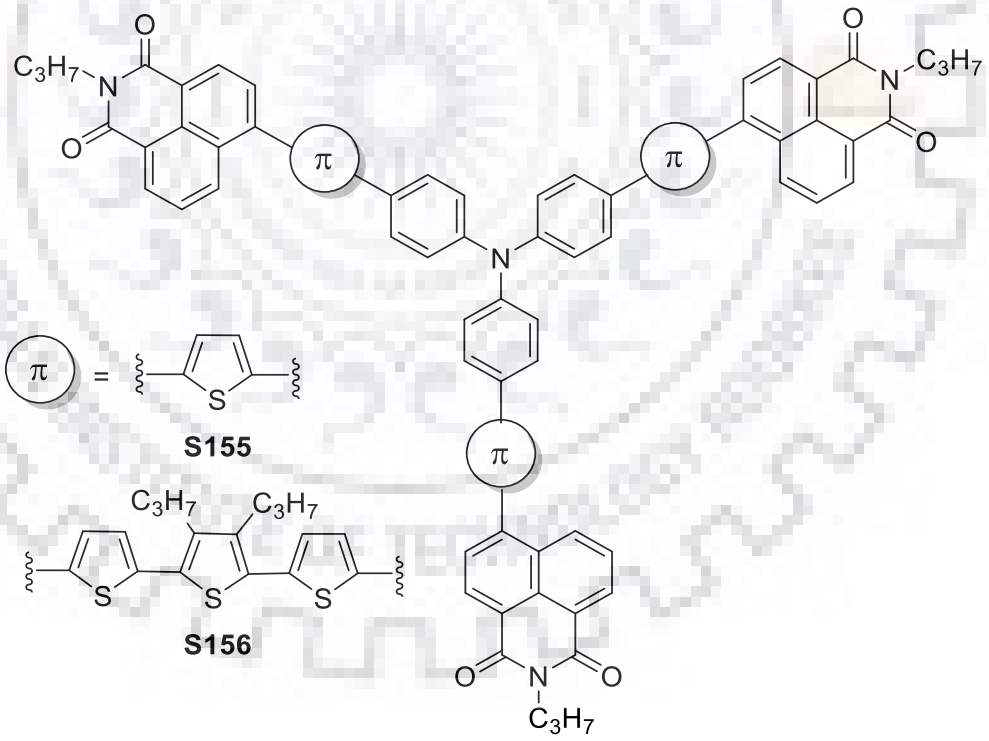

Chart 1.47 Structures of star-shaped donor-acceptor conjugated molecules (**S155-S156**)

1.4 Naphthalimide-based materials for electronics

1.4.1 Naphthalimide dyes as emitter or electron transporting material in OLEDs

Since the breakthrough work by Tang and Slyke in 1987,[43] OLEDs have grabbed researcher's interest to develop effective materials. OLED is a double charge injective diode which involves injection of electrical charge carriers with both polarities from the electrodes into the organic layers, subsequent transport and recombination of the charge carriers resulting in the formation of excitons followed by luminescence emission from emitting layer. Since the mobility of charge carriers is not same i.e. holes move faster than electrons, it is difficult to achieve better performance from single layer devices or two layer devices due to recombinational losses. Therefore, in order to attain better charge balance and high performance of the device, it is necessary to introduce additional layers such as ETL and HTL into the device architecture. The performance of OLED device is characterized by turn-on-voltage, current density, brightness, luminescence efficiency, and external quantum efficiency. The organic charge transporting material should meet the following requirements for better performance in OLEDs. It should have suitable HOMO and LUMO energy levels relative to the electrodes and to the adjacent layers for better injection of charge carriers and efficient transport and recombination possess. A high glass transition temperatures (T_g) and should be thermally and electrochemically stable. Furthermore, for the efficient flow of charges and working of device it is required that HTL should have a low IP and low EA while electron deficient molecules with high IP and high EA act as ETL as well as hole blocking materials. While, for an organic emitting material it should possess suitable energy levels for the efficient charge transportation from the adjacent layers, high thermal stability and high Φ_F. Herein, we have discussed naphthalimide containing chromophores as emitters, electron transporting materials and as host for PhOLEDs and FOLEDs.

Kolosov *et al.*[134] have synthesized four naphthalimide derivatives **E1-E4** for PhOLEDs doped with Ir-based complexes such as btpIr, btIr and Irppy (Chart 1.48). These naphthalimide derivatives were utilized as electron-transporting and doped luminescent layers as well as hole-blocking layers in electrophosphorescence. All the materials displayed a structured violet-blue fluorescence at ~380 nm and phosphorescent bands between 550 and 650 nm. All the dyes exhibited a reversible reduction wave with a potential of -1.55 eV for **E3**. Further, the HOMO and LUMO levels for **E3** were deep seated at -7.3 eV and -3.9 eV respectively which is suitable for them to behave as a good hole blocking layers and electron injecting layer. Two types of devices

were fabricated using these dyes. Type 1 OLEDs utilized them as phosphor-doped emitting layer and hole blocking layer while type 2 device used CBP as host and **E3** as hole blocking layers. The best PhOLED device was fabricated using btpIr doped **E3** with 3.2% as EQE at 6.3 V (Table 1.1).

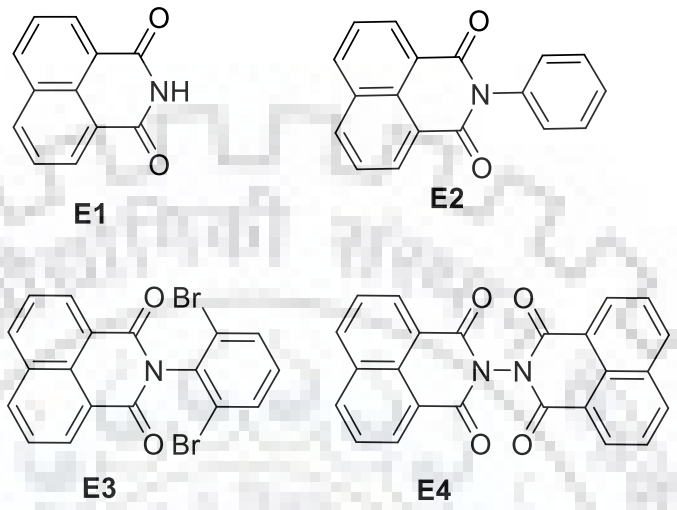

Chart 1.48 Structures of naphthalimide-based dopants and electron transporting materials in PhOLEDs (**E1-E4**)

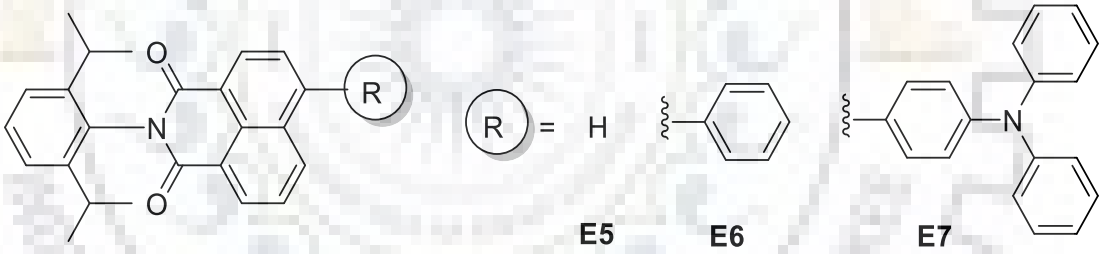

Chart 1.49 Structures of naphthalimide-based dyes for FOLEDs (**E5-E7**)

Zhang *et al.*[135] studied the influence of different substitution at 4th position of naphthalimide **E5-E7** on the photophysical and electrochemical properties as emitters in FOLEDs (Chart 1.49). **E5** exhibited a structured absorption bands arising from π–π* and n–π* transitions. While **E7** displayed two prominent absorption bands at λ = 430 nm and λ = 325 nm attributed to CT from triphenylamine to naphthalimide and π-π* transitions due to localized triphenylamine. However, **E6** exhibited only π-π* transition band at 350 nm and displayed deep blue emission at 416 nm, which was 36 nm red shifted compared to weakly emitting **E5**. **E7** exhibited a yellow emission at 586 nm due to strong CT transitions. In spite of CT emission, **E7** exhibited 57% quantum yield which is twice that of **E6** attributable to suppression of non-radiative decay in former. **E6** and **E7** display suppressed ISC compared to **E5** due to stabilized π-π* triplet state of former. Improvement

in emission intensity is observed for **E6** and **E7** due to conversion of singlet state to radiative π-π* transitions. At low temperature, dyes displayed phosphorescence. The suppression of intersystem crossing in **E6** and **E7** was related to larger ΔE_{ST} (0.66 eV, 0.31 eV) over **E5** (0.02 eV). **E7** displayed high lying HOMO energy level at -5.33 eV due to enhanced electronic richness. 6% doped OLED devices using **E6** and **E7** were fabricated with configuration ITO/PEDOT:PSS(40 nm)/NPB(40 nm)/TCTA(5 nm)/Emitter(20 nm)/TPBi(35 nm)/LiF(1 nm)/Al(100 nm) displayed in Table 1.2. **E6** displayed CIE coordinates (0.15, 0.07) corresponding to deep blue emission. **E6** based device displayed poor luminance of 948 cd m^{-2} and EQE of 1.58%. Device fabricated using **E7** exhibited superior performance with low V_{on} of 3.1 V, luminance of 64344 cd m^{-2} and EQE of 5.96%. Also, even at high brightness of 30000 cd m^{-2} device displayed a good efficiency indicating small efficiency roll off.

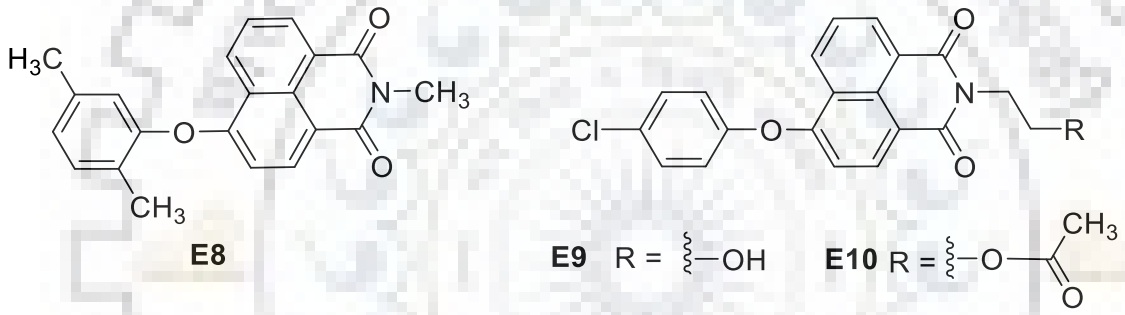

Chart 1.50 Structures of naphthalimide-based emitters for OLEDs (**E8-E10**)

Triboni *et al.*[136] synthesized and characterized a 4-(2-fenoxi-*p*-xileno)-*N*-methyl-1,8-naphthalimide **E8** as emitter in FOLED (Chart 1.50). It showed red shifted absorption band compared to unsubstituted 1,8-naphthalimide **E1** at 380 nm and a broad structureless emission band at 456 nm. The molecule displayed a reversible reduction wave at -1.0 V and an irreversible oxidation peak at 1.7 V arising from the reduction of naphthalimide and oxidation of substituent at 4^{th} position of the core. The molecule possessed HOMO and LUMO energy levels at 6.1 eV and 3.4 eV. The material was used as an emitting layer in OLED with device structure as ITO/PEDOT:PSS/**E8**/Al and CIE coordinates of 0.21, 0.31 lying in the blue region with an EL peak at 465 nm.(Table 1.2).

Ulla *et al.*[137] synthesized parachlorophenoxyl substituted two naphthalimide based electron transporting emitter materials **E9** and **E10** for OLEDs (Chart 1.50). Both the dyes displayed ICT absorption band at 362 nm due to typical donor-acceptor interactions. A 10 nm red shifted absorption band in thin film was observed for dyes arising from intermolecular interactions within the skeleton. **E10** exhibited a quasi-reversible reduction wave which was 60 mV cathodically

shifted than **E9** with reduction potential at -1.47 eV. Also, the oxidation potential of **E10** was positively shifted by 30 mV compared to **E9**. The dyes exhibited deep seated HOMO at 6.2 eV and low lying LUMO energy levels at 3.33 eV and 3.39 eV for **E9** and **E10**, respectively. The dyes were explored as electron transporting and emitting materials with different OLEDs configurations. Type 1 device FOLEDs were fabricated using device architecture of ITO (120 nm)/NPD (30 nm)/**E9-E10** (35 nm)/BCP (6 nm)/Alq_3 (35 nm)/LiF (1 nm)/Al (150 nm) using dyes as non-doped emitter (Table 1.2). Device using dye **E10** gave superior performance than **E9** with luminance of 1072 cdm^{-2} and EQE of 0.47%. In other type of FOLEDs devices, the dyes were used as emitting materials along with a hole transporting material F4TCNQ with device configuration of ITO (120 nm)/F4TCNQ (4 nm)/NPD (40 nm)/**E9-E10** (50 nm)/BCP (6 nm)/LiF (1 nm)/Al (150 nm) gave superior performance over other type of device without hole injecting layer and electron transporting layer. Device using dye **E9** achieved a low EQE of 0.24 % with luminance of 472 cd m^{-2}. However, other type of device for dye **E9** resulted in improved luminance of 1463 cd m^{-2} and EQE of 0.4%. However, another type of OLED resulted in blue emission with a high EQE of 0.71% for **E10** and 0.69% for **E9**, attributable to the confinement of additional holes in emitting layer (Table 1.2). The dyes were also used as electron transporting layer in PhOLEDs with $Ir(ppy)_3$ doped CBP as emitter layer (Table 1.1). The devices resulted in a high EQE of 1.39% for **E9** and 1.46% for **E10** compared to devices without ETL or with Alq_3

Luo *et al.*[138] reported dyes **E11-E18** exhibiting TICT comprised of 4-aryloxy-1,8-naphthalimide derivatives as promising sensor and EL materials (Chart 1.51). The photophysical and quantum chemical studies confirmed that rotation around central C-O bonds was responsible for the formation of a stable TICT state in **E11-E18**. Adjustable fluorescence ON-OFF switching responses and AIE activity towards different solvent polarity as well as good electroluminescent performance were observed for **E11-E18** due to the highly non-planar and twisted molecular geometries. **E16** displayed a strong TICT, high fluorescence in solid state, twisted ground state geometry and high thermal stability >400℃. A neat OLED device using **E16** as sky-blue emitter was fabricated with configuration of ITO/MoO_3 (7 nm)/(TAPC) (40 nm)/mCP(10 nm)/**E16** (10 nm)/Bphen (40 nm)/Mg:Ag (100 nm) with CIE coordinates of 0.17, 0.27 (Table 1.2). However, at high voltage, the device emitted orange EL due to the formation of exciplex between dye and TAPC. The device achieved a V_{on} of 3.0 V with luminance of 4780 cdm^{-2} and EQE of 1.6%.

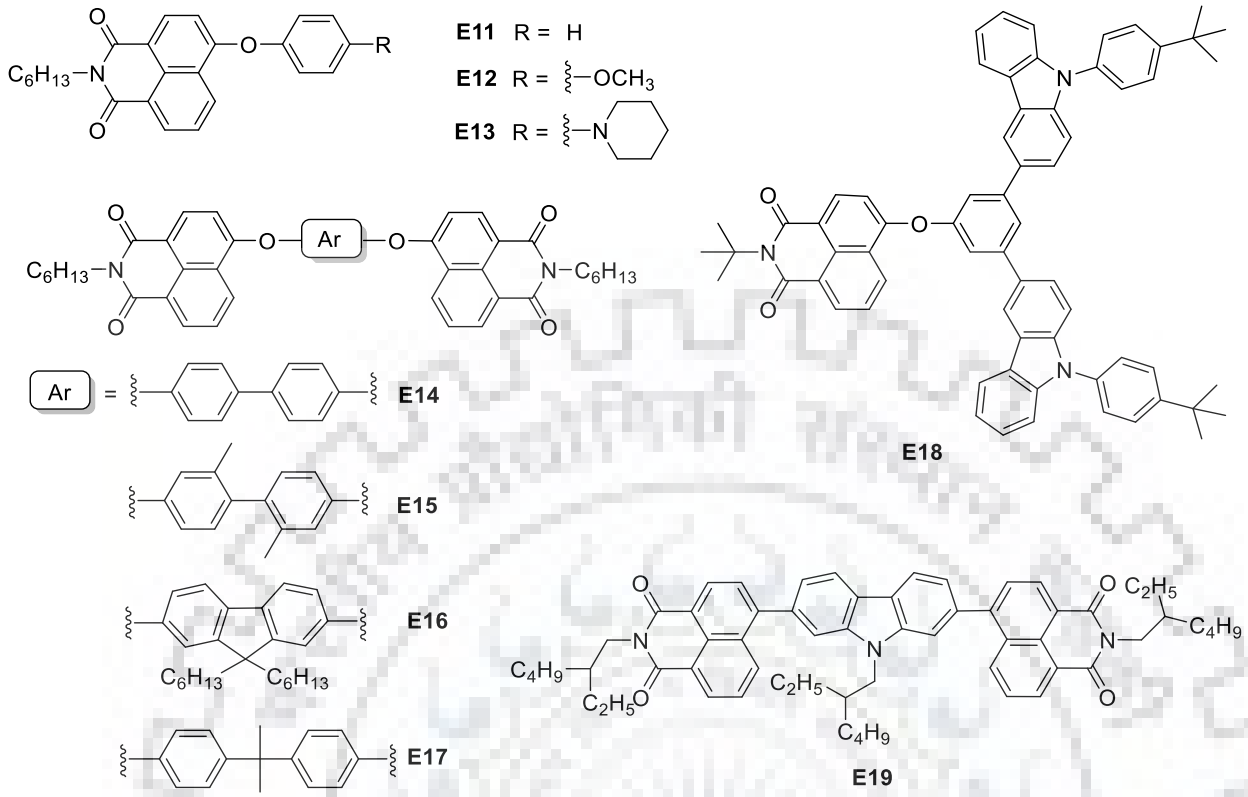

Chart 1.51 Structures of naphthalimide derivatives as emitter materials (**E11-E19**)

Li *et al.*[139] demonstrated pure white OLEDs utilizing non-doped 4-aryloxy-1,8-naphthalimide derivative **E16** which was blue emitting along with orange emitting exciplex at the interface of donor and **E16**. **E16** featured TICT and dual fluorescence at λ = 440 and 520 nm attributed to localized and TICT excited state in OLED fabrication. Four devices were fabricated using **E60** as emitting layer (Table 1.2). In detail, device based on planar structure of **E16** displayed a broad EL band at 680 nm arising from exciplex emission with high V_{on} of 4.4 V and low luminance. However, device with TAPC/**E16** exhibited two EL peaks at λ = 480 and 585 nm originating from radiative decay of dye and exciplex with 2.7 V as V_{on} and high luminance of 1550 cdm^{-2}. Another device exhibited emission from exciplex at 580 nm with low V_{on} of 2.2 V, EQE of 0.9% and CIE coordinates of 0.34, 0.34 closest to white emission. While, device with NPB/**E16** with film thickness of 30 nm exhibited 2.0 V as turn on voltage, luminance of 4500 cdm^{-2} and EQE of 1%.

Wang *et al.*[140] explored **E18** as a potential host material in FOLED and PhOLED (Chart 1.51). It was demonstrated that **E18** attain a highly twisted structure so that there is merely any HOMO-LUMO orbital overlap. The material showed a singlet CT state and triplet CT state differing by 0.05 eV. The low lying LUMO state at -3.1 eV is attributed to the high electron

affinity of naphthalimide unit. FOLED were fabricated using **E18** as host in device architecture of ITO (100 nm)/NPB (30 nm)/TCTA (10 nm)/**E18**: Dopant (20 nm)/Bphen (40 nm)/Mg:Ag (100 nm) with rubrene as fluorescent dyes and [(*t*-bt)$_2$Ir(acac)] as phosphorescent dyes (Table 1.1). It was found that doping concentration had no influence on the *J-V* curve for FOLEDs since there is no charge trapping. The lowest V_{on} of 2.9 V was observed for 5% rubrene doped device and a maximum EQE of 5% with the highest maximum luminance of 19,500 cdm^{-2} among the four devices. However, for PhOLEDs with increasing in doping concentration, the current density varied and displayed charge trapping. The device with 24% (*t*-bt)$_2$Ir(acac) as dopant achieved minimum turn-on voltage of 3.1 V with considerable luminance of 37,940 cdm^{-2} and EQE of 12%. However, maximum EQE of 16.5% was observed for 24% doped device with maximum luminance of 41,710cdm^{-2}.

Gudeika *et al.*[141] synthesized and characterized an electron transporting material **E19** composed of carbazole-coupled to 1,8-naphthalimide (Chart 1.51). The thermal, optical, photophysical, electrochemical and charge transporting properties of the dye were studied in detail. The dye exhibited an oxidation potential of substituted carbazole at 1.20 V and a reversible reduction peak at -1.68 V, which were attributed to the naphthalimide moiety. The energy levels for the dye were calculated to be -5.18 eV and -2.08 eV respectively. The dye showed a high thermal stability >400° C. Further the CIE coordinates (0.30; 0.27) of the emission of molecular mixture of the dye along with blue emitting dye 2-[4-(diphenylamino) phenyl]-1-phenyl-1*H*-phenanthro[9,10-*d*]imidazole were close to white color coordinates covering the whole range of visible light.

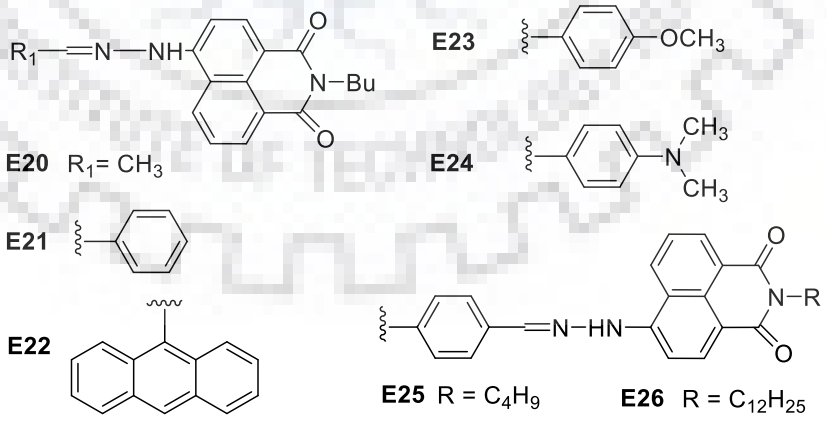

Chart 1.52 Structures of naphthalimide derivatives with different Schiff bases (**E20-E26**)

Gan *et al.*[142] synthesized a set of naphthalimide derivatives **E20-E26** with different Schiff bases for non-doped OLEDs (Chart 1.52). Compared to parent dye **E20**, **E21-E26** exhibited a red

shifted absorption band due to the extension of conjugating system or increase in donating strength of substituents. **E23** and **E24** displayed a 40 and 140 nm red shift in emission with quenched quantum yield due to strong push-pull interaction. However, the red shifted profile of **E25** and **E26** was ascribed due to the extended conjugation. Further, the fluorescence lifetime for **E22** was shortened to 0.22 ns compared to parent **E20** (8.14 ns), attributable to the rapid decay of the excited state. **E23** and **E24** showed a low reduction potential at -0.7 V due to the increased donating propensity. However, the HOMO of the dyes was deep seated inferring their use as good blocking layer in OLEDs. The OLED devices with configuration of ITO/CuPc(12 nm)/NPB(30 nm)/**E22**/sodium stearate (2 nm)/Al (100 nm) were fabricated (Table 1.2). **E22** gave a device current density of 2.9 mA cm^{-2} and a maximum brightness of 15.5 cd m^{-2} with a high turn-on voltage of 14 V and EL peak at λ = 620 nm.

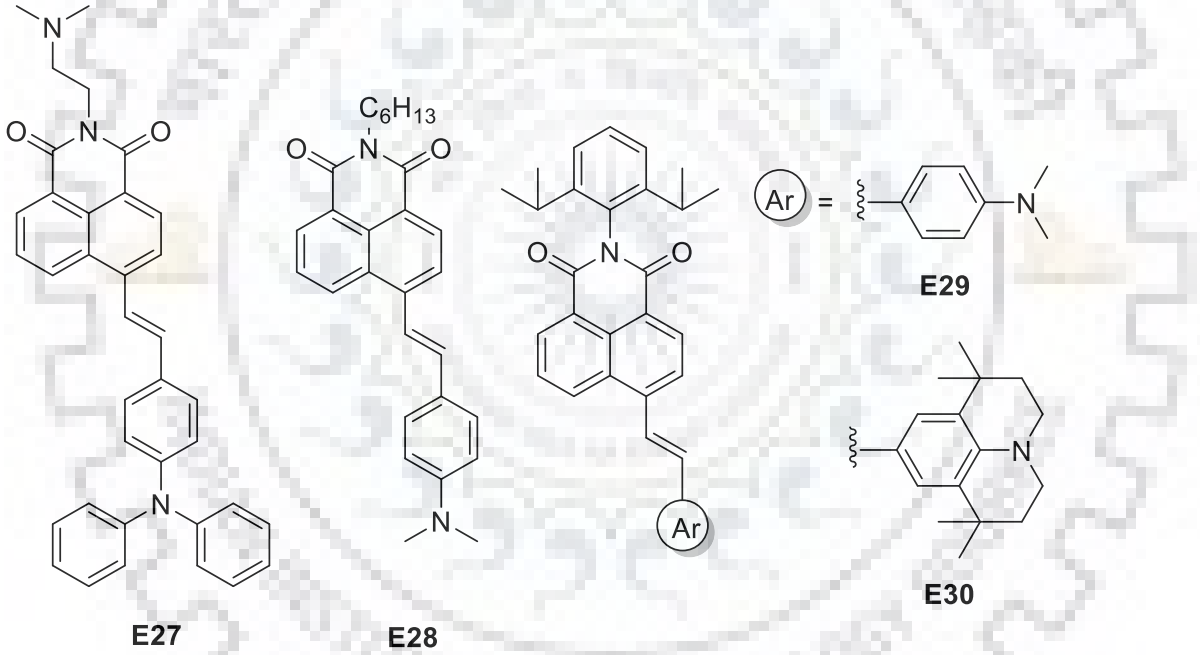

Chart 1.53 Structures of naphthalimide D-π-A derivatives (**E27-E30**)

Luo *et al.*[143] synthesized three red-emissive D-π-A derivatives **E27-E30** having aromatic amine as donor, vinyl as π- bridge, and 1,8-naphthalimide as acceptor units (Chart 1.53). Photophysical studies revealed that the presence of strong electron-rich 4-(dimethylamino)phenyl group in **E28** resulted in red shifted absorption and emission centered at 641 nm, compared to parent **E27**. Among the set of these dyes, **E28** suppressed the aggregation and intermolecular interaction due to the bulkiness of imidic group. Consistent with the absorption characteristics of **E27** and **E28-E30**, the PL emission band of **E30** was the most red-shifted to λ = 722 nm owing to

the strong D-A characteristics. All the dyes showed 20–30 nm red-shifted absorption bands in solvatochromic plots compared to **E29,** highlighting a polar and CT characteristics in ground state. Also, the alteration of the 4-(dimethylamino)phenyl by more electron-donating 1,1,7,7-tetramethyljulolidin-9-yl substituent in **E30** improved chromaticity in guest-doped film. The dye **E28** displayed a reversible reduction wave at -1.70 V due to the reduction of naphthalimide. Both **E29** and **E30** showed reversible reduction wave at -1.66 V indicating ease to reduce the core. However, **E28** and **E29** showed reversible oxidation waves at 0.24 V due to oxidation of 4-(dimethylamino)phenyl unit, compared to **E30** at 0.05 V. This was in agreement with the trend of electron richness of the donor units. When the dyes were utilized for OLED applications, **E30** as a dopant suppressed the intermolecular interactions. A device was fabricated using **E30** as the dopant with device configuration of ITO/MoO_3 (1 nm)/TCTA (40 nm)/**E18**: **E30** (14 wt%) (20 nm)/TPBI (45 nm)/LiF (1nm)/Al (80 nm). The OLED device exhibited parameters of CIE coordinates as 0.67, 0.32, maximum EQE of 1.8% and maximum current efficiency of 0.7 cd A^{-1} (Table 1.2). The three devices using these naphthalimide derivatives as dopants displayed comparable turn-on voltages of 3.1 V.

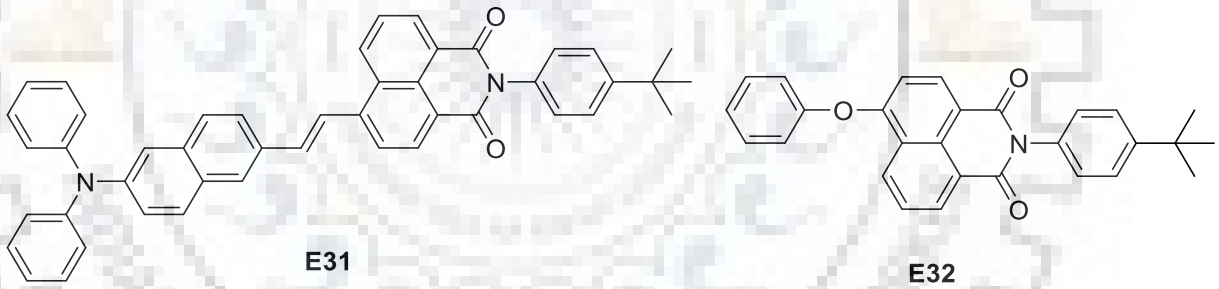

Chart 1.54 Structures of naphthalimide-based dyes (**E31-E32**)

Intrigued by **E18**, a potential TFDF host material, Zheng *et al.*[144] reported a linear D-π-A naphthalimide-based CT material **E31** (Chart 1.54). **E31** consisted of diphenylnaphthylamine as donor and naphthalimide as acceptor linked by vinyl linkage, suppressing intermolecular interactions. The emission spectra of the dye exhibited a positive solvatochromism of $\Delta\lambda$ = 47 nm on moving from Tol to DMSO indicative of highly polar CT excited state. Further, the DFT analysis depicted that the HOMO electron density was delocalized throughout the backbone of the dye while LUMO was localized on the linker and naphthalimide. **E31** displayed a reversible oxidation wave at 0.52 V due to the removal of electron from diphenylamine by naphthalimide. The HOMO and LUMO energy levels were calculated to be -5.32 eV and -3.0 eV, respectively. Similar to **E18**, **E31** was capable of harvesting triplet excitons *via* TTA path in OLED, attributable

to the presence of a lower-lying triplet excited state and low ΔE_{ST} of 0.24 eV. The dye was tested as a guest material with **E18** as an ICT host having variable doping concentrations as four devices. The orange OLED fabricated with 6 wt% **E31** doped **E18** displayed CE_{max} of 7.73 cdA^{-1}, L_{max} of 31940 cdm^{-2} and EQE_{max} of 5.83% (Table 1.2).

In 2014, Zhou *et al.*[145] reported a naphthalimide-based molecule **E18** as a promising host and as a TFDF material along with linear molecules **E32** as emitter and (*E*)-11-(tert-butyl)-4-(2-(7-(diphenylamino)-9,9-diethyl-9*H*-fluoren-2-yl)vinyl)-7*H*-benzo[*de*]benzo[4,5]imidazo[2,1-*a*]isoquinolin-7-one, **FN** as dopant (Chart 1.54). **E18** displays two main absorption bands assigned to the π-π* transition of carbazole at λ = 300 nm and naphthalimide unit at λ = 360 nm. The dye exhibited solvent dependent emission spectra due to the significant CT in the excited state irrespective of **E32**. The PLQY of former is found to be lower than latter due to the significant ICT in **E18**. Further, the dye displayed a vibrational structured emission in non-polar solvent while a dual fluorescence in polar solvent exhibiting a TICT character. In solid state, **E18** displayed a broad emission spectra centered at 493 nm and low quantum yield indicative of CT in solid state too. In fluorescence lifetime studies, under inert conditions, **E18** displayed a triple-exponential decay which decreases under air with short lived decay lifetime indicative of TICT emission with TTA. While the energy levels of the material were estimated to be -5.64 eV and -3.14 eV which are in accordance with the energy levels of different layers used in typical OLEDs. Thus, a non-doped device with **E18** as the emitter is fabricated with a structure of ITO/PEDOT(35 nm)/NPB (60 nm)/**E18** (30 nm)/TPBI (40 nm)/LiF (0.8 nm)/Al but failed at a high applied bias voltage when the magneto electroluminescence decreased gradually at higher magnetic field strength. Thus, another doped device using **E18** as a TFDF-featured host was fabricated with a structure of ITO/MoO_3 (10 nm)/NPB (35 nm)/TCTA (10 nm)/**FN**:**E18** (6 wt%, 30 nm)/TPBI (40 nm)/LiF (0.8 nm)/Al. It displayed a maximum brightness of 7250 cd m^{-2}. However, device using **E18** with **FN** was employed as an orange-red OLED with EQE of 3.59% with a maximum CE of 7.2 cdA^{-1} and a brightness of 16840 cdm^{-2} (Table 1.2). The EQE of the device was found to be far more than the theoretically predicted value of 2.5% attributed to the facile and efficient energy transfer of triplet excitons *via* TTA.

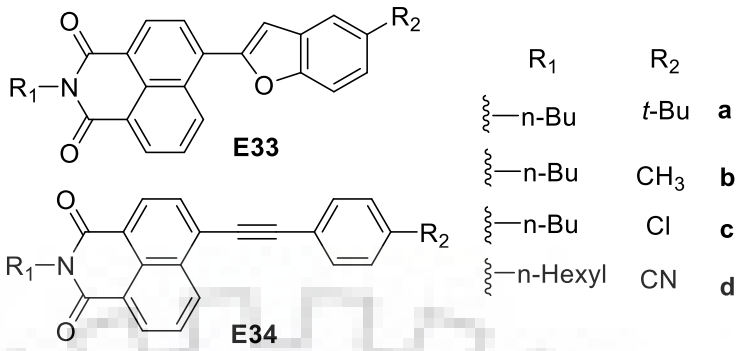

Chart 1.55 Structures of naphthalimide-based dyes as emitting layer in OLEDs

Shi *et al.*[146] reported naphthalimide-grafted dye molecules, **E33-E34** and investigated effects of side groups on the kinetics of charge carrier recombination in multilayer OLEDs (Chart 1.55). With the aid of transient EL charge carrier recombination coefficient, charge carriers were investigated for dye-doped CBP as emitting layer. All four devices obtained from **E33** displayed similar emission profile centered at λ = 500 nm. The dyes were used as dopants in fabrication of OLED with device architecture of ITO/NPB(40 nm)/CBP:**E33-E34** (1%) (20 nm)/BCP (20 nm)/Alq_3 (40 nm)/LiF (1 nm)/Al (200 nm) (Table 1.2). It was interesting to note that efficiency of the device was dependent on the charge recombination coefficients. Among the set of devices, device **E33a** exhibited the brightest luminance of 3640 cd m^{-2} with the highest CE of 3.7 cd A^{-1}. While device obtained from **E33d** having cyano group displayed the lowest CE of 0.8 cd A^{-1} with a luminance of about 760 cd m^{-2}. Among **E34**, **E34a** displayed EL efficiency of 2.6 cd A^{-1}, which was the highest in the series. However, **E34** displayed a poor EL efficiency compared to **E33**.

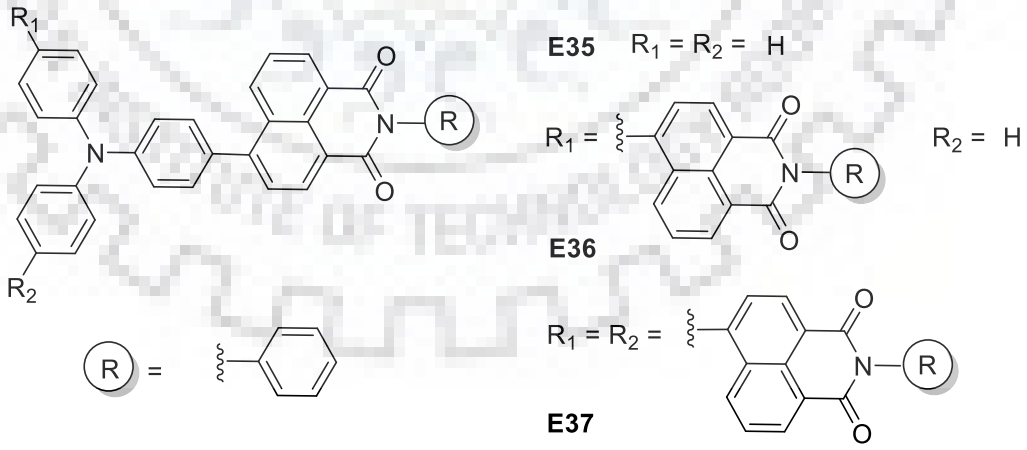

Chart 1.56 Structures of linear and star-shaped triphenylamino naphthalimides (**E35-E37**)

Arunchai *et al.*[147] reported a series of triphenylamino naphthalimides **E35-E37** using Suzuki cross coupling reactions between *N*-phenyl-1,8-naphthalimide and triphenylamine boronic

acids (Chart 1.56). The dyes exhibited ICT band at 430 nm and a characteristic π–π* transition band around 312-326 nm. However, an increase in the number of naphthalimide units shifted the emission band hypsochromically due to the decreased electron delocalization, originating from the molecular steric hindrance. Moreover, the fluorescence quantum yields of the dyes increased subsequently from 0.34 to 0.55 for **E35** to **E37** with an increase in the naphthalimide units arising from LE. The dyes show good thermal stabilities with the 10% weight loss above 350 °C. The dyes displayed a reversible oxidation peak at ca. 0.5 V attributable to the electron-donating ability of triphenylamine. The oxidation potential was found to be shifted cathodically with an increase in naphthalimide units, which stabilized the HOMO energy level and LUMO energy level was raised from -2.73 to -2.71 eV for **E37**. All the devices emitted a bright yellowish green EL similar to their thin-film PL spectra. This suggested that emission originated from the dyes indicative of efficient energy transfer from host to guest. The single-layered OLED device using **E37** resulted in poor device parameters with EQE of 0.006% and luminance of 133 cd m^{-2}. Considering all these parameters, the group fabricated multi-layered devices using dyes doped with CBP as the emissive layer. Using **E35**-doped BCP as a hole-transporting material, the device fabricated with ITO/PEDOT:PSS/Emitter:CBP/BCP/LiF/Al architecture resulted in yellowish green emission (CIE: 0.295, 0.6) with maximum brightness of 10404 cd m^{-2} at 19 V, a V_{on} of 5.8 V, and device luminance efficiency of 3.77 cd A^{-1} and EQE of 1.11% (Table 1.2).

Table 1.1 Electroluminescent properties of naphthalimide-based materials for PhOLEDs

Host	Dopant (wt%)	Device structure	V_{on}, V	EQE, %	CE, cdA^{-1}	PE, lmW^{-1}	L, cdm^{-2}	CIE
E3	BtpIr (6 wt%)	ITO/α-NPD (350 Å)/**E3**.Dopant	3.0	1.7	-	-	-	-
	BtIr (6 wt%)	(200 Å)/CBP (50 Å)/**E3** (100	3.0	0.4	-	-	-	-
	Ir(ppy) (6 wt%)	Å)/Alq_3 (200 Å)/Mg-Ag	4.5	0.3	-	-	-	-
CBP	BtpIr (6 wt%)	ITO/α-NPD (350	3.0	3.2	-	-	-	-
	BtIr (6 wt%)	Å)/CBP.Dopant (200 Å)/CBP	4.0	0.3	-	-	-	-
	Ir(ppy) (6 wt%)	(50 Å)/**E3** (100 Å)/Alq_3 (200 Å)/Mg-Ag	4.5	0.3	-	-	-	-
E9-E10	$Ir(ppy)_3$	ITO (120 nm)/ α-NPD (40 nm)/ CBP.Dopant (200 Å)/ (35 nm) /BCP (6 nm)/ LiF (1 nm)/Al (150 nm)	12.76	0.94	5.39	1.23	1714	
	$Ir(ppy)_3$	ITO (120 nm)/ α-NPD (40 nm)/ CBP.Dopant (200 Å)/ (35 nm) /Alq_3 (30 nm) BCP (6 nm)/ LiF (1 nm)/Al (150 nm)	9.09	1.70	9.79	2.71	9650	
E9	$Ir(ppy)_3$	ITO (120 nm)/ α-NPD (40 nm)/ CBP.Dopant (200 Å)/ (35 nm) /**E9** (30 nm) BCP (6 nm)/ LiF (1 nm)/Al (150 nm)	9.23	1.39	8.90	1.82	5341	
E10	$Ir(ppy)_3$	ITO (120 nm)/ α-NPD (40 nm)/ CBP.Dopant (200 Å)/ (35 nm) /**E10** (30 nm) BCP (6 nm)/ LiF (1 nm)/Al (150 nm)	9.14	1.46	9.04	1.98	5962	
E18	$bt_2Ir(acac)$ (8wt%)	ITO (100 nm)/NPB (30 nm)/ TCTA (10 nm)/**Host:**Dopant (20	3.2				31400	(0.52. 0.48)
	$bt_2Ir(acac)$ (16wt%)	nm)/Bphen (40 nm)/Mg: Ag (100 nm)	3.1	7.5	21.0	11.6	41020	(0.52. 0.47)
E18	$bt_2Ir(acac)$ (24wt%)	ITO (100 nm)/NPB (30 nm)/ TCTA (10 nm)/**Host:**Dopant (20	3.5	10.0	27.7	15.1	41710	(0.52. 0.47)
	$bt_2Ir(acac)$ (32wt%)	nm)/Bphen (40 nm)/Mg: Ag (100 nm)		16.5	44.2	33.3	37940	(0.53. 0.47)

Host	Dopant (wt%)	Device structure	V_{on}, V	EQE, %	CE, cdA^{-1}	PE, lmW^{-1}	L, cdm^{-2}	CIE
PEPCa	$bt_2Ir(acac)$/**E19**	ITO/ PEPCa.Dopant (1:10)/ LiF (1 nm)/Al (150 nm)	-	-12.0	33.0	16.3	-	(0.28. 0.38)

Table 1.2 Electroluminescent properties of naphthalimide-based materials for FOLEDs

Dye	Device structure	V_{on}, V	EQE, %	CE, cdA^{-1}	PE, lmW^{-1}	L, cdm^{-2}	CIE
E6	ITO/PEDOT:PSS(40 nm)/NPB(40 nm)/TCTA(5 nm)/**Emitter** (20 nm)/ mCP/TPBi(35 nm)/LiF(1 nm)/Al(100 nm)	3.8	1.58	0.90	0.68	948	(0.153, 0.066)
E7	ITO/PEDOT:PSS(40 nm)/NPB(40 nm)/TCTA(5 nm)/**Emitter** (20 nm)/ MADN/TPBi(35 nm)/LiF(1 nm)/Al(100 nm	3.1	5.96	15.5	12.0	64344	(0.291, 0.595)
E8	ITO/PEDOT:PSS(60 nm)/**Emitter** (100 nm)/Al(120 nm)	10.0	-	-	-	-	(0.21, 0.31)
E9	ITO (120 nm)/ α-NPD (30	7.03	0.41	0.89	0.21	889	(0.190, 0.283)
E10	nm)/**Emitter** (35 nm)/BCP (6 nm)/Alq_3 (35 nm)/LiF (1 nm)/Al (150 nm).	6.92	0.47	0.96	0.23	1072	(0.181, 0.279)
E9	ITO (120 nm)/ α-NPD (40 nm)/**E9** (50 nm) /LiF (1 nm)/Al (150 nm)	9.67	0.24	0.45	0.11	472	-
E9	ITO (120 nm)/F4TCNQ (4 nm)/ α-NPD (40 nm)/**E9** (50 nm)/LiF (1 nm)/Al (150 nm)	6.62	0.40	1.79	0.51	1493	-
E9	ITO (120 nm)/F4TCNQ (4 nm)/ α-NPD (40 nm)/**E9** (50 nm)/BCP (6 nm)/LiF (1 nm)/Al (150 nm)	6.35	0.69	1.87	0.86	1580	-
E10	ITO (120 nm)/F4TCNQ (4 nm)/ α-NPD (40 nm)/**E10** (50 nm)/BCP (6 nm)/LiF (1 nm)/Al (150 nm)	6.18	0.71	1.89	0.98	1681	-
E16	ITO/MoO_3 (7 nm)/ (TAPC) (40 nm)/ mCP(10 nm)/**Emitter** (10 nm)/ Bphen (40 nm)/Mg:Ag (100 nm)	3.0	1.6	3.0	2.8	4780	(0.17, 0.27)
E16	ITO/ m-MTDATA (35 nm)/**Emitter** (15 nm)/ Bphen (40 nm)/Mg:Ag	4.4	-	0.01	0.01	80	(0.68, 0.32)

Dye	Device structure	V_{on}, V	EQE, %	CE, cdA^{-1}	PE, lmW^{-1}	L, cdm^{-2}	CIE
E16	ITO/TAPC (35 nm)/**Emitter** (15 nm)/ Bphen (40 nm)/Mg:Ag	2.7	0.3	0.6	0.6	1550	(0.40, 0.42)
	ITO/NPB (35 nm)/**Emitter** (15 nm)/ Bphen (40 nm)/Mg:Ag	2.2	0.9	1.5	1.2	2800	(0.42, 0.34)
	ITO/NPB (35 nm)/**Emitter** (30 nm)/ Bphen (40 nm)/Mg:Ag	2.0	1.0	1.5	1.2	4500	(0.33, 0.33)
E18	ITO (100 nm)/NPB (30 nm)/ TCTA (10 nm)/**Host:**Dopant (1wt%) (20 nm)/ Bphen (40 nm)/Mg: Ag (100 nm)	3.5	2.5	7.8	6.4	15200	(0.48, 0.51)
	Dopant (3 wt%)	3.0	3.6	11.1	10.9	15290	(0.50, 0.50)
	Dopant (5 wt%)	2.9	5.0	15.0	16.6	19510	(0.50, 0.50)
	Dopant (7 wt%)	3.1	3.4	10.0	9.9	17250	(0.50, 0.49)
E22	ITO/CuPc (12 nm)/ NPB 30 nm/**Emitter**/sodium stearate(2 nm)/Al (100 nm)	14	-	2.9	-	15.5	-
E30	ITO/MoO_3 (1 nm)/TCTA (40 nm)/ **E18**: **Dopant** (2 wt %) (20 nm)/ TPBI (45 nm)/LiF (1nm)/Al (80 nm)	3.1	2.1	1.9	-	10900	(0.62, 0.37)
	ITO/MoO_3 (1 nm)/TCTA (40 nm)/ **E18**: **Dopant** (4 wt %) (20 nm)/ TPBI (45 nm)/LiF (1nm)/Al (80 nm)	3.1	1.8	1.1	-	6600	(0.65, 0.34)
	ITO/MoO_3 (1 nm)/TCTA (40 nm)/ **E18**: **Dopant** (14 wt %) (20 nm)/ TPBI (45 nm)/LiF (1nm)/Al (80 nm)	3.1	1.8	0.7	-	2660	(0.67, 0.32)
E31	ITO/MoO_3 (1 nm)/TCTA (40 nm)/ CBP (2 nm)/**Dopant** (20 nm)/ TPBI (45 nm)/ LiF (1 nm)/Al (80 nm),	4.2	0.59	0.53	-	5100	(0.64, 0.36)
	ITO/MoO_3 (1 nm)/TCTA (40 nm)/CBP (2 nm)/**E18**: **E31** (20 nm, 1.4 wt%)/TPBI (45 nm)/LiF (1 nm)/Al	2.6	2.49	3.19	-	24500	(0.47, 0.50)

Dye	Device structure	V_{on}, V	EQE, %	CE, cdA^{-1}	PE, lmW^{-1}	L, cdm^{-2}	CIE
E31	ITO/MoO_3 (1 nm)/TCTA (40 nm)/CBP (2 nm)/**E18**: **E31** (20 nm, 6 wt%)/TPBI (45 nm)/LiF (1 nm)/Al (80 nm)	2.8	5.83	7.73	-	31940	(0.51, 0.48)
	ITO/MoO_3 (1 nm)/TCTA (40 nm)/CBP (2 nm)/**E18**: **E31** (20 nm, 15 wt%)/ TPBI (45 nm)/LiF (1 nm)/Al (80 nm)	3.2	4.14	5.41	-	27640	(0.57, 0.43)
FN	ITO/ NPB (30 nm)/CBP (2 nm)/**FN**:**E18** (6 wt%, 20 nm)/Bphen (40 nm)/Mg:Al	4.0	3.59	7.2	-	16840	-
E33a	ITO/NPB(40 nm)/CBP:**Emitter** (1%)	-	-	3.7	-	-	-
E33b	(20 nm)/BCP (20 nm)/Alq_3 (40	-	-	3.0	-	3640	-
E33c	nm)/LiF (1 nm)/Al (200 nm)	-	-	2.5	-	2550	-
E33d	ITO/NPB(40 nm)/CBP:**Emitter** (1%)	-	-	0.8	-	1040	-
E34a	(20 nm)/BCP (20 nm)/Alq_3 (40	-	-	2.6	-	760	-
E34b	nm)/LiF (1 nm)/Al (200 nm)	-	-	1.9	-	-	-
E34c	ITO/NPB(40 nm)/CBP:**Emitter** (1%)	-	-	1.2	-	-	-
E34d	(20 nm)/BCP (20 nm)/Alq_3 (40 nm)/LiF (1 nm)/Al (200 nm)″ ″	-	-	1.0	-	-	-
E35	ITO/PEDOT:PSS/**Emitter**:CBP/BCP/ LiF/Al	5.8	1.11	3.77	0.68	10404	(0.29, 0.60)
E36	ITO/PEDOT:PSS/**Emitter**:CBP/BCP/ LiF/Al	6.2	0.73	2.49	0.32	5898	(31, 0.60)
E37	ITO/PEDOT:PSS/**Emitter**/LiF/Al	4.0	0.006	0.02	0.96	133	(0.48, 0.47)
	ITO/PEDOT:PSS/**Emitter**/BCP/LiF/Al	3.8	0.01	0.04	0.009	323	(0.48, 0.48)
E37	ITO/PEDOT:PSS/**Emitter**:CBP/ BCP/LiF/Al	5.5	0.27	0.93	0.02	877	(0.25, 0.57)

1.4.2 Naphthalimide-based materials in OSCs

Since the first report of organic solar cell in 1985,[39] the field of OPVs has become an area of intense research because these devices offer a potentially efficient, cost-effective, and scalable approach for solar energy conversion. Generally speaking, for better performance in BHJSCs, an organic electron-transporting material should have high electron affinity, deep LUMO of acceptor with respect to LUMO of donor, low band gap, broad absorption spectral profile, high molar absorption coefficient, high electron mobility and compatible active layer morphology. Although OPV efficiencies have been rapidly increasing, with multiple reports of PCE exceeding 10%, they still lag behind typical inorganic solar cells. In BHJSCs, both donor and acceptor, typically P3HT and fullerenes are blended to constitute an active layer.[148-150] A typical BHJSC possesses high efficiency and operational benefits such as low recombinational losses, effective exciton diffusion over single-layered or double layered solar cells using fullerenes and their derivatives, such as $PC_{61}BM$ and $PC_{71}BM$. These fullerenes are considered as dominant electron-acceptor materials because of their large electron affinity of 4.2 eV, good electron mobility in range of 10^{-3} $cm^2V^{-1}s^{-1}$ upto 1 $cm^2V^{-1}s^{-1}$. However, fullerenes have a few disadvantages such as weak absorption in the visible spectrum compared to typical donor polymers, high-cost production and purification, and an EA that is too large with respect to IP of a number of donor polymers, resulting in low V_{OC}. To address these problems, new electron acceptor materials are needed for OPVs applications following simple, inexpensive and highly productive synthetic processes with minimal steps. However, very few reports on solution-processed fullerene-free OPVs have shown PCEs approaching or exceeding 10%.[69, 151-162] Thus, increased efforts to develop effective non-fullerene-based acceptors are still needed.

1.4.2.1 Naphthalimide-based directly linked chromophoric materials

Lu *et al.*[163] synthesized corannulene-tethered naphthalimide derivative **E38** as non-fullerene acceptor using Suzuki cross coupling reaction for organic solar cells (Chart 1.57). The introduction of naphthalimide on the corannulune core was aimed at lowering LUMO level of corannulene to make it suitable for P3HT. The absorption profile of **E38** experienced a red shift ($\Delta\lambda$ = 77nm) compared to corannulene absorption at 288 nm. The band observed at 330-400 nm is attributed to ICT from corannulene to naphthalimide. The dye showed two reversible reduction waves at -1.0 V and -1.65 V corresponding to naphthalimide and corannulene, respectively. The introduction of naphthalimide on corannulene shifted its reduction potential from -1.75 V to -1.6

V and thus, the LUMO of corannulene from -2.65 eV to -3.24 eV for **E38**. The LUMO level of dye is more by 0.4 eV units promising a high V_{OC}. The DFT calculations revealed that LUMO is localized in naphthalimide while HOMO is spread over both corannulene and naphthalimide. The OSC device was designed using active blend in 1:1 ratio as ITO/ZnO/ **E38**:P3HT/LiF/Al (Table 1.3). The as-fabricated device achieved a PCE of 1.03% with a high V_{OC} of 0.82 V.

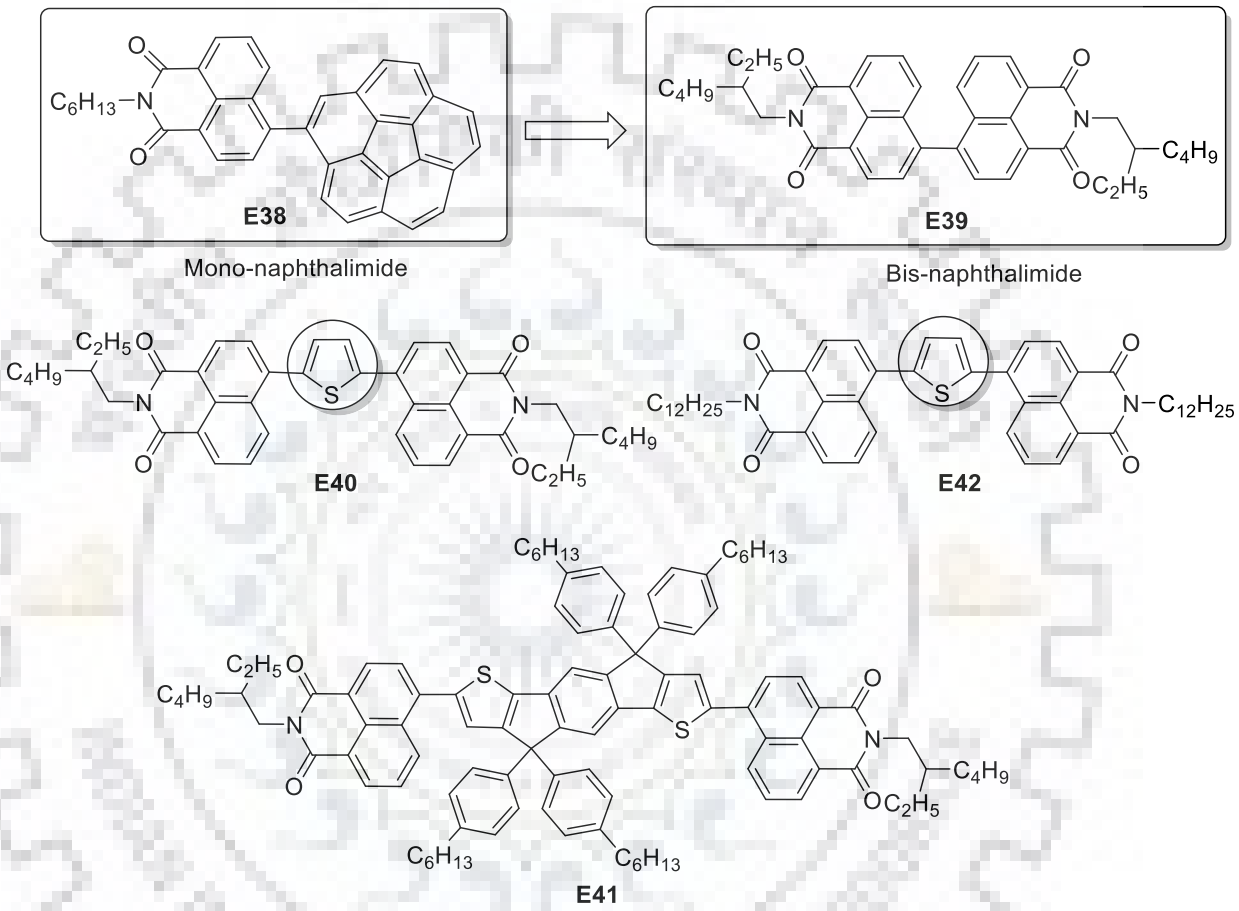

Chart 1.57 Structures of naphthalimide-based non-fullerene acceptors (**E38-E42**)

He *et al.*[164] synthesized three different as electron acceptors **E39-E41**, analogous to perylene diimides for solution-processed polymer solar cells (Chart 1.57). Specifically, these acceptors differ in terms of small and large π-conjugation units of thiophene and indacenodithiophene, respectively. These compounds showed excellent thermal stability with high decomposition temperatures. Increase in the conjugation length for **E41** compared to **E39** shifted the absorption profile from 358 nm to 482 nm. The absorption λ_{max} in thin film for all the dyes is further red shifted by 5-20 nm. The optical band gap decreased from 2.98 eV for **E39** to 2.25 eV for **E41**. The HOMO energy levels were upshifted from -6.18 to -5.67 eV and the LUMO energy levels were downshifted as the conjugation of the bridge between naphthalimide units increased.

The power conversion efficiencies of solar cells based on blends of P3HT donor and these acceptors increased from 0.28% to 2.36% attributed to enhanced V_{OC} and J_{SC} due to more light harvesting properties of **E41** (Table 1.3).

Zhang *et al.*[165] synthesized naphthalimide based non-fullerene acceptor **E42** for polymer solar cells with PCDTBT-C12 (Chart 1.57). The dye displayed an absorption upto 500 nm with a structured peak at λ_{max} = 399 nm, similar to **E40** which is attributed to the planarity of the molecule. In the solid state, **E42** exhibited a hypsochromic absorption profile due to the formation of H-aggregates which is contrary to **E40** which can be due to alkyl chain modification. The energy levels of the dye were determined to be -6.07 eV and -3.53 eV matching with the complementary polymer PCDTBT-C12, and promising a high open circuit voltage compared to former set of dyes, **E93-E41**. Owing to its electron deficiency **E42** exhibited an irreversible oxidation in high potential range at 1.27 V. The active layer was tested in polymer cell solar as ITO/PEDOT:PSS (30 nm)/PCDTBT-C12:**E42**/LiF (0.7 nm)/Al (100 nm) architecture. The modification in the donor-acceptor blend resulted in an improvement of PCE of the cell (Table 1.3). A low PCE of only 0.16% was observed for a device with active layer in 1:1 ratio without annealing. However, by increasing acceptor ratio to double, a tremendous hike in PCE of the cell to 0.84% was observed. For **E42**, a maximum PCE of 2.01% which is fourfold compared to **E40** was achieved with a high V_{OC} of 1.30 V using an active layer in a weight ratio of 1:4 annealed at 90 ˚C for 3 minutes.

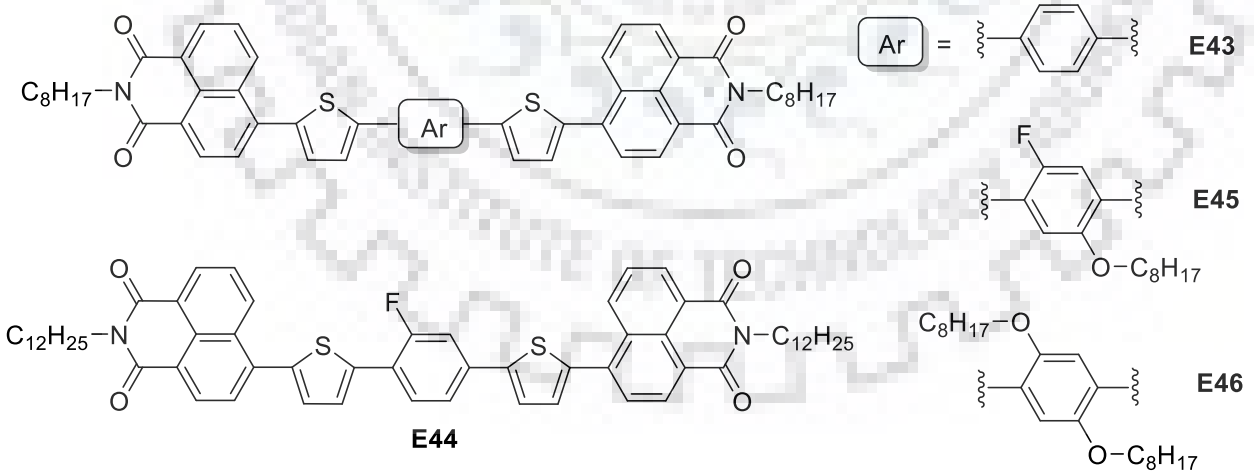

Chart 1.58 Structures of bis-naphthalimide-based non-fullerene acceptors (**E43-E46**)

Zhang *et al.*[166] synthesized a series of bis-naphthalimide-based small molecular acceptors **E43-E46** by C-H activation reactions (Chart 1.58). By introducing different substituents on the

central benzene ring, the dihedral angles between the two naphthalimide units increased from 34 ˚ to 89 ˚for **E43** to **E46**. The absorption profile experienced a red shift in solution spectra with the introduction of alkoxyl side chain due to increased donor strength. Moreover, tremendous red shift was observed for **E46** in the thin film due to molecular non-planarity. However, the planar small molecules were found to be beneficial for the electron transportation with enhanced electron mobility. This resulted into enhanced J_{SC} and PCE of the devices. The planar small molecule **E43** and PCDTBT-C12 blend films exhibited uniform morphology and acquired a PCE of 0.59% with a V_{OC} of 1.36 V (Table 1.3). However, the thermal annealing of dyes was found to have positive effect as increase of the PCE to a maximum of 2.78%. As an outlook, the planarity of small molecular acceptors has significant influences on the performance of non-fullerene OSCs and naphthalimide based planar acceptors are potential acceptors for wide band gap polymer based OSCs.

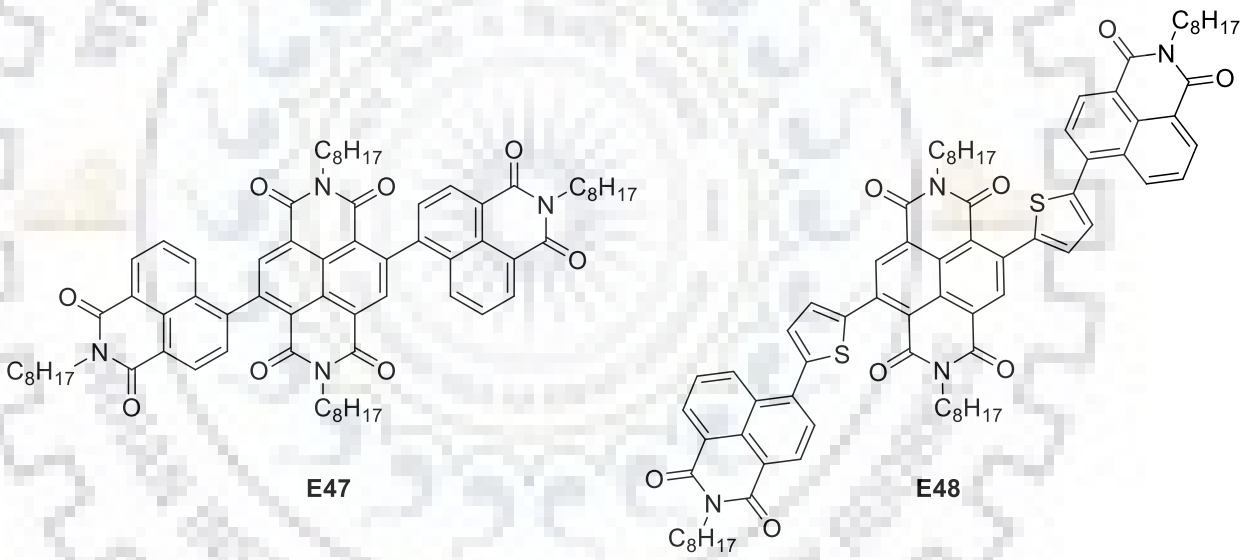

Chart 1.59 Structures of A-A-A type naphthalimide-based non-fullerene acceptors (**E47-E48**)

Srivani *et al*.[167] synthesized two non-fullerene electron acceptors based on naphthalenediimide and naphthalimide units **E47** and **E48** for solution processable bulk-heterojunction solar cells (Chart 1.59). The dyes had a basic A-A-A architecture where naphthalimide was flanked terminally on both the sides of central core. **E47** and **E48** displayed their absorption profiles in the range of 300-600 nm. Specifically, a 50 nm and 70 nm bathochromic shift was observed for **E48** in solution and film state, respectively. The theoretical calculations revealed that HOMO is located on peripheral naphthalimide and LUMO on the central naphthalene dimide. **E48** displayed a low lying LUMO level at -4.10 eV compared to -3.69

eV for **E47** due to introduction of thiophene units in former. The devices were fabricated with an architecture of (ITO)/ (PEDOT:PSS)/active layer/Ca (20 nm)/Al (100 nm) using both of the dyes (Table 1.3). The photovoltaic properties revealed the **E48** based device with an efficiency of 4.04% was superior over **E47**-based device (2.91%). The device from **E48** displayed a high V_{OC}, J_{SC}, *ff* of 0.81 V, 8.58 mA cm^{-2} and 0.58 respectively. Whereas, for P3HT:**E47** based 1:1 active blended device afforded cell parameters of 0.84 V, 6.13 mA cm^{-2} and 0.56.

Dang *et al.*[168] synthesized two naphthalimide-based acceptors **E49** and **E50** with an A_1-π-A-π-A_1 framework using end capped naphthalimide, benzothiadiazole and diketopyrrolopyrrole, respectively as the building groups (Chart 1.60). Both acceptor systems exhibited wide and broad absorption spectra covering a range of 300 nm to 700 nm with high lying LUMO energy levels complementary to the absorption spectra of polymer (PTB7-Th). The active blend were employed in non-fullerene BHJ-OSCs possessing a high V_{OC} values up to 1.01-1.12 V and PCE values of 1.23% and 1.64% for **E49** and **E50**, respectively (Table 1.3).

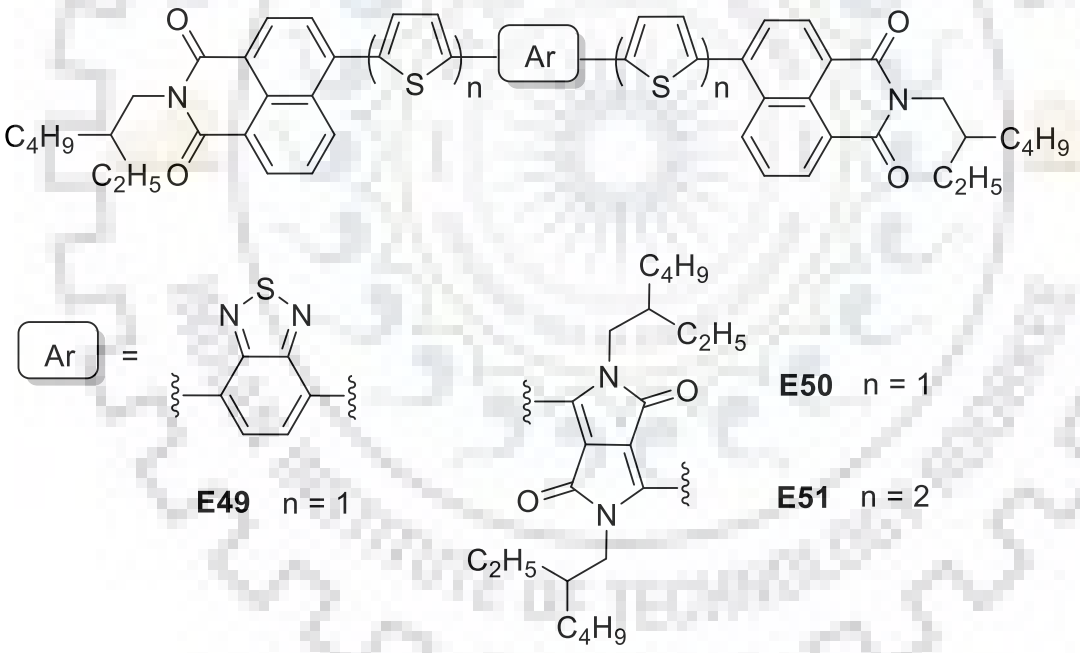

Chart 1.60 Structures of naphthalimide flanked dyes (**E49-E51**)

Another naphthalimide based organic dye **E51** possessing diketopyrrolopyrrole and bithiophene using Stille coupling was reported by Chen *et al.*[169] The dye was designed to act both as donor with PCBM and acceptor with P3HT in OSCs. It covered whole range of absorption spectra from 300-700 nm with two distinct bands arising from ICT and π-π* electronic transitions. The film spectra of **E51** observed a red shift by 40 nm. Due to the extended conjugation, **E51**

exhibited ca. 23 nm red shift in solution relative to that of **E50**. The LUMOs are delocalized across the whole molecular backbone while HOMOs located on the central bridged core. **E51** displayed a reversible two oxidation and one reduction waves located at about 0.56 eV and -1.16 eV, respectively, corresponding to HOMO (-5.40 eV) and LUMO (-3.61 eV) energy levels. The LUMO of the dye is low lying and found to be suitable for both P3HT and PCBM. A device with configuration ITO/PEDOT:PSS/**E51**:PCBM/LiF/Al using **E51** as donor with $PC_{61}BM$ was fabricated which achieved a low PCE of 0.58% with J_{SC} of 2.40 mA cm^{-2} and high V_{OC} of 0.80 V. Further, when blended with $PC_{71}BM$, **E51** exhibited a PCE of 0.76% with improved J_{SC} of 3.28 mA cm^{-2}. However, the P3HT:**E51**-based device achieved a PCE of 0.6% with a V_{OC} of 0.70 V, J_{SC} of 1.9 mA cm^{-2} (Table 1.3).

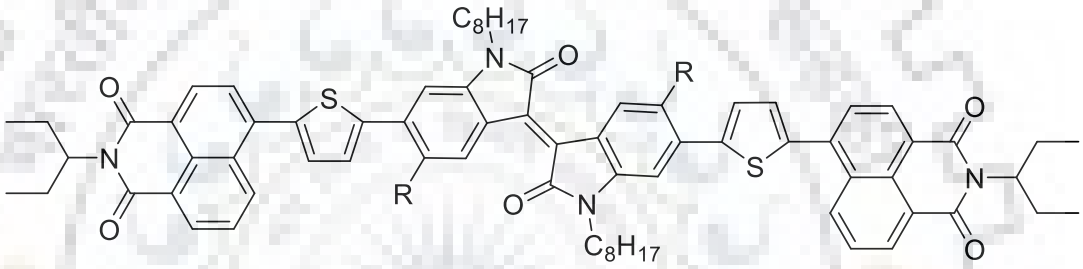

E52 R = H **E53** R = Cl

Chart 1.61 Structures of naphthalimide-based non-fullerene acceptors (**E52-E53**)

Two non-fullerene acceptors **E52** and **E53**-based on isoindigo as donor flanked by terminal naphthalimide acceptors were reported by McAfee *et al.*[170] shown in Chart 1.61. The influence of structural modification on the optical, electrochemical and thermal properties were assessed and correlated with DFT calculations. The small molecules exhibited two distinct absorption bands, a low-energy band at λ = 570 nm arising from charge transfer, and a high-energy band at λ = 450 nm owing to the π-π^* electronic transitions within the molecule. Notably, the induced molecular non-planarity in the conjugated backbone of **E52** by introduction of chlorine atoms hampers the electronic delocalization leading to visible effects in the absorption intensities. Unlike **E52**, in the solid state, **E53** exhibited a red-shift (Δ32 nm), which was attributed to the solid state self-assembly due to the presence of chlorine atoms, a factor responsible for the crystalline nature of **E53** (T_c~ 240). Both the dyes exhibited a reversible triple reduction profile attributed to the naphthalimide core. In terms of energy levels, **E53** exhibited a more stabilized energy levels. The incorporation of chlorine atoms in **E53** had a pronounced influence on lowering down LUMO energy level to -3.73 eV. The effect of substitution and the structure–property relationships were

investigated for their photovoltaic performance in solution-processable inverted BHJ devices as ITO/ZnO/p-DTS($FBTTh_2$)$_2$:**E52/E53**/MoO_3/Ag (Table 1.3). The synergy of non-planarity and enhanced electron affinity of the **E53** showed a maximum PCE of 1.9% with high V_{OC} of 0.87 V.

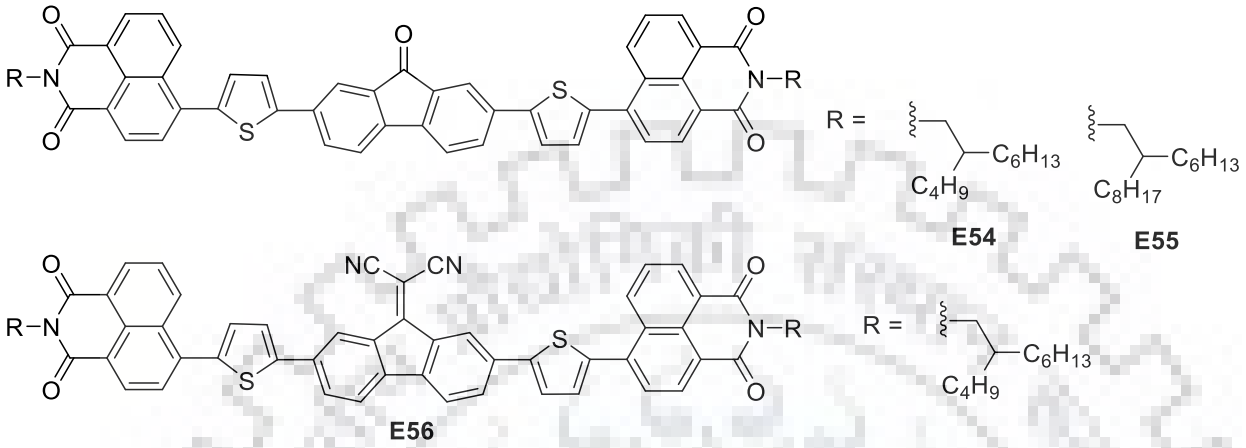

Chart 1.62 Structures of naphthalimide-based non-fullerene acceptors (**E54-E56**)

Do *et al.*[171] reported highly twisted non-fullerene acceptors based on alkylated naphthalimide and 9-fluorenone **E54** and **E55** with a basic module of A_1−D−A_2−D−A_1 (Chart 1.62). In particular, **E54** and **E55** were composed of naphthalimide as end-capping acceptor (A_1), fluorenone as electron-withdrawing central (A_2) group, and thiophene as a donor unit. In addition, dye **E56** was synthesized by introducing dicyano group on the fluorerone core, enhancing the acceptor strength of central acceptor unit. Whereas, **E54** and **E55** had similar absorption profile in the range of λ = 300−600 nm, **E56** showed two absorption bands due to the enhanced electronic conjugation and electron-withdrawing strength. The energy levels of **E54-E56** were found to be compatible with P3HT as donor in BHJSC. The deep HOMO and LUMO level at -6.0 eV and -4.0 eV with a narrow band gap is due to the high electron deficiency of the backbone. Interestingly, **E54** possessed a defused electron density on the backbone, whereas **E56** displayed a well separated electron density with LUMO centered on dicyanofluorene unit. Among three tested acceptor molecules for solar cell devices, **E54** exhibited the highest performance (3.6%) with a high V_{OC} of 0.88 V, J_{SC} of 9.1 mA cm^{-2} and *ff* of 0.45 (Table 1.3). The highest performance of **E54**-based device could be attributed to the enhanced nanoscale morphology of the active layer.

Table 1.3 Optical and photovoltaic properties of dyes **E38-E56**

Acceptor	Donor	Active blend ratio D:A (w/w)	$\lambda_{max,}$ nm	$\lambda_{max,}$ nm film	HOMO, eV	LUMO, eV	$E_{0\text{-}0,}$ eV	J_{SC} (mA/cm^2)	V_{OC} (V)	*ff*	η *(%)*
E38	P3HT	1:1	365	-	-	-3.24	3.04	2.75	0.82	0.46	1.03
E39	P3HT	1:1	358	360	-6.18	-3.59	2.98	0.51	0.20	0.31	0.03
		1.5:1						0.28	0.22	0.28	0.02
		1:1						0.57	0.28	0.41	0.06
		1:1.5[a]						0.83	0.56	0.35	0.16
		1:1.5[b]						0.79	0.79	0.45	0.28
E40	P3HT	1:1	396	420	-5.95	-3.62	2.49	0.69	0.49	0.33	0.11
		1.5:1						0.88	0.53	0.41	0.18
		1:1						1.08	0.53	0.28	0.16
		1:1.5[a]						0.73	0.61	0.48	0.21
		1:1.5[b]						1.47	0.80	0.49	0.58
E41	P3HT	1:1	482	488	-5.67	-3.60	2.25	3.15	0.96	0.33	0.99
		1.5:1						3.23	0.97	0.35	1.10
		1:1						3.20	0.97	0.34	1.05
		1:1.5[a]						4.85	1.06	0.46	2.36
		1:1.5[b]						3.33	1.08	0.35	2.25
E42	PCDTBT-C12	1:1	399	382	-6.07	-3.53	2.54	0.69	1.10	0.21	0.16
		1:2						0.29	1.21	0.30	0.84
		1:3						2.38	1.20	0.34	0.97
		1:4						2.46	1.22	0.36	1.12
		1:4[c]						2.91	1.30	0.53	2.01
E43	PCDTBT-C12	1:2	428	405	-5.93	-3.50	2.43	1.82	1.36	0.24	0.59
		1:2[c]						4.79	1.04	0.56	2.78
E44	PCDTBT-C12	1:2	424	415	-5.98	-3.62	2.36	1.10	1.19	0.26	0.34
		1:2 [c]						2.21	1.11	0.30	0.24
E45	PCDTBT-C12	1:2	437	448	-5.95	-3.68	2.27	0.42	1.11	0.26	0.14

Acceptor	Donor	Active blend ratio D:A (w/w)	λ_{max}, nm	λ_{max}, nm film	HOMO, eV	LUMO, eV	$E_{0\text{-}0}$, eV	J_{SC} (mA/cm^2)	V_{OC} (V)	*ff*	η (%)
E45		1:2 [c]						1.71	1.09	0.30	0.56
E46	PCDTBT-C12	1:2	458	492	-5.80	-3.65	2.15	0.34	1.25	0.26	0.11
		1:2 [c]						0.37	1.24	0.28	0.13
E47	P3HT	1:1	440	450	-5.95	-3.69	2.26	6.13	0.84	0.56	2.91
E48	P3HT	1:1	500	550	-5.86	-4.10	1.76	8.58	0.81	0.58	4.04
E49	PTB7-Th	1:1 [d]	480	509	-5.50	-3.35	2.01	3.84	1.02	0.31	1.23
	PTB7-Th	1:1 [e]						1.63	0.90	0.24	0.39
	PTB7-Th	1:1 [f]						2.42	1.02	0.27	0.72
E50	PTB7-Th	1:3 [d]	576	636	-5.51	-3.55	1.72	1.76	1.12	0.32	0.64
	PTB7-Th	1:3 [e]						3.12	1.06	0.46	1.64
	PTB7-Th	1:3 [f]						3.55	1.10	0.34	1.43
$PC_{61}BM$ [g]	**E51**	1:2.5	599	637	-5.40	-3.61	1.59	2.40	0.80	0.30	0.58
$PC_{71}BM$ [g]								3.48	0.79	0.29	0.76
E51 [h]	P3HT	1:2.5						1.91	0.70	0.45	0.60
E52	p-DTS(FBTTh$_2$)$_2$	1:1	450	709	-5.53	-3.70	1.83	1.29	0.68	0.44	0.38
E53	p-DTS(FBTTh$_2$)$_2$	1:1	482	711	-5.61	-3.73	1.88	5.27	0.87	0.42	1.93
E54	P3HT	1:1	411	426	-6.07	-3.96	2.11	9.1	0.86	0.45	3.6
E55	P3HT	1:1	411	425	-6.06	-3.98	2.08	7.2	0.86	0.41	2.5
E56	P3HT	1:1	586	625	-6.14	-4.21	1.93	3.0	0.56	0.36	0.6

[a]Thermal annealing at 120 ℃ for 20 min, [b] Solvent annealing, [c] Thermal annealing at 90 ℃ for 3 min, [d] device: ITO/PEDOT:PSS/active layer/Ca/Al, [e] ITO/PEDOT:PSS/active layer/PFN/Al, [f] ITO/ZnO/PFN/ active layer/MoO_3/Al, [g] Thermal annealing at 75 ℃ for 10 min and solvent annealing for 40 s, [h] vapour annealing for 1 hr followed by thermal annealing at 124 ℃ for 10 min

1.4.2.2 Naphthalimide-based vinyl-linked chromophoric materials

Bloking *et al.*[172] reported a symmetric naphthalimide based acceptor **E57** with benzothiadiazole in A_1-A_2-A_1 fashion (Chart 1.63). A broad absorption band at λ = 467 nm is observed attributable to the highly conjugating skeleton. The dye exhibited a high electron affinity of -3.4 eV. Due to the bulky steric interactions between neighboring hydrogen atoms in the naphthyl and vinyl moieties, a twist of 27.3 ° was induced resulting in poor electron transport. The device with an architecture of ITO/PEDOT:PSS (25 nm)/ P3HT:**E57** (ca. 80 nm)/LiF (1 nm)/Al (200 nm) was fabricated (Table 1.4). The device resulted in a low current density of 0.5 mA cm^{-2} and thus a poor PCE of 0.12% only.

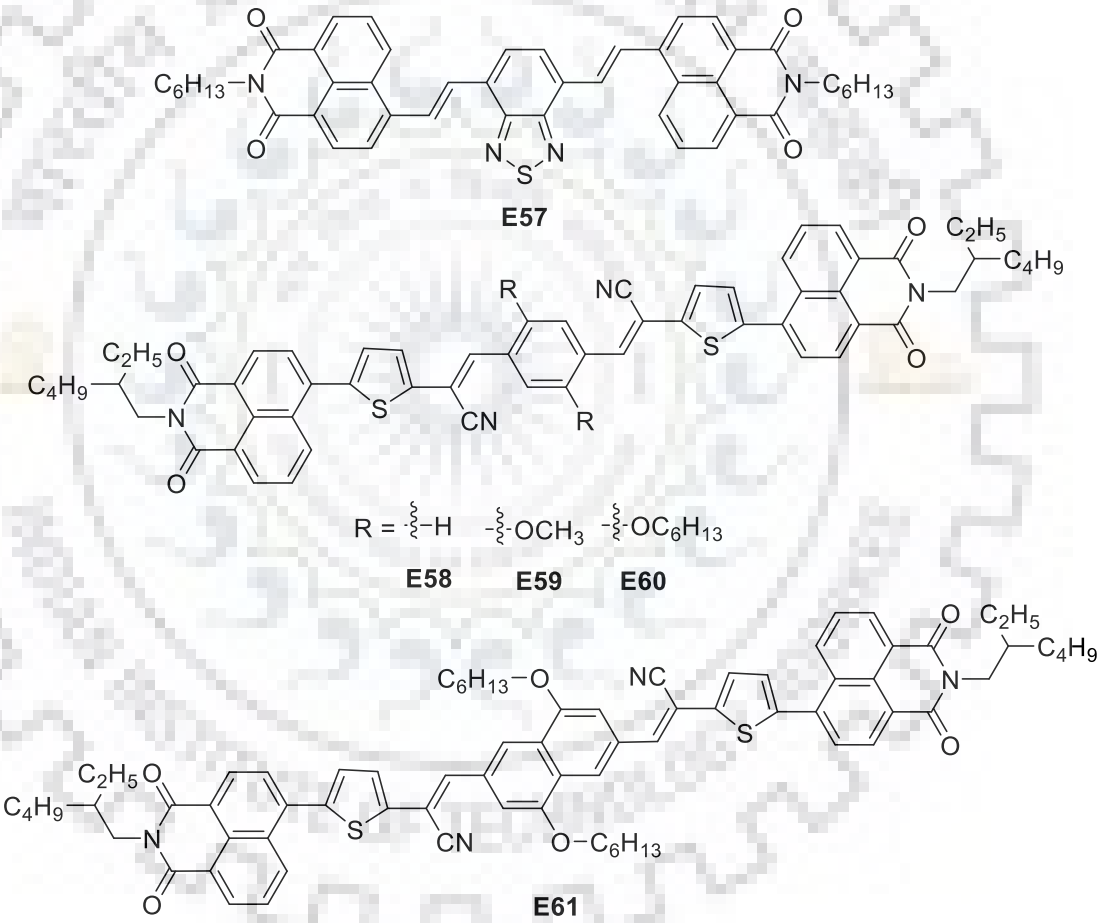

Chart 1.63 Structures of vinyl-linked bis-naphthalimides as non-fullerene acceptors (**E57-E61**)

In yet another work, Kwon *et al.*[173] aimed at synthesis and the characterization of non-fullerene naphthalimide end capped acceptors **E58** and **E59** having different substituents on the central phenyl unit (Chart 1.63). These dicyanodistyrylbenzene-appended acceptors were tested with P3HT as active layer in polymer solar cell. The presence of terminal naphthalimide units in

E58 and **E59** suppressed the molecular aggregation in addition to the twisted conformation of the molecule. Blue shifted absorption spectra were recorded for **E59** when annealed at 150 ˚C in contrast to **E60** which displayed a well resolved absorption band. These alterations inferred the molecular conformational changes arising from the non-planarity of the dyes. The dyes displayed multiple reduction waves due to their multiple reductions. The dyes possessed a high lying LUMO energy levels than $PC_{61}BM$ (-3.83 eV) at -3.42, -3.66 and -3.41 eV, respectively. The polymer solar cell with structure of ITO/PEDOT:PSS/ P3HT:**E58-E60**/Ca/Al was fabricated using an active layer in ratio of 1:2.5 (Table 1.4). The device fabricated using **E59** displayed a low PCE of 1.45% relative to **E58** (2.71%) attributable to a low lying LUMO level of **E59**. However, the device using **E60** exhibited a good efficiency of 2.55% with a high V_{OC} of 0.67 V and a maximum J_{SC} of 8.15 mA cm^{-2} (Table 1.4). The devices exhibited a broad IPCE plot covering a range of 400-650 nm with maximum IPCE of 61 % for **E58**.

Min *et al.*[174] studied the effect of addition of six solvent additives and a non-volatile molecular additive, di-2-thienyl-2,1,3-benzothiadiazole (DTBT), on the performance of BHJSC. All small molecule solar cell was fabricated using a BDTT-S-TR: **E58** system. The reference as casted device fabricated using the active blend showed a PCE of approximately 1.09%, which was enhanced to over 4.5% with addition of 0.75 vol% of DIO (Table 1.4). Also authors designed a device using DTBT as a non-volatile additive in addition to DIO to reduce D/A blending. The PCE was further improved to 5.33% by addition of 0.75 vol% DIO and 2 wt% DTBT into $CHCl_3$. This work suggests that the use of binary additives can control the bulk morphology of solution processed all-small molecule solar cells and other thin film devices.

E59 was demonstrated as an efficient non-fullerene small molecule acceptor along with a benzothiadiazole-based small molecule as donor (p-DTS$(PBTTh_2)_2$) in all small molecule solar cell.[175] In contrast to polymer-based solar cells, the all small molecule-based solar cell displayed a better efficiency, presumably, due to better fabrication in terms of batch-to-batch purifications and solution processing. The absorption profiles of both donor (λ_{max} = 680 nm) and acceptor (λ_{max} = 498 nm) were found complementary to each other to cover the visible region. It is interesting to note that the absorption spectra of either donor or acceptor did not change individually on thermal annealing, but the absorption spectra of the active layer significantly altered with a red shift of 50 nm. The HOMO and LUMO energy levels of **E59** were calculated to be -5.75 eV and -3.66 eV, respectively. The fabricated solar cell when subjected to thermal annealing at 90-150 °C displayed variation in efficiency. When annealed at high temperature 130˚

C, the efficiency drops down from 5.44% to 3.61% due to the sudden fall in J_{SC} value. Thus, naphthalimide based molecule showcased a promising PCE of 5.44% with V_{OC} of 0.85 V, J_{SC} of 9.68 mA cm^{-2}, and *ff* of 0.66.

Further, Kwon *et al.*[176] demonstrated an efficient non-fullerene organic solar cell with donor–acceptor crystalline structures using PPDT2FBT and **E60** as the donor and small molecular acceptor, respectively. The active layer morphology was found to be dependent on thermal annealing and the various morphological characteristics. The as-fabricated naphthalimide-based OPV device showed a high PCE of 7.64% (the highest observed efficiency till date) with a remarkably high V_{OC} of 1.03 V. This is among the highest observed efficiency in polymer solar cells with a small molecular non-fullerene acceptor. The highest performance of device could be attributed to the complementary absorption, well matched energy levels and balanced charge transport, and minimized charge recombination processes.

Kwon *et al.*[177] synthesized a new non-fullerene acceptor **E61**, an analog of **E60** (Chart 1.65). The dye was used with small molecular donor *p*-DTS$(FBTTh_2)_2$ in BHJSC devices with different processing solvents. **E61** displayed multiple reduction waves arising from dicyanostryl and naphthalimide units. The dye possessed a deep seated HOMO and LUMO at -5.88 eV and -3.63 eV. The highest PCE of 3.45% was achieved using chloroform as processing solvent, forming uniform morphology with device architecture of ITO/PEDOT:PSS/active layer/Ca/Al. Notably, **E61** exhibited an enhanced PCE compared to its analog dye **E60** with a V_{OC} of 1.04 V, J_{SC} of 5.94 mA cm^{-2}, and a *ff* of 0.56 (Table 1.4).

Table 1.5 Optical and photovoltaic properties of dyes (**E57-E61**)

Acceptor	Donor	Solvent/thermal Annealing w/w%/° C	Active blend ratio D:A (w/w)	$\lambda_{max,}$ nm	$\lambda_{max,}$ nm film	HOMO, eV	LUMO, eV	$E_{0\text{-}0,}$ eV	J_{SC} (mA/cm^2)	V_{OC} (V)	*ff*	η (%)
E57	P3HT	as cast	1:1.4	467	-	-5.70	-3.40	2.16	0.50	0.65	0.40	0.12
E58	P3HT	100° C/20 min	1:2.5	430	453	-5.90	-3.42	2.46	8.04	0.73	0.46	2.71
	BDTT-S-TR	as cast	1:0.8						3.59	1.12	0.27	1.09
		DIO (0.75)	1:0.8						8.29	0.97	0.58	4.67
		MT (0.50)	1:0.8						5.54	1.04	0.40	2.33
		NMP (0.20)	1:0.8						3.86	1.03	0.33	1.30
		CN (0.50)	1:0.8						6.13	1.03	0.42	2.67
		DPE (0.75)	1:0.8						7.19	1.00	0.45	3.26
		BrAni (0.50)	1:0.8						4.18	0.99	0.31	1.30
		DTBT (3.0)	1:0.8						6.26	1.00	0.37	2.36
		DIO (0.75)+ DTBT (2.0)	1:0.8						9.12	0.97	0.60	5.33
E59	P3HT	110° C/20 min	1:2.5	476	498	-5.75	-3.66	2.23	6.23	0.54	0.43	1.45
	p-DTS(PBTTh$_2$)$_2$	as cast	1:1						0.11	0.92	0.22	0.02
		90° C	1:1						8.42	0.83	0.44	3.25
		110° C	1:1						9.62	0.85	0.64	5.44
		130° C	1:1						5.54	0.92	0.68	3.61
E60	P3HT	90° C/20 min	1:2.5	476	517	-5.79	-3.41	2.28	8.15	0.67	0.47	2.55
	PPDT2FBT	as cast	1:2.5						11.50	1.03	0.54	6.38
		90° C	1:2.5						11.88	1.03	0.63	7.64
		130° C	1:2.5						8.24	0.94	0.54	4.15
E61	p-DTS(PBTTh$_2$)$_2$	CB	1:1	439	471	-5.88	-3.63	2.25	5.94	1.04	0.56	3.45
		CF	1:1						5.44	1.08	0.55	3.24
		THF	1:1						5.23	1.07	0.54	3.02
		Tol	1:1						6.06	1.08	0.50	3.30
		o-xyl	1:1						5.41	1.04	0.52	2.92

1.4.2.3 Naphthalimide-based ethynyl-linked chromophoric materials

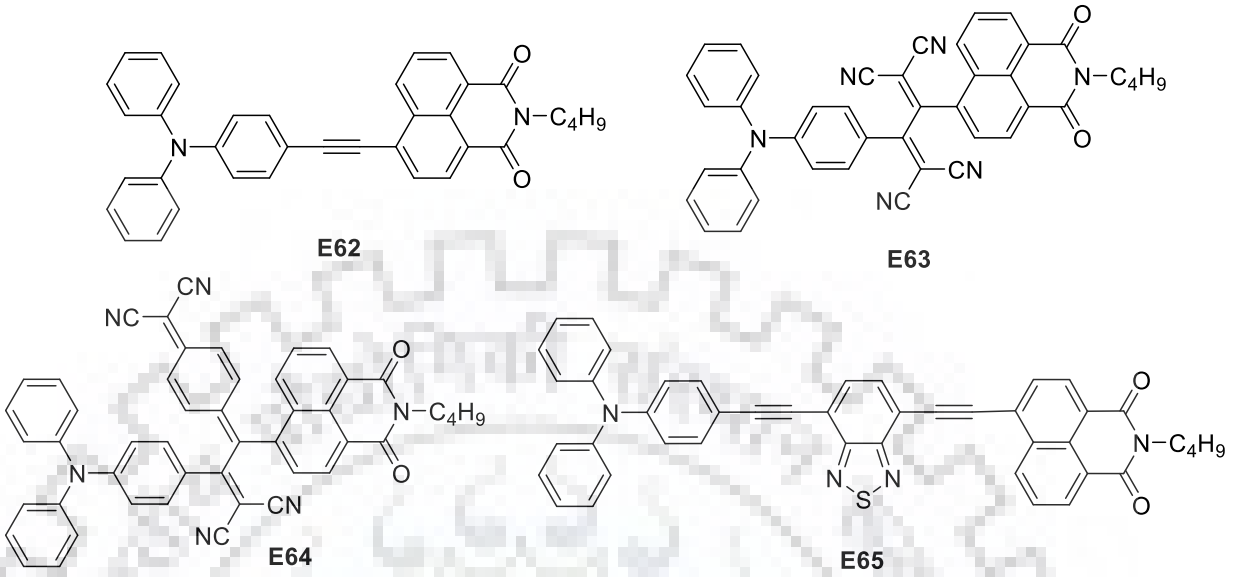

Chart 1.64 Structures of linear D-A based mono-naphthalimide dyes (**E62-E65**)

Gautam *et al.*[178] synthesized D-A-A modules based on triphenylamine-naphthalimide molecules **E63** and **E64** functionalized with tetracyanobutadiene and dicyanoquino-dimethane analogous to **E62** and used as fullerene free acceptors for BHJSCs (Chart 1.64). The dyes in blend with the polymer covered the whole visible region. Unlike **E62**, the incorporation of additional acceptors in **E63** and **E64** resulted in strong ICT. Moreover, dye **E64** exhibited a red shift profile near IR due to the presence of strong electron-withdrawing unit. Both **E63** and **E64** displayed multi-redox waves and possessed a LUMO level of -3.92 and -3.98 eV, respectively. The organic solar cells fabricated from **E64** displayed higher PCE of 6.11% than **E63** (4.94%) attributed to the broader absorption profile, more balanced charge transport and lower photon energy loss in **E64** The solar cells showed a larger value of V_{OC} of 1.06 V for **E64** without solvent annealing (Table 1.5). These two small molecules were found as effective non-fullerene acceptors and displayed good efficiencies with polymer (DTS(FBTTh).

In their successive work, the same group reported a small molecular acceptor **E65** [179] having D-π-A_1-π-A_2 configuration where triphenylamine, benzothiadiazole and naphthalimide units were respectively coupled as D, A_1 and A_2 through ethylene linkers (Chart 1.66). **E65** was used as an electron donor for solution-processed BHJSCs. The absorption spectrum of **E65** exhibited two distinct peaks at λ = 328 nm and 408 nm due to π-π* transitions and an ICT band at 494 nm. In the solid state, the dye displayed a red shift at λ = 548 nm. Such ICT is a characteristic of *J*-aggregates due to the facile ordered packing of dye. **E65** showed suitable HOMO (-5.30 eV)

and LUMO (-3.36 eV) energy levels to be used as donor along with $PC_{71}BM$ as acceptor. The small molecule organic solar cells based on the optimized blend of **E65** with $PC_{71}BM$ processed in $CHCl_3$ showed PCE of 2.21%, which was significantly improved upto 6.67%, when two-step annealing (TSA) treated blend was used as an active layer (Table 1.5).

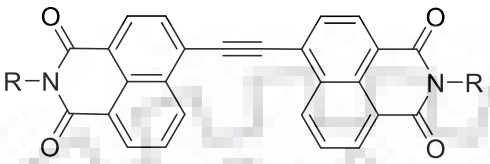

R = $-C_4H_9$ $-C_6H_{13}$ $-C_8H_{17}$

E66 **E67** **E68**

E69

Chart 1.65 Structures of naphthalimide-based non-fullerene acceptors (**E66-E69**)

Zhang *et al.*[184] reported three naphthalimide based non-fullerene acceptors **E66-E68** with different alkyl chains at the imidic position (Chart 1.65). It was found that the LUMO levels of **E66-E68** were high-lying and quite suitable for wide optical band gap polymer PBDTBT-C12. All acceptors were planar, crystalline and aggregated in the solid state facilitating the electron transport in blend films, and thus resulted a superior electron mobility and J_{SC}. A PCE of 4.05% with a V_{OC} of 1.08 V was obtained for PBDTBT-C12:**E67**-based PSCs in a very thin active layer (35 nm in thickness) with device architecture of ITO/PEDOT:PSS/active layer/LiF/Al (Table 1.6). Furthermore, the PCE of 4.05% was comparable to PBDTBTC12:$PC_{71}BM$-based optimized devices (4.07%) and even better than devices with an active layer thickness of ca. 30 nm (2.72%).

Zhang *et al.*[185] again reported a small molecular acceptor **E69** based on 1,8-naphthalimide. **E32** acceptor along with two wide band gap benzothiadiazole-based polymers as donors (BTDFTh, BTDFThO) was used in the fabrication of non-fullerene polymer OPVs (Chart 1.65). The dye exhibited a broad absorption band at λ = 376 nm in film with a blue shift ($\Delta\lambda$ = 21 nm) as compared to that of in the solution (397 nm), indicating the formation of H-aggregates in the solid state. The modeled structure of the dye supported highly planar and rigid molecular backbone which was believed to enhance the charge transportation in the solid state. The dye was found to

be crystalline in nature (T_C = 201.4° C) having a sharp melting at 216.0℃. The HOMO-LUMO energy levels of **E69** were determined to be -6.00 and -3.57 eV, respectively. Such a high lying LUMO level of dye is beneficial for reducing energy loss. **E69** displayed a PCE of 1.26% when used with BTDFTh polymer with a high V_{OC} of 1.06 V (Table 1.5). With the other polymer, BTDFThO the device exhibited an enhanced efficiency (2.91%). Solar cell devices based on fluorinated polymer BTDFThO achieved a good efficiency of 3.71% with additive addition displaying a high V_{OC} of 1.07 V.

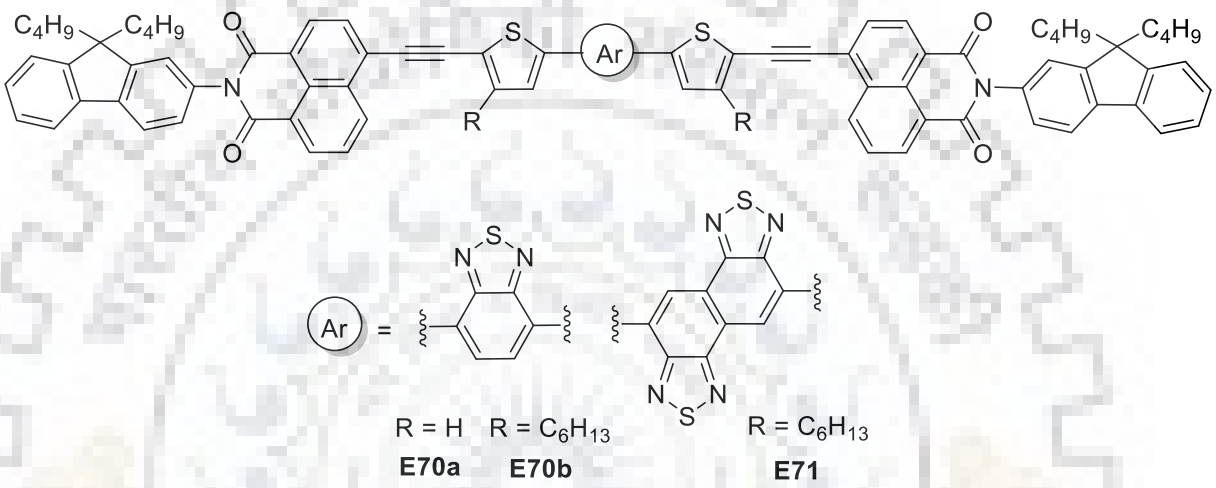

Chart 1.66 Structures of linear bis-naphthalimide-based non-fullerene acceptors (**E70-E71**)

Novel end-capped naphthalimide-based linear non-fullerene acceptors **E70a-b** and **E71** were reported by Chatterjee *et al.*[182] (Chart 1.66). The dyes possess conjugating π-backbone comprising of central acceptors (thiophene flanked benzothiadiazole and fused bisbenzothiadazole) linked by ethyl linkage to the terminal fluorene-appended naphthalimides. The dyes displayed an absorption band at λ = 500-540 nm, attributable to their transitions from HOMO to LUMO. **E70a** displayed an absorption band at λ_{max} = 503 nm, which experienced a red shift by 15 nm in film state. The dye possessed reversible multiple reduction peaks due to the reduction of naphthalimide and benzothiadiazole unit. The LUMO level of **E70a** was found at -3.43 eV, similar to **E70b**. Owing to its extended conjugated system, **E71** exhibited a significant bathochromic shift ($\Delta\lambda$ = 16 nm) relative to that of **E70b**. The film absorption spectra of **E71** were found to be further red shifted due to the intermolecular interactions within the dyes. Emergence of new absorption shoulder at λ = 620 nm for **E71** implied stronger intermolecular interactions. The dyes displayed multiple reversible reduction waves as depicted by **E70a**. The reduction aroused from benzothiadiazole, fused benzothiadiazole, and naphthalimide units. It was observed

that the first reduction potential of **E71** was cathodically shifted to -1.25 V compared to **E70b** (-1.34 V), which can be attributed to the more electron affinity of central core in former. Further, the second and third reduction potentials of **E71** were assigned to the reduction of naphthalimide unit. In contrast to **E70b** (-3.44 eV), **E71** displayed a low lying LUMO energy level at -3.60 eV due to the more electron deficiency of the **E71**. Also, the HOMO energy levels of both the dyes were deep seated at -6.0 eV. The dyes were tested in BHJSCs with a structure of (ITO)/ (PEDOT:PSS)/active layer/Ca/Al in 1:1 weight ratio, and thermal annealing at 140 ˚C (Table 1.5). Device fabricated using **E70a** exhibited efficiency of 1.16 % with J_{SC} of 3.92 mA cm^{-2} and V_{OC} of 0.75. Dye **E70b** displayed an improved device performance with PCE of 1.53 %, attributable to its larger V_{OC}. Compared to device fabricated using **E70b**, **E71** displayed better EQE spectra in the range of 300-720 nm with photocurrent response of 42% at 525 nm. Further, **E71** exhibited a maximum PCE of 2.81% with a V_{OC} of 0.90 and J_{SC} of 5.18 mA cm^{-2} when used with P3HT donor using co-solvent processing.

1.4.2.4 Star-shaped naphthalimide-based materials

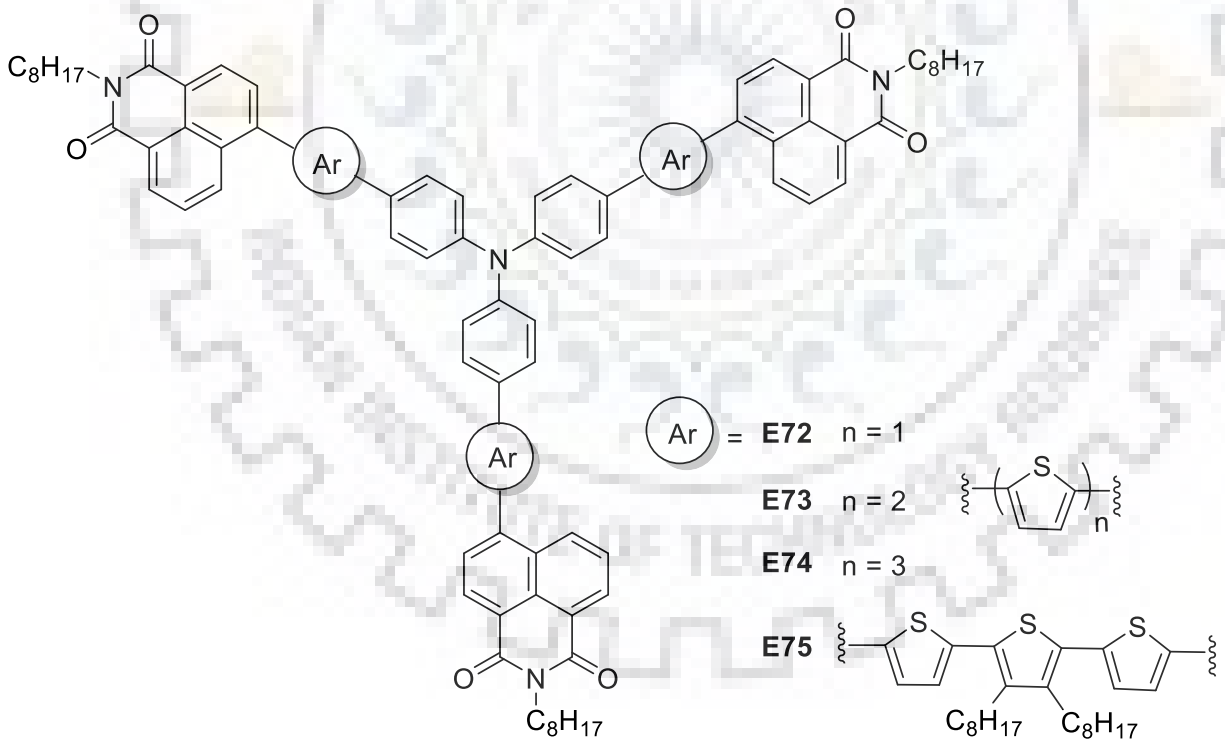

Chart 1.67 Structures of star-shaped naphthalimide triphenylamine derivatives **(E72-E75)**

Zhang *et al.*[183] demonstrated the application of star shaped D-π-A small molecules **E72-E75** as donors possessing triphenylamine as central donor core flanked by naphthalimide as terminal acceptors and oligothiophenes as spacer in OSCs shown in Chart 1.67. The molecules

were synthesized using direct arylation and Suzuki coupling reactions between the precursors. The materials displayed excellent light harvesting properties covering the whole range of absorption spectra (300-600nm). All the dyes displayed a broad absorption band in 400-500 nm region, originating from the ICT from triphenylamine to naphthalimide unit within the dyes. Further, the film absorption spectra of the dyes were found to be broad and red-shifted. Due to the presence of electron deficient naphthalimide and highly twisted structure the dyes displayed a deep HOMO energy level favorable for high V_{OC}. It was also observed that with increasing the length of thiophenes as in **E72** to **E74**, the HOMO energy levels were lifted and lowered the LUMO levels. The molecules were tested in BHJSCs as an architecture of ITO/PEDOT:PSS/**E72-E75**:$PC_{71}BM$/LiF/Al (Table 1.5). All the devices were fabricated using 1:3 weight ratio of donor and $PC_{71}BM$. For all OSCs, a donor to $PC_{71}BM$ weight ratio of 1:3 with or without annealing at 110 ˚C was used. The device efficiencies increased from 0.66% using **E72** to 2.32% for **E75** with a high V_{OC} of 0.94 V. It was successfully demonstrated that the use of spacer can significantly influence the optical and photovoltaic properties of D-A small molecules.

Table 1.5 Optical and photovoltaic parameters of dyes (**E62-E75)**

Acceptor	Donor	Solvent/thermal Annealing w/w%/° C	Active blend ratio D:A (w/w)	$\lambda_{max,}$ nm	$\lambda_{max,}$ nm film	HOMO, eV	LUMO, eV	$E_{0\text{-}0,}$ eV	J_{SC} (mA/cm^2)	V_{OC} (V)	*ff*	*η (%)*
E63	DTS(FBTTh)	as cast	1:2.5	451	-	-5.56	-3.92	1.64	6.14	1.06	0.36	2.34
		DIO	1:1						8.02	0.98	0.40	3.14
E64	DTS(FBTTh)	as cast	’’	722	-	-5.44	-3.98	1.46	9.15	1.02	0.54	4.94
		DIO	’’						11.26	0.92	0.59	6.11
$PC_{71}BM$	**E65**	as cast	’’	494	548	-5.30	-3.36	1.81	6.18	0.94	0.38	2.21
$PC_{71}BM$	**E65**	120° C/10min	1:2.5						11.54	0.90	0.66	6.67
E66	PCDTBT-C12	as cast	1:1	426	439	-6.05	-3.54	2.50	1.34	1.09	0.10	0.15
E67	PCDTBT-C12	as cast	’’	426	434	-6.04	-3.48	2.56	4.71	1.06	0.56	2.80
	PCDTBT-C12	CN (0.5%)	’’						6.24	1.06	0.61	4.05
E68	PCDTBT-C12	as cast	’’	426	438	-6.02	-3.47	2.55	4.43	1.07	0.55	2.61
	PCDTBT-C12	CN (0.5%)	’’						5.19	1.07	0.60	3.34
E69	BTDFTh	as cast	1:3	429	376	-6.00	-3.57	2.43	3.40	1.06	0.35	1.26
		CN (0.5%)	’’						4.10	1.06	0.43	1.87
	BTDFThO	as cast	’’						5.27	1.08	0.51	2.91
		CN (0.5%)	’’						6.29	1.07	0.55	3.71
E70a	P3HT	140° C/15min	1:1	503	518	-5.56	-3.43	2.13	3.92	0.75	0.36	1.16
E70b	P3HT	CB	1:1	517	-	-5.95	-3.44	1.82	3.52	0.94	0.46	1.53
E71		CB		533	-	-6.01	-3.60	1.73	5.31	0.90	0.52	2.48
E71		o-DCB							4.15	0.87	0.63	2.29
E71		CB/o-DCB(4:1)							5.18	0.0	0.60	2.81
$PC_{71}BM$	**E72**	as cast	1:3	458	466	-5.62	-3.57	2.23	3.15	0.74	0.29	0.66
		130° C							4.13	0.81	0.31	1.04
$PC_{71}BM$	**E73**	as cast	1:3	462	481	-5.57	-3.67	2.08	3.30	0.88	0.34	0.97
		130° C							4.98	0.83	0.37	1.54
$PC_{71}BM$	**E74**	as cast	1:3	450	467	-5.47	-3.74	1.91	5.97	0.90	0.36	1.87
		130° C							6.29	0.90	0.34	1.96
$PC_{71}BM$	**E75**	as cast	1:3	419	425	-5.39	-3.42	2.15	5.93	0.93	0/36	1.92
		130° C							6.38	0.94	0.39	2.32

1.4.3 Naphthalimide-based sensitizers in DSSCs

Another class of solar cell era is ruled by DSSCs after its invention by Grätzel *et al.*[40]. A DSSC is a composite of photoanode comprising mesoporous anatase TiO_2 and sensitizer, redox electrolyte (I_3^-/I^-, Br_3^-/Br^-, Co(II)/(III)), and platinum as counter electrode. The sensitizers play an important role on the device performance. Till now, a variety of dyes such as Ru(II)-polypyridyl-, porphyrin- and organic counterparts have been demonstrated as effective sensitizers achieving the efficiency upto >15%.[184, 185] Despite their high efficiencies, these dyes has certain disadvantages such as the use of expensive and toxic metals to synthesize sensitizers, tedious purification, limited resources, poor thermal stability and environmental pollution. On the other hand, organic dyes possess characteristics such as high molar extinction coefficient, easy purification, cost effectiveness and allow facile structural modifications to fine-tune the optical and photovoltaic properties.[186-188] An ideal sensitizer should possess the following characteristics such as extended conjugation to exhibit panchromatic absorption and appropriate energy levels for fast dye regeneration and electron injection. Therefore, a dye is designed and its molecular architecture is wisely modified to optimize the tuning of properties involving different types of donors, auxiliary acceptors, π-linkers and acceptors.

Huang *et al.*[189] synthesized naphthalimide-based four D-π-A type organic dyes **E76-E79** for DSSCs (Chart 1.68). The dyes comprised of triphenylamine or indoline and mono- or disubstituted naphthalimide units with a carboxylic group. Specifically, naphthalimide core played a role of π-conjugation and acceptor for improving ICT and electronic communication. The dyes exhibited two prominent absorption bands. A low energy band arise from the CT between donor to acceptor and a high energy band due to the π-π* electronic transitions. On contrary to **E76**, **E77** displayed a 39 nm red shift absorption profile due to the strong electron-donating strength of indoline unit. The bis-donor substituted **E78** and **E79** exhibited bathochromic shifts by 19 and 15 nm with higher molar extinction coefficients relative to those of **E76** and **E77** respectively. Among different set of dyes, the most red-shifted absorption spectra was observed for bis-indoline-based dye. Interestingly, unlike **E78-E79**, **E76-E77** displayed a blue shift when adsorbed on TiO_2 presumably due to the more non-planarity of the former. The oxidation potential of **E77** was anodically shifted to 0.79 V due to the electronic richness of indoline unit. Also, dyes having bis-donor groups facilitated the easy oxidation than those with mono-donor counterparts. However, the reduction potential of the dyes was observed at -1.4 V more negative than E_{CB} of TiO_2 (-0.5 V vs. NHE). For all the dyes, the LUMO orbitals was delocalized on naphthalimide moieties and isolated from carboxyl group

due to the presence of methylene group which hampered electron injection into the semiconductor. Thus, all dyes displayed a poor J_{SC} resulting from disruption of electron flow into TiO_2. **E76** and **E77** gave an efficiency of 1.10% and 1.18% while **E78** and **E79** exhibited η of 2.27% and 2.70% (Table 1.6). The improved efficiencies for **E78** and **E79** were ascribed to better light harvesting properties due to their broader absorption spectra.

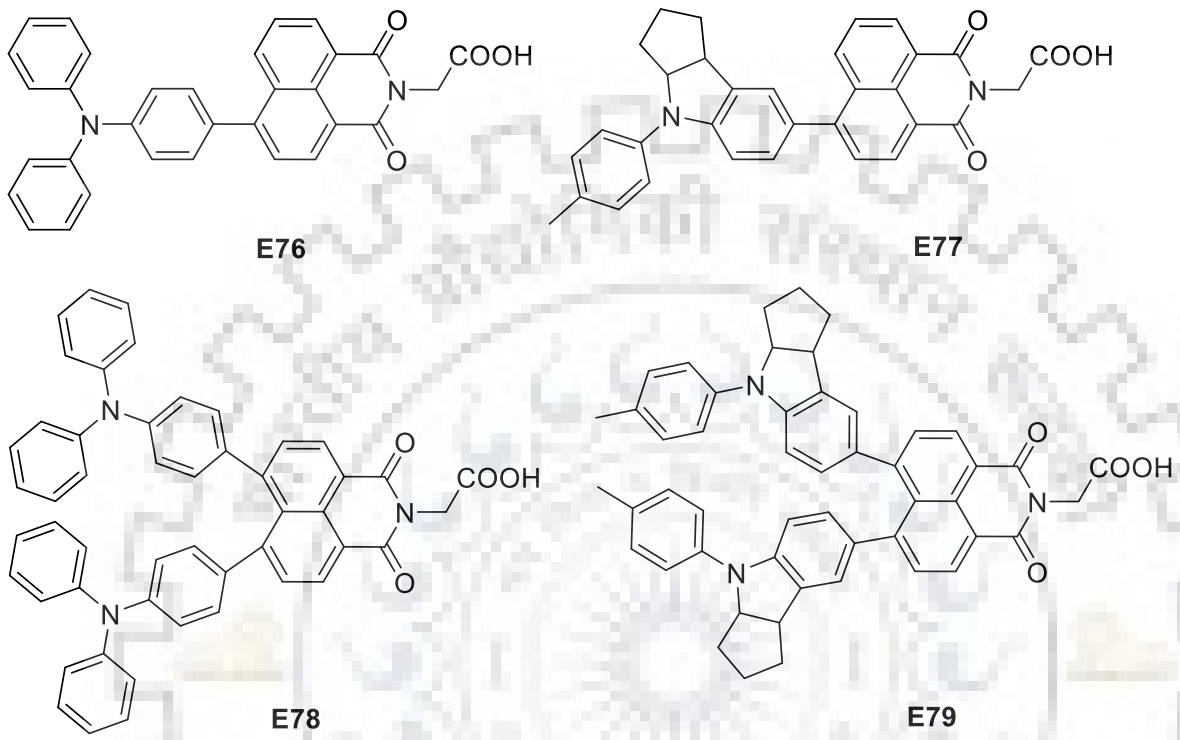

Chart 1.68 Structures of naphthalimide-based sensitizers (**E76-E79**) for DSSCs

Table 1.6 Optical and photovoltaic parameters of dyes (**E76-E79)**

Dye	$\lambda_{max,}$[a] nm (ε_{max} $\times 10^3$ M^{-1} cm^{-1})	$\lambda_{max,}$ nm on TiO_2	$E_{ox,}$ eV (*vs* NHE)	$E_{0\text{-}0,}$ eV	J_{SC} (mA/cm^2)	V_{OC} (mV)	*ff*	η (%)
E76	419 (8.2)	417	1.08	2.50	2.51	597	0.73	1.10
E77	458 (5.1)	437	0.79	2.24	2.90	594	0.68	1.18
E78	438 (14.7)	442	0.93	2.36	4.62	662	0.74	2.27
E79	473 (19.0)	506	0.61	2.07	5.42	664	0.75	2.70

[a] Recorded in methanol-chloroform (4:1, v/v) solutions.

1.5 Naphthalimide-based materials as anticancer and bioimaging agents

The 1,8-Naphthalimides constituted a class of antitumor agents since after its first report in 1970s came as a breakthrough by Braña and co-workers.[190] First reported 3-amino substituted naphthalimide derivative, Amonafide, **B1** displayed high cytotoxic activity against HeLa cells with IC_{50} value of 8.80 μM.[191] (Chart 1.69) It exhibited strong affinity towards DNA intercalation and enhanced activity against various carcinoma, leukemia and melanoma cell lines (Table 1.7). In 1980s, Braña *et al*.[192] reported a set of 3-nitro-naphthalimide derivatives **B2-B5** possessing relatively strong cytotoxic activity against HeLa and KB cell lining than amonafide (Chart 1.69). They studied the positive effect of introduction of electron withdrawing unit by replacement of $–NH_2$by $–NO_2$ group. The **B2-B5** were differ in basic side chain at imidic position of naphthalimide. Among the series, dye **B2** (Mitonafide) and **B4** displayed the most efficient cytotoxicity against HeLa and KB cell lines over dye **B3** and **B5** with a low IC_{50} values of 0.47, 0.80 and 0.60, 1.0 μM respectively. In 1993, Sami *et al.*[193] replaced naphthalene unit by anthracene unit in order to examine the potency of derivative towards cytotoxic activity. The as-modified, Azonafide, **B6** with similar imidic substituent displayed stronger cytotoxic affinity against leukemia (L1210 sens. and L1210 res.) and HeLa cells (Table 1.7). As such, the use of fused core was proved effective displaying enhanced cytotoxic activity and was explored further to design a variety of naphthalimide-based anticancer and imaging agents.

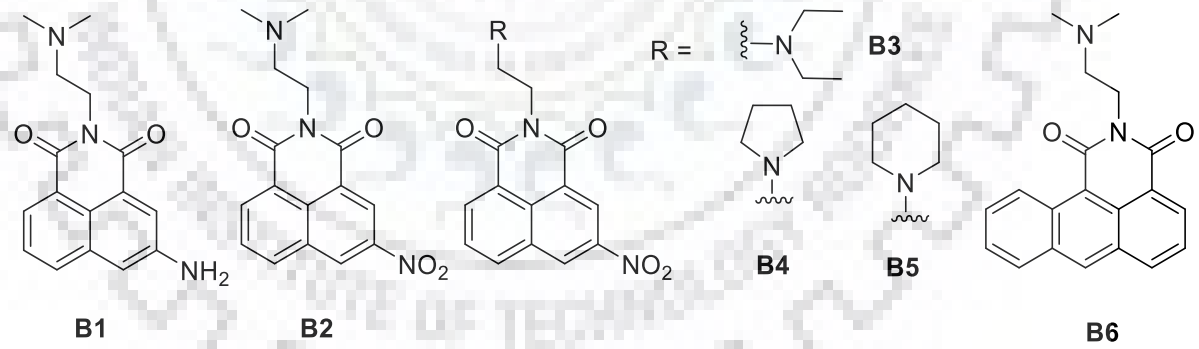

Chart 1.69 Structures of 3-substituted naphthalimide-based anticancer agents (**B1-B6**)

Table 1.7 In vitro cytotoxicity of dyes **B1-B6** against various cancer cell lines

Dye	IC_{50}, μM in various cell lines			
	HeLa	KB	L1210 sens.	L1210 res.
B1	8.80	-	-	-
B2	0.47	0.60	-	-
B3	7.00	10.20	-	-
B4	0.80	1.00	-	-
B5	5.80	5.60	-	-
B6	0.14	-	0.007	0.007

Considering the positive effect of substituent alteration at 3rd position of the naphthalimide core, Cheng *et al.*[194] 3, 6-disubstituted amino and nitro derivatives **B7** and **B8**, potential DNA binders and anticancer agents (Chart 1.70). These two derivatives displayed enhanced cytotoxicity against leukemia cells with IC_{50} values < 1 μM (0.33 μM and 0.036 μM). In particular, the disubstitution resulted in an improved anticancer activity compared to **B1** and **B2**.

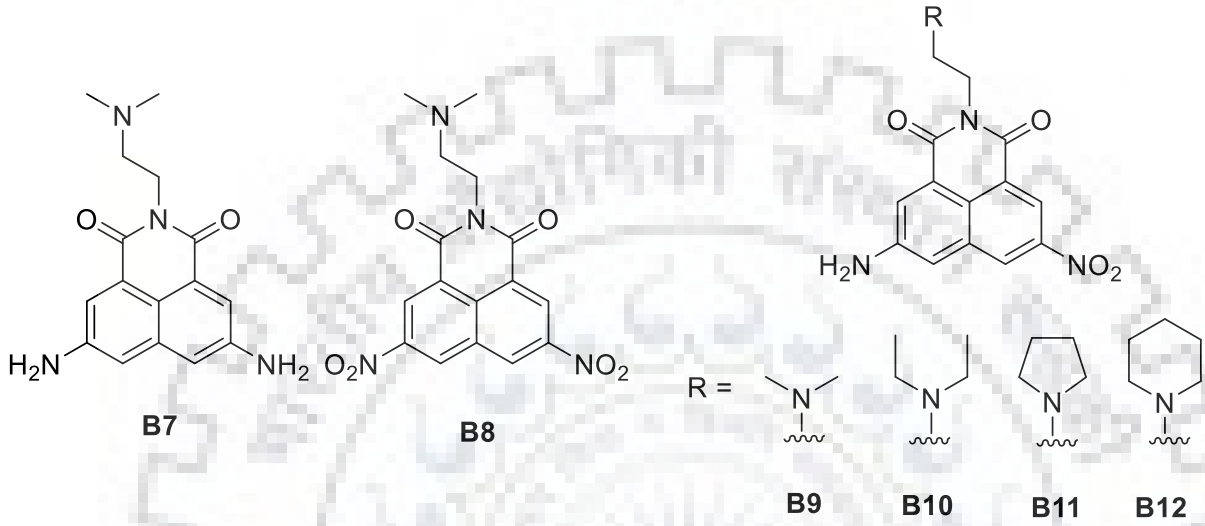

Chart 1.70 3, 6 disubstituted naphthalimide-based anticancer agents (**B7**-**B12**)

A decade later, Braña *et al.*[195] synthesized and studied 3-amino 6-nitro disubstituted mononaphthalimide asymmetric derivatives **B9**-**B12** as potential antitumor agents (Chart 1.70). These derivatives displayed high cytotoxicity against CX-1 colon and LX-1 lung carcinoma cells with IC_{50} less than 1 μM (Table 1.8). **B9** and **B11** displayed the most effective activity among this set, similar to those of compounds **B2** and **B4**. Interestingly, all derivatives exhibited better activity than reference **B1** and **B2**.

Table 1.8 In vitro cytotoxicity of dyes **B9**-**B12** against various colon and lung cancer cell lines

Dye	IC_{50}, μM in various cell lines	
	CX-1	LX-1
B9	0.06	0.05
B10	0.59	1.00
B11	0.06	0.13
B12	0.52	0.51

Apart from mono-naphthalimide derivatives, bis-naphthalimide derivatives have also been explored to enhance antitumor activity. The first bis-naphthalimide derivative, **B13** (Elinafide) was developed by Bousquet *et al.*[196] in 1995 (Chart 1.71). Though usually, the substituted naphthalimides having amino and nitro motifs display an improved cytotoxicity yet **B13** without any substituent exhibited high cytotoxicity against a variety of human cancer cell lines such as LX-1, LOX and CX-1. Furthermore, **B13** displayed an excellent structure activity

relationship and cytotoxicity assay against HT-29 colon cell line with low IC_{50} of 14 nM relative to those of **B1** and **B2**.

Before switching to bis-naphthalimide-based derivatives for cytotoxicity and bioimaging, we will discuss 3 and/or 4-substituted and imidic substituted mono-naphthalimide derivatives for biological applications.

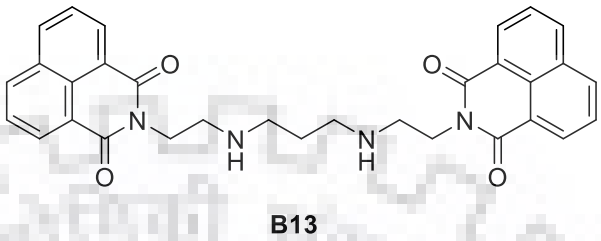

B13

Chart 1.71 Structure of first reported bis-naphthalimide **B13** (Elinafide)

1.5.1 Mono-naphthalimide-based derivatives

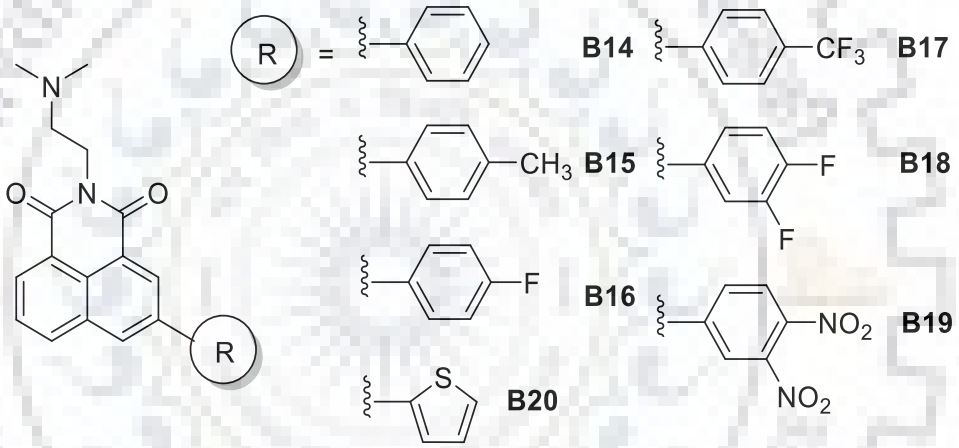

Chart 1.72 Structures of 3-substituted aryl-naphthalimides (**B14-B20**) as antitumor agents

Xie *et al.*[197] synthesized a set of 3-substituted naphthalimide derivatives **B14-B20** with different substituent to understand the antiproliferative activity against HeLa and P388D1 cell lines (Chart 1.72). Compared to parent dyes **B1** and **B2**, the incorporation of electron-withdrawing substituents in dyes **B16-B19** enhanced the antitumor activity as inferred by a low IC_{50} (Table 1.9). As such, all the dyes except **B15** displayed a stronger cytotoxic activity compared to amonafide, **B1**. This work reveals that introduction of aromatic heterocyclic unit on naphthalimide core can exhibit better apoptosis of cancerous cells.

Table 1.9 Cytotoxicity of naphthalimide derivatives **B14-B20** against various cell lines

Dye	IC_{50}, μM				
	HeLa	P388D1		HeLa	P388D1
B14	6.04 ± 0.09	0.68 ± 0.08	**B18**	5.54 ± 0.09	0.98 ±0.12
B15	36.28 ±0.11	2.19 ±0.10	**B19**	4.72 ± 0.08	0.38 ±0.09
B16	5.09 ± 0.08	-	**B20**	3.70 ± 0.08	0.68 ± 0.11
B17	4.51 ± 0.08	-	**B1**	6.45 ± 0.09	0.68 ± 0.08

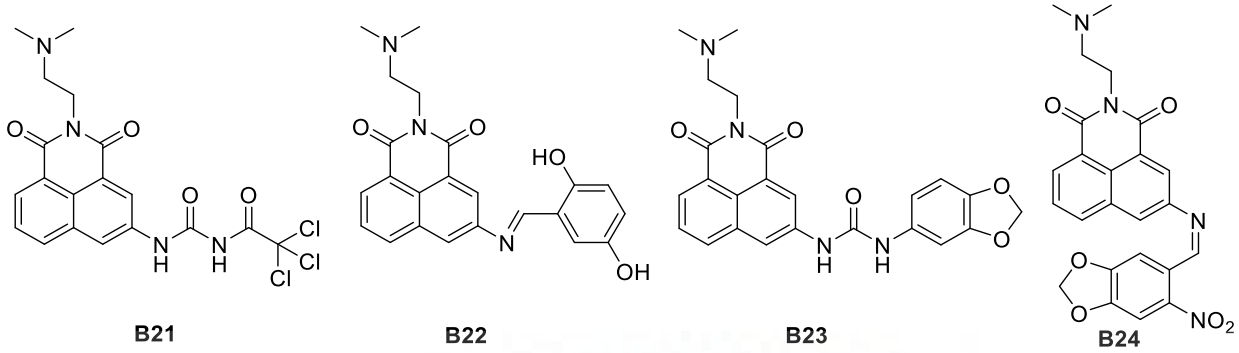

Chart 1.73 Structures of 3-substituted amino naphthalimides (**B21-B24**) as anticancer agents

Quaquebeke *et al.*[198] developed a series of 3-substituted amino naphthalimides with potent antitumor activities, analogous to amonafide, against various carcinoma cell lines. Among the set of dyes, the dyes **B21-B24** possessing having substitution at 3rd position displayed an excellent to moderate *in vivo* and *in vitro* activities (Chart 1.73). Among the series, **B21** exhibited no hematotoxicity and resist the growth of carcinoma cells better than other three and parent dye with extremely low IC_{50} of >1 μM. It is worth to note that these four dyes exhibited a high *in vivo* toxicity with index nearly 300% and high therapeutic window. Further, the urea substituted electron deficient derivative **B21** displayed the most effective growth inhibitory effect on cancer cell lines (Table 1.10).

Table 1.10 Cytotoxicity of dyes **B21-B24** derivatives against various cell lines

Dye	IC_{50}, μM			
	HS683	HCT-15	A549	MCF-7
B21	0.8	0.9	0.9	0.9
B22	>10.0	>10.0	8.4	9.1
B23	5.8	7.7	5.5	6.6
B24	>10.0	>10.0	>10.0	>10.0
B1	3.9	5.2	3.8	5.8
B2	3.7	2.6	2.4	-

Azab *et al.*[199] synthesized a series of nine *N*-substituted naphthalimides **B25a-B25i** to test and examine their antibacterial and antitumor evaluation against various tumor cell lines (Chart 1.74). Among set of dyes, **B25c**, **B25e** and **B25g** displayed the most active and broad spectrum as antibacterial agents. On the other hand, dyes **B25g**, **B25h** and **B25i** exhibited effective cytotoxicity against wide group of tumor cells (Table 1.11). Furthermore, dye **B25g** possessing three methoxy substituents exhibited better growth inhibition of the tumor cell lines than dye **B25i** having two chloro groups. It was found that aromatic electronegative substituents at imidic position can alter the activities of the dyes.

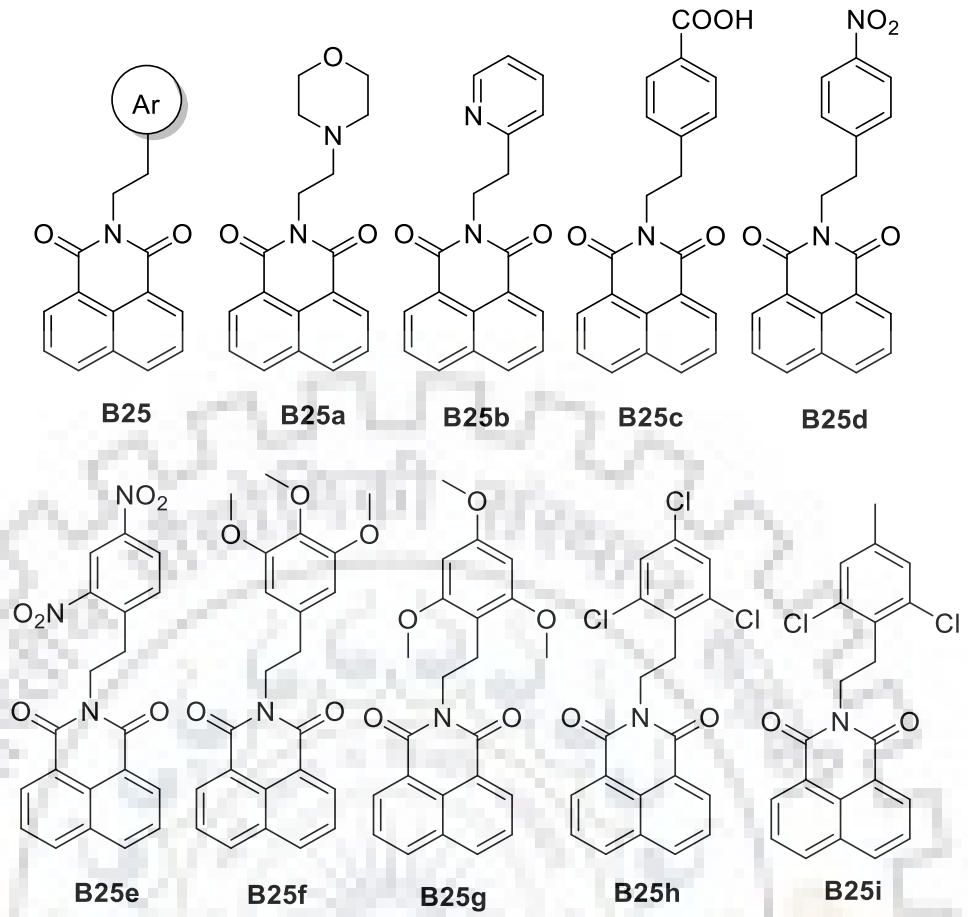

Chart 1.74 Structures of mononaphthalimides **B25a-B25i** with different imidic groups

Table 1.11 Growth inhibition of dyes **B25g-B25i** against various cancer cell lines

Dye	Growth inhibition, % at 10 μM					
	HOP-92	NCI-H522	SN12C	UO-31	SNB-75	MCF7
B25g	30.21	13.61	19.27	21.03	13.16	6.42
B25h	-15.52	5.32	3.72	26.75	6.64	-1.03
B25i	-	4.37	6.09	20.89	39.13	3.55

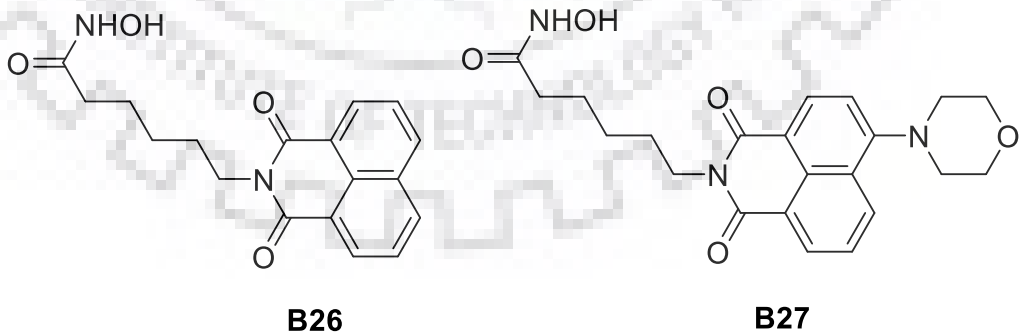

Chart 1.75 Structures of naphthalimide-based anticancer and cell imaging agents (**B26-B27**)

In another work, Fleming *et al.*[200] reported 4-substituted morpholinonaphthalimide **B27** as effective anticancer and cell imaging agent (Chart 1.75). In DMSO solution, **B27** exhibited the absorption and emission bands at λ = 399 nm and 534 nm, respectively, attributable to the ICT. The dye demonstrated effective visualization of cellular uptake particularly in the

cytoplasm of MDA-MB-231 cells as fluorescent green emission. The dye was tested against both isoforms of HDAC cell lines with extremely low IC_{50} of 12 nM for HDAC6 (Table 1.12). For other cell lines, IC_{50} was found in between 0.2 to 2.0 μM, and thus displayed better selectivity than reference scriptaid drug **B26**.

Table 1.12 Cytotoxicity of dyes **B26-27** against HDAC isoforms cell lines

Dye	IC_{50}, μM					
	HDAC1	HDAC3	HDAC6	HDAC8	HDAC11	KASUMI-1
B26	1.74 ± 0.06	0.37 ± 0.06	0.012 ± 0.002	1.52 ± 0.01	0.36 ± 0.03	0.49
B27	1.43 ± 0.13	0.32 ± 0.04	0.012 ± 0.001	1.81 ± 0.17	0.29 ± 0.02	0.29

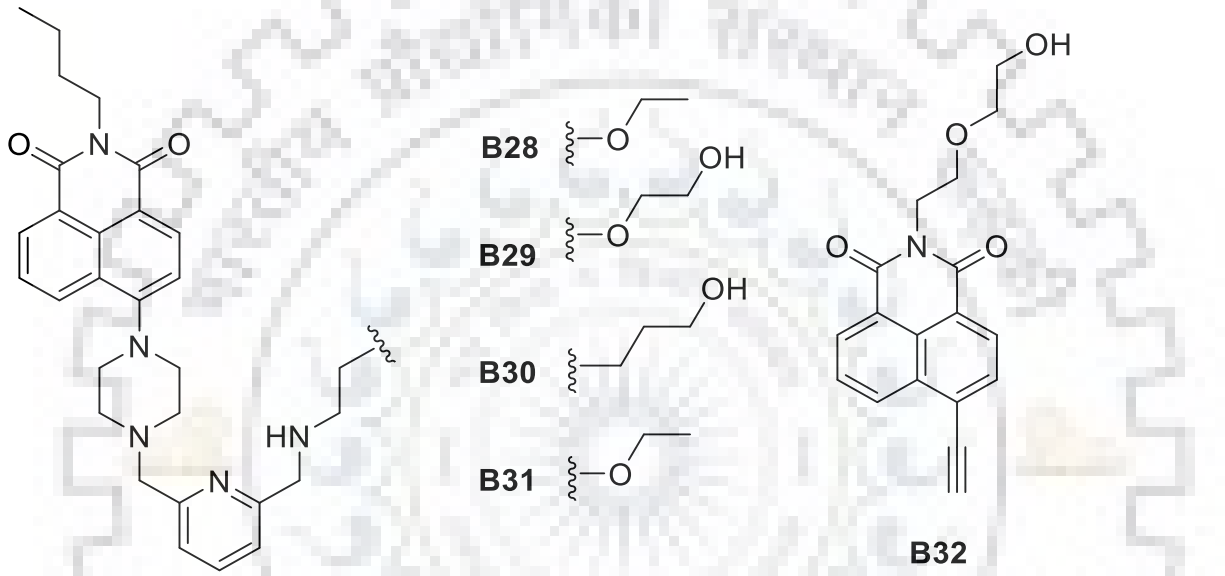

Chart 1.76 Structures of naphthalimide-based dyes (**B28-B32**) for cell imaging

Un *et al.*[201] synthesized a set of naphthalimide-based fluorescent dyes **B28-B31** for HeLa cell imaging (Chart 1.76). The dyes displayed a highly sensitive and selective fluorescence turn-on response toward Histidine in aqueous solution and acted as a pH sensor *in vivo*. When HeLa cells were treated with **B28**, a bright green fluorescence was observed due to an effective ICT, similar to that of **B27**. Moreover, **B28** exhibited good cell viability with a low cytotoxicity making it an ideal candidate for live cell imaging.

Zhou *et al.*[202] reported a 4-ethylnaphthalimide derivative **B32** as a potent cell imaging agent for biological applications (Chart 1.76). To improve its water solubility, the naphthalimide was appended with a long hydroxyldiethyl ether functional group at imidic position. The dye was tested in both living HeLa cells and larval zebrafish. Specifically, **B32** displayed high cell permeability and specificity for hydrazoic acid. It acted as an imaging agent within the cell and exhibited fluorescence enhancement with deep blue emission.

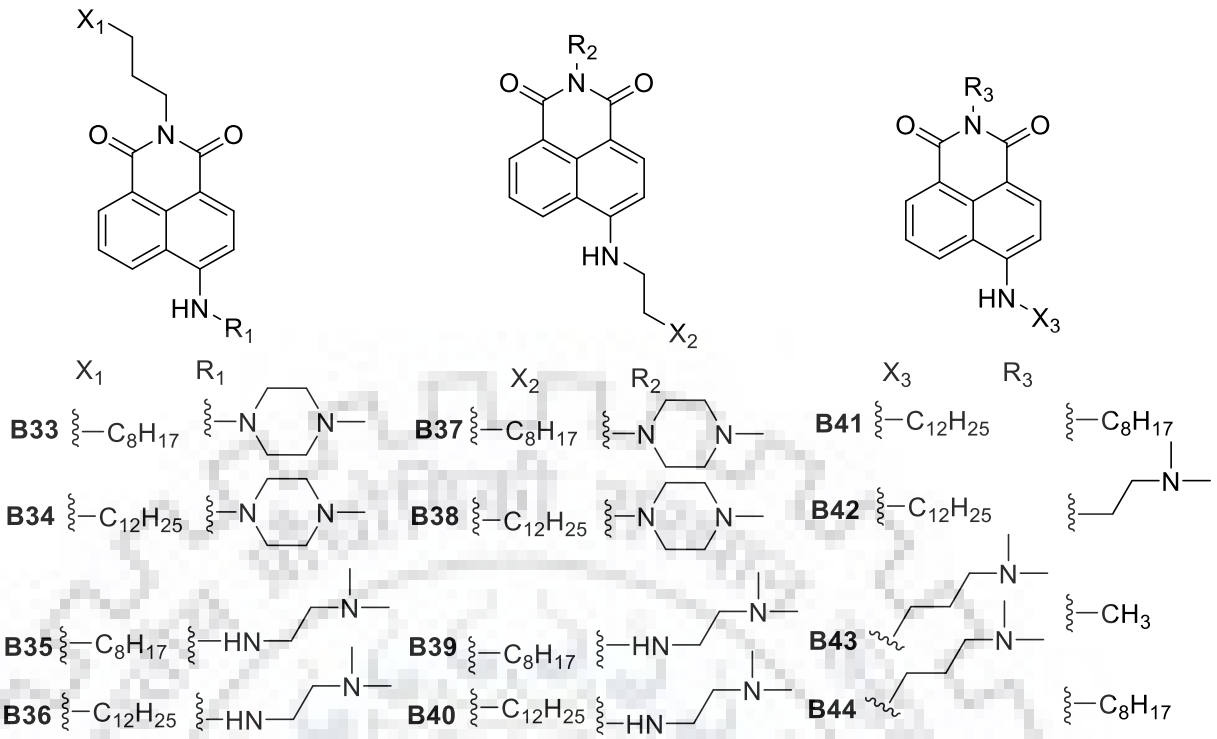

Chart 1.77 Structures of 4-substituted aminonaphthalimides (**B33-B44**) as antitumor agents

Table 1.13 Cytotoxicity of dyes **B33-B44** derivatives against various cell lines

Dye	IC_{50}, μM		
	HL-60	HeLa	MCF-7
B33	5.70	8.10	5.72
B34	2.98	2.89	2.48
B35	2.67	4.06	2.41
B36	4.04	4.71	2.56
B37	12.02	7.90	8.35
B38	7.05	5.45	2.79
B39	5.13	4.5	3.76
B40	6.63	16.84	4.52
B41	>50	46.43	>50
B42	5.32	9.13	3.57
B43	21.61	23.37	9.66
B44	5.53	8.52	5.15
B1	17.96	10.67	11.88

Chen *et al.*[203] synthesized 4-substituted aminonaphthalimides-based antitumor agents **B33** and **B44** inhibiting the proliferation of various cancer cell lines more effective than amonafide drug (Chart 1.77). The dyes exhibited a green fluorescence surrounding the nucleus of HeLa cells as they are localized in the cytoplasm of the cells. Notably, the dye **B34** displayed the most effective cell growth inhibition with low drug loading against five cancerous cell lines, namely, HeLa, HL-60, MCF-7, MKN45 and LS174 (Table 1.13). All the dyes except **B41** and **B43** exhibited better anticancer activities with low IC_{50} than amonafide loadings. It was observed that mono-amine containing dyes resulted in low cell inhibitory

growth than those of **B33-B40** possessing polyamines. The analysis depicted that the cytotoxicity of dyes was dependent on the nature and length of the side chains.

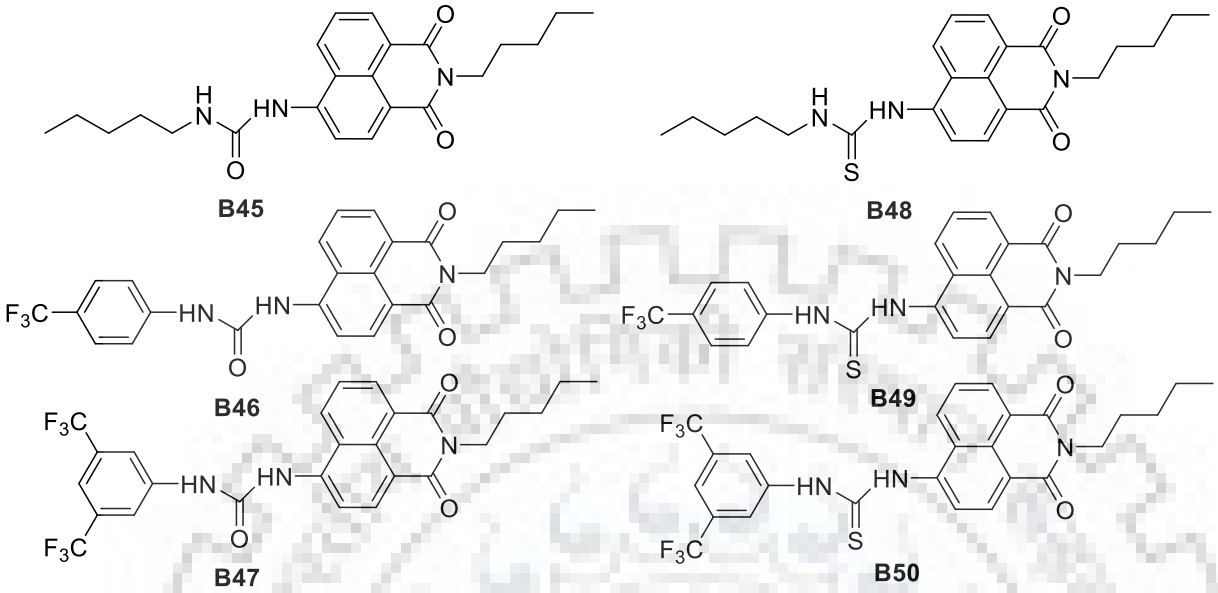

Chart 1.78 Structures of 4-substituted amino naphthalimides (**B45-B50**) as anticancer agents

Berry *et al.*[204] synthesized a series of fluorescent urea and thiourea naphthalimide-based trans-membrane anion transporters **B45-B50** (Chart 1.78). The dyes containing aromatic fluoro substituents induced cytotoxicity in cancer cell lines, namely A549 and MCF-7. In line with this, **B50** also induced apoptosis in A549 cells. It was found that the most lipophilic, aromatic-substituted transporters were found localized homogeneously throughout the cell and were toxic towards cancer cells. On the other hand, the least lipophilic alkyl-substituted transporters (**B45** and **B48**) were localized in specific vesicles and were found non-toxic to cancer cells. Among all the dyes, the highly fluorinated **B50** was the most effective compound towards cancer cells with low IC_{50} value against A549 and MCF-7 cell lines (Table 1.14). It is worth to mention here that thiourea naphthalimide-based derivatives **B48-B50** were more potent towards cytotoxicity compared to urea-based derivatives **B45-B47**.

Table 1.14 Cytotoxicity of dyes **B45-B50** derivatives against lung and breast cancer cell lines

Dye	IC_{50}, μM	
	A549	MCF-7
B45	>50	>50
B46	>50	>50
B47	22.6 ± 7.5	40.3 ± 3.0
B48	17.1 ± 3.0	12.7 ± 2.1
B49	7.7 ± 4.1	31.2 ± 3.2
B50	7.6 ± 1.1	12.3 ± 1.5

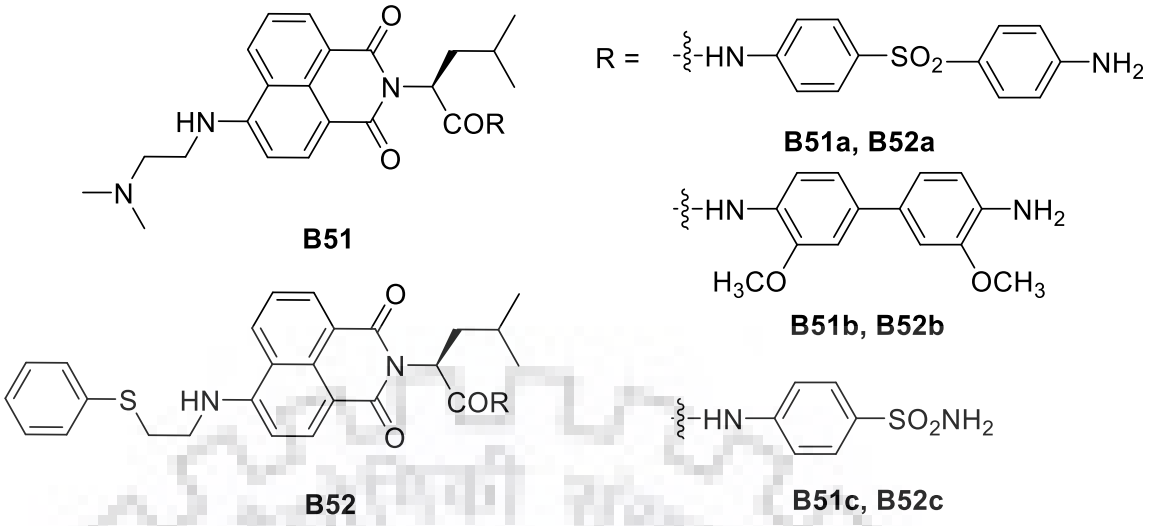

Chart 1.79 Structures of naphthalimide derivatives (**B51** and **B52**) possessing leucine side chain as anticancer agents

Wu *et al.*[205] synthesized chiral naphthalimide derivatives **B51** and **B52** possessing leucine side chain at imidic position with amino and thio-substituted chains at core position, and explored to them as effective antitumor agents against HeLa, P388, HL-60, A549, HCT-8, MCF-7, and A375 cancer cell lines (Chart 1.79). Among the set of dyes, the dye possessing thiophenyl substituent (**B52**) displayed superior antitumor activities against MCF-7 cells over other cell lines. However, **B51** displayed good cytotoxicity against MCF-7 and A375 cell lines with low IC_{50}values of 8.64 and 6.51 μM, respectively. The dyes with amino chain **B51** exhibited good cell growth inhibitory activity with low IC_{50} values (Table 1.15).

Table 1.15 Cytotoxicity of dyes **B51** and **B52** derivatives against various cell lines

Dye	IC_{50}, μM in various cell lines						
	HeLa	MCF-7	P388	HL-60	HCT-8	A375	A549[a]
B51a	>50	8.64	>50	>50	>50	>50	>50
B51b	6.74	15.02	7.67	22.79	>50	6.51	1.00
B51c	8.09	8.65	7.23	17.83	>50	6.60	>50
B52a	>50	24.55	>50	>50	>50	>50	>50
B52b	>50	9.45	>50	>50	>50	>50	>50
B52c	>50	12.56	>50	>50	>50	>50	>50

[a] cytotoxicity against cell line by sulphorhodamine B method after 72 hrs instead of MTT method after 48 hrs

Intrigued by an excellent cytotoxicity of **B59**, compared to amonafide and mitonafide, against various cell lines, Ott *et al.*[206] developed a series of thio-substituted naphthalimides **B53-B59**, and tested them for cell imaging, cellular uptake and as antitumor drugs (Chart 1.80). All the dyes except **B56** displayed a blue fluorescence under microscopic cell uptake by MCF-7 cells. The antiproliferative effects of dyes on MCF-7 and HT-29 cells were also studied. Although the reported dyes displayed a higher value of IC_{50} than **B59**, they were

highly active against tumor cells. Specifically, the dyes displayed a low IC_{50} in the range of 2-5 μM, which were found to be compatible with other antitumor agents such as cisplatin, 5-fluorouracil and amonafide (Table 1.16). However, **B58** lacking basic imidic unit did not display any antitumor activity, similar to **B52** dyes. These derivatives were also tested as efficient DNA photocleavers. It was demonstrated that the non-ring fused thionaphthalimides are useful for efficient cytotoxic and photocleaving activities. It is interesting to note that the effect of cytotoxicity against cancerous cell lines was enhanced by multifold for **B57** with increasing incubation time compared to other derivatives.

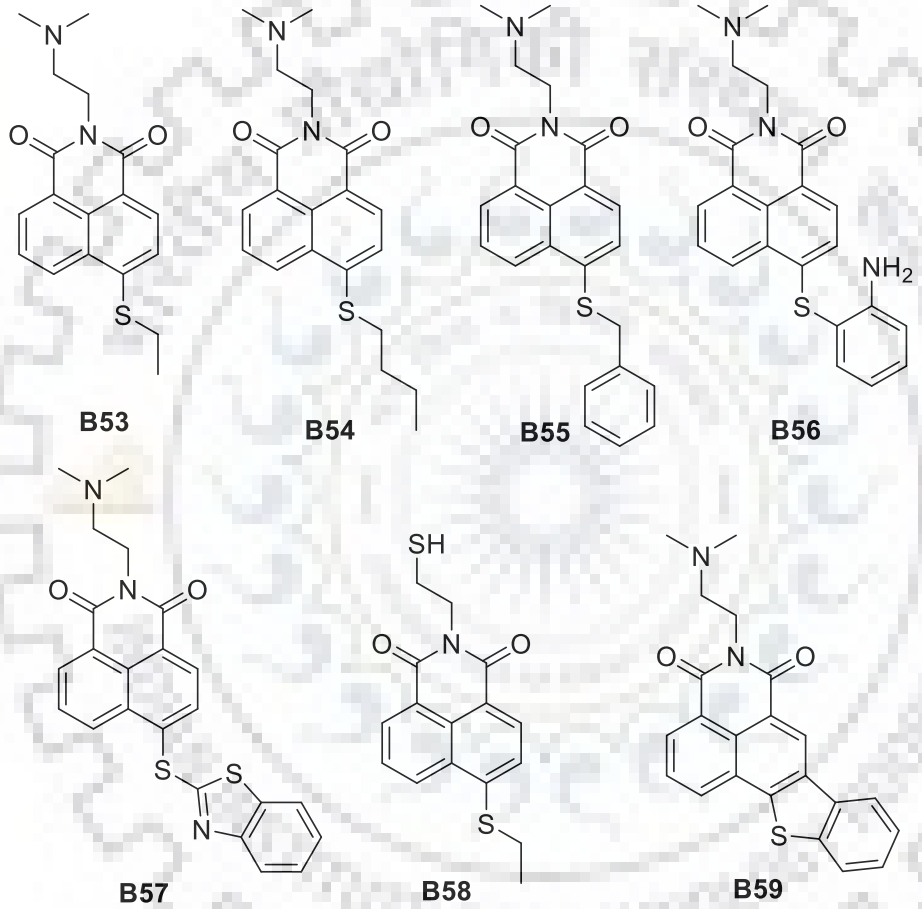

Chart 1.80 Structures of sulfur-substituted naphthalimides (**B53-B59**) as antitumor agents

Table 1.16 Cytotoxicity of dyes **B53-B59** derivatives against various cell lines

Dye	IC_{50}, μM			
	MCF-7		HT-29	
	24/72 hrs	96 hrs	24/48 hrs	72 hrs
B53	4.5	4.4	2.2	1.9
B54	5.7	2.6	4.3	4.6
B55	6.7	3.4	4.8	4.1
B56	4.8	2.6	2.8	2.9
B57	7.3	2.7	5.5	4.4
B58	>50	>50	>50	-
B59	0.17	0.20	0.23	0.62

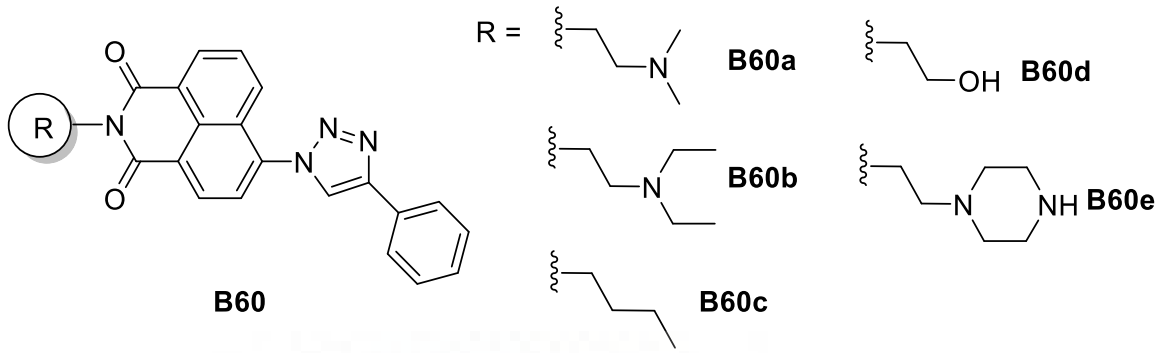

Chart 1.81 Structures of 4-phenyltriazol-naphthalimide derivatives (**B60a-B60e**) as anti-cancer agent

A series of 4-phenyltriazol-naphthalimide derivatives **B60a-B60e** were demonstrated as effective anti-cancer agent against MCF-7, HeLa and 7721 cancer cell lines by Li *et al.*[207] (Chart 1.81). All the derivatives were found to be potent over amonafide with low IC_{50} of upto 1 μM (Table 1.17). Whereas **B60a** displayed the most effective cytotoxicity against all the three set of cell lines, **B60d** possessing ethanol as side chain exhibited poor antitumor activity with IC_{50} of > 100 μM. The enhanced cytotoxicity of these derivatives was attributed due to the antitumor activity of triazole moiety as well as the naphthalimide unit having the basic substituents.

Table 1.17 Cytotoxicity of dyes **B60a-B60e** derivatives against various tumor cell lines

Dye	IC_{50}, μM		
	HeLa	MCF-7	7741
B60a	1.02	0.323	0.463
B60b	26.56	1.09	1.892
B60c	19.56	19.51	32.92
B60d	>100	>100	>100
B60e	96.7	0.836	1.545
B1	1.73	1.68	4.27

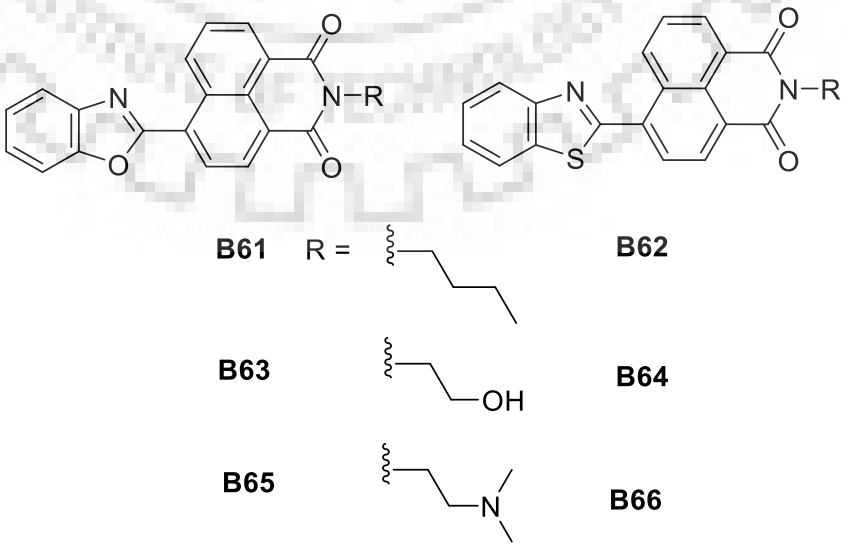

Chart 1.82 Structures of C4-benzazole naphthalimide derivatives (**B61-B66**)

Lu *et al.*[208] synthesized a C4-benzazole naphthalimide derivative **B61-B66** and used them as *in vitro* and *in vivo* anticancer drugs (Chart 1.82). Among the series, **B65** and **B66** were capable of suppressing lung tumor metastasis with low cytotoxicity compared to other analogs. Specifically, both the compounds having the same naphthalimide moiety as that of amonafide exhibited comparable biological activity against murine B16F10 melanoma cells *in vitro*. The cytotoxic activity of these derivatives was found to be dependent on side chain. The derivatives **B61-B64** were found to be non-toxic even at high concentration of 40 μM. Both **B65** and **B66** exhibited a strong affinity towards B15F10 cell lines with relatively low IC_{50} value of 7.8 and 4.5 μM, respectively, than that of **B1** (IC_{50} = 6.7 μM).

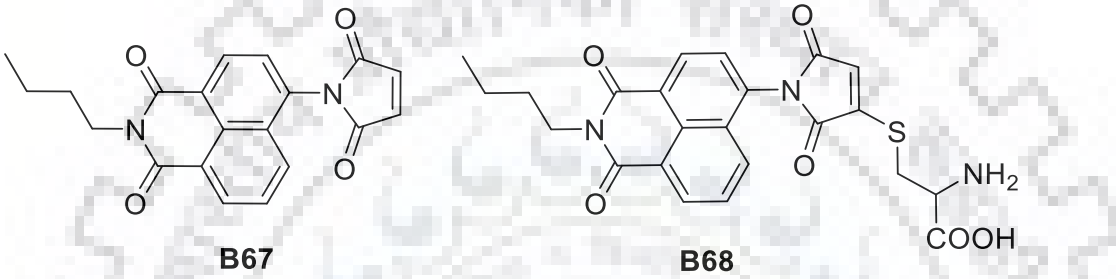

Chart 1.83 Structures of maleimide-coupled naphthalimide derivatives (**B67–B68**) as cell imaging agent

Liu *et al.*[209] reported a maleimide coupled naphthalimide **B67** as a two-photon fluorescent probe for cysteine detection (Chart 1.83). The dye displayed a weak emission at λ = 470 nm, which was enhanced by multi-fold upon addition of cysteine, due to restricted PET. **B68** possessed a selective fluorescent turn-on response towards cysteine. The dye **B68** was used in live imaging of HeLa cells, with red emission localized onto cell membrane.

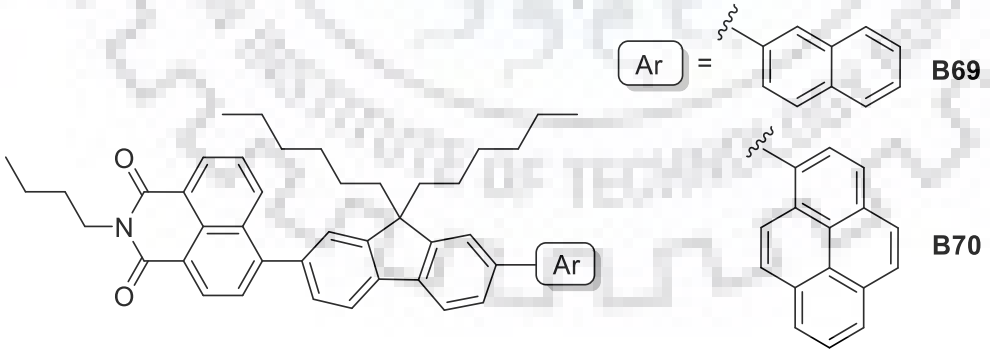

Chart 1.84 Structures of D-π-A naphthalimide-based TICT AIEgens (**B69–B70**) for cell imaging

In 2013, Li *et al.*[210] reported a naphthalimide-based bioprobe **B69** based on AIE for cell membrane tracking, lasting for 4 days (Chart 1.84). Due to its highly twisted molecular skeleton, **B69** dye exhibited a TICT, and a positive solvatochromism in polar excited state. On moving from hexane to ACN, the dye displayed a significant bathochromic shift (Δ 94 nm).

However, the AIE properties of dye **B69** was only recognized when a binary aqueous solvent system (1:1, v/v) was used. The dye exhibited good photostability and strong fluorescence making it suitable for imaging experiments. Specifically, **B69** displayed a low cytotoxicity against HepG-2 cell lines even at high loadings of 10-50 μM for 24 h.

In their successive work, Li *et al.*[211] reported yet another naphthalimide AIEgen, **B70** with TICT properties (Chart 1.84). In particular, the dye was composed of pyrene donor, 1,8-naphthalimide acceptor and fluorene as a linker. Such D-π-A architecture displayed a 109 nm red shift in solvatochromism and exhibited a strong emission band at 510 nm in aggregated state and high quantum yield of up to 0.62. When adsorbed onto SiO_2, the **B70** formed an AIE-active nano-composite structure (**B70**@SiO_2), which exhibited both anti-photobleaching ability and good biocompatibility. The composite was effectively utilized as mitochondria imaging reagent in experimented on KB and HeLa cells.

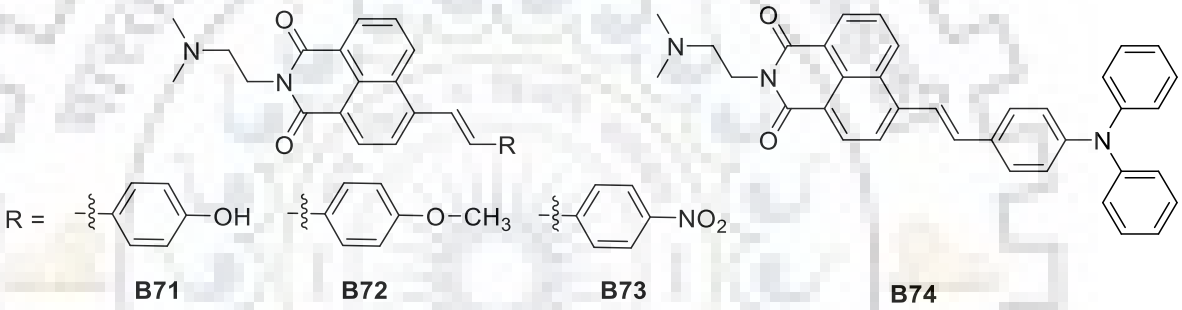

Chart 1.85 Structures of D–π–A naphthalimide derivatives (**B71-B74**) for cell imaging

Zheng *et al.*[212] demonstrated a vinyl-substituted naphthalimide based dye **B71** as a lysosome marker to distinguish cancer cells from non-cancer cells in cell imaging (Chart 1.85). The dye exhibited a typical D–π–A-structured skeleton with ICT emission in yellow region. The dye displayed an excellent cell permeability and only accumulated in lysosomes of cancerous cells such as HeLa, MCF-7 and 4T1.

In another work, Lin *et al.*[213] further reported three typical D–π–A-structured 1,8-naphthalimide derivatives **B72-74** (Chart 1.85). The dyes showed an excited state positive solvatochromism, depicting the bipolar nature of the excited state. Whereas, the absorption spectra of **B73** were blue shifted to 400nm ascribed to the electron-withdrawing nature of nitrobenzene. **B74** displayed a distinct positive solvatochromism due to having relatively a strong donor, triphenylamine. In the solid state, the dye **B74** emitted intensely having an orange fluorescence in the solid state centered at 597 nm. The large red shift in the solid state emission of **B74** could be attributed to the enhanced intermolecular interactions. The dyes **B71-B74** were found to display AIE properties due to the molecular twisting and non-planarity. This property of the molecules was explored for bioimaging. All the dyes were

found to penetrate the cellular membrane and showed cellular uptake. Among the set of dyes, **B74** resulted in bright imaging of cancer cells.

1.5.2 Bis-naphthalimide-based derivatives

Considering the superior cytotoxicity of **B13** over **B1** and **B2,** in terms of improved activity of bis-naphthalimides, a gallery of such derivatives was developed by differing length and size of alkylamino linkers or the introduction of substituents and fusion of rings on the naphthalimide core.

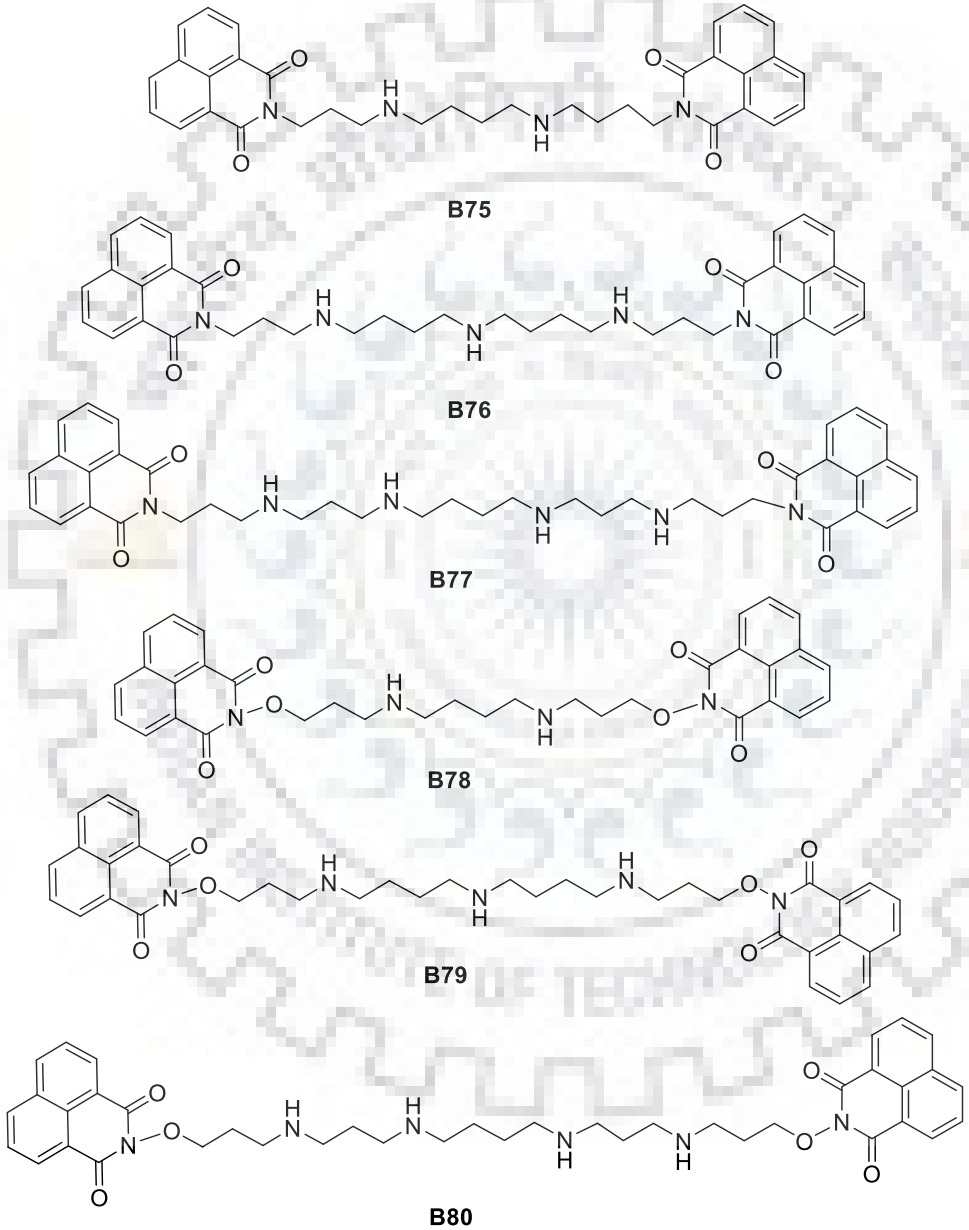

Chart 1.86 Structures of bis-naphthalimide derivatives as anticancer agents (**B75-B80**)

Dance *et al.*[214] reported analogs of elinafide, bis-naphthalimidopolyamines **B75-B80** and bisoxynaphthalimidopolyamines **B78-B80** to evaluate them against MCF-7 carcinoma cells (Chart 1.86). Bis-oxynaphthalimide polyamines exhibited poor cytotoxicity compared to

analogs **B76** and **B78** and exhibited high IC_{50} values of >30 μM (Table 1.18). Interestingly, the dyes displayed more potency towards cancer cells after 48 hrs of exposure with lower IC_{50} values. **B130** displayed IC_{50} value of 10.0 μM when exposed for 72 hrs. These derivatives were found to stabilize DNA and localized inside the nucleus. The potency of cytotoxicity was dependent on nature and length of linker since oxypolyamine derivatives displayed less toxicity compared to polyamine derivatives having low IC_{50} of 5.5 and 0.73 μM for **B76** and **B77**, respectively (Table 1.18).

Table 1.18 In vitro cytotoxicity of polyamine derivatives **B76-B80** against breast cancer cell lines

Dye	IC_{50}, μM against MCF-7 cells	
	24 hrs	48 hrs
B76	13.32 ± 0.63	5.5 ± 0.5
B77	1.50 ± 0.42	0.73 ± 0.17
B78	>50	>50
B79	>50	29.55 ± 8.01
B80	32.12 ± 6.14	±5.60

Rong *et al.*[215] synthesized a series of naphthalimide derivatives **B81a-B81f** to examine their cytotoxic activities against Hela, MCF-7, SGC-7901 and A549 cells (Chart 1.87). All the compounds exhibited selective cytotoxic activities in the tested cell lines and exhibited lower cytotoxic activities against MCF-7 cells except for **B81a**. In the tested cell lines, **B81a** displayed a better cytotoxic activity than the control drug (Table 1.19). DNA binding properties, fluorescence imaging and collective apoptosis were also investigated for the dyes. **B81a** as a DNA intercalator showed fluorescence enhancement upon binding with Ct-DNA and exhibited different impacts on the cell cycle when compared with **B1.** No significant hematoxicity and cardiotoxicity were observed for compound **B81a**.

Table 1.19 In vitro cytotoxicity of dyes **B81a-B81f** against various cancer cell lines

Dye	IC_{50}, μM			
	HeLa	MCF-7	SGC-7901	A549
B81a	2.31 ± 0.39	2.94 ± 0.16	0.88 ± 0.31	1.21 ± 0.04
B81b	>50	>50	3.63 ± 0.18	3.20 ± 0.02
B81c	>50	>50	4.46 ± 0.17	4.71 ± 0.02
B81d	>50	9.07 ± 0.05	2.30 ± 0.38	3.05 ± 0.03
B81e	1.05 ± 0.24	13.97 ± 0.23	2.47 ± 0.28	0.60 ± 0.05
B81f	3.65 ± 0.12	32.92 ± 0.10	23.23 ± 0.29	1.59 ± 0.12
B1	4.36 ± 0.13	8.02 ± 0.038	5.32 ± 0.20	1.59 ± 0.07

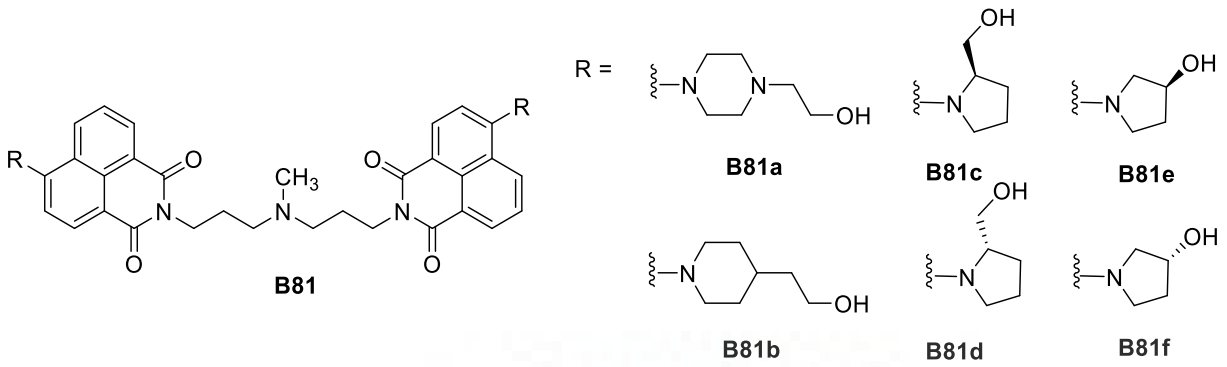

Chart 1.87 Structures of bis-naphthalimides **B81** with different imidic groups as anticancer agents.

Suzuki *et al*.[216] reported the properties of 3-nitronaphthalimide derivatives **B82** and **B83** as potent anti-cancer agents both *in vitro* and *in vivo* against AZ521 gastric cancer cells and LOX melanoma cell line (Chart 1.88). In particular, **B82** displayed a strong cytotoxicity with extremely low IC_{50} value of 3 nM in both the cell lines. The interactions of dyes with various DNA fragments were also tested. **B83** displayed a relatively stronger affinity towards G-C nucleobases than A-T fragments.

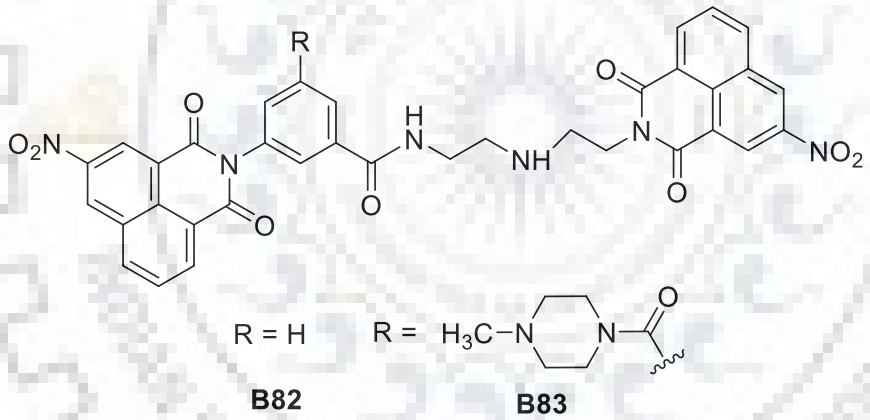

Chart 1.88 Structures of 3-nitrobisnaphthalimide derivatives (**B82** and **B83**)

1.6. Conclusions and outlook

Over the years, naphthalimide ensembles have gained a great deal of attention devoted to its photophysical, electrochemical, and theoretical studies because of their potential as *n*-type semiconductors. Naphthalimide derivatives have found numerous applications in organic electronics, biology and supramolecular chemistry. Employing naphthalimide as acceptor to design molecules along with other acceptors or donors has resulted into a huge gallery of small molecules for solar cells. Apart from their diverse applications, naphthalimide based derivatives exhibit high molecular and chemical versatility as they can be functionalized at both core and imidic positions to alter the molecular and electronic properties. Both conjugated and non-conjugated structures have been obtained by core and *N*-imide functionalization of the moiety. Conjugated donor–acceptor hybrids have been synthesized by directly linking the chromophores to the core positions of the naphthalimide moiety. A variety of bipolar, D-A molecules based on naphthalimide have been demonstrated as promising emitters and hosts in FOLEDs and PhOLEDs. Also, the naphthalimide derivatives have been used as electron-transporting layers in OLEDs and memory devices. Furthermore, they have been of major importance for establishing structure–property relationships and extrapolations of their outstanding properties including TICT, AIEgens and self-assembling. The naphthalimide-based conjugated materials have been found to be potent fluorescent cell imaging and as anticancer agents for medicinal applications. The feasible synthesis and tunable properties of naphthalimide-based materials make them promising functional materials. It is believed that further exploration of such materials will provide enhance the possibilities for organization of the core with molecular-level precision through rational design strategies in near future.

Chapter 2 Naphthalimide-Based Materials for Electronics and Biological Applications: Aim and Scope

The organic materials are known to be explored in diverse fields of material science such as electronics, sensing, biological, supramolecular and medicinal chemistry. The exploration of organic fluorophores in chemo/biosensing, bioimaging and optoelectronic materials with promise in various device applications has been a topic of interest for decades. Thus, the development of functional materials in the area of material science has increased tremendously over the last several decades. The state-of-the-art shows in terms of the molecular architecture, D–A derivatives have received more attention than solely D-D or A-A type of molecular scaffolds due to presence of prominent ICT. Also, the optoelectronic properties and energy levels of these molecules can be adjustable depending upon the nature of donors and acceptors in scaffold. As a result, a number of articles have been reported in the literature so far to unveil the structure-property relationship and their use in the material science. However, among *p*-type and *n*-type semiconductors, later has received great attention since synthesizing an air stable electron deficient molecule is tedious over electron rich dyes.[12-19] An ample amount of research has been executed on *p*-type semiconductors including oligothiophenes,[20-22] triarylamines,[12, 24] carbazoles,[24-28] fluorenes,[29-31] dithienopyrrole,[33-35] and phenothiazine[36-37]. A judicious focus on the molecular modifications to alter the properties makes them potential candidates as either *p*-type or *n*-type semiconductors. Since *n*-type semiconductors lag behind, organic semiconductors with electron transporting property have received great deal of research interest in recent years.[16-19, 47-64] The generic requirements of a dye to act as *n*-type semiconductor lies in high electron mobility, high solubility, thermal and chemical stability to minimize decomposition. Although *p*-type materials with high mobility have been successfully developed with a wide range of molecular designs, only a few *n*-type materials have shown promising properties. Thus, synthesis of π-conjugated electron acceptors will help to enrich the library of existing electron transporting materials.

Among the known frameworks, imides and amides π-conjugated molecules have received considerable attention as promising *n*-type organic semiconducting candidates (Figure 2.1). Within imides, rylene imides such as perylene and naphthalene mono- and bis-imides have been among the most explored cores in the development of *n*-type semiconductors owing to their ease of synthesis, chemical stability and strong electron-accepting properties. But due to the large

aromatic core, these materials show poor solubility for solution processing and results in severe aggregation in solid state.

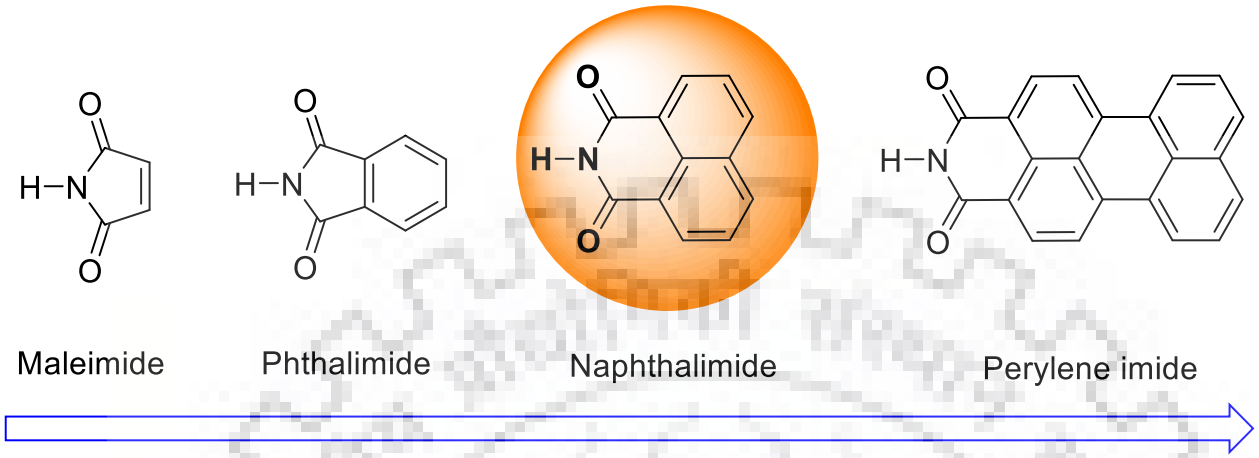

Figure 2.1 Treadmill of mono-imides as *n*-type aromatic core.

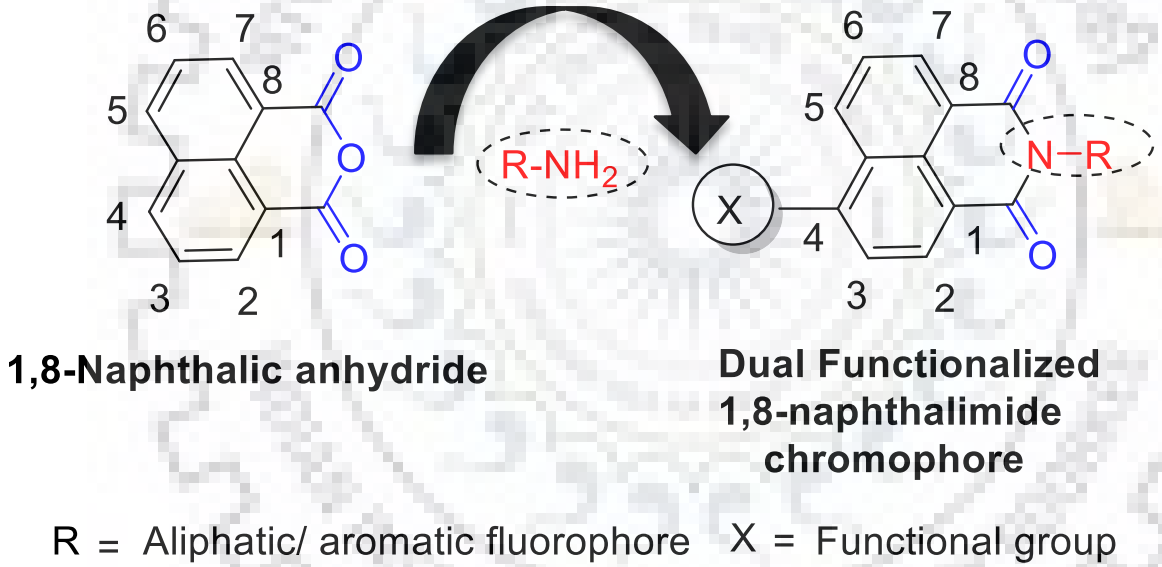

Figure 2.2 Core numbering and molecular engineering of naphthalimide unit.

Naphthalimide is an electron-deficient heterocyclic ring (Figure 2.2). 1,8-Naphthalimide (1*H*-benzo[*de*]isoquinoline-1,3(2*H*)-dione) compounds are an attractive class of electron-deficient organic materials similar to maleimide, phthalimide, and perylene imide is known to be used in *n*-type organic semiconducting materials. It can be tuned by functionalization to have wide energy gaps and low reduction potentials, making them good candidates for use as *n*-type materials in

organic electronics. It possesses naphthalene as a parent structure which is simple enough to functionalize and synthesize a wide variety of derivatives with minimum cost. The anhydridic group can be used to tag the fluorophore through the formation of the imide bond to another functional fragment and further substitution at 4^{th} position can be preferentially done. The high carrier mobilities, electron affinities, promising fluorescence properties, chemical and thermal stabilities and easy functionalization at active C-4 and N-atom positions makes it a suitable core. The imidic unit in naphthalimide acts as electron deficient part to realize good electron density and charge separated state. Although the imidic substituent is orthogonally linked to the *N*-atom of the core, since it helps in altering the properties with high thermal and electrochemical stability. Thus naphthalimide based chromophores exhibits dual functionalization (core and imidic) which would shift absorption bathochromically as compared to the π-system of naphthalimide which only absorbs at ~340 nm in the UV region. Also, it facilitates the long-range intermolecular charge delocalization of π-electron cloud. It has been widely employed as a highly ordered skeleton as acceptor moiety in the fabrication of OSCs, BHJSCs, DSSCs, OLEDs, memory storage devices, supramolecular chemistry and OTFTs. Further, they have been of major importance for establishing structure–property relationships and extrapolations of their properties in different areas. The progress of organic naphthalimide-based materials by a detailed description of its applications particularly in electronics and biological application are systematically summarized and discussed earlier in Chapter 1.

Naphthalimide core has been extensively investigated as material to be utilized in organic electronic devices, sensing and as a bioimaging and anticancer agent. The correlation of photophysical, electrochemical and thermal properties with their molecular structure is essential for exploration of organic materials for their application in broader field. Extensive studies toward new organic materials have been carried out to demonstrate their properties. This thesis surveys the different chromophoric and molecular functionalizations carried on naphthalimide with special attention to the photophysical and electrochemical properties and the relationship with their properties. The studies have allowed us to have a rational design of naphthalimide-based materials for various electronic and biological applications (Figure 2.3).

Herein, we have used 1,8-naphthalimide for synthesizing potential organic materials. We aim to synthesize a gallery of dyes based on naphthalimide as an acceptor flanked on or appended by different chromophores such as different acceptors like fluorenone, benzothiadiazole, quinoxaline and benzotriazole, PAH such as pyrene, heterocyclic donor such as carbazole, electron deficient

star-cored triazine and electron donating secondary amine. Thus, we have a set of different varieties of naphthalimide based small molecules which are attached to the chromophore directly through rigid acetylene linkage by Sonogashira reactions, C-C bond using Suzuki and Stille cross coupling reactions. It is aimed to explore how incorporation of core as a basic module in the molecular structures of the various designed dyes altered the photophysical, electrochemical and thermal properties and leads us on path towards exploration of *n*-type semiconductors. The materials aimed to synthesize for electronics such as OSCs, DSSCs and OLEDs are supposed to possess good light-harvesting properties in the region of 250-600 nm in the visible light, appropriate HOMO and LUMO energy levels for efficient charge injection, stable redox potentials. A high fluorescence quantum yields and excellent thermal properties are expected for dyes synthesized for OLEDs. The materials synthesized for cell imaging with variation in chromophoric units at imidic position are supposed to display structural influence on morphology of the dyes.

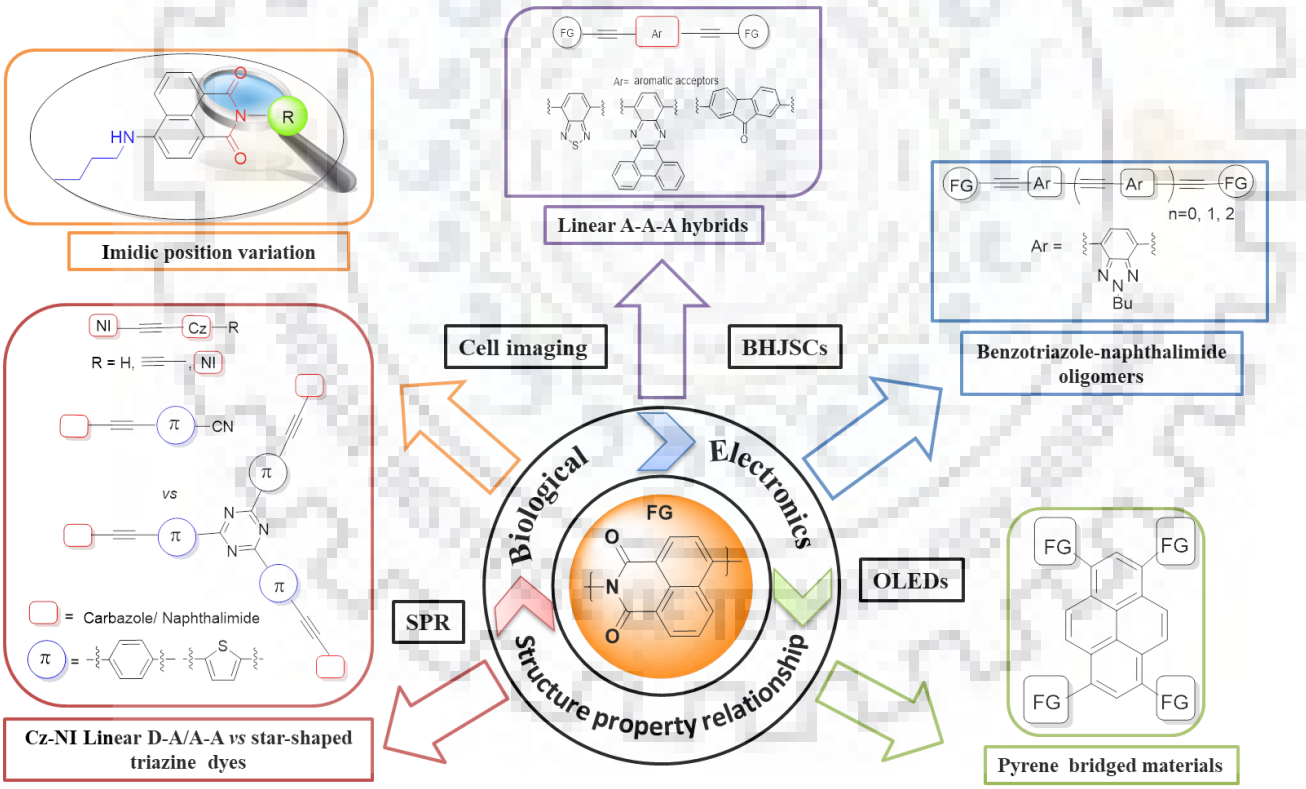

Figure 2.3 Pictorial representation of aim and scope of naphthalimide-based materials for electronic and biological applications.

Thus, in this thesis we aim to provide a systematic description of judicious molecular engineering which is expected to channelize structure property relationship study. We intend to set

a platform where one can correlate how and why the introduction of different chromophores tunes the optical and electrochemical properties of the dyes.

Chapter 3 Bis-Naphthalimides Bridged by Electron Acceptors

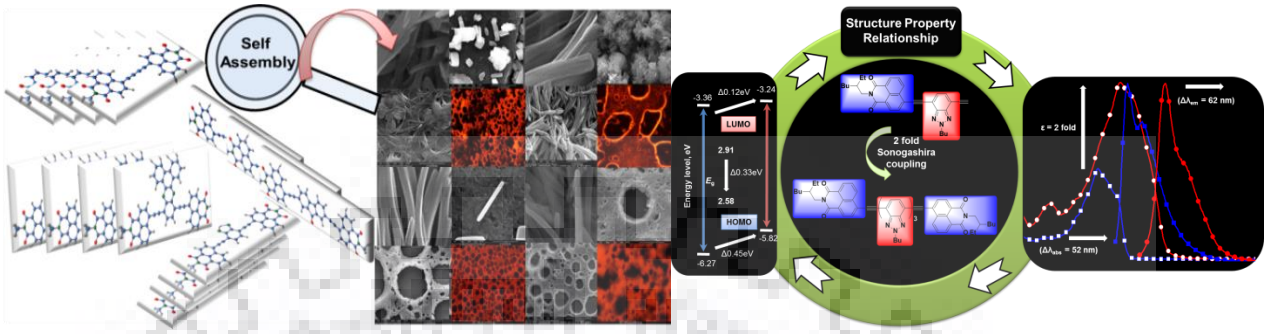

3.1 Introduction

After the advent of polyacetylene by Heeger[217] in 1977, π-conjugated semiconducting systems have gained considerable attention as revolutionary functional materials for the next generation organic electronics.[7, 11] In the field of materials science, small organic molecules exhibit defined chemical structures which make them quite attractive in terms of ease of synthesis and purification. Additionally improves the easy processing and device-fabrication reproducibility as compared to polymers and inorganic materials.[8, 218-226] To date, a large number of π-conjugated materials based on acenes,[227, 228] thienoacenes,[20, 229] heteroaromatics[1, 3] and imide derivatives[59, 64] has been synthesized and successfully expanded the pool of π-conjugated systems for organic electronics. A variety of aromatic π-conjugated small molecules have been investigated due to their easily tunable photophysical, electrochemical and electrical properties. These molecules exhibit interesting optical properties attributable to the narrow band gap. Also, the self-assembling properties of the small molecules into supramolecular materials have flagged its importance due to their high aspect ratio, unique optical and electronic properties.[230-269] It is documented that vinyl linked aromatic conjugating system displays enhanced charge mobilities than single bond bridged molecules due to the extension of π-system.[270, 271] Since these type of molecules exhibit rapid radiationless decay therefore, the incorporation of rigid triple bond maintains the molecular planarity and rigidity and thus nullifies the radiative relaxation.[272, 273] Also, the delocalization of electron density over the whole π-extended molecule enhances the intermolecular charge transport properties. The incorporation of alkyne group between aromatic building blocks is more adaptable to conformational and steric constraints than the alkene moiety due to the electronic symmetry. Moreover, the high stability of

these promising materials makes them attractive for potential application as organic semiconductors.

The organic materials possessing D-A architecture is well known for tons of application owing to accessibility of variety of blends. Although a molecular library comprising solely D-D or A-A is also reported but lack in comprehensive analyses. Since *n*-type organic semiconductors are far behind than their counterparts due to their mismatched energy levels, low mobility and poor solubility for solution processing and thus the stability factor.[16-19] Imides and π-conjugated molecules have received considerable attention. Other than this, several electron deficient moieties such as benzothiadiazole,[104, 172] diketopyrrolo[3,4-*c*]-pyrrole-1,4-dione,[105, 169] benzotriazole,[274-281] fluorenone,[260, 261] and quinoxaline,[23, 282, 283] have been explored as electron acceptor units. A number of polymers using benzotriazole as acceptor with different electron donating group to tune the polymeric properties are documented in literature.[284-294] Yet, only few reports are documented on benzotriazole-based small molecules.[277-281]

Several novel non-fullerene electron acceptors and small molecules based on naphthalimide and bis-naphthalimide derivatives are already discussed in Chapter 1. But no reports have addressed the study of effect of different acceptors in synergy with naphthalimide as small molecules and oligomers. Further, only few reports have addressed the crystalline nano or microscale *n*-type organic semiconductors. Therefore, we have opted to design a class of electron acceptors that could fulfil the lacuna addressed. The supramolecular self-assembly of π-conjugated alkynyl-linked dyes (**D1-D8**) into defined dimensional nanostructures provides a potential strategy to tune the optical and electronic properties shown in Chart 3.1. There are few reports known for the self-assembled well-defined nano-morphology of the organic chromophores. Chen *et al.*[295] revealed the tunable solvent-processed molecular aggregates depending on the self-assembly of carbazole-benzothiadazole ICT hybrids, **D2** and **D3** which is found to be different from their analog dye, **D1**. Zhao *et al.*[296] synthesized anthracene-based dyad, **D4a** which exhibited optical waveguiding and self-assembled to form microrods and microtubes depending on the solvent processing techniques. Later, Wang *et al.*[297] reported the self-assembly behaviors of anthracene-based cruciform, **D4a-D4c** with tunable molecular configuration to design single crystals as nanowires, ribbons and hexagon, respectively attributable to different π-π stacking direction owing to highly planar and rigid system. In 2014, Zhu *et al.*[298] synthesized rod-like anthracene-based oligomers, **D5a-D5d** to demonstrate the effect of length of substitution on the formation of supramolecular assemblies. Torres *et al.*[280,

281] reported rod like T-Shaped 2*H*-benzo[*d*][1,2,3]triazole derivatives, **D6a-D6d**, **D7a-D7c** and **D8a-D8i** to study their photophysical, optical waveguide and self-assembly properties.

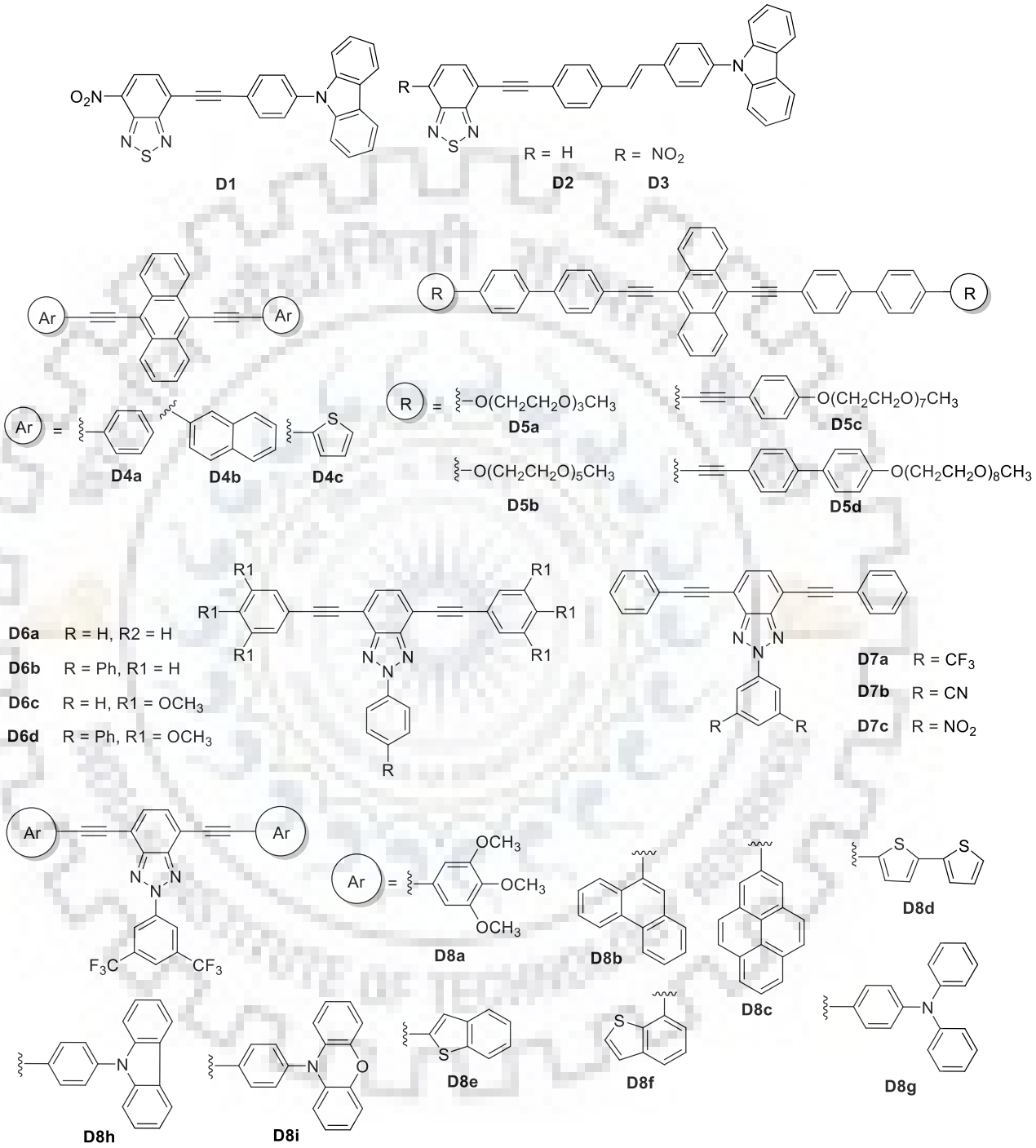

Chart 3.1 Structures of alkynyl-linked related linear dyes.

Considering the benefits of having a large planar and heteroaromatic system for facile and tunable properties, imide-based PAH cores are considered superior. Imide-based dyes are highlighted to show self-assembling supramolecular systems with the aid of various

methods.[299-312] From the literature survey, it is observed that the general strategy for designing a molecular system for effective intermolecular interactions is to have a larger, planar and extended π-core which enhance π-stacking and reduce steric interactions. The acetylene-based functionalized large aromatic core assemblies enhances π-π interactions, reduces the intermolecular spacing between molecules and therefore strengthening the non-covalent interactions. In this Chapter we describe the synthesis and characterization of 4-ethynyl-1,8-naphthalimide-based planar dyes obtained by palladium catalyzed Sonogashira cross-coupling reaction. A series of rod-like π-conjugating end-capped naphthalimide dyes are shown in Figure 3.1. In order to study the effect of electron withdrawing groups on bis-naphthalimide, we have synthesized small molecules bridged by different acceptors and investigated their optical and self-assembly properties.[313] They form self-assembled 1D to 3D nanostructures in a facile manner attributed to the effective intermolecular π-π stacking. While, we extended our approach to enrich the library of electron deficient conjugated molecules incorporating a strong 1,8-naphthalimide and a weak 1,2,3-benzotriazole as acceptors linked by ethynyl group for the following reasons: (a) The presence of lone pair on the nitrogen atom (*N*-2) of benzotriazole weaken the electron acceptor ability of the moiety and (b) it provides an additional advantage over other acceptor moieties as it helps in incorporating symmetrically distributed alkyl chains which assists the molecular structure to attain a more planar and close packing of the molecule. We intend to investigate the effect of the increasing number of benzotriazole unit on the properties of the dyes. All the dyes exhibit remarkable optical, electrochemical and thermal properties. The planar skeletons show high degree of crystallinity and solubilities in various organic solvents owing to the *n*-ethylhexyl chain introduced at *N*-position.

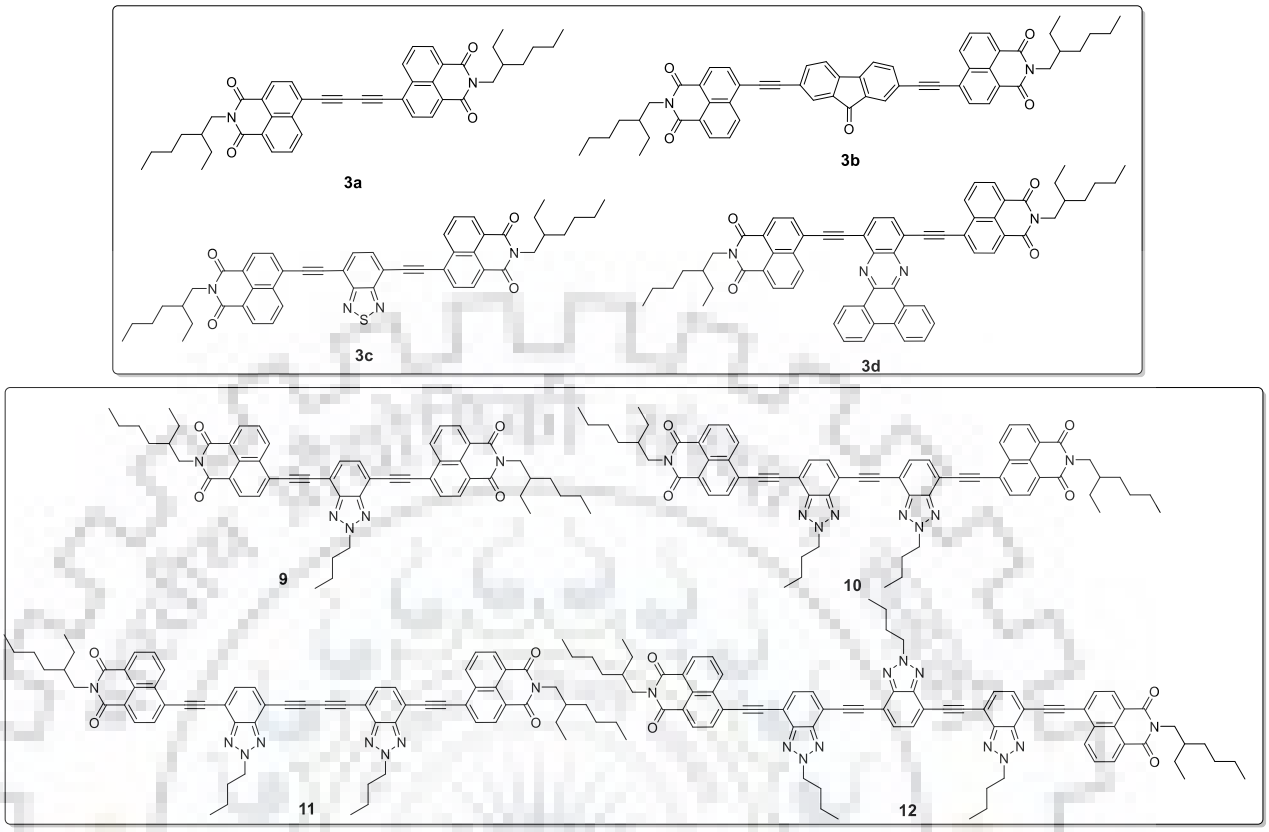

Figure 3.1 Structures of bis-naphthalimide end-capped dyes.

3.2 Results and Discussion

3.2.1 Synthesis and Characterization

3.2.1.1 Small molecules with different electron withdrawing groups

The synthetic pathway used for preparing the dyes (**3a-3d**) is shown in Scheme 3.1. Firstly, the acetylene derivative, **2** was synthesized by a two-step reaction involving Sonogashira coupling[314] of 4-bromo-*N*-(2-ethylhexyl)-1,8-naphthalimide (**1**) with trimethylsilyl acetylene. The later compound, **1** was synthesized by imidization of 4-bromonaphthalene anhydride according to literature procedure.[315] Finally, the naphthalimide-based functional materials were conveniently synthesized by Sonogashira cross-coupling reaction between **2** and respective aryl dibromides[316-319] using $Pd(PPh_3)_2Cl_2/PPh_3/CuI$ catalytic system in good to excellent yields. For **3b** 4-((7-bromo-9-oxo-9*H*-fluoren-2-yl)ethynyl)-*N*-(2-ethylhexyl)-1,8-naphthalimide was synthesized as major product due to the low reactivity of respective arylene dibromide. The dye **3a** was obtained as homocoupled byproduct in the cross coupling reactions targeted for the synthesis of other dyes **3b-3d**.

3.2.1.2 Oligomers with variable number of acceptors

The synthetic protocol followed for synthesizing the set of naphthalimide end-cappred benzotriazole-based oligomers is depicted in Scheme 3.2. The starting materials **2** and 4,7-dibromo-2-butyl-2*H*-benzo[*d*][1,2,3]triazole, **4** were synthesized according to a literature procedure.[373, 374] While 2-butyl-4,7-diethynyl-2*H*-benzo[*d*][1,2,3]triazole, **5** was synthesized *via* a two-step reaction involving the Sonogashira coupling of **4** with trimethylsilyl acetylene followed by deprotection to yield the desired product. The resulting functional dyes were obtained by utilizing Sonogashira coupling procedure. Compound **2** was reacted with **4** in different stoichiometric ratios to yield a bromo-intermediate 4-((7-bromo-2-butyl-2*H*-benzo[*d*][1,2,3]triazol-4-yl)ethynyl)-*N*-(2-ethylhexyl)-1,8-naphthalimide, **6** and dye 4,4'-((2-butyl-2*H*-benzo[*d*][1,2,3]triazole-4,7-diyl)bis(ethyne-2,1-diyl))bis(*N*-(2-ethylhexyl)-1,8-naphthalimide, **7** in good yields. Further, the intermediate **6** was converted to terminal acetylene 4-((2-butyl-7-ethynyl-2*H* benzo[*d*][1,2,3]triazol-4-yl)ethynyl)-*N*-(2-ethylhexyl)-1,8-naphthalimide, **8** by Sonogashira coupling reaction with trimethylsilyl acetylene *via* formation of intermediate 4-((2-butyl-7-((trimethylsilyl)ethynyl)-2*H*-benzo[*d*][1,2,3]triazol-4-yl)ethynyl)-*N*-(2-ethylhexyl)-1,8-naphthalimide, **7**. The compound **8** was coupled with bromo derivative **6** to yield oligomer, **10** and homo coupled product, **11**. The final dye of the series, **12** was obtained by coupling **6** with **5** in moderate yield.

All the dyes are intensely colored (yellow or orange) and exhibited bright solid state luminescence. The dyes were thoroughly characterized by various spectroscopic techniques such as ^{1}H and ^{13}C NMR spectroscopy, IR spectroscopy and HRMS and the data is found to be consistent with the proposed structures. All of the molecules are reasonably soluble in common organic solvents such as Tol, DCM, $CHCl_3$, THF, and DMF and are highly fluorescent both in solution and solid state.

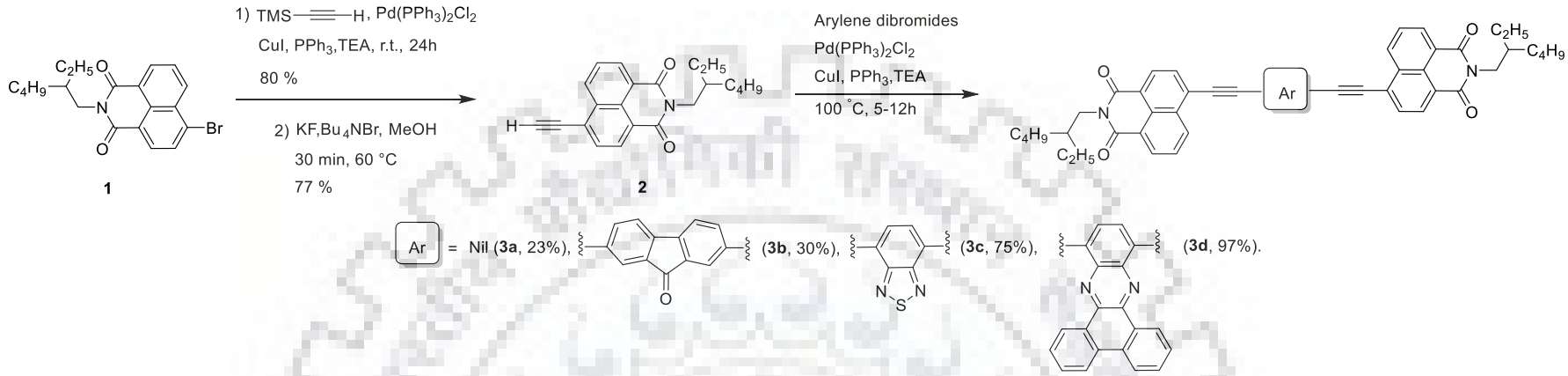

Scheme 3.1 Synthesis of the small molecules.

Table 3.1 Optical and electrochemical data of the dyes **3a-3d** recorded in DCM.

Dye	λ_{max}, nm (ε_{max}, $M^{-1}cm^{-1} \times 10^3$)	λ_{em}, nm (Φ_F, %)[a]	Stokes shift, cm^{-1}	E_{ox},[b] V	E_{red},[b] V	HOMO,[d] eV	LUMO,[c] eV	$E_{0\text{-}0}$,[e] eV
3a	423 (42.4), 392 (47.8), 371 (28.9)	438, 464 (sh) (62)	810	1.51	–1.43	–6.31	–3.37	2.94
3b	445 (sh) (20.9), 400 (70.0), 291 (41.8)	540 (24)	6798	1.17, 1.31	–1.50, –1.66	–5.97	–3.30	2.67
3c	463 (39.8), 439 (46.4), 380 (18.1), 354 (15.6), 329 (14.6), 279 (14.6)	490, 518 (sh) (70)	1237	1.23	–1.32, –1.84	–6.03	–3.48	2.55
3d	470 (41.5), 447 (41.9), 422 (39.5), 398 (35.8), 302 (32.7)	500, 526 (sh) (82)	1322	1.16	–1.48, –1.84	–5.96	–3.32	2.64

[a] Relative quantum yield was obtained by comparing with standard coumarin-6, [b] Redox potentials are reported with reference to the ferrocene internal standard using tetrabutylammonium perchlorate as electrolyte. [c] Deduced from the reduction potential using the formula LUMO= -(4.8 - $|E_{red}|$). [d] Obtained from the DPV oxidation potential peak. [e] Calculated using formula $E_{0\text{-}0}= E_{HOMO}\text{-}E_{LUMO}$.

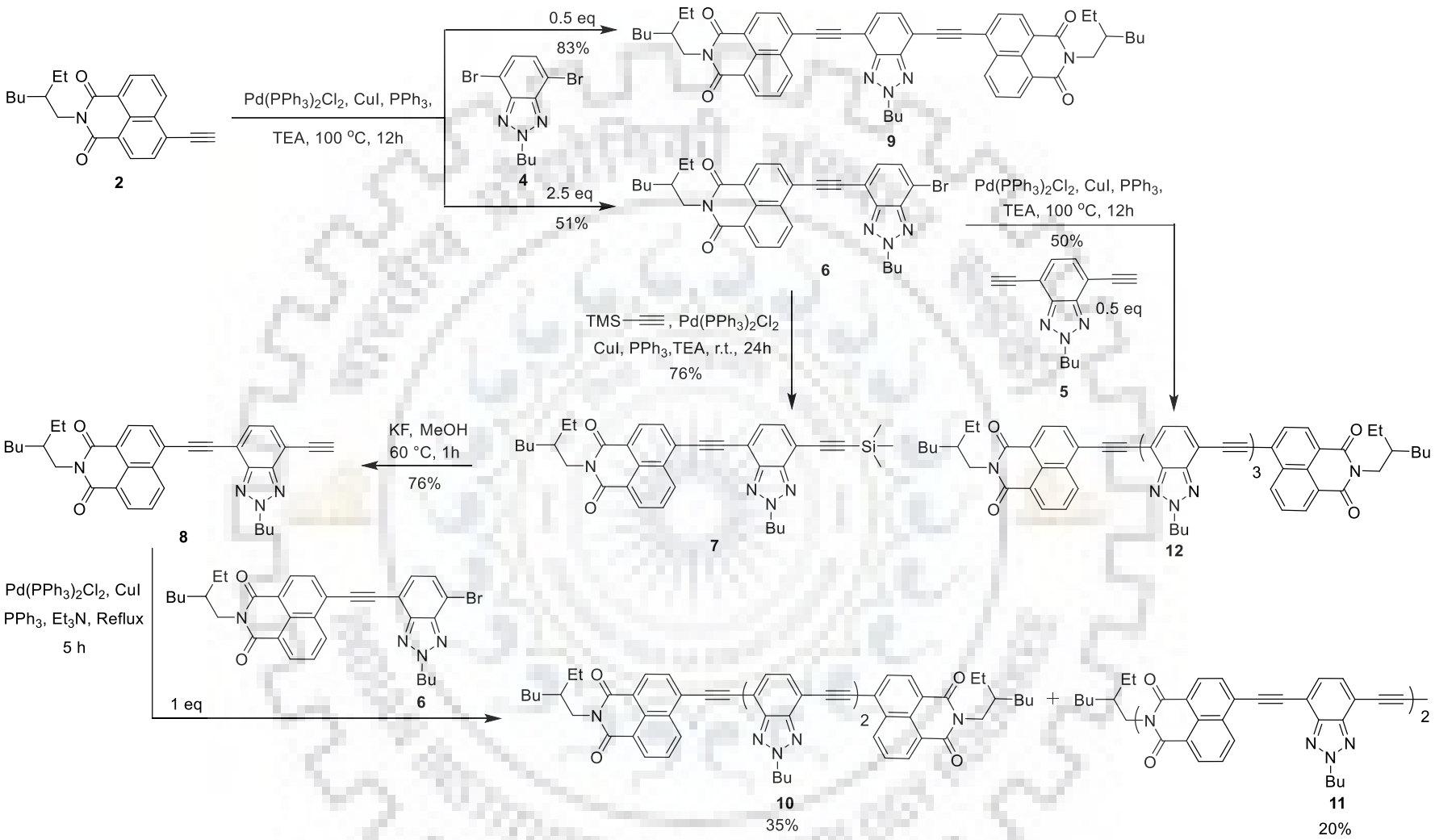

Scheme 3.2 Synthetic scheme of the oligomers.

Table 3.2 Absorption and emission data of the dyes **3a-3d** recorded in different solutions, thin film and solid state.

Dyes	λ_{max}, nm (ε_{max}, M^{-1} cm^{-1} × 10^3)					λ_{em}, nm (Φ_F, %) [a]					
	Tol	THF	$CHCl_3$	DMF	Thin film	Tol	THF	$CHCl_3$	DMF	Thin film [a]	Solid
3a	424 (36.3), 392 (40.5), 373 (25.0)	420 (41.9), 389 (50.3), 369 (32.5)	425 (49.9), 394 (57.4), 372 (34.8)	423 (45.4), 392 (52.6), 372 (33.6)	441, 408, 384	436, 464	434, 462	440, 466	447, 466	519, 547	534 (05)
3b	444 (sh) (16.4), 398 (53.9), 289 (30.6)	439 (sh) (17.0), 395 (49.2), 289 (28.4)	400 (56.5), 292 (34.6)	518, 438, 402, 295	524, 483, 429	510, 540	511, 540	544	551	554	578 (01)
3c	466 (40.6), 441 (45.5), 380 (sh) (18.4), 356 (17.4), 334 (15.5), 285 (17.4)	462 (40.6), 438 (45.2), 376 (sh) (17.1), 354 (15.5), 328 (14.8), 279 (14.7)	466 (43.4), 441 (51.8), 379 (20.5), 356 (18.2), 329 (16.8), 281 (16.7)	464, 439, 332, 276	494, 460	485, 514	489, 517	491, 519	494	566	592 (31)
3d	471 (28.9), 448 (29.5), 423 (28.5), 401 (25.9), 303 (25.7)	469 (25.2), 445 (25.6), 421 (24.6), 398 (22.7), 302 (20.8)	471 (39.8), 449 (40.2), 422 (37.9), 399 (33.8), 303 (31.9)	517, 472, 447, 443, 420, 302	504, 471, 447, 416	498, 532	502, 532	498, 525	507	532, 565	589 (24)

[a] Absolute quantum yield of dyes obtained using integrating sphere

3.2.2 Photophysical Properties

3.2.2.1 Effect of electron withdrawing groups

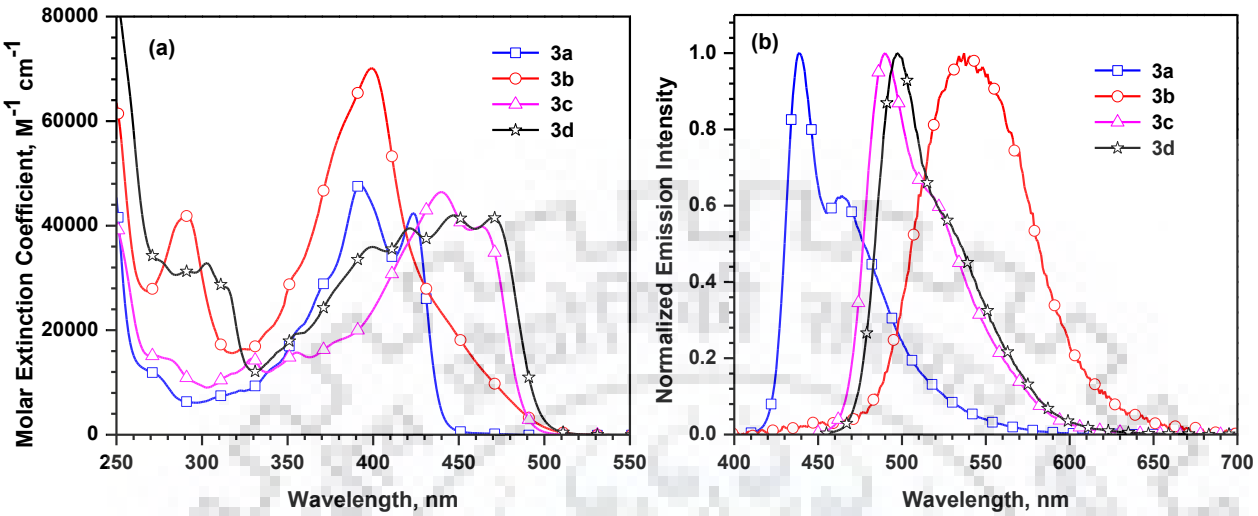

Figure 3.2 (a) Absorption and (b) emission spectra of dyes recorded in DCM.

The UV-visible absorption and emission spectra of the dyes were measured in DCM and displayed in Figure 3.2. The corresponding optical parameters are listed in Table 3.1. The absorption spectra of dyes are complex with multiple overlapping π-π* transition bands ranging from 350 to 500 nm. Naphthalimide moiety shows absorbance band at 350-366 nm.[67] In the present dyes additional red-shifted absorption peaks were noticed. Among the dyes, the dyes containing benzothiadiazole (**3c**) and dibenzo[*a*,*c*]phenazine (**3d**) in the conjugation pathway exhibited most red-shifted absorption peaks. The bathochromic shift is attributed to the extension of conjugation by introduction of an additional electron accepting π-conjugating chromophore. Additional peaks attributable to the localized absorptions originating from the fluorenone and dibenzo[*a*,*c*]phenazine chromophores were observed for the compounds **3b** and **3d**.[260, 320] All the dyes except the fluorenone derivative are brightly luminescent in dilute solutions. The fluorescence spectra recorded for the compounds **3a-3d** in dilute DCM solution is displayed in Figure 3.2(b). The emission peak wavelengths showed the trend similar to that of the absorption with the exception of **3b**. The emission profiles of the compounds **3a**, **3c** and **3d** exhibited vibronic features attesting the rigidity of the molecules.[321] However, **3b** featured broad structureless emission. The Stokes shift is also significantly large for **3b** in the series. Additionally the quantum yield of **3b** is lowest in the group. The above observations

suggest that the dye **3b** probably undergoes structural relaxation in the excited state prior to emission.[321]

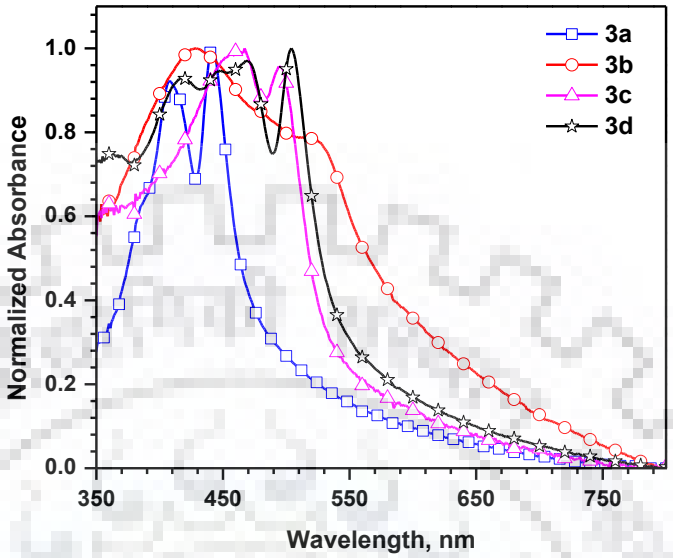

Figure 3.3 Normalized absorption spectra of dyes as drop-casted thin films.

Further, the UV−vis absorption and emission spectra of compounds in thin film, and solid state (Figures 3.3, 3.4, Table 3.3) are carried out to understand the intermolecular interaction and the self-assembly process. A red-shifted absorption bands by 20-70 nm observed in thin film as compared to solution spectra attributed to stronger electronic interaction between the individual molecular skeleton in the solid state.[124, 253, 322] Also, the broad featureless absorption band with emergence of new band was observed attributed to the intermolecular π-π packing interactions or *J*-aggregation[323, 324] as reported in literature.[325] Such an ordered packing of small molecule is effective for long range charge carrier mobility and self-assembly. It is well known that the fluorescence spectral shifts and changes in the quantum yield for solid with respect to solution depend on the molecular packing in the solid state.[301, 326] The presence of strong π−π interactions between cofacially stacked molecules leads to red-shifted fluorescence and a decrease in emission yield. In thin film emission spectra of the compounds (Figure 3.4(a)), a bathochromic spectral shift and broadening clearly indicates the presence of intermolecular interactions. Furthermore, the emission of the compounds in the solid state (Figure 3.4(b)) is further red-shifted when compared to that in thin film; accompanied by a significant broadening of fluorescence band with large FWHM (~90 nm) which is common for solid emitting materials.[327-330] Moreover Φ_F for solid is found to be quenched

(Table 3.2) in comparison to Φ_F in DCM solvent supporting the molecular self-assembly arising from the strong π-π intermolecular interactions.

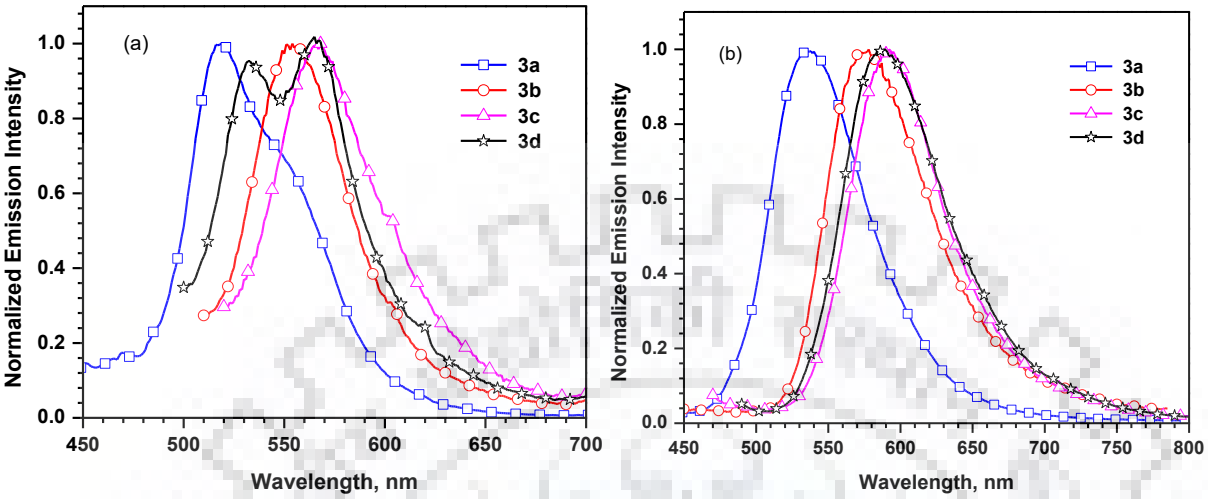

Figure 3.4 Emission spectra of the dyes as (a) drop-cast thin films and (b) solid powder.

To investigate the effect of solvent polarity on the optical properties of the molecules the solvatochromic study was performed for all of the dyes in solvents of different polarity (Figures 3.5, 3.6) and the data obtained is displayed in Table 3.2. The absorption spectra showed negligible changes in the profiles on changing the polarity of the solvent suggesting that the ground state of these molecules is relatively non-polar and devoid of significant solvent effects. However, the emission spectra showed a positive solvatochromism[330] particularly for fluorenone derivative attributed to the stability of the more polarized excited state by the polar solvents than in the ground state. All of the compounds except **3b** showed vibronic transitions in the emission spectra recorded in different solutions particularly in less-polar solvent proving the rigidity of the structure.

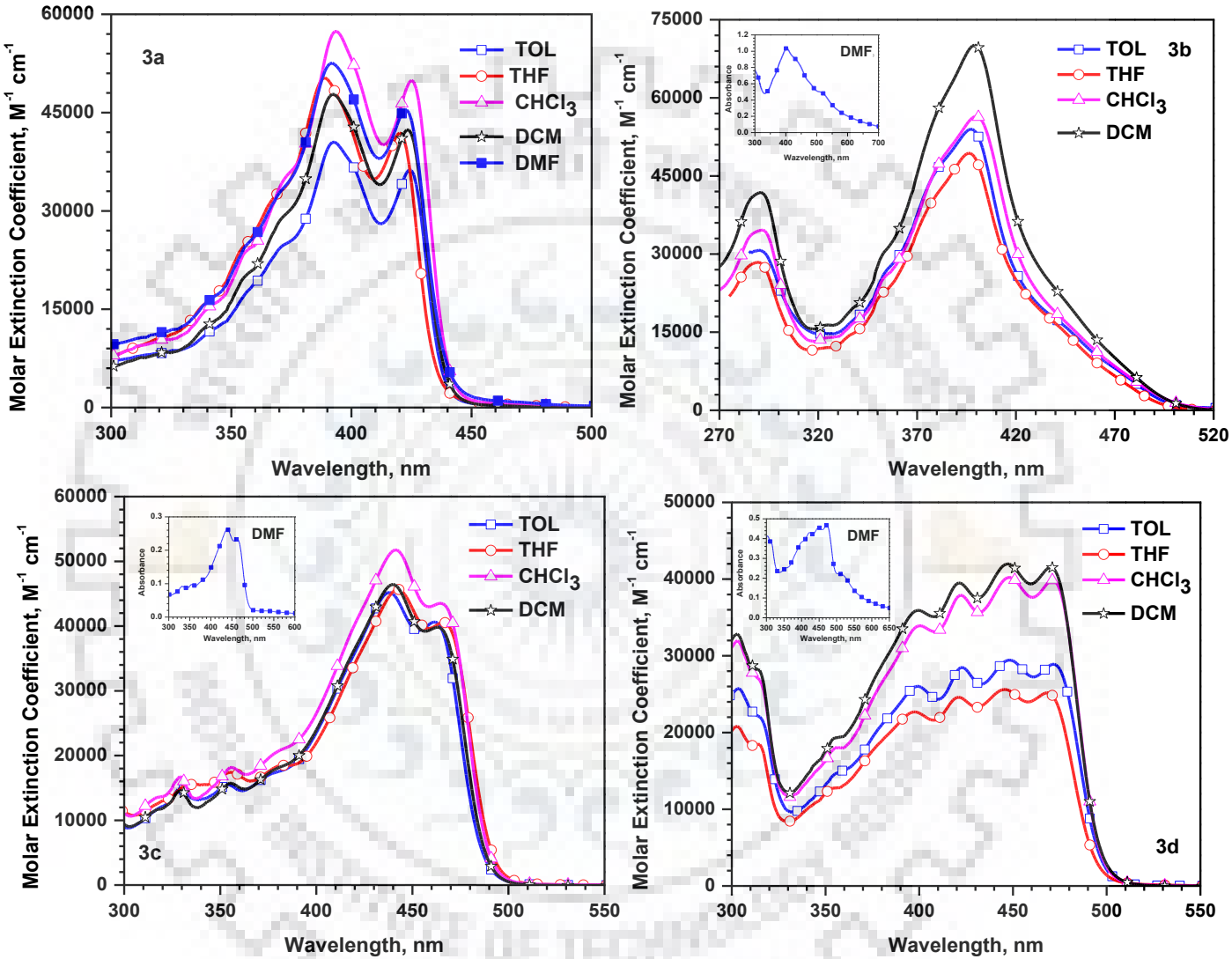

Figure 3.5 Absorption spectra of dyes **3a-3d** recorded in different solutions.

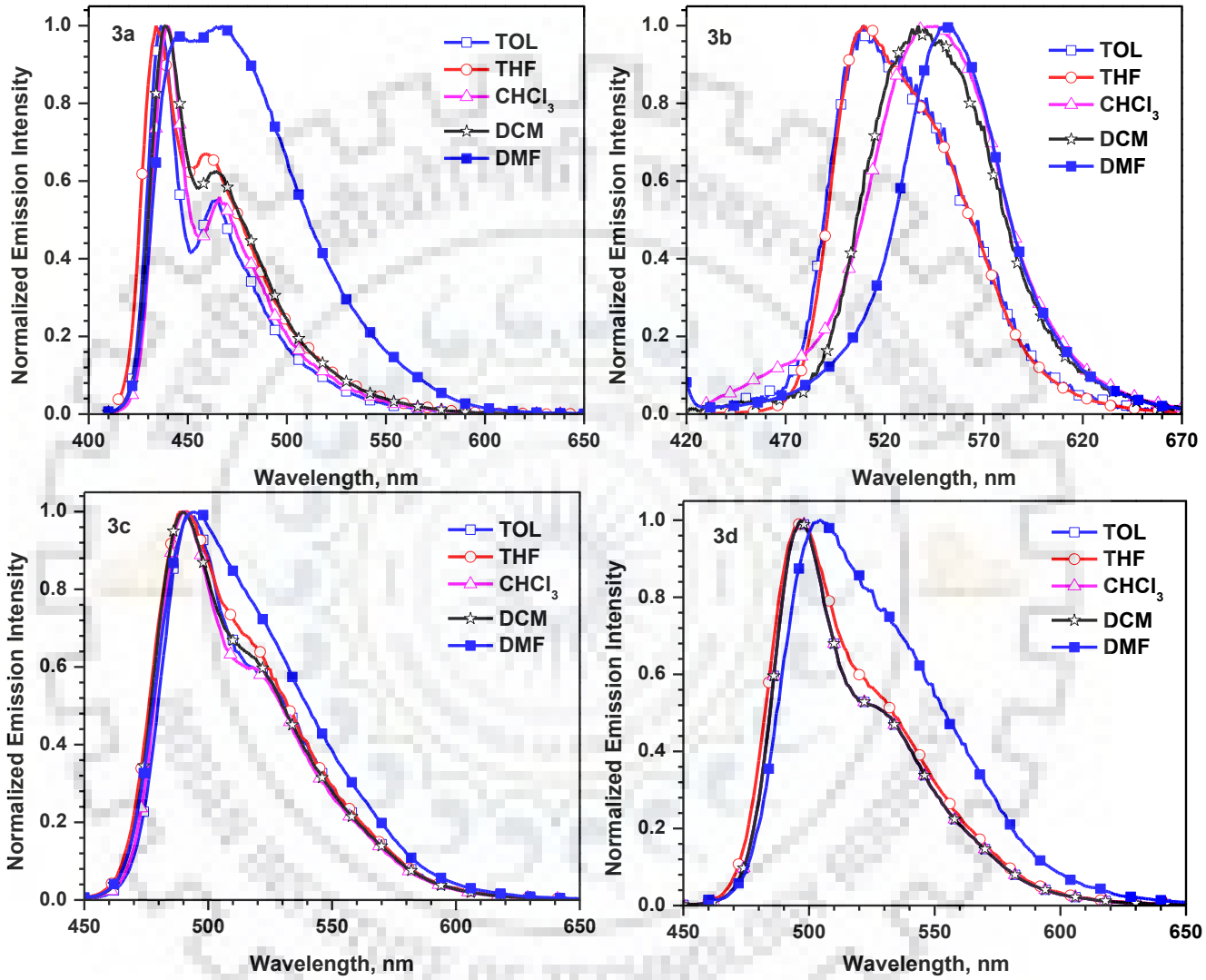

Figure 3.6 Normalized emission spectra of dyes **3a-3d** recorded in different solutions.

Table 3.3 Optical and electrochemical data of the oligomers, **8-12** recorded in DCM.

Dye	λ_{max}, nm, (ε_{max}, $M^{-1}cm^{-1} \times 10^3$)	λ_{em}, nm; Φ_F, %[a]	Stokes shift, cm^{-1}	λ_{max},[b] nm	λ_{em},[b] nm	Stokes shift, cm^{-1}	λ_{em},[c] nm	E_{red}, V[d] (ΔE_p)	LUMO,[e] eV	HOMO,[f] eV	$E_{0\text{-}0}$,[g] eV
8	423 (sh) (31.5), 392 (42.9), 313 (10.8), 244 (48.7)	440, 465 (sh); 59	913	441, 414	525	3628	527	-1.48 (54), -1.56 (52)	-3.36	-6.27	2.91
9	451 (43.2), 427 (49.4), 312 (10.2), 243 (42.6)	475, 500 (sh); 71	1169	478, 446	550	2739	564	-1.50 (81)	-3.30	-6.01	2.71
10	463 (45.8), 438 (57.9), 314 (13.8), 243 (43.5)	487, 515 (sh); 86	1055	506, 468	570	2219	596	-1.52 (125)	-3.28	-5.92	2.64
11	465 (41.5), 437 (54.3), 313 (12.7), 242 (39.7)	489, 520 (sh); 88	963	505, 469	573, 595 (sh)	2350	620, 660 (sh)	-1.51 (86)	-3.29	-5.90	2.61
12	475 (sh) (42.2), 448 (66.9), 428 (73.0), 313 (22.8)	502, 535 (sh); 95	1132	515, 469	576	2094	620, 660 (sh)	-1.56 (98)	-3.24	-5.82	2.58

[a] Relative quantum yield was obtained by comparing with standard coumarin-6. [b] calculated for film obtained by drop casting. [c] Obtained for soild powder form. [d] Reduction potentials are reported with reference to the ferrocene internal standard. [e] Deduced from the reduction potential using the formula LUMO= -(4.8 + E_{red}). [f] Calculated using the formula HOMO = -|LUMO + $E_{0\text{-}0}$|. [g] Calculated from the intersection of absorption and emission spectra.

3.2.2.1 Effect of number of benzotriazole units in oligomers

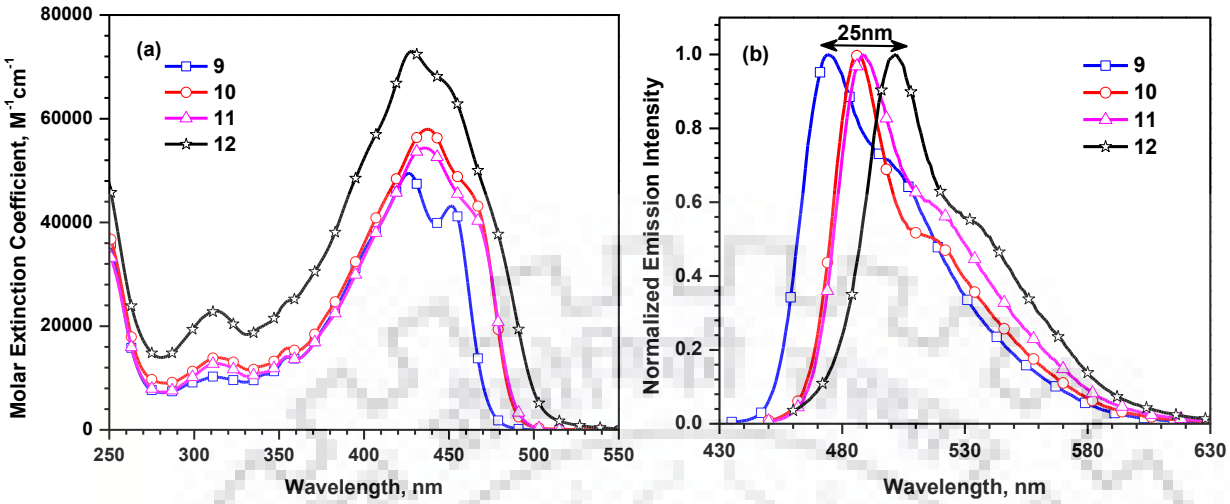

Figure 3.7 (a) Absorption, (b) Normalized emission spectra of the dyes recorded in DCM.

Optical properties of the oligomers were evaluated by measuring absorption and emission spectra in dichloromethane. The absorption and emission spectra of the dyes in the solution are displayed in Figure 3.7 and the pertinent data collected in Table 3.3. The absorption spectra of the dyes show π–π* transition bands ranging from 250 to 500 nm. The absorption band lying in high energy region originates from a π–π* electronic transitions arising from benzotriazole at 280-330nm.[275, 276] The absorption band at longer wavelength arises from multiple π-π* transitions within the conjugated system. It is noteworthy to mention that the series of oligomers depict a progressive bathochromic shift of λ_{max} accompanied by increase in molar absorption coefficients with increase in π-conjugation length and follows the trend **9** < **10** = **11** < **12**. While, within the set of dyes **10** and **11** there is no significant increment in the absorption parameters which means it is independent of the presence of an acetylene group. Comparative study of **8** (Figure 3.8) with its building blocks **2** and **5** displays the synergy of naphthalimide and benzotriazole resulted in a large bathochromic shift of 56 nm and 113 nm respectively with increase in molar extinction coefficient of **8** by more than two fold. Among the series of oligomers the introduction of naphthalimide brings a red shift of λ_{max} by 50 nm for **8** and **9** and benzotriazole by 20 nm for dyes **9** to **10** with higher ε values compared to the preceding oligomer because of the extension in conjugation. Moreover when compared to dye **3a**, dye **9** exhibited a red shifted absorption by 25 nm due to introduction of benzotriazole between the two naphthalimide units. Compared to **D6a**, introduction of naphthalimide on benzotriazole unit as in dye **9** resulted in bathochromic shift ($\Delta\lambda$ = 77 nm). Thus, the combinational effect of benzotriazole and naphthalimide led to superior photophysical properties.

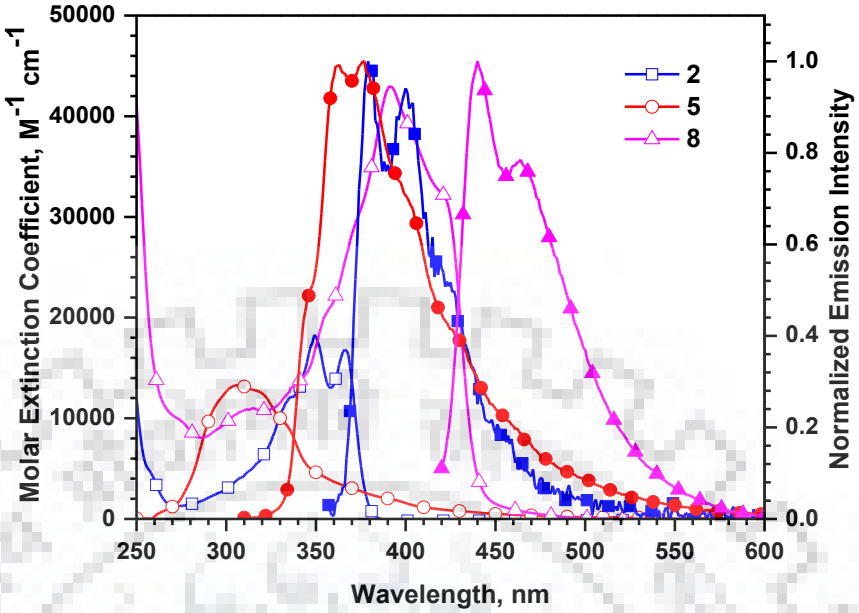

Figure 3.8 Absorption and emission spectra of **2**, **5** and **8** recorded in DCM.

The benzotriazole based dyes display blue-green to highly fluorescent green emissions in dilute DCM solutions. The emission spectra of the dyes exhibit a trend similarly observed in absorption spectra as displayed in Figure 3.7(b). The dye **12** exhibits the most red-shifted emission band at ~500nm in series of dyes. The dye **10** displays a ~15 nm bathochromic shift in emission band on introduction of an additional benzotriazole unit in dye **9**. Moreover, the combinational effect of **2** and **5** compared to **8** results in a large red shift of emission band by 60 nm and 80 nm attributed to the incorporation of benzotriazole and naphthalimide unit, respectively (Figure 3.8). Further, the emission profiles for dyes exhibit a structured vibronic pattern attesting their molecular rigidity. It is observed that the fluorescence spectra are mirror images of the absorption bands suggesting that the geometry of the molecules in its relaxed Frank-Condon excited state is not very different from that of the ground state molecule. This is in accordance with the dyes described in previous section and reported linear naphthalimide-based dyes.[124, 313] Comparison of **3a** and **D6a** with dye **9**, a red-shift in emission profile by 37 nm and 33 nm is observed attributable to extended conjugation by benzotriazole and naphthalimide units, respectively. Further, the Stokes shift for oligomers lies in the range of 900-1100 cm^{-1} which is larger than **3a**. The Stokes shift of **9** is the smallest among the set of dyes. This indicates that the dye **11** undergoes lesser structural reorganization in the excited state. This is reasonable as the dye **11** is more planar when compared to the other dyes attributed to the highly rigid skeleton present in **3a**. The dyes displayed good to excellent fluorescence quantum yield (>70%-95%). Successive

introduction of benzotriazole moiety enhanced the fluorescence quantum yield for dye **12** compared to rest of the dyes. Strong emission makes them suitable to be used in OLEDs as emitting layer.

The absorption spectra of the series of oligomers in thin film casted from toluene solution showcase a red-shift in absorption as displayed in Figure 3.9(a). In particular, the dyes show an emergence of new peak which is further red-shifted when observed in solution implying *J*-aggregation[124] in the solid state. This is attributed to the intermolecular π–π stacking or aggregation within the molecular skeleton as displayed by our previously synthesized dyes. This also highlights the rigidity and planarity of the molecules supported by the optimized geometry of the dyes. Due to their planar aromatic skeletons, these molecules exhibited self-aggregation behavior in solid state. This type of ordered packing of small molecules is effective for long range charge carrier mobilities in field of organic electronics. In the emission spectra (Figure 3.9(b)), a broad structureless emission band is observed attributable to the strong π-π interactions between stacked molecules. The presence of *J*-aggregation results into bathochromic spectral fluorescence shift when compared to solutions. Furthermore, the Stokes shift observed for film state is larger than that observed in solution depicting the role of strong intermolecular interactions. Inspite of this, the dyes display solid state emission (Figure 3.9(c)) which is further red-shifted and broadened than that observed for film.

To study the role of solvent effect on the solvatochromism of the dyes, absorption and emission were recorded in different solvents (Figures 3.10, 3.11 Tables 3.4, 3.5). The absorption spectra showed negligible changes in the profiles suggesting the non-polar nature of the ground state. However, the emission spectra displayed a slight positive solvatochromism attributable to the stabilization of polarized excited state in polar solvents. All the dyes have shown vibronic transitions in the emission spectra proving the planarity of molecular skeleton. Further, the Stokes shift observed in different solvents particularly for non-polar solvents is the least among the series (Table 3.6).

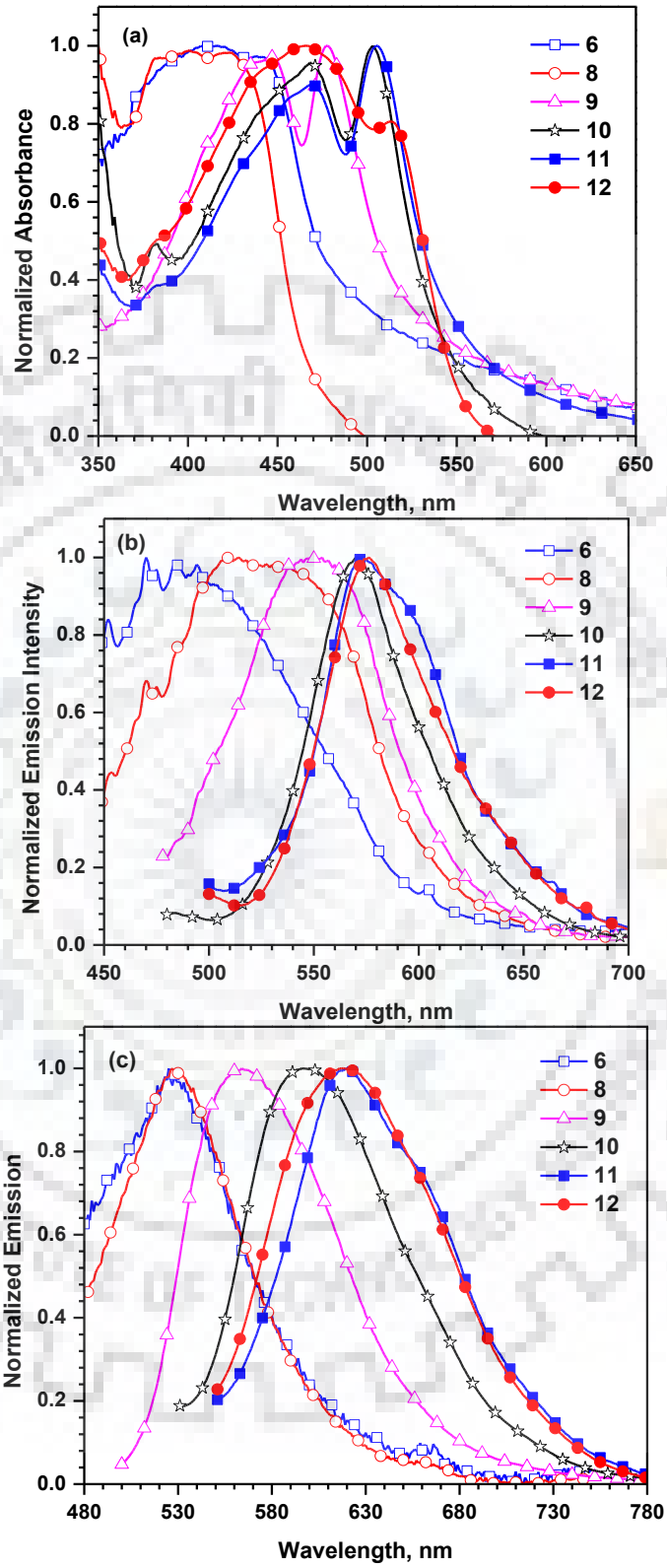

Figure 3.9 (a) Normalized absorption spectra, (b) Normalized emission spectra of dyes **6**, **8-12** recorded on drop casted thin films. (c) Normalized emission spectra of the solid powder.

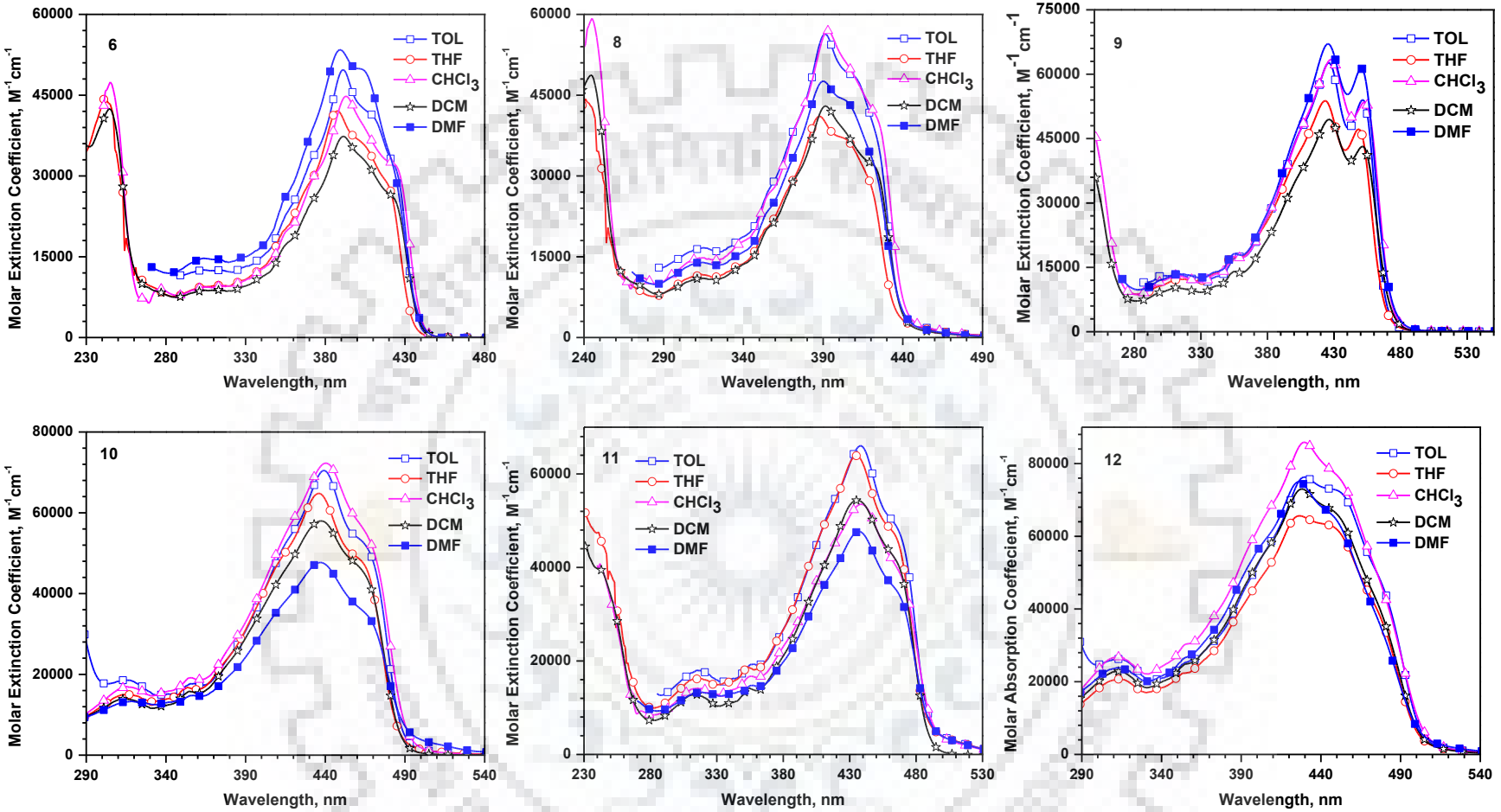

Figure 3.10 Absorption spectra of dyes **6**, **8-12** recorded in different solutions.

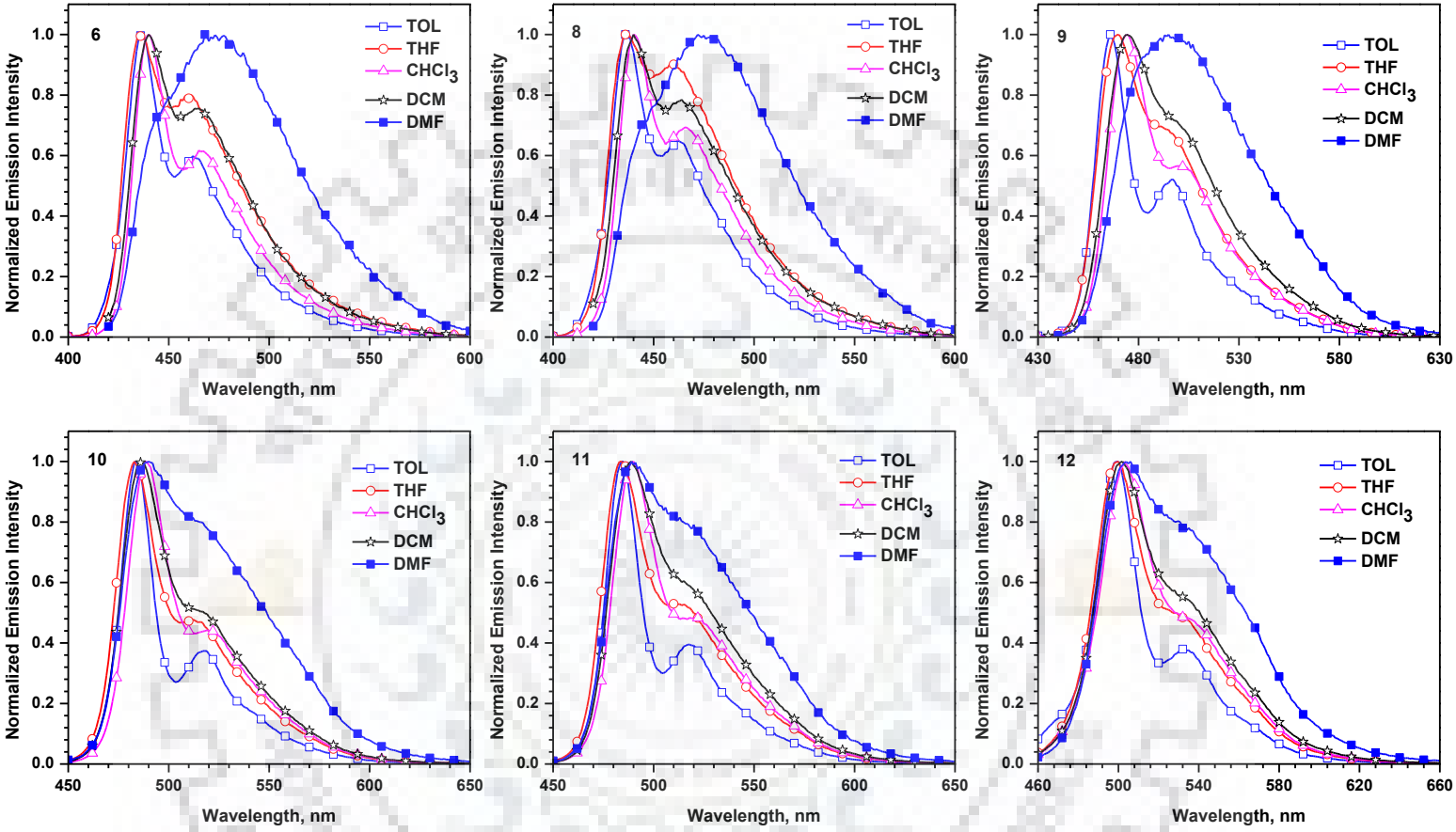

Figure 3.11 Normalized emission spectra of dyes **6, 8-12** recorded in different solvents.

Table 3.4 Absorption data for dyes **6**, **8-12** recorded in different solvents.

Dye	λ_{max}, nm, (ε_{max}, $M^{-1}cm^{-1} \times 10^3$)					
	TOL	THF	$CHCl_3$	DCM	DMF	Film
6	424 (31.6), 409 (41.4), 391 (49.7), 310 (12.4)	419 (sh) (28.6), 404 (35.9), 388 (42.1), 310 (9.6), 243 (43.9)	424 (sh) (32.1), 393 (44.8), 311 (9.4), 245 (47.4)	423 (sh) (25.9), 392 (37.3), 313 (8.8), 245 (42.5)	423 (sh) (31.4), 404 (49.7), 389 (53.4), 312 (14.4)	421, 400, 382
8	424 (sh) (40.7), 393 (56.9), 311 (14.6), 245 (59.3)	418 (sh) (39.8), 405 (36.7), 388 (41.1), 310 (11.5), 242 (43.7)	424 (sh) (40.7), 493 (56.9), 310 (14.6), 245 (59.3)	423 (sh) (31.5), 392 (42.9), 313 (10.8), 244 (48.7)	422 (sh) (32.0), 405 (43.8), 391 (47.5), 311 (13.9)	441, 414
9	452 (53.9), 426 (62.7), 311 (13.2)	449 (47.2), 423 (53.8), 312 (12.2)	453 (53.5), 428 (63.4), 312 (13.2), 244 (51.7)	451 (43.2), 427 (49.4), 312 (10.2), 243 (42.6)	452 (58.8), 426 (64.9), 313 (12.9)	478, 446
10	464 (49.3), 438 (66.0), 312 (17.5)	463 (47.5), 436 (63.8), 311 (15.9), 440 (47.3)	464 (40.7), 438 (53.5), 312 (14.1), 242 (40.8)	463 (45.8), 438 (57.9), 314 (13.8), 243 (43.5)	464 (35.6), 437 (47.7), 311 (12.8)	506, 468
11	466 (48.4), 439 (65.9), 313 (17.7)	466 (45.8), 437 (63.8), 312 (16.1), 241 (47.6)	465 (40.3), 438 (53.5), 312 (14.1), 242 (40.8)	465 (41.5), 437 (54.3), 313 (12.7), 242 (39.7)	466 (34.8), 437 (47.7), 312 (13.0)	505, 469
12	475 (sh) (50.1), 453 (71.8), 431 (76.2), 312 (26.2)	474 (sh) (40.9), 450 (61.9), 428 (65.6), 312 (20.7), 239 (52.4)	476 (sh) (48.9), 455 (73.8), 431 (85.7), 312 (26.8), 242 (66.6)	475 (sh) (42.2), 448 (66.9), 428 (73.0), 313 (22.8)	474 (sh) (38.9), 449 (64.9),427 (75.0), 312 (23.8)	514, 469

Table 3.5 Emission data for dyes **6**, **8-12** recorded in different solvents.

Dye	λ_{em}, nm; Φ_F						
	TOL	THF	$CHCl_3$	DCM	DMF	Film	Solid
6	437, 462 (sh)	437, 461 (sh)	440, 467 (sh)	440, 465 (sh); 48	445 (sh), 474	485	525
8	436, 463 (sh)	436, 460 (sh)	440, 466 (sh)	440, 465 (sh); 59	445 (sh), 475	525	527
9	466, 497 (sh)	470, 497 (sh)	474, 501 (sh)	475, 500 (sh); 71	498	550	564
10	483, 517 (sh)	483, 517 (sh)	488, 521 (sh)	487, 515 (sh); 86	490, 517 (sh)	570	596
11	484, 518 (sh)	484, 517 (sh)	490, 523 (sh)	489, 520 (sh); 88	489, 520 (sh)	573, 595 (sh)	620, 660 (sh)
12	500, 534 (sh)	500, 534 (sh)	503, 535 (sh)	502, 535 (sh); 95	506, 535 (sh)	576	620, 660 (sh)

[a]Relative quantum yield was obtained by comparing with standard coumarin-6

Table 3.6 Stokes shift data for dyes **6**, **8-12** recorded in different solvents.

Dye	Stokes shift, cm^{-1}					
	TOL	THF	$CHCl_3$	DCM	DMF	Film
6	702	983	858	913	1169	3134
8	649	988	858	913	1225	3628
9	763	847	978	1169	2044	2739
10	848	894	1060	1055	1144	2219
11	798	798	1097	963	1009	2350
12	1053	1097	1128	1132	1334	2094

3.2.3 Self-assembly studies of small molecules

The self-assembly of the compounds **3a-3d** were investigated by absorption and emission measurements in binary THF: H_2O solvent system (Figures 3.12-3.15). The aggregation behaviors of the compounds were confirmed by gradual change in ratio of water and solvent. The solution color of dyes is found to change from 100% THF to 40-60% H_2O accompanied by a new 20-30 nm red shifted absorption shoulder as compared to the π-π* transitions in pure THF solvent. On moving from 100% THF to 90% water, the absorption spectra showed hypochromic shift on increasing water content suggesting π-stacking among the chromophores. Levelling off of the spectra at longer wavelength region observed at high water content is attributed to the scattering of light due to formation of aggregates. This result clearly pointed towards the occurrence of π–π stacking in the aggregates due to the formation of self-assembled structures.

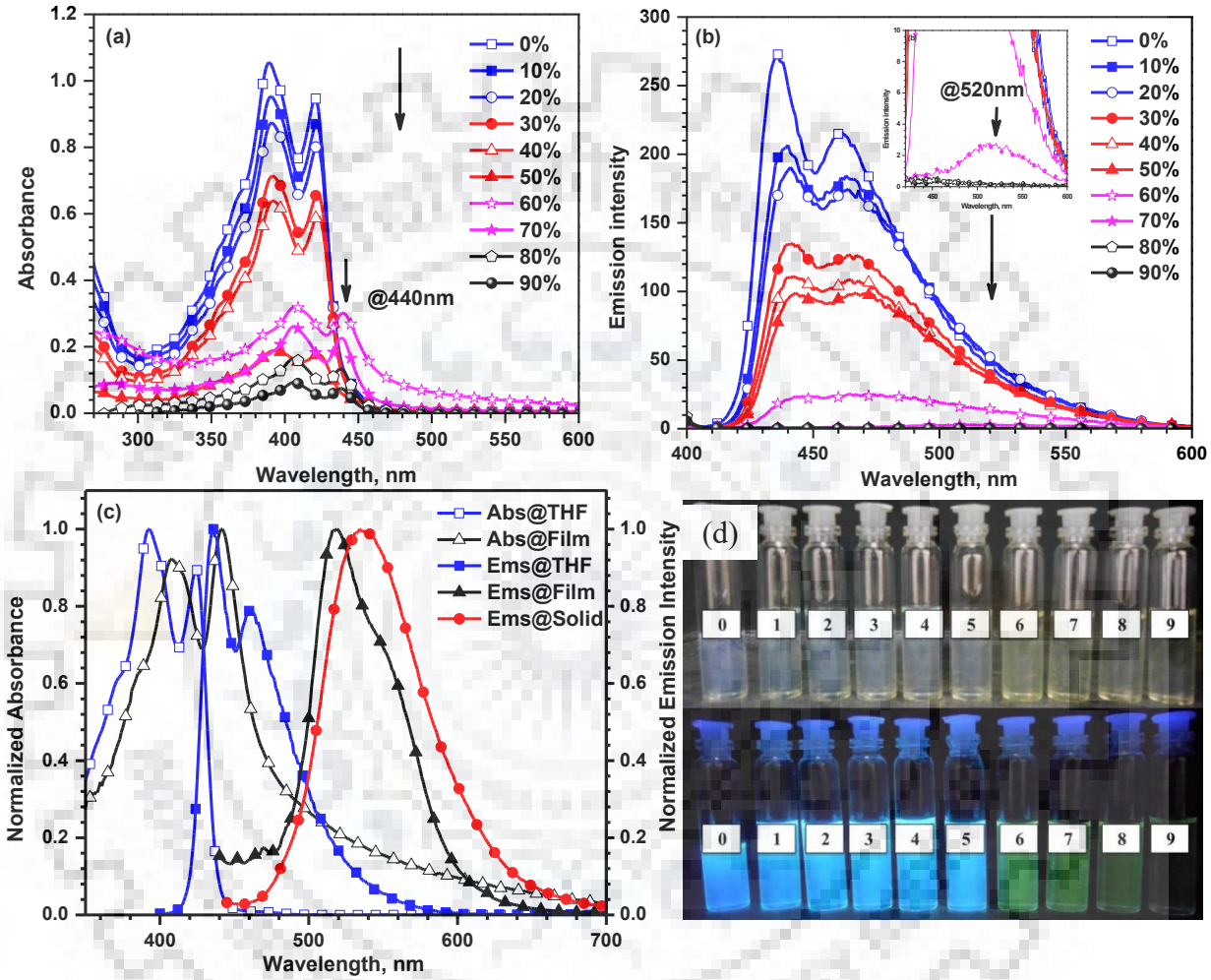

Figure 3.12 (a, b) Absorption and emission spectra of **3a** with THF:H_2O titration studies respectively. (c) Normalized absorption and emission spectra of THF solution, thin film and solid state (d) Images of solution (above under normal light, below under UV light) obtained by varying water concentration in THF solvent for **3a** (left to right – increasing water concentration 0-90%).

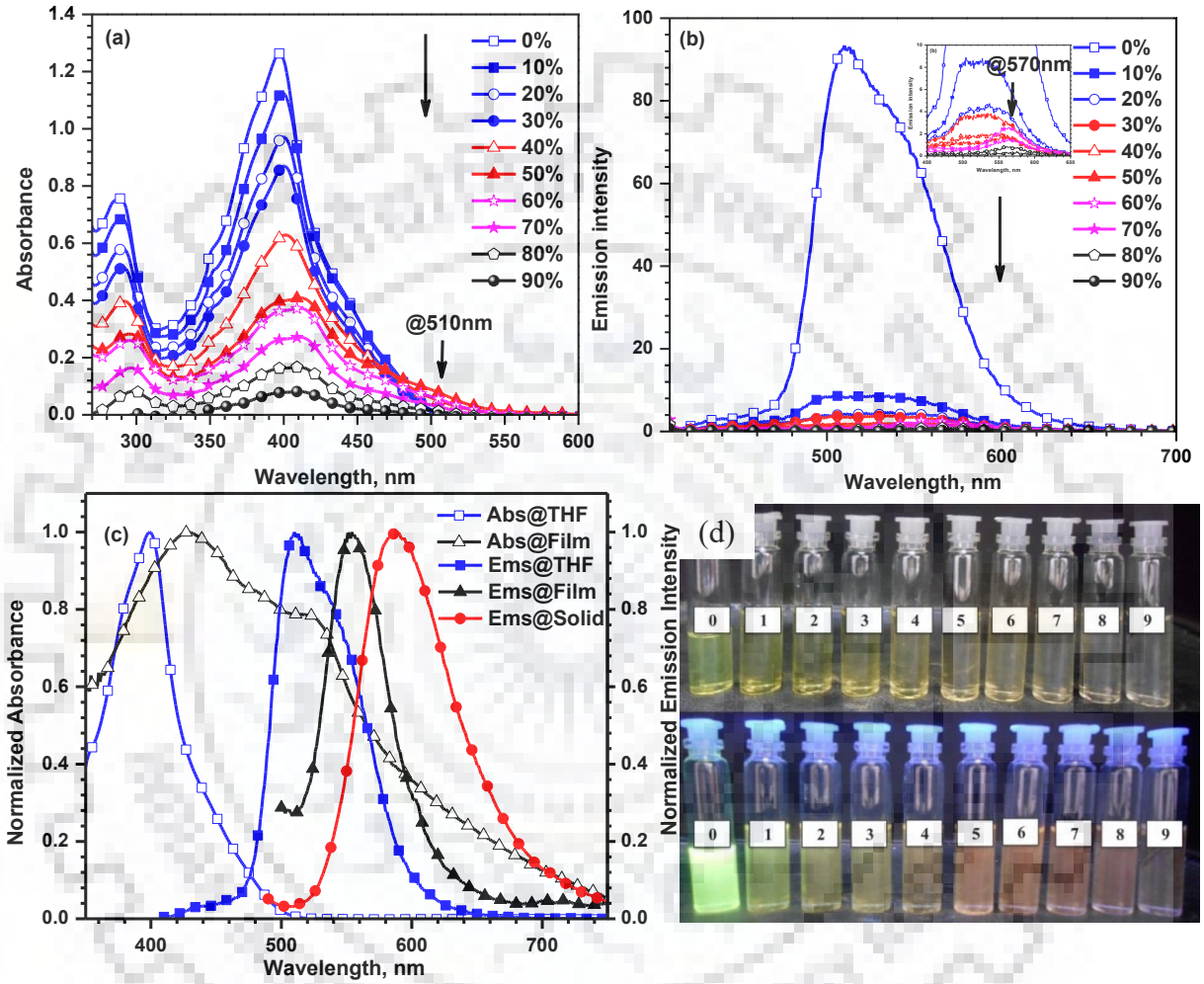

Figure 3.13 (a, b) Absorption and emission spectra of **3b** with THF:H_2O titration studies respectively. (c) Normalized absorption and emission spectra of THF solution, thin film and solid state (d) Images of solution (above under normal light, below under UV light) obtained by varying water concentration in THF solvent for **3b** (left to right – increasing water concentration 0-90%).

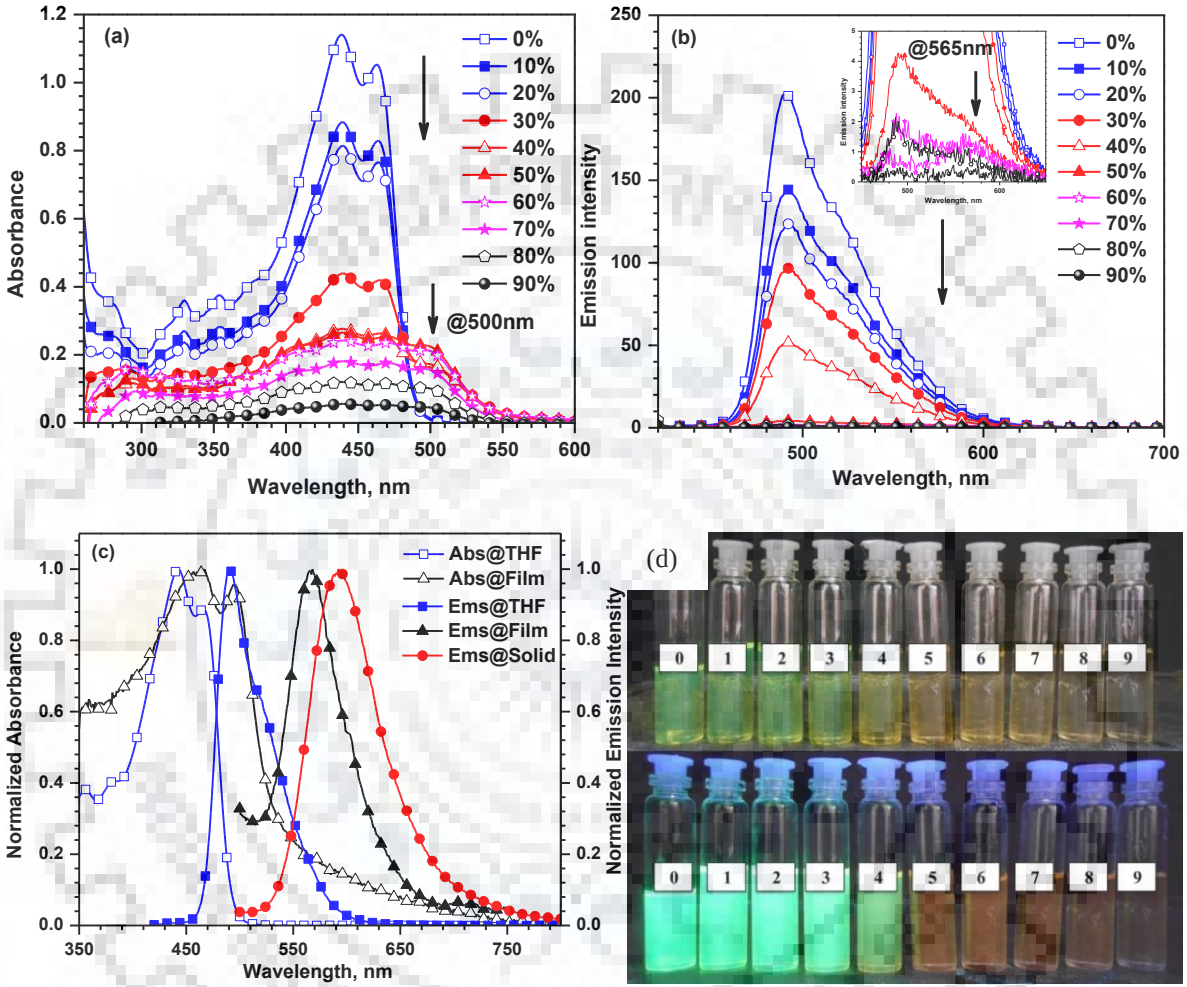

Figure 3.14 (a, b) Absorption and emission spectra of **3c** with THF:H_2O titration studies, respectively (c) Normalized absorption and emission spectra in THF solution, thin film and solid state (d) Images of solution (above under normal light, below under UV light) obtained by varying water concentration in THF solvent for **3c** (left to right – increasing water concentration 0-90%).

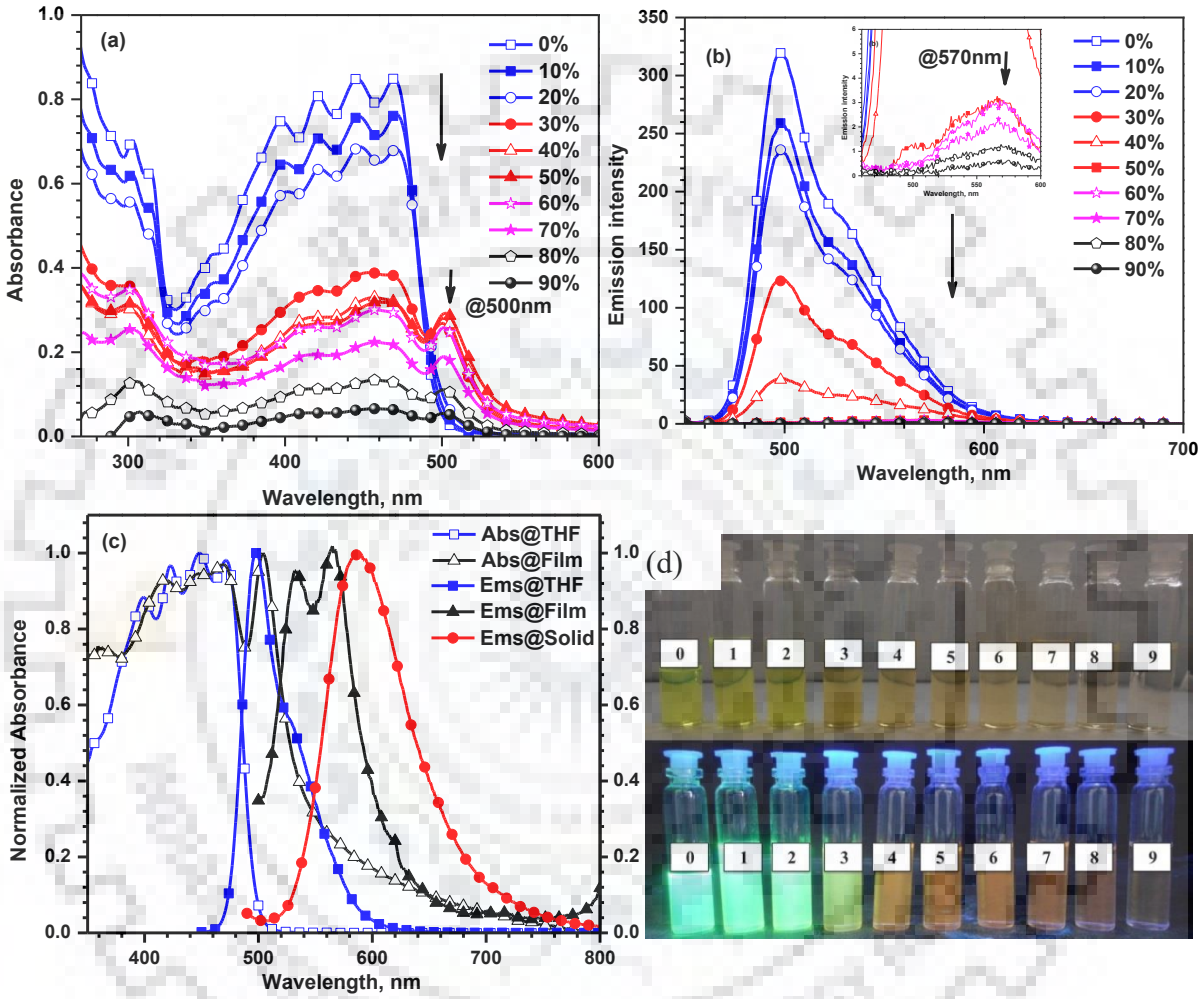

Figure 3.15 (a, b) Absorption and emission spectra of **3d** with THF:H_2O titration studies respectively. (c) Normalized absorption and emission spectra of THF solution, thin film and solid state (d) Images of solution (above under normal light, below under UV light) obtained by varying water concentration in THF solvent for **3d** (left to right – increasing water concentration 0-90%).

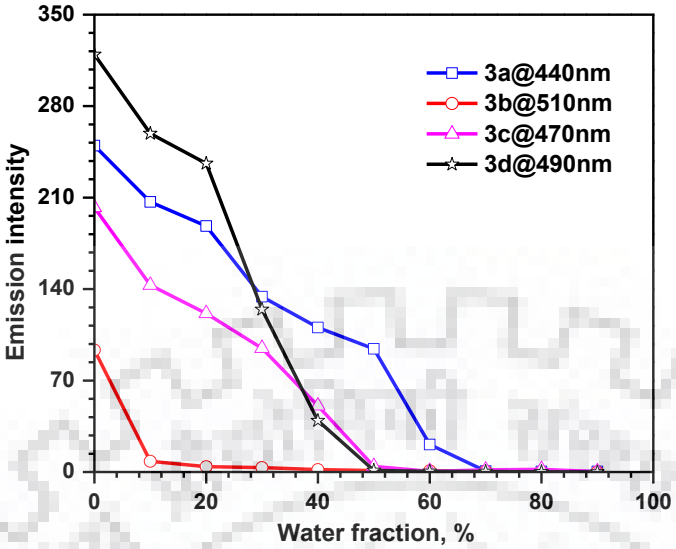

Figure 3.16 Plot of emission intensity *vs* water fraction in THF solvent for dyes.

In the fluorescence spectra, the aggregate emission bathochromically shifts towards the solid state emission region. The fluorescence emission intensity in THF solution is 3-5 folds higher than that of (1:1) THF: H_2O system. Such red-shifted and quenched emission intensity at high water content (Figure 3.16) could be attributed to the presence of π–π stacking interactions that induce the self-assembly. This supports the formation of aggregates driven by non–covalent interactions which is corroborated by red shifted absorption and emission bands and emission quenching in solid state.

3.2.4 Excited State Decay Dynamics

3.2.4.1 Effect of electron withdrawing groups on aggregation

In order to investigate and analyze the effect of aggregation on radiative and non-radiative transition rates (k_r, k_{nr}) time resolved fluorescence lifetime decay measurements were carried out for compounds in THF solution and 90% water-THF mixture (Figure 3.17, Table 3.7). Fluorescence lifetime measurements displayed multi-exponential behavior of emission decay which was best fitted with a double or triple exponential function (Table 3.8). According to Sillen *et al*.[331] the amplitude average lifetime is an effective parameter to derive the transition rate constants of multi-exponential decays caused by the exposure of fluorescent molecules to different environments. The calculated average lifetime[322] (τ_{avg}) of excited state of dyes in solution is found to be long lived than corresponding aggregates. This can be correlated to the quenching of Φ_F in aggregated and solid state. Furthermore, the lifetime calculated out is found to be consistent with the order

of quantum yields observed in solution, aggregates and solid state of the dyes. The correlated data revealed that a long lifetime value of 3.58 ns in solution for **3d** is attributed to the delayed radiative rate decay i.e. high quantum yield. Moreover, in aggregated state the lifetime is acquired to be shorter indicating more efficient non-radiative decay pathway. This is clearly reflected by magnitude of k_{nr} which is significantly larger than k_r value for aggregates. Also, Spano *et al*. [332] had theoretically studied exciton delocalization in molecular aggregates due to exciton-vibration coupling. Thus on comparing radiative decay rate of solution (0.4 ns^{-1}) and aggregates for **3b** (1 ns^{-1}) and **3c** (8 ns^{-1}) radiative decay rate is greatly enhanced which is characteristics for *J*-aggregates referred as super-radiance.[333, 334] This is a clear evidence of formation of *J*-aggregates in solid state. Whereas the non-radiative decay rate for the aggregation state are observed to be faster than the corresponding k_{nr} values in solution which reflects effective intermolecular interactions resulting into significant decline in fluorescence quantum yield.

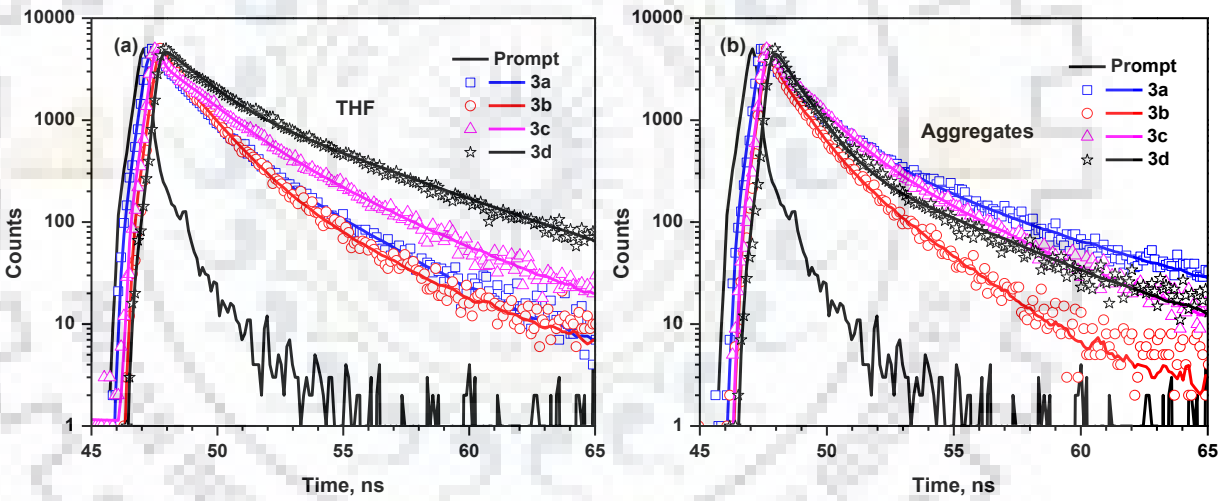

Figure 3.17 Fluorescence decay profiles of dyes in (a) THF solution, (b) 90% water-THF mixture aggregates for $2x10^{-5}$M solution.

If we look into the calculated lifetimes of dyes, the first lifetime (τ_a) is equivalent to that of the **3a** lifetime and, therefore, can be ascribed to the emission from the naphthalimide skeleton.[67] Whereas lifetime less than 1 ns time scale with ultrafast decay channels can be correlated to the non-emissive aggregated state of the dyes. We found it interesting to correlate these fluorescence decay analysis with degree of assembling properties of the dyes. A long lifetime value of 1.84 ns of aggregates for **3d** as compared to 0.01 ns for rest two dyes in 90% water-THF system reflects the better self-assembly properties and solid

state quantum yield of the corresponding dye. While for **3a** τ_{avg} is 0.7 ns longer than in solution i.e. monomeric state. This could be due to stronger intermolecular interactions in excited state.[124] Also the longer life time in the aggregated state and micro structured flower like morphology for this dye is possibly due to the involvement of large number of molecules in these aggregates. Thus fluorescence lifetime decay data for solution and aggregates offer us sufficient evidences for existence of molecular aggregation in solid state.

Table 3.7 Time-resolved fluorescence and photophysical data for the dyes in THF and 90% water-THF mixtures.

Dye	τ_{avg},[a] ns		Φ_F[b]		k_r,[c] ns^{-1}		k_{nr},[d] ns^{-1}	
	Sol.	Agg.	Sol.	Agg.	Sol.	Agg.	Sol	Agg.
3a	1.73	2.43	0.66	0.06	0.38	0.03	0.20	0.39
3b	1.40	0.01	0.52	0.01	0.37	1.00	0.34	99.00
3c	1.83	0.01	0.74	0.08	0.40	8.00	0.14	92.00
3d	3.58	1.84	0.90	0.15	0.25	0.08	0.03	0.46

[a]τ_{avg} = Fluorescence lifetime decay measured as $\tau_{avg} = (A_1 \times \tau_1) + (A_2 \times \tau_2) + (A_3 \times \tau_3)$ in ns. [b]Fluorescence relative quantum yield calculated using coumarin 6 as reference (0.78 in EtOH). [c]Radiative decay rates (k_r) calculated using $k = \Phi_F/\tau$. [d]Non-radiative decay rate (k_{nr}) calculated using $\Phi_F = k_r/(k_r+k_{nr})$.

Table 3.8 Time-resolved fluorescence spectroscopy data of dyes in THF and 90% water -THF mixtures.

Dye	A_1	τ_1, ns	τ_a, ns	A_2	τ_2, ns	τ_b, ns	A_3	τ_3, ns	τ_c, ns	τ_{avg}, ns	χ^2
3a Sol.	0.66	0.99	0.65	0.34	3.17	1.08	-	-	-	1.73	1.01
3a Agg.	0.26	0.28	0.07	0.46	1.69	0.78	0.28	5.67	1.58	2.43	0.97
3b Sol.	0.61	1.26	0.77	0.15	3.84	0.58	0.24	0.20	0.05	1.40	1.32
3b Agg.	0.001	0.85	0.001	0.00	2.43	0.00	0.99	0.01	0.01	0.01	1.40
3c Sol.	0.53	1.30	0.69	0.28	3.94	1.10	0.19	0.17	0.03	1.83	1.15
3c Agg.	0.00	1.64	0.00	0.00	4.08	0.00	1.00	0.01	0.01	0.01	1.44
3d Sol.	0.39	1.30	0.51	0.61	5.06	3.07	-	-	-	3.58	1.02
3d Agg.	0.73	0.89	0.65	0.27	4.43	1.19	-	-	-	1.84	0.97

Where τ_1/ τ_2 /τ_3, Life time of different decay channels from FLS experiment in ns using 405 nm as excitation wavelength; $A_1/A_2/A_3$, Contribution of different decay channels in solution; fitted by either double or triple exponential; χ^2, correlation of exponential fit; τ_{avg} = Fluorescence lifetime decay measured as $\tau_{avg} = (A_1 \times \tau_1) + (A_2 \times \tau_2) + (A_3 \times \tau_3)$ in ns.

3.2.4.2 Effect of number of benzotriazole units in oligomers

In order to have a deep insight into the excited state dynamics of the dyes, the fluorescence decay in DCM ($2x10^{-6}$ M) were recorded by exciting 405 nm and fixing the emission monochromator at corresponding emission maxima (Figure 3.18). The data is compiled and summarized in Tables 3.9 and 3.10. The fluorescent decay profiles were fitted by double exponential kinetics and average excited state lifetime were calculated as relatively short approximately 1 ns. This portrays that the dyes are highly fluorescent in nature and exhibited a strongly allowed S_0-S_1 transition. This can further be infered from the computed electronic parameters and a correlation between the fluorescence lifetime and quantum yield. The quantum yield is the highest for dye **12** exhibiting longer lifetime when compared to other oligomers **10** and **11**. Also, the analysis pointed that the average lifetime of excited states gradually decreased with the incorporation of benzotriazole unit on moving from **9** to **12** in the set of oligomers. While among the dyes **10** and **9**, the later exhibited a long lived lifetime (1.34 ns) than parent dye, **8** attributed to the additional functionalized naphthalimide core. Also, it is found that the lifetime of **8** (1.23 ns) is long lived than the core 1,8-naphthalimide molecule (0.52 ns)[335] which is supported by enhanced quantum yield for the same. The observed short lived and ultrafast decay channels of the oligomers than parent dye can be correlated to k_r and k_{nr} determined from the excited state lifetime and fluorescence quantum yields. The calculated k_r and k_{nr} values are in aggrement with the observed quantum yield and lifetime. All the dyes have possessed a faster radiative decay rates than the non-radiative rate decay constants contributed to the high fluorescence efficiency. The calculated parameters such as the slowest k_{nr} value and short lived excited state lifetime shows a moderate fit to the most fluorescent dye **10**. The two components of the dyes i.e. benzotriazole and naphthalimide contributed to the existence of biexponential decays to different extends in the dyes. The fast and slow component (τ_a and τ_b) could be assigned to the benzotriazole and naphthalimide units due to the gradual decrease in the corresponding component by the introduction of respective moiety. The module thus provided a platform to predict and visualize the role of two units in the excited state dynamics sufficient for the decay analysis relationship among the set of oligomers.

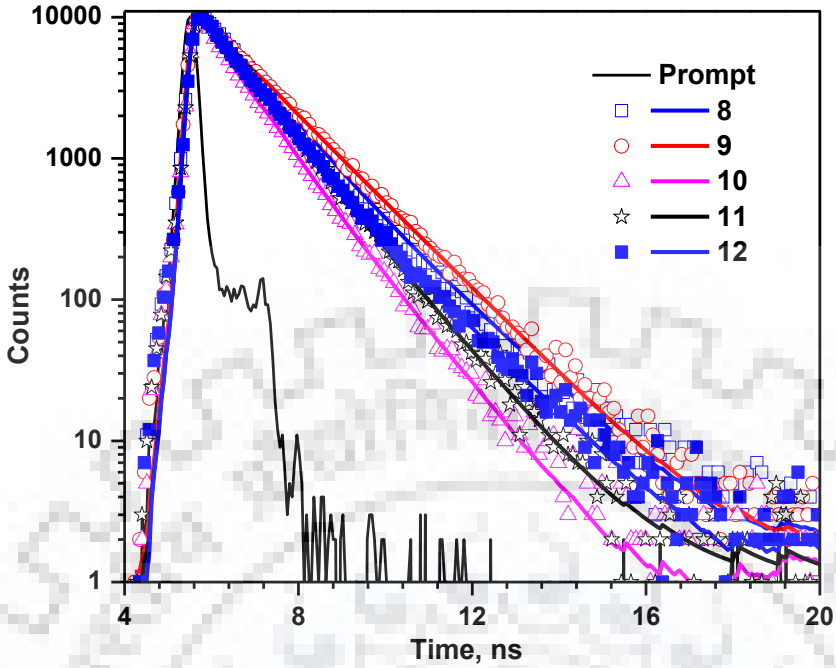

Figure 3.18 Fluorescence decay profiles of dyes in DCM ($2x10^{-6}$ M).

Table 3.9 Time-resolved fluorescence and photophysical data for the dyes in DCM (2×10^{-6}).

Dye	τ_{avg},[a] ns	Φ_F [b]	k_r,[c] ns^{-1}	k_{nr},[d] ns^{-1}
8	1.23	0.59	0.48	0.33
9	1.34	0.71	0.53	0.22
10	0.92	0.86	0.94	0.15
11	0.89	0.88	0.99	0.13
12	1.10	0.95	0.86	0.05

[a] τ_{avg} = Fluorescence lifetime decay measured as $\tau_{avg.} = (A_1 \times \tau_1) + (A_2 \times \tau_2)$ in ns. [b] Fluorescence relative quantum yield calculated using coumarin 6 as reference (0.78 in EtOH). [c] Radiative decay rates (k_r) calculated using $k_r = \Phi_F/\tau$. [d] Non-radiative decay rate (k_{nr}) calculated using $\Phi_F = k_r/(k_r+k_{nr})$.

Table 3.10 Time-resolved fluorescence spectroscopy data for the dyes in DCM

Dye	τ_1, ns	A_1	τ_2, ns	A_2	τ_a, ns	τ_b, ns	τ_{av}, ns	χ^2
8	1.02	0.68	1.68	0.32	0.69	0.54	1.23	1.1
9	0.57	0.10	1.42	0.90	0.06	1.28	1.34	1.1
10	0.58	0.36	1.11	0.64	0.21	0.71	0.92	1.1
11	0.86	0.56	1.29	0.44	0.32	0.57	0.89	1.0
12	0.85	0.62	1.52	0.38	0.53	0.57	1.10	1.1

Where τ_1/ τ_2, Life time of different decay channels from FLS experiment in ns using 405 nm as excitation wavelength; A_1/A_2, Contribution of different decay channels in solution; fitted by double exponential; χ^2, correlation of exponential fit; $\tau_{avg.}$ = Fluorescence lifetime decay measured as $\tau_{avg.} = (A_1 \times \tau_1) + (A_2 \times \tau_2)$

3.2.5 Electrochemical Properties

3.2.5.1 Effect of electron withdrawing groups

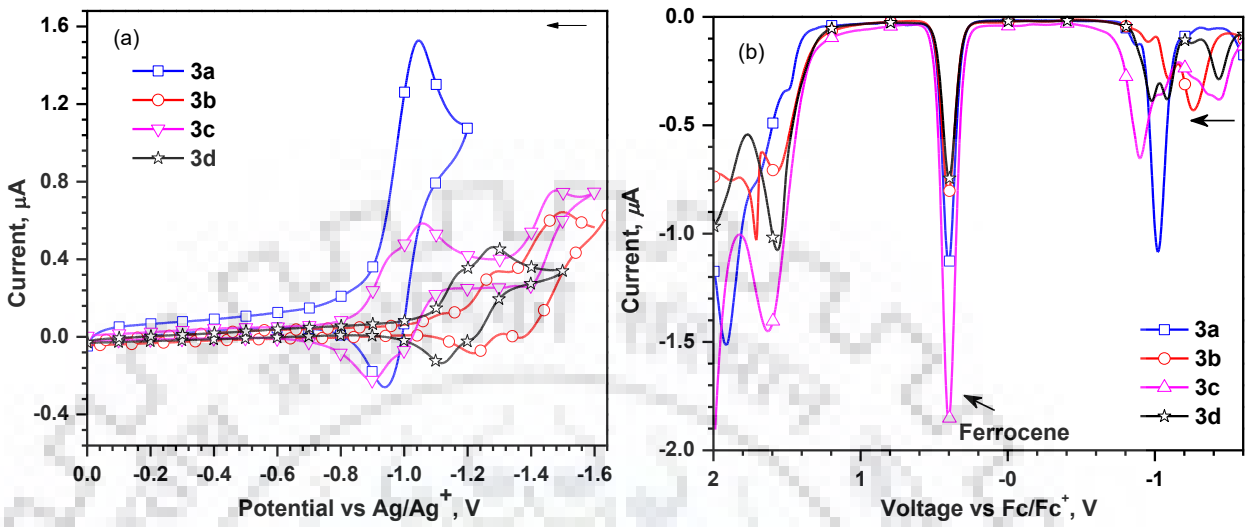

Figure 3.19 (a) CV showing reduction region (b) DPV of the dyes, **3a-3d**.

The electrochemical analysis of the dyes was carried out using CV and DPV measurements and the results are summarized in Table 3.1. All the compounds exhibited a reversible redox couple attributed to the reduction of naphthalimide unit (Figure 3.19(a)).[67] Compound **3a** exhibited a single two-electron reduction while the other dyes showed two or more reduction couples. It clearly indicates the reduction propensity of the molecules is enhanced on introduction of additional acceptor in the conjugation pathway. However, it is interesting that only the benzothiadiazole derivative **3c** possessed reduction potential larger that the dimer **3a**. It clearly points that extension of conjugation by incorporation of fluorenone and dibenzo[*a*,*c*]phenazine increases slightly the electron richness due to the presence of π-electrons. Benzothiadiazole derivative, **3c** displayed a third reduction couple attributable to the reduction of benzothiadiazole moiety. The LUMO energy values deduced from the reduction potentials are close to -3.3 eV which lies among those of typical air stable *n*-type organic semiconductors.[16] High electron affinity across the π-conjugated backbone afforded by the two naphthalimide and an electron deficient central unit help to deepen HOMO energy level and lies in the range of -5.9 eV to -6.3 eV. All the dyes exhibited an irreversible oxidation peak. It is worth to mention that the electronic structure of the naphthalimide core is finely tuned by the introduction of electron withdrawing moieties and the energy levels of all dyes are favorable to act as *n*-type semiconducting materials in OLEDs, OSCs and OTFTs.

3.2.5.2 Effect of number of benzotriazole units in oligomers

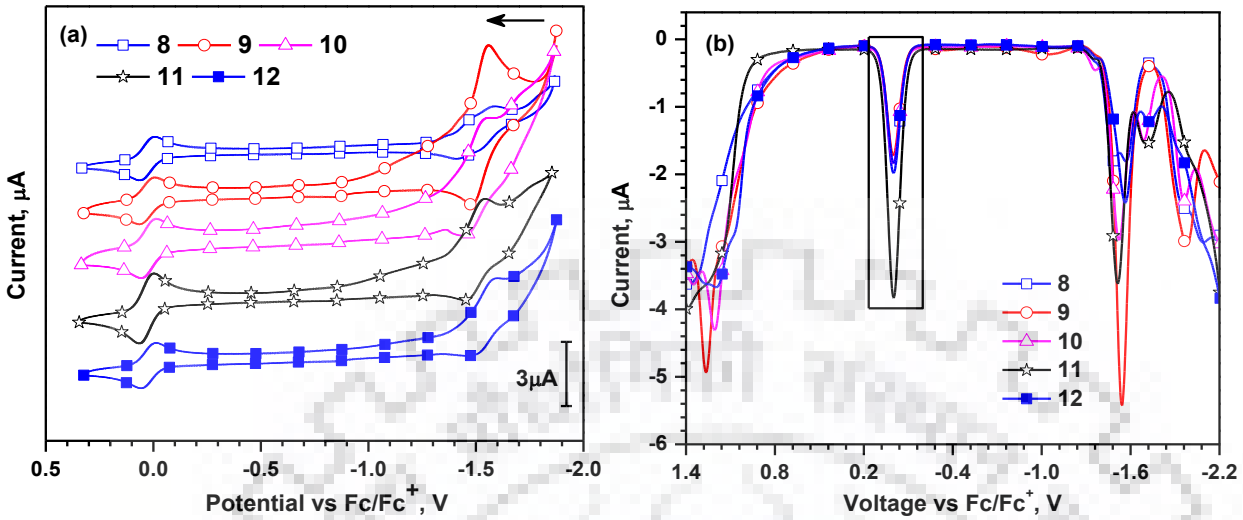

Figure 3.20 (a) CV and (b) DPV of the dyes recorded in DCM.

The electrochemical properties of the dyes **8-12** were also studied by CV and DPV in order to estimate their orbital energy levels (Figure 3.20). The energy level calculations carried out using electrochemical analysis of the dyes are summarized in Table 3.3. The electrochemical behavior of the compounds exhibit a reversible redox couple attributed to the reduction of naphthalimide unit resulting from the addition of electron across the highly electron deficient moieties. The reduction potentials of the first wave shifts towards cathodic regime on successive addition of benzotriazole illustrating that introduction of benzotriazole unit alter the electronic configuration and thus the electrochemistry of the backbone. From DPV plot, the first reduction peaks corresponds to the naphthalimide moiety which indicates that latter dominates the reductive properties of the molecule. High electron affinity across the π-conjugated backbone afforded by the naphthalimide and benzotriazole unit deepen HOMO energy level lying in the range of -5.8 eV to -6.3 eV and thus maintain high oxidation potentials. While the LUMO energy levels lies in range of -3.2 to -3.3 eV. The analysis depicts that the presence of the multiple acceptors in the oligomer resulted in lowering energy level corresponding to HOMO and LUMO. It is also observed that as the number of chromophore unit increases, the energy band gap of the series of oligomers decreases which is consistent with the observation obtained from the theoretically computed electronic parameters of the oligomers. The reduction potential of **3a** is positively shifted by 70 mV compared to dye **9** which is observed at -1.50 V. This indicated that benzotriazole introduced electronic richness since HOMO and LUMO energy level is lifted by

300 meV and 70 meV respectively compared to -6.31 eV and -3.37 eV observed for **3a**. It is thus concluded that energy levels of the dyes are suitable enough which enable them to behave as *n*-type semiconducting materials.

3.2.6 Theoretical Studies

To understand the electronic features of the compounds, DFT computations were performed on the model structures of the compounds in which long alkyl chains are approximated to methyl. The geometry of the compounds were optimized using B3LYP functional and 6-31G(d, p) basis set (Figure 3.21). The optimized structures were then used for TDDFT computations at (M06-2x/6-31G(d,p)) levels (Table 3.11). The optimized structures assumed coplanar arrangement of functional entities which ensure close packing arrangement of molecules in the solid state. This ensures the effective conjugative communication between the chromophore units.

3.2.6.1 Effect of electron withdrawing groups

The FMOs of the dyes, **3a-3d** is displayed in Figure 3.22. The HOMO of the molecules is mainly contributed by the π- linker and the naphthalene segment of the naphthalimide while the HOMO-1 orbital is mainly spread over the naphthalimide unit. In compound **3d**, the dibenzo[*a*,*c*]phenazine unit also contributed to the formation of HOMO−1. The LUMO is mainly constructed by the central π-linker with little contribution from the naphthalimide units. Interestingly, the LUMO+1 is restricted to the naphthalimide unit in all the compounds. The observed electronic distributions in the molecules are suggestive of the electron-withdrawing nature of the constituting units. Prominent contribution of the π-linker to the LUMO suggests the electron deficiency of the central bridge over the naphthalimide periphery.

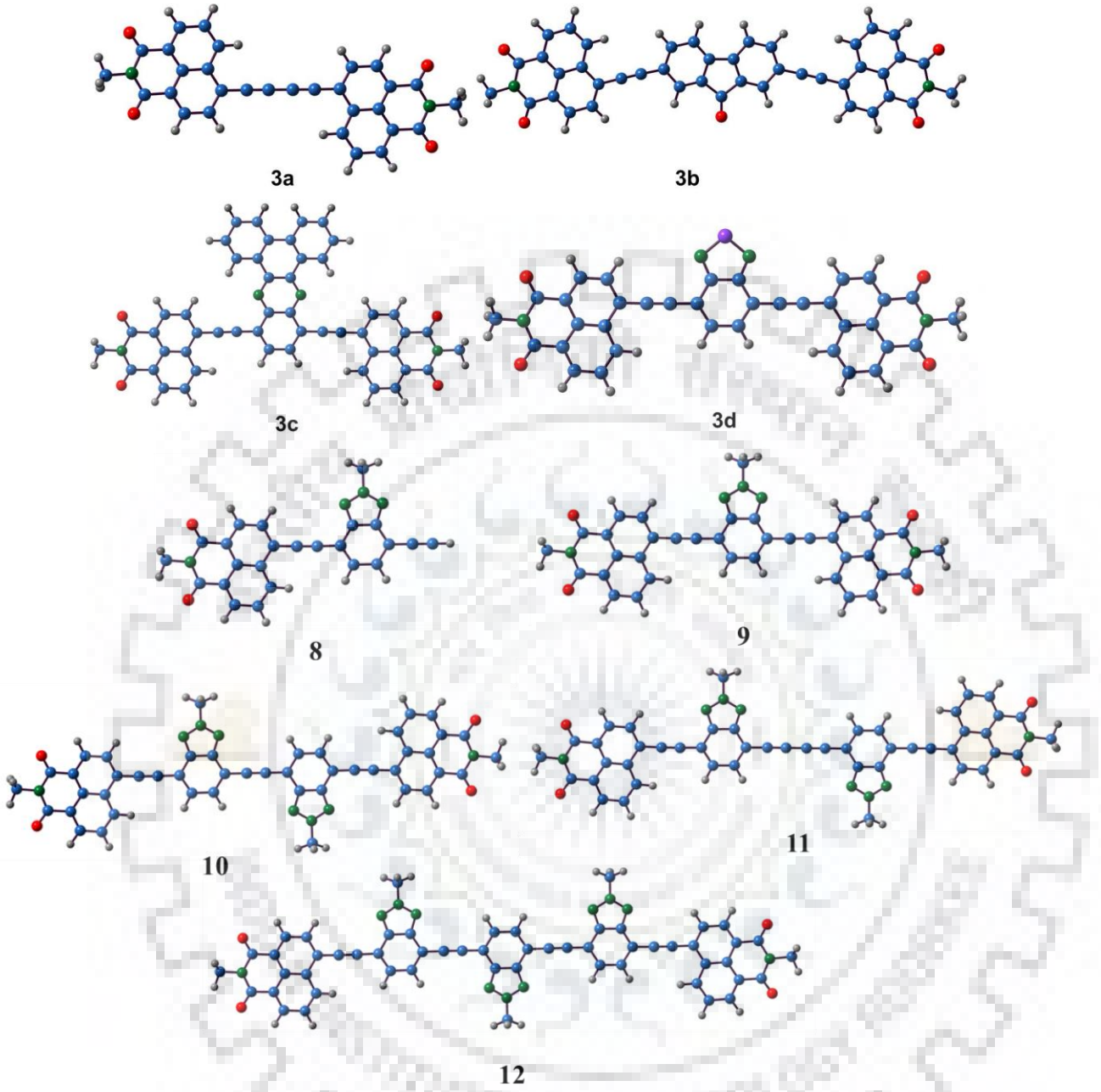

Figure 3.21 Optimized geometries for model dyes by DFT calculations using B3-LYP 6-31G(d, p) functionals.

3.2.6.2 Effect of number of benzotriazole units in oligomers

The computed frontier molecular orbitals HOMO, HOMO–1, LUMO and LUMO+1 of the dyes are shown in Figures 3.23 and 3.24. In the dyes, the HOMO is spread on the π-linker and majorly on benzene segment of the benzotriazole which become more pronounced as we move from **9** to **10** and **12**. This highlights the electronic richness enhancement on introduction of benzotriazole. However, HOMO-1 is contributed by the naphthalimide unit in all dyes and

partially by adjacent benzotriazole units in dye **10** and **12**. The LUMO is mainly constructed by the central π-linkers with little contribution from the naphthalimide units. Thus, the LUMO tends to delocalize over the whole conjugated backbones. This dictates the electron deficiency of the constituting units. Whereas LUMO+1 in all the dyes is constrained to the more electron withdrawing naphthalimide segment. The TDDFT computations at the (M06-2x/6-31G(d,p)) level were used on the optimized structures to determine the computed electronic parameters. Computed vertical transition, their oscillator strengths and their orbital contributions are listed in Table 3.11. The π-π* vertical transition is mainly contributed by the HOMO to LUMO electronic excitations followed by minor contributions from HOMO-1 to LUMO+1. It is worth to mention that the order of theoretically calculated absorption maxima and energy band gap for the dyes is well matched with the absorption trend observed experimentally. Also, the introduction of additional benzotriazole unit renders narrowing the band gap. Furthermore, due to relative electron richness of benzotriazole unit, dye **8** displays high lying LUMO compared to other analogs, **3c-3d.**

Table 3.11 Computed electronic parameters for the compounds by the TDDFT (M06-2x/6-31G(d,p)) method.

Dye	λ_{max}, nm	f	Composition	HOMO, eV	LUMO, eV	E_g, eV
3a	390	1.49	HOMO → LUMO (91%)	-6.13	-3.17	2.96
3b	406	1.70	HOMO → LUMO (79%), HOMO-1 → LUMO+1 (7%)	-5.93	-3.08	2.85
	349	0.95	HOMO → LUMO+2 (63%), HOMO -1 → LUMO+1 (16%)			
3c	446	1.81	HOMO → LUMO (93%)	-5.92	-3.37	2.55
	328	0.29	HOMO → LUMO+2 (77%), HOMO-1 → LUMO+1 (14%)			
3d	436	1.62	HOMO → LUMO (92%)	-5.79	-3.18	2.61
	361	0.38	HOMO-1 → LUMO (52%), HOMO → LUMO+1 (24%), HOMO-3 → LUMO (10%)			
8	392	1.43	HOMO → LUMO (94%)	-5.78	-2.77	3.01
9	422	2.19	HOMO → LUMO (91%), HOMO-1 → LUMO+1 (6%)	-5.77	-3.07	2.70
10	463	3.36	HOMO → LUMO (85%), HOMO-1 → LUMO+1 (8%)	-5.51	-3.03	2.48
11	466	3.75	HOMO → LUMO (83%), HOMO-1 → LUMO+1 (10%)	-5.52	-3.07	2.45
12	482	4.27	HOMO → LUMO (80%), HOMO-1 → LUMO+1 (11%)	-5.34	-2.99	2.35

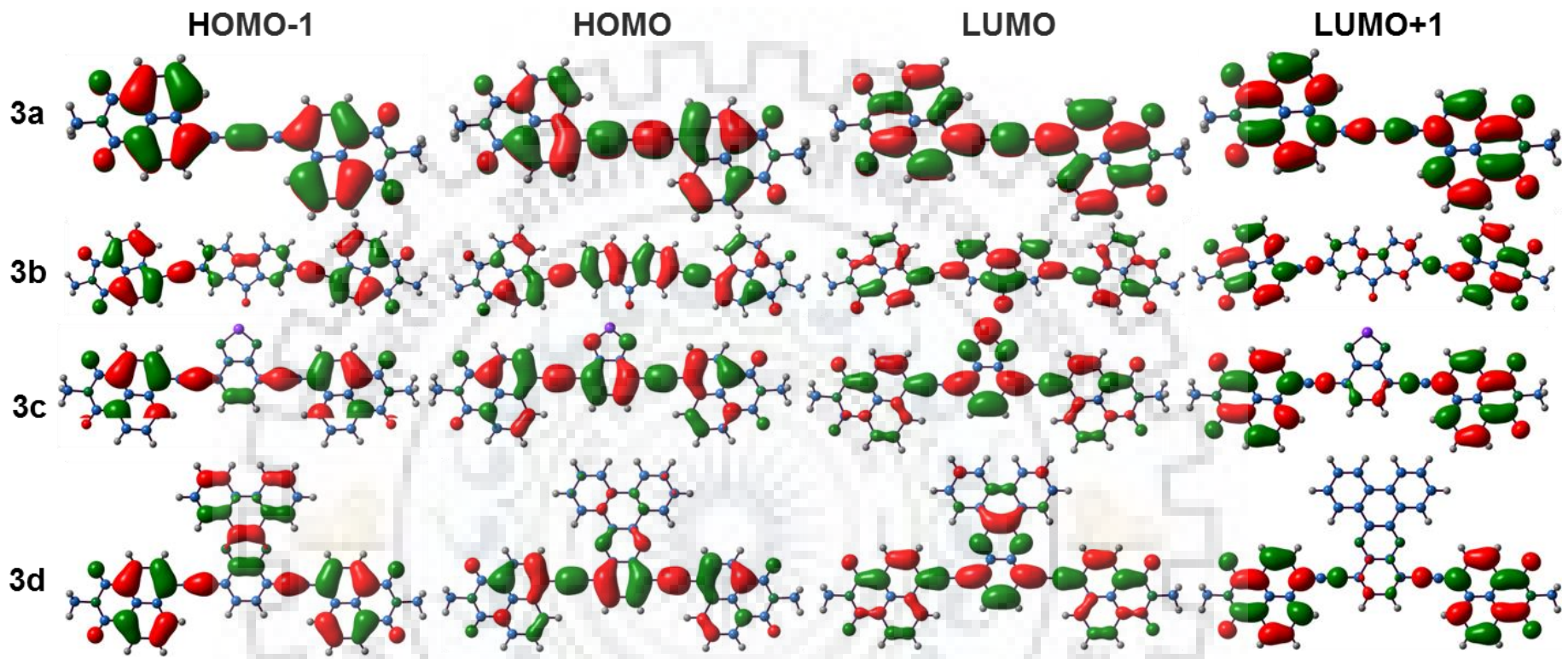

Figure 3.22 Electronic distribution in the frontier molecular orbitals of the model compounds **3a-3d**.

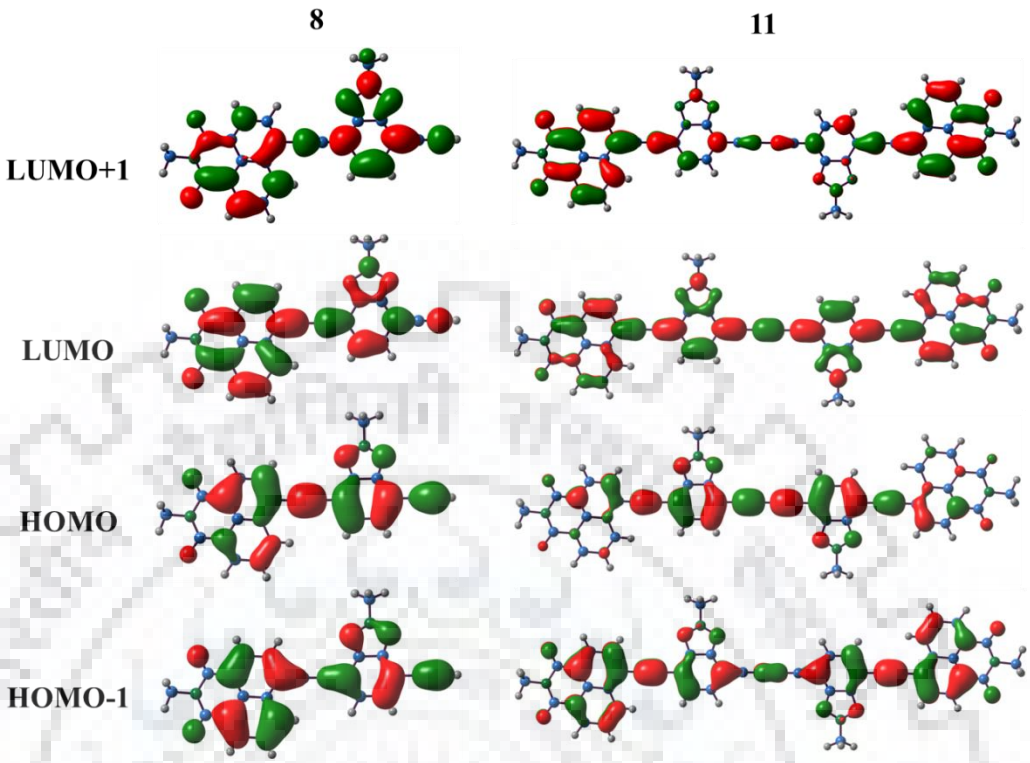

Figure 3.23 Frontier molecular orbitals of the dyes **8** and **11**.

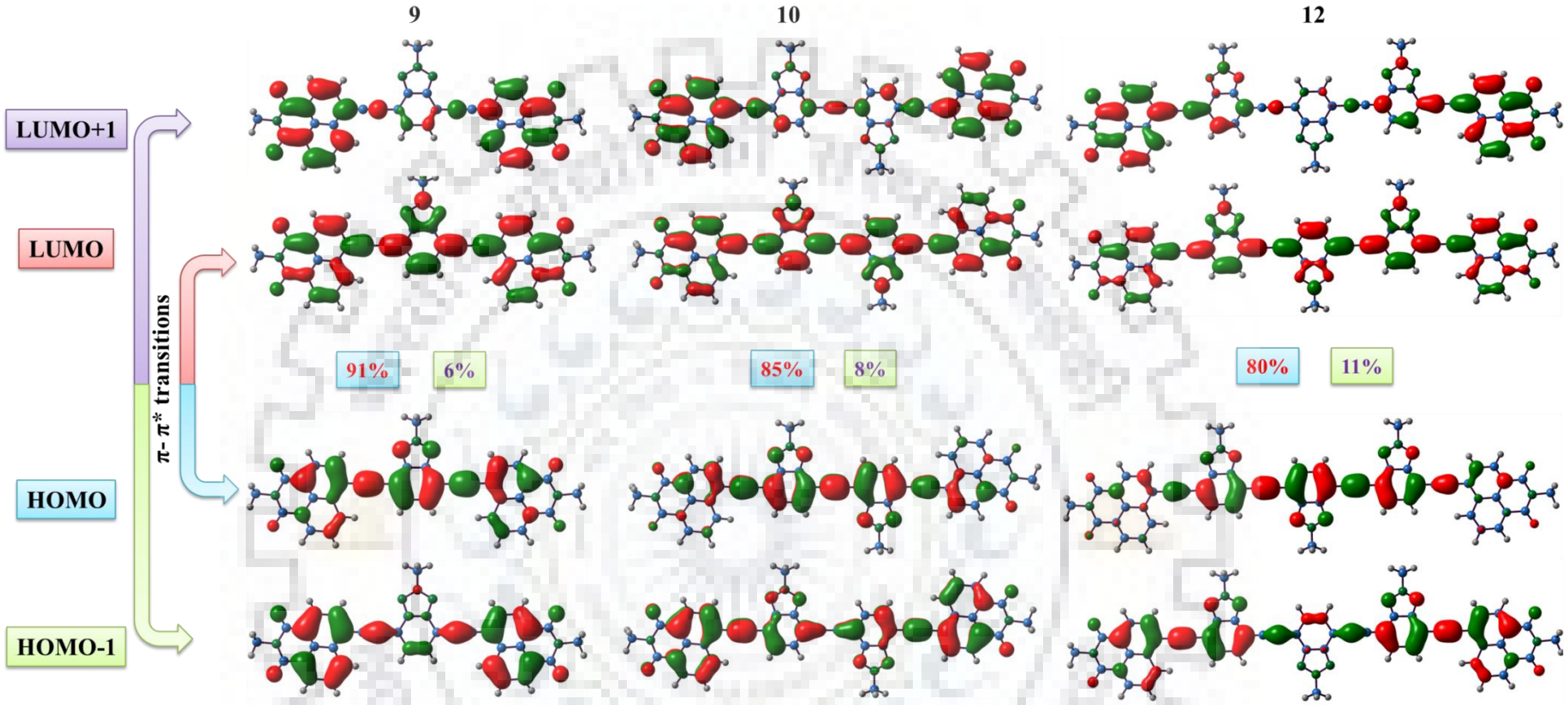

Figure 3.24 Frontier molecular orbitals and major vertical transition of the dyes.

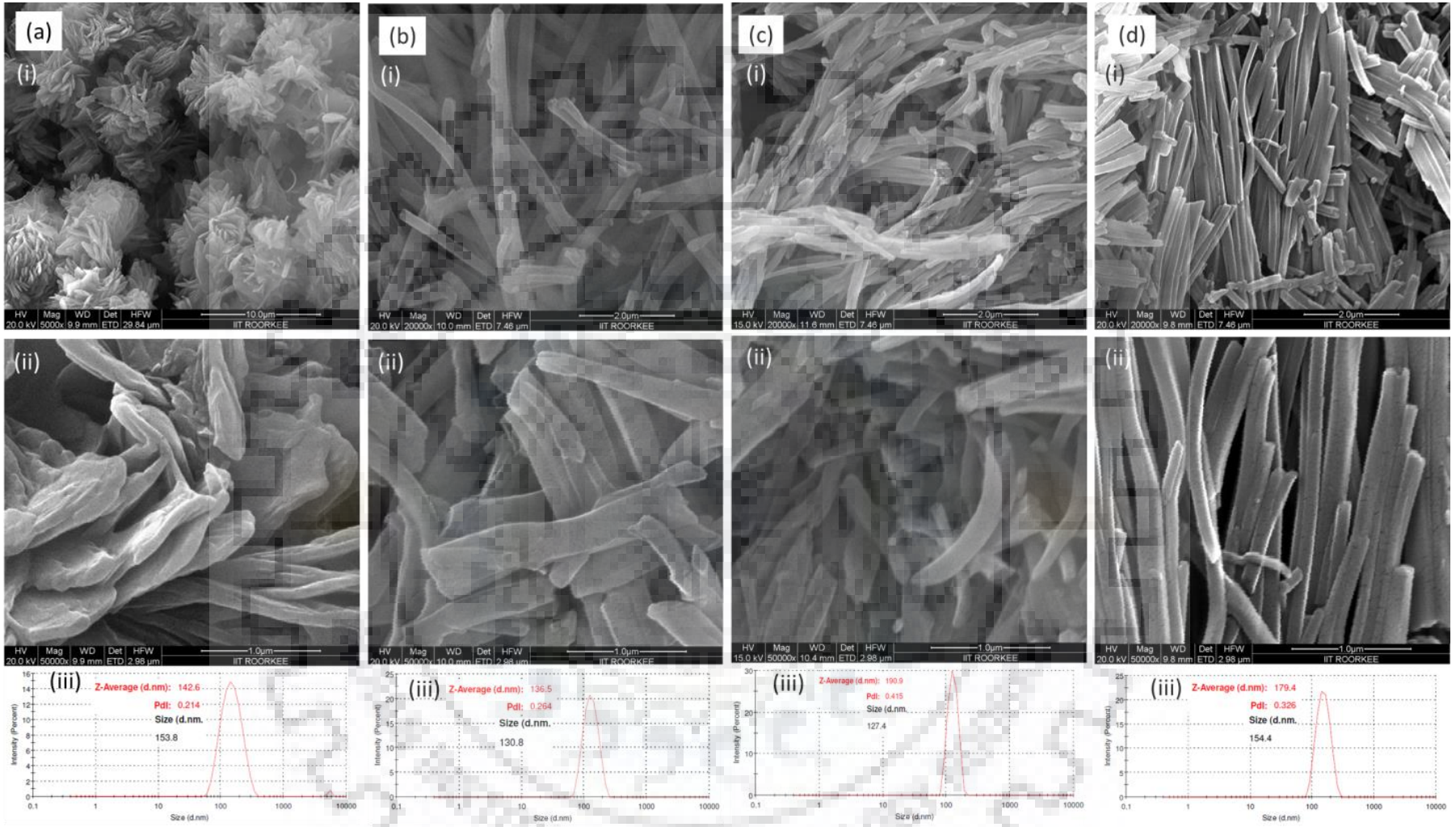

Figure 3.25 FESEM images of as synthesized compounds (a-d) **3a-3d** respectively; scale bar: (a) (i) 10 μm, (ii) 1 μm; (b-c) (i) 2 μm, (ii) 1 μm and (iii) DLS-determined size distribution profiles for the aggregates formed from (a-d) **3a-3d** in THF/H_2O (1:9; 2×10^{-5} M), respectively.

3.2.7 Morphological Properties

The morphologies of the as synthesized small molecules with different electron withdrawing groups and those obtained from solvent system were investigated by FESEM. SEM images of as synthesized samples (Figure 3.25) reveal the presence of an ample amount of rod like nanostructures with diameters and lengths in the range of hundreds of nanometers to several micrometers, respectively. The rods/belts have uniform nano-sized diameter along their lengths. SEM images show that the typical diameter of the nanostructures is about 120±20 nm. The dyes **3b**-**3d** possessing skeleton derived from elongated conjugation exhibits nanorods/belts while **3a** forms microflowers (6±1 μm) composed of a number of nanoflakes as petals in nanodimensions. Thus, the morphological difference between these chromophores is supposed to be attributed to the difference in the conjugation length. Also, it is seen that SEM images of compound **3d** revealed the formation of well-defined nanorods compared to others for as synthesized compound due to the effective intermolecular interactions arising from the more extended planar π-conjugated aromatic system. The mechanism for formation of rods arises from the effective π-π intermolecular head to tail stacking between the molecules. While flower like morphology for **3a** is formed by the arrangement of a number of nanopetals driven by the intermolecular interactions which can be correlated to results obtained from UV-Vis spectroscopy and powder XRD analysis. It is also observed that as the density of sample increases, the number of aggregates increases, as seen at the core center in the SEM images resulting in the formation of heaps of cluster. When the stacking forces between the molecules are too large, then ill-defined super structural assemblies are formed. It is also confirmed by SEM images of compounds shown in Figure 3.26.

In Figure 3.27, the FESEM images of the aggregates **3c** obtained from the binary THF: H_2O mixtures at 50% and 90% H_2O prepared for absorption and emission studies clearly supports the formation of aggregates due to the solvophobicity and π-π intermolecular interactions resulting into a long-range ordering and finally induced the formation of nanostructures. Very long and thin fibrous nano to micro scale structures of several micrometer lengths are obtained for sample at 50% THF: H_2O mixture. While for 90% H_2O mixture bunch of nanosized rigid aggregates are seen, revealing the formation of nanorods.

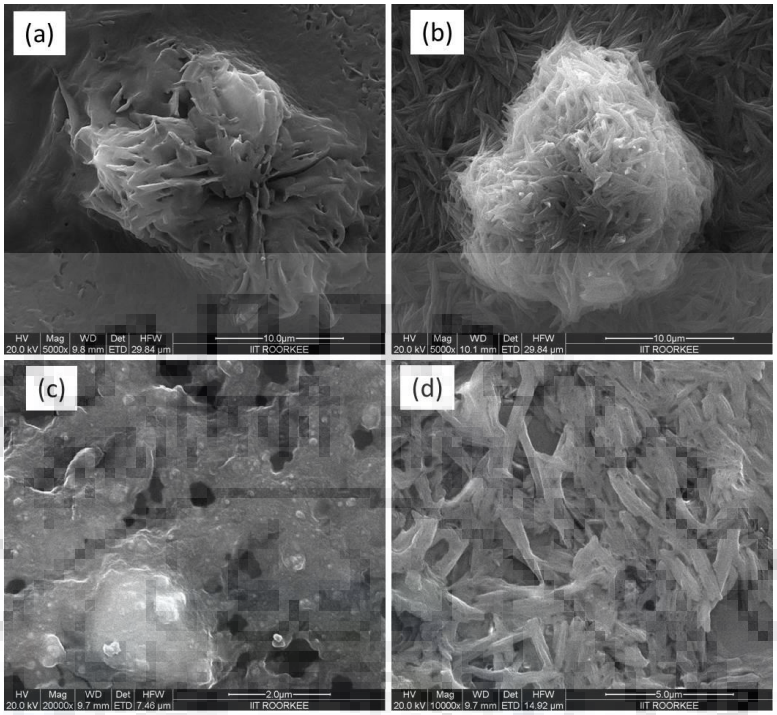

Figure 3.26 FESEM images (a-d) of compounds **3a-3d** respectively showing formation of ill-defined aggregated cluster owing to poor control over concentration and aggregation, scale bar: 10, 10, 2, 4 μm respectively.

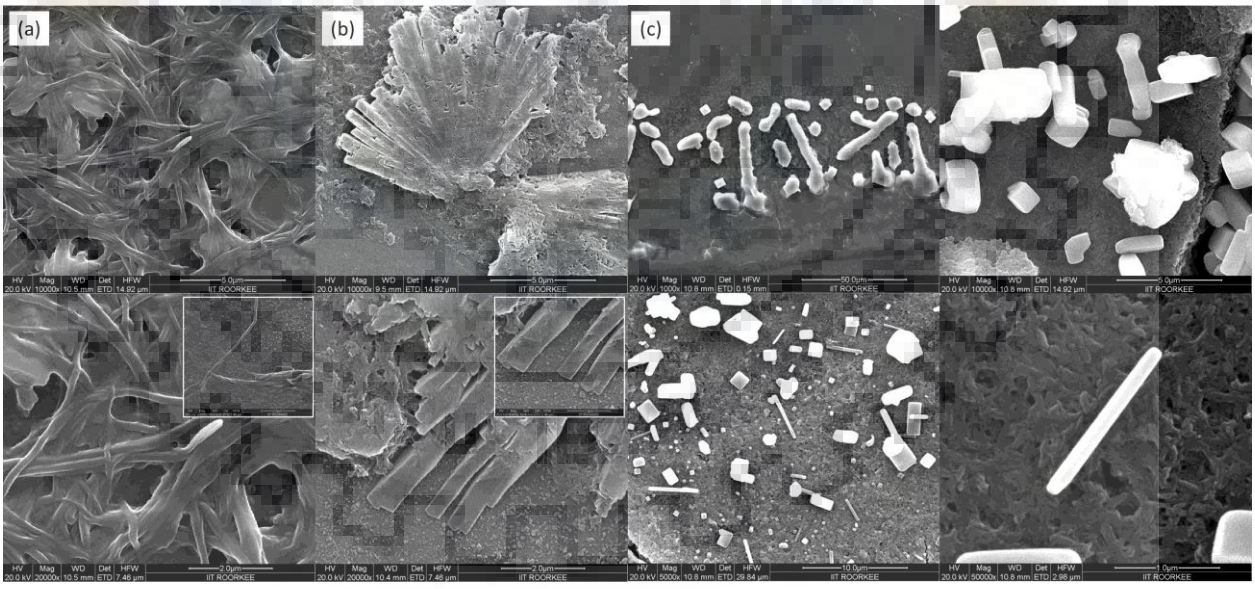

Figure 3.27 FESEM images of **3c** (a) long entangled fibres in 50% THF: H_2O; scale bar: (i) 5 μm, (ii) 2 μm; inset showing a long fibrous strand; scale bar 2 μm (b) formation of nanorods in 90% THF: H_2O; scale bar: (i) 5 μm, (ii) 2 μm; inset showing magnified image of nanorods at scale bar 1 μm (c) (i-iv) formation of crystalline 3-D rods, cubes at different scale bar 50, 10, 5, 1 μm respectively from 90% THF: H_2O after 1 week.

Moreover after 1 week at room temperature the same sample solution gives nano to micro scale crystalline SEM images in form of typical rods and cubes of nano dimension due to the facile crystallization induced by effective intermolecular forces between the aromatic conjugated core and hydrophobicity of alkyl chains. Furthermore, the fine and uniform nanostructures obtained for compound **3d** allow us to investigate the SEM images of the drop-casted precipitates obtained from the DMF solution at low concentration of 1mM which gives spindle shaped thin and long fibers of diameter 120±10 nm and length of approximately 10μm throughout the sample area under investigation. Moreover, the presence of strong intermolecular interactions and formation of thin fibrous network like assemblies motivated us to organogelate the compound.[336, 337] Therefore, supersaturated sample of 1 wt% (16 mM) DMF solution concentration is prepared by heating-cooling method but due to the crystalline nature of compound it reprecipitated out during cooling process. SEM images of the reprecipitated crystalline compound shows uniform sized cubic crystals of approximately $1\times1\mu m^2$ throughout the glass plate which assembles to form large crystals in form of cuboids and rods driven by minimization of surface area as shown in Figure 3.28(a, b). We tried to grow crystal of the dyes in number of solvent systems for single crystal X-ray diffraction studies but were unsuccessful to obtain which could diffract and ended with fibers or mosaic. On the other hand for **3a** (Figure 3.28(c, d)) exhibits clusters of nanoflakes as heaps in 1mM DMF while it precipitates out as supramolecular sheets and flowers from 1wt% DMF solution system. These morphological changes are supposed to be due to the concentration dependence in self-aggregation.

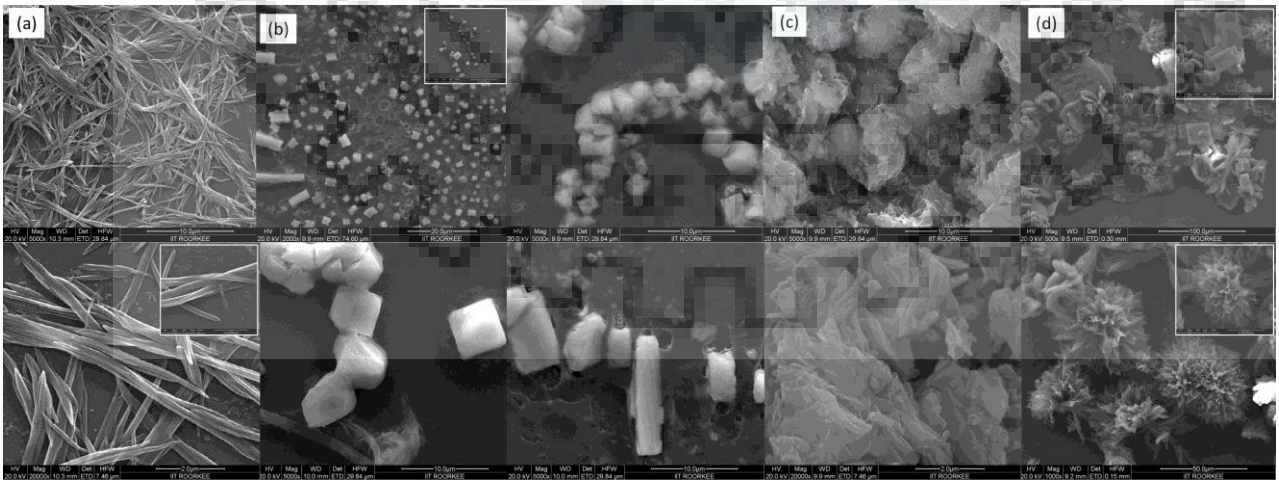

Figure 3.28 FESEM images of (a) **3d** from 1mM DMF showing spindle shaped nanofibers; scale bar (i) 10 μm, (ii) 2 μm, inset 1 μm (b) (i-iv) **3d** crystalline 3-D structures from 1 wt% DMF (c) **3a** from 1mM DMF; scale bar (i) 10 μm, (ii) 2 μm (d) Precipitates of

3a from 1 wt% DMF as sheets and flowers; scale bar (i) 100 μm, inset 50 μm, (ii) 50 μm, inset 20 μm.

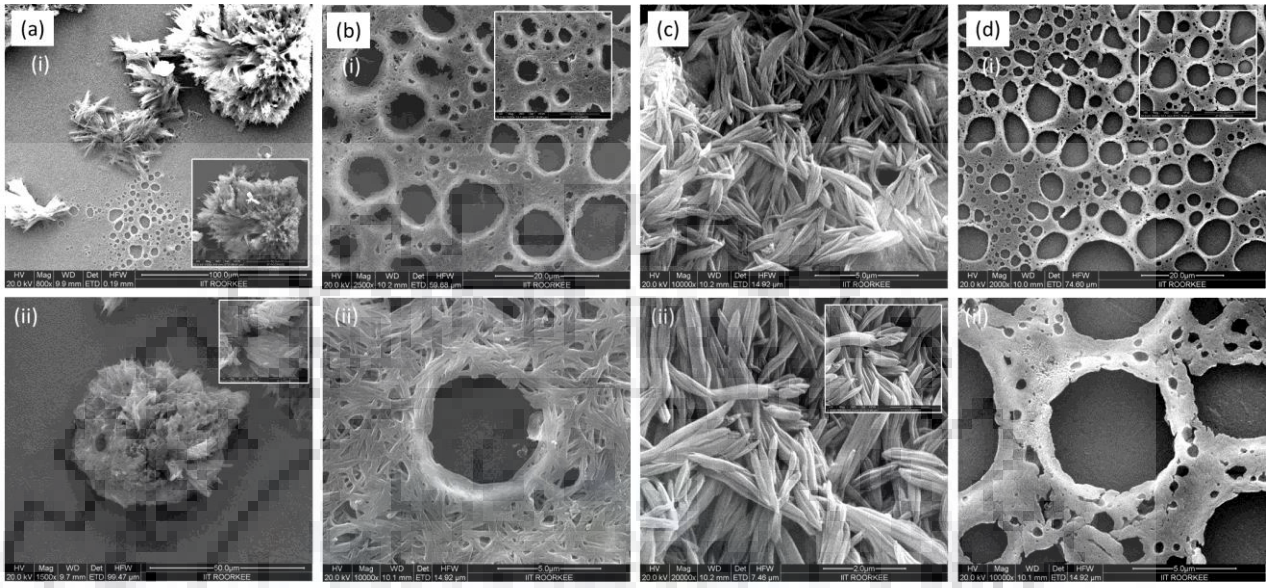

Figure 3.29 FESEM images of drop-casted samples from 1mM DCM solution (a) **3a** scale bar (i) 100 μm; inset 50 μm, (ii) 50 μm; inset 1 μm (b) **3b** showing sieves (i) 20 μm; inset 10 μm, (ii) 5 μm (c) **3c** scale bar (i) 5 μm, (ii) 2 μm; inset 1 μm, (d) **3d** showing sieves (i) 20 μm; inset 10μm, (ii) 5 μm.

To understand more about the effect of addition of highly volatile solvent and concentration on the morphology of the self-assembly, samples are drop-casted from 1mM DCM solution on glass slides. We observed porous vesicular morphology for the obtained film for **3b**, **3d** after slow evaporation of solvent at room temperature as shown in Figure 3.29. The size of the pores so formed by the self-assembling is around 5 μm. However, **3c** and **3a** show different morphological shapes due to highly agglomerated assemblies. The mechanism of formation of sieves (Figure 3.30) is ascribed to the process of volatilization of the solvent which resulted in rupturing of the shell-like structure around the surface of the solvent. This resulted in the movement of the molecules resulting in re-aggregation. The molecules aggregated in the gap between adjacent vesicles arising from the solvent evaporation to form the honey comb like molecular sieve pattern. It has been noted that in multilayer formation, the micro pores were overlapped and allowed to form a cross bedded pattern. The sieve pattern could be obtained only if the vesicles were closely packed and arranged in an orderly manner. It has been seen that in the more diluted samples or at the edge of the film, a number of scattered and broken vesicles can be detected as number of

molecules are very less to fill into the generated gaps. Whereas on the contrary, at peripheral part of the sample slide due to the more concentration a number of collapsed and crowded vesicles can be seen owing to random collisions which is unfavourable for formation of regular porous morphology. Thus it can be stated that the facile tunable morphology at nanoscale of the planar and rigid end-capped naphthalimide based organic *n*-type semiconductors is of great importance for a large number of efficient device applications.

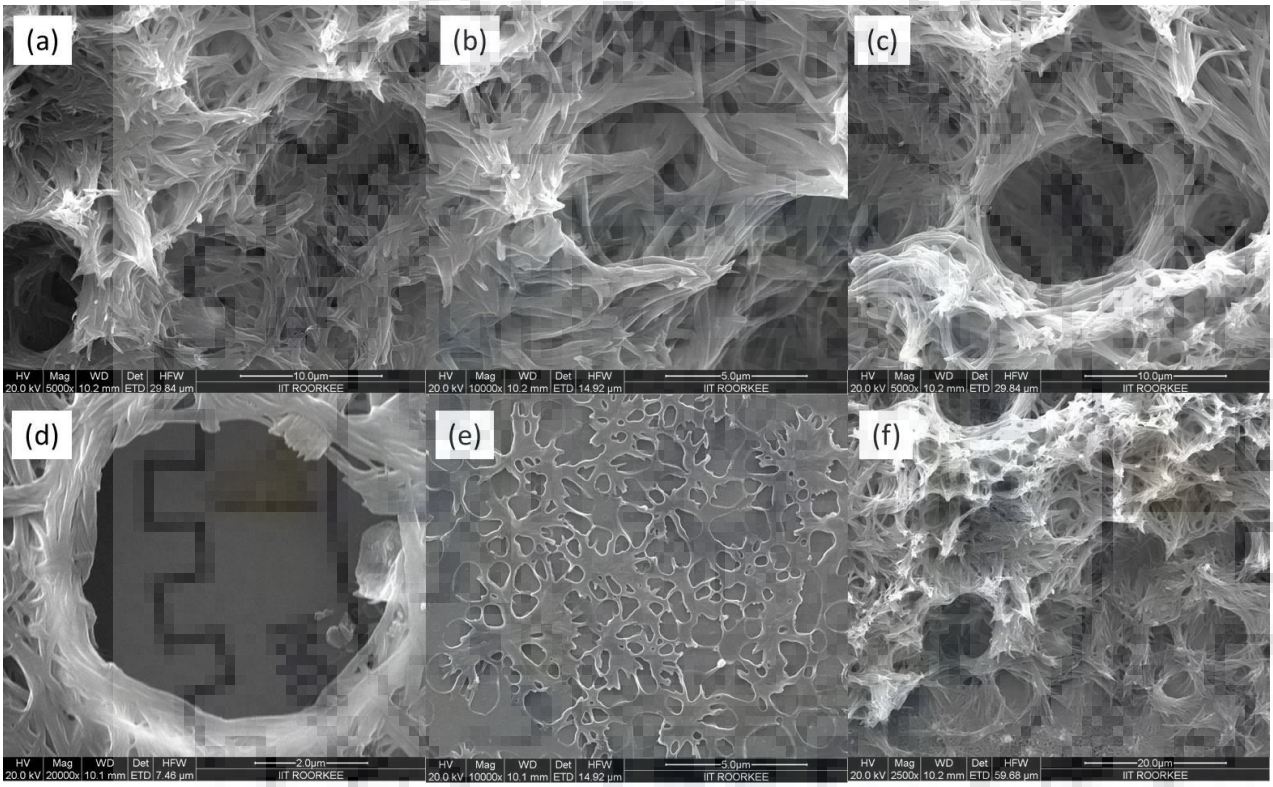

Figure 3.30 FESEM images of dropcasted **3b** from 1mM DCM solution showing (a) mechanism for formation of sieves, scale bar 10 μm (b) self-rearrangement of nanofibres to form micropores, scale bar 5 μm (c) cross bedded pattern due to multilayer formation, scale bar 10 μm (d) ordered arrangement of nanofibers to form a micropore of diameter ~5 μm, scale bar 2 μm (e) scattered and broken vesicles due to less concentration at edges, scale bar 5 μm (f) collapsed and crowded vesicles due to more concentration at periphery, scale bar 20 μm.

3.2.8 Dynamic Light Scattering Analysis

DLS determined particle size distribution of aggregates of the dyes in THF:H_2O mixtures (2×10^{-5}M) with water fractions (f_w) of 90% indicates the homogenous dispersion (Figure 3.25(iii)). The median diameter (d_m) and average diameter (d_{avg}) for the aggregates is found to be in range of ~125-155 nm and >200 nm respectively (Table 3.12) which is in good agreement with SEM data. The particle size distribution peak for **3b-3d** is narrower than **3a,** suggesting the well-ordered particle distribution.[338] Bimodal distributions is observed for **3a** while others exhibited unimodal distributions. An additional less intense peak observed for **3a** dispersion centered at ~6 μm is attributed to diameter of the flower like morphology as seen in FESEM images also.

Table 3.12 Data of DLS-determined size distribution by intensity for the aggregates formed from dyes in THF: H_2O (90%, 2×10^{-5} M).

Dye	d_{avg}, nm	d_m, nm
3a	142.6	153.8
3b	151.4	130.8
3c	190.9	127.4
3d	179.4	154.4

3.2.9 Fluorescence Microscopy Analysis

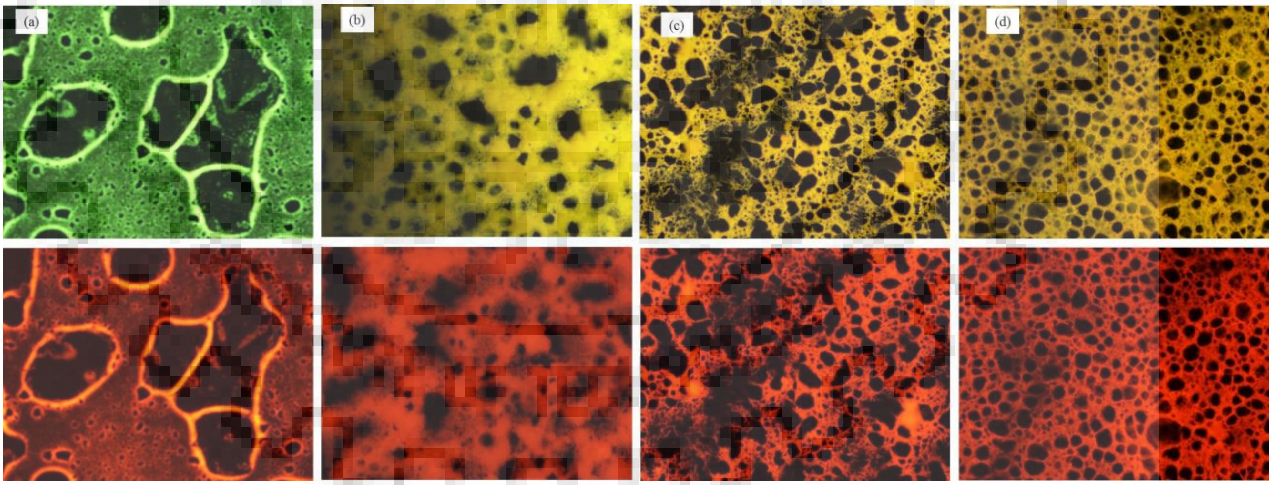

Figure 3.31 Fluorescence microscopy images of the dyes **(**a-d**) 3a-3d** respectively obtained from DCM solution (1mM), above row under excitation by blue light (450-490 nm), below row under green light (510-550 nm).

Furthermore, the fluorescence images of the dyes (Figure 3.31) were investigated using optical fluorescence microscopy exhibiting multicolor emission[339] under different light source due to the broad emission region. The drop-casted film obtained from

dichloromethane solution (1mM) shows bright yellow-green and orange-red fluorescence upon excitation with blue and green light, respectively. Hence the multicolor emission properties of these small molecules are useful for the design and fabrication of displays and flat screens.

3.2.10 Powder X-ray Diffraction Analysis

To investigate the molecular arrangement in the solid state, PXRD is measured and depicted in Figure 3.32(a). The calculated d-spacing values are summarized in Table 3.13. The correlation of d-spacing and 2θ is represented in Figure 3.32(b). The pattern so obtained clearly shows intensive and sharp peaks within the range of 2θ = 5˚ to < 50˚ suggesting a well-ordered crystalline structure. The intermolecular distance calculated from the peak positions is found to be effective for π-π intermolecular interactions. The sharp diffraction peak at 2θ = ~25˚ corresponding to d-spacing of 3.49 Å, 3.43 Å, 3.55 Å and 3.49 Å for **3a-3d**, respectively could be attributed to the π–π stacking intermolecular distance responsible for the self-assembling. Whereas a sharp diffraction peak at 2θ = ~6˚ with a d-spacing of ~13Å can be attributed to the translational slip stacking of the small molecules into *J*-aggregates as reported in earlier reports.[258] Therefore, we conclude that the pattern obtained reflects an organized assembly and crystallinity of these π-conjugated molecules in the solid state suitable for excellent charge transportation.

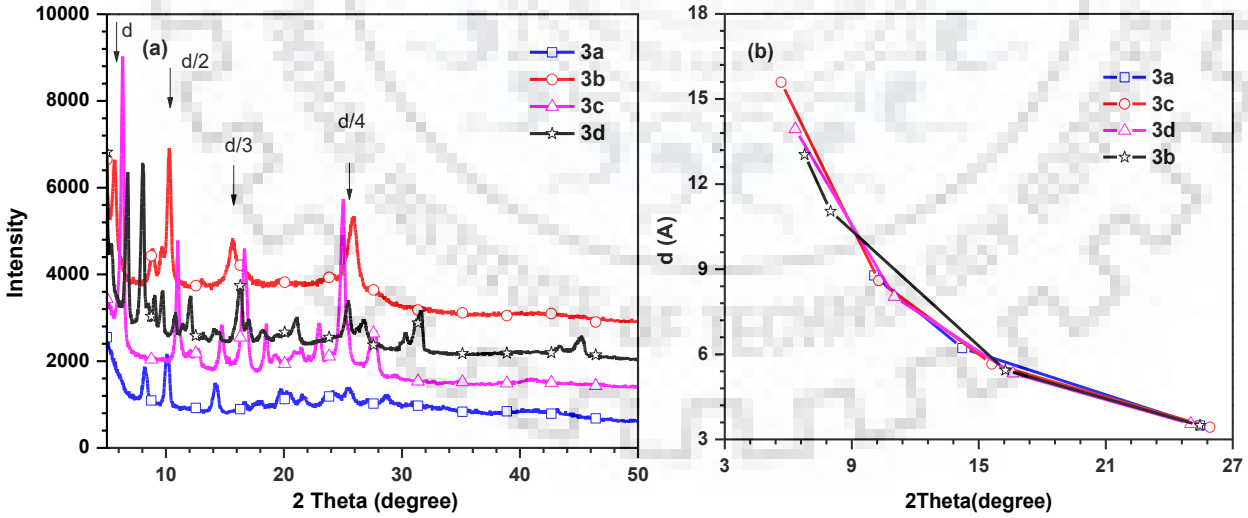

Figure 3.32 (a) PXRD and (b) correlation of d-spacing and 2θ of the small molecules.

Table 3.13 Calculated interplanar distances, d (Å) using Braggs equation (nλ=2dSinθ) from the peaks obtained in powder X-ray diffraction of the small molecules.

Dye	2θ (d, Å), d/4	2θ (d, Å), d/3	2θ (d, Å), d/2	2θ (d, Å), d
3a	25.46 (3.49)	14.22 (6.22)	10.06 (8.78)	-
3b	25.92 (3.43)	15.62 (5.66)	10.27 (8.60)	5.66 (15.59)
3c	25.02 (3.55)	16.61 (5.33)	11.01 (8.03)	6.33 (13.94)
3d	25.47 (3.49)	16.26 (5.44)	8.00 (11.04)	6.77 (13.04)

3.2.11 Thermal Properties

Thermal stability of the organic materials is of paramount importance for the construction of electronic devices to withstand high operational temperature. Thus, the thermal resistance is essential.

3.2.11.1 Effect of electron withdrawing groups

We investigated melting temperature (T_m) and decomposition temperatures (T_d) of the compounds by DSC and TGA. The relevant traces are shown in Figure 3.33 and data summarized in Table 3.14. The endothermic sharp peak in DSC plots represent T_m which increases in order of **3a** < **3c** < **3d** < **3b** pointing to the increasing trend of molecular interactions and presence of some degree of molecular ordering within the molecules. While a broad exothermic peak above 300 ˚C corresponds to the weight loss of compound because of deimidization process. Furthermore, crystalline behavior of compounds is proven by absence of glass transition temperature (T_g). The excellent thermal stability is confirmed by a two-step decomposition pathway with T_d at 10% weight loss above 400 ˚C. The weight loss in the first step between 400-550 ˚C may be due to the degradation of the alkyl chains and other labile units while the second step between 500-700 ˚C corresponds to the loss of aromatic residue and other stronger bonds. Thus both the thermal analysis clearly reflects the crystalline behavior and high thermal stability of the non-covalent interactions based self- assemble small molecules.

Table 3.14 Thermal analysis data of the naphthalimide-based small molecules.

Dye	T_{onset}, ˚C[a]	T_d, ˚C	T_m, ˚C
3a	426	484, 582	199
3b	446	476, 643	296
3c	431	482, 669	272
3d	456	475, 620	286

[a]Decomposition temperature corresponding to 10% weight loss

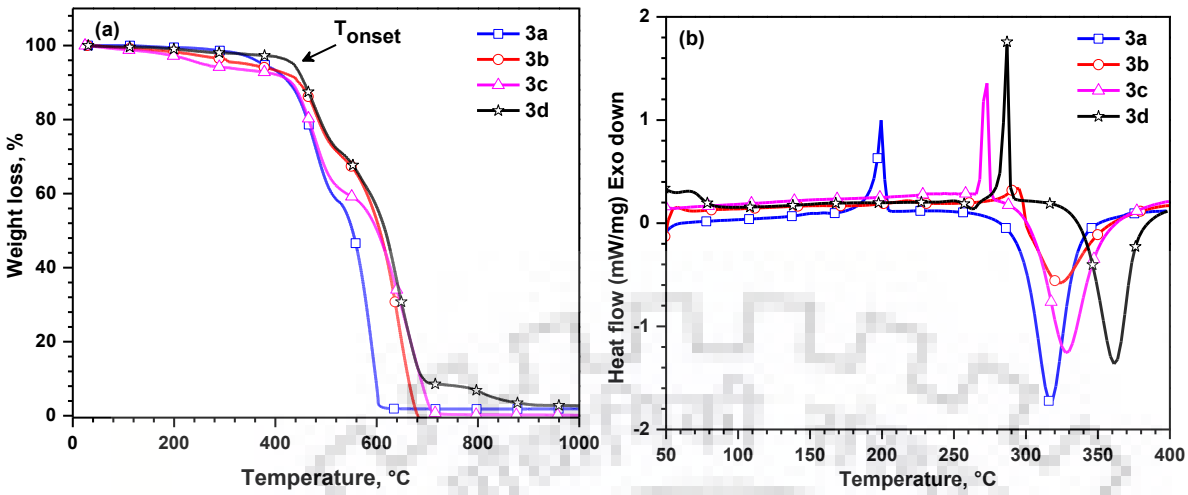

Figure 3.33 (a) TGA and (b) DSC curves of the small molecules.

3.2.11.2 Effect of number of benzotriazole units in oligomers

The thermal properties of oligomers were evaluated by TGA as shown in Figure 3.34. The oligomers exhibit high thermal stability upto 400℃ at a weight loss of 10%. The dyes display a two-step decomposition pathway similar as previous set of dyes where in the first step the weight loss between 400-500℃ may be due to the defragmentation of the alkyl chains. Whereas, the second step between 550-700℃ results from the degradation of aromatic residue and other labile bonds as observed for dyes **3a-3d**. However, with the increase in the benzotriazole unit from one to three in **9** and **12** respectively, decreased the T_d due to the labile alkyl groups in later. Yet, the thermal analysis indicates the sufficient thermal stability of the dyes for organic electronic applications.

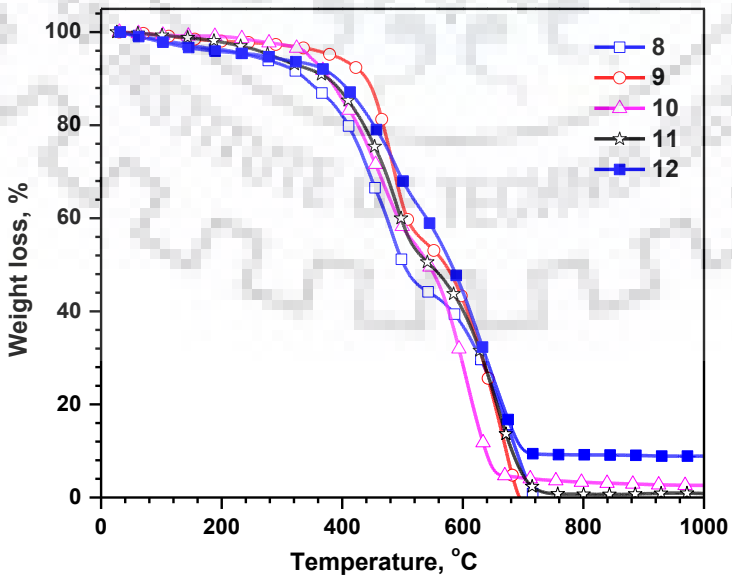

Figure 3.34 TGA curves of the dyes.

3.3 Conclusions

In this Chapter, we shed light on the optical, electrochemical, theoretical and thermal properties of the linear and rigid electron deficient π-conjugated bis-naphthalimide derivatives synthesized by Sonogashira coupling reaction. The structure property relationship of a series of rod-like planar small molecules and oligomers with different electron withdrawing groups and variable number of benzotriazole units were demonstrated in order to access their optical properties, excited state characteristics and energy levels. The dyes displayed successive red-shift of absorption band and extinction coefficient attributed to the increase in π-conjugation length and enhanced electronic transitions. The strong structured emission band and small Stokes shifts observed for all dyes is reflection of their rigid and planar structure. Solvent polarity has a negligible influence on the optical properties of dyes. However, these molecular scaffold exhibits high fluorescent quantum yields and thus offers a chance to be used as emitters in OLEDs. The lifetime studies were performed to unravel the excited state dynamics of the molecules. The solution, thin film and solid state optical properties of the small molecules support the presence of intermolecular interactions and π–π stacking which is supposed to enhance charge transport properties. This is further supported by XRD analysis of the as synthesized samples. The morphology patterns observed in the FESEM images for these organic molecules confirm π–π stacking interactions and establish well-defined formation of nanostructures with rod shaped or flower like morphology in solid state. It is also found that the morphology varies with concentration and solvent. DLS analysis further strengthens the formation of nanomorphology for the aggregates. Furthermore, the thermal and electrochemical data indicate high thermal stability, crystallinity and suitable energetics which support high electron deficiency of the molecules and deep HOMO energy levels suitable to be used as electron accepting semiconductors. Further, electrochemical analysis reveal that these dyes acquire suitable LUMO levels in range of -3.2 to - 3.3 eV to be used as non-fullerene electron acceptors in OSCs. From the studies of oligomers, it is found that with increasing number of benzotriazole unit in the oligomer LUMO is stabilized and HOMO is destabilized, thus leading to narrow band gap. DFT investigations highlighted the electronic properties and ensure the coplanar geometries of the compounds. The dyes possess excellent thermal stability. Hence exploring such a design of molecules as potential luminescent organic materials can contribute to ever growing understanding of the use of small molecules and oligomers in optoelectronics where both the aromatic system and solubilizing alkyl chains plays a pivotal role. As an outlook,

judicious and efficient tuning the property of such class of functional materials could be beneficial for *n*-type organic semiconducting materials to study electronic transport properties in a number of solution processed nano-optoelectronic devices

3.4 Experimental Section

3.4.1 General Methods and Instrumentation

All commercial chemicals were used as received. Column chromatography was performed by using silica gel (100−200 mesh) as stationary phase. All solvents used in synthesis and spectroscopic measurements were distilled over appropriate drying and/or degassing reagents. ^{1}H and ^{13}C NMR spectra were recorded on a FT-NMR spectrometer operating at Bruker 500, 125 MHz and JEOL 400, 100 MHz, respectively, in $CDCl_3$. Me_4Si (0.00 ppm) or residual signals for $CHCl_3$ (^{1}H NMR, δ = 7.26 ppm; ^{13}C NMR, δ = 77.23/ 77.00 ppm) served as internal standard. IR spectra were measured on a FT-IR spectrometer. High resolution mass spectra were measured in an electron spray ionization (ESI) mode using a Bruker TOF-Q ESI mass spectrometer operating in positive ion mode. UV/Vis spectra were recorded at RT in quartz cuvettes on a Cary UV-100 spectrophotometer. Fluorescence measurements by using freshly prepared dilute solutions were performed on a RF-5301-PC Shimadzu spectrofluorophotometer. Drop-cast thin films on quartz plates were prepared from toluene solution and used for the measurement of solid state photoluminescence. Solid state emissions of the powders were recorded on Horiba FluoroMax-4 spectrofluorometer. The fluorescence quantum yields (Φ_F) were determined using the formula $\Phi_s = (\Phi_r \times A_r \times I_s \times \eta_s^2)/ (A_s \times I_r \times \eta_r^2)$ where A is the absorbance at the excitation wavelength, I is the integrated area under the fluorescence curve, and η is the refraction index. Subscripts r and s refer to the reference and to the sample of unknown quantum yield, respectively. For 90% water-THF mixture refraction index (η) 0.34 is calculated using formula $\eta_{water} \times V_{water} + \eta_{THF} \times V_{THF}/ V_{water} + V_{THF}$. Coumarin-6 in ethanol (Φ_F =0.78) were taken as the reference. Absolute solid state fluorescent quantum yield (±3% accuracy) was measured by integrating sphere method using Edinburgh FLS980 fluorescence spectrometer. Fluorescence lifetimes decay measurements were recorded in 1 cm quartz cell on a Horiba Jobin Yvon "FluoroCube Fluorescence Lifetime System" equipped with NanoLEDs and LDs as excitation source(s) and an automated polarization accessory (Model 5000 U-02). CV measurements were performed using BASi Epsilon

electrochemical analyzer. All measurements were carried out at room temperature for the DCM solutions with a conventional three-electrode configuration consisting of a glassy carbon working electrode, a platinum wire counter, and a nonaqueous acetonitrile $Ag/AgNO_3$ reference electrode under nitrogen atmosphere. The potential are quoted against ferrocene internal standard. The solvent in all experiments was dichloromethane DCM and the supporting electrolyte was 0.1 M TBAP at a scan rate of 100 mV/s. TGA were performed under nitrogen atmosphere at heating rate of 10 °C/min using a SII 6300 EXSTAR analyser. The thermal transitions of the dyes were investigated on a DSC using Netzsch DSC 204F1 Phoenix under nitrogen atmosphere at a heating rate of 10 °C/min. Powder X-ray diffraction was performed using a Bruker D8 Advance diffractometer over the 2θ range of 5–90° and the scan rate was 1° min^{-1} as copper target (Cu-K_α; λ = 1.5406 Å). The SEM images of the samples on substrate sputtered by gold were recorded using FE-SEM Quanta 200 FEG instrument. Samples for SEM analysis were investigated as powder form or prepared by a drop-cast method from dye aggregates in various solvent systems on glass substrate operated at 15-20 kV. The DLS particle size distribution by intensity of the aggregates was measured on a Malvern Zetasizer Nano-ZS90. Fluorescence microscopic images were acquired using a Nikon Eclipse LV100 microscope by air drying a drop of the diluted samples on a glass slide under various excitation filters such as B-2A (450-490 nm) and G-2A (510-560 nm) filter excitation. All images were taken at 100X magnification.

3.4.2 Sample preparation for THF: H_2O titration studies

Prepared stock solution of dyes in THF (2×10^{-4} M) and diluted ten times to 2×10^{-5} M. Sample solutions (10 mL) with varying water concentration (distilled water) from 0% to 90% in THF solution with same concentration is prepared for absorption. The same solution system is diluted 10 times with THF and water keeping constant concentration of 2×10^{-6} M for emission.

3.4.3 Sample preparation for optical microscopy morphological studies

The 1 mM sample solution in DCM is drop casted on glass plates and evaporated at room temperature. The fluorescence images are captured from the slides observed under excitation using blue and green light.

3.4.4 Synthesis

3.4.4.1 *N*-(2-ethylhexyl)-4-ethynyl-1,8-naphthalimide (2)

To a round bottomed flask was added 4-bromo-*N*-(2-ethylhexyl)-1,8-naphthalimide (**1**) (13.0 g, 33.5 mmol), PPh_3 (176 mg, 0.2 mmol, 2 mol%), CuI (64 mg, 0.1 mmol, 1 mol%), $Pd(PPh_3)_2Cl_2$ (235 mg, 0.1 mmol, 1 mol%), and purged N_2 for 10 min. Then added trimethylsilylacetylene (4.0 g, 40.2 mmol, 1.2 eq) and passed N_2 for next 5 min and added distilled degassed TEA 160 mL immediately and kept on stirring at r.t. After completion of reaction confirmed by TLC, extracted the TMS intermediate using DCM and washed with brine water, dried over Na_2SO_4 and solvent evaporated to yield brown liquid which is purified by silica column chromatography(eluent: $CHCl_3$:Hexane, 1:1) followed by deprotection in 50 mL distilled methanol was added to the resulting intermediate and 30 mmol each of KF and Bu_4NBr and 10 mL distilled DCM and stirred for 30 minutes at 60 °C. Cooled and added water, extracted with DCM and washed thoroughly with water and dried to obtain viscous liquid which solidified on cooling and adsorbed on silica for chromatography(eluent: $CHCl_3$: Hexanes,1:1). Yellow solid; yield 7.0 g (77%); mp: 82-84 °C. ; IR (KBr, cm^{-1}) 1698 ($\nu_{C=O}$), 2098 ($\nu_{C\equiv C}$), 3218 ($\nu_{C\equiv CH}$); ^1H NMR ($CDCl_3$, 500 MHz) δ 8.66 (d, J = 8.5 Hz, 2H), 8.63 (d, J = 7.0 Hz, 1H), 7.94 (d, J = 7.5 Hz, 1H), 7.83 (t, J = 7.5 Hz, 1H), 4.14-4.07 (m, 2H), 3.73 (s, 1H), 1.96-1.91 (m, 1H), 1.40-1.29 (m, 8H), 0.93 (t, J = 7.5 Hz, 3H), 0.87 (t, J = 7.0 Hz, 3H); ^{13}C NMR ($CDCl_3$, 100 MHz) δ 164.5, 164.3, 132.3, 132.1, 131.94, 131.85, 130.4, 128.1, 127.9, 126.3, 123.1, 123.0, 86.7, 86.5, 44.4, 38.1, 30.9, 28.9, 24.2, 23.3, 14.3, 10.9; HRMS (ESI, *m/z*) $[M]^+$ calcd. for $C_{22}H_{23}NO_2$: 333.1723; found 333.1748.

General procedure for the synthesis of dyes 3b-d and byproduct 3a

In a two neck R.B. flash added aryl dibromide (1mmol), *N*-(2-ethylhexyl)-4-ethynyl-1,8-naphthalimide (**2**) (0.7 g, 2 mmol) and passed N_2 gas for 5 minutes and added $Pd(PPh_3)_2Cl_2$ (14 mg, 0.02 mmol), CuI (4 mg, 0.02 mmol), PPh_3 (11 mg, 0.04 mmol) and purged nitrogen for 10 minutes. Then degassed distilled TEA (20 mL) was added under nitrogen atmosphere. Kept the reaction mixture on reflux for next 5-12 h. Monitored the reaction with TLC and on completion added water and quenched the reaction. Extracted with DCM and washed thoroughly with water. Solvent was evaporated and absorbed on silica for purification.

3.4.4.2 4,4'-(Buta-1,3-diyne-1,4-diyl)bis(*N*-(2-ethylhexyl)-1,8-naphthalimide (3a)

Silica column chromatography, eluent; $CHCl_3$: Hexanes (3:2). Yellow solid; Yield: 0.15 g (23%), mp: 119 ˚C; IR (KBr, cm^{-1}) 1699 ($\nu_{C=O}$); ^1H NMR ($CDCl_3$, 500 MHz) δ 8.70 (d, J = 8.5 Hz, 2H), 8.67 (d, J = 8.5 Hz, 2H), 8.57 (d, J = 7.5 Hz, 2H), 8.05 (d, J = 7.5 Hz, 2H), 7.89 (t, J = 7.5 Hz, 2H), 4.17-4.08 (m, 4H), 1.97-1.92 (m, 2H), 1.41-1.28 (m, 16H), 0.94 (t, J = 7.0 Hz, 6H), 0.88 (t, J = 7.0 Hz, 6H); ^{13}C NMR ($CDCl_3$, 100 MHz) δ 164.3, 164.0, 132.8, 132.5, 132.1, 132.1, 130.3, 128.3, 128.2, 125.3, 123.6, 123.4, 82.2, 81.7, 44.5, 38.1, 30.9, 28.9, 24.2, 23.3, 14.3, 10.8; HRMS (ESI, *m/z*) $[M+H]^+$ calcd. for $C_{44}H_{44}N_2O_4$:665.3373; found 665.3342.

3.4.4.3 4,4'-((9-Oxo-9*H*-fluorene-2,7-diyl)bis(ethyne-2,1-diyl))bis(*N*-(2-ethylhexyl)-1,8-naphthalimide (3b)

Purification by silica column chromatography using $CHCl_3$: Hexanes mixture (7:3) as eluent to yield desired orange solid and yellow solid 0.4 g mono-coupled bromoderivative. Yield: 0.3 g (30%); mp: 296 ˚C; IR (KBr, cm^{-1}) 1699 ($\nu_{C=O}$), 2200 ($\nu_{C\equiv C}$); ^1H NMR ($CDCl_3$, 500 MHz) δ 8.68 (d, J = 8.0 Hz, 2H), 8.65 (d, J = 6.0 Hz, 2H), 8.55 (d, J = 7.5 Hz, 2H), 7.97-7.95 (m, 4H), 7.86 (t, J = 7.5 Hz, 2H), 7.82 (d, J = 8.5 Hz, 2H), 7.62 (d, J = 8.5 Hz, 2H), 4.15-4.07 (m, 4H), 1.96-1.93 (m, 2H), 1.39-1.30 (m, 16H), 0.93 (t, J = 7.5 Hz, 6H), 0.87 (t, J = 7.0 Hz, 6H); ^{13}C NMR ($CDCl_3$, 100 MHz) δ 191.8, 164.4, 164.1, 143.9, 138.4, 134.5, 132.1, 131.9, 131.6, 131.2, 130.4, 128.1, 127.9, 126.7, 123.9, 123.2, 122.6, 121.2, 97.9, 88.7, 44.4, 38.1, 30.9, 28.9, 24.2, 23.3, 14.3, 10.8; HRMS (ESI, *m/z*) $[M]^+$ calcd. for $C_{57}H_{50}N_2O_5$: 842.3714; found 842.3724.

3.4.4.4 4,4'-(Benzo[*c*][1,2,5]thiadiazole-4,7-diylbis(ethyne-2,1-diyl))bis(*N*-(2-ethylhexyl)-1,8-naphthalimide (3c)

Purification by silica column chromatography using $CHCl_3$: Hexanes mixture (1:1) as eluent. Orange solid; Yield: 0.6 g (75%); mp: 272 ˚C; IR (KBr, cm^{-1}) 1704 ($\nu_{C=O}$), 2199 ($\nu_{C\equiv C}$); ^1H NMR ($CDCl_3$, 500 MHz) δ 9.02 (d, J = 8.5 Hz, 2H), 8.84 (d, J = 7.0 Hz, 2H), 8.59 (d, J = 8.5 Hz, 2H), 8.08 (d, J = 8.5 Hz, 2H), 7.97 (d, 2 H), 7.94 (t, J = 7.5 Hz, 2H), 4.17-4.08 (m, 4H), 1.98-1.93 (m, 2H), 1.42-1.29 (m, 16H), 0.94 (t, J = 7.5 Hz, 6H), 0.88 (t, J = 7.0 Hz, 6H); ^{13}C NMR ($CDCl_3$, 100 MHz) δ 164.4, 164.2, 154.6, 132.9, 132.6, 132.0, 131.9, 131.4, 130.5, 128.3, 128.2, 126.5, 123.2, 123.2, 117.4, 95.1, 94.4, 44.4, 38.0, 30.8, 28.8, 24.1, 23.2, 14.2, 10.7; HRMS (ESI, m/z) $[M+H]^+$ calcd. for $C_{50}H_{46}N_4O_4S$: 799.3312; found 799.3298.

3.4.4.5 4,4'-(Dibenzo[*a*,*c*]phenazine-10,13-diylbis(ethyne-2,1-diyl))bis(*N*-(2-ethylhexyl)-1,8-naphthalimide (3d)

Recrystallized with hexanes and $CHCl_3$. Orange solid; Yield: 0.92 g (97%); mp: 286 ˚C; IR (KBr, cm^{-1}) 1698 ($\nu_{C=O}$), 2200 ($\nu_{C\equiv C}$); ^{1}H NMR ($CDCl_3$, 500 MHz) δ 8.88 (d, J = 7.5 Hz, 2H), 8.68 (d, J = 8.0 Hz, 2H), 8.36 (d, J = 6.5 Hz, 2H), 8.27 (d, J = 7.0 Hz, 2H), 8.12 (d, J = 8.0 Hz, 2H), 7.62 (d, J = 7.5 Hz, 2H), 7.59-7.50 (m, 6H), 7.35 (t, J = 7.0 Hz, 2H), 4.11-4.00 (m, 4H), 1.98-1.93 (m, 2H), 1.44-1.35 (m, 16H), 0.98-0.91 (m, 12H); ^{13}C NMR ($CDCl_3$, 100 MHz) δ 163.7, 163.5, 141.7, 140.8, 132.6, 131.9, 131.5, 130.8, 130.4, 130.3, 129.6, 128.8, 127.3, 127.2, 126.9, 126.5, 125.8, 122.9, 122.5, 121.9, 95.9, 94.1, 44.3, 38.1, 30.9, 28.9, 24.1, 23.4, 14.4, 10.7; HRMS (ESI, m/z) $[M+Na]^+$ calcd. for $C_{64}H_{54}N_4O_4$: 942.4139; found 942.4170.

3.4.4.6 2-Butyl-4,7-diethynyl-2*H*-benzo[*d*][1,2,3]triazole (5)

It was synthesized following the same procedure as for **2**, but with 4,7-dibromo-2-butyl-2*H*-benzo[*d*][1,2,3]triazole, **4** and 3 eq. of trimethylsilylacetylene. The residues were purified by column chromatography (eluent: $CHCl_3$: hexanes:: 1:1) on silica gel. Light brown solid; Yield: 0.4 g (30%), mp: 54-56 ˚C; IR (KBr, cm^{-1}) 3289 ($\nu_{C\equiv H}$), 2959, 2928, 2872 ($\nu_{CHstretch}$), 2104 ($\nu_{C\equiv C}$), 1563 ($\nu_{C=C}$), 1414 (ν_{C-N}); ^{1}H NMR ($CDCl_3$, 400 MHz) δ 7.52 (s, 2H), 4.80-4.75 (t, J = 7.2 Hz, 2H,), 3.59 (s, 2H), 2.14-2.10 (m, 2H), 1.42-1.37 (m, 2H), 0.96 (t, J = 7.2 Hz, 3H); ^{13}C-NMR (100 MHz, $CDCl_3$) δ 144.5, 130.5, 113.1, 84.2, 79.1, 56.9, 32.3, 19.8, 13.5; HRMS calcd for $C_{14}H_{13}N_3$ [M] *m/z* 223.1109, found 223.1112.

3.4.4.7 4-((7-Bromo-2-butyl-2*H*-benzo[*d*][1,2,3]triazol-4-yl)ethynyl)-*N*-(2-ethylhexyl)-1,8-naphthalimide (6)

To a flask was added **4** (1.7 g, 5 mmol), **2** (0.67 g, 2 mmol) and added $Pd(PPh_3)_2Cl_2$ (14 mg, 0.02 mmol), CuI (4 mg, 0.02 mmol), PPh_3 (11 mg, 0.04 mmol) under inert atmosphere. Then added degassed distilled TEA (20 mL) to it and kept the reaction mixture on reflux for 5 h. Monitored the reaction with TLC and the reaction was quenched with addition of water. Extracted with DCM and washed thoroughly with water. Solvent was evaporated and absorbed on silica for chromatography (eluent: DCM: hexanes (6:4-7:3). Yellow solid; Yield: 0.6 g (51%), mp: 122-124 ˚C; IR (KBr, cm^{-1}) 2961, 2919, 2860 ($\nu_{CHstretch}$), 2200 ($\nu_{C\equiv C}$), 1697, 1656 ($\nu_{C=O}$), 1563 ($\nu_{C=C}$), 1414 (ν_{C-N}); ^{1}H NMR ($CDCl_3$, 400 MHz) δ 8.96 (d, J = 8.2 Hz, 1H), 8.67 (d, J = 6.9 Hz, 1H), 8.59 (d, J = 7.8 Hz,1H), 8.07 (d, J = 7.8 Hz, 1H), 7.93-7.87 (m, 1H), 7.64 (d, J = 7.8 Hz, 1H), 7.59 (d, J = 7.8 Hz, 1H), 4.89-4.80 (m, 2H), 4.12 (q, J = 7.2 Hz, 2H), 2.20 (t, J = 7.3 Hz, 1H), 1.48 (q, J = 7.5

Hz, 2H), 1.39 (q, *J* = 6.6 Hz, 2H), 1.35-1.24 (m, 8H), 1.02 (t, *J* = 7.3 Hz, 3H), 0.97-0.85 (m, 6H); ^{13}C-NMR ($CDCl_3$,100 MHz) δ 164.3, 164.1, 144.4, 143.7, 134.3, 132.5, 131.7, 131.1, 130.9, 130.3, 128.9, 128.1, 127.6, 126.9, 122.9, 122.5, 112.6, 111.9, 93.9, 92.3, 57.1, 44.2, 37.9, 32.1, 30.7, 28.7, 23.9, 23.1, 19.8, 14.1, 13.5, 10.6; HRMS calcd for $C_{34}H_{33}N_4O_2Br$ [M] *m/z* 584.1781, found 584.1784.

3.4.4.8 4-((2-Butyl-7-((trimethylsilyl)ethynyl)-2*H*-benzo[*d*][1,2,3]triazol-4-yl)ethynyl)-*N*-(2-ethylhexyl)-1,8-naphthalimide (7)

It was synthesized following the same procedure as for TMS derivative of **2**, but with **6** and 2 eq. of trimethylsilylacetylene. The brown liquid obtained was purified by silica column chromatography ($CHCl_3$: hexanes:: 1:1) to yield yellow solid. Yield: 0.22 g (76%), mp: 156-158 ˚C; IR (KBr, cm^{-1}) 2960, 2928, 2869, 2857 ($\nu_{CHstretch}$), 2148 ($\nu_{C\equiv C}$), 1699, 1659 ($\nu_{C=O}$), 1587 ($\nu_{C=C}$), 1409 (ν_{C-N}); ^{1}H NMR ($CDCl_3$, 400 MHz) δ 8.98 (dd, *J* = 8.2, 0.9 Hz, 1H), 8.69 (m, 1H), 8.58 (d, *J* = 7.2 Hz, 1H), 8.05 (d, *J* = 7.8 Hz, 1H), 7.90 (dd, *J* = 8.2, 7.3 Hz, 1H), 7.69-7.54 (m, 2H), 4.85 (t, *J* = 7.3 Hz, 2H), 4.22-4.05 (m, 2H), 2.28-2.13 (m, 1H), 1.95 (q, *J* = 5.5 Hz, 2H), 1.45-1.28 (m, 8H), 1.07-0.99 (m, 2H), 0.91 (td, *J* = 14.7, 7.5 Hz, 9H), 0.34 (s, 9H); ^{13}C-NMR ($CDCl_3$,100 MHz) δ 164.1, 163.8, 144.3, 132.6, 132.3, 131.95, 131.87, 130.9, 130.7, 130.4, 130.1, 128.1, 127.6, 125.1, 123.4, 123.2, 113.1, 112.9, 94.7, 93.0, 81.9, 81.5, 56.9, 44.3, 37.9, 32.1, 32.0, 30.7, 28.7, 24.0, 23.1, 19.9, 14.1, 13.6, 10.6, 1.0; HRMS calcd for $C_{37}H_{42}N_4O_2Si$ [M] *m/z* 602.3071, found 602.3073.

3.4.4.9 4-((2-Butyl-7-ethynyl-2*H* benzo[*d*][1,2,3]triazol-4-yl)ethynyl)-*N*-(2-ethylhexyl)-1,8-naphthalimide (8)

It was synthesized following the same procedure as for **2**, but with **7** (0.24 g, 0.4 mmol). It was purified using short silica column (1:1 hexanes: $CHCl_3$) to yield light orange solid. Yield: 0.16 g (76%), mp: 138-140 ˚C; IR (KBr, cm^{-1}) 3242 ($\nu_{C\equiv Hstretch}$), 2958, 2927, 2860 ($\nu_{C-Hstretch}$), 2197 ($\nu_{C\equiv Cstretch}$), 1699 ($\nu_{C=O\ asym.}$), 1659 ($\nu_{C=O\ sym.}$), 1586 ($\nu_{C=C}$), 1517 (ν_{C-N}). ^{1}H NMR ($CDCl_3$, 400 MHz) δ 8.98 (d, *J* = 8.0 Hz, 1H), 8.72-8.65 (m, 1H), 8.59 (m, 1H), 8.06 (t, *J* = 7.6 Hz, 1H), 7.92-7.86 (m, 1H), 7.68 (d, *J* = 7.2 Hz, 1H), 7.62 (d, *J* = 7.6 Hz, 1H), 4.87-4.84 (m, 2H), 4.19-4.08 (m, 2H), 3.66 (s, 1H), 2.24-2.16 (m, 1H), 1.97-1.94 (m, 2H), 1.52-1.42 (m, 2H), 1.41-1.29 (m, 8H), 1.02 (t, *J* = 7.6 Hz, 3H), 0.94 (t, *J* = 7.2 Hz, 3H), 0.88 (t, *J* = 7.2 Hz, 3H); ^{13}C-NMR ($CDCl_3$, 100 MHz) δ 164.2, 163.9, 144.3, 132.5, 132.4, 131.6, 130.9, 130.6, 130.2, 129.9, 127.9, 127.5, 124.9, 122.9, 122.5, 113.6, 113.5, 94.3, 93.1, 84.7, 81.9, 79.1, 56.9, 44.2, 37.9, 32.1, 30.7, 28.6, 24.0, 23.0, 19.8, 14.0, 13.5, 10.6; HRMS calcd for $C_{34}H_{34}N_4O_2$ [M] *m/z* 530.2676, found 530.2675.

3.4.4.10 4,4'-((2-Butyl-2*H*-benzo[*d*][1,2,3]triazole-4,7-diyl)bis(ethyne-2,1-diyl))bis(*N*-(2-ethylhexyl)-1,8-naphthalimide (9)

It was synthesized following the same procedure as for **6**, but with **6** and **2**. Eluent: $CHCl_3$: Hexane mixture (7:3) as eluent to yield desired yellow solid. Yield: 0.7 g (83%); mp: 178-180 ˚C; IR (KBr, cm^{-1}) 1696.96 ($\nu_{C=O)}$, 2198.51 ($\nu_{C\equiv C}$); ^{1}H NMR ($CDCl_3$, 400 MHz) δ 8.99 (d, J = 8.5 Hz, 2H), 8.67 (d, J = 7.0 Hz, 2H), 8.59 (d, J = 7.5 Hz, 2H), 8.08 (d, J = 7.5 Hz, 2H), 7.89 (t, J = 7.5 Hz, 2H), 7.76 (s, 2H), 4.92 (t, J = 7.0 Hz, 2H), 4.17-4.08 (m, 4H), 2.31-2.2 (m, 2H), 1.98-1.93 (m, 2H), 1.57-1.51 (m, 2H), 1.42-1.31 (m, 16H), 1.077(t, J = 7.5 Hz, 3H), 0.94 (t, J = 7.5 Hz, 6H), 0.88 (t, J = 7.0 Hz, 6H); ^{13}C-NMR ($CDCl_3$,100 MHz) δ 164.52, 164.24, 144.63, 132.75, 132.04, 131.92, 131.84, 130.65, 130.41, 128.27, 127.89, 126.99, 123.18, 122.83, 114.09, 94.69, 93.92, 57.19, 44.45, 38.04, 32.23, 30.92, 28.89, 24.22, 23.29, 20.12, 14.34, 13.84, 10,84; HRMS calcd for $C_{54}H_{55}N_5O_4$ [M+Na] *m/z* 860.4146, found 860.4136.

3.4.4.11 4,4'-((Ethyne-1,2-diylbis(2-butyl-2*H*-benzo[*d*][1,2,3]triazole-7,4-diyl)) bis(ethyne-2,1-diyl))bis(*N*-(2-ethylhexyl)-1,8-naphthalimide (10)

It was synthesized following the same procedure as for **6**, but with **8** and **6**. Eluent: hexanes: EtOAc (9:1) and hexanes: EtOAc (8:2)) to yield desired orange solid. Yield: 35 mg (35%); mp: > 250 ˚C; IR (KBr, cm^{-1}) 2960, 2925, 2855 ($\nu_{C\text{-}Hstretch}$), 2195 ($\nu_{C\equiv Cstretch}$), 1697 ($\nu_{C=Oasym.}$), 1655 ($\nu_{C=Osym.}$), 1583 ($\nu_{C=C}$), 1384 ($\nu_{C\text{-}N}$). ^{1}H-NMR (400 MHz, $CDCl_3$) δ 8.98 (d, J = 8.4 Hz, 2H), 8.68 (d, J = 6.8 Hz, 2H), 8.60 (d, J = 7.8 Hz, 2H), 8.08 (d, J = 7.6 Hz, 2H), 7.90 (t, J = 8.0 Hz, 2H), 7.70 (s, 4H), 4.91-4.86 (4H, m), 4.19-4.08 (4H, m), 2.27-2.19 (4H, m), 1.98-1.94 (2H, m), 1.50 (q, J = 7.5 Hz, 4H), 1.44-1.28 (16H, m), 1.05 (t, J = 7.6 Hz, 6H), 0.94 (t, J = 7.2 Hz, 6H), 0.88 (t, J = 6.8 Hz, 6H); ^{13}C-NMR ($CDCl_3$, 100 MHz) δ 164.2, 164.1, 144.6, 144.4, 132.6, 131.8, 131.6, 131.1, 130.4, 130.0, 128.1, 127.7, 126.8, 123.0, 122.7, 114.2, 113.2, 94.4, 93.9, 81.3, 80.1, 57.0, 44.2, 37.9, 32.1, 30.7, 28.7, 24.0, 23.1, 19.9, 14.1, 13.6, 10.6; HRMS calcd for $C_{66}H_{66}N_8O_4$ [M+Na] *m/z* 1057.5099, found 1057.5095.

3.4.4.12 4,4'-((Buta-1,3-diyne-1,4-diylbis(2-butyl-2*H*-benzo[*d*][1,2,3]triazole-7,4-diyl))bis(ethyne-2,1-diyl))bis(*N*-(2-ethylhexyl)-1,8-naphthalimide (11)

This was obtained as a homo-coupled product from reaction for synthesizing **10**. Eluent: Hexanes:EtOAc (8:2). Orange solid; Yield: 20 mg (20%); mp: > 250 ˚C; IR (KBr, cm^{-1}) 2958, 2925, 2855 ($\nu_{C\text{-}Hstretch}$), 2197 ($\nu_{C\equiv Cstretch}$), 1698 ($\nu_{C=Oasym.}$), 1658 ($\nu_{C=Osym.}$), 1584 ($\nu_{C=C}$), 1384 ($\nu_{C\text{-}N}$). ^{1}H-NMR (400 MHz,$CDCl_3$) δ 8.99 (dd, J = 11.0, 8.7 Hz, 2H,), 8.68 (d, J = 7.3 Hz, 2H), 8.60 (dd, J = 7.8, 1.8 Hz, 2H), 8.08 (dd, J = 7.8, 2.3 Hz, 2H), 7.90 (td, J = 7.7, 2.7 Hz, 2H), 7.80 (d, J = 7.2

Hz, 1H), 7.75 (d, *J* = 8.0 Hz, 1H), 7.69 (s, 2H), 4.89 (q, *J* = 7.5 Hz, 4H), 4.25-4.03 (m, 4H), 2.36-2.14 (m, 4H), 1.96 (t, *J* = 6.2 Hz, 2H), 1.55-1.45 (m, 4H), 1.42-1.27 (m, 12H), 1.05 (m, 6H), 0.94 (t, *J* = 7.3 Hz, 6H), 0.89 (t, *J* = 6.9 Hz, 6H); ^{13}C-NMR ($CDCl_3$, 100 MHz) δ 164.4, 164.1, 144.6, 144.4, 144.3, 144.2, 132.6, 131.7, 131.6, 131.1, 130.9, 130.6, 130.4, 130.3, 130.2, 130.1, 128.1, 121.7, 126.9, 126.8, 122.9, 122.5, 114.3, 114.1, 113.3, 113.1, 94.6, 94.4, 93.9, 93.4, 92.5, 81.2, 80.1, 57.0, 56.9, 44.2, 37.9, 32.11, 32.06, 30.7, 28.7, 23.1, 19.9, 14.1, 13.6, 10.6; HRMS calcd for $C_{68}H_{66}N_8O_4$ [M] *m/z* 1058.5201, found 1058.5220.

3.4.4.13 4,4'-((((2-Butyl-2*H*-benzo[*d*][1,2,3]triazole-4,7-diyl)bis(ethyne-2,1-diyl))bis(2-butyl-2*H*-benzo[*d*][1,2,3]triazole-7,4-diyl))bis(ethyne-2,1-diyl))bis(*N*-(2-ethylhexyl)-1,8-naphthalimide (12)

It was synthesized following the same procedure as for **6**, but with **5** and **8** in 1:2 ratio. Eluent: 7:3 $CHCl_3$: hexanes). Dark orange solid; Yield: 0.1 g (40%), mp: >250 ˚C; IR (KBr, cm^{-1}) 2958, 2922, 2863 ($\nu_{CHstretch}$), 2194 ($\nu_{C\equiv C}$), 1696, 1653 ($\nu_{C=O}$), 1572 ($\nu_{C=C}$), 1414 (ν_{C-N}); ^{1}H NMR ($CDCl_3$, 400 MHz) δ 9.02 (d, *J* = 8.2 Hz, 2H), 8.68 (d, *J* = 6.4 Hz, 2H), 8.61 (d, *J* = 7.3 Hz, 2H), 8.09 (d, *J* = 7.8 Hz, 2H), 7.91 (t, *J* = 7.8 Hz, 2H), 7.84-7.71 (m, 6H), 4.89 (q, *J* = 7.6 Hz, 6H), 4.21-4.08 (m, 4H), 2.25 (q, *J* = 7.5 Hz, 6H), 1.96 (d, *J* = 6.4 Hz, 2H), 1.54-1.46 (m, 6H), 1.45-1.27 (m,16H), 1.06 (t, *J* = 7.1 Hz, 9H), 0.95 (t, *J* = 7.3 Hz, 6H), 0.89 (t, *J* = 7.1 Hz, 6H); ^{13}C-NMR ($CDCl_3$,100 MHz) δ 164.4, 164.1, 144.2, 132.6, 131.7, 130.9, 130.6, 130.5, 130.4, 130.2, 130.1, 128.1, 127.7, 126.9, 122.9, 122.6, 114.5, 113.9, 113.3, 94.7, 93.4, 92.7, 92.3, 56.9,44.3, 37.9, 32.1, 30.7, 28.7, 24.0, 23.1, 19.9, 14.1, 13.6, 10.6; HRMS calcd for $C_{78}H_{77}N_{11}O_4$ [M+ Na] *m/z* 1254.6052, found 1254.6058.

3.4.5 Computational Methods

Gaussian 09 program package was employed for performing all fully optimized without any symmetry constrains employing the DFT using Becke's three parameters hybrid functional[340] and Lee, Yang and Parr's correlational functional B3LYP[341] using the 6-31G* basis set on all atoms in vacuum. The confirmation of the structure was performed by vibrational analyses on the optimized structures. The excitation energies and oscillator strengths for the lowest 10 singlet–singlet transitions at the optimized geometry in the ground state were obtained by TD-DFT calculations using (M06-2x/6-31G(d,p))[342] method.

Chapter 4 Pyrene-Naphthalimide Hybrids: Synthesis and Effects of Substitution Pattern on Optical, Electrochemical and Thermal Properties

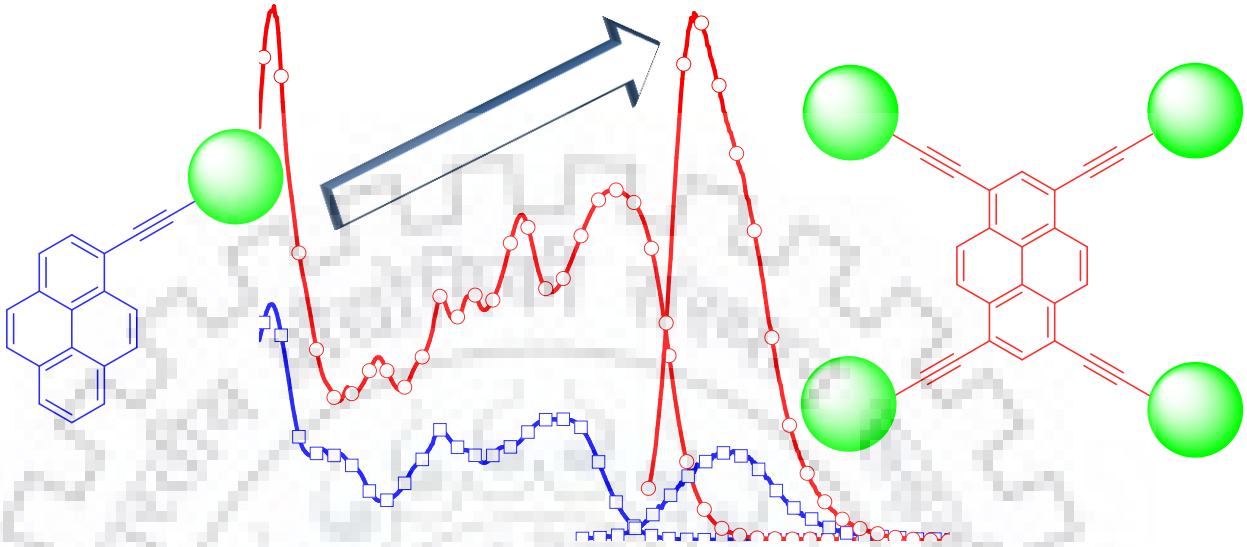

4.1 Introduction

The tremendous ongoing development in the field of organic functional materials is still of great interest to exploit the optical and electronic properties over polymers and inorganic counterparts. The applicability of semiconducting organic molecules is anticipated to widely explore the market of optoelectronics which is in fast competition with its polymeric and silicon-based materials. The rapid alterations for affording them as flexible, cheap and stable scaffolds in electronic devices such as OSCs, DSSCs, OLEDs and OTFTs have gathered immense attention. In the last decades, remarkable progress in designing of organic semiconductor based small molecular devices with the long-term stability on basis of deeper studies on their electronic and optoelectronic properties have been reported.[9, 11, 13, 343] Until now, use of spontaneous but controlled synthetic strategies is in application to develop well-defined small molecules using PAHs,[344, 345] heterocyclic chromophores and imide-based molecules as potential candidates for organic electronic devices. An indispensable need for cost-effective synthesis of *n*-type semiconductors is in demand. Further, to generalize push-pull chromophore with direct or vinyl-linkage which exists in their highly distorted ICT excited state are supposed to exhibit rapid radiationless decay. Whereas the incorporation of rigid acetylene bridging group prevents the molecular deformation keeping the molecular rigidity and symmetry intact and thus avoiding the radiative relaxation. Moreover, the molecular coplanarity and architectures of π-conjugated organic molecules bring

importance to the charge hopping that facilitates the intramolecular and intermolecular interactions.

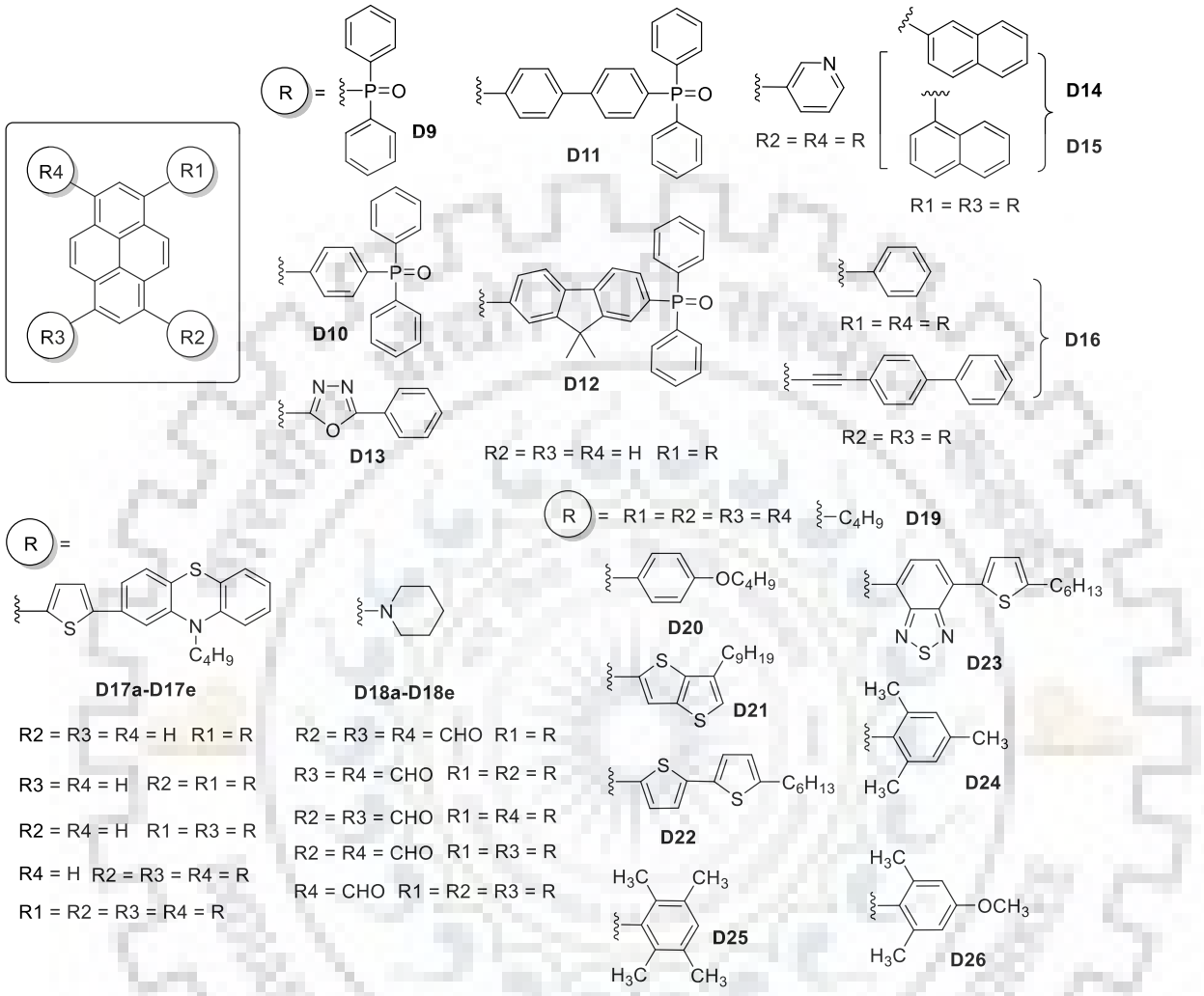

Chart 4.1 Structures of documented chromophore-substituted pyrene-based organic materials.

Among the various PAHs, pentacenes[346, 347] and pyrene[348] have gained prominent attention owing to its good molecular and electronic flexibility. However, due to constrained multiple substitution and poor stability of pentacenes, pyrene core is preffered. It is renowned for its multiple substitution at 1, 3, 6, 8, or 2, 7 or 4, 5, 9, 10 positions. The chemical methods to substitute at 1, 3, 6, 8 positions are more facile than other sites. Moreover, the chromophore displays a planar π-conjugating system with long lifetime and high quantum efficiency. To gain an insight of multi-functionalized pyrene core as organic semiconductor several research groups have characterized the dyes to reveal the pioneering application as *p*-type or *n*-type semiconducting backbone.[349-354] Pyrene chromophore have been studied widely in the field of material science in combination with different electron rich and electron deficient fluorescent moieties to serve as

typical D-A functional materials, **D9-D32**.[352-370] Structures of few chromophore-tethered pyrene-based organic materials are shown in Charts 4.1 and 4.2.

Recently, Mallesham *et al.*[353] have synthesized a series of mono-substituted pyrene dyes, **D9-D12** exploring pyrene as donor end-capped with electron deficient diphenyl phosphine–oxide, acceptor to develop highly efficient electron transporting blue-emitters. Konidena *et al.*[358].synthesized multi-substituted C-C linked pyrene-phenothiazine conjugates, **D17a-D17e** to study the structure-function correlation for OLEDs. Recently, Niko *et al.*[361] have explored the four positions of pyrene to construct asymmetric derivatives appended with both donor and acceptors to synthesize polar dyes, **D18a-D18e**. Sonar *et al.*[362] presented a straight forward synthesis for D-D or D-A star shaped 1, 3, 6, 8-tetra-sustituted pyrene, **D20-D23** as solution processable blue to orange emitters for OLEDs. Moorthy *et al.*[363] synthesized sterically hindered 1, 3, 6, 8-tetra-substituted pyrenes, **D24-D26** coupled to multiple methyl substituted phenyl rings by Suzuki cross coupling as blue light emitting materials. Thomas *et al.*[321] reported blue to yellow emitting OLEDs based on planar fluorene-pyrene hybrids, **D30-D31** exhibiting charge transfer Ji *et al.*[365] studied the molecular effect of 1, 6- and 1, 8-bis(phenylethynyl) pyrenes, **D32b** and **D32c** on the charge transfer as an efficient fluorescent thiol probe for bioimaging in living cells.

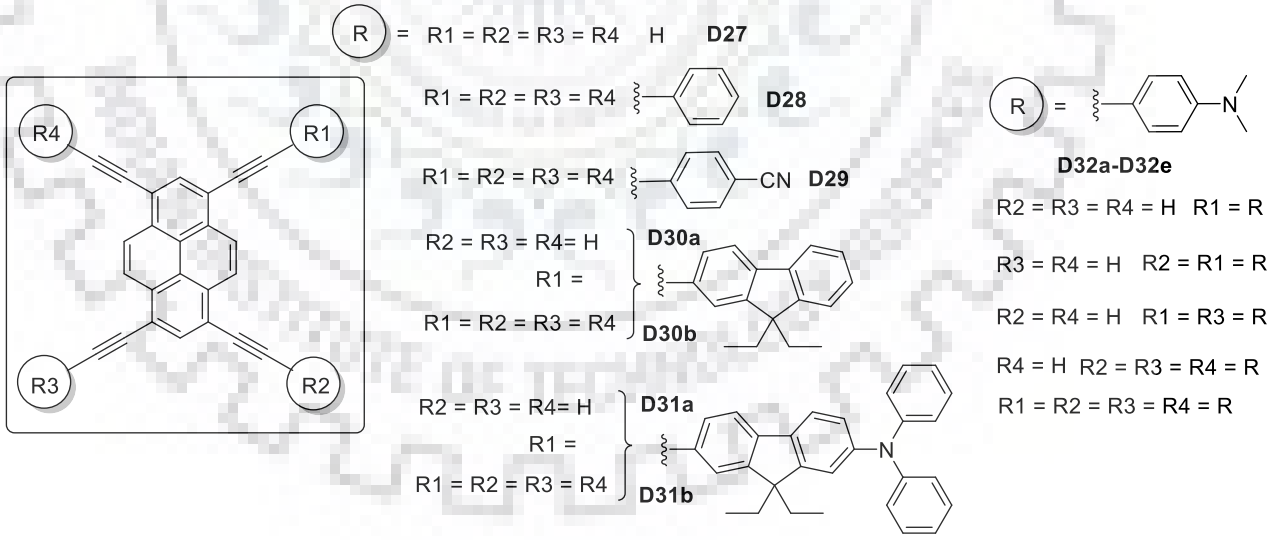

Chart 4.2 Structures of known pyrene-based rigid organic materials.

Thus, to the best of our knowledge only a few articles are reported where pyrene is flanked by electron deficient moieties solely or in combination with electron donating units. Imides are considered as electron deficient organic core which are known for their strong electron affinity and stability as described in previous chapters too. The series of various imide derivatives such as

perylene bisimide, rylene imides, bis-naphthalimides, naphthalimides and phthalimide are well known. 1,8-naphthalimide is an imide-based electron deficient pivotal scaffold that provides a ease of functionalization at aromatic core as well as imidic position to behave as a promising *n*-type organic semiconductor. The small molecular derivatives based on naphthalimide possess a high electron affinity that makes it a suitable candidate as electron transporting materials in OLEDs and non-fullerene acceptor in OSCs. A variety of naphthalimide based D-A molecules with different topology are documented and discussed in Chapter 1. Chai *et al.*[103] have theoretically investigated photophysical and electronic properties of naphthalimide-substituted fluorene derivatives and characterized them as D-A molecules possessing ICT. Arunchai *et al.*[147] have synthesized three triphenylamino naphthalimides directly linked *via* C-C bond with mono to tri substituted core. It was found that with increase in naphthalimide units there is a decrease in electron delocalization between the donor and the acceptor and stabilization of HOMO energy level attributed to the electron withdrawing characteristic of naphthalimide unit. Gudieka *et al.*[118] have reported three D-A molecules composed of triphenylamine and naphthalimide linked by double bond in order to improve the extent of conjugation. It was found that the HOMO was localized entirely on donor while LUMO was centered on naphthalimide while mono and di-substituted derivatives exhibit higher hole mobilities than tri-substituted derivative. Further, Gudeika *et al.*[119] synthesized triphenylamine-naphthalimide hybrids comprising different number of acceptors linked *via* ethynyl bridge. These dyes exhibited enhanced intensity of the low-energy band with the increasing number of 1,8-naphthalimide and show superior thermal stabilities over their single and double bond linked analog derivatives. Jin *et al.*[132] modeled star-shaped D–π–A molecules comprising triphenylamine, 1,8-naphthalimide linked by different π-bridges and studied their properties as organic solar cell materials. The results suggested that molecules possessing ethyne π-bridge displayed better charge transfer rates attributed to a more efficient orbital overlap. Seifert *et al.*[364] have synthesized a highly planar electron-deficient nanographene composed of *N*-(2,6-diisopropylphenyl)-1,8-naphthalimide dehydrogenated on pyrene core possessing a narrow band gap with deep seated LUMO and HOMO energy level at 3.81 eV and 5.83 eV respectively. Thus, naphthalimide is capable to tune the properties of its derivatives by incorporating planarity, strong emission and altering LUMO energy levels. The illustrated molecules in literature supports that structural variation in the D-A molecules to control the position, orientation and linkage of the tethered chromophore is fruitful for the practical application of organic molecules.

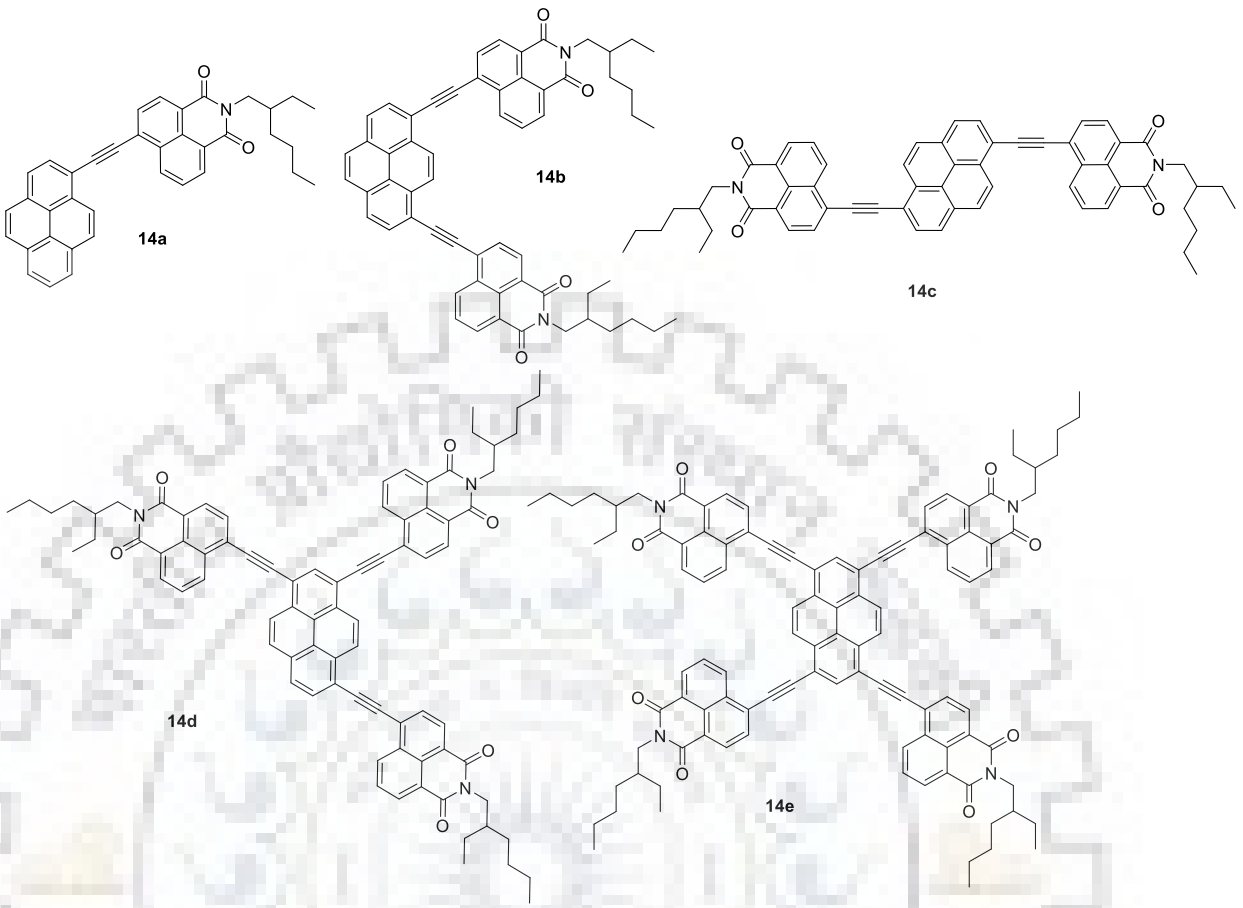

Figure 4.1 Structures of pyrene derivatives containing naphthalimides peripheries.

We have synthesized a series of compounds where pyrene and naphthalimide units are tethered together in a single molecule to offer a route to new fluorescent materials with interesting properties. Herein this chapter, we present the synthesis and analysis of a set of small molecules which consist of pyrene core and 1,8 naphthalimide group as terminal acceptors linked by acetylene bridge synthesized by Sonogashira cross coupling reactions as depicted in Figure 4.1. The photophysical behavior of the dyes depends solely on the architecture, framework and number of substituents on the pyrene core. The tetra-substituted pyrene compound absorbs bathochromically in the set of dyes and emits light strongly in solution state compared to other dyes attributed to elongation in the conjugation. The dyes possess positive solvatochromism in the excited state indicative of more polarized excited state supported by low quantum yield and long lived fluorescence lifetime in polar solvent. Theoretical computations are performed to investigate the electronic structure of the dyes. The dyes exhibited electronic distribution facile for charge transfer in excited state and electron deficiency with low lying LUMO energy level. The low

reduction potential and high thermal stability make these materials promising *n*-type semiconducting candidates for electronic applications.

4.2 Results and Discussion

4.2.1 Synthesis and Characterization

The dyes (**14a**-**14e**) were synthesized by following a synthetic protocol displayed in Scheme 4.1. The reaction involve Sonogashira cross coupling reaction using Pd catalyst. The bromo-derivatives of pyrene as key intermediates were obtained by following literature procedures.[372, 373] The respective bromo-derivatives such as 1-bromopyrene (**13a**), 1,8-dibromopyrene (**13b**), 1,6-dibromopyrene (**13c**), 1,3,6-tribromopyrene (**13d**), 1,3,6,8-tetrabromopyrene (**13e**) were coupled with *N*-(2-ethylhexyl)-4-ethynyl-1,8-naphthalimide, **2** to obtain the target compounds, **14a-14e** in moderate to good yields. The dyes are orange or red in colour and are reasonably soluble in most of common organic solvents such as TOL, DCM, THF, $CHCl_3$, DMF but insoluble in alcohols. They were characterized by ^1H, ^{13}C-NMR, IR and mass analyses and the data found to be consistent with the proposed molecular structures.

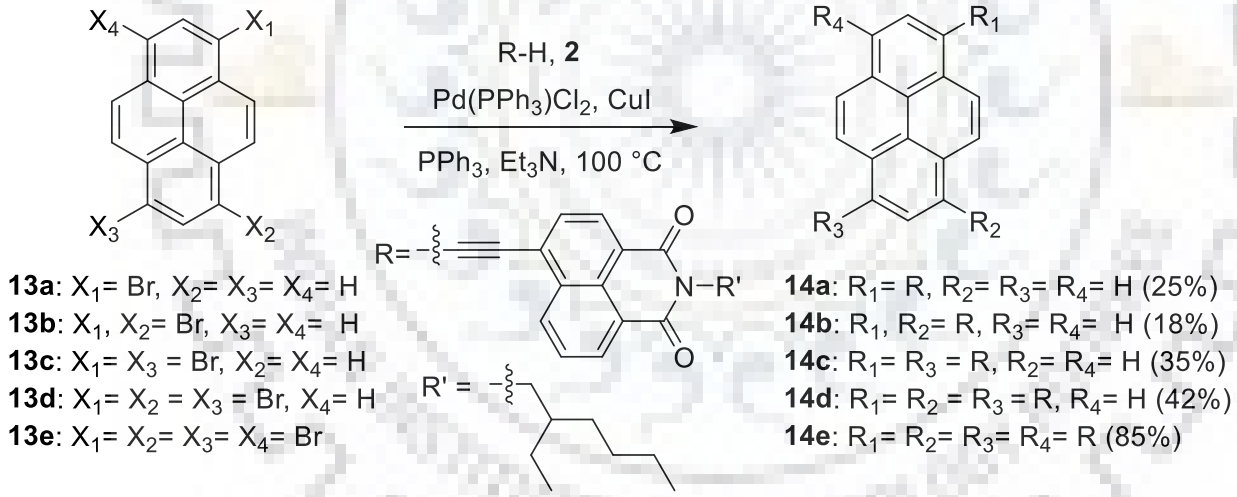

Scheme 4.1 Synthetic route to the compounds **14a**-**14e**

4.2.2 Photophysical Properties

The absorption spectra of the dyes recorded in DCM are shown in Figure 4.2(a). The corresponding optical data is summarized in Table 4.1. All the dyes display complex structured absorption profile covering the entire 230-550 nm region. The intense band appearing at higher energy wavelength (~240 nm) is due to the localized π-π* transitions originating from the naphthalene core of naphthalimide whereas the resolved and sharp absorption bands in 300-400 nm region originates from the π-π* delocalized electronic transition in naphthalimide and pyrene

units. The longer wavelength band appearing in 400-550 nm is attributed to the multiple transitions from the entire molecule which depends on the chromophore density. Compared to the absorption spectrum of pyrene[374, 375] which shows three well-resolved sharp bands, dyes **14a-14e** display a red-shifted broad spectra attributable to the extended π-conjugation system. The photophysical properties of the dyes are dependent on the peripheral chromophore density, molecular symmetry and substitution pattern on the pyrene core. The optical properties were found to be attenuated monotonically from mono, di, tri to tetra substituted derivatives. Among the dyes, the tetra-substituted dye **14e**, displayed the most bathochromic absorption owing to the extension in conjugation. Interestingly, among the 1,6- and 1,8-isomers, former displayed red shifted absorption profile attributed to the extended conjugation over 1,8-analog. The molar extinction coefficients of the dyes showed progressive increase on moving from mono to tetra derivative attributable to the increase in naphthalimide density. When compared to phenylethynylpyrene[366] reported by Yang *et al.*, **14a** displayed a bathochromically shifted absorption ($\Delta\lambda$ = 55 nm) as a result of extension in conjugation due to replacement of phenyl with naphthalimide. Moreover, **14a** possesses a red-shifted absorption ($\Delta\lambda$ = 47 nm) than the typical donor-acceptor molecule *N*,*N*-dimethylanilinoethynylpyrene, **D32a**[366]. Similarly, the tetra-substituted derivative **14e** show a red-shifted band ($\Delta\lambda$ = 58 nm) compared to 1,3,6,8-tetraethynylpyrene, **D27**.[367]

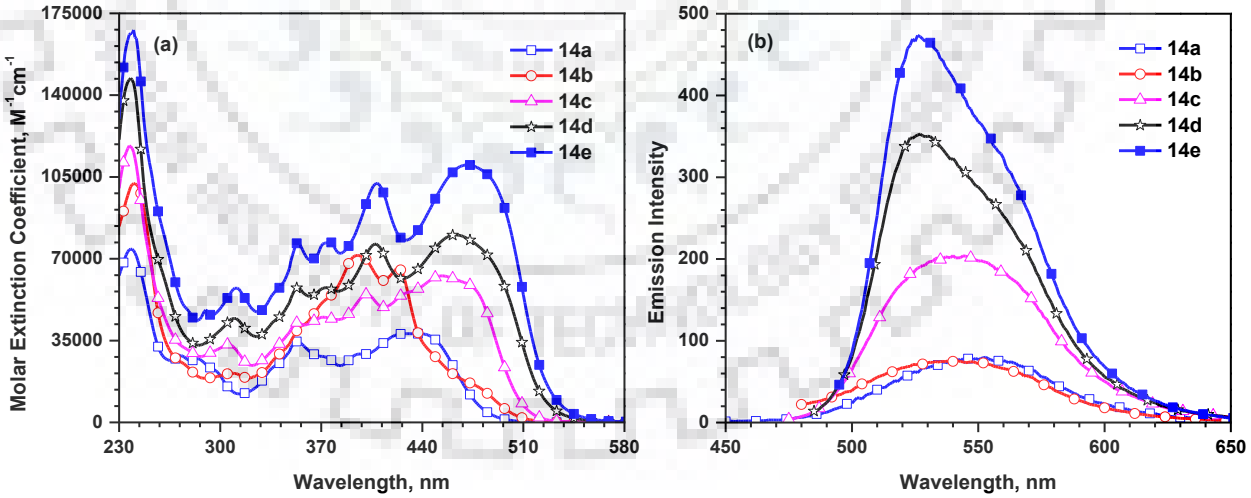

Figure 4.2 (a) Absorption and (b) emission spectra of the dyes recorded in DCM.

The emission spectra of the dyes recorded in DCM solvent is displayed in Figure 4.2(b). Unlike the absorption profile, the emission spectra of the dyes remain unaltered and centered at 550 nm irrespective of naphthalimide count. This emission band observed is due to ICT from pyrene to naphthalimide chromophore in the excited state. A successive increment in the emission

yield was observed on moving from mono- to tri-substituted derivative which is saturated then. The Stokes shift of **14a** is doubled that of **14e**. This points that the highly rigid and planar framework of latter prevents structural reorganization in the excited state. This also validates the most significant charge transfer in **14a** is due to the non-competitive and unidirectional transfer of charge in excited state. Furthermore, this is also supported by the trend of fluorescence quantum yield (Φ_F) calculated for the series of compounds in range of 32-81% relative to coumarin-6 (78% in EtOH). It is stated that the charge transfer generally brings a decrement in the quantum yield attributed to the more pronounced dipolar relaxation in the excited state. Moreover, tetra-substituted functionalized phenylethynyl pyrenes[368-371] reported in literature displayed low quantum yield owing to the rapid nonradiative decay of the excited state. However, interestingly the present dye **14e** exhibited a relatively high quantum efficiency. Compound **14a** displayed red shifted emission than documented phenylethynylpyrene ($\Delta\lambda$ = 150 nm) and dimethylanilinoethynylpyrene, **D32a** ($\Delta\lambda$ = 50 nm). This could be attributed to the strong charge transfer in the excited state of the dye where pyrene acts as donor and naphthalimide as strong acceptor.

Table 4.1 Optical data of the dyes **14a-14e**.

Dye	λ_{max}, nm ($\mathcal{E}_{max}$, M^{-1} cm^{-1} × 10^3)		λ_{em}, nm (Φ_F, %)[a]			Stokes shift, cm^{-1}
	DCM	Film	DCM	Film	Solid	DCM
14a	435 (37.9), 372 (28.1), 353 (34.6), 285 (27.2), 274 (28.4)	504, 440, 379	552 (32)	560 (s), 600	560 (s), 612	4873
14b	478 (s) (15.4), 424 (65.8), 395 (71.4), 312 (20.7), 241 (102.1)	512, 435, 405	542 (41)	575	586	2470
14c	475 (s) (57.9), 455 (62.6), 402 (54.8), 371 (45.0), 353 (42.6), 305 (33.3), 237 (118.4)	515, 477, 416	545 (74)	590	602	2704
14d	463 (80.2), 409 (75.9), 372 (57.5), 355 (57.3), 310 (44.5), 236 (145.6)	525, 477, 418	530, 557 (s) (81)	605, 645 (s)	623	2730
14e	480 (108.4), 409 (102.2), 373 (76.7), 313 (56.9), 240 (167.8)	530, 485, 421	530, 558 (s) (79)	611, 650 (s)	634	1965

[a] Fluorescence quantum yield (Φ_F) calculated relative to standard coumarin-6 (78% in EtOH)

The absorption and emission spectra of dyes in a series of solvents of varying polarity were recorded to ascertain the solvatochromic properties (Table 4.2). The solvatochromism in the absorption and fluorescence spectra is displayed for the dyes in Figures 4.3 and 4.4, respectively. The absorption of the dyes is insensitive to change in solvent polarity indicating the ground state is devoid of solvent specific stabilization. However, the emission profiles of the dyes shifted from

green to orange region on changing polarity of solvent. All the dyes displayed positive solvatochromism in the excited state. This clearly indicates that the dyes are more solvated in the excited state than in ground state. The compounds show structured emission spectra in non-polar solvent whereas in highly polar solvent such as DMF it is broad and structureless. This is a result of polar solvent specific stabilization of the charge transfer excited state. However, among the dyes, **14d** and **14e** display structured emission spectra even in polar solvents such as DCM and THF indicating a less polar excited state. Moreover a large Stokes shift is observed for polar solvents indicating the polarized excited state and effective solvation of dyes by polar solvents. A Stokes shift change from 2147 cm^{-1} to 5330 cm^{-1} is observed for **14a** on moving from TOL to DMF which is largest in the series (Table 4.3). This may be due to the competitive charge transfer to multiple naphthalimides which reduce the overall dipole of the molecule. Also, the rigid rod-like extended in conjugation present in the compound **14b-14e** may resist structural changes in the excited state. Further the reduction of quantum yield in polar solvents support the presence of polarized excited state which is relaxed non-radiatively in polar solvents.

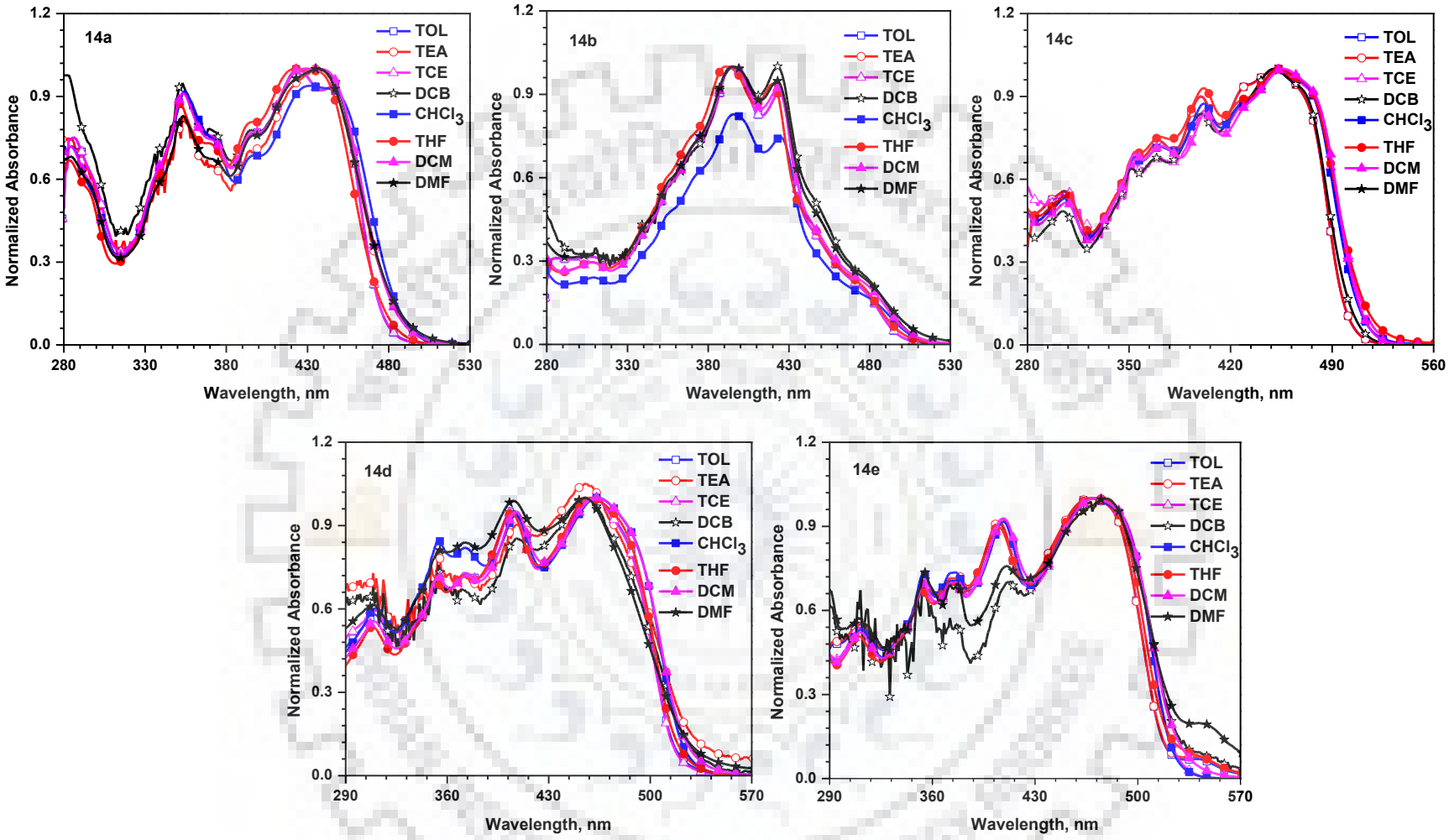

Figure 4.3 Normalized absorption spectra of the dyes **14a-14e** recorded in different solvents.

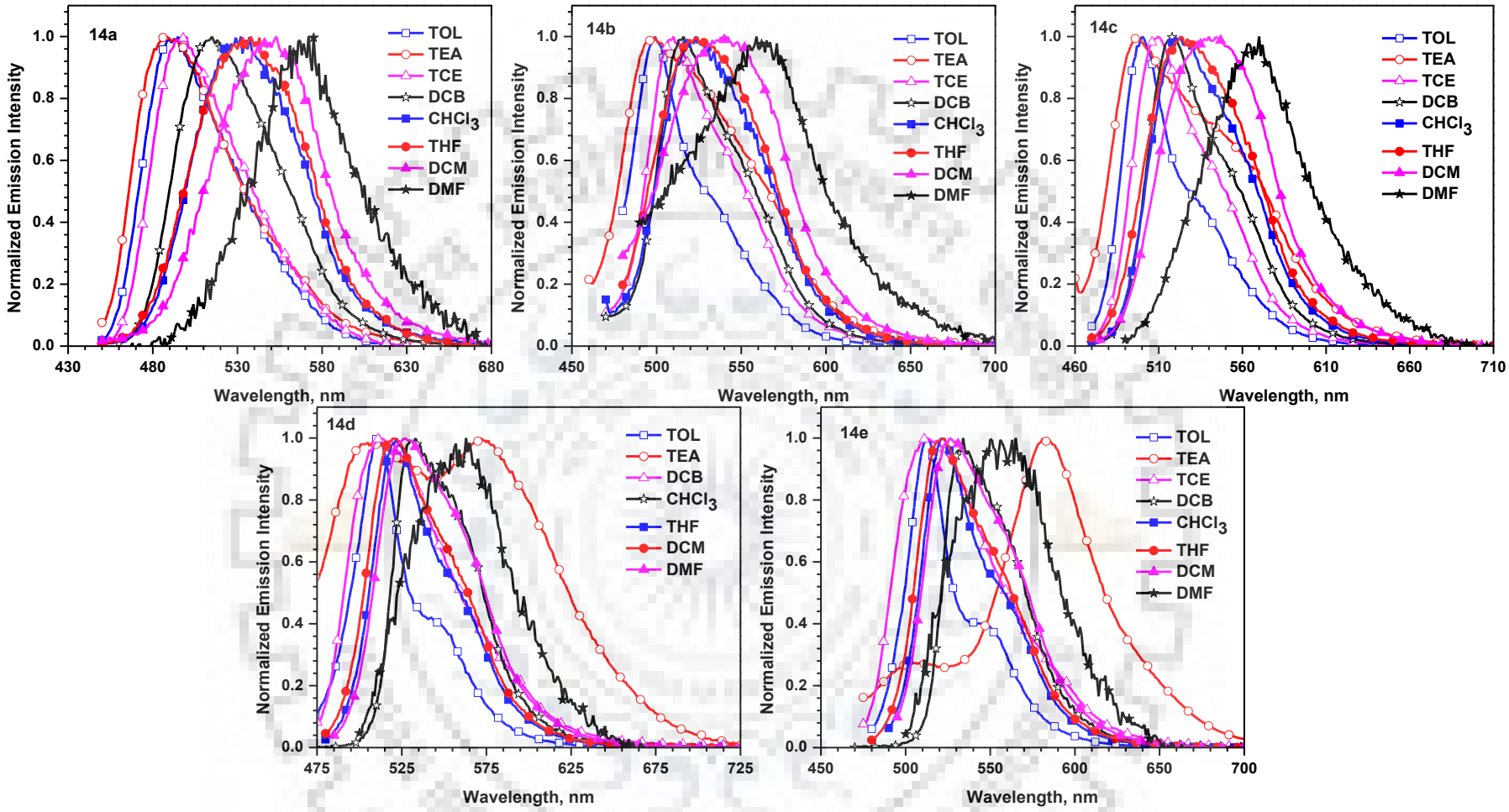

Figure 4.4 Normalized emission spectra of the dyes **14a-14e** recorded in different solvents.

Table 4.2 Absorption spectral data of dyes **14a-14e** in different solvents.

Dye	λ_{max}, nm						
	TOL	TEA	TCE	DCB	$CHCl_3$	THF	DMF
14a	445 (s), 430, 396, 370, 355, 285	434, 353, 283	445 (s), 426, 353, 285	431, 353, 282	440, 395, 373, 355, 286	438, 420, 395, 372, 352, 284	436, 370, 353, 286
14b	472 (s), 424, 395, 311	474 (s), 421, 395, 310	475 (s), 424, 395, 308	475 (s), 423, 395, 310	474 (s), 425, 396, 310	478 (s), 420, 393, 310, 246, 240	483 (s), 422, 395, 312
14c	472 (s), 454, 399, 371, 355, 305	470 (s), 454, 399, 371, 355, 305	472 (s), 455, 399, 370, 355, 304	471 (s), 455, 400, 371, 355, 305	474 (s), 455, 402, 279, 354, 307	475 (s), 450, 400, 370, 355, 304	478 (s), 456, 401, 371, 354, 307
14d	461, 405, 372, 354, 310	460, 405, 372, 354, 310	460, 405, 372, 354, 310	460, 410, 372, 354, 310	463, 407, 372, 354, 311	460, 405, 373, 354, 311, 236	460, 408, 373, 356, 313
14e	480, 468, 405, 374, 354, 313	480, 405, 374, 354, 313	490, 405, 374, 354, 313	544 (s), 490, 405, 374, 354, 313	480, 408, 375, 354, 312	480, 472, 406, 373, 352, 313	542 (s), 481, 410, 373, 354, 312

Table 4.3 Emission spectral data for **14a-14e** dyes in different solvents.

Dye	λ_{em}, nm (Φ_F %)							Stokes shift, (cm^{-1})						
	TOL	TEA	TCE	DCB	$CHCl_3$	THF	DMF	TOL	TEA	TCE	DCB	$CHCl_3$	THF	DMF
14a	492, 533 (s) (75)	488	495	515	529 (64)	536 (49)	568 (12)	2147	2550	3272	3784	3824	4174	5330
14b	499, 533 (s) (55)	499, 536 (s)	510, 542 (s)	516, 549 (s)	527 (51)	533 (40)	559 (23)	1146	1097	1445	1673	2122	2159	2815
14c	500, 540 (s) (91)	498, 547 (s)	512, 538 (s)	519, 548 (s)	521, 557 (s) (78)	530 (84)	570 (26)	1186	1196	1655	1964	2312	2185	3377
14d	511, 546 (s) (83)	505, 572 (s)	513	533, 554 (s)	522, 557(s) (79)	522, 553 (s) (79)	565 (23)	2123	1937	2246	2977	2441	2582	3818
14e	513, 548 (s) (92)	500, 583	512	534	521, 557 (s) (90)	523, 554 (s) (87)	565 (25)	1340	833	915	1682	1639	1713	3091

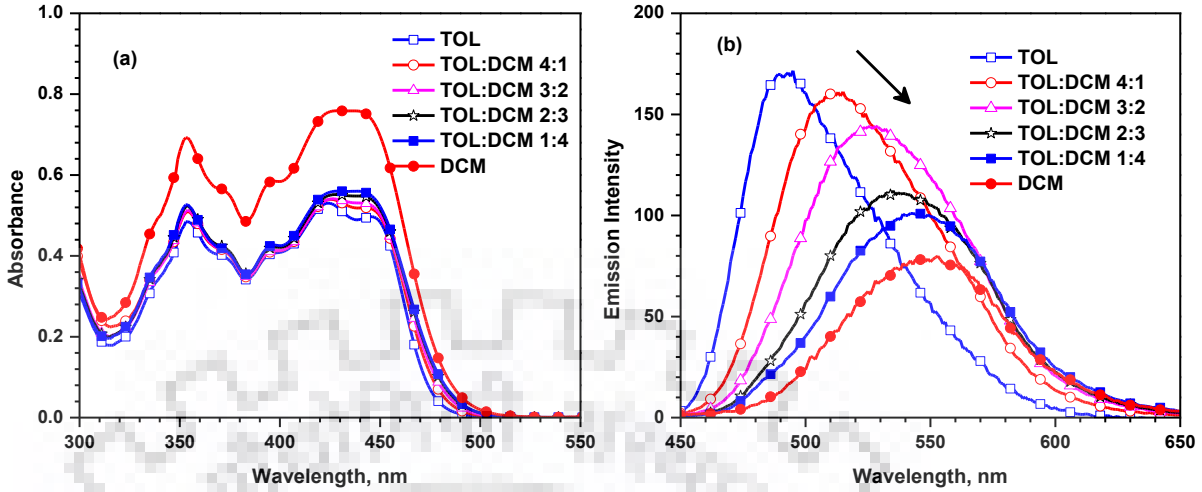

Figure 4.5 (a) Absorption and (b) Emission spectra of **14a** in TOL-DCM mixture.

Photophysical studies in binary solvent mixture are recorded for **14a** in varying proportion of non-polar solvent (TOL) and polar solvent (DCM) in order to study the effect of solvation of polar excited ICT state on variation in solvent polarity. Figures 4.5(a-b) display the variation in the absorption and emission spectra of **14a** in TOL: DCM binary solvent system. In absorption spectra, there is negligible effect on the absorption properties of the dye as the ratio of polar solvent is increased from 0% to 100% pointing towards the non-polar character of the ground state of the dye and absence of CT in ground state. While in emission spectra we observed a gradual continuous red shift in the peak with increment of polar solvent showing positive solvatochromism from 490 to 550 nm. This highlights that the emission peak observed is due to CT from electron rich pyrene to electron deficient naphthalimide unit. Furthermore, it is clear that the dye is polarized and exhibits CT interactions in excited state.

In order to get further insights into the effect of solvent polarity on excited state, Lippert-Mataga correlations[376, 377] were performed (Figure 4.6). The dyes exhibited a positive slope and displayed a reasonable linear correlation highlighting the positive solvatochromism in the excited state for the dyes. Furthermore, it is clear that the dye is polarized and exhibits CT interactions in excited state. In the series, dye **14a** displayed the largest slope which highlights a more polarized excited state for this when compared to other dyes. The dyes **14d** and **14e** show deviation from the linearity for aromatic solvents in Lippert-Mataga plot. The larger Stokes shift observed for both the dyes could be attributed to either better solvation, aggregation or higher degree of change in the electron density distribution between the ground state and excited state.[378]

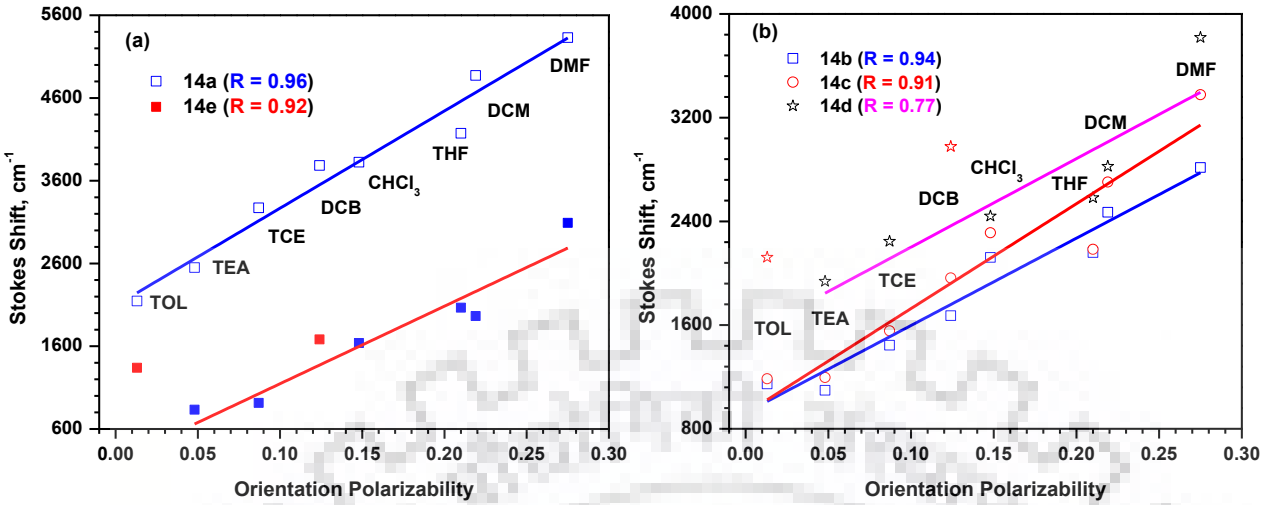

Figure 4.6 Lippert-Mataga plot for (a) **14a** and **14e** and (b) **14b-14d** dyes.

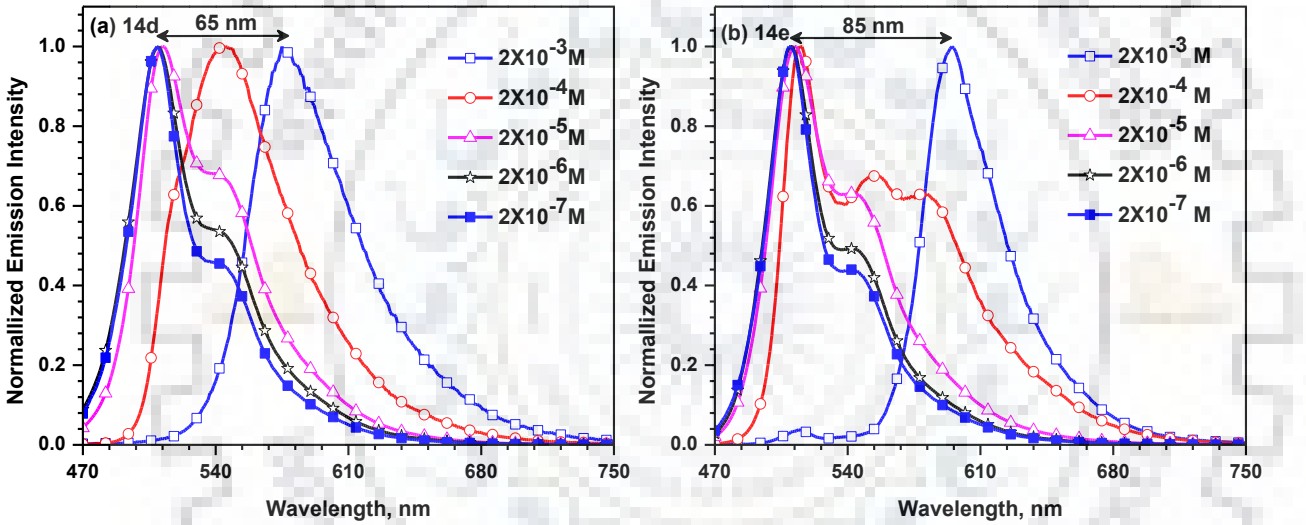

Figure 4.7 Concentration dependent normalized emission spectra of dye (a) **14d** and (b) **14e** recorded in TOL.

The concentration dependent fluorescence spectra of the dyes **14d** and **14e** were recorded in Tol to study the effect of aggregation (Figure 4.7). Both the dyes display a red-shifted and structureless emission band in concentrated solution ($2x10^{-3}$ M) compared to the spectra observed in diluted solutions. The vibronic bands that appeared at concentration lower than $2x10^{-4}$ M disappear at higher concentrations. This red-shift and broadening of the band could be attributed to the formation of aggregates at higher concentrations. The study has shown the existence of the dyes in different states *i.e.* monomer and aggregate. Dye **14e** displayed a more red-shifted ($\Delta\lambda$ = 85 nm) emission band at λ = 595 nm than dye **14d** ($\Delta\lambda$ = 65 nm) observed at λ = 575 nm. The band observed for both the dyes is narrower and bathochromically shifted than dimeric pyrene excimer (λ = 475 nm). This may be due to the enhanced conjugation length, increased intermolecular interactions and conformational disorder

preferably in dye **14e** than dye **14d**. At a concentration of $2x10^{-4}$ M, dye **14e** display a red-shifted shoulder at λ = 580 nm along with monomeric emission in contrast to the broad band observed for dye **14d** at λ = 545 nm.

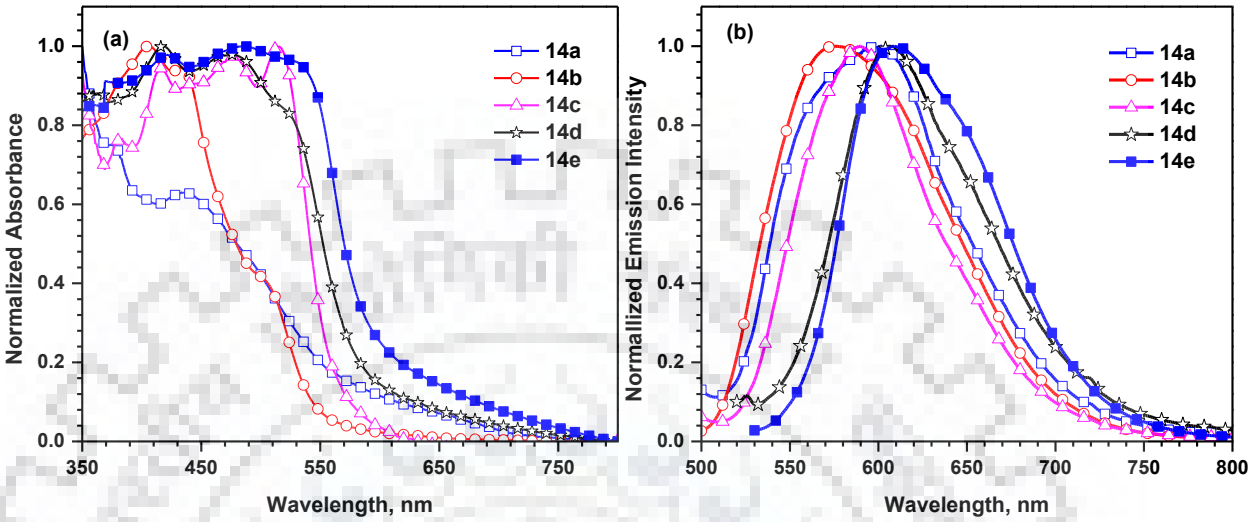

Figure 4.8 Normalized (a) absorption and (b) emission spectra of the dyes recorded on film prepared by drop cast method.

Further, to investigate the optical properties for the dyes in solid state we have recorded absorption and emission spectra in thin film and solid state. The absorption bands were found to be bathochromically shifted for the dyes (Figure 4.8(a)). Thus, thin films obtained from the dyes tend to give *J*-aggregates indicating enhanced intermolecular interactions in the solid state which is confirmed by SEM images of powder samples (Figure 4.9). The FESEM images revealed the presence of different morphologies in nanometers (nm) to micrometers (μm) sizes. The dye **14a** exhibited spherical morphology with a typical diameter of nanostructures 80±20 nm. Interestingly, both the dyes **14b** and **14c** displayed nanoflakes (60-70 nm). It is worth to mention here that **14c** displayed more organized and well defined flakes compared to **14b** which can be due to the effective intermolecular interactions arising from compact and planar π-conjugated aromatic system. While more extended systems **14d** and **14e** displayed ill-defined superstructures with network-like morphology in micrometer range. It is observed that as the chromophore density on pyrene core increases, the morphology changed drastically which could be attributed to the difference in intermolecular forces between the molecules. The morphological difference in the series is attributed to the variation in the molecular conjugation density. We recorded PXRD spectra for the dyes to evaluate the grain size (Figure 4.10). However, a broad profile centered at 2θ = 20-30 Å (d = ~3.5 Å) is observed attributed to the amorphous nature of the dyes.

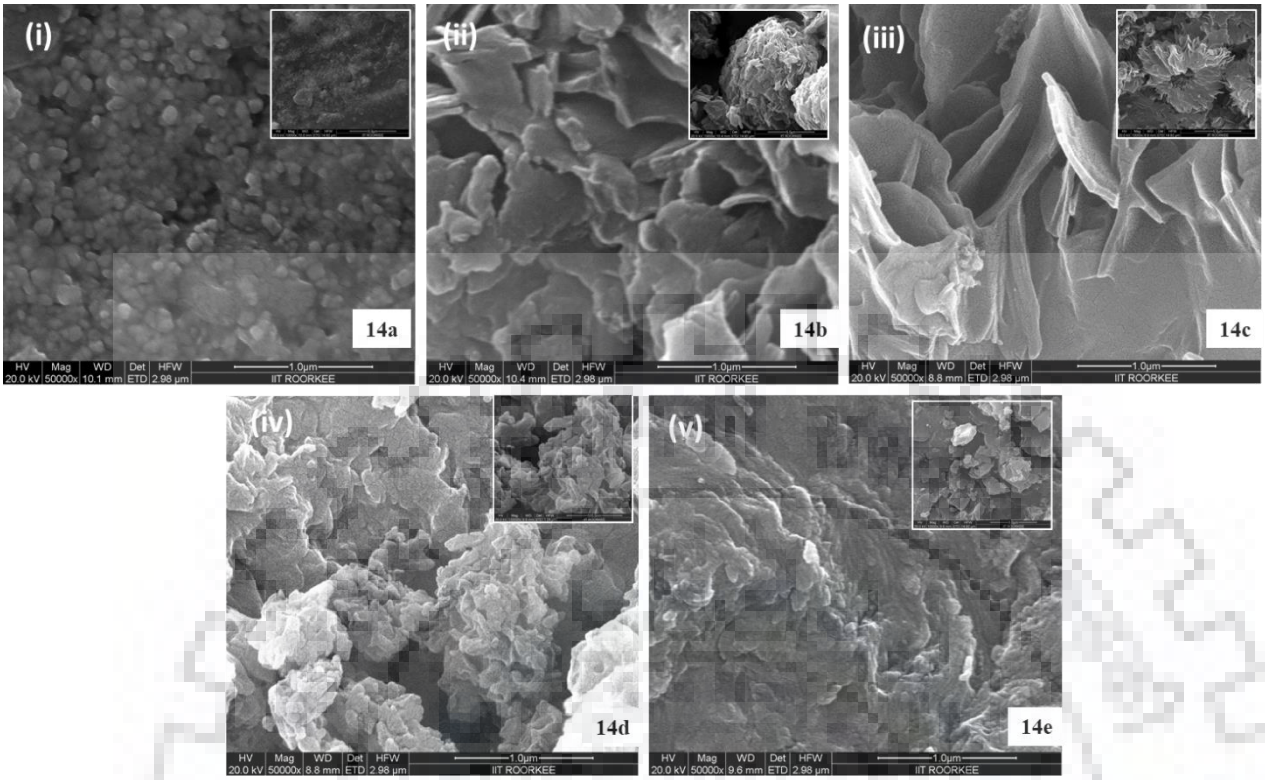

Figure 4.9 FESEM images of as synthesized compounds (i-v) **14a-14e,** respectively; scale bar: 1 μm.

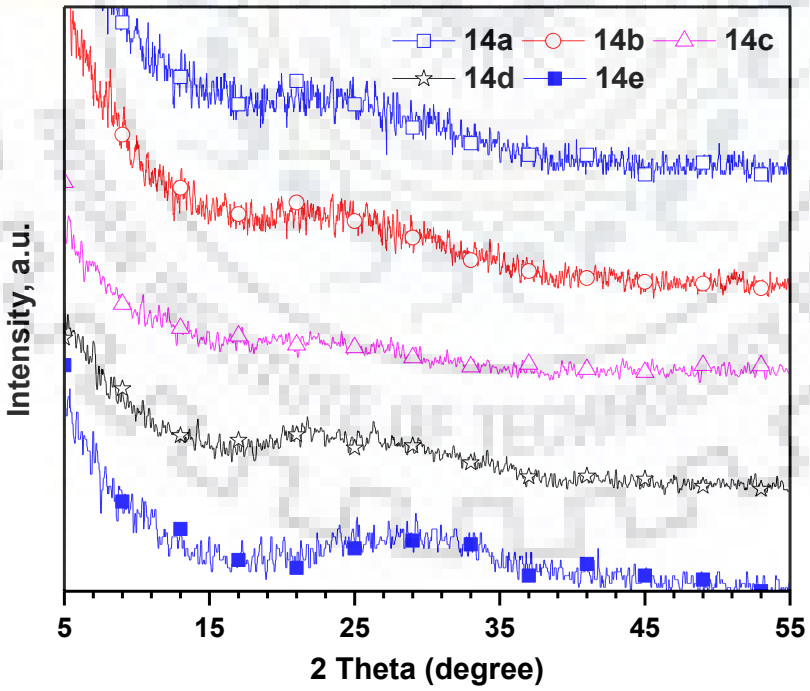

Figure 4.10 PXRD spectra of the dyes.

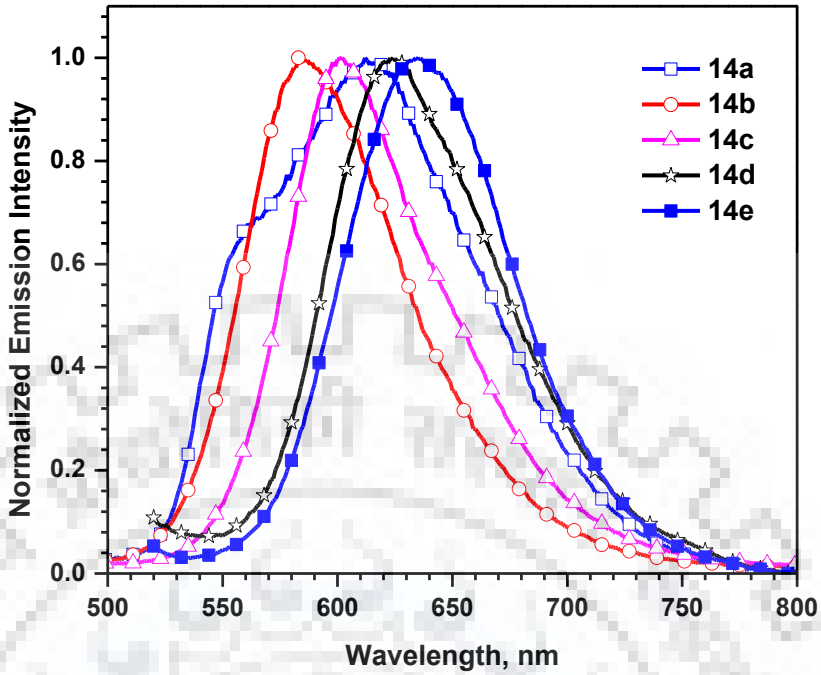

Figure 4.11 Normalized solid state emission spectra of the dyes.

Also, the emission of films casted on quartz (Figure 4.8(b)) of the corresponding compounds and of powder solid samples (Figure 4.11) were also recorded. A large divergence was observed between the fluorescence properties of the films, solid state and solutions. The dyes display red-shifted emissions compared to the solution emission highlighting strong intermolecular interaction in the solid state.

4.2.3 Time Resolved Fluorescence Studies

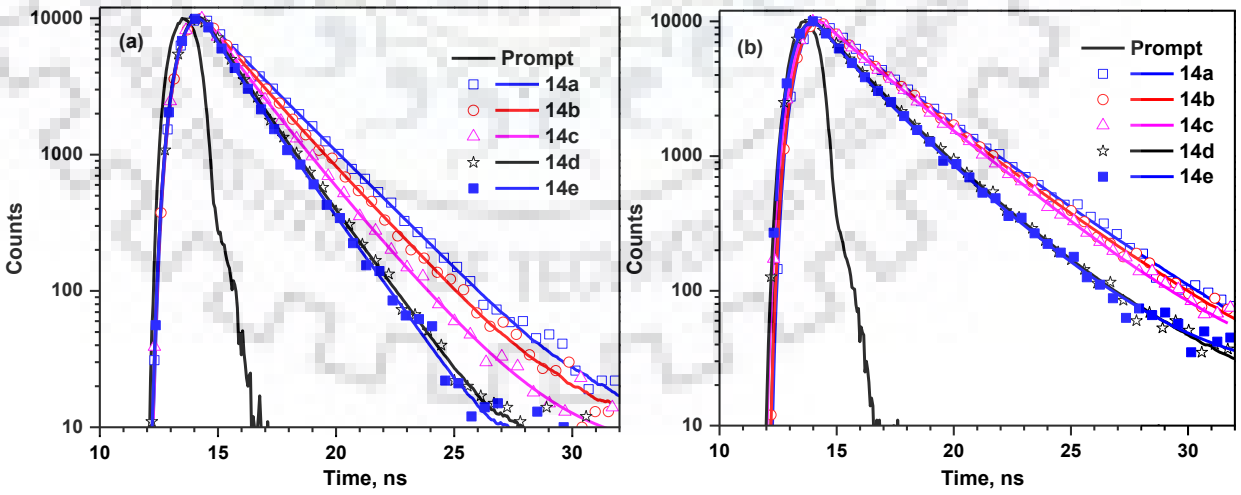

Figure 4.12 Fluorescence decay data for the dyes in (a) TOL and (b) DCM.

Further, to investigate the decay dynamics and effect of solvent polarity on the excited state, time-resolved fluorescence studies (Figure 4.12) were conducted in TOL and DCM. Table 4.4 summarizes the time-resolved fluorescence data such as fluorescence lifetimes, quantum yields, k_r

and k_{nr} decay rate constants of the dyes. The fluorescence decay profiles for the dyes in both solvents follow tri-exponential kinetics as detailed in Table 4.5. The average lifetime calculated for the dyes are found to be 1.5-3.5 ns which are relatively shorter than the parent unsubstituted pyrene core.[351, 360] The occurrence of ultrafast decay *i.e.* shorter lifetime can be related to the allowed S_0-S_1 transitions in the dyes compared to forbidden transitions in pyrene.[351] Further, the correlated fluorescence decay analysis reveal that τ_{avg} of the excited state increases with increase in solvent polarity. This elicits the long lived excited state in more polar solvent than non-polar solvent. It highlights the probability of the excited state to undergo faster non-radiative decay. Among the dyes, **14a** exhibits a large lifetime decrement ($\Delta\tau$ = 1.17 ns) with change in solvent polarity. This can be attributed to the highly asymmetric structure. Dye **14e** possessing high fluorescence quantum yield display a lifetime calculated to be the least (1.51 ns) among the series. This type of trend is the characteristic for the polarized excited state of dyes. The shorter lifetime as displayed by **14e** indicates a rapid radiative pathway among the dyes. Radiative decay rate slows down with increase in solvent polarity. This supports the longer fluorescence lifetime for non-polar solvent. Further, the magnitude of k_r is larger than k_{nr} for non-polar solvent. This is in aggrement with the trend of fluorescence quantum yield. This means that radiative pathway is facilitated over non-radiative decay for non-polar solvent than polar solvent owing to the solvent specific stabilization of the polar excited state in the later.

Table 4.4 Time-resolved fluorescence and photophysical data for the dyes in TOL and DCM (2×10^{-6}).

Dye	τ_{avg},[a] ns		Q.Y.,[b] Φ_F %		k_r,[c] ns^{-1}		k_{nr},[d] ns^{-1}	
	TOL	DCM	TOL	DCM	TOL	DCM	TOL	DCM
14a	2.25	3.42	75	32	0.33	0.09	0.11	0.20
14b	2.10	3.06	55	41	0.26	0.13	0.21	0.19
14c	1.92	2.51	91	74	0.47	0.29	0.05	0.10
14d	1.54	2.37	83	81	0.54	0.34	0.11	0.08
14e	1.51	2.18	92	79	0.61	0.36	0.05	0.09

[a] τ_{avg} = Fluorescence lifetime decay measured as $\tau_{avg} = (A_1 \times \tau_1) + (A_2 \times \tau_2) + (A_3 \times \tau_3)$ in ns. [b] Fluorescence relative quantum yield calculated using coumarin 6 as reference (78% in EtOH). [c] Radiative decay rates (k_r) calculated using $k_r = \Phi_F/\tau$. [d] Non-radiative decay rate (k_{nr}) calculated using $\Phi_F = k_r/(k_r+k_{nr})$.

Table 4.5 Time-resolved fluorescence spectroscopy data for the dyes in TOL and DCM, respectively

Dye	τ_1, ns	A_1	τ_2, ns	A_2	τ_3, ns	A_3	τ_a, ns	τ_b, ns	τ_c, ns	τ_{avg}, ns	χ^2
14aTOL	1.12	0.0352	2.52	0.8718	0.009	0.0930	0.039	2.20	0.008	2.25	1.10
14aDCM	1.30	0.0011	3.20	0.0108	3.43	0.9881	0.001	0.035	3.39	3.42	1.08
14bTOL	1.63	0.2992	0.136	0.0635	2.52	0.6373	0.488	0.009	1.60	2.10	1.04
14bDCM	0.111	0.0518	3.71	0.6456	2.15	0.3026	0.006	2.40	0.652	3.06	1.11
14cTOL	0.165	0.0230	1.47	0.3876	2.28	0.5894	0.004	0.57	1.34	1.92	1.01
14cDCM	1.69	0.1206	0.002	0.2431	3.61	0.6364	0.020	0.005	2.30	2.51	1.08
14dTOL	1.10	0.1992	1.86	0.7038	0.008	0.0970	0.022	1.31	0.007	1.54	1.09
14dDCM	0.009	0.0932	2.00	0.6223	3.91	0.2845	0.008	1.25	1.11	2.37	1.19
14eTOL	0.937	0.1644	1.80	0.7507	0.112	0.0849	0.154	1.35	0.009	1.51	1.10
14eDCM	1.50	0.0002	2.97	0.0003	2.18	0.9995	0.0003	0.0009	2.18	2.18	1.26

Where τ_1/ τ_2/ τ_3, Life time of different decay channels from FLS experiment in ns using 463 nm as excitation wavelength; $A_1/A_2/A_3$, Contribution of different decay channels in solution; fitted by triple exponential; χ^2, correlation of exponential fit; τ_{avg} = Fluorescence lifetime decay measured as $\tau_{avg} = (A_1 \times \tau_1) + (A_2 \times \tau_2) + (A_3 \times \tau_3)$ in ns.

4.2.4 Electrochemical Properties

Electrochemical analysis was performed to investigate the redox characteristics of the dyes in DCM. The redox parameters deduced from CV and DPV of the dyes are compiled in Table 4.6. All the dyes displayed a reversible reduction couple (Figure 4.13) and an irreversible oxidation wave (Figure 4.14(a)). The reduction peak for each compound with quite similar onset potentials can be assigned to the reduction of the 1,8-naphthalimide unit. This reduction potential lies in the range of -1.4 to -1.6 V. The reduction potential was found to be shifted anodically for **14b-14e** compared to **14a** indicating more electron-withdrawing capability for the former set of dyes. While the peak in the anodic region assigned to the removal of electrons is obtained from the oxidation of the conjugation backbone. The respective energy levels were calculated from the potential of first reduction and oxidation wave (E_{onset}). The LUMO energies were found to be at ca. -3.2 to -3.3 eV which is lower when compared to phenylethynylpyrene (-3.88 eV). The LUMO levels of these compounds are close to that of the widely used non-fullerene acceptors and electron-transport materials indicating the materials can serve as potential *n*-type materials. While, the HOMO levels of these molecules are reasonably low lying (-5.6 to -5.9 eV) due to electron deficiency. The energy band gap narrowed down in the series by 0.2 eV on moving from for **14a** to **14e** suggestive of the role of chromophore density. The band gap of **14a** is found to be lowered by 0.62 eV when compared to phenylethynylpyrene (3.14 eV) attributed to the presence of electron deficient naphthalimide unit instead of phenyl. Also, the band gap for the dyes, **14a-14e**) is narrower than the pyrene derivatives reported in literature.[353, 359, 360]

Table 4.6 Electrochemical and Thermal data of the dyes.

Dye	E_{red}, mV[a] (ΔE_p)	E_{ox}, mV[b]	HOMO,[c] eV	LUMO,[d] eV	E_g,[e] eV	$E_{0\text{-}0}$,[f] eV	T_m (°C)	T_{onset} (°C)[g]	T_d (°C)[g]
14a	-1623 (98)	898	-5.70	-3.18	2.52	2.58	189	380	459, 634
14b	-1487 (69)	986	-5.79	-3.31	2.48	2.56	152	429	482, 617
14c	-1573 (99)	927	-5.73	-3.23	2.50	2.53	260	446	487, 615
14d	-1568 (151)	789	-5.59	-3.23	2.36	2.45	236	438	476, 634
14e	-1523 (80)	820	-5.62	-3.28	2.32	2.43	258	444	490, 623

[a, b] Redox potentials are reported with reference to the ferrocene internal standard using tetrabutylammonium perchlorate as electrolyte from CV and DPV respectively. [c] Obtained from the oxidation potential using the formula -(4.8 + E_{ox}) [d] Deduced from the reduction potential using the formula LUMO= -(4.8 - E_{red}) [e] Calculated using formula $E_g = E_{HOMO} - E_{LUMO}$. [f] Calculated from optical edge. [g] Calculated from TGA plot recorded at heating rate of 10 °C/ min under nitrogen atmosphere, T_{onset} wrt 10% wt. loss, T_d = Decomposition temperature.

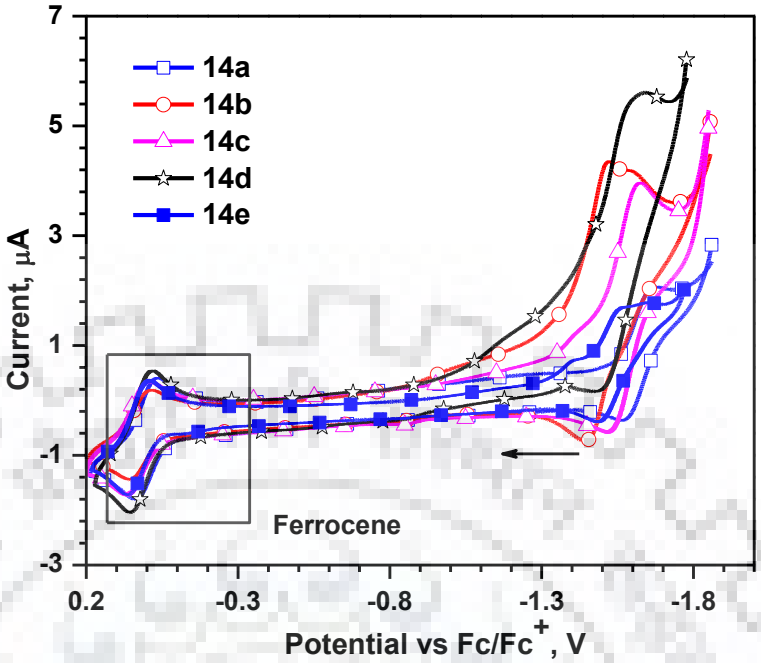

Figure 4.13 CV of the dyes (cathodic region) recorded in DCM.

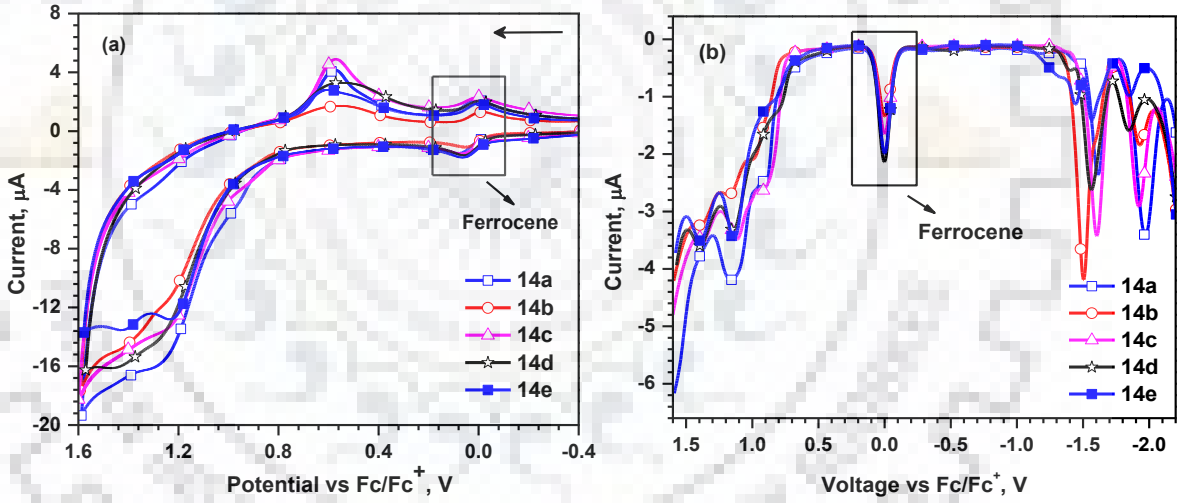

Figure 4.14 (a) CV (anodic region) and (b) DPV recorded in DCM.

4.2.5 Theoretical Studies

To understand the electronic configuration of the compounds, density functional computational calculations were performed on model dyes **14a-14e** where lengthy alkyl chain is approximated to methyl group (Figure 4.15). The dyes were found to be planar which probably facilitates the intermolecular interactions within the dyes. Figure 4.16 displays electronic distribution in the frontier molecular orbitals HOMO, HOMO–1, LUMO and LUMO+1 of the dyes. In all the compounds, the HOMO is mainly constrained on pyrene core and naphthalene part of naphthalimide. This clearly demonstrates that pyrene acts as electron donating moiety. The

LUMO is spread over the entire molecule except **14e** where it is constituted by pyrene. The LUMO+1 is localized on the naphthalimide unit. Thus, the HOMO to LUMO transitions occurring in the dyes at longer wavelength region involves charge transfer from pyrene to naphthalimide in **14a**-**14c** while in **14d** and **14e** it is mainly a pyrene localized transition. Table 4.7 summarizes the computed electronic parameters such as vertical transition, their oscillator strengths, their orbital contributions and energy of the HOMO and LUMO levels using TDDFT at the (M06-2x/6-31G(d,p)) level. The major vertical electronic transitions are contributed by the HOMO to LUMO excitations. It is worth to mention that the order of theoretically calculated absorption maxima and energy band gap for the dyes followed the same trend as observed experimentally.

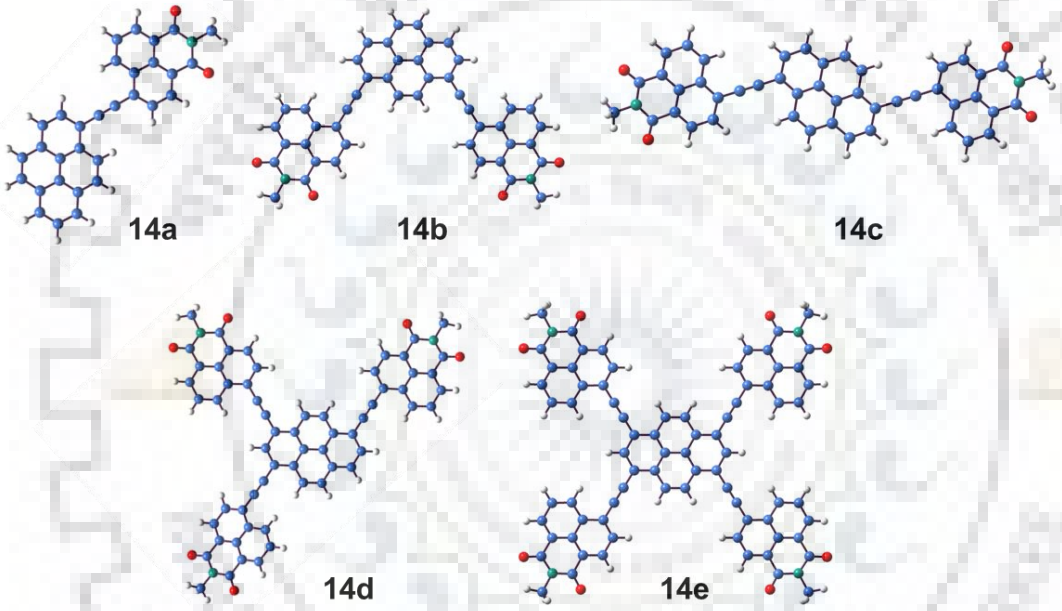

Figure 4.15 Optimized molecular geometries of the modeled dyes.

Table 4.7 Computed electronic parameters for the dyes using M06-2x/6-31G(d,p)) method.

Dye	λ_{max}, nm	f	Composition	HOMO, eV	LUMO, eV	E_g, eV
14a	420	1.41	HOMO → LUMO (88%)	-6.55	-2.10	4.45
	322	0.11	HOMO-1→ LUMO (54%), HOMO → LUMO+2 (15%), HOMO-2 → LUMO (10%)			
14b	458	1.53	HOMO → LUMO (88%)	-6.52	-2.31	4.21
	385	1.10	HOMO → LUMO+1 (73%), HOMO-1 → LUMO (19%)			
14c	457	2.55	HOMO → LUMO (88%)	-6.52	-2.32	4.20
14d	478	1.90	HOMO → LUMO (90%)	-6.53	-2.49	4.04
	395	1.51	HOMO → LUMO+1 (67%)			
14e	516	2.11	HOMO → LUMO (92%)	-6.50	-2.70	3.80
	398	2.63	HOMO → LUMO+1 (62%), HOMO-1 → LUMO (17%)			

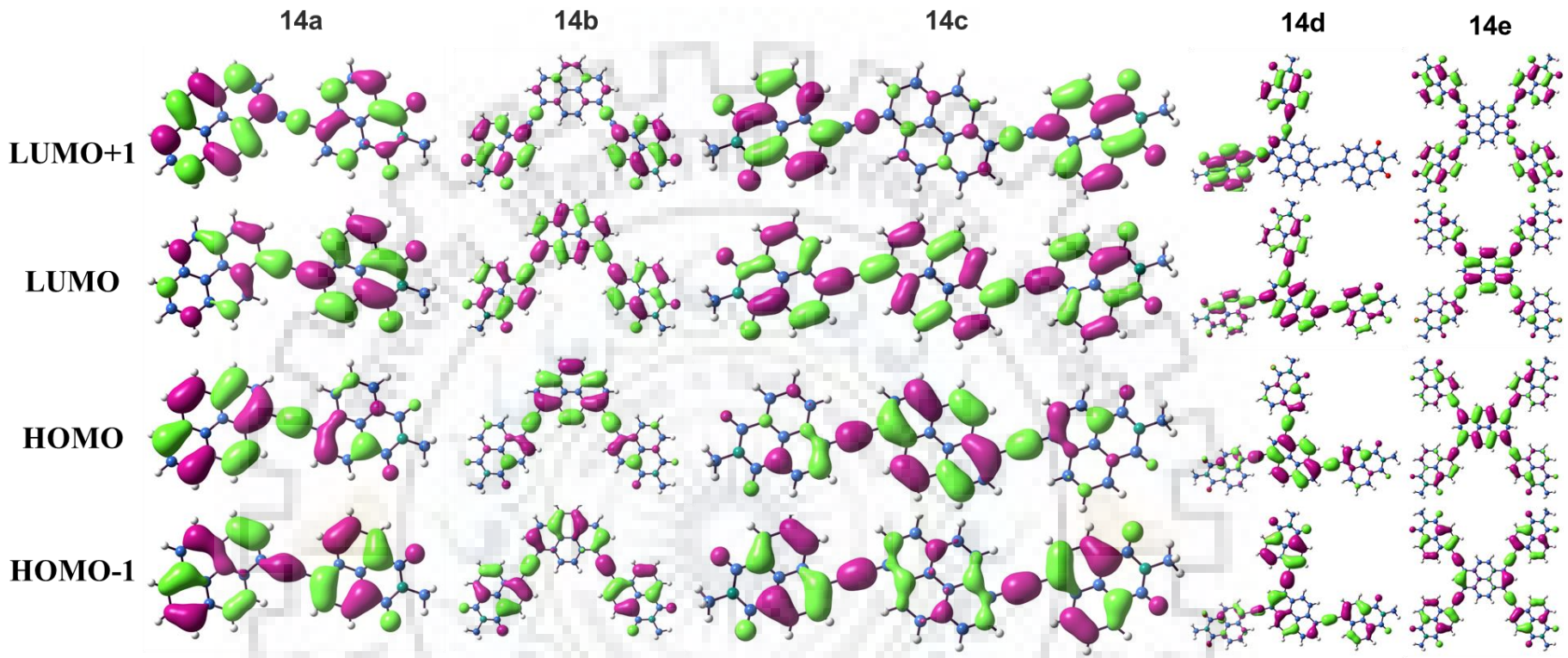

Figure 4.16 FMO of the dyes computed by using TDDFT at the B3LYP level.

4.2.6 Thermal Properties

The thermal properties of the pyrene-naphthalimide hybrids were estimated by TGA (Figure 4.17) and the data compiled in Table 4.6. All the dyes exhibit good thermal stability upto 380℃ and display a T_d above 450℃. All the compounds display a two-step decomposition path in the range of 350-550℃ and 550-650℃ attributed to the loss of alkyl chain and aromatic ring, respectively. The dyes are thermally more stable than the previously reported dyes with either acetylene, vinyl or directly linked pyrene-based compounds with other chromophores highlighting the combined rigidity of pyrene and naphthalimide.[369, 370]

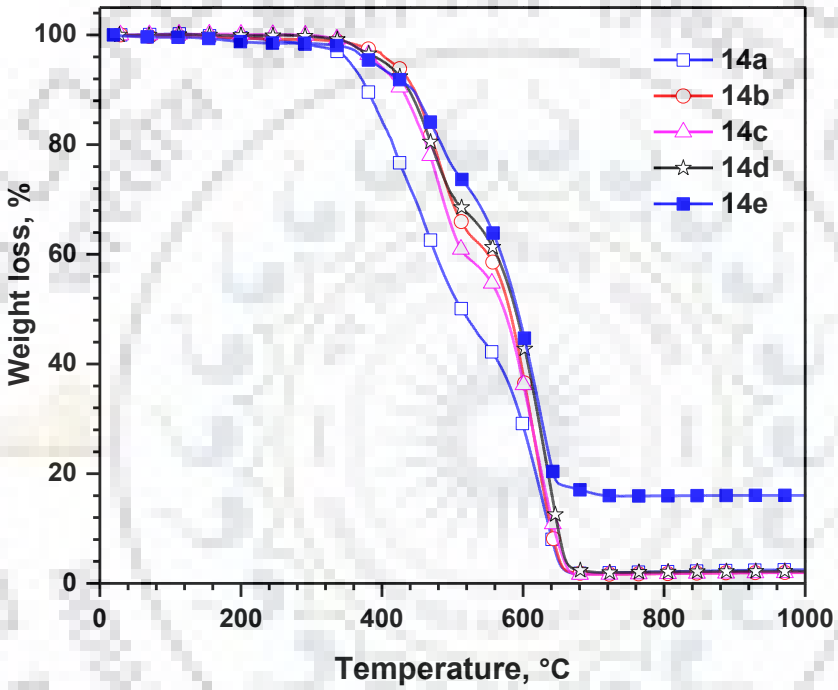

Figure 4.17 TGA curves of the dyes.

4.3 Conclusions

A series of naphthalimide decorated pyrene were synthesized by Sonogashira coupling reactions. The optical properties of the dyes show changes attributable to the degree of substitution on pyrene core. Among the 1,6-di-substituted and 1,8-di-substituted isomers, former displayed red shifted absorption profile attributed to the extended configuration possessing longer conjugation pathway. The molar extinction coefficient of the dyes increased monotonously from mono to tetra-substituted compound attributed to the elongation of conjugation. The compounds are green to orange fluorescent and display dependence on solvent polarity confessing a intra molecular charge transfer in excited state. Further, it is supported by large Stokes shifts, low quantum yield in polar solvents, linear trend in Lippert-Mataga plots and prolonged lifetime fluorescence decay

in polar solvents. The dyes show good thermal stability and reduction originating from naphthalimide unit. DFT studies exposed the presence of charge transfer in the molecules. The observed optical and electrochemical properties of the new dyes position them as promising *n*-type semiconductors for electronic applications.

4.4 Experimental Section

4.4.1 General Methods and Instrumentation

The general methodology is similar as described in Chapter 3.

4.4.2 Synthesis

4.4.2.1 *N*-(2-ethylhexyl)-4-(pyren-1-ylethynyl)-1,8-naphthalimide (14a)

A mixture of **13a** (0.56 g, 2 mmol), *N*-(2-ethylhexyl)-4-ethynyl-1,8-naphthalimide (0.67 g, 2 mmol) were purged with nitrogen followed by addition of $Pd(PPh_3)_2$ Cl_2 (14 mg, 0.02 mmol), CuI (4 mg, 0.02 mmol), PPh_3 (11 mg, 0.04 mmol) and degassed distilled TEA (20 mL). The reaction mixture was kept on reflux for 12 h and the reaction was monitored with TLC and on completion water was added to quench the reaction. The organic part was extracted with $CHCl_3$ to give orange solution and washed thoroughly with water. Solvent was evaporated and absorbed on silica for chromatography (eluent: $CHCl_3$: Hexane, 2:3 -7:3) to yield light orange solid. Yield: 0.25 g (25%), mp: 189 ^oC, IR (KBr, cm^{-1}) 2188, $\nu_{(C\equiv C)}$ 2966, 2925, 2860 $\nu_{(C\text{-}Hstretch)}$, 1695, 1648, 1563 $\nu_{(C=O,\ C=Carene)}$, 1414 $\nu_{(C\text{-}N)}$; ^{1}H-NMR (400 MHz, $CDCl_3$) δ 8.96 (d, J = 9.6 Hz, 1H), 8.84 (d, J = 9.2 Hz, 1H), 8.74 (d, J = 9.2 Hz, 1H), 8.69 (d, J = 6.0 Hz, 1H), 8.63 (d, J = 7.3 Hz, 1H), 8.54 (d, J = 9.2 Hz, 1H), 8.40-8.33 (m, 1H), 8.32-8.18 (m, 3H), 8.17-8.06 (m, 3H), 7.92 (t, J = 7.8 Hz, 1H), 4.21-4.01 (m, 2H), 2.01-1.94 (m, 1H), 1.46-1.27 (m, 8H), 0.96 (t, J = 8.0 Hz, 3H), 0.90 (t, J = 7.6 Hz, 3H); ^{13}C-NMR (100 MHz, $CDCl_3$) δ 164.3, 164.1, 132.2, 132.1, 131.9, 131.5, 131.1, 130.84, 130.78, 130.7, 130.65, 130.60, 130.56, 130.5, 130.34, 130.28, 129.9, 128.9, 128.8, 127.4, 127.2, 126.4, 126.0, 125.1, 124.6, 122.9, 92.0, 91.9, 44.2, 37.9, 30.7, 28.7, 24.0, 23.1, 14.1, 10.6; HRMS: m/z calcd for $C_{38}H_{31}NO_2$: 556.2247 ($M + Na^+$); found: 556.2248.

4.4.2.2 4,4'-(Pyrene-1,8-diylbis(ethyne-2,1-diyl))bis(*N*-(2-ethylhexyl)-1,8-naphthalimide) (14b)

It was obtained from compound **13b** (0.36 g, 1 mmol), *N*-(2-ethylhexyl)-4-ethynyl-1,8-naphthalimide (0.67 g, 2 mmol) and $Pd(PPh_3)_2$ Cl_2 (14 mg, 0.02 mmol), 4 mg, 0.02 mmol), PPh_3 (11 mg, 0.04 mmol) by following the procedure described above for **14a**. The dye was purified by silica column chromatography. Eluent: $CHCl_3$: Hexane: EtOAc (7:3:0 -6:2:2) to yield light orange

solid. Yield: 0.15 g (18%), mp: 152 °C; IR (KBr, cm^{-1}) 2959, 2925, 2863 $\nu_{(C\text{-}Hstretch)}$, 2192 $\nu_{(C\equiv C)}$, 1699, 1658, 1564 $\nu_{(C=O,\ C=Carene)}$, 1413 $\nu_{(C\text{-}N)}$; ^{1}H-NMR (400 MHz, $CDCl_3$) δ 8.93 (d, J = 8.2 Hz, 1H), 8.89 (s, 1H), 8.71-8.68 (m, 2H), 8.67 (dd, J = 7.3, 0.9 Hz, 2H), 8.61 (dd, J = 7.6, 2.1 Hz, 1H), 8.57 (d, J = 7.8 Hz, 2H), 8.39 (d, J = 7.8 Hz, 1H), 8.25 (d, J = 7.8 Hz, 1H), 8.15 (d, J = 7.8 Hz, 1H), 8.04 (d, J = 7.3 Hz, 2H), 8.00 (d, J = 7.8 Hz, 1H), 7.97 (d, J = 7.3 Hz, 1H), 7.92-7.85 (m, 2H), 4.17-4.09 (m, 4H), 1.99-1.90 (m, 2H), 1.42-1.28 (m, 16H), 0.93 (t, J = 7.6 Hz, 6H), 0.88 (t, J = 7.2 Hz, 6H); ^{13}C-NMR (100 MHz, $CDCl_3$) δ 164.1, 163.8, 137.9, 132.6, 132.2, 132.1, 131.9, 131.8, 131.7, 131.5, 131.1, 130.8,130.3, 130.1, 129.4, 128.1, 127.9, 127.6, 127.3, 126.8, 125.1, 124.0, 123.3, 123.2, 113.7, 97.5, 90.7, 81.9, 81.5, 44.3, 37.9, 30.7, 24.0, 23.1, 14.1, 10.6; HRMS: m/z calcd for $C_{60}H_{52}N_2O_4$: 865.3999 ($M + H^+$); found: 865.3992.

4.4.2.3 4,4'-(Pyrene-1,6-diylbis(ethyne-2,1-diyl))bis(*N*-(2-ethylhexyl)-1,8-naphthalimide) (14c)

It was obtained from compound **13c** (0.36 g, 1 mmol), *N*-(2-ethylhexyl)-4-ethynyl-1,8-naphthalimide (0.67 g, 2 mmol) and $Pd(PPh_3)_2$ Cl_2 (14 mg, 0.02 mmol), 4 mg, 0.02 mmol), PPh_3 (11 mg, 0.04 mmol) by following the procedure described above for **14a**. The dye was purified by silica column chromatography (Eluent: $CHCl_3$: Hexane (1:1-7:3) to yield orange solid. Yield: 0.3 g (35%), mp: 260 °C; IR (KBr, cm^{-1}) 2963, 2922, 2860,$\nu_{(C\text{-}Hstretch)}$, 2190 $\nu_{(C\equiv C)}$, 1697, 1645, 1563 $\nu_{(C=O,\ C=Carene)}$, 1413 $\nu_{(C\text{-}N)}$; ^{1}H-NMR (400 MHz, $CDCl_3$) δ 8.91-8.82 (m, 2H), 8.73 (d, J = 9.0 Hz, 2H), 8.64 (dd, J = 7.3, 1.1 Hz, 2H), 8.57 (dd, J = 7.6, 4.4 Hz, 2H), 8.37 (dd, J = 8.0, 4.4 Hz, 2H), 8.26-8.19 (m, 3H), 8.13 (d, J = 6.8 Hz, 1H), 8.11-8.08 (m, 1H), 8.04 (d, J = 7.6 Hz, 1H), 7.93-7.84 (m, 2H), 4.20-4.08 (m, 4H), 1.99-1.93 (m, 2H), 1.43-1.26 (m, 16H), 0.97-0.86 (m, 12H); ^{13}C-NMR (100 MHz, $CDCl_3$) δ 164.1, 163.9, 131.9, 131.4, 131.1, 130.7, 130.4, 130.1, 128.5, 127.8, 127.3, 127.1, 126.4, 126.2, 125.5, 123.6, 122.8, 121.9, 117.6, 97.9, 92.7, 44.2, 37.9, 30.7, 28.6, 23.9, 23.1, 14.1, 10.6; HRMS: m/z calcd for $C_{60}H_{52}N_2O_4$: 865.3999 ($M + H^+$); found: 865.3998.

4.4.2.4 4,4',4''-(Pyrene-1,3,6-triyltris(ethyne-2,1-diyl))tris(*N*-(2-ethylhexyl)-1,8-naphthalimide) (14d)

It was obtained from compound **13d** (0.22 g, 0.5 mmol), *N*-(2-ethylhexyl)-4-ethynyl-1,8-naphthalimide (0.5 g, 1.5 mmol) and $Pd(PPh_3)_2Cl_2$ (11 mg, 0.015 mmol), CuI (3 mg, 0.015 mmol), PPh_3 (8 mg, 0.03 mmol) by following the procedure described above for **14a**. The dye was purified by silica column chromatography $CHCl_3$: Hexane: EtOAc (7:3:0 -1:1:0-7:2:1) to yield red solid. Yield: 0.3 g (42%), mp: 236 °C; IR (KBr, cm^{-1}) 2957, 2925, 2863 $\nu_{(C\text{-}Hstretch)}$, 2193 $\nu_{(C\equiv C)}$, 1699, 1653, 1563 $\nu_{(C=O,\ C=Carene)}$, 1413 $\nu_{(C\text{-}N)}$; ^{1}H-NMR (400 MHz, $CDCl_3$) δ 8.79 (d, J = 8.2 Hz,

1H), 8.73-8.65 (m, 2H), 8.63 (s, 1H), 8.61-8.51 (m, 3H), 8.51-8.48 (m, 1H), 8.48 (d, *J* = 1.8 Hz, 1H), 8.45-8.42(m, 1H), 8.30 (dd, *J* = 7.8, 6.0 Hz, 2H), 8.18-8.06 (m, 3H), 8.07-7.93 (m, 4H), 7.91-7.77 (m, 3H), 4.17-4.05 (m, 6H), 2.00-1.85 (m, 3H), 1.40-1.25 (m, 24H), 0.96-0.84 (m, 18H); ^{13}C-NMR (100 MHz, $CDCl_3$) δ 163.4, 163.3, 131.4, 131.20, 131.15, 131.0, 130.9, 130.8, 130.7, 130.65, 130.6, 130.44, 130.39, 129.7, 129.5, 128.9, 127.5, 127.3, 127.1, 127.0, 126.1, 125.9, 125.3, 125.2, 122.8, 122.6, 122.5, 122.3, 122.1, 121.9, 121.8, 117.2, 117.1, 97.1, 96.2, 93.3, 92.9, 44.2, 37.9, 30.7, 28.6, 23.9, 23.1, 14.1, 10.5; HRMS: m/z calcd for $C_{82}H_{73}N_3O_6$: 1196.5572 ($M + H^+$); found: 1196.5564.

4.4.2.5 4,4',4'',4'''-(Pyrene-1,3,6,8-tetrayltetrakis(ethyne-2,1-diyl))tetrakis(*N*-(2-ethylhexyl)-1,8-naphthalimide) (14e)

It was obtained from compound **13e** (1 g, 1 mmol), *N*-(2-ethylhexyl)-4-ethynyl-1,8-naphthalimide (1.33 g, 4 mmol) and $Pd(PPh_3)_2$ Cl_2 (28 mg, 0.04 mmol), CuI (8 mg, 0.04 mmol), PPh_3 (22 mg, 0.08 mmol) by following the procedure described above for **14a**. The dye was purified by silica column chromatography ($CHCl_3$: Hexane, 2:3 -1:1) to yield red solid. Yield: 1.3 g (85%), mp: 258 ^{o}C; IR (KBr, cm^{-1}) 2958, 2924, 2860 $\nu_{(C\text{-}Hstretch)}$, 2191 $\nu_{(C\equiv C)}$, 1699, 1657, 1586, $\nu_{(C=O,\ C=Carene)}$ 1415 $\nu_{(C\text{-}N)}$; ^{1}H-NMR (400 MHz, $CDCl_3$) δ 8.58 (d, *J* = 8.1 Hz, 1H), 8.52-8.36 (m, 3H), 8.36-8.29 (m, 2H), 8.27 (dd, *J* = 7.3, 1.8 Hz, 2H), 8.22 (dd, *J* = 9.4, 4.2 Hz, 2H), 8.19 (s, 2H), 8.17-8.09 (m, 3H), 8.07-8.03 (m, 1H), 8.01-7.95 (m, 2H), 7.92-7.82 (m, 2H), 7.80-7.71 (m, 2H), 7.70-7.62 (m, 2H), 7.58 (dd, *J* = 14.9, 7.1 Hz, 1H), 7.50 (d, *J* = 7.5 Hz, 1H), 4.19-3.86 (m, 8H), 1.94-1.85 (m, 4H), 1.45-1.19 (m, 32H), 1.00-0.77 (m, 24H); ^{13}C-NMR (100 MHz, $CDCl_3$) δ 163.4, 163.3, 163.2, 163.1, 131.2, 131.1, 130.9, 130.74, 130.68, 130.6, 130.5, 130.4, 130.3, 130.1, 129.9, 129.7, 129.64, 129.60, 129.4, 129.1, 128.9, 128.8, 127.5, 127.2, 127.1, 127.0, 126.0, 125.9, 125.82, 125.77, 125.4, 125.3, 125.2, 122.9, 122.7, 122.5, 122.4, 122.1, 121.9, 121.8, 120.9, 120.6, 118.3, 118.2, 117.7, 117.6, 117.12, 117.06, 97.0, 96.1, 95.8, 95.6, 95.3, 93.9, 93.5, 93.3, 93.0, 92.9, 44.1, 37.8, 30.6, 28.5, 23.9, 23.1, 14.1, 10.6, 10.4; HRMS: m/z calcd for $C_{104}H_{94}N_4O_8$: 1526.7072 (M^+); found: 1526.7069.

4.4.3 Computational Methods

All the computational methodology used is similar as described in Chapter 3.

Chapter 5 Carbazole-Naphthalimide-Based Linear D-A and Star-shaped Triazine-Cored Molecules

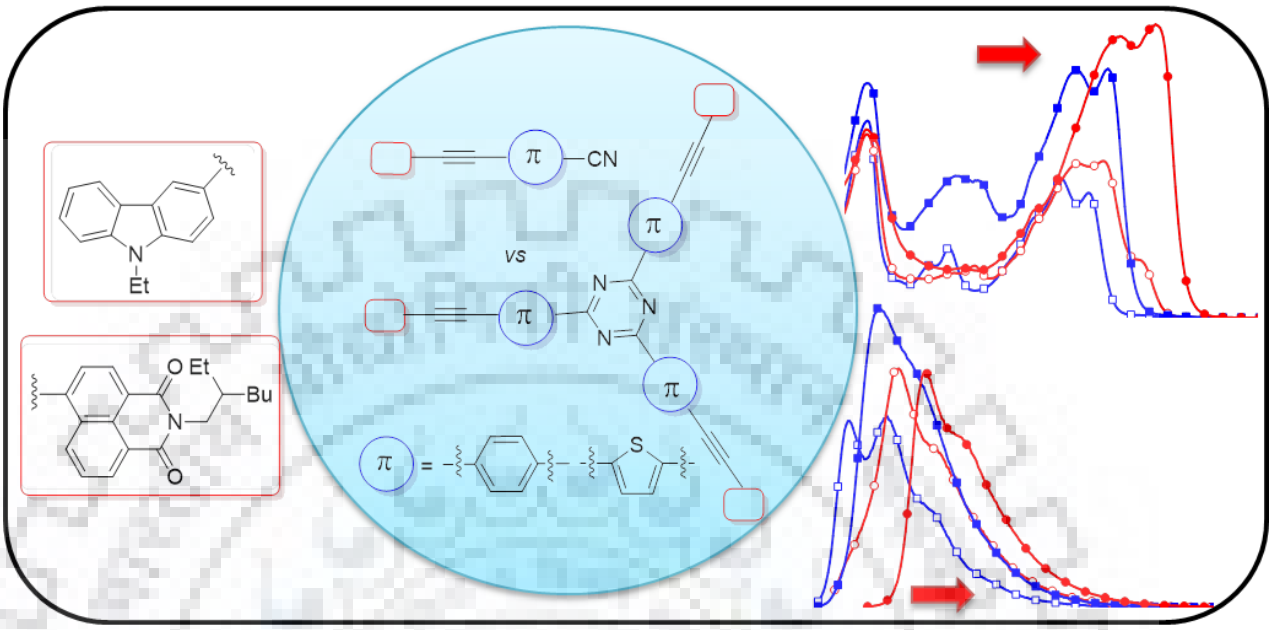

5.1 Introduction

The organic small molecules have gained tremendous attention as an important class of materials attributed to their unique optical and electronic properties. Their tunable properties make them attractive for applications in various organic electronic devices. There is a prompt progress in the field of large π-heteroaromatic conjugated molecules in organic electronics. Among various heteroaromatic cores, carbazole as electron rich and 1,8-naphthalimide as electron deficient core possessing C2 symmetric planar conjugated structure are preferably considered in developing conjugated materials. Owing to their planar extended system and easy functionalization, they offer great potential application in OLEDs, OPVs, OFETs, and fluorescent sensors.

Depending on the molecular topology of the conjugated derivatives, they are classified into linear and star-shaped molecules. Star-shaped organic materials represent a family of compounds featuring a central core unit linked to conjugating side arms that emanate as spikes from a central axle. The star-shaped molecules exhibit superior properties over linear molecules similar to dendrimers.[379-391] They possess well-defined molecular structures while retaining good solution processability, film-forming properties, and easy tunable properties. Such compounds tend to show distinct advantages over linear analogs in terms of molecular conformation, charge and energy transfer, self-assembly and thermal properties. Apart from these, the multiple conjugated side arms of star-shaped molecules benefits by tremendously altering the optical

properties of the dyes. However, with respect to efficient synthesis, such compounds in general require repetitive synthetic steps involving multiple couplings with overall low yields. So, utilizing a facile synthetic strategy that facilitates avoiding lengthy procedure is desirable.

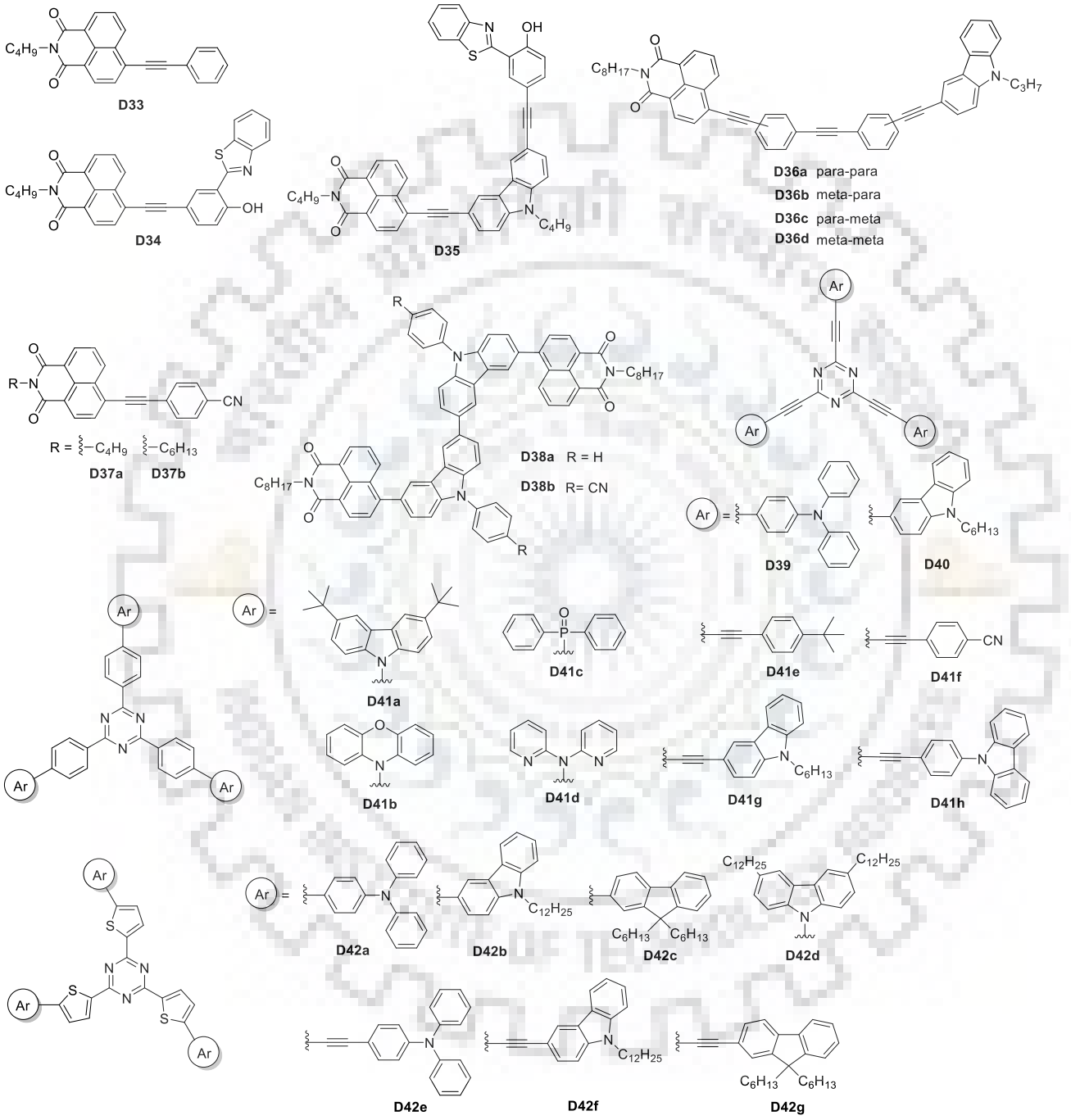

Chart 5.1 Structures of the related dyes.

Owing to the superior physico-chemical characteristics, a number of functional materials with different topology of the chromophores are designed and studied to unveil the properties of the dyes. A typical D-A linear shaped dyes, cyano-containing dyes and triazine molecules are

considered as a promising class of chromophores. A class of well-defined star-shaped compounds possessing triazine as the core and various chromophores as the branching arms has been synthesized and studied conveniently owing to its ease in synthesis and highly promising dipolar properties.[392-401] With this in regard, the development of D-A linear dyes and star-shaped triazine based-derivatives with particularly, donor groups are reported and their investigation are subjected to intense interest. Chart 5.1 displays the structures of related linear carbazole and naphthalimide-based and star-shaped triazine cored-dyes, **D33-D42**. Ma *et al*.[402] synthesized naphthalimide conjugated compounds, **D33-D35**. Dye **D35** exhibited the most red-shifted absorption band at 433 nm with $\Delta\lambda$ = 47 and 59 nm compared to that of **D34** and **D33**, respectively. Introduction of carbazole unit in **D35** resulted in extended π-conjugation. Lee *et al*.[403] synthesized linear and non-linear isomeric D-π-A dyes, **D36a-d** comprising carbazole donor and naphthalimide acceptor. The effect of difference in linkage is studied and found that the when compared to other isomers, *meta* linkage hampered the TPA properties, attributable to the poor D-A interactions in the ground state. Yang *et al*.[404] synthesized benzonitrile substituted dyes, **D37a** and **D37b** that absorbs at 372 nm and emits at 428 nm which is blue shifted compared to **D33**. However, dyes **D37a-b** displayed superior thermal stability. Zhang *et al*.[405] reported a D-A type naphthalimide-carbazole hybrid compounds, **D38a** and **D38b**, differing in cyano-substitution in later for organic memory storage devices. **D38b** displayed excellent memory storage attributable to facile energy level. The cyano-group benefited in lowering the E_{LUMO} compared to **D38a**, enhanced thermal stability, induced intermolecular interactions and effective film formation. Zhang *et al*.[406] synthesized star-shaped triazine-cored ($(D–\pi–)_3A$) compounds, **D39** and **D40** with different electron donating groups, namely, triphenylamine and carbazole, respectively exhibiting excellent two-photon absorption properties. **D39** displayed 35 nm red shifted absorption compared to that of **D40** attributed to extended π-π* conjugation in former. Matulaitis *et al*.[407] synthesized and characterized tri-substituted symmetric triazine-carbazole based electroluminescent materials, **D41a** and **D41g** differing in linking topologies of carbazole unit. Although dye **D41a** displayed superior thermal properties, **D41g** possessed a narrow band gap attributed to low-lying LUMO level and low oxidation potential of carbazole. This highlighted the ease of ICT in **D41g** compared to **D41a**. Tanaka *et al*.[408] synthesized a highly twisted triazine-substituted phenoxazine-based TADF active compound, **D41b** which displayed an EQE of 13.3 ±0.5% with yellow-orange emission arising from ICT. Jia *et al*.[409] reported tri-substituted triazine-phosphine oxide dye, **D41c** as an electron transporter for blue PHOLEDs with

low turn on-voltage of 2.5 V. **D41c** displayed deep seated HOMO and LUMO energy levels lying at -6.6 eV and -3.4 eV, respectively owing to its strong electron affinity. Pang *et al.*[410] synthesized a star burst triazine cored-di-pyridylaminophenyl substituted dye, **D41d** and characterized it as a blue emitters in electroluminescent devices that it absorbs at 386 nm and strongly emit at 440 nm in solution and solid state. It possesses a high lying HOMO level at -4.99 eV attributable to its electron deficiency. Aihara *et al.*[411] synthesized a blue emitter, **D41e** possessing phenylethynyl as brancing arms on triazine core and studied its EL properties with emission at 406 nm. Ranganathan *et al.*[412] synthesized a highly rigid and symmetric triazine-cored cyano-substituted phenylacetylene derivative, **D41f** that absorbs at 353 nm and exhibited a sharp emission peak at 386 nm. It displayed a strong π-stacking interaction owing to effective inter-molecular interactions. Zhang *et al*.[413] synthesized a carbazole-triazine cored dye, **D41h** and found that it absorbs at 361 nm and emit strongly at 500 nm possessing a solvent stabilized charge transfer in excited state ($\Delta\lambda$ = 60 nm). Zou *et al*.[414] synthesized and compared a set of C-C single and C-C triple bonded star-shaped D-π-A dyes, **D42a-c** and **D42e-g**, respectively. It was found that dyes **D42e-g** exhibited superior photophysical properties and deep seated energy levels over their C-C- bonded analogs. Further, the optical properties of these dyes were investigated to exhibit a red-shifted absorption compared to their phenyl-linked analogs. Yasuda *et al*.[415] synthesized a propeller-shaped D-π-A type triazine-cored carbazole based dye, **D42d** which absorbs at 415 nm and exhibited a broad fluorescence band at 503 nm. However, it was revealed that the *N*-carbazolyl units behave as an independent electronic entity with poor electronic coupling towards triazine-core. It is revealed from the illustrated examples that the C–C triple bond exhibited improved stability compared to its C-C double and single bonded D-A based analogs. It also helped in extension of conjugation and facile electronic coupling. Further, introduction of cyano-group to the molecular scaffold lies in strengthening the electron deficiency, thermal properties and tuning the energy level of the compounds. While, the advantages of tailoring the linear organic materials to star-shaped architecture rely in improving the conformational effects, molar extinction coefficients, charge transfer and thermal stability. The synergy of π-electron-rich thienyl group and a C-C triple bond into the triazine-cored dyes were illustrated to be effective with superior photophysical properties. Moreover, among the triazine-cored dyes, there is no report with naphthalimide to study the effect of improvised electron deficiency. All these aspects prompted us to introduce these in newly designed dyes.

In this Chapter, we have discussed and highlighted the design strategy of carbazole and naphthalimide units as star-shaped molecules and compared their unique physico-chemical properties with their linear analogs (Figure 5.1). We have synthesized triazine-cored star shaped compounds with electron rich and electron deficient side arms for comparison and investigated the effect of substitution on optical, electrochemical and thermal properties compared to control linear analogs.

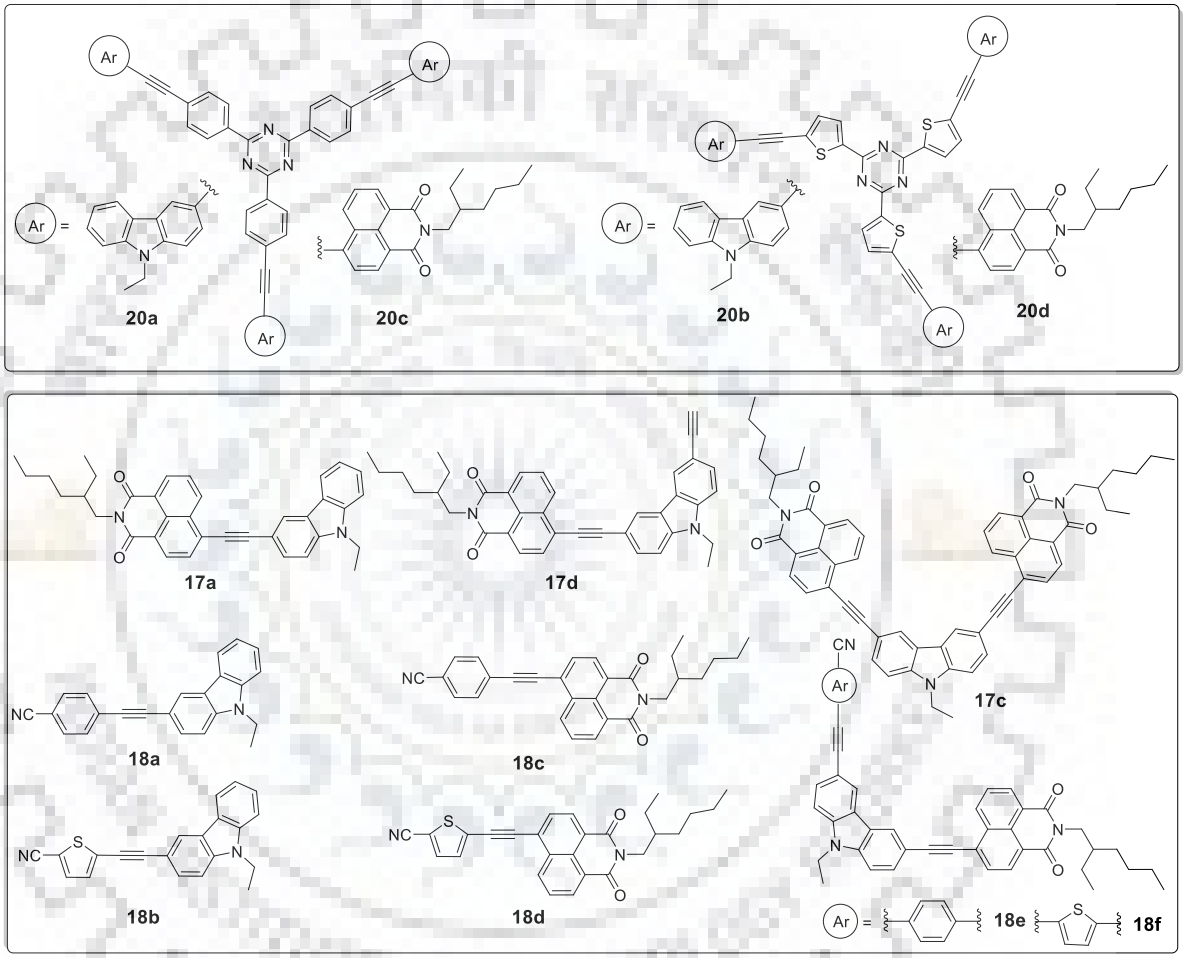

Figure 5.1 Structures of target star-shaped dyes and control linear dyes.

5.2 Results and Discussion

5.2.1 Synthesis and Characterization

The synthetic protocol of the control linear and star-shaped dyes is displayed in Scheme 5.1, 5.2 and 5.3. The dyes **17a-17d** were synthesized using Sonogashira coupling reaction between respective terminal acetylene (**2** or **15**) and mono- or di-bromo-derivative (**1** or **16**). **17c** was obtained as di-substituted product along with **17b**. The intermediate **17b** was subsequently treated with trimethylsilylacetylene and deprotected to obtain the required terminal acetylene, **17d**. The target star-shaped triazine-cored dyes, **20a-20d** were obtained in two step initiated by following literature procedure for acid catalyzed trimerization of bromo-arylnitriles [410, 412, 415] to yield tri-bromo substituted triazine core, **19a** and **19b** followed by Sonogashira coupling reaction with **2** and **15** in moderate yields. We obtained mono- and di-bromo substituted triazine-cored compounds as side-products. We made an attempt to synthesize asymmetric triazine-cored dyes and symmetrically substituted triazine dyes with **17d** but failed to obtain the desired products. Thus, we planned to synthesize another set of control dyes as linear carbazole and/ or naphthalimide-based cyano analogs, **18a-18f**. They were synthesized by employing Sonogashira reaction between terminal acetylene, **2**, **15** and **17d** with respective bromo-arylnitrile in good to moderate yield. All the compounds were thoroughly characterized by spectroscopic techniques such as NMR and mass spectral studies. The spectral data of the dyes are consistent with the proposed structures. The dyes show moderate solubility in common organic solvents such as Tol, TEA, TCE, DCB, $CHCl_3$, DCM, THF and DMF.

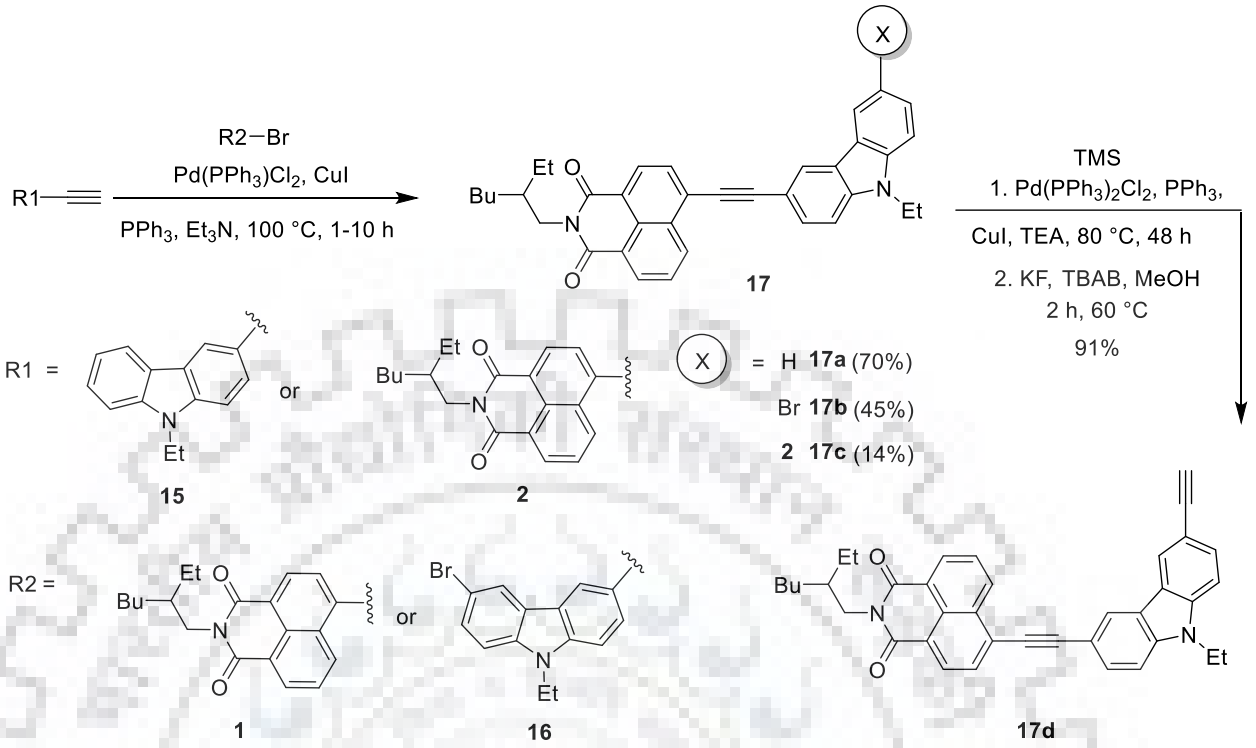

Scheme 5.1 Synthetic protocol for carbazole and naphthalimide-based linear D-A dyes.

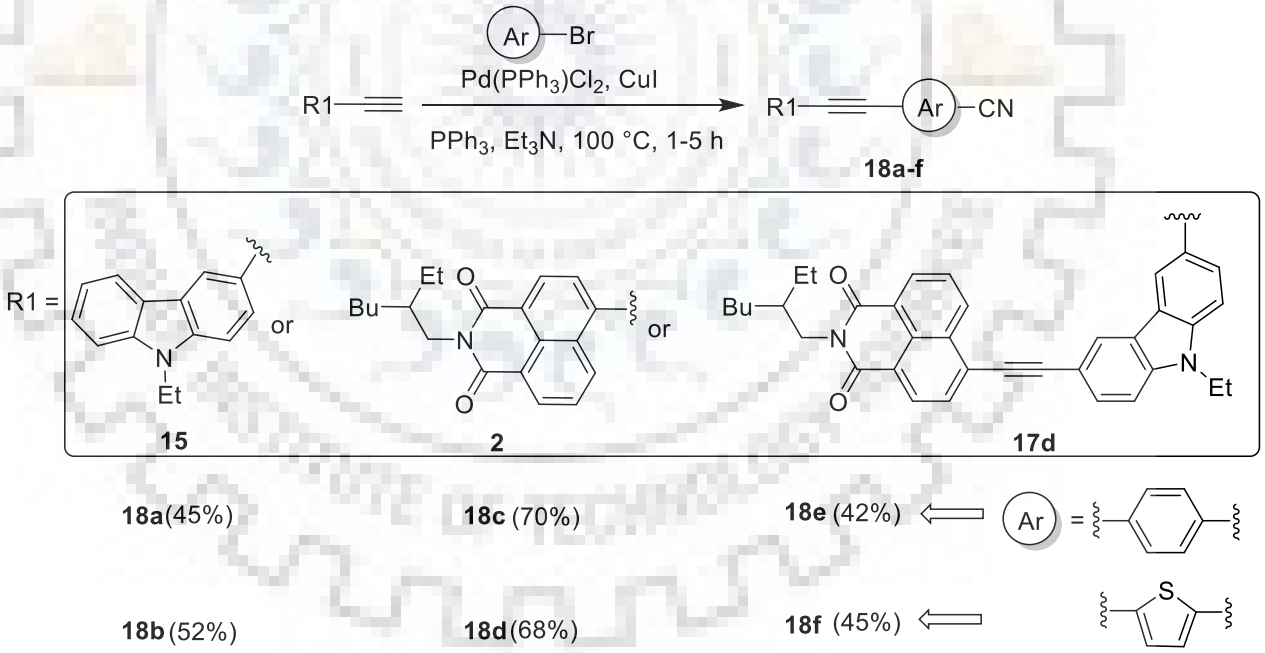

Scheme 5.2 Synthetic protocol for carbazole and/or naphthalimide-based linear D-A cyano analogs.

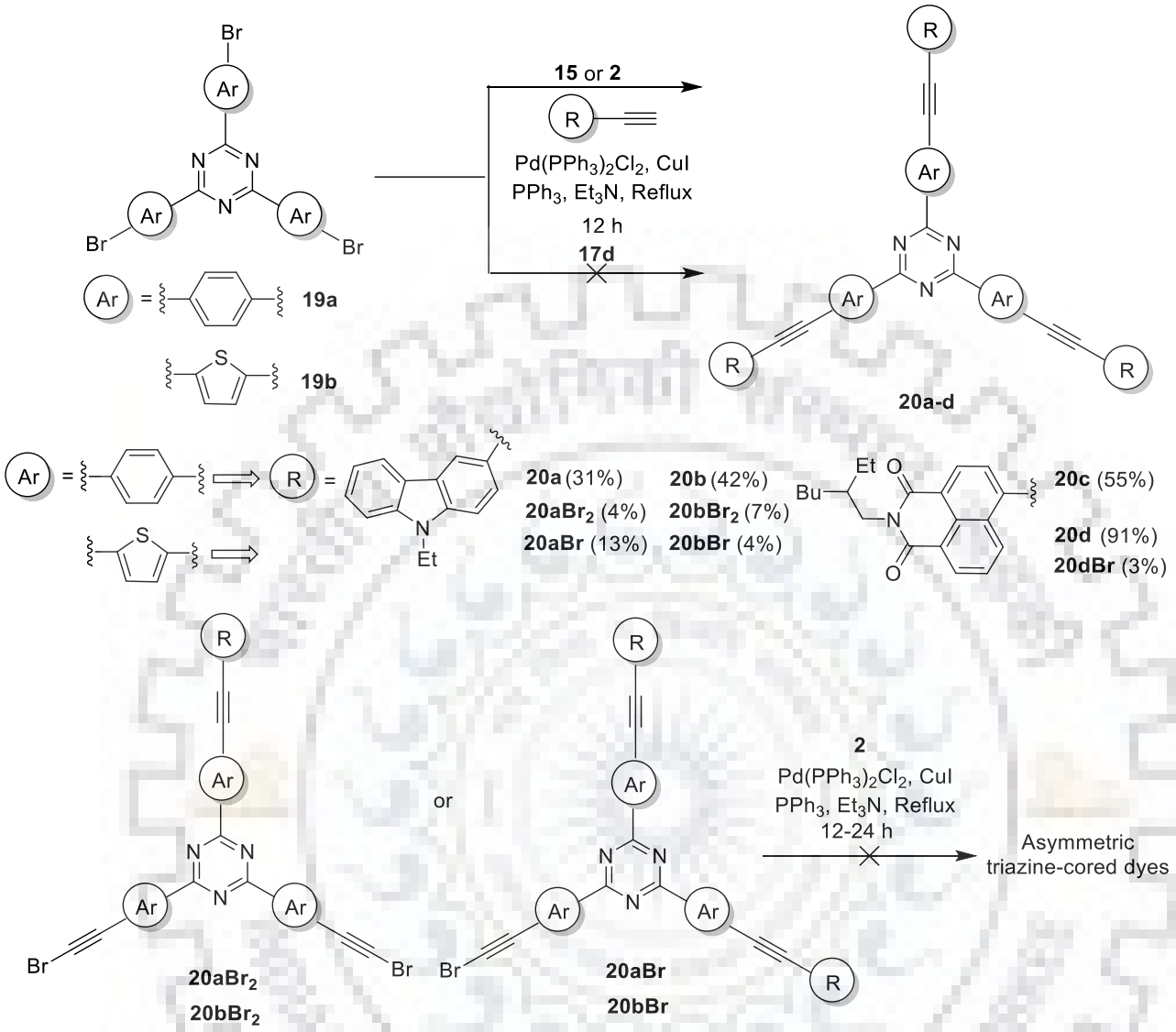

Scheme 5.3 Synthetic protocol for carbazole or naphthalimide-based star-shaped triazine-cored target dyes.

5.2.2 Photophysical Properties

The absorption spectra of the linear analogs and star-shaped dyes recorded in DCM are displayed in Figure 5.2 and the relevant photophysical data listed in Tables 5.1 and 5.2, respectively. The typical D-A carbazole-naphthalimide-based linear dyes, **17a**, **17d** and **17c** exhibit two distinctive absorption bands, originating from carbazole localized π-π* at shorter wavelength, 280-320 nm and other at longer wavelength, 430 nm which is assigned to the conjugated naphthalimide unit (Figure 5.2(a)). The hypochromic vibronic bands observed at 340-370 nm is attributed to the n-π* transitions of carbazole and naphthalimide.[416] A hyperchromic shift of longer wavelength band is observed for **17c** compared to other two analogs, attributable to presence of additional naphthalimide unit. While, among the set of cyano- containing dyes, **18a-18f**, the red-shift in absorption wavelength is observed due to the elongation in the conjugating length of the molecular skeleton (Figure 5.2(b)). All the dyes exhibit two prominent bands. The shorter wavelength band is assigned to the characteristic absorption band due to localized π-π* transitions of the building blocks such as carbazole and naphthalimide units. While, the absorption band at longer wavelength corresponds to the π-π* transitions arising from the conjugated system except for **18e** and **18f**, where it corresponds to conjugated naphthalimide unit similar to dye **17a**. Dyes **18c** and **18d** possess structured absorption band when compared to their carbazole analogs. The presence of thienyl-group helps in effective conjugation pathway which red-shifted the absorption profile due to the coplanar arrangement. Thus, the thienyl-based dyes display a bathochromic shift of 10 nm when compared to their respective phenyl-analogs except **18e** and **18f**. Dyes **18e** and **18f** display absorption profile similar to their analog, **17d**. The introduction of carbazole unit induces a red shift by 38 and 27 nm, respectively for phenyl and thienyl-dyes, **18c** and **18d**. While the incorporation of naphthalimide with **18a** and **18b** brings a large bathochromic shift of 64 nm and 55 nm, when compared to **18e** and **18f**. The star-shaped dyes (**20a-20d)** display prominently two absorption bands, one at shorter wavelength attributed to the triazine core and other at longer wavelength corresponding to the π-conjugated system (Figure 5.2(c)). The absorption profile displays that replacement of carbazole by naphthalimide results in bathochromic shift by 10-15 nm which is however, less compared to linear analogs. This could be due to the disruption of π-conjugation in the star-shaped dyes. However, the absorption peaks of all the dyes ascribed to the combined n-π* and π-π* transitions is red-shifted compared to 1,3,5-triazine (210 nm), 2,4,6-triphenyl-1,3,5-triazine (270 nm) and 2,4,6-tris(thiophen-2-yl)triazine (314 nm) attributed to the extended π–π* transition of the branched structure. Further, the molar extinction coefficient of

these dyes is enhanced corresponding to the transition probabilities compared to linear analogs. The thienyl-triazine dyes, **20b** and **20d** show a bathochromic λ_{max} ascribed to the strengthened π-electron density of the 1,3,5-triazine-based star shaped dyes. The λ_{max} of **20b** at 427 nm is red-shifted by 42 nm relative to that of **20a**. Similarly, **20d** exhibits a 30 nm bathochromic shift when compared to **20c**.

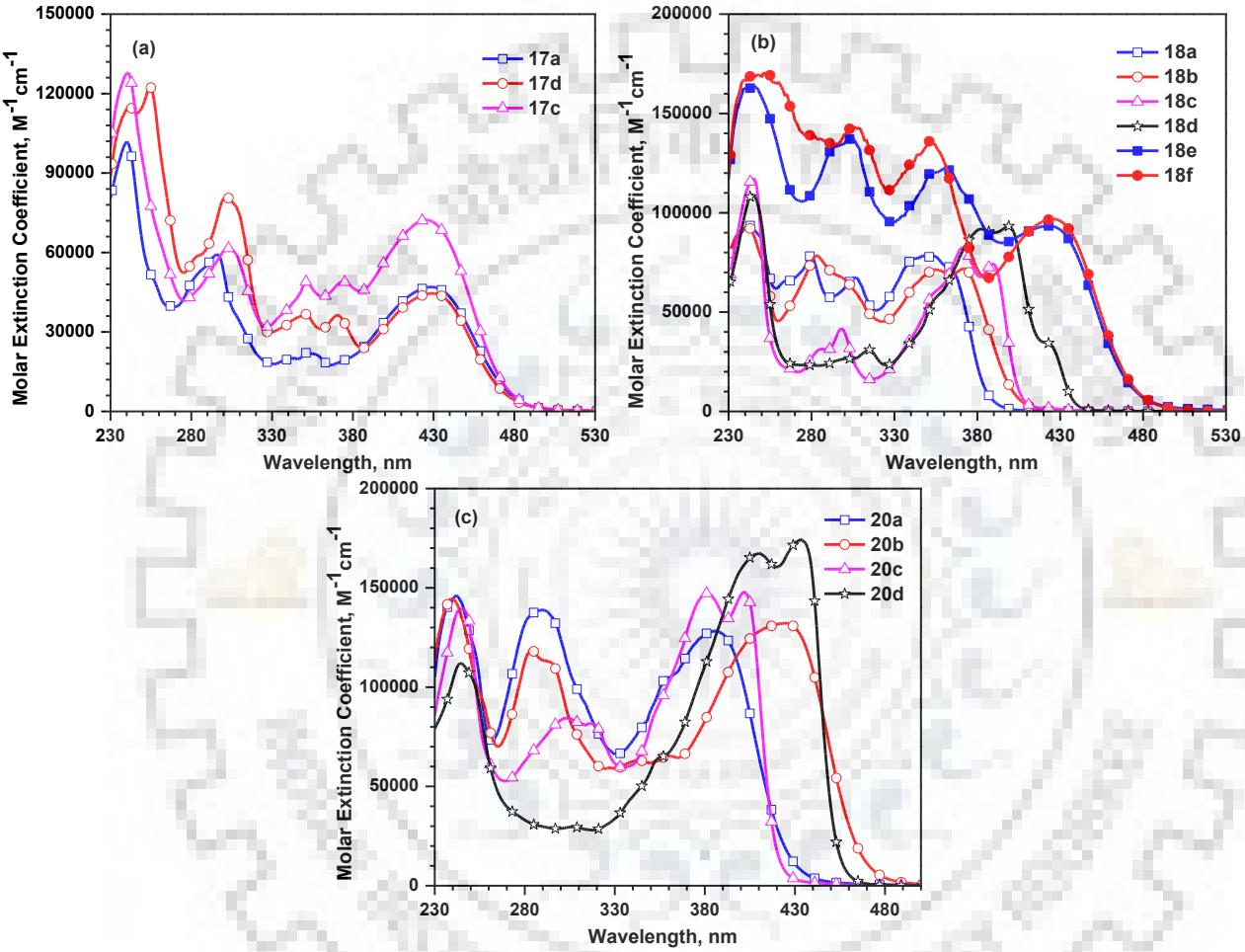

Figure 5.2 Absorption spectra of the dyes recorded in DCM.

The emission spectra of the dyes recorded in DCM are displayed in Figures 5.3. The typical linear D-A dyes, **17a**, **17c** and **17d** displayed a broad emission band at ~550 nm attributable to CT in excited state. However, the fluorescence spectra of naphthalimide-based cyano-containing linear analogs, **18c** and **18d** display structured vibronic peaks compared to carbazole-analogs, **18a** and **18b**. While, **18e** and **18f** show the most red-shifted broad emission band similar to **17a**. It is observed that carbazole-based dyes, **18a** and **18b** display red-shifted emission compared to that of naphthalimide-based dyes, **18c** and **18d**. This could be ascribed to the formation of typical CT excited state in the former. Among these dyes, thienyl-based dyes display red-shifted emission attributed to extension in

conjugation length. For the star-shaped dyes, **20a** and **20b** exhibit typical D-A behavior attributed to electron donating carbazole and electron deficient triazine unit. The dyes depict similar behavior as their linear analogs with red-shifted emission. Dyes **20c** and **20d** show structured profile due to molecular rigidity and strong electron deficiency. Further, the dyes **20b** and **20d** exhibit a bathochromic shift by 20 and 30 nm, respectively compared to their phenyl-analogs. This is ascribed to the electron density provided by thienyl-group. Also, the star-shaped phenyl-based dyes, **20a** and **20c** has shown a bathochromically shifted emission with respect to parent core, triphenyl-triazine core which emits at 366 and 475 nm corresponding to monomeric and excimer emission, respectively.[409] This is due to the extended π-conjugation introduced by carbazole and naphthalimide units. It is worth to note that the naphthalimide-based linear and triazine star shaped dyes, **18c-18d** and **20c-20d** exhibit smaller Stokes shift when compared to carbazole-based and other D-A analogs due to absence of significant CT owing to the electron deficiency induced by naphthalimide.

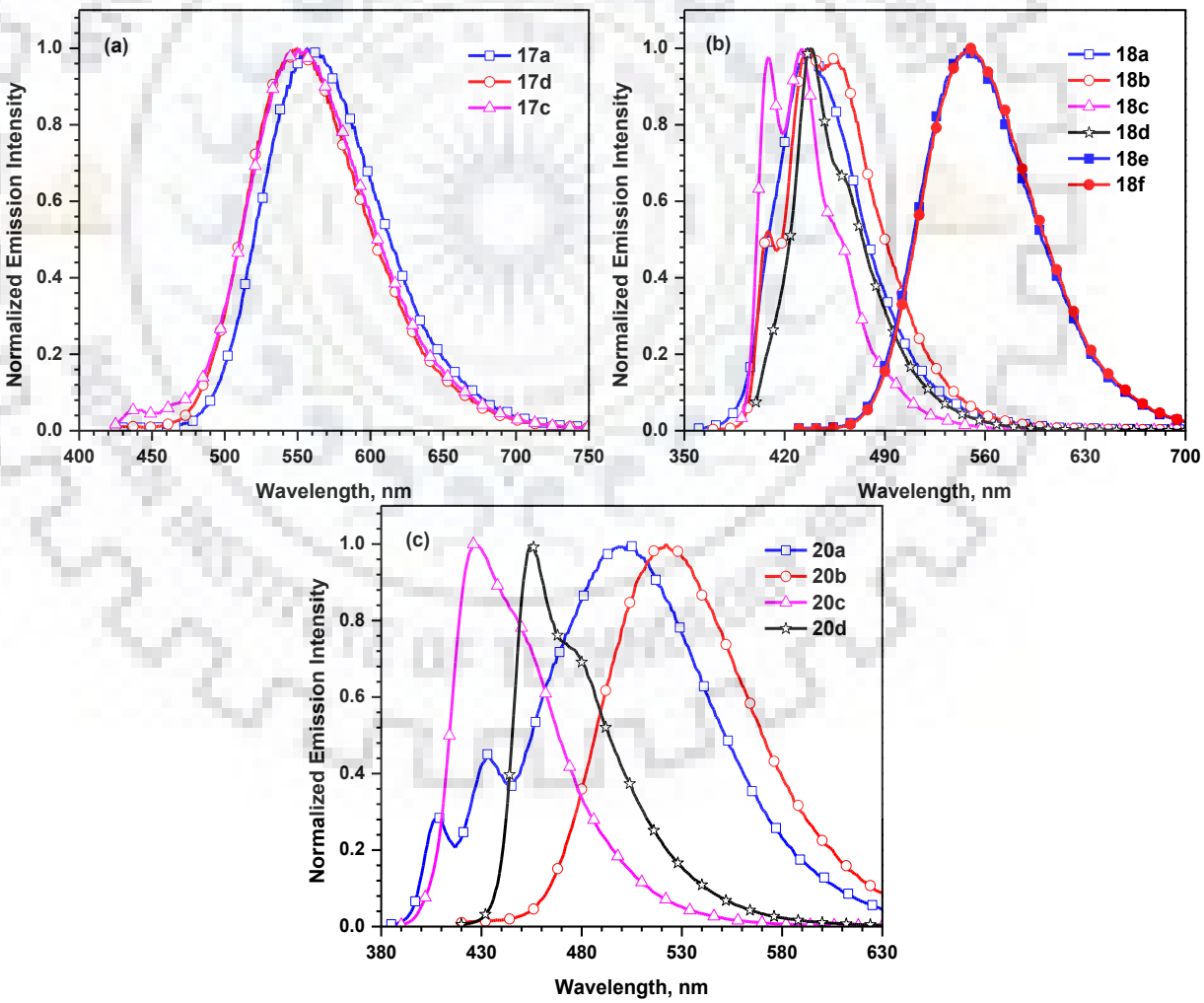

Figure 5.3 Normalized emission spectra of the dyes recorded in DCM.

Table 5.1 Optical, electrochemical and thermal data of linear control dyes.

Dye	λ_{max}, nm (ε_{max}, $10^3 \times M^{-1} cm^{-1}$)	λ_{em}, nm	Stokes Shift, cm^{-1}	E_{ox},[a] V	E_{red},[a] V	HOMO,[b] eV	LUMO,[c] eV	E_{0-0},[d] eV	T_d,[e] °C
17a	429 (46.9), 354 (21.8), 342 (20.1), 296 (59.2)	550	5128	0.75	-1.69	-5.55	-3.11	2.44	360
17d	432 (44.3), 370 (3.3), 351 (36.7), 303 (80.6)	550	4966	0.91	-1.64	-5.71	-3.16	2.55	435
17c	428 (72.0), 374 (49.9), 351 (48.9), 303 (61.6)	550	5183	0.88	-1.66	-5.68	-3.14	2.54	374
18a	364 (72.2), 350 (78.3), 306 (67.4), 280 (78.4)	435	4484	0.75	-	-5.55	-3.11	3.14	295
18b	372 (71.9), 356 (71.3), 300 (66.5), 284 (78.2)	445	4410	0.78	-	-5.71	-3.16	3.08	350
18c	390 (74.2), 372 (82.5), 298 (41.7), 285 (31.2)	409, 432 (sh)	1191	-	-1.58	-6.21	-3.22	2.99	356
18d	400 (92.9), 382 (91.8), 315 (31.1), 298 (26.1)	436, 462 (sh)	2064	-	-1.41	-6.27	-3.39	2.88	365
18e	428 (92.5), 360 (122.2), 305 (137.4)	547	5083	0.80	-1.69	-5.60	-3.15	2.49	336
18f	427 (96.8), 352 (136.6), 308 (142.1)	550	5238	0.80	-1.64	-5.60	-3.16	2.44	367

[a] Oxidation and reduction potentials are reported with reference to ferrocene, [b] Deduced from the oxidation potential using the formula, HOMO = -(4.8 + E_{ox}), [c] Deduced from the reduction potential using the formula, LUMO = -(4.8 + E_{red}),[d] Obtained from intersection of absorption and emission band or using formula, E_{HOMO}-E_{LUMO}, [e] thermal decomposition temperature at 5% weight loss.

Table 5.2 Optical, electrochemical and thermal data of star-shaped target dyes.

Dye	λ_{max}, nm (ε_{max}, $10^3 \times M^{-1} cm^{-1}$)	λ_{em}, nm	Stokes Shift, cm^{-1}	E_{ox},[a] V	E_{red},[a] V	HOMO,[b] eV	LUMO,[c] eV	E_{0-0},[d] eV	T_d,[e] °C
20a	385 (128.2), 289 (138.80, 240 (146.2)	500	5974	0.66	-	-5.46	-2.58	2.88	442
20b	427 (131.9), 284 (118.6), 241 (143.9)	522	4262	0.48	-	-5.28	-2.69	2.59	429
20c	402 (148.0), 382 (147.1), 307 (83.5), 245 (13.9), 245 (111.85)	426, 450 (sh)	1401	-	-1.61	-6.18	-3.19	2.99	428
20d	433 (174.2), 409 (166.8), 245 (111.85)	456, 478 (sh)	1165	-	-1.56	-6.02	-3.24	2.78	436

[a] Oxidation and reduction potentials are reported with reference to ferrocene, [b] Deduced from the oxidation potential using the formula, HOMO = -(4.8 + E_{ox}), [c] Deduced from the reduction potential using the formula, LUMO = -(4.8 + E_{red}),[d] Obtained from intersection of absorption and emission band or using formula, E_{HOMO}-E_{LUMO}, [e] thermal decomposition temperature at 5% weight loss.

Table 5.3 Photophysical data of the linear dyes.

Dye	λ_{max}, nm							λ_{em}, nm							
	TOL	TEA	TCE	DCB	$CHCl_3$	THF	DMF	TOL	TEA	TCE	DCB	$CHCl_3$	THF	DMF	Solid
17a	430	426	428	435	434	426	430	467	467	500	517	537	547	615	735
17d	432	430	432	436	435	432	427	478	478	498	513	528	539	600	718
17c	425	420	427	430	428	422	426	469	469	498	512	532	539	610	720
18a	364	360	365	368	365	364	364	384	384	400	416	420	430	463	697
18b	372	370	375	372	370	372	374	408	408	422	432	436	437	480	660
18c	390	-	390	390	390	387	390	409, 432 (sh)	-	409, 432 (sh)	410, 432 (sh)	409, 432 (sh)	408, 430 (sh)	432	692
18d	400	-	400	402	400	397	399	436, 461 (sh)	-	436, 461 (sh)	437, 461 (sh)	436, 461 (sh)	435, 459 (sh)	460	677
18e	429	430	430	430	430	423	426	465	465	491	507	526	540	602	673
18f	429	432	432	432	432	422	426	464	465	490	505	525	538	605	650

Table 5.4 Photophysical data of the star-shaped dyes.

Dye	λ_{max}, nm							λ_{em}, nm							
	TOL	TEA	TCE	DCB	$CHCl_3$	THF	DMF	TOL	TEA	TCE	DCB	$CHCl_3$	THF	DMF	Solid
20a	392	392	395	397	392	390	392	440, 466 (sh)	440, 466 (sh)	461	472	496	503	555	730
20b	430	430	430	432	432	430	432	452, 470 (sh)	452, 470 (sh)	470	487	495	517	570	710
20c	402	-	402	405	402	400	401	418, 438 (sh)	-	419, 438 (sh)	418, 438 (sh)	419, 438 (sh)	420, 438 (sh)	445	713
20d	433	-	433	435	435	430	433	450, 475 (sh)	-	452, 475 (sh)	450, 475 (sh)	451, 475 (sh)	450, 471 (sh)	470	696

Table 5.5 Stokes shift of the dyes.

Dye	Stokes Shift, cm^{-1}						
	TOL	TEA	TCE	DCB	$CHCl_3$	THF	DMF
17a	1842	2061	3365	3646	4419	5193	6996
17d	2228	2335	3068	3443	4049	4595	6752
17c	2207	2488	3339	3725	4567	5144	7081
18a	1431	1736	2397	3135	3588	4217	5874
18b	2372	2517	2970	3734	4091	3998	5905
18c	1191	-	1191	1191	1251	1329	2493
18d	2064	-	2064	1992	2064	2200	3324
18e	1804	1750	2889	3532	4244	5122	6863
18f	1758	1643	2740	3346	4101	5109	6945
20a	2783	2783	3625	4003	5349	5760	7492
20b	1132	1132	1979	2614	2946	3913	5604
20c	952	-	1009	971	1009	1190	2466
20d	872	-	971	766	816	1034	1818

In order to get insight into the effect of solvent polarity on the photophysical properties of the dyes, solvatochromism of the dyes were measured (Table 5.3). The change in the nature of solvent does not bring significant shifts in the absorption spectra of the dyes (Figures 5.4, 5.5 and 5.6). This means the dyes are non-polar in the ground state.

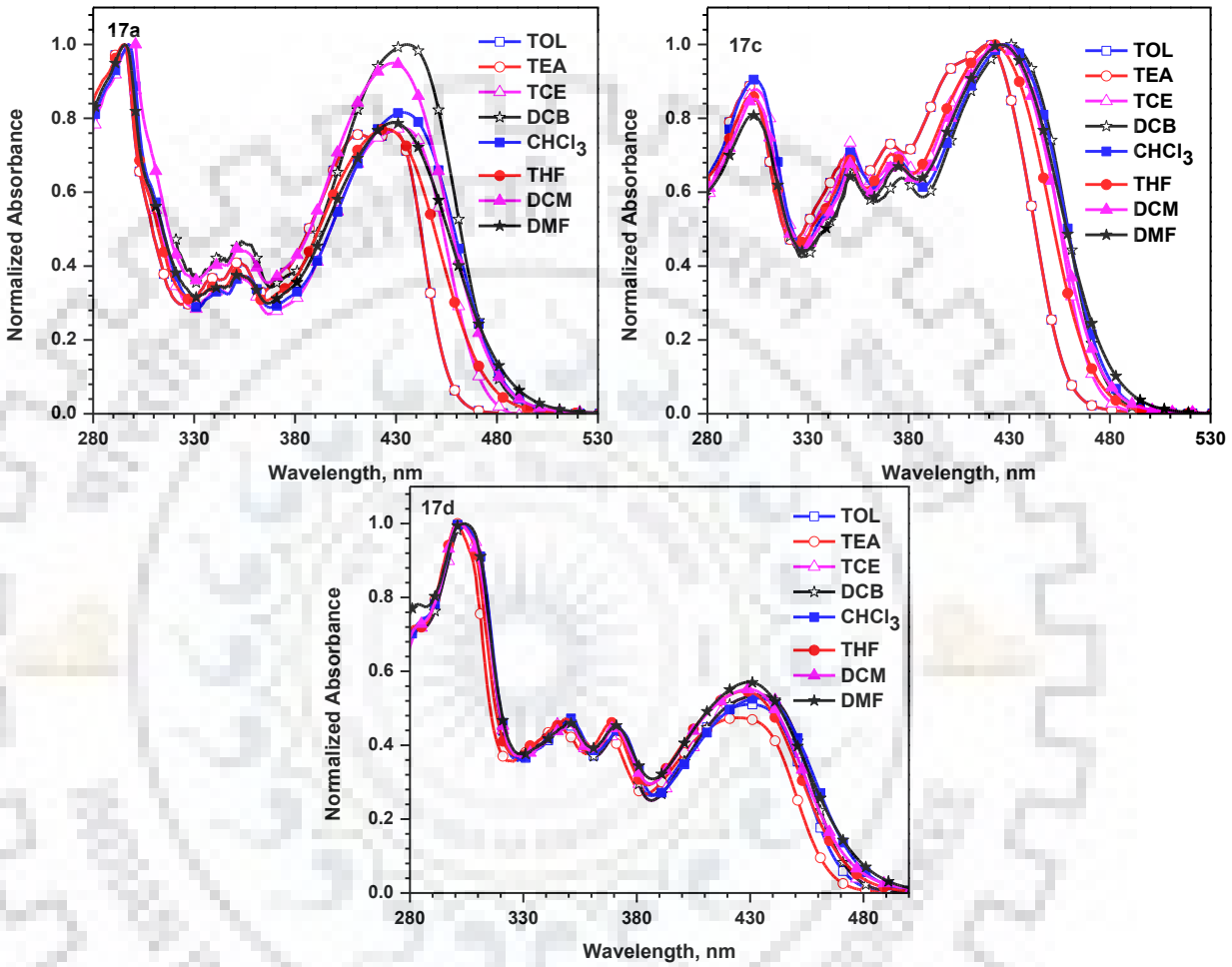

Figure 5.4 Absorption spectra of the dyes **17a**, **17c** and **17d** recorded in different solvents.

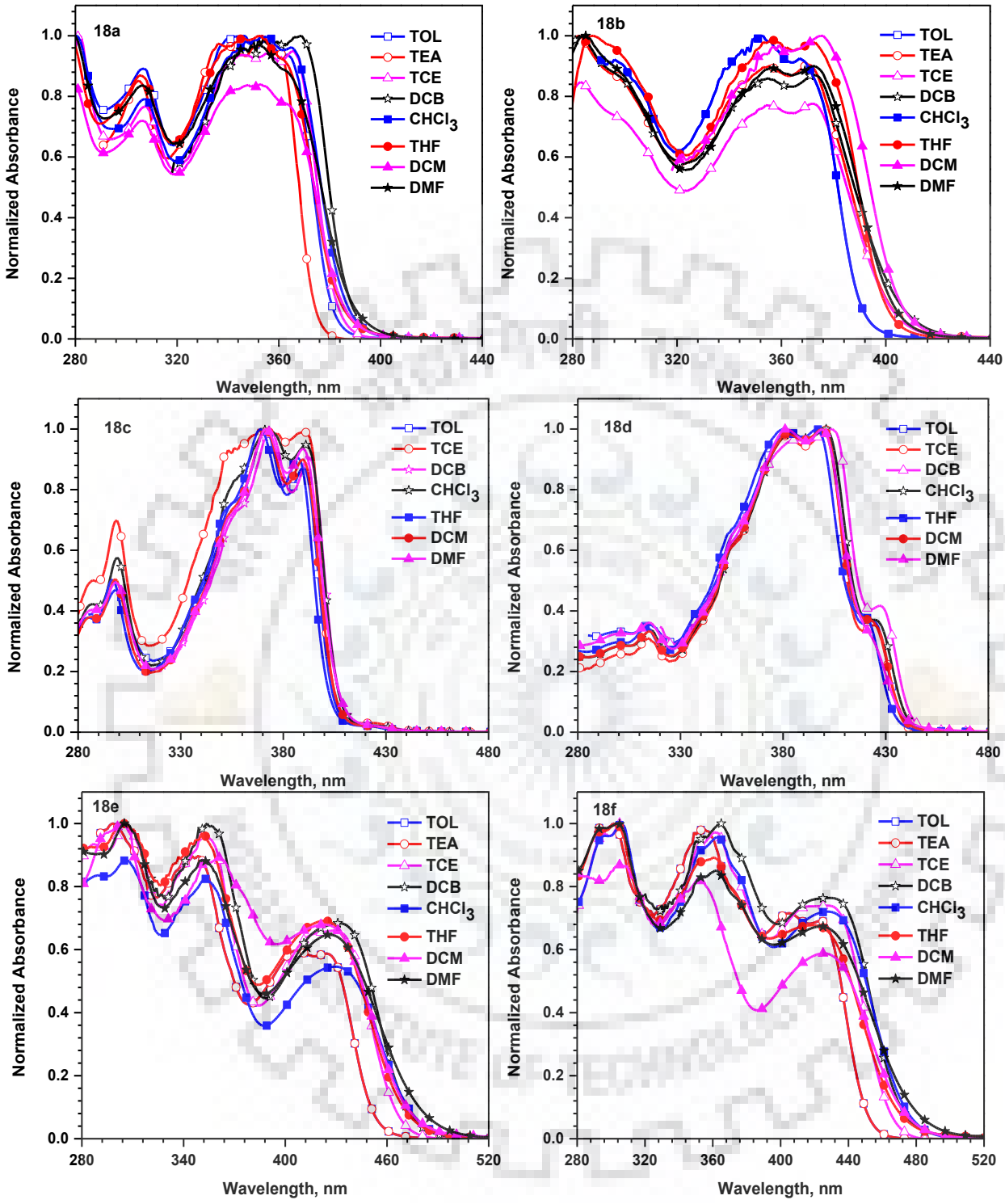

Figure 5.5 Absorption spectra of the dyes **18a-18f** recorded in different solvents.

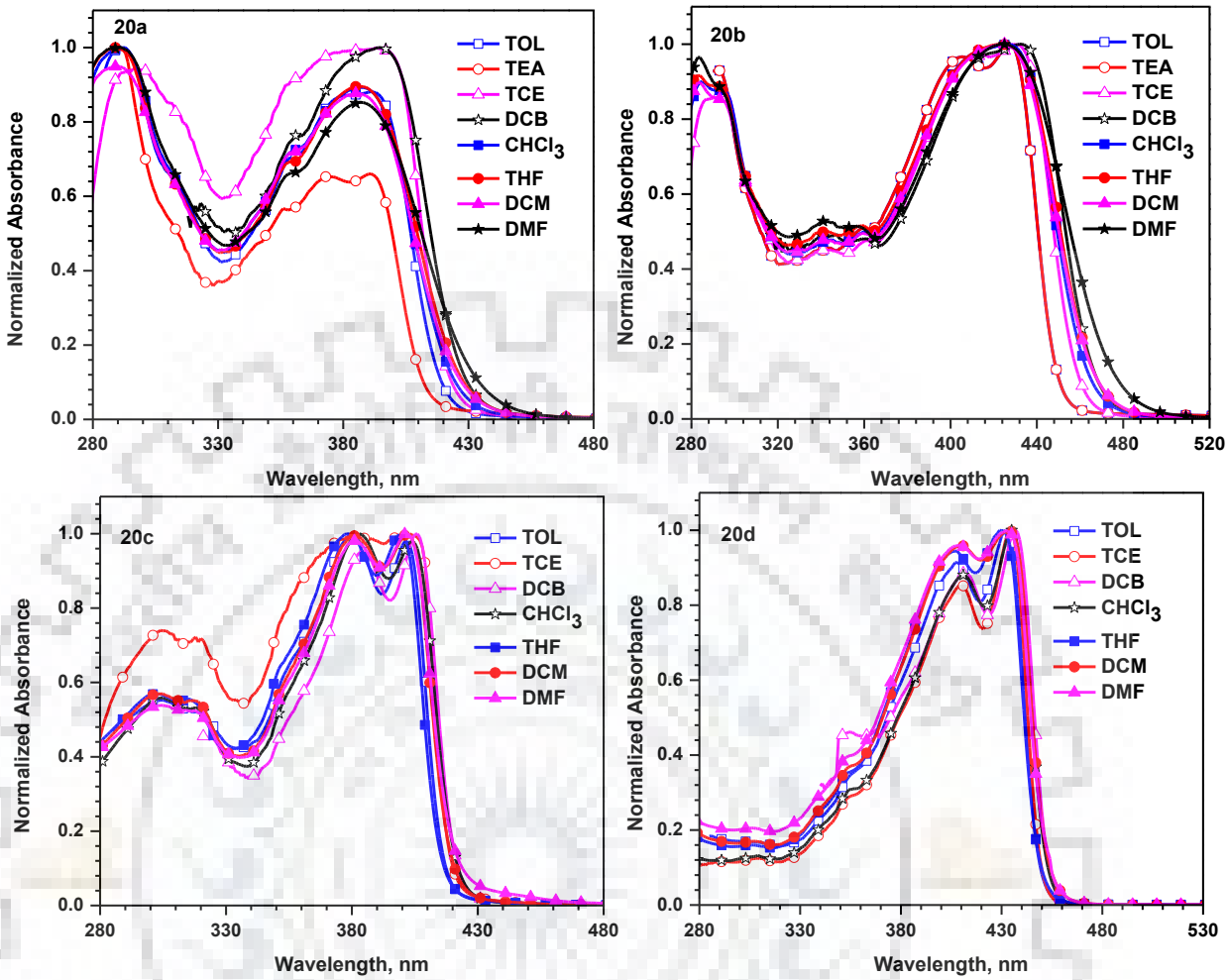

Figure 5.6 Absorption spectra of the dyes **20a-20d** recorded in different solvents.

In general, the photophysical properties of dyes with CT excited state display solvatochromism as the polarity of the solvent increases. To investigate the stability of the CT states of the dyes, we recorded their emissive properties. The fluorescence spectra for linear and star-shaped dyes recorded in different solvents is displayed in Figures 5.7, 5.8 and 5.9 and pertinent data compiled in Tables 5.3 and 5.4. It was observed that naphthalimide-based dyes (**18c**, **18d**, **20c** and **20d)** display a fluorescence band exhibiting vibronic features attributable to the rigidness and electron deficiency of the dyes. Furthermore, all the dyes except the former dyes display red-shifting and broadening of the emission spectra as the solvent polarity increases due to bipolar nature of the dyes. This confirmed the CT nature of the excited state with respect to the absorption profile. Similarly, dyes **17a**, **17c** and **17d** show structureless emission band attributed to the formation of stable CT excited state due to presence of typical dipolar nature of the dyes as mentioned earlier. Dyes **18a** and **18b** display a prominent positive solvatochromism compared to

dyes, **18c** and **18d**. The presence of pronounced polar character in the excited state than ground state is supported by large Stokes shift in polar solvents (Table 5.5).

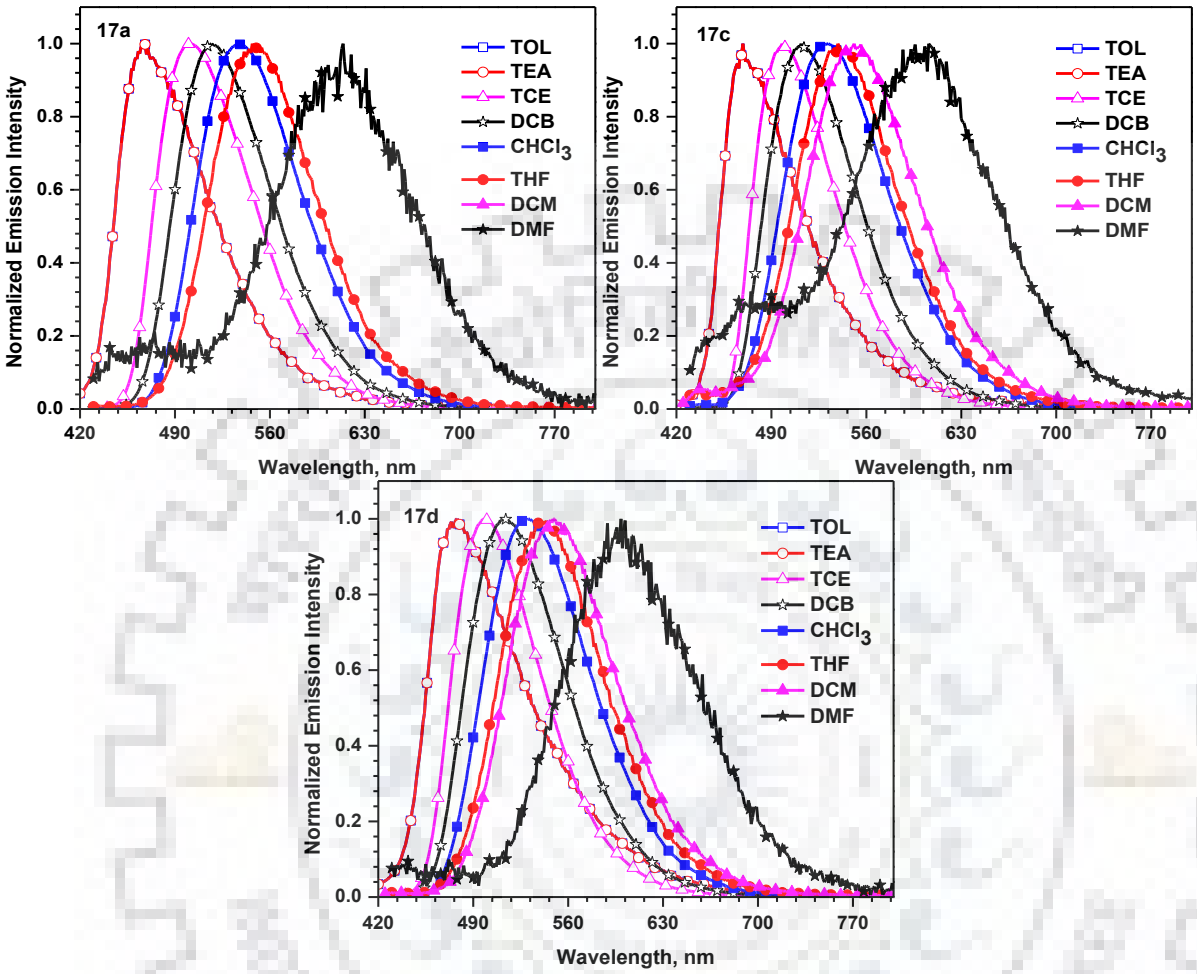

Figure 5.7 Normalized emission spectra of the dyes **17a**, **17c** and **17d** recorded in different solvents.

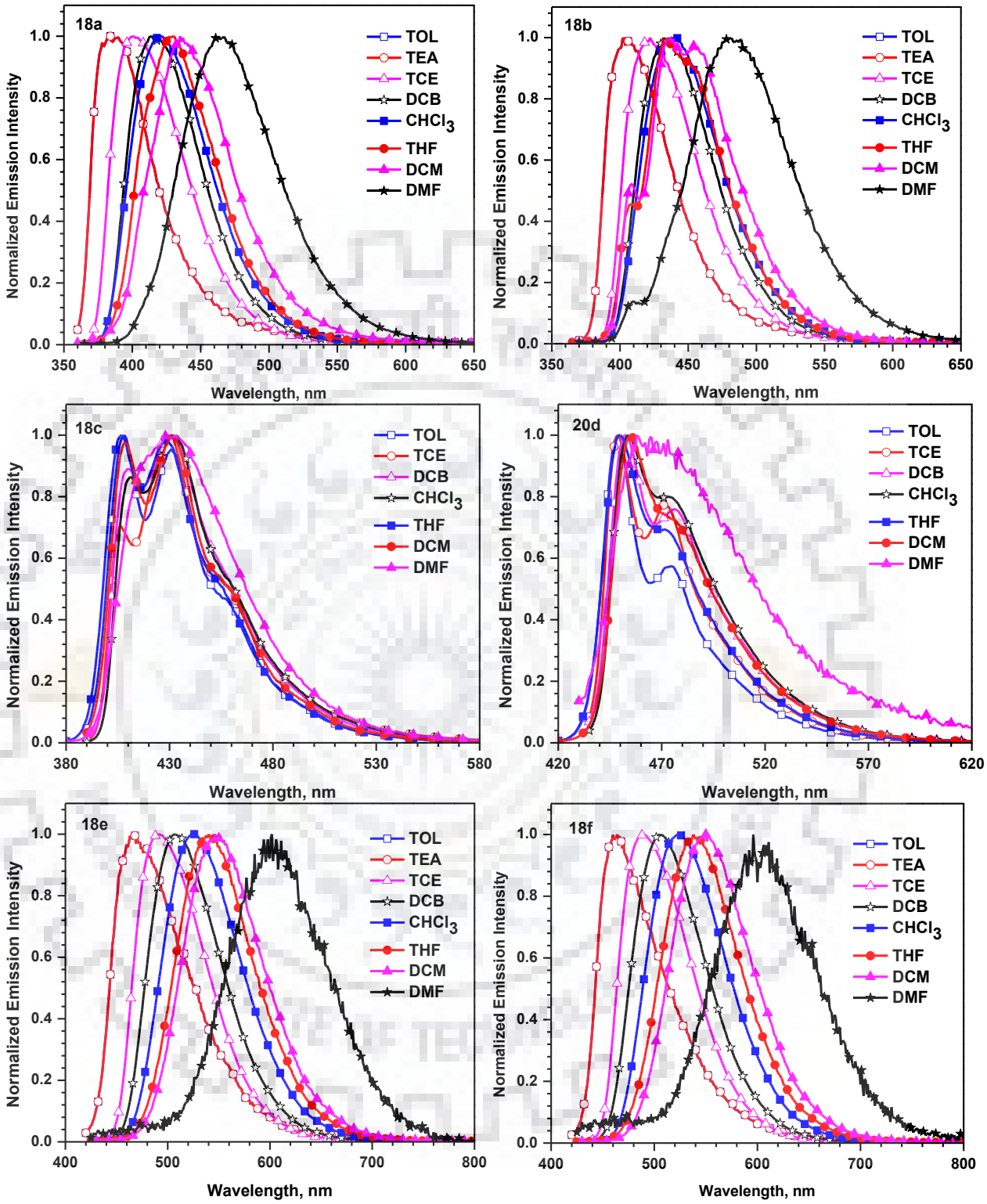

Figure 5.8 Normalized emission spectra of the dyes **18a-18f** recorded in different solvents.

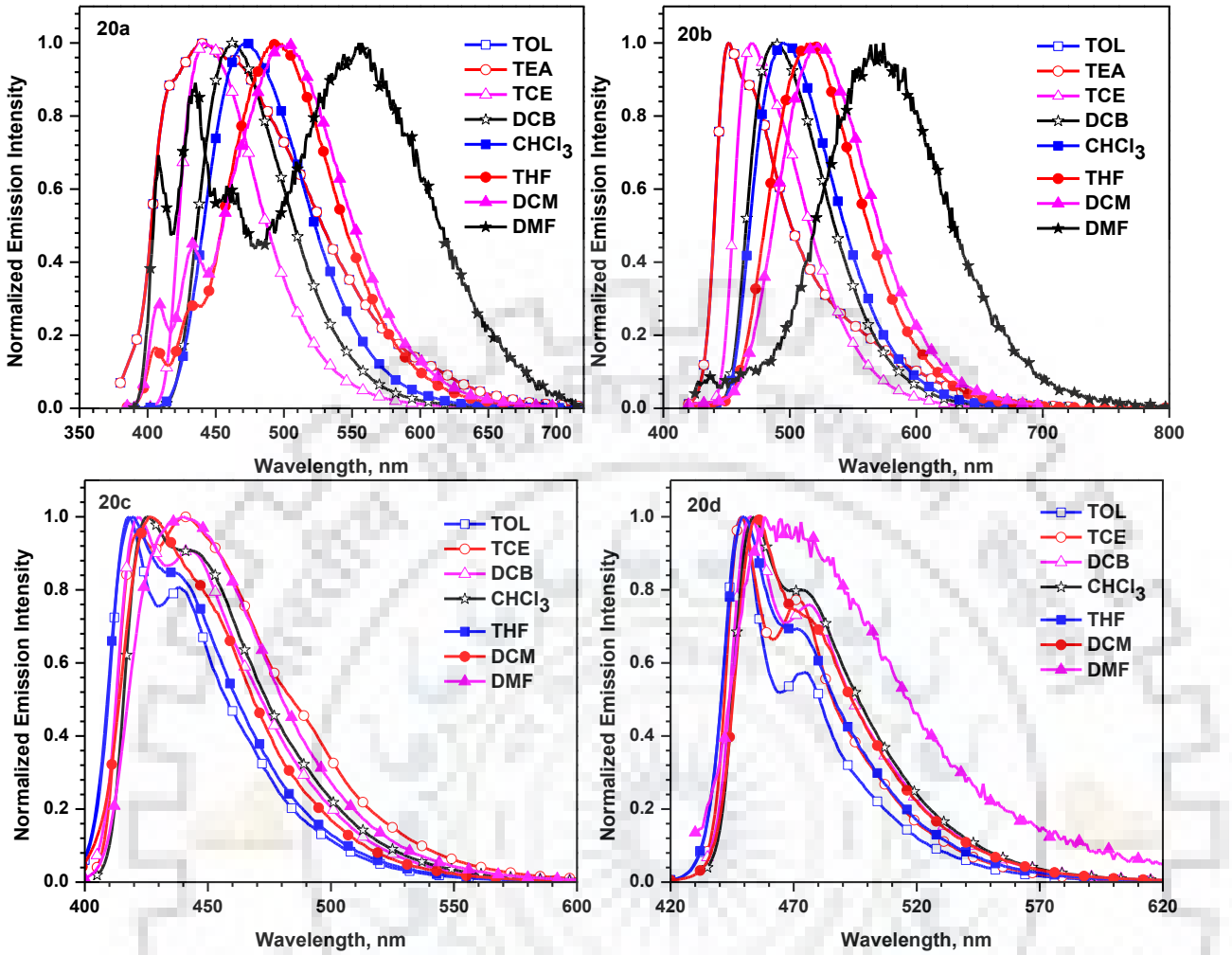

Figure 5.9 Normalized emission spectra of the dyes **20a-20d** recorded in different solvents.

The solvatochromism data of the CT possessing dyes were analysed by Lippert−Mataga plot as displayed in Figure 5.10. The dyes exhibited linearity in the correlation highlighting the effect of solvent polarity, which is typical for polar molecules in excited state.

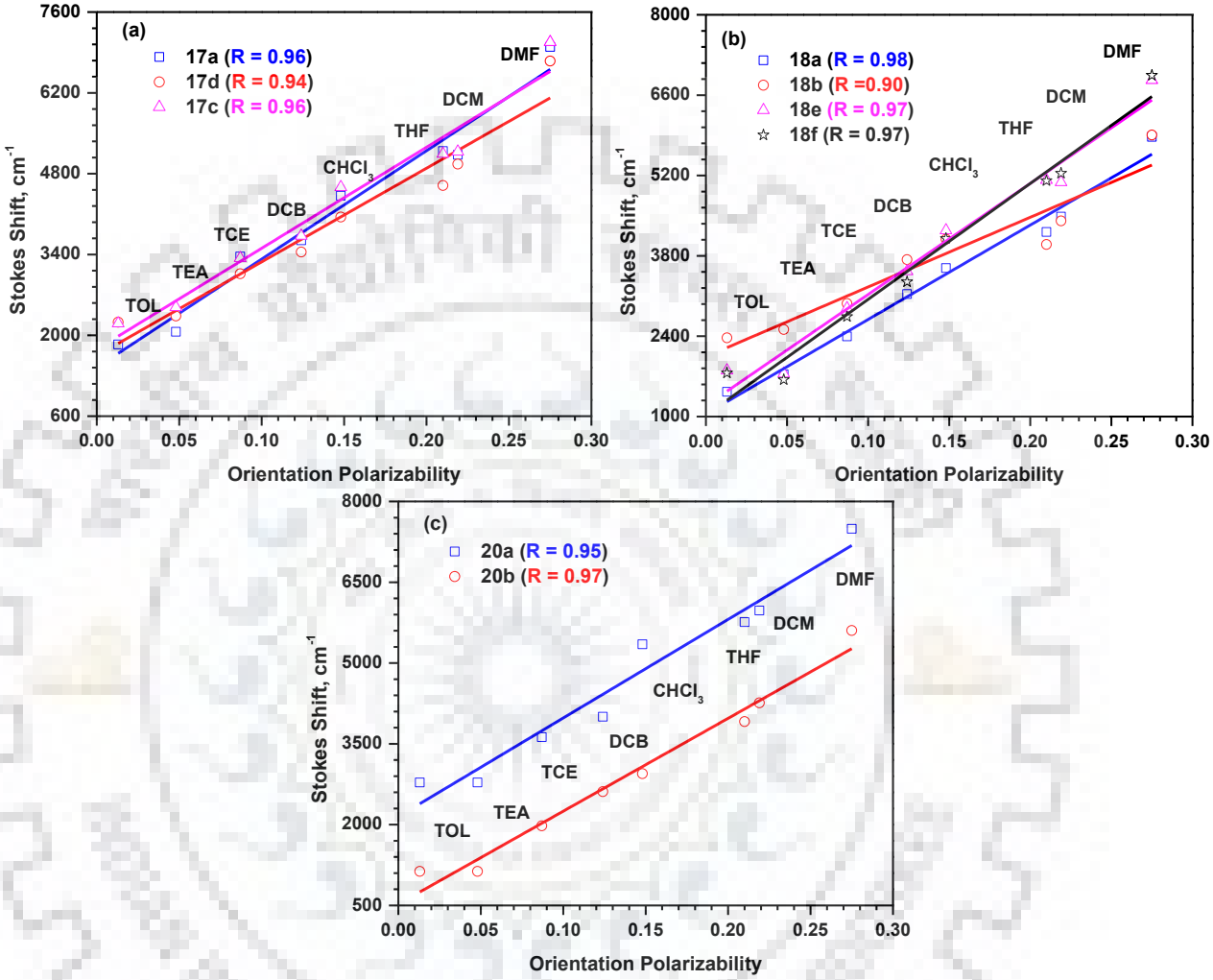

Figure 5.10 Lippert-Mataga plot for (a) **17a**, **17c** and **17d**, (b) **18a**, **18b**, **18e** and **18f** and (c) **20a** and **20b** dyes.

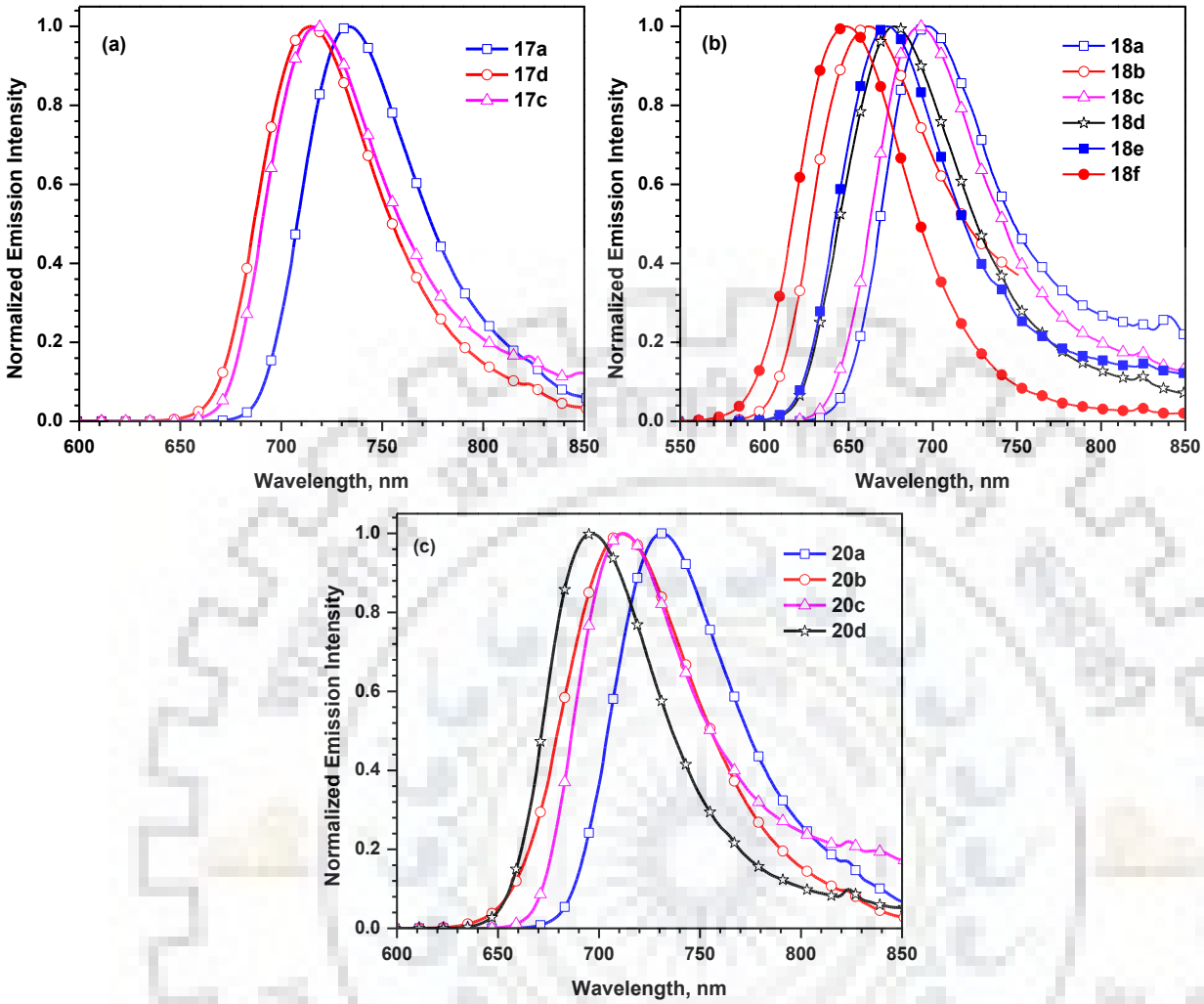

Figure 5.11 Solid state emission spectra of the dyes.

The dyes display bathochromically shifted broad emission band in the solid state compared to spectra in solution (Figure 5.11). This reflects the presence of strong intermolecular interactions in the solid state attributed to the *J*-aggregation which is beneficial for charge transport in their thin films. It is interesting to mention that phenyl-substituted dyes display large bathochromic shift ($\Delta\lambda$ = ~20 nm) than thienyl-substituted dyes. This could be due to presence of effective intermolecular interactions in thienyl-possessing dyes.

5.2.3 Time Resolved Fluorescence Studies

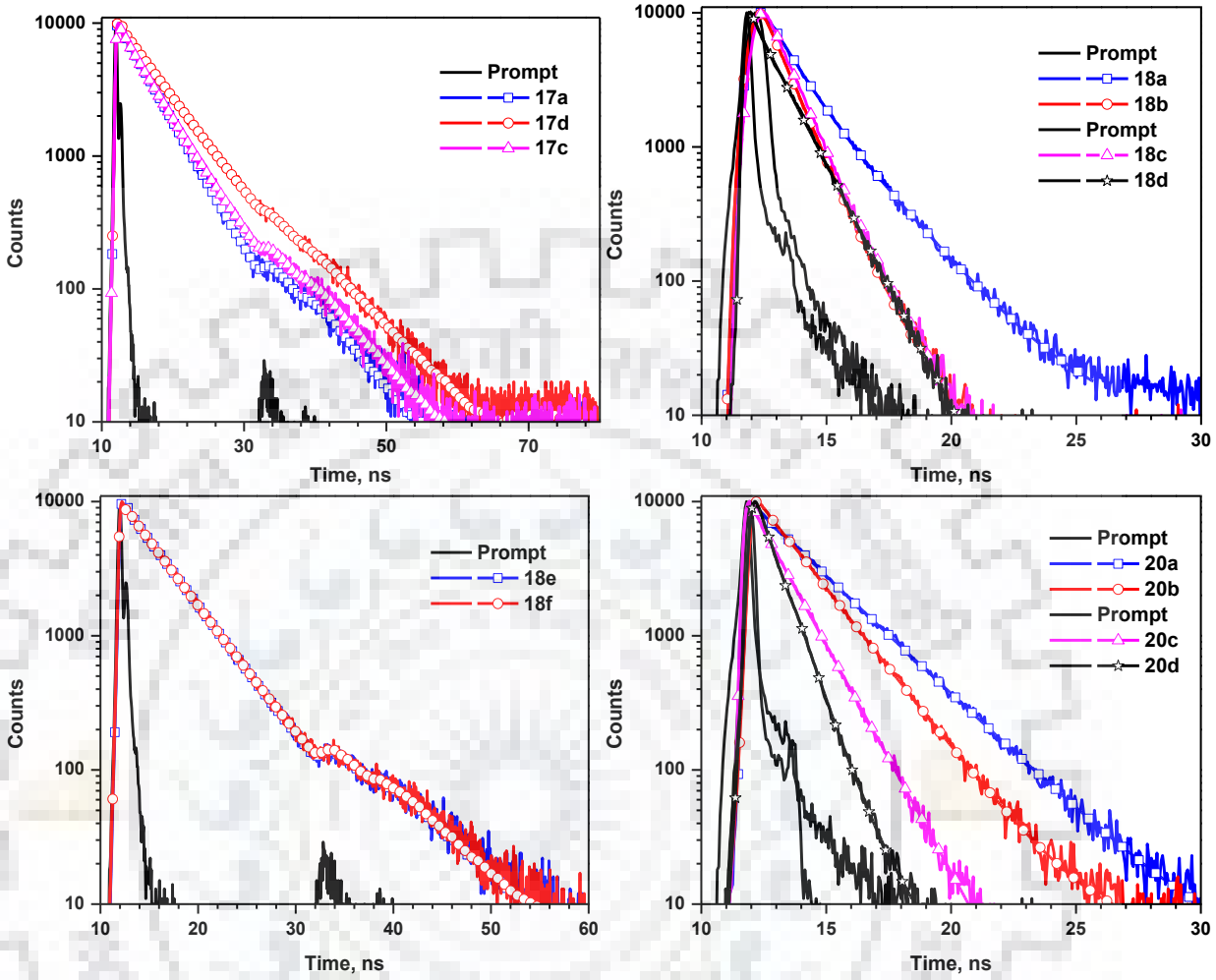

Figure 5.12 Fluorescence lifetime decay plots of the dyes.

To understand the process of excited state of the dyes, the fluorescence decay profiles in DCM is recorded (Figure 5.12) and the data is summarized in Tables 5.6 and 5.7. The average excited state lifetime were calculated and correlated to the molecular topology. The analysis predicted that the lifetime of excited states of the linear D-A dyes, **17a**, **17c** and **17d** and structurally similar dyes **18e** and **18f** is long lived attributed to CT excited state. Other cyano-containing dyes (**18a-18d)** display a relatively shorter lifetime in a range of 1.0 to 1.5 ns. However, all the naphthalimide-based dyes exhibit a longer lifetime compared to naphthalimide unit (0.52 ns). Also, it is found that the lifetime of carbazole-based star shaped (**20a** and **20b**) is long lived than the naphthalimide-based analogs (**20c** and **20d**) which is similar to typical CT exhibiting dyes. The short lived and ultrafast decay channels of the star-shaped dyes compared to linear analogs can be correlated to k_r and k_{nr}. The star-shaped dyes possess a faster radiative decay than their linear analogs corresponding to their high fluorescence efficiency.

Table 5.6 Time-resolved fluorescence and photophysical data for the dyes in DCM.

Dye	τ_{avg},[a] ns	Q.Y., Φ_F[b]	k_r,[c] ns^{-1}	k_{nr},[d] ns^{-1}
17a	4.21	0.48	0.11	0.12
17d	6.08	0.40	0.06	0.10
17c	4.89	0.37	0.08	0.13
18a	1.52	0.16	0.11	0.55
18b	0.90	0.19	0.21	0.90
18c	1.59	0.11	0.07	0.56
18d	1.14	0.11	0.10	0.78
18e	4.12	0.26	0.06	0.18
18f	4.50	0.36	0.08	0.14
20a	2.44	0.69	0.28	0.13
20b	1.75	0.23	0.13	0.44
20c	0.59	0.48	0.81	0.88
20d	0.74	0.40	0.54	0.81

[a] τ_{avg} = Fluorescence lifetime decay measured as $\tau_{avg.} = (A_1 \times \tau_1) + (A_2 \times \tau_2)$ in ns. [b] Absolute quantum yield calculated using integrating sphere. [c] Radiative decay rates (k_r) calculated using $k_r = \Phi_F/\tau$. [d] Non-radiative decay rate (k_{nr}) calculated using $\Phi_F = k_r/(k_r+k_{nr})$.

Table 5.7 Time-resolved fluorescence spectroscopy data for the dyes in DCM.

Dye	$\tau_{1,}$ ns	A_1	$\tau_{2,}$ ns	A_2	$\tau_{a,}$ ns	$\tau_{b,}$ ns	$\tau_{avg,}$ ns	χ^2
17a	0.22	0.06	4.47	0.94	0.01	4.20	4.21	1.2
17d	5.52	0.75	7.76	0.25	4.14	1.94	6.08	1.2
17c	3.98	0.50	6.04	0.48	1.99	2.90	4.89	1.2
18a	0.97	0.53	2.14	0.47	0.51	1.01	1.52	1.1
18b	0.90	1.00	-	-	0.90	-	0.90	1.1
18c	0.86	0.06	1.64	0.94	0.05	1.54	1.59	0.9
18d	0.13	0.05	1.19	0.95	0.01	1.13	1.14	1.1
18e	0.24	0.07	4.41	0.93	0.02	4.10	4.12	1.1
18f	4.16	0.74	5.46	0.26	3.08	1.42	4.50	1.2
20a	1.23	0.04	2.49	0.96	0.05	2.39	2.44	1.2
20b	0.69	0.07	1.83	0.93	0.05	1.70	1.75	1.2
20c	0.59	0.04	0.59	0.96	0.02	0.57	0.59	1.2
20d	0.67	0.82	1.08	0.18	0.55	0.19	0.74	1.2

Where τ_1/ τ_2, Life time of different decay channels from FLS experiment in ns; A_1/A_2, Contribution of different decay channels in solution; fitted by single/ double exponential; χ^2, correlation of exponential fit.

5.2.4 Electrochemical Properties

The redox properties of the dyes were characterized by recording CV and DPV shown in Figures 5.13-15 and relevant data listed in Tables 5.1 and 5.2. It is demonstrated that all the D-A hybrids undergo both electrochemical irreversible oxidation and quasi-reversible reduction processes. However, dyes possessing solely carbazole or naphthalimide unit display either oxidation or reduction waves, respectively. All the three dyes, **17a**, **17c** and **17d** possess an irreversible oxidation attributable to carbazole and quasi-reversible reduction attributed to naphthalimide. Among the linear dyes, **18a-18f**, the dyes having carbazole (**18a** and **18b**) are easily oxidized and dyes **18e** and **18f** show similar redox behavior as **17a**. However, dyes **18c** and **18d** display reduction potential at lower range due to more electron affinity. Further, star-shaped dye **20b** possessing an electron rich branching arm display an oxidation peak at 0.48 V which is 0.18 V less positive than **20a**. Both of these dyes are easily oxidizable than analogous linear dyes. Also, dyes **20c** and **20d** being more electron deficient display E_{red} at higher values than linear dyes. The reduction of the triazine core appears in DPV as a peak in the range of -1.8 to -1.9 V. The low lying HOMO and LUMO energy levels of all the naphthalimide-based compounds display the electron deficiency of the unit. Also, as a result of the strong electron-accepting ability of the triazine-cored dyes, **20c** and **20d**, they exhibit a deep seated HOMO level at ~6.0 eV. The electrochemical analysis shows that the thienyl-linked dyes possess a narrow band gap attributed to high lying HOMO and low lying LUMO energy level revealing the enhanced electron density of the core. Also, the band gap decreases for the dyes with the electron-donating branching arm among the star-shaped dyes.

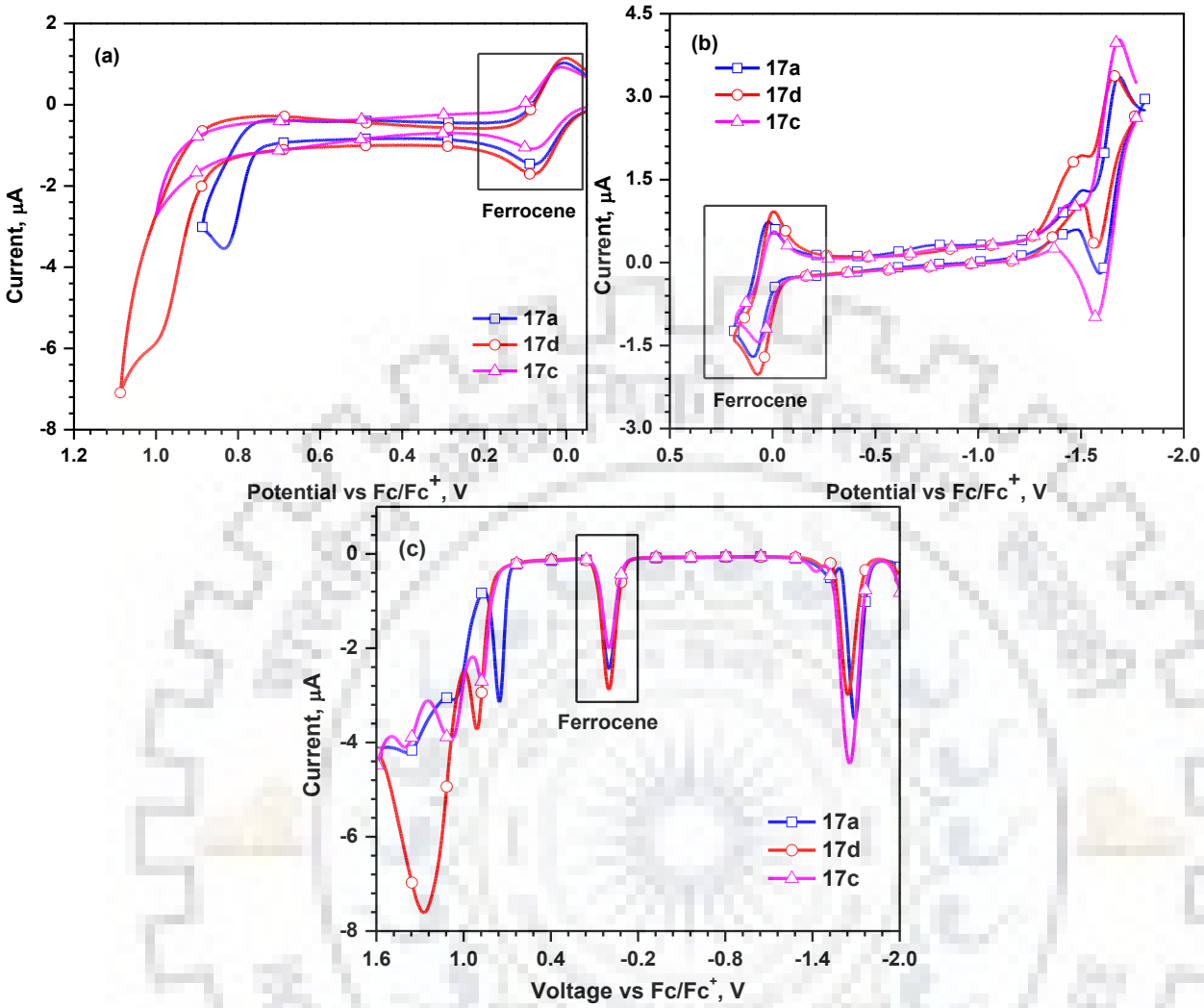

Figure 5.13 (a, b) CV and (c) DPV of the dyes **17a**, **17c** and **17d**.

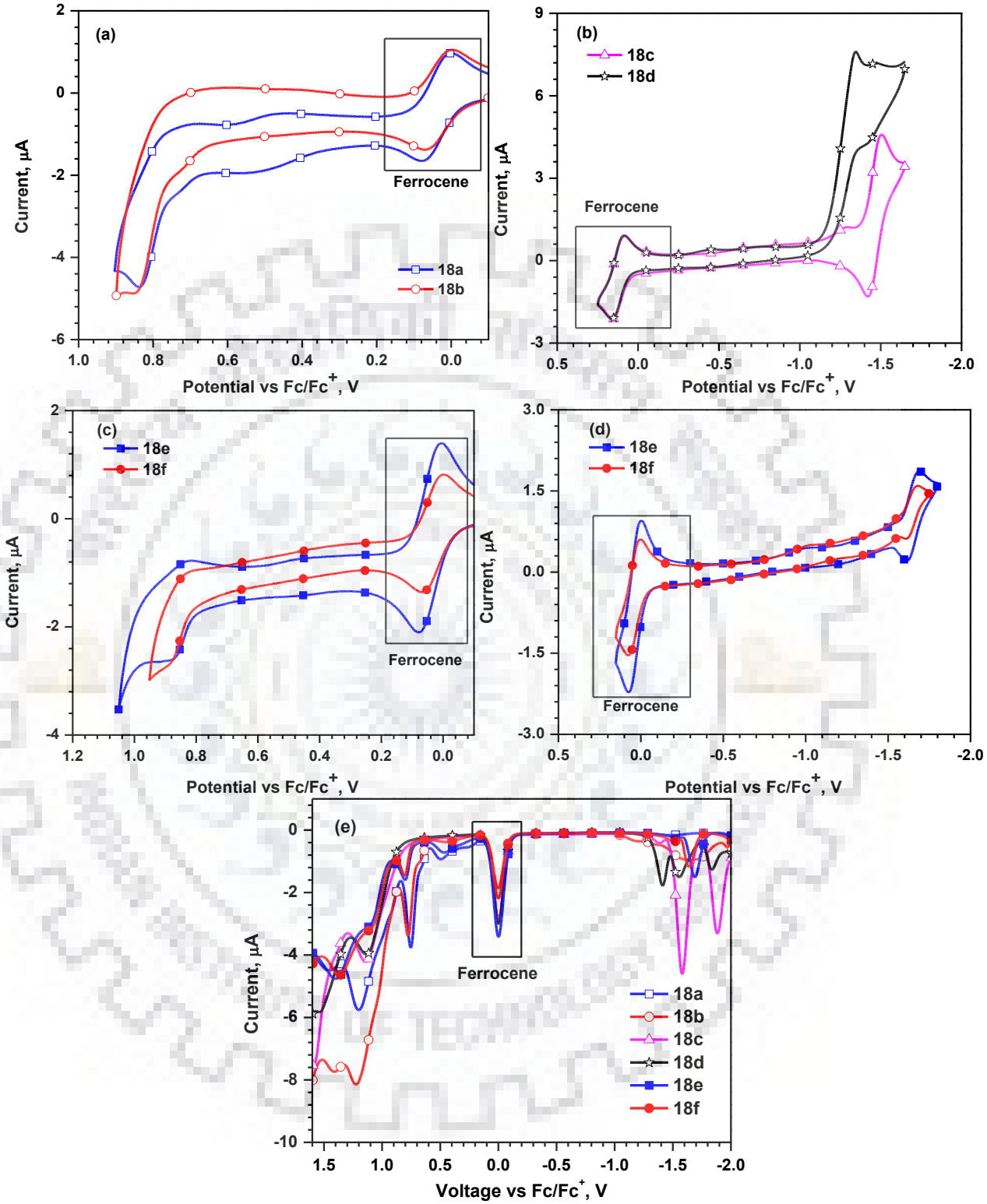

Figure 5.14 (a-d) CV and (e) DPV of the dyes **18a-18f**.

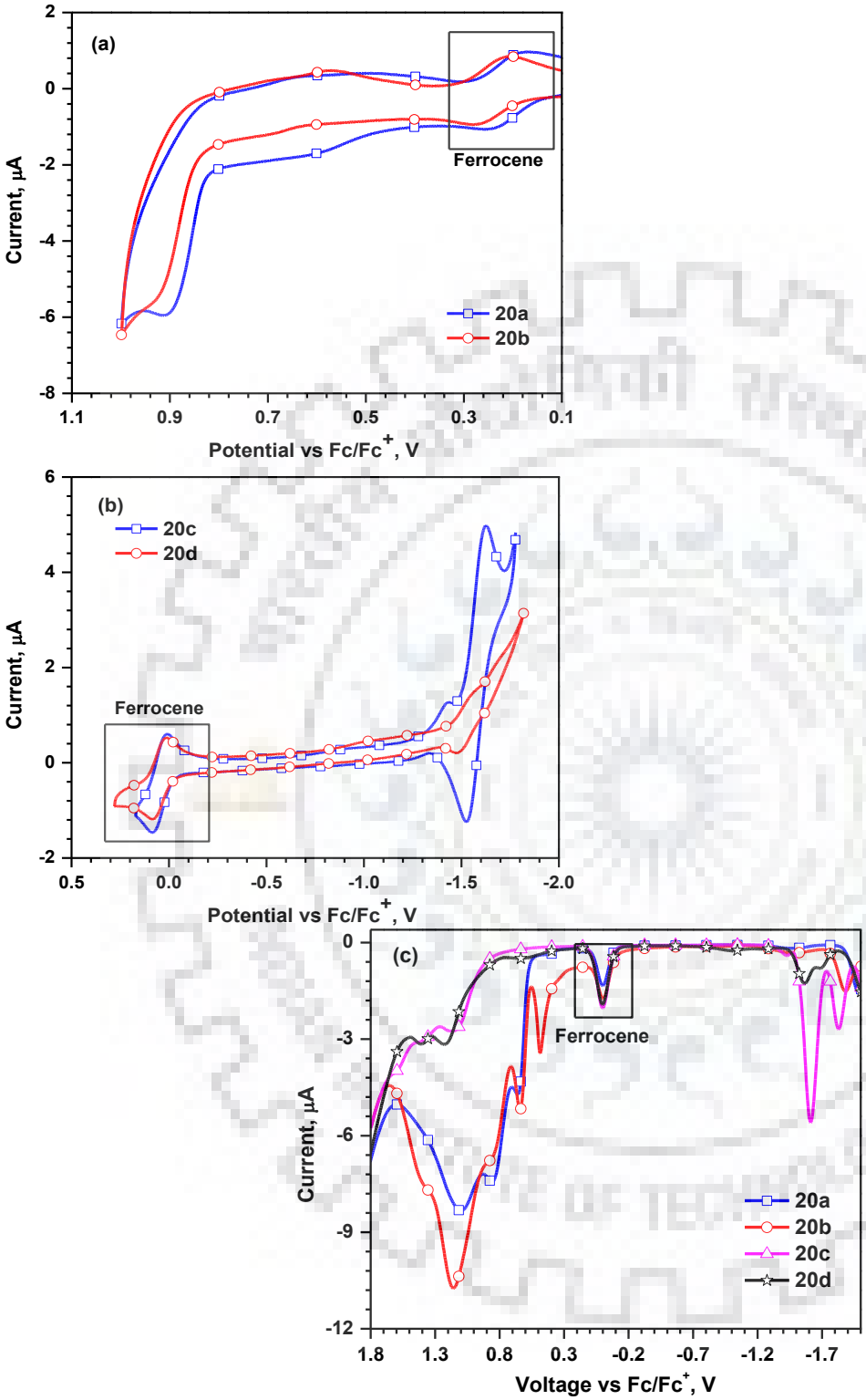

Figure 5.15 (a, b) CV and (c) DPV of the dyes **20a-20d**.

5.2.5 Thermal Properties

The thermal performance of the dyes is significant since it influence the stability of their thin films during device operation. The thermal properties of the linear and star-shaped dyes were investigated

by TGA as shown in Figure 5.16 and data compiled in Table 5.1 and 5.2, respectively. All the compounds exhibited a high thermal stability till 340 °C. The thermal decomposition temperatures with 5% weight loss were measured for the dyes. The T_d of the star-shaped dyes is higher (>425 °C) than the linear analogs attributed to the strong molecular interactions arising from planar arrangement in the solid state. Among the linear dyes, **17d** displays superior thermal stability with respect to **17a** and **17c**. Dye **17c** exhibit higher thermal stability than **17a** owing to additional naphthalimide unit, but less than **17d** due to presence of more alkyl group which decomposes easily. It is interesting that among the set of cyano-possessing dyes, **18a-18f**, thienyl-based dyes display superior stability than phenyl analogs which can be attributed to the induced strong intermolecular interactions and π–π interactions.

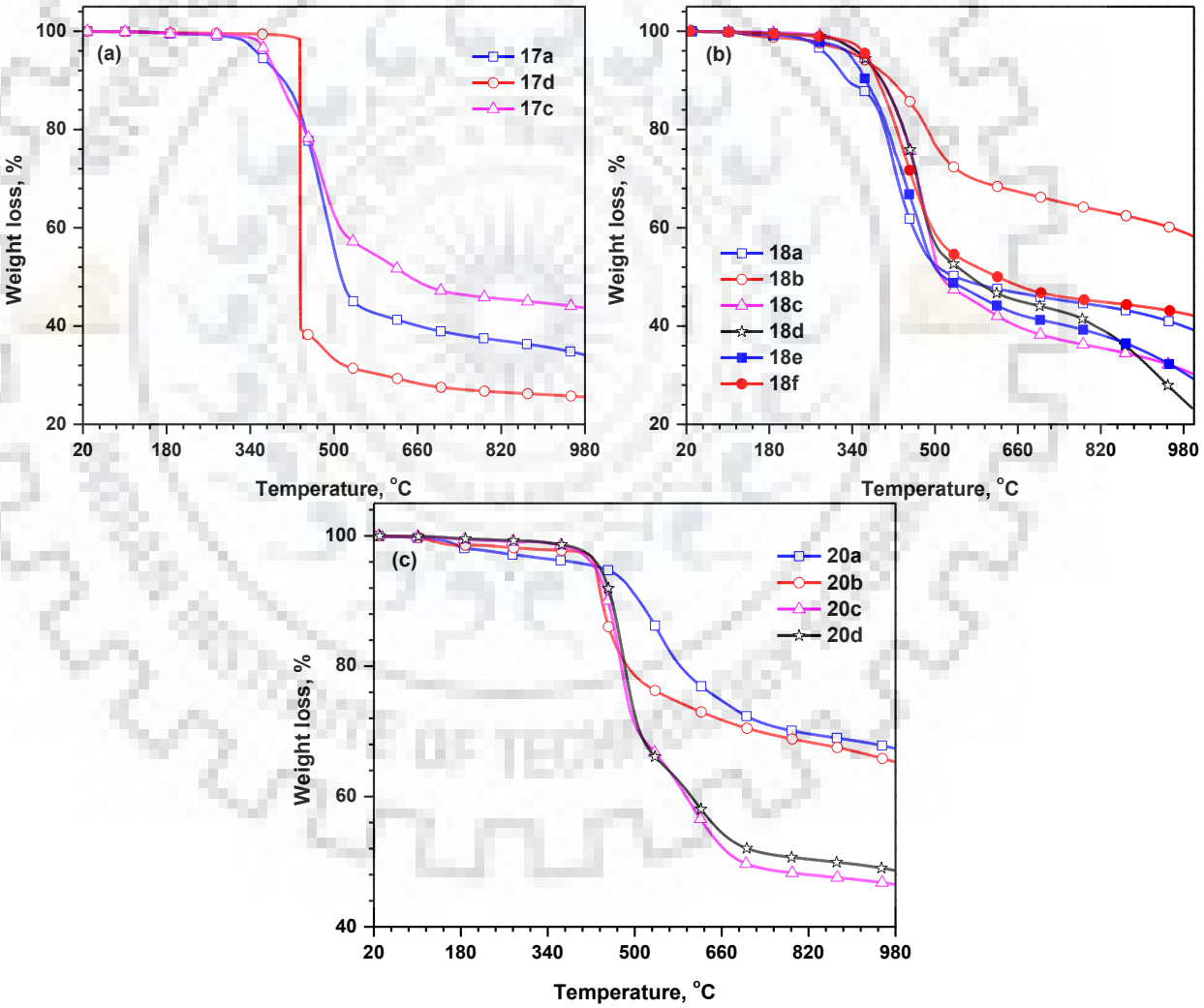

Figure 5.16 TGA curves of the linear and star-shaped dyes.

5.3 Conclusions

A series of 'ethyne-linked' compounds, containing carbazole and/ or 1,8-naphthalimide moiety were synthesized by a stepwise route involving a Pd/Cu catalyzed Sonogashira coupling reaction. The thermal, optical, and electrochemical properties of the dyes were investigated. The results indicated that these compounds possess improved optical and thermal properties by introducing the electron-transporting and emitting naphthalimide unit in conjugation with carbazole or in place of carbazole moiety. These compounds act as a good blue to green light-emitting materials. The star shaped triazine-cored dyes displayed superior optical, thermal and electrochemical properties compared to linear cyano analogs, attributable to the extended aromatic planar and C3-symmetric structure. The introduction of the thienyl-group into triazine-based dyes enriched the electron density for the star-shaped dyes and thus, influenced their photophysical and electrochemical properties. We intended to study the structure property relationship by the structural modification of carbazole and/ or naphthalimide as an aspect for improving the optoelectronic performance. Thus, designing the molecule to exhibit diverse structures and properties with remarkable benefits in the pool of various organic semiconductors has provided a new horizon to execute.

5.4 Experimental Section

5.4.1 General methods and Instrumentation

The general methodology is similar as described in previous Chapter.

5.4.2 Synthesis

The starting materials 9-ethyl-3-ethynyl-9*H*-carbazole (**15**), 3,6-dibromo-9-ethyl-9*H*-carbazole (**16**), 2,4,6-tris(4-bromophenyl)-1,3,5-triazine (**19a**) and 2,4,6-tris(5-bromothiophen-2-yl)-1,3,5-triazine (**19b**) were synthesized following literature procedure.[315, 402, 405]

5.4.2.1 4-((9-Ethyl-9*H*-carbazol-3-yl)ethynyl)-*N*-(2-ethylhexyl)-1,8-naphthalimide (17a)

A mixture of **1** (150 mg, 0.4 mmol), **15** (85 mg, 0.4 mmol), $Pd(PPh_3)_2Cl_2$ (3.5 mg, 1mol%), PPh_3 (3 mg, 2 mol%) and CuI (1mg, 1 mol%) suspended in TEA was refluxed under nitrogen atmosphere. The progress of the reaction was monitored by TLC. After completion of reaction, it was quenched by the addition of water. The organic product was extracted with $CHCl_3$. The collected organic layer was thoroughly washed with brine solution and dried over anhydrous Na_2SO_4. The orange residue was further purified by washing with hexanes and reprecipitation from $CHCl_3$: hexenes solvent system. Orange solid; Yield: 150 mg, 70 %; mp: 175 °C; IR (KBr, cm^{-1}) 3057, 2959, 2927 ($\nu_{CHstretch}$), 2191 ($\nu_{C\equiv C}$), 1694, 1654 ($\nu_{C=O}$), 1585 ($\nu_{C=C}$), 1485 (ν_{C-N});^{1}H-NMR (400 MHz, $CDCl_3$) δ 8.86 (dd, J = 8.3, 1.0 Hz, 1H), 8.66 (dd, J = 7.3, 1.0 Hz, 1H), 8.57 (d, J

= 7.7 Hz, 1H), 8.44 (d, *J* = 1.0 Hz, 1H), 8.16 (d, *J* = 7.7 Hz, 1H), 7.98 (d, *J* = 7.7 Hz, 1H), 7.87 (dd, *J* = 8.3, 7.3 Hz, 1H), 7.78 (dd, *J* = 8.4, 1.5 Hz, 1H), 7.53 (dd, *J* = 7.1, 1.2 Hz, 1H), 7.46 (d, *J* = 8.5 Hz, 2H), 7.34-7.28 (m, 1H), 4.42 (q, *J* = 7.3 Hz, 2H), 4.21-4.05 (m, 2H), 2.03-1.88 (m, 1H), 1.49 (t, *J* = 7.2 Hz, 3H), 1.44-1.25 (m, 8H), 0.94 (t, *J* = 7.4 Hz, 3H), 0.88 (t, *J* = 7.0 Hz, 3H); ^{13}C-NMR (100 MHz, $CDCl_3$) δ 164.5, 164.2, 140.4, 140.2, 132.5, 131.6, 130.6, 130.2, 129.5, 128.4, 128.2, 127.2, 126.4, 124.6, 123.1, 122.9, 122.4, 121.4, 120.7, 119.7, 112.1, 108.9, 108.7, 101.4, 85.1, 44.2, 37.9, 37.8, 30.7, 28.7, 24.0, 23.2, 14.1, 13.8, 10.7; HRMS calcd for $C_{36}H_{34}N_2O_2$ [M+Na] *m/z* 549.2512, found 549.2535.

5.4.2.2 4-((6-Bromo-9-ethyl-9*H*-carbazol-3-yl)ethynyl)-*N*-(2-ethylhexyl)-1,8-naphthalimide (17b)

It was synthesized following same procedure as of **17a** but using a mixture of **2** and **16**. Eluent: 50% Hexanes: $CHCl_3$. Yellow solid; Yield: 820 mg (45%); mp: 177 °C; IR (KBr, cm^{-1}) 2959, 2927, 2858 ($\nu_{CHstretch}$), 2196 ($\nu_{C\equiv C}$), 1696, 1656 ($\nu_{C=O}$), 1585 ($\nu_{C=C}$), 1484 (ν_{C-N}); ^{1}H-NMR (400 MHz, $CDCl_3$) δ 8.83 (d, J = 7.9 Hz, 1H), 8.66 (d, J = 6.8 Hz, 1H), 8.57 (d, J = 7.9 Hz, 1H), 8.38 (s, 1H), 8.26 (s, 1H), 7.98 (d, J = 7.3 Hz, 1H), 7.87 (t, J = 7.6 Hz, 1H), 7.80 (d, J = 8.5 Hz, 1H), 7.60 (dd, J = 8.5, 1.8 Hz, 1H), 7.45 (d, J = 8.5 Hz, 1H), 7.33 (d, J = 8.5 Hz, 1H), 4.39 (q, J = 7.1 Hz, 2H), 4.22-4.05 (m, 2H), 2.03-1.89 (m, 1H), 1.47 (t, J = 7.3 Hz, 3H), 1.44-1.25 (m, 8H), 0.94 (t, J = 7.3 Hz, 3H), 0.89 (t, J = 6.7 Hz, 3H); ^{13}C-NMR (100 MHz, $CDCl_3$) δ 164.4, 164.2, 140.3, 138.9, 132.4, 131.5, 131.4, 130.4. 130.2, 130.1, 129.1, 128.13, 128.09, 127.2, 124.8, 124.1, 123.4, 122.9, 122.1, 121.5, 112.7, 112.5, 110.2, 108.9, 100.8, 85.3, 44.2, 37.9, 30.7, 28.7, 24.1, 23.1, 14.1, 13.8, 10.6; HRMS calcd for $C_{36}H_{33}N_2O_2Br$ [M] *m/z* 604.1720, found 604.1736.

5.4.2.3 4,4'-((9-Ethyl-9*H*-carbazole-3,6-diyl)bis(ethyne-2,1-diyl))bis(*N*-(2-ethylhexyl)-1,8-naphthalimide (17c)

It was obtained as a product along with **17b**. Orange solid; Yield: 380 mg (14%); mp: 162 °C; IR (KBr, cm^{-1}) 2958, 2925, 2858 ($\nu_{CHstretch}$), 2195 ($\nu_{C\equiv C}$), 1699, 1658 ($\nu_{C=O}$), 1585 ($\nu_{C=C}$), 1443 (ν_{C-N}); ^{1}H-NMR (400 MHz, $CDCl_3$) δ 8.80 (t, J = 8.2 Hz, 2H), 8.71-8.63 (m, 2H), 8.62-8.54 (m, 2H), 8.38 (s, 1H), 8.25 (s, 1H), 8.09 (s, 1H), 8.03-7.94 (m, 2H), 7.94-7.84 (m, 2H), 7.65 (d, J = 8.7 Hz, 1H), 7.49 (d, J = 8.7 Hz, 1H), 7.37 (d, J = 8.2 Hz, 1H), 4.97-4.93 (m, 2H), 4.20-4.05 (m, 4H), 2.03-1.87 (m, 2H), 1.48-1.25 (m, 16H), 0.95 (t, J = 7,2 Hz, 6H), 0.89 (t, J = 7.4 Hz, 6H); ^{13}C-NMR (100 MHz, $CDCl_3$) δ 164.2, 164.0, 163.9, 163.8, 139.2, 138.5, 135.5, 131.9, 131.7, 131.4, 131.4, 131.2, 130.3, 130.2, 129.9, 127.9, 127.6, 127.2, 126.7, 125.6, 123.5, 123.2, 123.1, 122.9, 122.4, 113.4, 113.0, 110.4, 109.1, 104.6, 98.9, 95.4, 90.3, 85.9, 44.2, 39.0, 37.9, 30.7, 28.7, 24.0, 23.1, 15.4, 14.1, 10.6; HRMS calcd for $C_{58}H_{55}N_3O_4$ [M] *m/z* 857.4187, found 857.4189.

5.4.2.4 4-((9-Ethyl-6-ethynyl-9*H*-carbazol-3-yl)ethynyl)-*N*-(2-ethylhexyl)-1,8-naphthalimide (17d)

A pressure tube charged with **17b** (0.24 g, 0.4 mmol), $Pd(PPh_3)_2Cl_2$ (7 mg, 0.01 mmol), CuI (2 mg, 0.01 mmol) and PPh_3 (3 mg, 0.02 mmol) under inert atmosphere followed by addition of dry TEA (25 mL) and ethynyltrimethylsilane (1.5 mL). The reaction mixture was then stirred at for 24h at 80℃. After the reaction was completed, organic fraction was extracted with $CHCl_3$, dried over Na_2SO_4 and solvent was evaporated to dryness. The residue was purified by short silica

column chromatography. Eluent: 50 % $CHCl_3$ in hexanes. Yellow solid; Yield: 220 mg (91%); mp: 154 °C; IR (KBr, cm^{-1}) 2955, 2926, 2859 ($\nu_{CHstretch}$), 2194 ($\nu_{C\equiv C}$), 1701, 1658 ($\nu_{C=O}$), 1588 ($\nu_{C=C}$), 1482 (ν_{C-N}); ^{1}H-NMR (400 MHz, $CDCl_3$) δ 8.78 (dd, *J* = 8.2, 1.4 Hz, 1H), 8.68 (dd, *J* = 7.3, 0.9 Hz, 1H), 8.59 (d, *J* = 7.8 Hz, 1H), 8.23 (dd, *J* = 6.8, 1.3 Hz, 2H), 7.95 (d, *J* = 7.3 Hz, 1H), 7.93-7.86 (m, 3H), 7.64 (dd, *J* = 8.5, 1.6 Hz, 1H), 7.38 (d, *J* = 8.7 Hz, 1H), 5.18-4.79 (m, 2H), 4.19-4.08 (m, 2H), 1.99-1.94 (m, 1H), 1.60 (t, *J* = 7.1 Hz, 3H), 1.48-1.22 (m, 8H), 0.94 (*t*, J = 7.3 Hz, 3H), 0.89 (t, *J* = 7.1 Hz, 3H), 0.31 (s, 9H); ^{13}C-NMR (100 MHz, $CDCl_3$) δ 164.3, 164.0, 140.5, 138.5, 135.6, 132.1, 131.8, 131.6, 130.7, 130.4, 130.3, 128.2, 127.7, 127.2, 125.9, 124.6, 123.9, 123.1, 122.3, 122.0, 114.8, 114.2, 108.9, 105.8, 104.8, 104.2, 96.1, 93.2, 92.6, 89.8, 44.3, 39.1, 37.9, 30.7, 28.7, 24.0, 23.1, 15.4, 14.1, 10.7, 0.10; HRMS calcd for $C_{41}H_{42}N_2O_2Si$ [M+H] *m/z* 623.3088, found 623.3070. 4-((9-Ethyl-6-((trimethylsilyl)ethynyl)-9*H*-carbazol-3-yl)ethynyl)-*N*-(2-ethylhexyl)-1,8-naphthalimide (**17bd**) as intermediate (220 mg, 0.35 mmol) was suspended in 10 ml of methanol and 5 mL DCM, to which powdered KF (0.1 g) and TBAB (0.1 g) was added. The mixture was heated for 2 h at 60℃. After desilylation, the product was filtered and washed with water and hexanes and purified by silica column chromatography. Eluent: 50 % $CHCl_3$ in hexanes. Orange solid; Yield: 150 mg (77%); mp: 175 °C; IR (KBr, cm^{-1}) 2958, 2928, 2861 ($\nu_{CHstretch}$), 2195, 2104 ($\nu_{C\equiv C}$), 1795, 1692, 1656 ($\nu_{C=O}$), 1589 ($\nu_{C=C}$), 1485 (ν_{C-N}); ^{1}H-NMR (400 MHz, $CDCl_3$) δ 8.83 (d, *J* = 8.2 Hz, 1H), 8.66 (d, *J* = 7.3 Hz, 1H), 8.57 (d, *J* = 7.6 Hz, 1H), 8.40 (s, 1H), 8.30 (s, 1H), 7.98 (d, *J* = 7.5 Hz, 1H), 7.93-7.83 (m, 1H), 7.79 (d, *J* = 8.4 Hz, 1H), 7.65 (d, *J* = 8.4 Hz, 1H), 7.46 (d, *J* = 8.5 Hz, 1H), 7.39 (d, *J* = 8.5 Hz, 1H), 4.40 (q, *J* = 7.2 Hz, 2H), 4.21-4.06 (m, 2H), 3.10 (s, 1H), 1.95 (q, *J* = 6.2 Hz, 1H), 1.48 (t, *J* = 7.2 Hz, 3H), 1.44-1.27 (m, 8H), 0.94 (t, *J* = 7.3 Hz, 3H), 0.88 (t, *J* = 6.6 Hz, 3H); ^{13}C-NMR (100 MHz, $CDCl_3$) δ 164.4, 164.2, 140.5, 140.2, 132.4, 131.5, 131.4, 130.5, 130.3, 130.3, 129.9, 128.2, 128.1, 127.2, 124.9, 124.7, 122.9, 122.6, 122.3, 121.5, 113.0, 112.8, 108.9, 108.8, 100.9, 85.3, 84.6, 75.6, 44.2, 37.9, 30.7, 28.7, 24.0, 23.1, 14.1, 13.9, 10.63; HRMS calcd for $C_{38}H_{34}N_2O_2$ [M+Na] *m/z* 574.2591, found 574.2593.

5.4.2.5 4-((9-Ethyl-9*H*-carbazol-3-yl)ethynyl)benzonitrile (18a)

A mixture of 4-bromobenzonitrile (182 mg, 1mmol), **15** (220 mg, 1mmol), $Pd(PPh_3)_2Cl_2$ (7 mg, 1mol%), PPh_3 (6 mg, 2 mol%) and CuI (2 mg, 1mol%) suspended in 20 mL TEA was refluxed under nitrogen atmosphere for 5 h. The progress of the reaction was monitored by TLC. After completion of reaction, it was quenched by the addition of water. The organic product was extracted with $CHCl_3$. The collected organic layer was thoroughly washed with brine solution and

dried over anhydrous Na_2SO_4. Evaporation of the volatiles gave off white residue. It was further purified by washing with hexanes multiple times and finally dried to yield product. Off white; Yield: 160 mg (45%); mp: 130 °C; IR (KBr, cm^{-1}) 3052, 2976, 2928 ($\nu_{CHstretch}$), 2209 ($\nu_{C\equiv N}$), 1593, 1499 ($\nu_{C=C}$), 1471 (ν_{C-N});^{1}H-NMR (400 MHz, $CDCl_3$) δ 8.32 (s, 1H), 8.11 (d, J = 7.8 Hz, 1H), 7.68-7.60 (m, 5H), 7.52 (t, J = 7.6 Hz, 1H), 7.44 (d, J = 8.2 Hz, 1H), 7.40 (d, J = 8.2 Hz, 1H), 7.32 (m, 1H), 4.39 (q, J = 7.0 Hz, 2H), 1.46 (t, J = 7.1 Hz, 3H); ^{13}C-NMR (100 MHz, $CDCl_3$) δ 140.3, 140.0, 132.0, 131.8, 129.4, 128.9, 128.4, 126.3, 124.5, 123.0, 122.4, 120.6, 119.6, 118.7, 112.0, 110.7, 108.8, 108.6, 95.8, 86.3, 37.7, 13.8; HRMS calcd for $C_{23}H_{16}N_2$ [M+Na] *m/z* 343.1205, found 343.1204.

5.4.2.6 5-((9-Ethyl-9*H*-carbazol-3-yl)ethynyl)thiophene-2-carbonitrile (18b)

It was synthesized following same procedure as of **18a** but using 5-bromothiophene-2-carbonitrile. It was purified by washing with hexanes and finally reprecipitation from $CHCl_3$: hexanes solvent system. Pale yellow solid; Yield: 170 mg (52%); mp: 135 °C; IR (KBr, cm^{-1}) 3090, 3058, 2970, 2922 ($\nu_{CHstretch}$), 2197 ($\nu_{C\equiv N}$), 1627, 1597, 1519 ($\nu_{C=C}$), 1477 (ν_{C-N}); ^{1}H-NMR (400 MHz, $CDCl_3$) δ 8.30 (d, J = 1.0 Hz, 1H), 8.10 (d, J = 7.7 Hz, 1H), 7.63 (dd, J = 8.4, 1.5 Hz, 1H), 7.55-7.48 (m, 2H), 7.44 (d, J = 8.1 Hz, 1H), 7.40 (d, J = 8.5 Hz, 0H), 7.31-7.27 (m, 1H), 7.21 (d, J = 3.9 Hz, 1H), 4.39 (q, J = 7.3 Hz, 2H), 1.46 (t, J = 7.2 Hz, 3H); ^{13}C-NMR (100 MHz, $CDCl_3$) δ 140.3, 140.1, 137.3, 131.7, 130.6, 129.2, 126.4, 124.4, 123.0, 122.3, 120.6, 119.7, 113.9, 111.3, 108.9, 108.8, 108.7, 98.8, 79.1, 37.7, 13.8; HRMS calcd for $C_{21}H_{14}N_2S$ [M+Na] *m/z* 349.0770, found 349.0779.

5.4.2.7 4-((Benzonitril-4-yl)ethynyl)-*N*-(2-ethylhexyl)-1,8-naphthalimide (18c)

It was synthesized following same procedure as of **18a** but using **2**. Yellow residue obtained was purified by washing with hexanes and reprecipitation from $CHCl_3$: hexenes solvent system. Yellow solid; Yield: 300 mg (70%); mp: 170 °C; IR (KBr, cm^{-1}) 2958, 2929, 2861 ($\nu_{CHstretch}$), 2229 ($\nu_{C\equiv N}$), 16969, 1659 ($\nu_{C=O}$), 1589, 1508 ($\nu_{C=C}$), 1486 (ν_{C-N}); ^{1}H-NMR (400 MHz, $CDCl_3$) δ 8.71-8.64 (m, 2H), 8.61-8.55 (dd, J = 5.2, 0.8 Hz,1H), 8.03-7.97 (m, 1H), 7.87 (td, J = 7.9, 1.2 Hz, 1H), 7.80-7.71 (m, 4H), 4.21-4.05 (m, 2H), 1.96-1.93 (t, J = 5.7 Hz, 1H), 1.48-1.21 (m, 8H), 1.01-0.91 (m, 3H), 0.88 (dd, J = 6.4, 5.0 Hz, 3H); ^{13}C-NMR (100 MHz, $CDCl_3$) δ 164.2, 163.9, 132.4, 131.8, 131.3, 130.3, 127.8, 127.0, 126.1, 123.1, 122.9, 118.2, 112.6, 96.4, 90.1, 44.3, 37.9, 30.7, 28.7, 24.0, 23.1, 14.1, 10.6; HRMS calcd for $C_{29}H_{26}N_2O_2$ [M] *m/z* 434.1989, found 434.1984.

5.4.2.8 4-((Thieno-2-nitril-5-yl)ethynyl)-*N*-(2-ethylhexyl)-1,8-naphthalimide (18d)

It was synthesized following same procedure as of **18b** but using **2**. Yellow solid; Yield: 300 mg (68%); mp: 145 °C; IR (KBr, cm^{-1}) 2957, 2925, 2859 ($\nu_{CHstretch}$), 2217 ($\nu_{C\equiv N}$), 1699, 1659 ($\nu_{C=O}$), 1586, 1510 ($\nu_{C=C}$), 1435 (ν_{C-N}); ^{1}H-NMR (400 MHz,$CDCl_3$) δ 8.65 (d, J = 6.4 Hz, 1H), 8.58 (dd, J = 13.5, 8.5 Hz, 2H), 7.98 (d, J = 7.1 Hz, 1H), 7.88 (d, J = 7.3 Hz, 1H), 7.66-7.55 (m, 1H), 7.40 (t, J = 2.5 Hz, 1H), 4.17-4.05 (m, 2H), 1.95-1.93 (m, 1H), 1.42-1.26 (m, 8H), 0.97-0.84 (m, 6H); ^{13}C-NMR (100 MHz, $CDCl_3$) δ 164.1, 163.8, 137.3, 132.7, 132.6, 131.9, 131.7, 131.3, 130.2, 129.2, 128.0, 127.9, 125.4, 123.2, 123.1, 113.3, 111.5, 93.2, 89.1, 44.3, 37.9, 30.7, 28.7, 24.0, 23.1, 14.1, 10.6; HRMS calcd for $C_{27}H_{24}N_2O_2S$ [M+H] *m/z* 441.1631, found 441.1622.

5.4.2.9 4-((9-Ethyl-9*H*-carbazol-3-yl)ethynyl)-benzonitril-6-yl)-(*N*-(2-ethylhexyl))-1,8-naphthalimide (18e)

It was synthesized following same procedure as of **18a** but using **17d**. It was purified by short silica column chromatography. Eluent: 50% $CHCl_3$ in Hexanes. Yellow solid; Yield: 27 mg (42%); mp: 155 °C; IR (KBr, cm^{-1}) 3055, 2956, 2925, 2857 ($\nu_{CHstretch}$), 2196 ($\nu_{C\equiv N}$), 1693, 1655 ($\nu_{C=O}$), 1584, 1507 ($\nu_{C=C}$), 1482 (ν_{C-N}); ^{1}H-NMR (400 MHz, $CDCl_3$) δ 8.91-8.78 (m, 1H), 8.66 (d, J = 7.3 Hz, 1H), 8.57 (d, J = 7.3 Hz, 1H), 8.43 (d, J = 1.2 Hz, 1H), 8.36 (d, J = 0.9 Hz, 1H), 7.98 (d, J = 7.3 Hz, 1H), 7.87 (t, J = 7.9 Hz, 1H), 7.83-7.74 (m, 2H), 7.70 (dd, J = 8.5, 1.8 Hz, 1H), 7.65 (s, 2H), 7.52-7.40 (m, 3H), 4.42 (q, J = 7.3 Hz, 2H), 4.19-4.09 (m, 2H), 2.06-1.87 (m, 1H), 1.54-1.46 (m, 3H), 1.40 (q, J = 6.9 Hz, 4H), 1.36-1.28 (m, 4H), 0.94 (t, J = 7.3 Hz, 3H), 0.89 (t, J = 7.0 Hz, 3H); ^{13}C-NMR (100 MHz, $CDCl_3$) δ 164.4, 164.2, 140.5, 140.4, 134.7, 132.1, 131.8, 131.6, 131.5, 131.4, 130.5, 130.3, 130.1, 129.5, 128.7, 128.1, 127.9, 127.2, 124.8, 124.6, 122.9, 122.6, 122.5, 121.5, 118.7, 113.1, 112.9, 110.9, 109.1, 100.7, 95.2, 86.7, 85.4, 44.2, 38.0, 37.9, 30.7, 28.7, 24.0, 23.1, 14.1, 13.9, 10.6; HRMS calcd for $C_{45}H_{37}N_3O_2$ [M] *m/z* 649.2723, found 649.2721.

5.4.2.10 4-((9-Ethyl-9*H*-carbazol-3-yl)ethynyl)-thieno-2-carbonitril-5-yl)-(*N*-(2-ethylhexyl))-1,8-naphthalimide (18f)

It was synthesized following same procedure as of **18e** but using 5-bromothiophene-2-carbonitrile. It was purified by short silica column chromatography. Eluent: 50% $CHCl_3$ in Hexanes. Yellow solid; Yield: 30 mg (45%); mp: 142 °C; IR (KBr, cm^{-1}) 3049, 2969, 2926, 2854 ($\nu_{CHstretch}$), 2195 ($\nu_{C\equiv N}$), 1691, 1653 ($\nu_{C=O}$), 1580, 1505 ($\nu_{C=C}$), 1480 (ν_{C-N}); ^{1}H-NMR (400 MHz, $CDCl_3$) δ 8.84 (d, J = 7.9 Hz, 1H), 8.67 (d, J = 7.3 Hz, 1H), 8.58 (t, J = 4.0 Hz, 1H), 8.43 (s, 1H), 8.35 (s, 1H), 7.99 (t, J = 3.7 Hz, 1H), 7.91-7.85 (m, 1H), 7.82 (d, J = 8.5 Hz, 1H), 7.73-7.42 (m, 4H), 7.35 (s, 1H),), 4.46-4.42(m, 2H), 4.16-4.12 (m, 2H), 1.97-1.89 (m, 1H), 1.51 (t, J = 7.0 Hz, 3H), 1.45-1.27 (m,

8H), 0.95 (t, *J* = 7.3 Hz, 3H), 0.88 (t, *J* = 6.4 Hz, 3H); ^{13}C-NMR (100 MHz, $CDCl_3$) δ 164.4, 164.2, 140.5, 137.3, 134.6, 134.2, 134.1, 132.2, 131.6, 131.5, 130.8, 130.5, 130.3, 129.9, 129.6, 128.4, 127.9, 127.2, 124.8, 124.6, 122.9, 122.6, 121.5, 113.8, 113.1, 112.4, 109.1, 100.7, 98.2, 85.4, 79.5, 44.2, 38.0, 37.9, 30.7, 28.7, 23.9, 23.1, 14.1, 13.9, 10.6; HRMS calcd for $C_{43}H_{35}N_3O_2S$ [M+Na] *m/z* 680.2342, found 630.2345.

5.4.2.11 2,4,6-Tris(4-((9-ethyl-9*H*-carbazol-3-yl)ethynyl)phenyl)-1,3,5-triazine (20a)

It was synthesized following same procedure as of **17a** but using a mixture of **15** and **19a**. The desired product was further purified by silica column chromatography. Eluent: 1:1-4:1 $CHCl_3$: Hexanes. Mustard yellow solid; Yield: 300 mg (31%); mp: 220 °C; IR (KBr, cm^{-1}) 3055, 2967, 2925, 2855 ($\nu_{CHstretch}$), 2205 ($\nu_{C\equiv C}$), 1597, 1569 1506 ($\nu_{C=C}$), 1404 (ν_{C-N}); ^{1}H-NMR (400 MHz, $CDCl_3$) δ 8.81 (d, *J* = 7.3 Hz, 6H), 8.38 (s, 3H), 8.14 (d, *J* = 7.3 Hz, 3H), 7.83-7.75 (d, *J* = 7.6 Hz, 6H), 7.75-7.67 (d, *J* = 8.8 Hz, 3H), 7.55-7.48 (m, 3H), 7.43 (t, *J* = 8.5 Hz, 6H), 7.30 (d, *J* = 7.3 Hz, 3H), 4.40 (q, *J* = 7.0 Hz, 6H), 1.48 (t, *J* = 6.9 Hz, 9H);^{13}C-NMR (100 MHz, $CDCl_3$) δ 171.0, 140.3, 139.8, 135.1, 131.6, 129.4, 128.9, 128.3, 126.2, 124.4, 120.6, 119.4, 112.7, 108.7, 108.5, 94.1, 87.7, 37.7, 13.8; HRMS calcd for $C_{69}H_{48}N_6$ [M+H] *m/z* 961.4013, found 961.4024.

5.4.2.12 3-((4-(4,6-Bis(4-bromophenyl)-1,3,5-triazin-2-yl)phenyl)ethynyl)-9-ethyl-9*H*-carbazole (20aBr_2)

It was obtained as a product while synthesizing **20a**. Eluent: 1:1 $CHCl_3$: Hexanes. Yellow solid; Yield: 30 mg (4%); mp: 158 °C; IR (KBr, cm^{-1}) 2962, 2923, 2854 ($\nu_{CHstretch}$), 2202 ($\nu_{C\equiv C}$), 1595, 1568, 1504 ($\nu_{C=C}$), 1401 (ν_{C-N}); ^{1}H-NMR (400 MHz, $CDCl_3$) δ 8.76 (d, *J* = 8.5 Hz, 2H), 8.66 (d, *J* = 8.5 Hz, 1H), 8.59 (d, *J* = 8.5 Hz, 2H), 8.37 (s, 1H), 8.13 (d, *J* = 7.9 Hz, 1H), 7.77 (d, *J* = 8.5 Hz, 2H), 7.71 (t, *J* = 7.9 Hz, 4H), 7.50 (d, *J* = 7.3 Hz, 1H), 7.43 (t, *J* = 9.2 Hz, 2H), 7.29 (d, *J* = 7.9 Hz, 1H), 7.18 (d, *J* = 6.4 Hz, 1H), 7.13 (d, *J* = 7.3 Hz, 1H), 4.40 (q, *J* = 7.1 Hz, 2H), 1.47 (t, *J* = 7.3 Hz, 3H); ^{13}C-NMR (100 MHz, $CDCl_3$) cannot be recorded due to insufficient amount and poor solubility; HRMS calcd for $C_{37}H_{24}Br_2N_4$ [M+Na] *m/z* 705.0260, found 705.0269.

5.4.2.13 3,3'-(((6-(4-Bromophenyl)-1,3,5-triazine-2,4-diyl)bis(4,1-phenylene))bis(ethyne-2,1-diyl))bis(9-ethyl-9*H*-carbazole) (20aBr)

It was obtained as a product while synthesizing **20a**. Eluent: 40% $CHCl_3$ in Hexanes. Pale yellow solid; Yield: 100 mg (13%); mp: 145 °C; IR (KBr, cm^{-1}) 2962, 2923, 2854 ($\nu_{CHstretch}$), 2202($\nu_{C\equiv C}$), 1595, 1568, 1504 ($\nu_{C=C}$), 1401 (ν_{C-N}); ^{1}H-NMR (400 MHz, $CDCl_3$) δ 8.76 (d, *J* = 7.8 Hz, 4H), 8.65 (d, *J* = 7.8 Hz, 2H), 8.37 (s, 2H), 8.13 (d, *J* = 8.0 Hz, 2H), 7.77 (d, *J* = 7.8 Hz, 4H), 7.71 (t, *J* = 7.3 Hz, 4H), 7.51 (t, *J* = 7.6 Hz, 2H), 7.42 (dd, *J* = 11.0, 8.7 Hz, 4H), 7.29 (d, *J* = 7.3 Hz, 2H), 4.39 (q,

J = 7.0 Hz, 4H), 1.47 (t, *J* = 7.1 Hz, 6H); ^{13}C-NMR (100 MHz, $CDCl_3$) cannot be recorded due to insufficient amount and poor solubility; HRMS calcd for $C_{53}H_{36}BrN_5$ [M+H] *m/z* 822.2227, found 822.8222.

5.4.2.14 2,4,6-Tris(5-((9-ethyl-9H-carbazol-3-yl)ethynyl)thiophen-2-yl)-1,3,5-triazine (20b)

It was synthesized following same procedure as of **20a** but using a mixture of **15** and **19b**. The desired product was further purified by silica column chromatography. Eluent: 50%-80% $CHCl_3$ in Hexanes. Orange solid; Yield: 410 mg (42%); mp: 175 °C; IR (KBr, cm^{-1}) 2969, 2925, 2858 ($\nu_{CHstretch}$), 2193 ($\nu_{C\equiv C}$), 1624, 1598, 1501 ($\nu_{C=C}$), 1482, 1440 (ν_{C-N}); ^{1}H-NMR (400 MHz, $CDCl_3$) δ 8.34 (s, 3H), 8.18 (q, *J* = 1.8 Hz, 3H), 8.12 (d, *J* = 7.9 Hz, 3H), 7.67 (d, *J* = 7.9 Hz, 3H), 7.51 (dd, *J* = 8.2, 7.0 Hz, 3H), 7.42 (dd, *J* = 11.0, 8.5 Hz, 6H), 7.37-7.35 (m, 3H), 7.29 (d, *J* = 7.3 Hz, 3H), 4.39 (q, *J* = 7.1 Hz, 6H), 1.47 (t, *J* = 7.3 Hz, 9H); ^{13}C-NMR (100 MHz, $CDCl_3$) cannot be recorded due to poor solubility; HRMS calcd for $C_{63}H_{42}N_6S_3$ [M+Na] *m/z* 1001.2525, found 1001.2525.

5.4.2.15 3-((5-(4,6-Bis(5-bromothiophen-2-yl)-1,3,5-triazin-2-yl)thiophen-2-yl)ethynyl)-9-ethyl-9*H*-carbazole) (20bBr$_2$)

It was obtained as a product while synthesizing **20b**. Eluent: 50% $CHCl_3$ in Hexanes. Yellow solid; Yield: 50 mg (7%); mp: 150 °C; IR (KBr, cm^{-1}) 2968, 2924, 2855 ($\nu_{CHstretch}$), 2191 ($\nu_{C\equiv C}$), 1593, 1569, 1502 ($\nu_{C=C}$), 1403 (ν_{C-N}); ^{1}H-NMR (400 MHz, $CDCl_3$) δ 8.32 (s, 1H), 8.14 (d, *J* = 4.1 Hz, 1H), 8.11 (d, *J* = 7.6 Hz, 1H), 7.98 (q, *J* = 4.1 Hz, 2H), 7.65 (dd, *J* = 8.5, 1.6 Hz, 1H), 7.51 (t, *J* = 7.6 Hz, 1H), 7.42 (dd, *J* = 12.6, 8.0 Hz, 2H), 7.34 (d, *J* = 3.7 Hz, 1H), 7.29 (d, *J* = 7.3 Hz, 1H), 7.18 (d, *J* = 4.1 Hz, 2H), 4.39 (q, *J* = 7.3 Hz, 2H), 1.46 (t, *J* = 7.3 Hz, 3H); ^{13}C-NMR (100 MHz, $CDCl_3$) δ 166.9, 141.2, 140.3, 139.9, 132.3, 131.7, 130.8, 129.2, 128.5, 126.3, 124.2, 123.0, 122.5, 120.6, 119.5, 112.3, 108.8, 108.6, 97.9, 81.2, 37.7, 13.8; HRMS calcd for $C_{31}H_{18}Br_2N_4S_3$ [M+Na] *m/z* 722.8952, found 722.8948.

5.4.2.16 3,3'-(((6-(5-Bromothiophen-2-yl)-1,3,5-triazine-2,4-diyl)bis(thiophene-5,2-diyl))bis(ethyne-2,1-diyl))bis(9-ethyl-9*H*-carbazole) (20bBr)

It was obtained as a product while synthesizing **20b**. Eluent: 50%-70% $CHCl_3$ in Hexanes. Dark yellow solid; Yield: 30 mg (4%); mp: 138 °C; IR (KBr, cm^{-1}) 2965, 2923, 2853 ($\nu_{CHstretch}$), 2193 ($\nu_{C\equiv C}$), 1595, 1568, 1504 ($\nu_{C=C}$), 1405 (ν_{C-N}); ^{1}H-NMR (400 MHz, $CDCl_3$) δ 8.32 (s, 2H), 8.15 (d, *J* = 4.3 Hz, 2H), 8.11 (d, *J* = 7.9 Hz, 2H), 7.99 (d, *J* = 4.3 Hz, 1H), 7.66 (d, *J* = 9.2 Hz, 2H), 7.51 (t, *J* = 7.6 Hz, 2H), 7.41 (dd, *J* = 13.7, 8.9 Hz, 4H), 7.34 (d, *J* = 4.3 Hz, 2H), 7.29 (d, *J* = 7.9 Hz, 2H), 7.18 (d, *J* = 4.3 Hz, 1H), 4.38 (q, *J* = 7.1 Hz, 4H), 1.46 (t, *J* = 7.0 Hz, 6H); ^{13}C-NMR (100

MHz, $CDCl_3$) δ 166.9, 142.6, 140.9, 140.3, 139.9, 132.3, 131.8, 131.1, 129.2, 126.3, 124.2, 123.0, 122.5, 120.6, 119.5, 112.3, 108.7, 108.6, 98.2, 81.2, 37.7, 13.8; HRMS calcd for $C_{47}H_{30}BrN_5S_3$ [M] *m/z* 839.0841, found 839.0864.

5.4.2.17 4,4',4''-(((1,3,5-Triazine-2,4,6-triyl)tris(benzene-4,1-diyl))tris(ethyne-2,1-diyl))tris(*N*-(2-ethylhexyl))-1,8-naphthalimide (20c)

It was synthesized following same procedure as of **20a** but using a mixture of **2** and **19a**. The product was further purified by silica column chromatography. Eluent: $CHCl_3$; Yellow solid; Yield: 0.25 g (55%), mp: 303 °C; IR (KBr, cm^{-1}) 2957, 2928, 2857 ($\nu_{CHstretch}$), 2203 ($\nu_{C\equiv C}$), 1701, 1659 ($\nu_{C=O}$), 1569 ($\nu_{C=C}$), 1408 (ν_{C-N}); ^{1}H-NMR (400 MHz, $CDCl_3$) δ 8.77 (d, *J* = 8.0 Hz, 6H), 8.72 (d, *J* = 8.4 Hz, 3H), 8.63 (d, *J* = 7.2 Hz, 3H), 8.59 (d, *J* = 8.8 Hz, 3H), 8.54 (d, *J* = 7.6 Hz, 3H), 7.98 (d, *J* = 7.6 Hz, 3H), 7.83 (d, *J* = 8.4 Hz, 6H), 7.71 (d, *J* = 8.4 Hz, 3H), 4.18-4.07 (m, 6H), 1.97-1.93 (m, 3H), 1.42-1.25 (m, 24H), 0.97-0.83 (m, 18H); ^{13}C-NMR (100 MHz, $CDCl_3$) δ 170.8, 164.2, 163.9, 136.3, 134.6, 132.1, 132.0, 131.7, 131.5, 131.1, 130.4, 130.3, 129.0, 128.0, 127.9, 127.6, 126.8, 126.6, 123.1, 122.5, 98.3, 89.0, 44.3, 37.9, 30.8, 28.7, 24.1, 23.1, 14.1, 10.6; HRMS calcd for $C_{87}H_{78}N_6O_6$ [M+Na] *m/z* 1325.5875, found 1325.5865.

5.4.2.18 4,4',4''-(((1,3,5-Triazine-2,4,6-triyl)tris(thieno-5,2-diyl))tris(ethyne-2,1-diyl))tris(*N*-(2-ethylhexyl))-1,8-naphthalimide (20d)

It was synthesized following same procedure as of **20b** but using a mixture of **2** and **19b**. The desired product was further purified by silica column chromatography. Eluent: $CHCl_3$, Yellow solid; Yield: 1.2 g (91%), mp: 300 °C; IR (KBr, cm^{-1}) 2956, 2926, 2860 ($\nu_{CHstretch}$), 2193 ($\nu_{C\equiv C}$), 1702, 1661 ($\nu_{C=O}$), 1588, 1504($\nu_{C=C}$), 1444 (ν_{C-N}); ^{1}H-NMR (400 MHz, $CDCl_3$) δ 8.49 (d, *J* = 6.9 Hz, 3H), 8.43 (d, *J* = 8.2 Hz, 3H), 8.37 (d, *J* = 7.3 Hz, 3H), 8.08 (d, *J* = 3.7 Hz, 3H), 7.76 (d, J = 8.0 Hz, 3H), 7.72 (t, *J* = 7.8 Hz, 3H), 7.42 (d, *J* = 3.7 Hz, 3H), 4.08 (m, 6H), 1.94-1.91 (m, 3H), 1.41-1.27 (m, 24H), 0.94 (t, *J* = 7.3 Hz, 9H), 0.89 (t, *J* = 6.9 Hz, 9H); ^{13}C-NMR (100 MHz, $CDCl_3$) cannot be recorded due to poor solubility; HRMS calcd for $C_{81}H_{72}N_6O_6S_3$ [M+H] *m/z* 1321.4748, found 1321.4736.

5.4.2.19 4,4'-(((6-(5-Bromothiophen-2-yl)-1,3,5-triazine-2,4-diyl)bis(thiophene-5,2-diyl))bis(ethyne-2,1-diyl))bis(*N*-(2-ethylhexyl))-1,8-naphthalimide (20dBr)

It was obtained as a product while synthesizing **20d**. Eluent: Hexanes:EtOAc (4:1), Pale yellow solid; Yield: 30 mg (3%), mp: 280 °C; IR (KBr, cm^{-1}) 2955, 2924, 2858 ($\nu_{CHstretch}$), 2190 ($\nu_{C\equiv C}$), 1701 1661 ($\nu_{C=O}$), 1590 ($\nu_{C=C}$), 1460 (ν_{C-N}); ^{1}H-NMR (400 MHz, $CDCl_3$) δ 8.65 (m, 4H), 8.54 (m, 2H), 8.27 (d, *J* = 3.7 Hz, 1H), 8.21 (d, *J* = 4.1 Hz, 1H), 8.17 (d, *J* = 4.4 Hz, 1H), 7.95 (d, *J* = 7.6

Hz, 2H), 7.86 (t, *J* = 7.8 Hz, 2H), 7.67 (d, *J* = 5.0 Hz, 1H), 7.52 (d, *J* = 4.1 Hz, 2H), 4.20-4.05 (m, 4H), 1.98-1.92 (m, 2H), 1.42-1.29 (m, 16H), 0.94 (t, *J* = 7.6 Hz, 6H), 0.89 (t, *J* = 6.9 Hz, 6H); ^{13}C-NMR (100 MHz, $CDCl_3$) δ 166.6, 164.2, 163.9, 143.3, 134.3, 131.9, 131.7, 131.1, 131.0, 130.7, 130.2, 130.1, 128.6, 128.4, 127.9, 127.7, 126.3, 122.9, 122.5. 92.9, 91.9, 44.2, 37.9, 30.7, 28.7, 23.9, 23.1, 14.1, 10.6; HRMS calcd for $C_{59}H_{50}BrN_5O_4S_3$ [M+H] *m/z* 1068.2281, found 1068.2282.

Chapter 6 Effect of Non-conjugated Chromophores on Photophysics, Electrochemistry, Morphology and Bioimaging Applications of Naphthalimide Derivatives

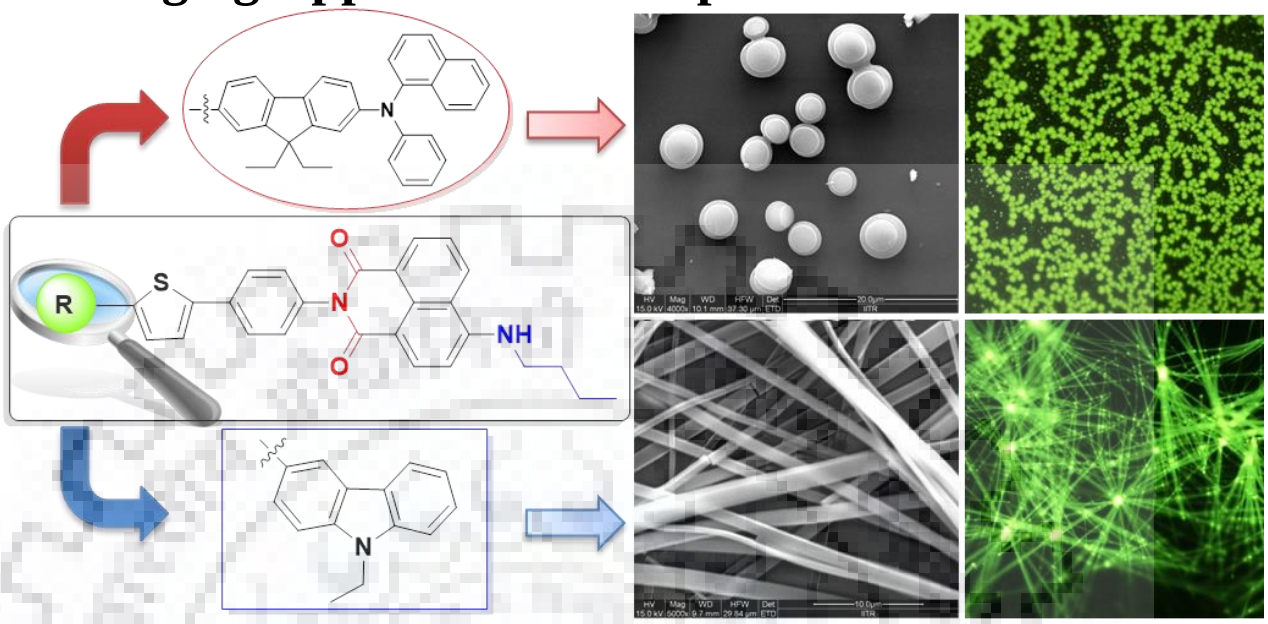

6.1 Introduction

Organic materials receive immense attention owing to their wide practical use in electronic devices and biological applications. Organic molecules containing discrete molecular structure and small molecular weights are advantageous over polymeric materials due to their straightforward synthesis, easy purification, high quantum efficiency, wide structural variability and simple fabrication methodologies. Such small molecules containing donor and acceptor moieties either interacting via conjugation or attached through a non-conjugating node have been synthesized and demonstrated for application in optoelectronics and biosensors. Systematic understanding of structure-property relationship in D-A molecules helps to fine tune structural components required to assemble functional materials of specific application. Triarylamines and electron rich heterocycles such as carbazole, phenothiazine and dithienopyrrole were routinely used as donors while electron-deficient fragments such as benzothiadiazole, benzotriazole, oxadiazole, phthalimide, naphthalimide and perylenediimide explored as acceptors.

Among the known acceptor chromophores, 1,8-naphthalimides have gained much attention due to its high electron affinity, optical, thermal and chemical stabilities, promising electron-transporting and tunable fluorescent properties. Wide variety of organic dyes possessing naphthalimide unit have found application as discussed in Chapter 1 in OLEDs, OSCs, biological and chemical sensors.[417-421] Naphthalimide can be functionalized at naphthalene nucleus or

imidic nitrogen with different substituents and offers pathways to fine-tune the photophysical and electronic properties of the targets. It is well established that optical and electrochemical properties of naphthalimides can be altered by extending the π-conjugation at C4. The behaviour of the substituents (electron-donating or withdrawing) at C4 scale the extend of charge transfer and thus the fluorescent and redox properties of the resulting derivatives. However, naphthalimides without functionalization at nucleus display poor fluorescence due to the presence of an upper lying triplet excited state isoenergetic with the lowest singlet excited state which facilitates intersystem crossing. Further, naphthalimides provide wide scope for functionalization at the imide nitrogen as well. Though the effect of chromophore attached to nitrogen has negligible or no influence on the electronic properties otherwise dominated by naphthalimide core, they help to modulate the interchromophoric interactions in the solid state and consequently the charge transporting properties. Among the pool of aromatic electron rich chromophores, carbazole, triphenylamine, and fluorene are widely explored due to the easy oxidizability and the ability to transport charges *via* the radical-cation species. Integration of a hole transporting moiety with an electron transporting unit is beneficial to balance charge transport in molecular layer. Chart 6.1 represents the structures of related typical D-A based materials. Wang *et al.*[422] synthesized naphthalimides, **D43** featuring fluorene at the imidic nitrogen and found to exhibit good electron-transporting characteristics in electroluminescent devices. Zhu *et al.*[423] synthesized carbazole containing naphthalimide derivatives, **D44** and **D45** and found to possess bipolar character which was beneficial for the realization of single layer electroluminescent device.

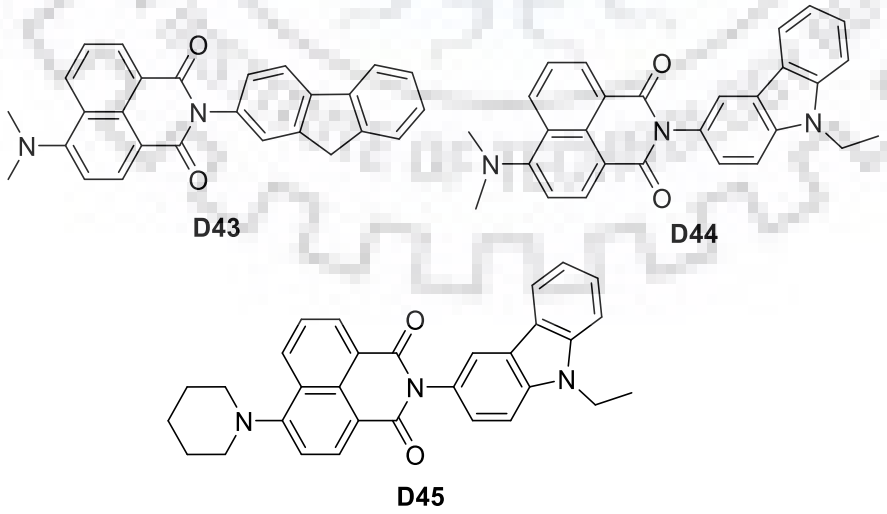

Chart 6.1 Structures of related naphthalimide-based D-A dyes.

In this Chapter, we present a series of 1,8-naphthalimides (Figure 6.1) containing different chromophoric units at imidic nitrogen.[424] The motivation behind the choice of fluorene and carbazole is that they display promising photophysical and thermal properties due to their rigid structure and offer multiple nuclear positions for chemical modifications. We investigated the effect of structural variation on photophysical and electrochemical properties of the dyes and correlated the trends with theoretical results. Interestingly, the differences in the structural composition of these dyes result in significant morphological changes in the solid state as determined by electron microscopy analyses. They are highly fluorescent in nature, which pave way for exploration in cellular staining. These new compounds are potential candidates for cellular imaging applications and showed remarkable biocompatibility.

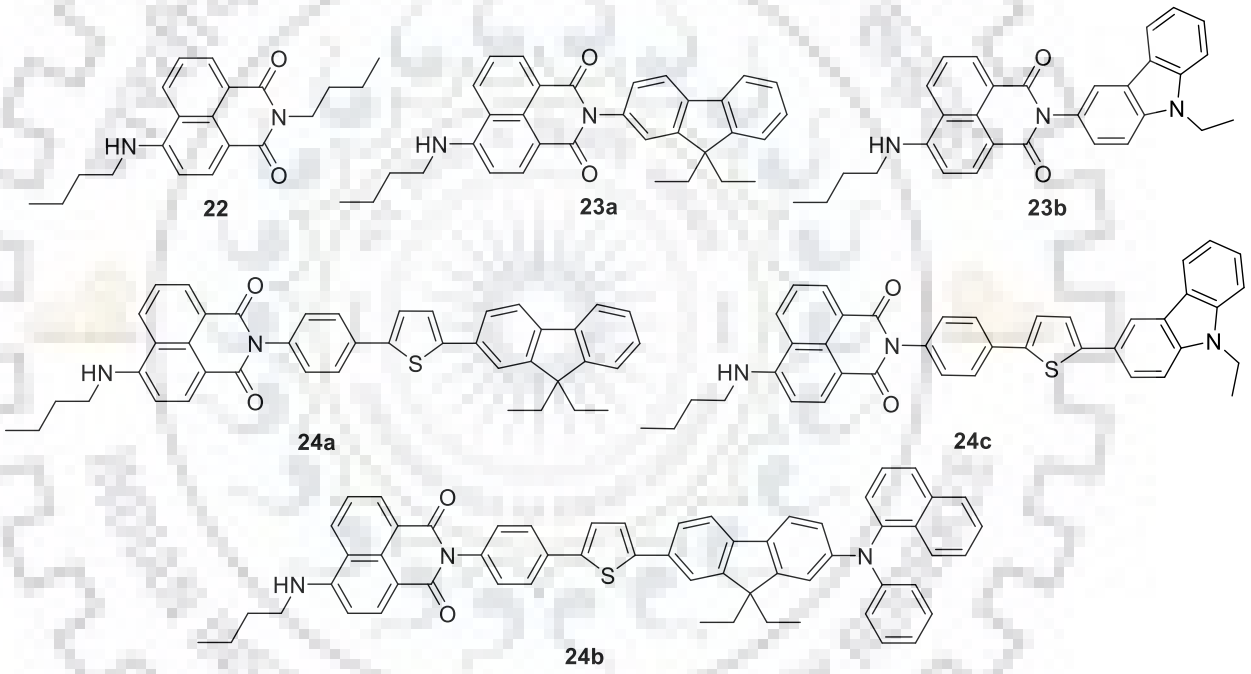

Figure 6.1 Structures of the naphthalimide-based D-A small molecules.

6.2 Results and Discussion

6.2.1 Synthesis and Characterization

The synthetic protocol used to obtain the dyes **22**, **23a**, **23b**, **24a, 24b** and **24c** is shown in Scheme 6.1. The synthesis of these dyes involves imidization of 4-bromo-1,8-naphthalic anhydride, followed by nucleophilic substitution with *n*-butylamine and Stille coupling reaction with suitable tin reagent.[425] Since the basicity of the aromatic amine is much weaker than that of aliphatic amine, the imidization of 4-bromo-1,8-naphthalic anhydride with fluorenyl, carbazolyl and 4-bromophenyl amine to yield intermediates **21a-21c** required harsh conditions such as zinc

acetate catalyst. This step is followed by nucleophilic attack of *n*-butylamine on 4th-position of naphthalimide to give **23a**-**23c**. Whereas dye **22** was synthesized with ease using excess of *n*-bulylamine under milder conditions. The dyes **24a**-**24c** were synthesized by Stille coupling reaction of appropriate tin reagents with **23c**. All compounds were characterized by IR, NMR (^{1}H and ^{13}C) and mass spectral methods. The spectral data of the dyes are consistent with the proposed structures. The bright yellow coloured dyes are moderately soluble in common organic solvents such as TOL, $CHCl_3$, THF, DCM, DMSO, DMF, ACN, and MeOH.

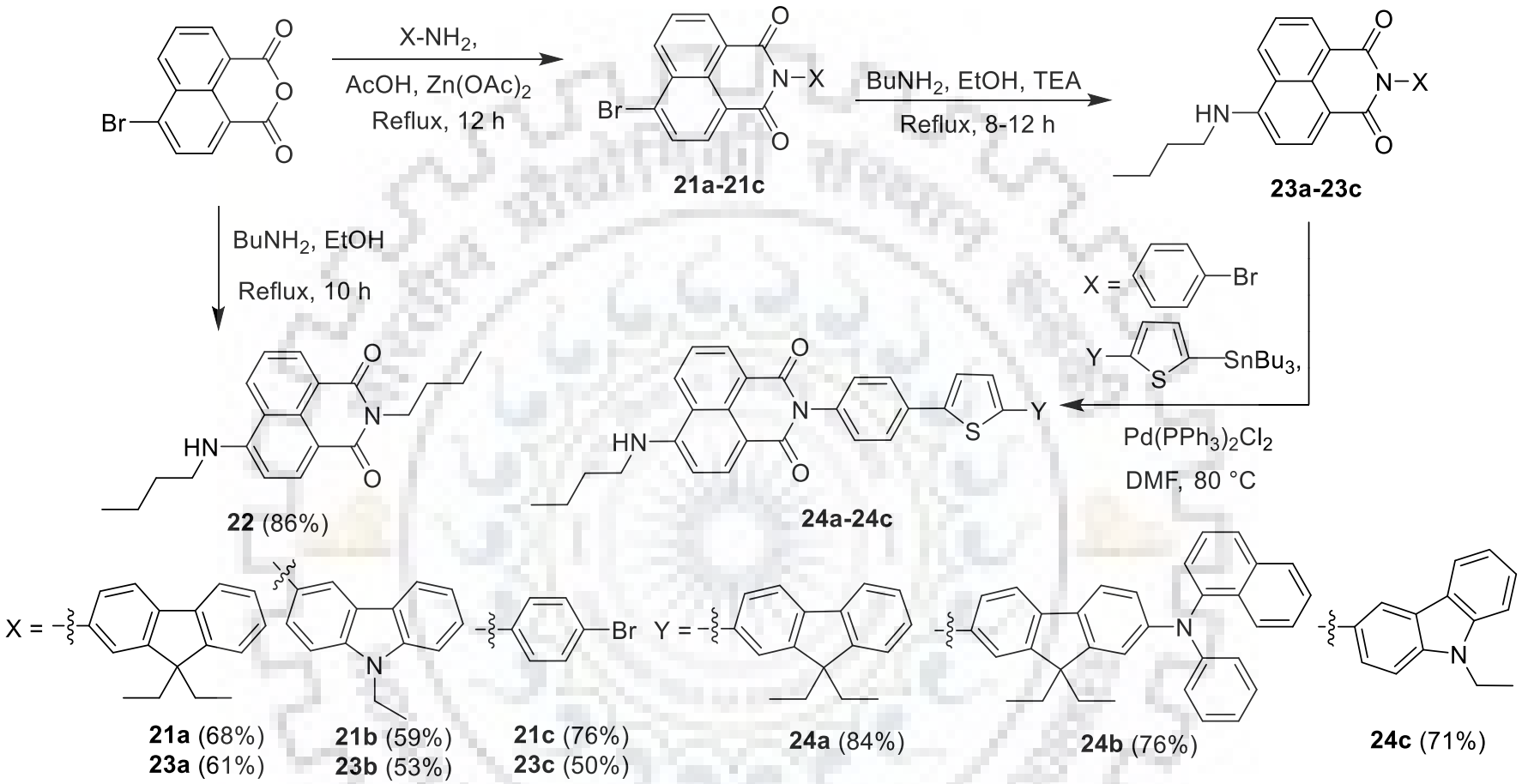

Scheme 6.1 Synthesis of the dyes.

6.2.2 Theoretical Studies

To understand the electronic structure of the dyes, the geometries of the dyes were first optimized by DFT using B3LYP hybrid functional and 6-31G(d,p) basis set. The optimized structures assumed non-planar arrangement of functional entities as depicted in Figure. 6.2. The non-planarity of the model compounds can be highlighted in terms of the large dihedral angle (60-88°) between the imidic chromophore and the naphthalimide planes. While for the extended π-conjugated dyes (**24a**, **24b** and **24c**) the dihedral angles between the peripheral chromophore, thiophene ring and the phenylene ring are in range 25-28°, which suggested further twisting in the conjugation framework.

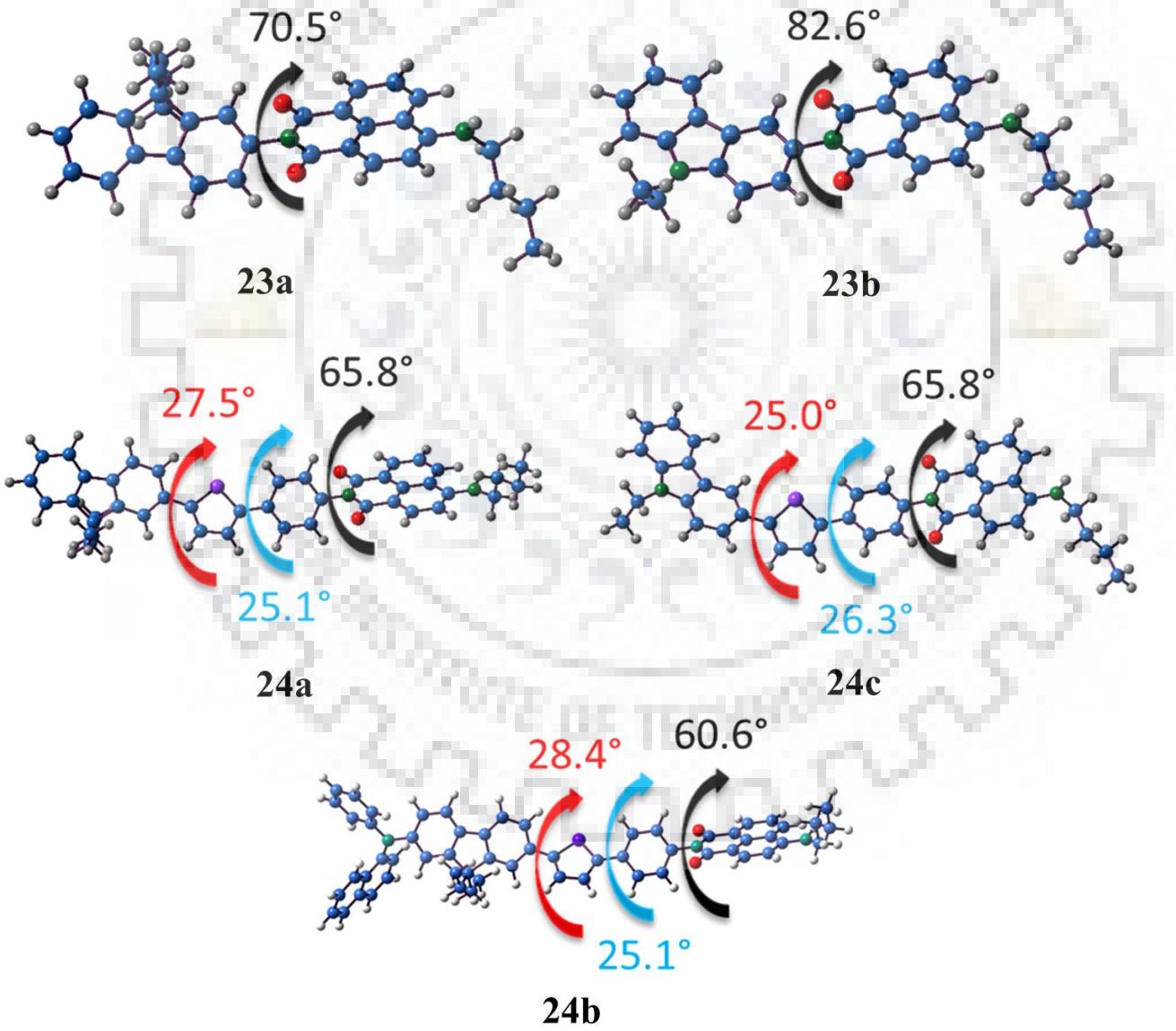

Figure 6.2 Optimized geometries and interchromic dihedral angles for the compounds.

Figure 6.3 shows the electronic distribution in frontier molecular orbitals, HOMO and LUMO of the selected dyes **22** and **24a**. The computed energies of the vertical excitations and their orbital contributions using TDDFT in the B3LYP level are compiled in Table 6.1. The HOMO of the dyes **23b**, **24a**, **24b** and **24c** containing donor segment is largely delocalized over the entire π-system at the imidic position (Figure 6.4). While in **22** and **23a**, which lack donor, it is constituted by naphthalimide unit. In all the dyes, the LUMO is mainly localized on the naphthalimide unit. It is interesting to highlight that although the dyes are structurally different at the imidic position the computed electronic transitions at low energy region are found to be closely related and originating from the common chromophore. The prominent absorption appearing at ~410 nm is mainly originating from HOMO to LUMO electronic excitation in **22** and **23a**, while in **23b**, **24a**, **24b** and **24c** it is due to HOMO-1 to LUMO electronic transition. As these orbitals are mainly composed of naphthalimide unit, this absorption is assigned to naphthalimide-based π-π* transition. Moreover, in dyes **24a**-**24c** an additional HOMO to LUMO electronic excitation occurs due to aromatic π-system present in imidic nitrogen. This assignment is confirmed from the orbitals (Figure 6.3) involved in these transitions. Also, these π-π* transitions are consistent with the trend in the absorption wavelength conjugation length of the imidic chromophore.

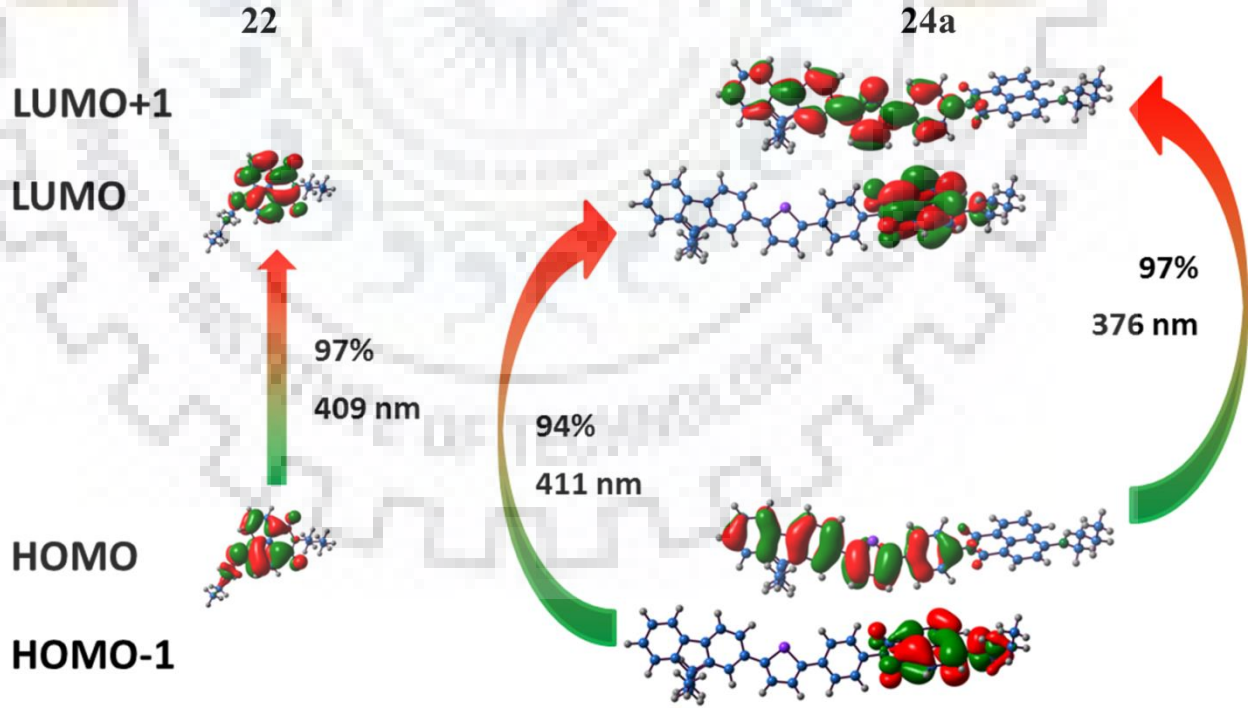

Figure 6.3 Electronic distributions in the frontier molecular orbitals of the dyes **22** and **24a** responsible for prominent absorptions.

Dye	HOMO-1	HOMO	LUMO	LUMO+1
23a	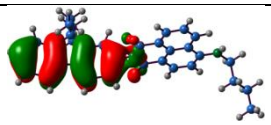	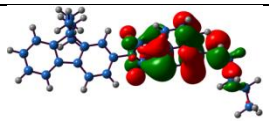	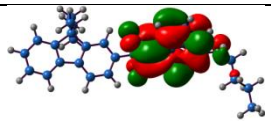	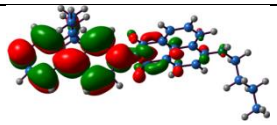
23b	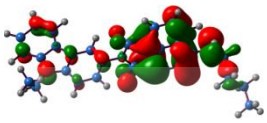	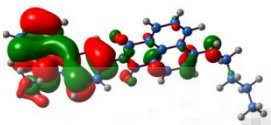	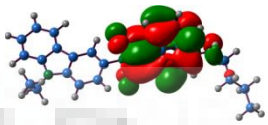	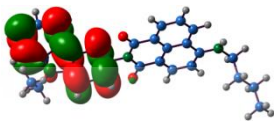
24b	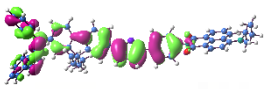	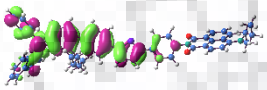	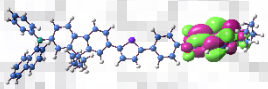	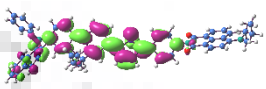
24c	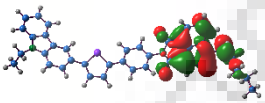	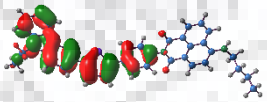	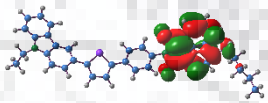	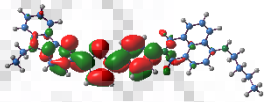
22	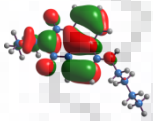	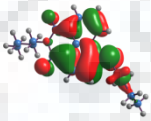	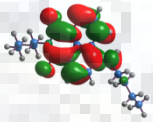	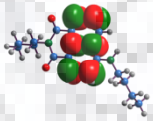

Figure 6.4 Electronic distributions in the frontier molecular orbitals of the dyes.

Table 6.1 Computed electronic parameters of the dyes in DCM.

Dye	λ_{max}, nm	*f*	Composition
23a	410	0.36	HOMO → LUMO (97%)
23b	408	0.33	HOMO-1 → LUMO (97%)
24a	411	0.59	HOMO-1 → LUMO (94%)
	376	1.46	HOMO → LUMO+1 (97%)
24b	431	1.70	HOMO → LUMO+1 (90%)
	411	0.15	HOMO-2 → LUMO (51%), HOMO-1 → LUMO (41%)
24c	412	0.52	HOMO-1 → LUMO (95%)
	372	1.06	HOMO → LUMO+1 (97%)
22	409	0.30	HOMO → LUMO (97%)

6.2.3 Photophysical Properties

The absorption spectra for the dyes recorded in DCM (2×10^{-5} M) are displayed in Figure 6.5(a). The relevant photophysical data is compiled in Table 6.2. All the compounds exhibit a common absorption at ca. 410 nm attributable to the n-π* electronic excitation localized within naphthalimide as predicted by theoretical calculations. This absorption is closely matching with the theoretically predicted values. Interestingly, the absorption maxima of other reported dyes with different substituent at 4th position of naphthalimide are found to be centered in same region. 4-(*N*,*N*-dimethylamino)-*N*-(2-fluorenyl)-1,8-naphthalimide, **D43** and 4-dimethylamino-*N*-(9-ethyl-9*H*-carbazol-3-yl)-1,8-naphthalimide, **D44** displayed absorption in range of 409-415 nm. This further supports the existence of common electronic excitation which is localized within naphthalimide. Further, compounds **24a-24c** exhibited an additional higher energy absorption arising from the aromatic chromophores attached to the imidic nitrogen. This π-π* absorption wavelength showed a trend attributable to the conjugation length of the chromophore. Thus, the dye **24b** displayed the most red-shifted absorption in this series.

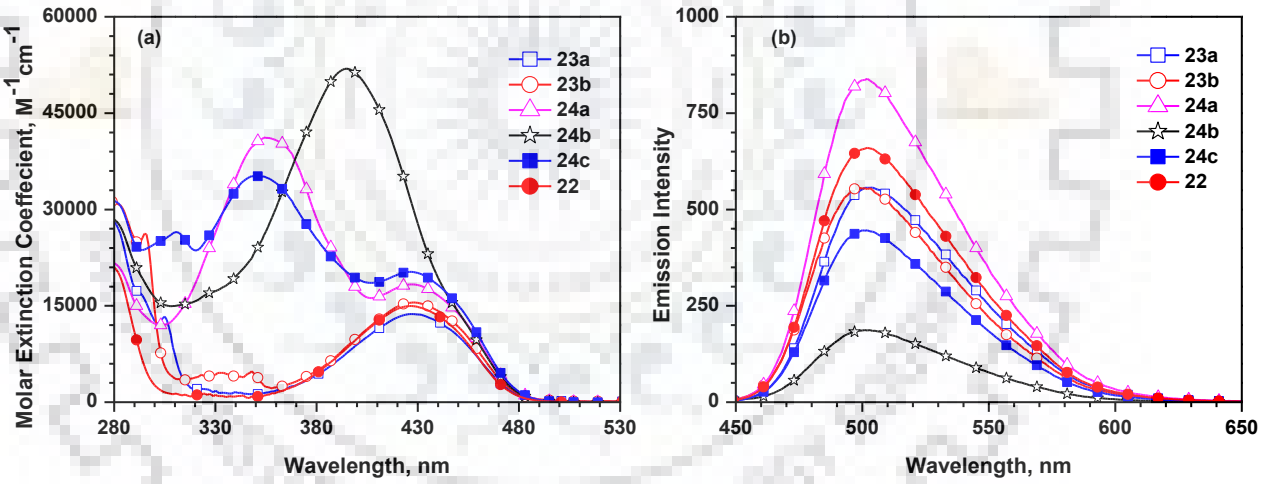

Figure 6.5 (a) Absorption and (b) emission spectra of dyes recorded in DCM.

The compounds are intensely emitting in yellow to green region. All dyes exhibit a broad and structureless band centered at ~500 nm irrespective of the nature of the chromophore in the molecule (Figure 6.5(b)). This indicates the excited state is similar in all the compounds and probably originates from the naphthalimide unit. The introduction of additional chromophores in **23a-23b** and **24a-24c** does not alter the emission properties of the dyes. This could be due to the orthogonal orientation of the units at the imidic nitrogen of naphthalimide, which blocks effective electronic communication. Further, the absence of residual emission from the *N*-chromophore suggests the effective energy transfer from it to the naphthalimide moiety. The values of the

Stokes shift for these dyes are in the range of 3300–3500 cm^{-1} which is in accordance with other similar 1,8-naphthalimide derivatives. Such values of Stokes shift points toward the existence of non-radiative relaxation pathways due to the non-planarity and significant geometric rearrangements in the excited state of the molecule. Further, the solid state emission of the dyes exhibit broad band accompanied by quenching of fluorescence which is common for planar conjugated emitting materials. All the dyes exhibited red-shift of 15-20 nm in the solid state (Table 6.2) when compared to their solution. This reflects the presence of intermolecular interactions in the solid state of the dyes.

The solvatochromism study was performed for all of the dyes to evaluate the effect of solvent polarity on the optical properties of the dyes (Figures 6.6 and 6.7). The absorption and emission data observed for the dyes in different solvents are listed in Tables 6.3 and 6.4. All the dyes showed negligible changes in shorter wavelength region peak arising from localized π-π* transition while the naphthalimide-based electronic transition exhibits positive solvatochromism (~25 nm) on varying the polarity of the solvent. Furthermore, the dyes show prominent positive solvatochromism (~50 nm) in the emission spectra since the excited state is stabilized by polar solvents resulting in red shift in emission. This also shows that the dyes are more polarized in the excited state than in the ground state. The structureless emission pattern observed for the dyes in all the solvents can be described to the structural reorganization. The large Stokes shift in polar solvents supported pronounced polar character in the excited state than ground state.

The solvatochromic data of the dyes were analysed by Lippert−Mataga plot and Stokes shift versus E_T (30) parameter as displayed in Figure 6.8. The dyes exhibited linearity in the above correlations indicating the role of general solvent effect, which is typical for polar molecules. While a deviation from linearity for MeOH can be due to the specific interactions *i.e*. hydrogen bonding. The relative fluorescence quantum yield (Φ_F) measured by comparing with the standard show a quantum yield (>45%) except for **24b** and **24c**. The relatively low quantum yields observed for these compounds may be due to the electron transfer quenching from donor such as carbazole and triarylamine, which is a nonradiative deactivation pathway for the excited state.

Table 6.2 Optical, electrochemical and thermal data of the dyes.

Dye	λ_{max}, nm (ε_{max}, M^{-1} cm^{-1} × 10^3)	λ_{em}, nm (Φ_F %)[a]	Stokes shift, cm^{-1}	λ_{em},[b] nm	E_{ox},[c] mV (ΔE_p)	E_{red},[c] mV	HOMO,[d] eV	LUMO,[e] eV	E_{0-0},[f] eV	T_{onset} (°C)	T_d[g] (°C)
23a	429 (13.7), 306 (12.8)	502 (66)	3390	522	668, 976	-1516	-5.46	-3.28	2.18	306	440
23b	428 (15.5), 296 (26.1)	501 (88)	3404	524	676, 740	-1440	-5.48	-3.36	2.11	374	490
24a	427 (18.3), 354 (41.2)	502 (47)	3499	524	684, 772	-1636	-5.48	-3.16	2.32	430	525
24b	430 (sh), 395 (51.9)	501 (03)	3296	524	368 (65), 688 (64), 748	-1632	-5.17	-3.17	2.00	456	544
24c	426 (20.3), 352 (35.2), 311 (26.5)	500 (11)	3474	526	500, 664	-1696	-5.30	-3.10	2.20	427	527
22	428 (14.9), 280 (20.9)	502 (68)	3444	520	652	-1520	-5.45	-3.28	2.17	295	382

Recorded in DCM [a] Relative quantum yield was obtained by comparing with standard coumarin-6, [b] Solid state emission, [c] Redox potentials are reported with reference to the ferrocene internal standard using tetrabutylammonium perchlorate as electrolyte. [d] Obtained from the oxidation potential using the formula HOMO = -(4.8 + E_{ox}). [e] Deduced from the reduction potential using the formula LUMO = -(4.8 - |E_{red}|). [f] Calculated using formula E_{0-0}= E_{HOMO}-E_{LUMO}. [g] Decomposition temperature wrt 5% wt. loss.

Table 6.3 Absorption data for dyes recorded in different solvents.

Dye	λ_{max}, nm ($\mathcal{E}_{max}$, M^{-1} cm^{-1} × 10^3)						
	Tol	$CHCl_3$	THF	DMSO	DMF	ACN	MeOH
23a	421 (18.4), 306 (20.3)	428 (10.9), 306 (11.5)	428 (14.9), 306 (18.2)	443 (19.3), 306 (26.8)	440 (19.3), 306 (25.4)	432 (13.7), 306 (13.9)	443 (12.7), 306 (15.2)
23b	419 (09.1), 295 (15.9)	428 (15.9), 296 (27.6)	426 (35.6), 330 (11.2), 295 (21.0)	443 (13.5), 296 (26.4)	439 (12.9), 296 (25.0), 286 (25.5)	432 (13.3), 294 (19.6), 283 (20.3)	442 (08.5), 295 (15.8), 285 (15.5)
24a	418 (11.3), 357 (26.4)	427 (18.9), 355 (41.5)	425 (18.7), 355 (43.9)	442 (21.7), 362 (49.1)	437 (17.2), 360 (40.2)	431 (21.4), 354 (21.4)	440 (04.8), 352 (10.9)
24b	395 (49.4)	395 (45.1)	393 (58.1)	396 (57.4)	394 (51.3)	390 (37.3)	390 (-)
24c	417 (13.4), 351 (25.4), 311 (18.4)	427 (18.9), 348 (32.9), 311 (25.1)	427 (14.6), 348 (27.9), 310 (20.6)	442 (19.3), 356 (34.2), 311 (25.9)	437 (13.8), 354 (25.2), 310 (19.7)	431 (10.6), 349 (19.1), 311 (14.3)	443 (06.0), 349 (09.8), 311 (08.0)
22	420 (15.2)	429 (19.6), 280 (26.3), 262 (30.1)	429 (19.5), 280 (28.2), 262 (37.1)	443 (13.5), 296 (26.4)	440 (29.2), 283 (38.7)	432 (19.3), 280 (24.8), 260 (25.2)	443 (18.4), 283 (21.8), 260 (21.9)

Table 6.4 Emission and Stokes shift data for dyes recorded in different solvents.

Dye	λ_{em}, nm (Φ_F, %)[a]							Stokes shift, cm^{-1}						
	Tol	$CHCl_3$	THF	DMSO	DMF	ACN	MeOH	Tol	$CHCl_3$	THF	DMSO	DMF	ACN	MeOH
23a	484	494	502	527	523	518	535 (32)	3092	3122	3444	3598	3607	3843	3882
23b	483	495	500	527	522	517	533 (47)	3162	3162	3474	3598	3622	3806	3935
24a	484	494	502	528	523	523	530 (36)	3262	3122	3609	3685	3763	4081	3607
24b	485	494	500	526	524	519	537 (-)	-	-	-	-	-	-	-
24c	483	494	501	528	524	524	537 (07)	3277	3176	3459	3685	3799	4118	3951
22	482	497	507	526	522	517	531 (35)	3063	3244	3641	3562	3570	3806	3741

[a]Relative quantum yield was obtained by comparing with standard coumarin-6 (EtOH = 78%).

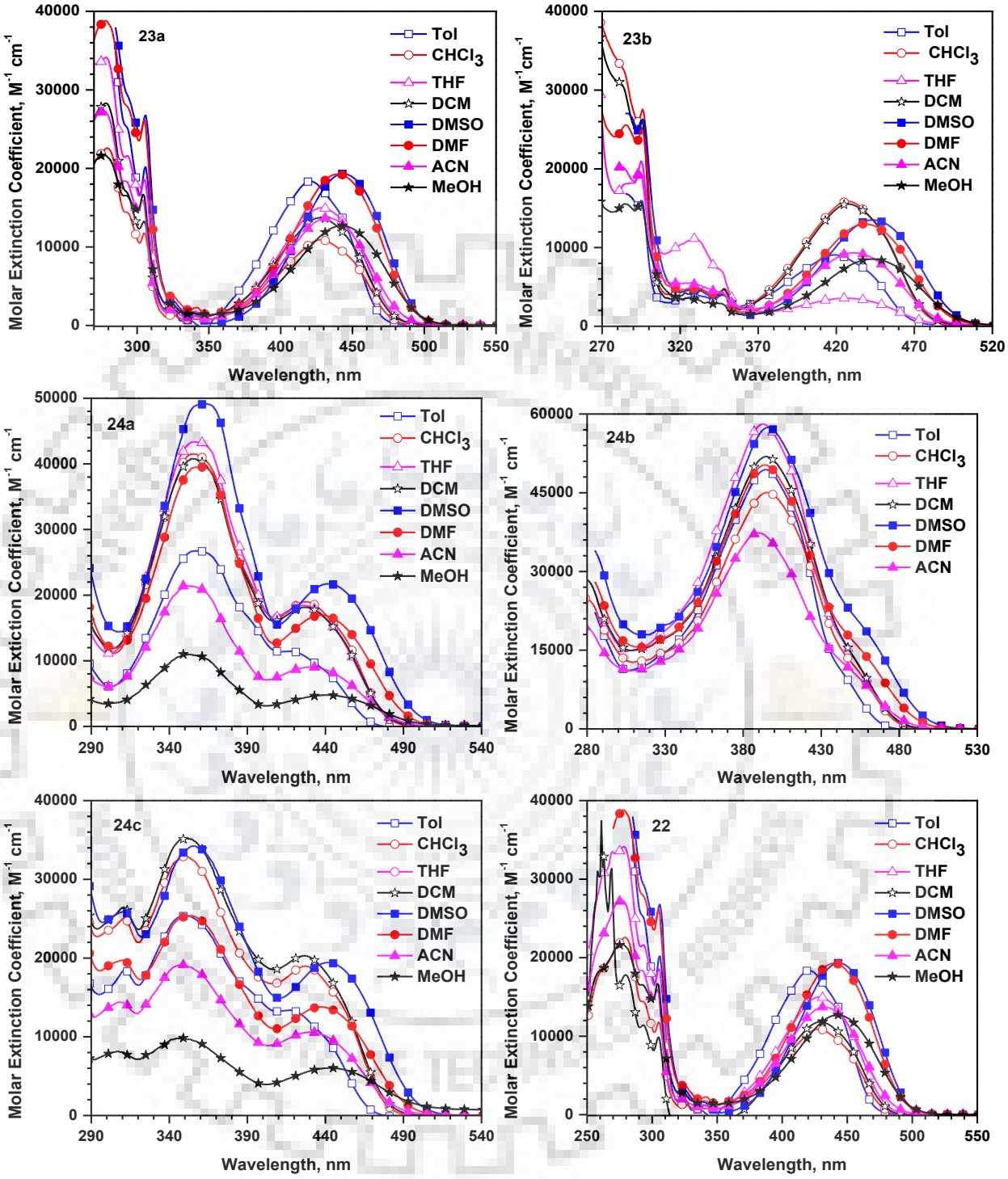

Figure 6.6 Absorption spectra of the dyes recorded in different solvents.

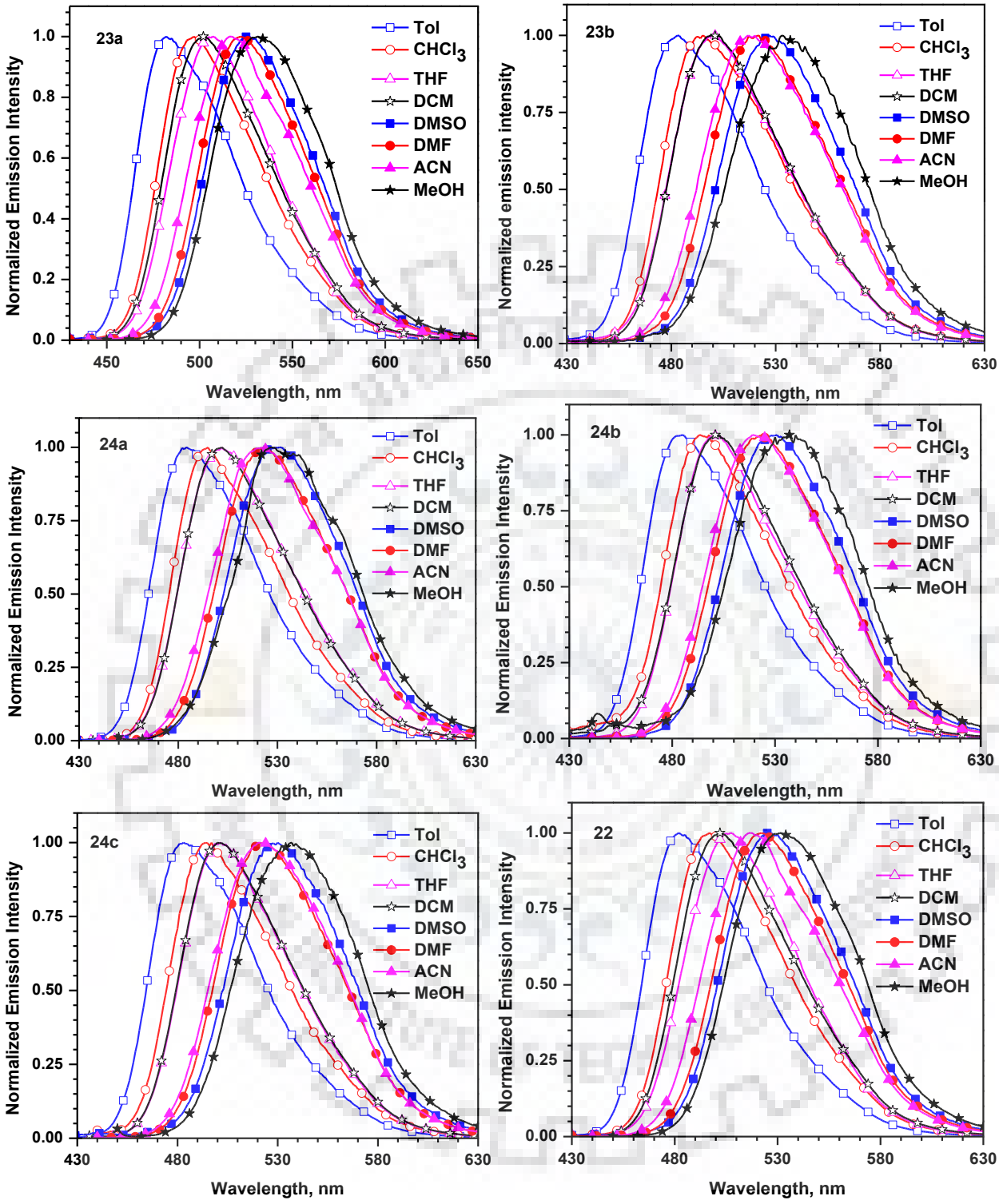

Figure 6.7 Normalized emission spectra of the dyes recorded in different solvents.

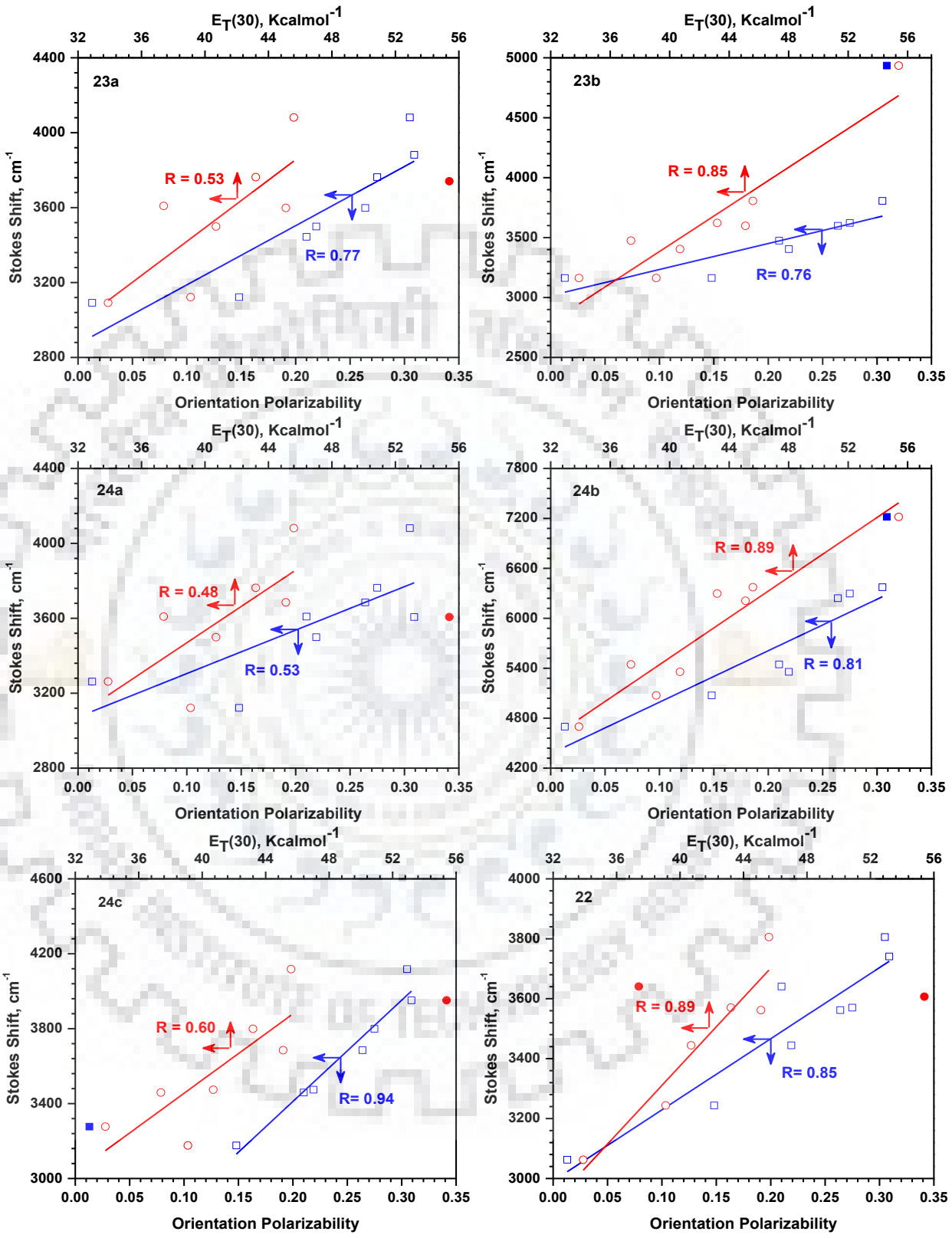

Figure 6.8 Lippert−Mataga and Stokes shift vs E_T (30) plot for the dyes.

6.2.4 Electrochemical Properties

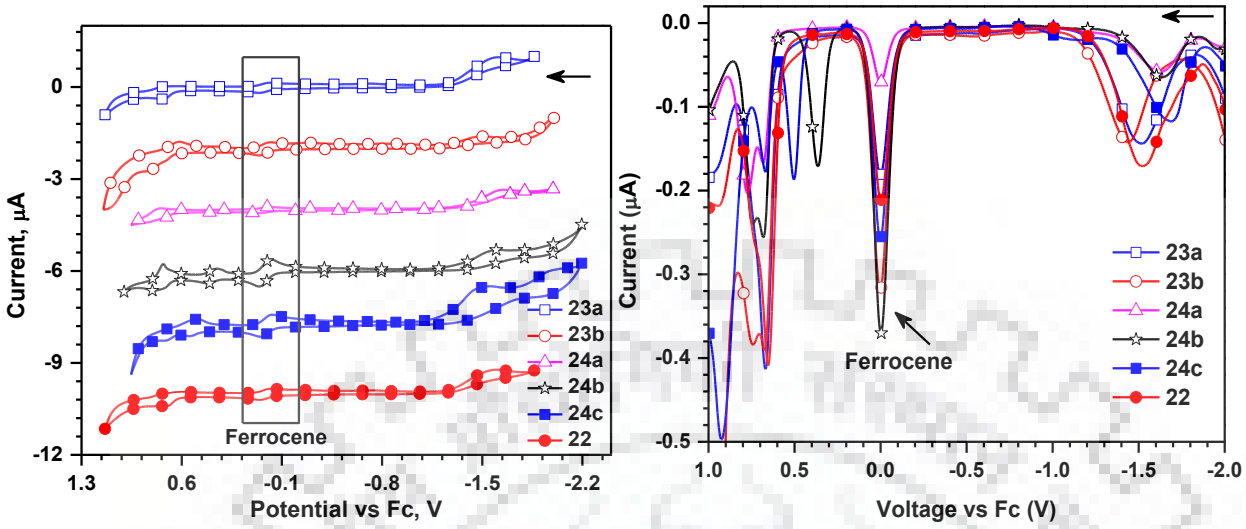

Figure 6.9 (a) CV) and (b) DPV of the dyes recorded in DCM.

The electrochemical analysis of the dyes was carried out using CV and DPV measurements (Figure 6.9). The results are summarized in Table 6.2. The CV plots exhibited signature waves attributable to the reduction of naphthalimide unit and the oxidation of donor moieties in the dyes. The reduction potential of the dyes is centered at -1.4 to -1.6 V. This reduction potential is shifted cathodically by 0.4-0.5 V when compared to the unsubstituted naphthalimides which generally showcase a reversible reduction wave at -1.0 to -1.1 V.[96] The oxidation peak centered at ~0.6 V for the dyes corresponds to the removal of electrons from butyl amino unit. Additional oxidation potentials are also observed for dyes, which are attributed to the oxidation of chromophoric units tethered on imidic nitrogen of naphthalimide core except for the reference dye **22**. It is interesting to note that oxidation potentials of the dyes **24a**, **24b** and **24c** shifts anodically when compared to the dyes **23a** and **23b** due to the enhanced electron richness of the chromophores such as carbazole and triarylamine attached to phenyl-thiophene linker. This is clearly understandable from the electronic distribution in the frontier molecular orbitals (*vide supra*) discussed earlier. An additional one electron reversible oxidation potential is observed for dye **24b** corresponding to the electron removal from *N*-naphthalenyl-(phenyl) amine moiety. The HOMO and LUMO energy levels of all the dyes were calculated by using a ferrocene as internal standard (-4.80 eV). The HOMO energy of the dyes falls in range of -5.2 to -5.5 eV, whereas the LUMO energies lie in the range -3.1 to -3.3 eV. This indicates that the dyes can show the good electron-transporting ability due to the low-lying LUMO levels when used as electron-transporting electroluminescent materials in OLEDs.

6.2.5 Thermal Properties

In order to determine the thermal stability of the dyes, TGA under nitrogen atmosphere at a heating rate of 10 °C/min was performed. Thermogravimetric traces of the dyes are shown in Figure 6.10. The dyes possess superior thermal stability with high thermal decomposition temperatures (T_d) falling in the range, 440-545 ˚C as compared to reference dye **22** (Table 6.2). The substituents at the *N*-position of the naphthalimide unit played an important role in determining the thermal stability of these compounds. Owing to bulkiness, dye **24b** exhibited highest T_d among the series. Furthermore, carbazole bearing dyes (**23b** and **24c**) showed superior thermal stability in comparison to respective fluorene analogs (**23a** and **24a**) in keeping with the literature precedence.[426, 427]

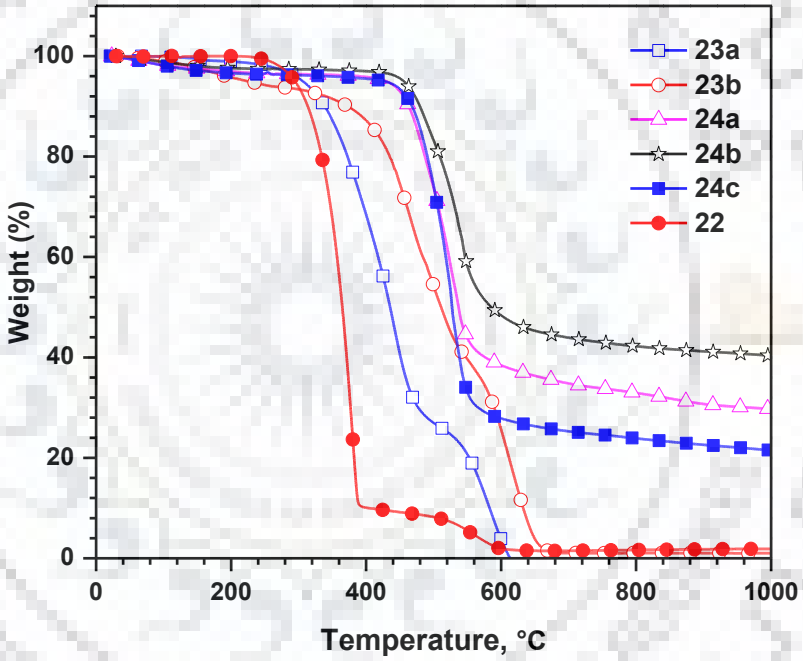

Figure 6.10 TGA curves of the dyes.

6.2.6 Morphological Properties

To gain further insight into the influence of structural variation on the morphologies of the dyes FESEM and TEM studies were performed. It was observed that these new molecules exhibit different types of morphologies depending upon the nature of chromophore on the imidic nitrogen. The SEM images for as synthesized samples show different non-uniform, ill-defined and bulky morphology in micrometer range as plates, rods, flakes and fibers (Figure 6.11). Whereas, the images examined for the film casted samples from DMSO solution exhibit fine and uniformly distributed morphology (Figures 6.12 and 6.13).

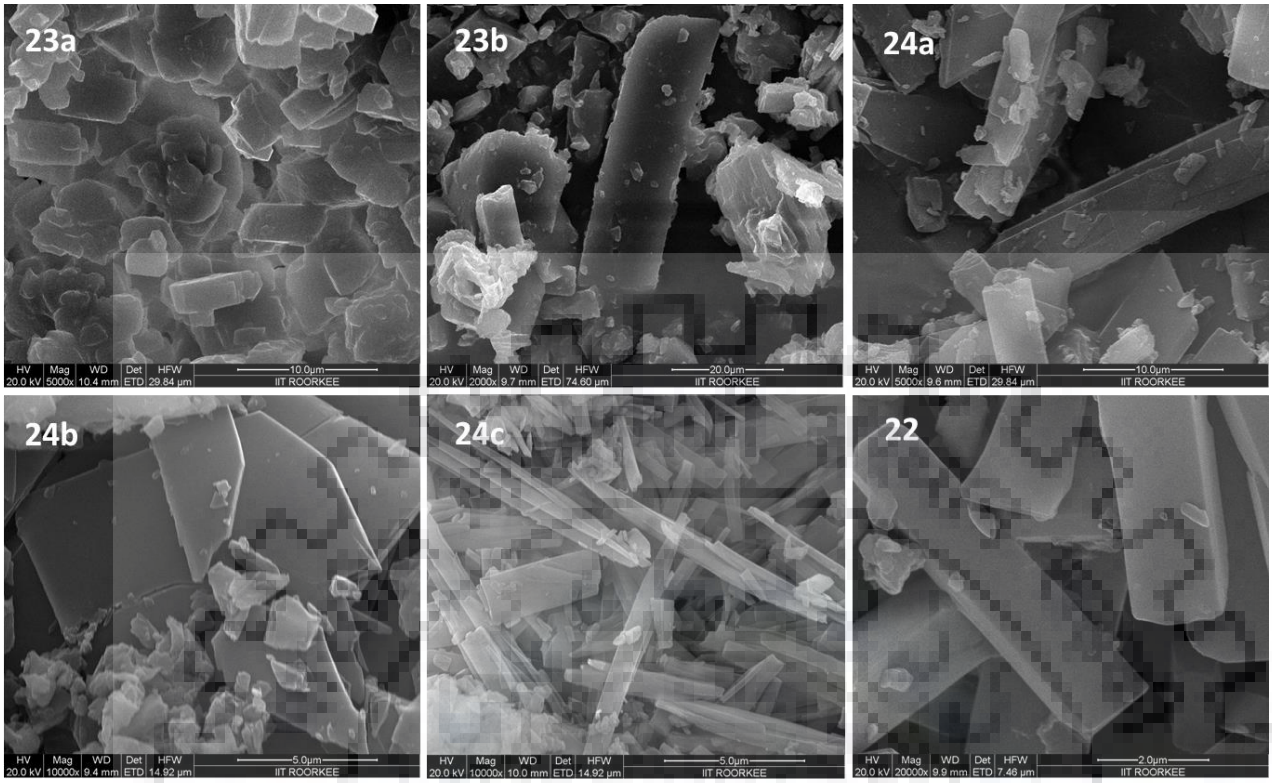

Figure 6.11 FESEM images of as synthesized dyes. Scale bar: **23a** (10 μm), **23b** (20 μm), **24a** (10 μm), **24b** (5 μm), **24c** (5 μm), **22** (2 μm), respectively.

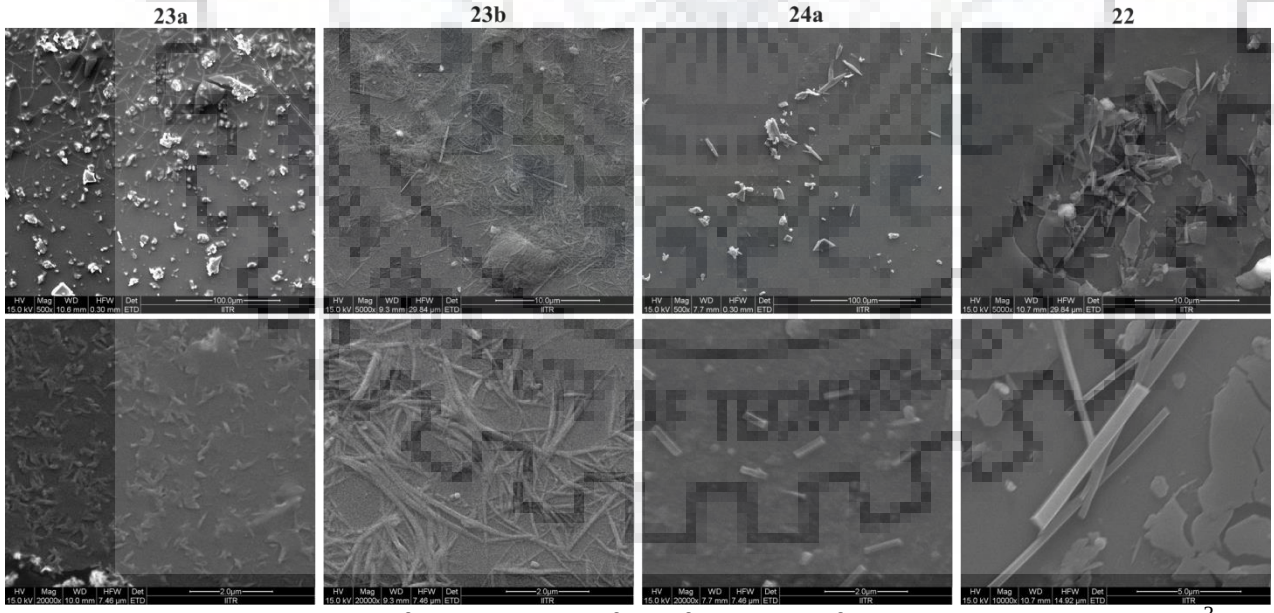

Figure 6.12 FESEM images of dyes obtained from film casted from DMSO solution (2×10^{-3} M). Scale bar = (above row) **23a**, **24a** (100 μm), **23b**, **26** (10 μm); (below row) **23a**, **23b**, **24a** (2 μm), **22** (5 μm).

The SEM images for dye **24b** reveal the presence of well-defined micro-spheres of uniform size with average diameter of 1 μm. While the dye **24c** exists as uniformly entangled network of wires of dimensions ~500 nm thick and several hundreds of microns in length. The shape and size of these samples are further confirmed by TEM analysis (Figures 6.13C, 13D). Further, the SAED image clearly established the amorphous nature of the compounds since diffuse rings with no bright spots were observed. Also, we have examined the influence of concentration (Figures 6.14 and 6.15) of the dyes **24b** and **24c** on the morphology. Fragmented and smaller sizes of the aggregates for both of the dyes were obtained at low concentrations, which point that the formation of well-defined and oriented morphology is concentration dependent. These SEM images provide to some extent detailed information on the mechanism for the morphology of the dyes. The diversity in shape and size of the morphology is probably arising from the difference in the conjugation length of the chromophore. The discrete morphological variation of dyes varying from rods, fibers, chips, spheres to wires revealed the significant role of intermolecular interactions arising from the conjugated aromatic chromophore. Hence, it can be stated that the facile tunable structural design of the functional materials is of immense importance for inducing changes in morphology.

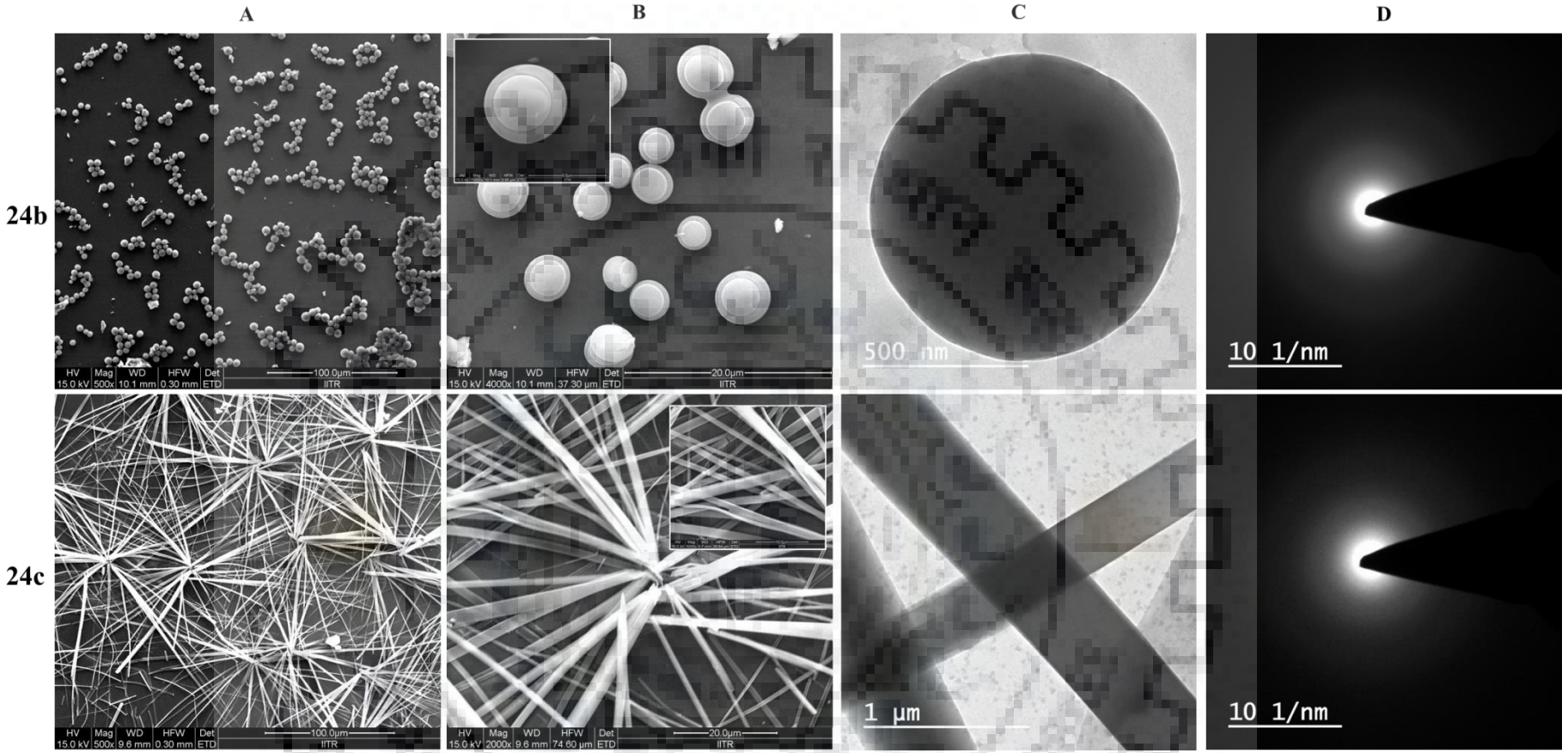

Figure 6.13 Morphology of dyes **24b** and **24c** (A, B) FESEM images obtained from film casted from DMSO solution (2×10^{-3} M). Scale bar = 100 µm, 20 µm respectively, (C) TEM image and (D) SAED image.

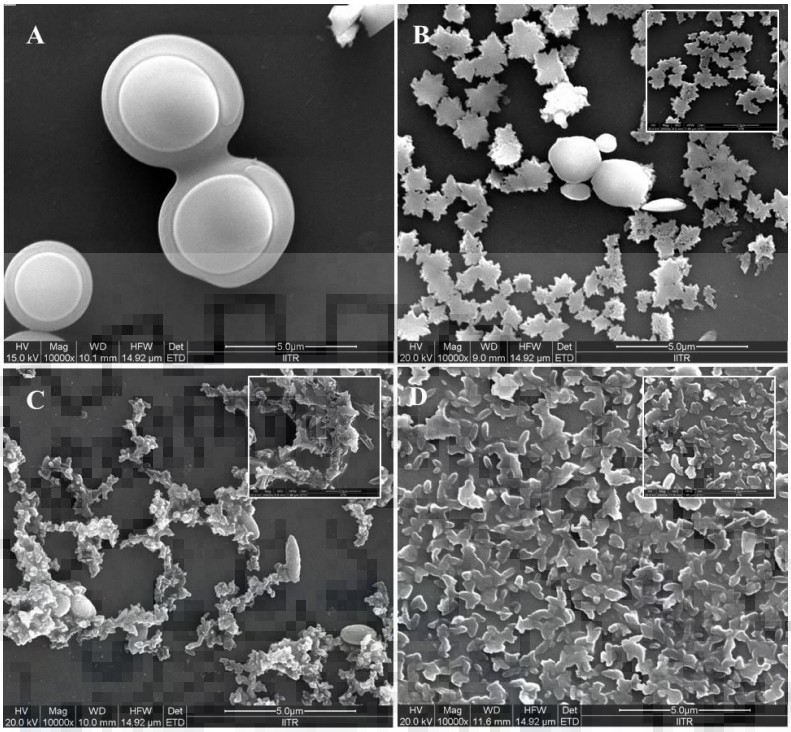

Figure 6.14 FESEM images of dye **24b** obtained for samples from DMSO solution at different concentrations (A) 2×10^{-3} M, (B) 2×10^{-4} M, (C) 2×10^{-5} M, (D) 2×10^{-6} M, Scale bar = 5 μm).

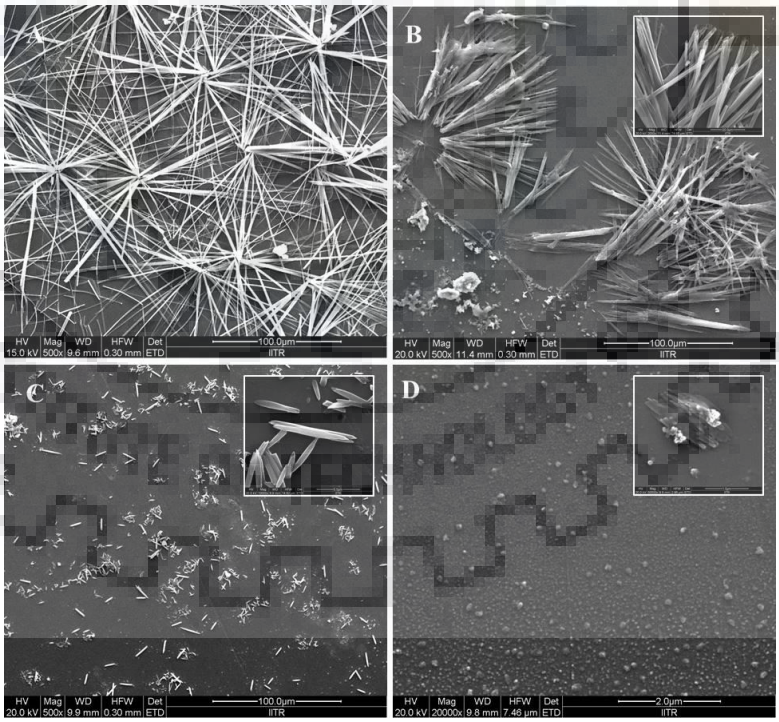

Figure 6.15 FESEM images of dye **24c** obtained for samples from DMSO solution at different concentrations (A) 2×10^{-3} M, (B) 2×10^{-4} M, (C) 2×10^{-5} M, (D) 2×10^{-6} M, Scale bar = 100 μm, 2 μm).

6.2.7 Fluorescence Microscopy Analysis

The fluorescence images of the dyes (Figures 6.16 and 6.17) were captured using optical fluorescence microscopy exhibiting multicolor emission under different light source owing to the broad emission range (*vide supra*). The drop-cast sample obtained from DMSO solution displays bright yellow-green and red fluorescence upon excitation with UV, blue and green light, respectively. The fluorescence images of the dyes are in good agreement with the SEM images of the dyes. All the dyes showed strong emission. The fine structures of the fluorescent spheres and wires were observed for **24b** and **24c**. Both the spherical balls and long micro-wires were uniformly spread and displayed both green and red emission. The highly fluorescent images were obtained for dye **24c** with entangled wires. Interestingly, the tips and the knot region of these wires were found to be significantly bright and may be helpful in optical wave-guiding. The multicolor and bright emission displayed by the reported dyes is of great importance for the design and fabrication of displays, OLEDs and for biological applications.

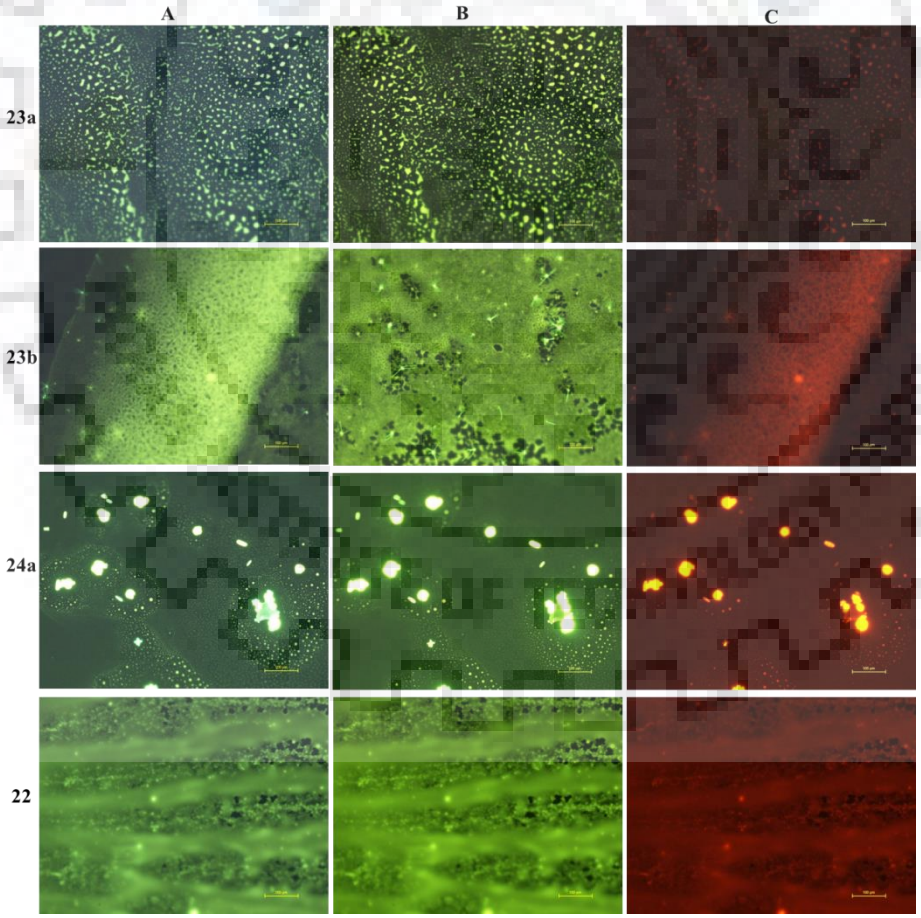

Figure 6.16 Fluorescence microscopy images of the dyes **23a, 23b, 24a** and **22**. Images captured under filter excitation (A) UV-2A, (B) B-2A, (C) G-2A. Scale = 100 μm.

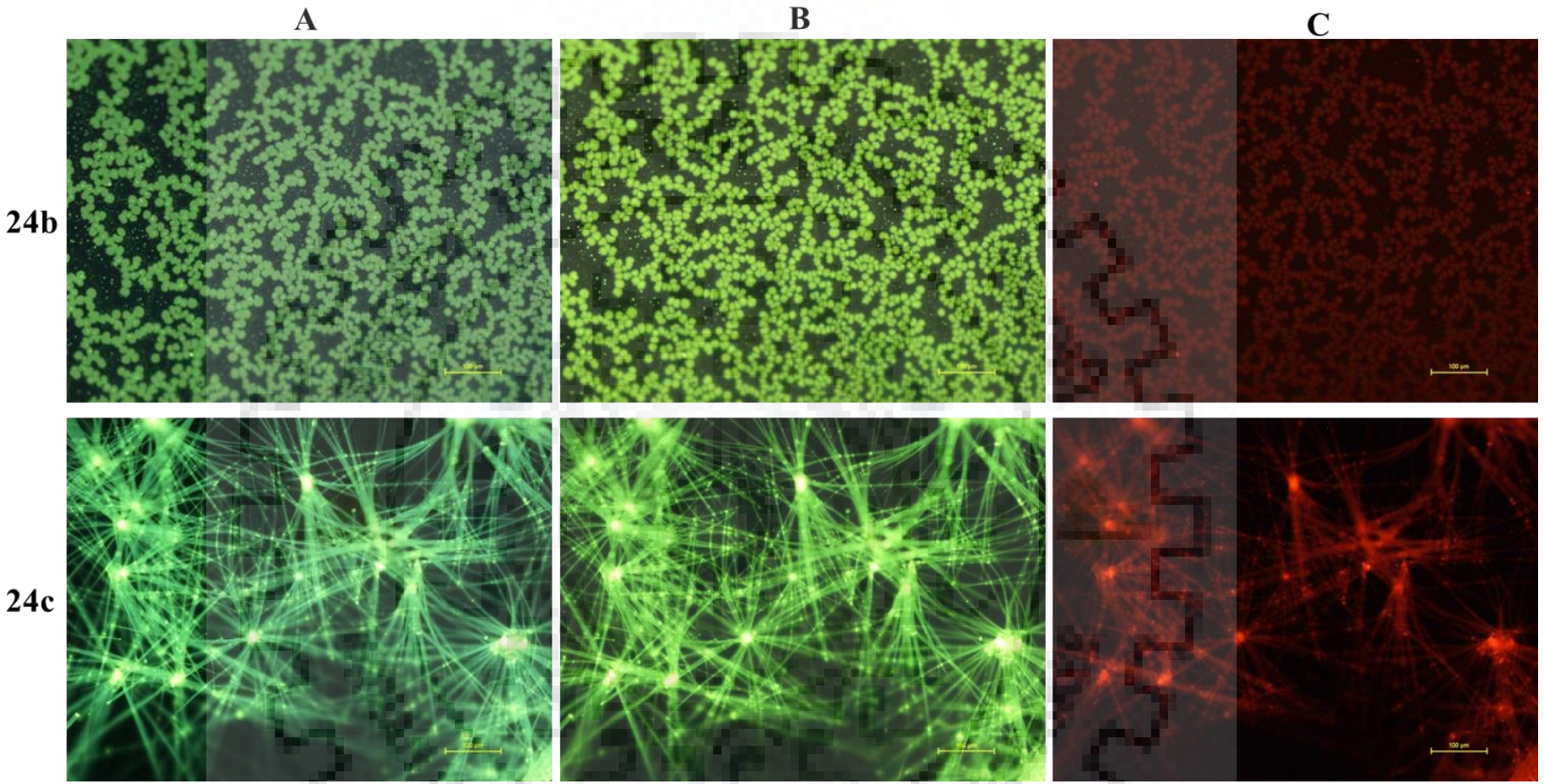

Figure 6.17 Fluorescence microscopy images of the dyes **24b** and **24c**. Images captured under filter excitation (A) UV-2A, (B) B-2A, (C) G-2A. Scale = 100 μm.

6.2.8 Biological Studies

To examine the bio-imaging potential of dyes, their cellular uptake behaviour was evaluated by fluorescence microscopy. Figures 6.18 and 6.19 show the cellular uptake of tested dyes used at a concentration of 30 μM. Distinct bright blue and green fluorescence was seen in A549 cells incubated with dyes **23a**, **23b** and **22** and while only green fluorescence was observed for cells incubated with dyes **24a-24c** owing to the strong fluorescence and broad emission range. As can be seen in the fluorescence images, dark areas were surrounded by either blue or green fluorescence. These dark areas correspond to the cell nucleus, thereby suggesting the cytoplasmic uptake by the endocytosis route for internalization of dyes. Also, it can be mentioned that due to the larger size of the dyes than the cell nucleus pore, the fluorescent dyes cannot enter the cell nucleus directly. Interestingly, dyes **24a-24c** displayed faint green emission (*vide supra*) due to their variable extents of aggregation inside the cytoplasm of the cells. It is noticeable to mention that the dyes possessing carbazole moiety (**23b** and **24c**) displayed brighter cell imaging comparable to dye **22** than fluorene containing naphthalimide dyes (**23a**, **24b** and **24c**) which can be attributed to the difference in cellular uptake biocompatibility.

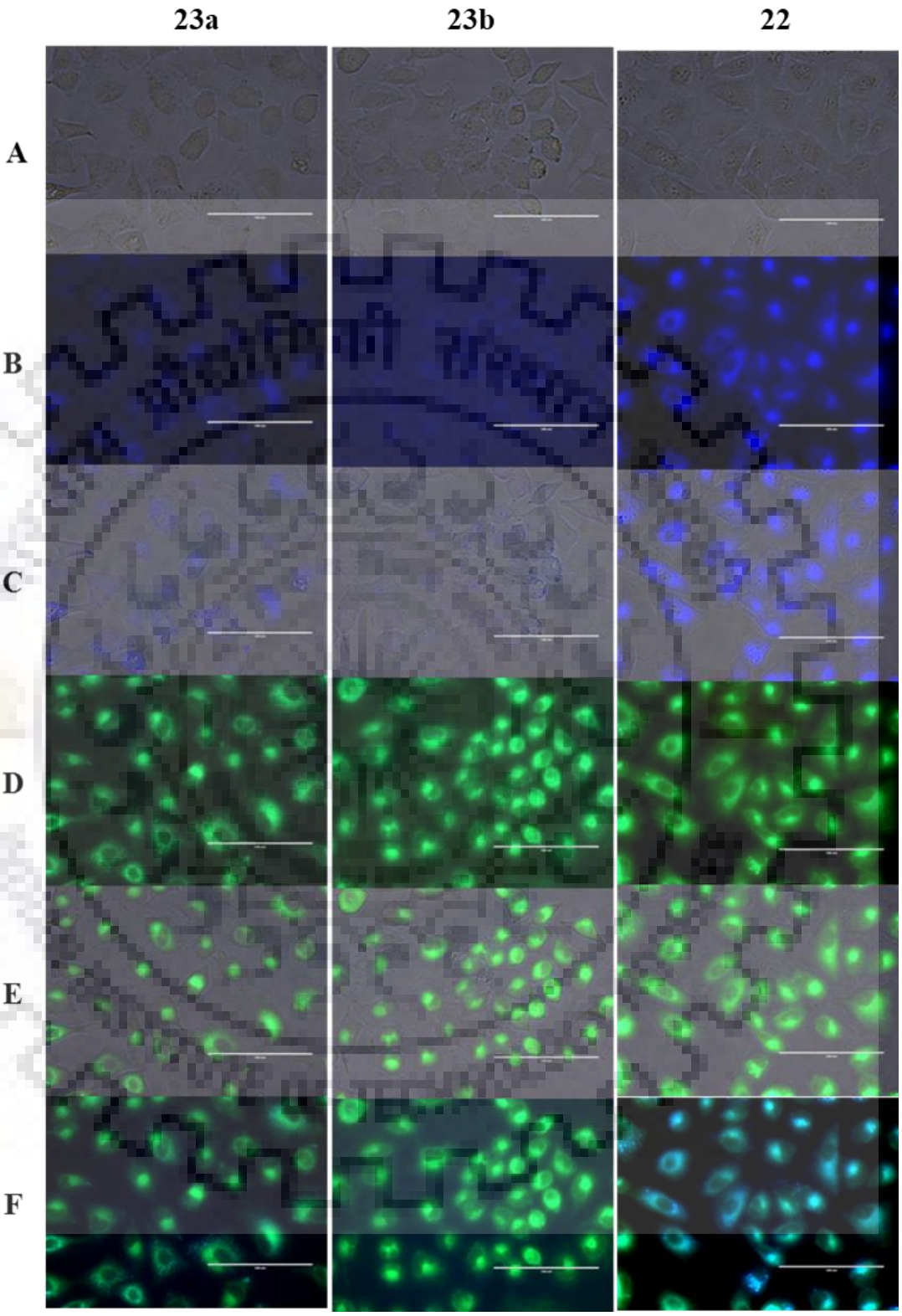

Figure 6.18 Microscopy images of A549 cells incubated with 30 μM of dyes **23a**, **23b** and **22** for 12 h. Images captured under (A) bright field, (B) DAPI filter, (C) merge image of A and B, (D) GFP filter, (E) merge image of A and D, (F) merge image of B and D. Scale bar = 100 μm.

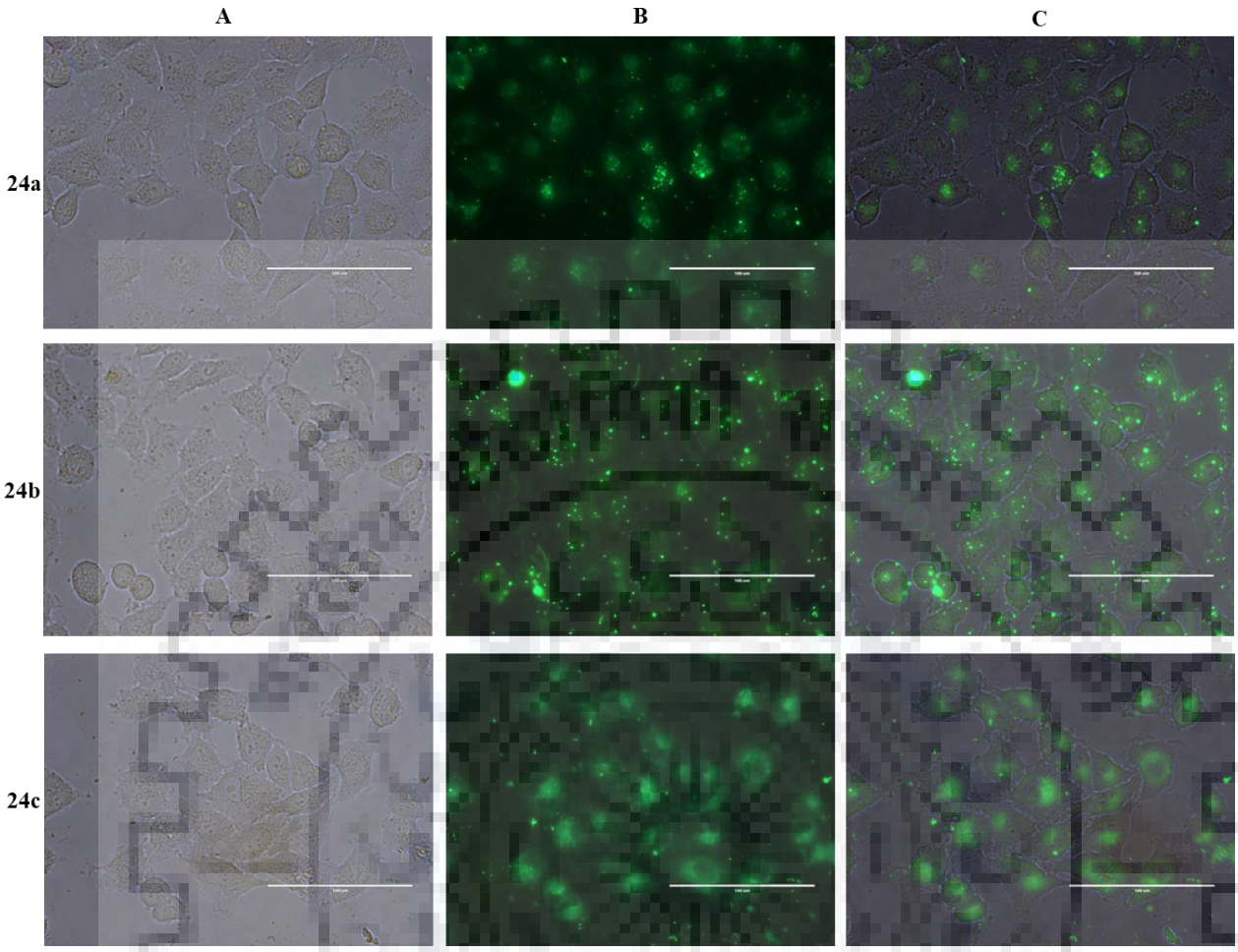

Figure 6.19 Microscopy images of A549 cells incubated with 30 μM of dyes **24a-24c** for 12 h. Images captured under (A) bright field, (B) GFP filter, (C) merge image of A and B. Scale bar = 100 μm.

Furthermore, in order to study the cytotoxic effect of the dyes, MTT assay was performed. It can be inferred that viability of the cells are not much affected by the dyes since absorbance is not varied drastically by varying concentration of the dyes. In Figure 6.20 and Table 6.5, the percentage cell viability of A549 cells at various concentrations of dyes is presented. As observed the cells grew normally in culture medium containing dyes in the concentration range of 5–50 μM, with almost no effect on its physiology, proliferation and does not cause cell apoptosis. No significant difference in cell viability was found between untreated and treated cells. The concentrations of dyes used for bioimaging did not cause any severe cytotoxic effects, which is in accordance with the MTT results. Hence it is concluded that these fluorescent dyes portray biocompatibility for imaging of cells.

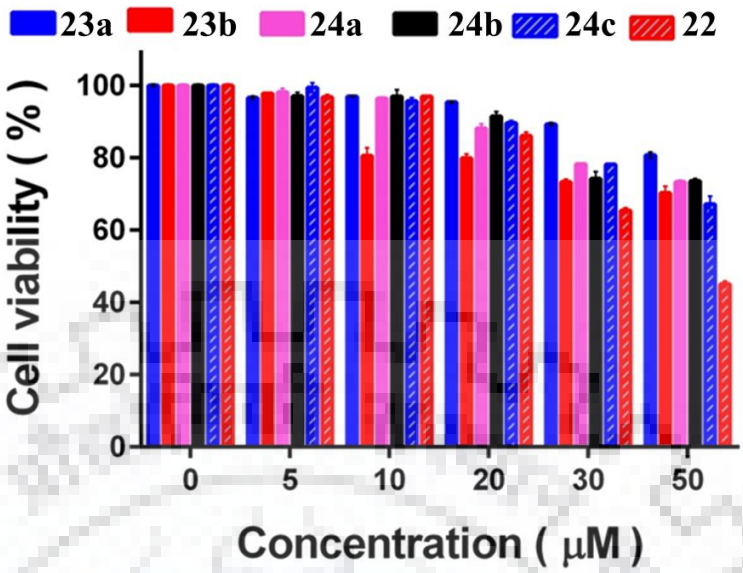

Figure 6.20 Cell viability of dyes with human lung carcinoma A549 cells incubated with 0 to 50 μM concentrations of dyes for 12 h. The data are presented as mean±SEM values of two individual experiments.

Table 6.5 Cell viability, cytotoxicity and cell proliferation effect of dyes of human lung carcinoma A549 cells estimated from the MTT assay.

Dye Conc. (μM)	Cell viability %					
	23a	**23b**	**24a**	**24b**	**24c**	**22**
0	100	100	100	100	100	100
5	97	98	98	97	99	97
10	97	81	96	97	96	97
20	95	80	88	91	90	86
30	89	73	78	74	78	65
50	81	70	73	74	67	45

6.3 Conclusions

We have successfully synthesized and characterized naphthalimide-based D-A small molecules and demonstrated in cellular bioimaging. The model compounds were optimized and theoretically investigated using DFT to gain insight into the electronic distribution in the frontier molecular orbitals. These dyes reflect the properties as predicted from the theoretical calculations. As a consequence the fluorescent dyes exhibited excellent photophysical, electrochemical and thermal properties attributed to the structural composition of the dyes. The photophysical and electrochemical studies revealed that these dyes are electronically similar although structurally different from each other. Whereas the structural variations helped to fine tune the morphology of

the dyes at microscopic level. The synthesized small molecules reflect unique and uniform morphology depending on their molecular structure. They show considerably different morphology which is solvent and concentration dependent. Finally, potential biological applications of the reported dyes are evaluated by investigating their biocompatibilities and cell uptake behaviors. It is observed that carbazole-based dyes exhibited supremacy in terms of brighter cell imaging than fluorene-naphthalimide analogs. It can be inferred that strategic structural modifications in designing the molecules play a crucial role in determining the properties and behavior of the functional materials.

6.4 Experimental Section

6.4.1 General methods and Instrumentation

All the general methodology is similar as described in Chapter 3.

6.4.2 Synthesis

6.4.2.1 4-(Butylamino)-*N*-butyl-1,8-naphthalimide (22)

A solution of 4-bromo-1,8-naphthalic anhydride (0.3 g, 1 mmol) and *n*-butylamine (3 mL, 4 mmol) in 15 mL of ethanol was refluxed for 8 h. After removal of ethanol, the residue was purified by silica column chromatography using EtOAc:Hexanes (1:10) as eluent to afford **22**. Yellow solid; Yield: 0.3 g (86%); mp: 122-124 °C; IR (KBr, cm^{-1}) 3383 (ν_{N-H}), 2956, 2930, 2865 (ν_{C-H}), 1685 ($\nu_{C=O}$), 1635, 1572 ($\nu_{C=C}$), 1348 (ν_{C-N}); ^{1}H-NMR (400 MHz, $CDCl_3$) δ 8.58 (d, J = 7.3 Hz, 1H), 8.47 (d, J = 8.2 Hz, 1H), 8.07 (d, J = 8.2 Hz, 1H), 7.62 (t, J = 8.0 Hz, 1H), 6.73 (d, J = 8.2 Hz, 1H), 5.21 (s, 1H), 4.16 (t, J = 7.6 Hz, 2H), 3.41 (dd, J = 12.4, 7.3 Hz, 2H), 1.85-1.75 (m, 2H), 1.75-1.65 (m, 2H), 1.56-1.37 (m, 4H), 1.03 (t, J = 7.2 Hz, 3H), 0.96 (t, J = 7.6 Hz, 3H); ^{13}C-NMR (100 MHz, $CDCl_3$) δ 164.9, 164.4, 149.6, 134.6, 131.3, 129.9, 125.9, 124.8, 123.4, 120.3, 110.4, 104.5, 43.6, 40.2, 31.3, 30.5, 20.7, 20.6, 14.1, 14.1; HRMS (ESI, *m/z*) $[M+Na]^+$ calcd. for $C_{20}H_{24}N_2O_2$: 347.1730; found 347.1734.

General procedure for the synthesis of dyes 21a-21c

A flask was charged with 4-bromonapthalic anhydride (1.1 g, 4 mmol), respective amine (6 mmol), a pinch of $Zn(OAc)_2$, and 15 mL acetic acid. The reaction mixture was refluxed for 12 h. On completion of reaction, it was quenched by pouring into cold water. The resultant solid was either filtered and recrystallized or extracted with $CHCl_3$. The residue obtained was adsorbed on silica gel and purified by column chromatography to obtain the desired product.

6.4.2.2 4-Bromo-*N*-(9,9-diethyl-9*H*-fluoren-2-yl)-1,8-naphthalimide (21a)

Eluted with $CHCl_3$:Hexanes mixture (4:1); Off white solid; Yield: 1.4 g (68%); mp: 164-166 °C; IR (KBr, cm^{-1}) 2959, 2929, 2864 (ν_{C-H}), 1705 ($\nu_{C=O}$), 1672, 1586 ($\nu_{C=C}$), 1364 (ν_{C-N}); ^{1}H-NMR (500 MHz, $CDCl_3$) δ 8.74-8.63 (m, 2H), 8.48-8.44 (m, 1H), 8.13-8.08 (m, 1H), 7.94-7.84 (m, 2H), 7.74 (d, *J* = 6.0 Hz, 1H), 7.38-7.32 (m, 3H), 7.28 (s, 1H), 7.25-24 (m, 1H), 1.96-1.95 (m, 4H), 0.68 (t, *J* = 6.0 Hz, 6H); ^{13}C-NMR (100 MHz, $CDCl_3$) δ 164.14, 164.10, 151.9, 151.4, 141.7, 140.5, 135.0, 134.5, 133.9, 133.8, 132.6, 131.9, 131.8, 131.4, 130.8, 128.8, 128.4, 127.6, 127.2, 127.1, 123.7, 123.1, 122.7, 120.5, 120.2, 55.7, 42.8, 17.5, 14.8; HRMS (ESI, *m/z*) $[M+Na]^+$ calcd. for $C_{29}H_{22}BrNO_2$: 518.0726; found 518.0716.

6.4.2.3 4-Bromo-*N*-(9-ethyl-9*H*-carbazol-3-yl)-1,8-naphthalimide (21b)

Eluted with $CHCl_3$:Hexanes mixture (4:1); Off white solid; Yield: 1.1 g (59%); mp: 286-288 °C; IR (KBr, cm^{-1}) 2961, 2925, 2855 (ν_{C-H}), 1702 ($\nu_{C=O}$), 1668, 1586 ($\nu_{C=C}$), 1340 (ν_{C-N}); ^{1}H-NMR (400 MHz, $CDCl_3$) δ 8.75 (dd, *J* = 7.3, 1.4 Hz, 1H), 8.66 (dd, *J* = 8.5, 1.1 Hz, 1H), 8.50 (d, *J* = 7.8 Hz, 1H), 8.10 (d, *J* = 7.8 Hz, 1H), 8.06-8.00 (m, 2H), 7.95-7.87 (m, 1H), 7.57 (d, *J* = 8.7 Hz, 1H), 7.53-7.41 (m, 2H), 7.38 (dd, *J* = 8.4, 2.4 Hz, 1H), 7.22 (td, *J* = 7.3, 0.9 Hz, 1H), 4.43 (q, *J* = 7.3 Hz, 2H), 1.49 (t, *J* = 7.1 Hz, 3H); ^{13}C-NMR (100 MHz, $CDCl_3$) δ 164.69, 164.66, 140.6, 139.9, 133.8, 132.7, 131.8, 131.4, 130.9, 130.8, 129.6, 128.4, 126.2, 125.6, 123.8, 123.6, 122.9, 122.8, 120.9, 120.8, 119.2, 109.4, 108.8, 37.9, 14.1; HRMS (ESI, *m/z*) $[M+Na]^+$ calcd. for $C_{26}H_{17}BrN_2O_2$: 491.0365; found 491.0366.

6.4.2.4 4-Bromo-*N*-(4-bromophenyl)-1,8-naphthalimide (21c)

Recrystallized from acetone; Off white solid; Yield: 1.3 g (76%); mp: 291-293 °C; IR (KBr, cm^{-1}) 1778, 1733 ($\nu_{C=O}$), 1669, 1591, 1534 ($\nu_{C=C}$), 1385 (ν_{C-N}); ^{1}H-NMR (400 MHz, $CDCl_3$) δ 8.70 (d, *J* = 7.3 Hz, 1H), 8.65 (d, *J* = 8.2 Hz, 1H), 8.46 (d, *J* = 7.8 Hz, 1H), 8.09 (d, *J* = 7.8 Hz, 1H), 7.90 (t, *J* = 8.0 Hz, 1H), 7.68 (d, *J* = 8.2 Hz, 2H), 7.20 (d, *J* = 8.7 Hz, 2H); ^{13}C-NMR (100 MHz, $CDCl_3$) δ 163.81, 163.79, 134.3, 134.1, 132.9, 131.9, 131.5, 131.2, 131.0, 130.6, 130.5, 129.5, 128.5, 123.21, 123.15, 122.3; HRMS (ESI, *m/z*) $[M+Na]^+$ calcd. for $C_{18}H_9Br_2NO_2$: 451.8892; found 451.8891.

General procedure for the synthesis of dyes 23a-23c

To a respective 4-bromonapthalimide **(21a, 21b** or **21c)** (0.5 g, 1.2 mmol) suspended in 15 mL ethanol was added *n*-butylamine (5 mL, 6 mmol) and trimethylamine (2 mL). This mixture was refluxed for 8-12 hours. Colour of the reaction mixture turned off white to yellow with passage of time. After completion of reaction, it was allowed to cool to room temperature. Solvent was

removed under vacuum to yield crude yellow solid, which was washed with hexanes. The residue was adsorbed on silica gel and purified by column chromatography to obtain the required compound.

6.4.2.5 4-(Butylamino)-*N*-(9,9-diethyl-9*H*-fluoren-2-yl)-1,8-naphthalimide (23a)

Eluted with $CHCl_3$:hexanes:EtOAc mixture (7:2:1); Yellow solid; Yield: 0.4 g (61%); mp: 134-136 °C; IR (KBr, cm^{-1}) 3382 (ν_{N-H}), 2954, 2928, 2869 (ν_{C-H}), 1692 ($\nu_{C=O}$), 1649, 1577 ($\nu_{C=C}$), 1357 (ν_{C-N}); ^{1}H-NMR (400 MHz, $CDCl_3$) δ 8.64 (d, J = 7.3 Hz, 1H), 8.52 (d, J = 8.4 Hz, 1H), 8.14 (d, J = 8.2 Hz, 1H), 7.83 (d, J = 7.8 Hz, 1H), 7.76-7.70 (m, 1H), 7.66 (t, J = 7.8 Hz, 1H), 7.39-7.27 (m, 4H), 7.25-7.23 (m, 1H), 6.77 (d, J = 8.7 Hz, 1H), 5.29 (s, 1H), 4.12 (q, J = 7.2 Hz, 2H), 3.44 (q, J = 6.4 Hz, 2H), 1.99-1.91 (m, 4H), 1.83 (t, J = 7.6 Hz, 2H), 1.04 (t, J = 7.3 Hz, 3H), 0.67 (t, J= 5.0 Hz, 6H); ^{13}C-NMR (100 MHz, $CDCl_3$) δ 165.2, 164.6, 151.6, 151.4, 149.8, 141.1, 140.8, 135.1, 134.7, 131.7, 131.3, 130.5, 127.5, 127.3, 126.9, 124.99, 124.85, 123.9, 123.1, 120.4, 120.1, 110.5, 104.6, 104.5, 55.6, 43.7, 42.8, 31.2, 20.6, 17.5, 14.8, 14.1; HRMS (ESI, *m/z*) $[M]^+$ calcd. for $C_{33}H_{32}N_2O_2$: 488.2458; found 488.2468.

6.4.2.6 4-(Butylamino)-*N*-(9-ethyl-9*H*-carbazol-3-yl)-1,8-naphthalimide (23b)

Eluted with hexanes:$CHCl_3$ mixture(1:4); yellow solid; Yield: 0.3 g (53%); mp: 130-132 °C; IR (KBr, cm^{-1}) 3383 (ν_{N-H}), 2967, 2926, 2870 (ν_{C-H}), 1686 ($\nu_{C=O}$), 1642, 1566 ($\nu_{C=C}$), 1354 (ν_{C-N}); ^{1}H-NMR (400 MHz, $CDCl_3$) δ 8.63 (d, J = 7.1 Hz, 1H), 8.52 (d, J = 8.5 Hz, 1H), 8.13 (d, J = 8.5 Hz, 1H), 8.03 (d, J = 1.8 Hz, 1H), 7.99 (d, J = 7.8 Hz, 1H), 7.61 (t, J = 7.9 Hz, 1H), 7.52 (d, J = 8.5 Hz, 1H), 7.50-7.44 (m, 1H), 7.42 (s, 1H), 7.41-7.36 (m, 1H), 7.23-7.15 (m, 1H), 6.73 (d, J = 8.5 Hz, 1H), 5.41 (s, 1H), 4.42-4.35 (m, 2H), 3.40 (q, J = 5.2 Hz, 2H), 1.85-1.76 (m, 2H), 1.54 (q, J = 7.6 Hz, 2H), 1.46 (t, J = 7.2 Hz, 3H), 1.03 (t, J = 7.3 Hz, 3H); ^{13}C-NMR (100 MHz, $CDCl_3$) δ 165.8, 165.2, 149.9, 140.6, 139.7, 135.1, 131.7, 130.5, 127.3, 126.4, 125.9, 124.9, 123.8, 123.6, 123.1, 120.96, 120.91, 120.5, 119.1, 110.5, 109.2, 108.7, 104.5, 43.7, 37.9, 31.2, 20.6, 14.14, 14.08; HRMS (ESI, *m/z*) $[M+H]^+$ calcd. for $C_{30}H_{27}N_3O_2$: 462.2176; found 462.2170.

6.4.2.7 4-(Butylamino)-*N*-(4-Bromophenyl)-1,8-naphthalimide (23c)

Eluted with hexanes:EtOAc mixture (4:1); Yellow solid; Yield: 0.3 g (50%); mp: 170-172 °C; IR (KBr, cm^{-1}) 3370 (ν_{N-H}), 2961, 2926, 2859 (ν_{C-H}), 1693 ($\nu_{C=O}$), 1644, 1542 ($\nu_{C=C}$), 1365 (ν_{C-N}); ^{1}H-NMR (400 MHz, $CDCl_3$) δ 8.62 (d, J = 7.3 Hz, 1H), 8.50 (d, J = 8.7 Hz, 1H), 8.14 (d, J = 8.2 Hz, 1H), 7.69-7.60 (m, 3H), 7.19 (d, J = 8.7 Hz, 2H), 6.76 (d, J = 8.4 Hz, 1H), 5.32 (s, 1H), 3.55-3.25 (m, 2H), 1.88-1.75 (m, 2H), 1.53 (q, J = 7.5 Hz, 2H), 1.04 (t, J = 7.3 Hz, 3H); ^{13}C-NMR (100 MHz, $CDCl_3$) δ 164.9, 164.2, 150.1, 135.3, 135.2, 132.7, 131.9, 130.8, 130.5, 126.5, 124.9, 123.3,

122.6, 120.5, 110.0, 104.7, 43.7, 31.2, 20.6, 14.1; HRMS (ESI, *m/z*) $[M+H]^+$ calcd. for $C_{22}H_{19}BrN_2O_2$: 423.0703; found 423.0703.

6.4.2.8 4-(Butylamino)-*N*-(4-(5-(9,9-diethyl-9*H*-fluoren-2-yl)thiophen-2-yl)phenyl)-1,8-naphthalimide (24a)

A mixture of **23c** (1.06 g, 2.5 mmol), tributyl(5-(9,9-diethyl-9*H*-fluoren-2-yl)thiophen-2-yl)stannane (1.78 g, 3.0 mmol), $Pd(PPh_3)_2Cl_2$ (35 mg) and DMF (10 mL) was heated at 80 °C for 18h. After completion of the reaction, it was poured into ice-water and the precipitates collected by filtration. This crude product was purified by column chromatography on silica gel using hexane/DCM mixture (1:1) as eluent. Yellow solid; Yield: 1.36 g (84%); mp: 258-260 °C; IR (KBr, cm^{-1}) 3366 (ν_{N-H}), 2960, 2926, 2870 (ν_{C-H}), 1695 ($\nu_{C=O}$), 1672, 1586 ($\nu_{C=C}$), 1364 (ν_{C-N}); ^{1}H-NMR (500 MHz, $CDCl_3$) δ 8.65 (d, *J* = 8.5 Hz, 1H), 8.52 (d, *J* = 8.5 Hz, 1H), 8.15 (d, *J* = 8.5 Hz, 1H), 7.82-7.58 (m, 7H), 7.37-7.31 (m, 7H), 6.82 (bs, 1H), 5.31 (s, 1H), 3.45 (t, *J* = 8.5 Hz, 2H), 2.1-2.05 (m, 4H), 1.85-1.80 (m, 2H), 1.59-1.53 (m, 2H), 1.04 (t, *J* = 8.5 Hz, 3H), 0.37 (t, *J* = 7.5 Hz, 6H); ^{13}C-NMR (100 MHz, $CDCl_3$) δ 165.1, 164.5, 150.9, 150.3, 149.9, 144.9, 142.8, 141.4, 141.3, 135.3, 135.2, 134.7, 133.3, 131.8, 130.5, 129.5, 127.3, 127.1, 126.7, 126.4, 124.9, 124.8, 124.0, 123.5,123.1, 120.5, 120.3, 120.2, 119.9, 110.3, 104.7, 56.4, 45.0, 43.7, 33.0, 31.3, 20.6, 14.1, 8.8; HRMS (ESI, *m/z*) $[M+Na]^+$ calcd. for $C_{43}H_{38}N_2O_2S$: 669.2546; found 669.2547.

6.4.2.9 4-(Butylamino)-*N*-(4-(5-(9,9-diethyl-7-(naphthalen-1-yl(phenyl)amino)-9*H*-fluoren-2-yl)thiophen-2-yl)phenyl)-1,8-naphthalimide (24b)

It was prepared by following the procedure described above for **24a** but using 9,9-diethyl-*N*-(naphthalen-1-yl)-*N*-phenyl-7-(5-(tributylstannyl)thiophen-2-yl)-9*H*-fluoren-2-amine instead of tributyl(5-(9,9-diethyl-9*H*-fluoren-2-yl)thiophen-2-yl)stannane. Yellow solid; Yield: 1.64 g (76%); mp: 258-260 °C; IR (KBr, cm^{-1}) 3385 (ν_{N-H}), 2958, 2926, 2870 (ν_{C-H}), 1693 ($\nu_{C=O}$), 1647, 1576 ($\nu_{C=C}$), 1361 (ν_{C-N}); ^{1}H-NMR (500 MHz, $CDCl_3$) δ 8.64 (d, *J* = 7.0 Hz, 1H), 8.53 (d, *J* = 8.5 Hz, 1H), 8.14 (d, *J* = 8.5 Hz, 1H), 7.95 (d, *J* = 8.5 Hz, 1H), 7.89 (d, *J* = 8.5 Hz, 1H), 7.78 (d, *J* = 8.5 Hz, 3H), 7.66 (t, *J* = 8.0 Hz, 1H), 7.59 (d, *J* = 6.0 Hz, 2H), 7.53-7.42 (m, 5H), 7.35-7.30 (m, 6H), 7.22 (t, *J* = 7.5 Hz, 3H), 7.07 (d, *J* = 6.0 Hz, 3H), 6.95 (s, 1H), 6.77 (d, J = 8.5 Hz, 1H), 5.31 (s, 1H), 3.44 (t, J = 7.0 Hz, 2H), 2.00-1.87 (m, 2H), 1.86-1.78 (m, 4H), 1.60-1.50 (m, 4H), 1.05 (t, *J* = 7.5 Hz, 3H), 0.36 (t, *J* = 7.5 Hz, 3H); ^{13}C-NMR (100 MHz, $CDCl_3$) δ 165.1, 164.5, 151.6, 150.8, 149.9, 148.9, 148.3, 145.1, 144.1, 142.5, 141.4, 135.5, 135.4, 135.24, 135.21, 134.8, 132.3, 131.8, 129.5, 129.3, 128.6, 126.9, 126.6, 126.5, 126.41, 126.37, 126.3, 124.95, 124.85, 124.8, 124.6, 123.8, 123.5, 122.1, 121.8, 121.7, 120.53, 120.49, 119.9, 119.5, 117.1, 56.3, 44.9, 43.7,

32.9, 31.2, 20.6, 14.1, 8.8; HRMS (ESI, *m/z*) $[M+Na]^+$ calcd. for $C_{59}H_{49}N_3O_2S$: 886.3437; found 886.3437.

6.4.2.10 4-(Butylamino)-*N*-(4-(5-(9-ethyl-9*H*-carbazol-3-yl)thiophen-2-yl)phenyl)-1,8-naphthalimide (24c)

It was obtained from 9-ethyl-3-(5-(tributylstannyl)thiophen-2-yl)-9*H*-carbazole and **23c** by following a procedure similar to that described above for **24a**. Yellow solid; Yield: 1.1 g (71%); mp: 254-256 °C, IR (KBr, cm^{-1}) 3364 (ν_{N-H}), 2958, 2926, 2858 (ν_{C-H}), 1694 ($\nu_{C=O}$), 1639, 1588 ($\nu_{C=C}$), 1369 (ν_{C-N}); ^{1}H-NMR (400 MHz, $CDCl_3$) δ 8.66 (t, J = 7.3 Hz, 1H), 8.54 (t, J = 7.8 Hz, 1H), 8.38 (d, J = 6.0 Hz, 1H), 8.16 (q, J = 8.2 Hz, 2H), 7.80 (q, J = 8.4 Hz, 3H), 7.67-7.64 (m, 1H), 7.50 (t, J = 7.6 Hz, 1H), 7.44 (t, J = 7.8 Hz, 2H), 7.40-7.31 (m, 4H), 7.28 (s, 1H), 6.79 (t, J = 8.0 Hz, 1H), 5.31 (s, 1H), 4.47-4.35 (m, 2H), 3.51-3.39 (m, 2H), 1.90-1.77 (m, 2H), 1.58-1.54 (m, 2H), 1.47 (t, J = 7.2 Hz, 3H), 1.06 (t, J = 7.5 Hz, 3H); ^{13}C-NMR (100 MHz, $CDCl_3$) δ 165.1, 164.5, 149.9, 145.8, 141.9, 140.6, 139.8, 135.2, 135.1, 134.9, 131.8, 129.5, 126.6, 126.3, 126.2, 125.8, 124.98, 124.85, 124.3, 123.1, 123.6, 123.6, 123.1, 120.9, 120.5, 119.3, 117.9, 108.99, 108.87, 104.69, 43.7, 37.9, 31.3, 20.6, 14.1; HRMS (ESI, *m/z*) $[M+Na]^+$ calcd. for $C_{40}H_{33}N_3O_2S$: 642.2185; found 642.2185.

6.4.3 Computational Methods

The computational methodology used is similar as described in Chapter 3. The ground-state geometries were optimized employing B3LYP functional and 6-31G (d,p) basis set for all atoms in the DCM solvent.

6.4.4 Microscopy Analyses

The SEM images of the dyes on substrate sputtered by gold were recorded using FE-SEM Quanta 200 FEG instrument. Samples for SEM analysis were as prepared powders or films prepared by a drop-cast method from dye aggregates in various solvent systems on glass substrate operated at 15-20 kV. TEM images and SAED patterns were obtained using a FEI TECNAI G2 transmission electron microscope at 200 kV voltage. For the TEM analysis, the sample solution of 2×10^{-3} M in DMSO was used. Then, one drop of the solution was kept on a carbon coated copper grid and allowed to dry at room temperature. Fluorescence microscopic images were acquired using a Nikon Eclipse LV100 microscope by air drying a drop of the diluted samples on a glass slide under various excitation filters such as UV-2A (330–380 nm), B-2A (450-490 nm) and G-2A (510-560 nm) filter excitation. All images were taken at scale of 100 μm.

6.4.5 Fluorescence-based Bioimaging

Bioimaging potential of various dye samples was explored by seeding $2x10^5$ A549 cells in 3 cm culture dishes in 2 mL of DMEM medium. The cells were allowed to attach overnight. After the attachment of the cells, dye samples (working concentration-30 μM) were added to respective dishes and incubated for 6 h. Dye containing medium was then removed and cells were washed twice with PBS to remove the unbound dye and any media traces left over. For bioimaging, cells were retained in PBS. Dye stained cells were examined under a fluorescent inverted microscope (EVOS® FL Color, AMEFC 4300). Microscopy images of cells were taken under bright field, DAPI (excitation 360 nm, emission 447 nm), and GFP (excitation 470 nm, emission 525 nm) light cubes, respectively and under combination of filters to develop merged images.

6.4.6 Cell Culture

For in *vitro* studies, A549 (human lung adenocarcinoma) cells were procured from National Centre for Cell Sciences (NCCS), Pune, India. The cell line was maintained in Dulbecoo's modified Eagle's medium (DMEM, Sigma-Aldrich) supplemented with 10% (v/v) fetal bovine serum (FBS) and 1% penicillin-streptomycin solution (Sigma -Aldrich, USA) at 5% CO_2 in a humidified incubator at 37 °C.

6.4.7 MTT Assay

In order to determine the cell viability, MTT, assay was performed which is based on the ability of mitochondrial dehydrogenases enzyme activity in living cells to transform yellow colour water soluble tetrazolium salt MTT solution to a purple water-insoluble formazan product . 10^4 cells/ well were seeded in 96-well tissue culture plates and allowed to attach for 12 h. Subsequently, these cells were then incubated with medium containing different concentrations ranging from 0 to 50 μM of the tested compounds in DMSO solution for 12 h. Upon the completion of incubation period, medium from each well was removed and cells were washed once with phosphate buffer saline (PBS). Afterwards, 100 μL of fresh medium containing 10 μL of MTT solution (5 mg/mL in PBS) was added to each well and incubated for another 4 h to allow the formation of formazan crystals. Medium containing MTT was aspirated slowly and formazan crystals were dissolved by adding 150 μL of DMSO was added to each well. Multi-mode microplate reader (Biotek, Cytation 3) was used to record the absorbance of each well was at 570 nm. The untreated cells (in DMEM) were used as control. Relative cell viability (mean% $\pm$ SEM, n = 2) was calculated as:

$$\% \text{ Cell viability} = (A_{570} \text{ in treated sample} / A_{570} \text{ in control sample}) \times 100\%$$

Chapter 7 Conclusions and Outlook

7.1 Conclusions

In this thesis, we have developed naphthalimide-based organic materials exploring its dual functionalization. The naphthalimide unit was explored for different functionalization employing palladium-catalyzed C-C bond coupling reactions such as Sonogashira, Suzuki-Miyaura and Stille to obtain the target dyes. The newly synthesized intermediates and final target dyes were thoroughly analyzed by spectroscopic techniques. The dyes synthesized were studied for either self-assembly, structure property relationships, or biological applications such as cell imaging. We have synthesized and fine-tuned the linear A-A-A/ D-A/ or star shaped $(A\text{-}\pi_2)_3\text{-}\pi_1\text{-}A$ naphthalimide-based dyes. The intrinsic properties of the dyes were broughtout with the aid of absorption, emission spectroscopy, cyclic voltammetry, theoretical computations and thermal analysis. The fine tuning of the photophysical, electrochemical or morphological properties of the naphthalimide derivatives were systematically addressed by appending different chromophore on aromatic system and imidic position of naphthalimide unit. The HOMO and LUMO alteration were arising due to the incorporation of various chromophores.

The overview and the outcome of the thesis work is summarized Chapter wise below and a snap shot provided in Figure 7.1.

Chapter 3 Bis-Naphthalimides Bridged by Different Electron Acceptors

In this Chapter depending upon the molecular modification implied, we have categorized the bis-naphthalimides into two sets and illustrated their structure property relationships. Firstly we studied the effect of different electron withdrawing units such as fluorenone, quinoxaline as a linker in conjugated rigid rods. Then benzotriazole oligomer bridged molecular wires terminated with naphthalimides were constructed. Nature of bridging unit on electronic properties were insvestivated.

- Synthesized linear bis-naphthalimide-based electron deficient small molecules and oligomers comprising benzotriazole by employing Pd-catalyzed Sonogashira cross coupling reaction.
- The dyes possessed multiple π-π* transitions arising from the conjugated system and depicted a progressive bathochromic shift of λ_{max} accompanied by increase in molar absorption coefficients with increase in π-conjugation length.
- The thermal and electrochemical data indicated high thermal stability, and suitable energetics which support pronounced electron deficiency for the molecules with high electron affinity and deep HOMO energy levels.

- Self-assembly of naphthalimide-based electron deficient organic small molecules into nanostructures is demonstrated. These resulted in formation of controlled morphologies and well-defined nanosized aggregates developed from *J*-aggregated solid state packing.
- Fluorescence lifetime analysis of the oligomers showed that the average lifetime of excited states gradually decreased with the incorporation of benzotriazole unit facilitating faster radiative decay.
- The electronic features and coplanar arrangement of functional entities established by theoretical computations revealed close packing arrangement of the molecules in the solid state.

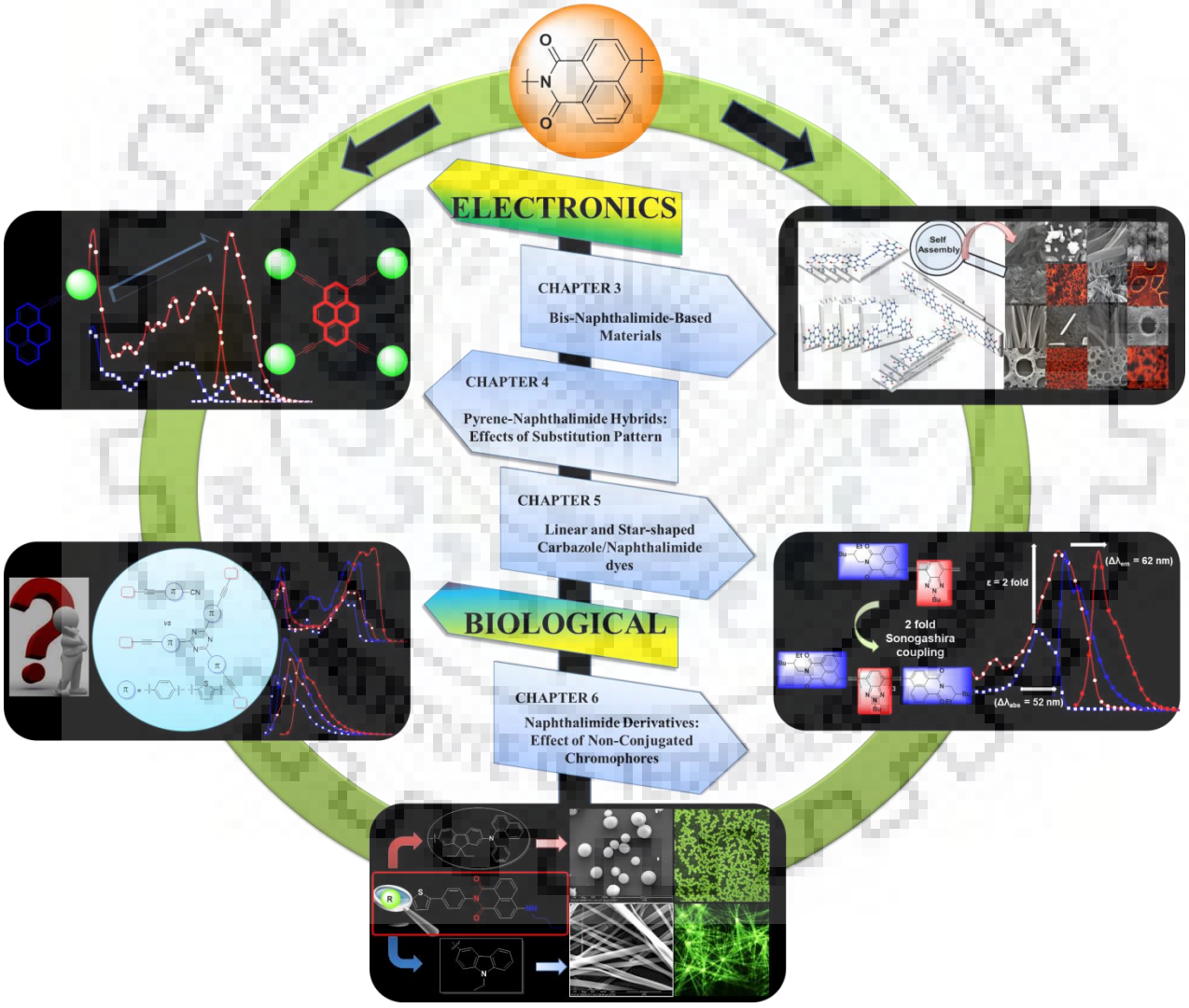

Figure 7.1 Pictorial representation of summary of the work accomplished.

Chapter 4 Pyrene-Naphthalimide Hybrids: Synthesis and Effects of Substitution Pattern on Optical, Electrochemical and Thermal Properties

- A series of pyrene derivatives decorated with one to four naphthalimide units were synthesized and characterized by optical, electrochemical, thermal and theoretical studies.
- The molar extinction coefficients of the dyes showed progressive increase on moving from mono to tetra derivative attributable to the increase in naphthalimide density while showing absence of charge transfer in the ground state.
- Among the 1,6-di-substituted and 1,8-di-substituted two isomers, former display red shifted absorption profile attributed to the extended conjugation length.
- The emission band is centered at 550 nm attributed to the charge transfer from pyrene to naphthalimide in the excited state.
- The compounds are green to orange fluorescent and display dependence on solvent polarity confessing an intra molecular charge transfer in excited state.
- The HOMO and LUMO energies were found to be low lying ca. -5.6-5.9 eV and -3.2 to -3.3 eV due to pronounced electron deficiency of the dyes.
- DFT simulation reveals the localization of HOMO/LUMO orbitals on the donor-acceptor moieties except for tetra-substituted dye where it is pyrene localized implying the significant charge transfer occurring during electronic excitation.

Chapter 5 Carbazole-Naphthalimide-Based Linear D-A and Star-shaped Triazine-Cored Molecules

- A set of carbazole and naphthalimide-based linear control dyes and star-shaped triazine-cored dyes were synthesized using Sonogashira coupling reactions and characterized successfully.
- The star-shaped triazine cored dyes displayed superior photophysical and electrochemical properties compared to their linear analogs.
- The dyes displayed emission in blue to green region. It was found that introduction of naphthalimide moiety in place of carbazole exhibited better emission profiles.
- The carbazole-based dyes displayed solvatochromism attributed to typical D-A interactions.
- The excited state lifetime of linear analogs were longer than star-shaped analogs.
- Among the star-shaped triazine-based compounds, naphthalimide containing dyes possessed low lying energy levels attributed to their electron deficiency.

Chapter 6 Effect of Non-conjugated Chromophores on Photophysics, Electrochemistry, Morphology and Bioimaging Applications of Naphthalimide Derivatives

- A series of 1,8-naphthalimide-based fluorescent small molecules featuring chromophores, differing in conjugation and electron richness, at imidic nitrogen are synthesized, characterized and demonstrated in cellular bioimaging.
- The fluorescent dyes exhibited excellent photophysical, electrochemical and thermal properties attributable to the structural composition of the dyes.
- The photophysical and electrochemical studies revealed that these dyes are electronically similar although structurally different from each other.
- The structural variations helped to fine tune the morphology of the dyes at microscopic level. They display unique and uniform morphology depending on their molecular structure.
- The dyes were evaluated by investigating their biocompatibilities and cell uptake behaviors. It was observed that carbazole-based dyes exhibited supremacy in terms of brighter cell imaging than fluorene-naphthalimide analogs.

7.2 Future Scope

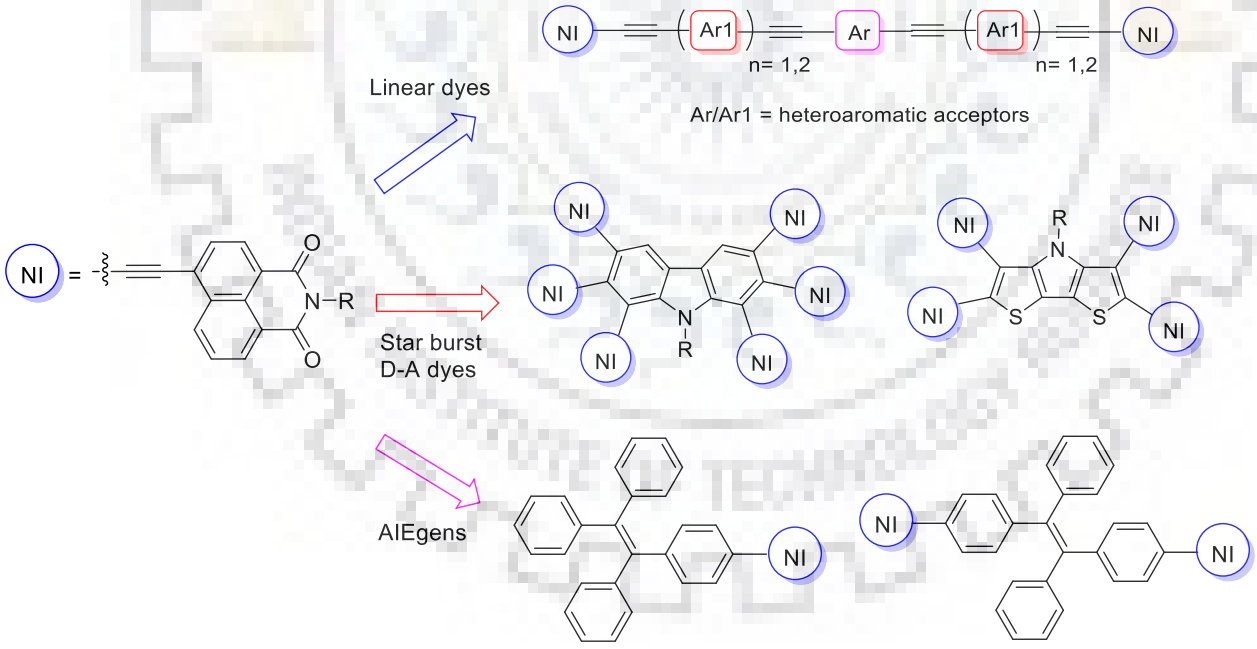

Chart 7.1 The proposed naphthalimide-based linear and star-burst functional materials.

As an outlook to the proposed work in this thesis, we envision that judicious and efficient tuning of the property of the synthesized dyes could lead to effective non-fullerene acceptors and electron transporting materials suitable for nano-optoelectronic devices. The results obtained through

inspecting the scaffold of the tuned dyes lead us on a path approaching to the development of new tailored naphthalimide-based organic materials. We propose to synthesize some more linear organic dyes by introduction of two different bridging acceptors between two naphthalimide units. Multi-substituted star-burst carbazole and dithienopyrrole-based dyes linked with naphthalimide unit can act as effective D-A type dyes for effective charge balancing. They could be effective light harvesting materials for OSCs. Further, the use of naphthalimide moiety in construction of AIEgens in combination with tetraphenylethylene can provide a new perspective to study the properties of AIE active and inactive blended molecules.

References

[1] Anthony, J. E. Functionalized Acenes and Heteroacenes for Organic Electronics. *Chem. Rev*. **2006**, *106* (12), 5028-5048.

[2] Heeger, A. J. Semiconducting Polymers: The Third Generation. *Chem. Soc. Rev*. **2010**, *39*, 2354-2371.

[3] Dou, L.; Liu, Y.; Hong, Z.; Li, G.; Yang, Y. Low-Bandgap Near-IR Conjugated Polymers/Molecules for Organic Electronics. *Chem. Rev.* **2015**, *115* (23), 12633-12665.

[4] Miao, Q.; Mamada, M.; Yamashita, Y. *S-Containing Polycyclic Heteroarenes: Thiophene-Fused and Thiadiazole-Fused Arenes as Organic Semiconductors.* Wiley-VCH: Weinheim, 2015.

[5] Lin, Y.; Li, Y.; Zhan, X. Small Molecule Semiconductors for High-Efficiency Organic Photovoltaics. *Chem. Soc. Rev.* **2012**, *41* (11), 4245-4272.

[6] Hu, W. *Organic Optoelectronics*; Wiley-VCH: Weinheim, 2013.

[7] Forrest, S. R.; Thompson, M. E. Introduction: Organic Electronics and Optoelectronics. *Chem. Rev.* **2007**, *107*, 923-925.

[8] Roncali, J.; Leriche, P.; Blanchard, P. Molecular Materials for Organic Photovoltaics: Small Is Beautiful. *Adv. Mater*. **2014**, *26* (23), 3821-3838.

[9] Henson, Z. B.; Müllen, K.; Bazan, G. C. Design Strategies for Organic Semiconductors beyond the Molecular Formula. *Nat. Chem*. **2012**, *4*, 699-704.

[10] Zhu, X.-H.; Peng, J.; Cao, Y.; Roncali, J. Solution-Processable Single-Material Molecular Emitters for Organic Light-Emitting Devices. *Chem. Soc. Rev.* **2011**, *40* (7), 3509-3524.

[11] Li, H.; Kim, F. S.; Ren, G.; Jenekhe, S. A. High Mobility n-Type Conjugated Polymers for Organic Electronics. *J. Am. Chem. Soc.* **2013**, *135*, 14920-14923.

[12] Wang, J.; Liu, K.; Ma, L.; Zhan, X. Triarylamine: Versatile Platform for Organic, Dye-Sensitized, and Perovskite Solar Cells. *Chem. Rev*. **2016**, *116*, 14675-14725.

[13] Wang, C.; Dong, H.; Hu, W.; Liu, Y.; Zhu, D. Semiconducting π-Conjugated Systems in Field-Effect Transistors: A Material Odyssey of Organic Electronics. *Chem. Rev.* **2012**, *112*, 2208-2267.

[14] Shirota, Y.; Kageyama, H. Charge Carrier Transporting Molecular Materials and Their Applications in Devices. *Chem. Rev.* **2007**, *107*, 953-1010.

References

[15] Liu, X.; Chen, H.; Tan, S. Overview of High-efficiency Organic Photovoltaic Materials and Devices. *Renewable Sustainable Ener. Rev*. **2015**, *52*, 1527-1538.

[16] Usta, H.; Facchetti, A.; Marks, T. *n*-Channel Semiconductor Materials Design for Organic Complementary Circuits. *Acc. Chem. Res.* **2011**, *44*, 501-510.

[17] Jones, B. A.; Facchetti, A.; Wasielewski, M. R.; Marks, T. J. Tuning Orbital Energetics in Arylene Diimide Semiconductors. Materials Design for Ambient Stability of n-Type Charge Transport. *J. Am. Chem. Soc.* **2007**, *129*, 15259-15278.

[18] Li, H.; Kim, F. S.; Ren, G.; Hollenbeck, E. C.; Subramaniyan, S.; Jenekhe, S. A. Tetraazabenzodifluoranthene Diimides: New Building Blocks for Solution Processable N-Type Organic Semiconductors. *Angew. Chem. Int. Ed.* **2013**, *52*, 5513-5517.

[19] Anthony, J. E.; Facchetti, A.; Heeney, M.; Marder, S. R.; Zhan, X. N-Type Organic Semiconductors in Organic Electronics. *Adv. Mater.* **2010**, *22* (34), 3876-3892.

[20] Perepichka, I. F.; Perepichka, D. F. *Handbook of Thiophene-Based Materials: Applications in Organic Electronics and Photonics*. John Wiley & Sons: New York, 2009.

[21] Mishra, A.; Ma, C. Q.; Bäuerle, P. Functional Oligothiophenes: Molecular Design for Multidimensional Nanoarchitectures and Their Applications. *Chem. Rev.* **2009**, *109* (3), 1141-1176.

[22] Zhang, C.; Zhu, X. Thieno[3,4-*b*]thiophene-Based Novel Small-Molecule Optoelectronic Materials. *Acc. Chem. Res.* **2017**, *50*, 1342-1350.

[23] Irfan, M.; Belfield, K. D.; Saeed, A. Carbazole/Fluorene Based Conjugated Small Molecules: Synthesis and Comparative Studies on the Optical, Thermal and Electrochemical Properties. *RSC Adv*. **2015**, *5*, 48760-48768.

[24] Liang, M.; Chen, J. Arylamine Organic Dyes for Dye-Sensitized Solar Cells. *Chem. Soc. Rev.* **2013**, *42*, 3453-3488.

[25] Venkateswararao, A.; Thomas, K. R. J.; Lee, C. P.; Li, C. T.; Ho, K. C. Organic Dyes Containing Carbazole as Donor and π-Linker: Optical, Electrochemical, and Photovoltaic Properties. *ACS Appl. Mater. Interfaces* **2014**, *6* (4), 2528–2539.

[26] Sathiyan, G.; Sivakumar, E. K. T.; Ganesamoorthy, R.; Thangamuthu, R.; Sakthivel, P. Review of Carbazole Based Conjugated Molecules for Highly Efficient Organic Solar Cell Application. *Tetrahedron Lett.* **2016**, *57* (3), 243-252.

[27] Wex, B.; Kaafarani, B. R. Perspective on Carbazole-Based Compounds as Organic Emitters and Hosts in TADF Applications. *J. Mater. Chem. C* **2017**, *5* (34), 8622-8653.

References

[28] Thomas, K. R. J.; Lin, J. T.; Tao, Y. T.; Chuen, C. H. Green and Yellow Electroluminescent Dipolar Carbazole Derivatives: Features and Benefits of Electron-Withdrawing Segments. *Chem. Mater.* **2002**, *14* (9), 3852-3859.

[29] Morales, A. R.; Frazer, A.; Woodward, A. W.; Ahn-White, H.-Y.; Fonari, A.; Tongwa, P.; Timofeeva, T. V.; Belfield, K. D. Design, Synthesis, Structural and Spectroscopic Studies of Push-Pull Two-Photon Absorbing Chromophores with Acceptor Groups of Varying Strength. *J. Org. Chem*. **2013**, *78*, 1014-1025.

[30] Kurhuzenkau, S. A.; Woodward, A. W.; Yao, S.; Belfield, K. D.; Shaydyuk, Y. O.; Sissa, C.; Bondar, M. V.; Painelli, A. Ultrafast Spectroscopy, Superluminescence and Theoretical Modeling of a Two-photon Absorbing Fluorene Derivative. *Phys. Chem. Chem. Phys.* **2016**, *18*, 12839-12846.

[31] Thomas, K. R. J.; Baheti, A. Fluorene-based Organic Dyes for Dye-sensitized Solar Cells: Structure Property Relationships. *Mater. Technol*. **2013**, *28*, 71-87.

[32] Mukherjee, S.; Thilagar, P. Recent Advances in Purely Organic Phosphorescent Materials. *Chem. Commun*. **2015**, *51*, 10988-11003.

[33] Grisorio, R.; Allegretta, G.; Suranna, G. P.; Mastrorilli, P.; Loiudice, A.; Rizzo, A.; Mazzeo, M.; Gigli, G. Monodispersed vs. Polydispersed Systems for Bulk Heterojunction Solar Cells: The Case of Dithienopyrrole/anthracene Based Materials. *J. Mater. Chem.* **2012**, *22* (37), 19752-19760.

[34] Kumar, S.; Thomas, K. R. J.; Li, C.-T.; Ho, K.-C. Synthesis and Photovoltaic Properties of Organic Dyes Containing N-Fluoren-2-yl dithieno[3,2-b:2′,3′-d]pyrrole and Different Donors. *Org. Electron.* **2015**, *26*, 109-116.

[35] Weidelener, M.; Wessendorf, C. D.; Hanisch, J.; Ahlswede, E.; Götz, G.; Lindén, M.; Schulz, G.; Mena-Osteritz, E.; Mishra, A.; Bäuerle, P. Dithienopyrrole-Based Oligothiophenes for Solution-Processed Organic Solar Cells. *Chem. Commun.* **2013**, *49* (92), 10865-10867.

[36] Huang, Z.-S.; Meier, H.; Cao, D. Phenothiazine-Based Dyes for Efficient Dye-Sensitized Solar Cells. *J. Mater. Chem. C* **2016**, *4* (13), 2404-2426.

[37] Neena, K. K.; Sudhakar, P.; Dipak, K.; Thilagar, P. Diarylboryl-Phenothiazine Based Multifunctional Molecular Siblings. *Chem. Commun*. **2017**, *53*, 3641-3644.

[38] Grätzel, M. Photoelectrochemical cells. *Nature*, **2001**, *414*, 338-344.

[39] Tang, C. W. Two-layer Organic Photovoltaic Cell. *Appl. Phys. Lett.* **1986**, *48*, 183-185.

References

[40] O'Regan, B.; Gratzel, M. A Low-Cost, High-Efficiency Solar Cell Based on Dye-Sensitized Colloidal TiO_2 Films. *Nature* **1991**, *353*, 737-740.

[41] Brabec, C. J. Organic Photovoltaics: Technology and Market. Sol. *Energy Mater. Sol. Cells* **2004**, *83*, 273-292.

[42] Hagfeldt, A.; Boschloo, G.; Sun, L.; Kloo, L.; Pettersson, H. Dye-Sensitized Solar Cells. *Chem. Rev.* **2010**, *110*, 6595-6663.

[43] Tang, C. W.; VanSlyke, S. A. Organic Electroluminescent Diodes *Appl. Phys. Lett*. **1987**, *51*, 913-915.

[44] Sun, Y.; Giebink, N. C.; Kanno, H.; Ma, B.; Thompson, M. E.; Forrest, S. R. Management of Singlet and Triplet Excitons for Efficient White Organic Light-Emitting Devices. *Nature* **2006**, *440*, 908-912.

[45] Mei, J.; Diao, Y.; Appleton, A. L.; Fang, L.; Bao, Z. Integrated Materials Design of Organic Semiconductors for Field-Effect Transistors. *J. Am. Chem. Soc.* **2013**, *135*, 6724-6746.

[46] Sirringhaus, H. 25th Anniversary Article: Organic Field-Effect Transistors: The Path Beyond Amorphous Silicon. *Adv. Mater.* **2014**, *26*, 1319-1335.

[47] Parker, T. C.; Patel, D. G.; Moudgil, K.; Barlow, S.; Risko, C.; Brédas, J.-L.; Reynolds, J. R.; Marder, S. R. Heteroannulated Acceptors Based on Benzothiadiazole. *Mater. Horiz.* **2015**, *2* (1), 22-36.

[48] Wang, Y.; Michinobu, T. Benzothiadiazole and Its π-Extended, Heteroannulated Derivatives: Useful Acceptor Building Blocks for High-Performance Donor–acceptor Polymers in Organic Electronics. *J. Mater. Chem. C* **2016**, *4* (26), 6200-6214.

[49] Lincker, F.; Delbosc, N.; Bailly, S.; De Bettignies, R.; Billon, M.; Pron, A.; Demadrille, R. Fluorenone-Based Molecules for Bulk-Heterojunction Solar Cells: Synthesis, Characterization, and Photovoltaic Properties. *Adv. Funct. Mater.* **2008**, *18* (21), 3444-3453.

[50] Eakins, G. L.; Alford, J. S.; Tiegs, B. J.; Breyfogle, B. E.; Stearman, C. J. Tuning HOMO–LUMO Levels: Trends Leading to the Design of 9-Fluorenone Scaffolds with Predictable Electronic and Optoelectronic Properties. *J. Phys. Org. Chem.* **2011**, *24* (11), 1119-1128.

[51] Hayashi, S.; Nishioka, N.; Nishiyama, H.; Koizumi, T. π-Conjugated Alternating Copolymer Based on the 3,5-Dinitro-9-Fluorenone for Electron-Acceptor Type Materials. *Synth. Met.* **2012**, *162*, 1485-1489.

References

[52] Chandrasekharan, A.; Hambsch, M.; Jin, H.; Maasoumi, F.; Shaw, P. E.; Raynor, A.; Burn, P. L.; Lo, S. C.; Meredith, P.; Namdas, E. B. Effect of Capping Group on the Properties of Non-Polymeric Diketopyrrolopyrroles for Solution-Processed Bulk Heterojunction Solar Cells. *Org. Electron.* **2017**, *50*, 339-346.

[53] Qu, S.; Tian, H. Diketopyrrolopyrrole (DPP)-Based Materials for Organic Photovoltaics. *Chem. Commun.* **2012**, *48* (25), 3039.

[54] Li, Y.; Sonar, P.; Murphy, L.; Hong, W. High Mobility Diketopyrrolopyrrole (DPP)-Based Organic Semiconductor Materials for Organic Thin Film Transistors and Photovoltaics. *Energy Environ. Sci.* **2013**, *6* (6), 1684.

[55] Gedefaw, D.; Mario Prosa, M.; Bolognesi, M.; Siri, M.; Andersson, M. R. Recent Development of Quinoxaline Based Polymers/Small Molecules for Organic Photovoltaics. *Adv. Energy Mater*. **2017**, *7* (21), 1700575.

[56] Segura, J. L.; Juárez, R.; Ramos, M.; Seoane, C. Hexaazatriphenylene (HAT) Derivatives: From Synthesis to Molecular Design, Self-Organization and Device Applications. *Chem. Soc. Rev.* **2015**, *44* (19), 6850-6885.

[57] Chen, Y.; Du, Z.; Chen, W.; Liu, Q.; Sun, L.; Sun, M.; Yang, R. Benzo[1,2-b:4,5-b']dithiophene and Benzotriazole Based Small Molecule for Solution-Processed Organic Solar Cells. *Org. Electron.* **2014**, *15* (2), 405-413.

[58] Patel, D. G.; Feng, F.; Ohnishi, Y. Y.; Abboud, K. A.; Hirata, S.; Schanze, K. S.; Reynolds, J. R. It Takes More than an Imine: The Role of the Central Atom on the Electron-Accepting Ability of Benzotriazole and Benzothiadiazole Oligomers. *J. Am. Chem. Soc.* **2012**, *134* (5), 2599-2612.

[59] Zhan, X.; Facchetti, A.; Barlow, S.; Marks, T. J.; Ratner, M. A.; Wasielewski, M. R.; Marder, S. R. Rylene and Related Diimides for Organic Electronics. *Adv. Mater*. **2011**, *23*, 268-284.

[60] Guide, M.; Pla, S.; Sharenko, A.; Zalar, P.; Fernández-Lázaro, F.; Sastre-Santos, Á.; Nguyen, T.-Q. A Structure–property–performance Investigation of Perylenediimides as Electron Accepting Materials in Organic Solar Cells. *Phys. Chem. Chem. Phys*. **2013**, *15* (43), 18894-18899.

[61] Suraru, S.-L.; Würthner, F. Strategies for the Synthesis of Functional Naphthalene Diimides. *Angew. Chem. Int. Ed.* **2014**, *53*, 7428-7448.

References

[62] Peebles, C.; Piland, R.; Iverson, B. L. More than Meets the Eye: Conformational Switching of a Stacked Dialkoxynaphthalene-Naphthalenetetracarboxylic diimide (DAN-NDI) Foldamer to an NDI-NDI Fibril Aggregate. *Chem. Eur. J.* **2013**, *19*, 11598-11602.

[63] Fernández-Lázaro, F.; Zink-Lorre, N.; Sastre-Santos, Á. Perylenediimides as Non-Fullerene Acceptors in Bulk-Heterojunction Solar Cells (BHJSCs). *J. Mater. Chem. A* **2016**, *4* (24), 9336–9346.

[64] Liu, Z.; Zhang, G.; Cai, Z.; Chen, X.; Luo, H.; Li, Y.; Wang, J.; Zhang, D. New Organic Semiconductors with Imide/Amide-Containing Molecular Systems. *Adv. Mater.* **2014**, *26*, 6965-6977.

[65] Middleton, R. W.; Parrick, J.; Clarke, E. D. Wardman, P. Synthesis and Fluorescence of *N*-Substituted-1,8-Naphthalimides. *J. Heterocyclic Chem.* **1986**, *23*, 849-855.

[66] Pardo, A.; Poyato, J. M. L.; Martin, E. Photophysical Properties of 1,8-Naphthalimide Derivatives. *J. Photochem.* **1987**, *36*, 323-329.

[67] Alexiou, M. S.; Tychopoulos, V.; Ghorbanian, S.; Tyman, J. H.; Brown, R. G.; Brittain, P. I. The UV-Visible Absorption and Fluorescence of Some Substituted 1,8-Naphthalimides and Naphthalic Anhydrides. *J. Chem. Soc. Perkin Trans.* **1990**, *2*, 837-842.

[68] Kucheryavy, P.; Li, G.; Vyas, S.; Hadad, C.; Glusac, K. D. Electronic Properties of 4-Substituted Naphthalimides. *J. Phys. Chem. A* **2009**, *113*, 6453-6461.

[69] Chen, W.; Zhang, Q. Recent Progress in Non-Fullerene Small Molecule Acceptors in Organic Solar Cells (OSCs). *J. Mater. Chem. C* **2017**, *5*, 1275-1302.

[70] Duke, R. M.; Veale, E. B.; Pfeffer, F. M.; Kruger, P. E.; Gunnlaugsson, T. Colorimetric and Fluorescent Anion Sensors: An Overview of Recent Developments in the Use of 1,8-Naphthalimide-Based Chemosensors. *Chem. Soc. Rev.* **2010**, *39*, 3936-3953.

[71] Peebles, C.; Alvey, P. M.; Lynch, V; Iverson, B. L. Time-Dependent Solid-State Polymorphism of a Series of Donor-Acceptor Dyads. *Cryst. Growth Des*. **2014**, *14*, 290-299.

[72] Gopikrishna, P.; Meher, N.; Iyer, P. K. Functional 1,8-Naphthalimide AIE/AIEEgens: Recent Advances and Prospects. *ACS Appl. Mater. Interfaces* **2017**, DOI: 10.1021/acsami.7b14473.

[73] Banerjee, S.; Veale, E. B.; Phelan, C. M.; Murphy, S. A.; Tocci, G. M.; Gillespie, L. J.; Frimannsson, D. O.; Kelly, J. M.; Gunnlaugsson, T. Recent Advances in the Development of 1,8-Naphthalimide Based DNA Targeting Binders, Anticancer and Fluorescent Cellular

Imaging Agents. *Chem. Soc. Rev.* **2013**, *42* (4), 1601-1618.

[74] Tandon, R.; Luxami, V.; Kaur, H.; Tandon, N.; Paul, K. 1,8-Naphthalimide: A Potent DNA Intercalator and Target for Cancer Therapy. *Chem. Rec.* **2017**, *17* (10), 956-993.

[75] Ge, S.; Li, B.; Meng, X.; Yan, H.; Yang, M.; Dong, B.; Lu, Y. Aggregation-Induced Emission, Multiple Chromisms and Self-Organization of *N*-Substituted-1,8-Naphthalimides. *Dyes Pigm.* **2018**, *148*, 147–153.

[76] Srivastava, A. K.; Singh, A.; Mishra, L. Tuning of Aggregation Enhanced Emission and Solid State Emission from 1,8-Naphthalimide Derivatives: Nanoaggregates, Spectra, and DFT Calculations. *J. Phys. Chem. A* **2016**, *120* (26), 4490–4504.

[77] Ledwon, P.; Brzeczek, A.; Pluczyk, S.; Jarosz, T.; Kuznik, W.; Walczak, K.; Lapkowski, M. Synthesis and Electrochemical Properties of Novel, Donor–Acceptor Pyrrole Derivatives with 1, 8-Naphthalimide Units and Their Polymers. *Electrochim. Acta* **2014**, *128*, 420–429.

[78] Grepioni, F.; d'Agostino, S.; Braga, D.; Bertocco, A.; Catalanoa, L.; Ventura, B. Fluorescent Crystals and Co-Crystals of 1,8-Naphthalimide Derivatives: Synthesis, Structure Determination and Photophysical Characterization. *J. Mater. Chem. C* **2015**, *3*, 9425-9434.

[79] Liu, Y-H.; Chen, L-F.; Wang, H-Y.; Wan, Y.; Wu, H. Synthesis and Photophysical Properties of Novel Fluorescent Materials containing 2,4,6-Triphenylpyridine and 1,8-Naphthalimide Units using Suzuki Reaction. *RSC Adv.* **2016**, *6*, 94833-94839.

[80] Dong, L.; Li, G.; Yu, A. D.; Bo, Z.; Liu, C. L.; Chen, W. C. Conjugated Donor-Acceptor-Acceptor (D-A-A) Molecule for Organic Nonvolatile Resistor Memory. *Chem. - Asian J.* **2014**, *9* (12), 3403–3407.

[81] Meher, N.; Iyer, P. K. Pendant Chain Engineering To Fine-Tune The Nanomorphologies And Solid State Luminescence of Naphthalimide AIEEgens: Application to Phenolic Nitro-Explosive Detection In Water. *Nanoscale* **2017**, *9*, 7674–7685

[82] Zhuang, H.; Zhou,Q.; Li, Y.; Zhang, Q.; Li, H.; Xu, Q.; Li, N.; Lu, J.; Wang, L. Adjustment of ON-State Retention Ability Based on New Donor–Acceptor Imides through Structural Tailoring for Volatile Device Applications. *ACS Appl. Mater. Interfaces* **2014**, *6* (1), 94–100.

[83] Sun, F.; Jin, R. Optical and Charge Transport Properties of *N*-Butyl-1,8-Naphthalimide Derivatives as Organic Light-Emitting Materials: A Theoretical Study. *J. Lumin.* **2014**,

149, 125-132.

[84] Greiner, R.; Schlücker, T.; Zgela, D.; Langhals, H. Fluorescent Aryl Naphthalene Dicarboximides with Large Stokes Shifts and Strong Solvatochromism Controlled by Dynamics and Molecular Geometry. *J. Mater. Chem. C* **2016**, *4* (47), 11244–11252.

[85] Mallia, A. R.; Salini, P. S.; Hariharan, M. Nonparallel Stacks of Donor and Acceptor Chromophores Evade Geminate Charge Recombination. *J. Am. Chem. Soc.* **2015**, *137* (50), 15604–15607.

[86] Wang, H, Liang, Y.; Xie, H.; Lu, H.; Zhao, S.; Feng, S. Unexpected $SiMe_3$ Effect on Color-Tunable and Fluorescent Probes of Dendritic Polyphenyl Naphthalimides with Aggregation-Induced Emission Enhancement. *J. Mater. Chem. C* **2016**, *4*, 745-750.

[87] Keerthi, A.; Hou, I. C.-Y.; Marszalek, T.; Pisula, W.; Baumgarten, M.; Narita, A. Hexa-*Peri* -Hexabenzocoronene with Different Acceptor Units for Tuning Optoelectronic Properties. *Chem. - Asian J.* **2016**, *11* (19), 2710–2714.

[88] Qu, Y.; Wang, L.; Wu, J.; Rui, Y.; Cao, J.; Xu, J. 4-Phenyl-1,8-Naphthalimides: Brightness and Tuning Emission over Widely Visible Gamut in Different Aggregated States. *Dyes Pigm.* **2018**, *148*, 99–107.

[89] Meher, N.; Chowdhury, S. R.; Iyer, P. K. Aggregation Induced Emission Enhancement And Growth Of Naphthalimide Nanoribbons *Via* J-Aggregation: Insight into Disaggregation Induced Unfolding and Detection of Ferritin at the Nanomolar Level. *J. Mater. Chem. B* **2016**, *4*, 6023-6031.

[90] Ulla, H.; Kiran, M. R.; Garudachari, B.; Ahipa, T. N.; Tarafder, K.; Adhikari, A. V.; Umesh, G.; Satyanarayan, M. N. Blue Emitting 1,8-Naphthalimides with Electron Transport Properties for Organic Light Emitting Diode Applications. *J. Mol. Struct.* **2017**, *1143*, 344–354.

[91] Rémy, C.; Allain, C.; Leray, I. Synthesis and Photophysical Properties of Extended π Conjugated Naphthalimides. *Photochem. Photobiol. Sci.* **2017**, *16* (4), 539–546.

[92] Zhengneng, J.; Najun, L.; Chuanfeng, W.; Huajiang, J.; Jianmei, L.; Qizhong, Z. Synthesis and Fluorescence Property of Some Novel 1, 8-Naphthalimide Derivatives Containing a Thiophene Ring at the C-4 Position. *Dyes Pigm.* **2013**, *96* (1), 204–210.

[93] Gudeika, D.; Reghu, R. R.; Grazulevicius, J. V.; Buika, G.; Simokaitiene, J.; Miasojedovas, A.; Jursenas, S.; Jankauskas, V. Electron-Transporting Naphthalimide-Substituted Derivatives of Fluorene. *Dyes Pigm.* **2013**, *99* (3), 895–902.

References

[94] Mallia, A. R.; Hariharan, M. Self-Assembled Donor-Acceptor Trefoils: Long-Lived Charge Separated State through Aggregation. *J. Phys. Chem. C* **2017**, *121* (9), 4778–4788.

[95] Gudeika, D.; Grazulevicius, J. V.; Volyniuk, D.; Butkute, R.; Juska, G.; Miasojedovas, A.; Gruodis, A.; Jursenas, S. Structure-Properties Relationship of the Derivatives of Carbazole and 1,8-Naphthalimide: Effects of the Substitution and the Linking Topology. *Dyes Pigm.* **2015**, *114*, 239–252.

[96] Inari, T.; Yamano, M.; Hirano, A.; Sugawa, K.; Otsuki, J. Photophysical and Electrochemical Properties of Thienylnaphthalimide Dyes with Excellent Photostability. *J. Phys. Chem. A* **2014**, *118* (28), 5178–5188.

[97] Jin, R.; Tang, S. Theoretical Study on Optical and Electronic Properties of Bipolar Molecules with 1 , 8-Naphthalimide and Triphenylamine Moieties as Organic Light-Emitting Materials. *J. Mol. Graph. Model.* **2013**, *42*, 120–128.

[98] Mallia, A. R.; Philip, A. M.; Bhat, V.; Hariharan, M. Persistent Charge-Separated States in Self-Assembled Twisted Nonsymmetric Donor-Acceptor Triads. *J. Phys. Chem. C* **2017**, *121* (9), 4765–4777.

[99] Li, Y.; Li, H.; He, J.; Xu, Q.; Li, N.; Chen, D.; Lu, J. Inserting Thienyl Linkers into Conjugated Molecules for Efficient Multilevel Electronic Memory: A New Understanding of Charge-Trapping in Organic Materials. *Chem. – Asian J.* **2016**, *11* (6), 906-914.

[100] Zhang, Q.; Miao, S.; Li, H.; He, J.; Li, N.; Xu, Q.; Chen, D.; Lu, J. A Novel Bat-Shaped Dicyanomethylene-4 *H* -Pyran-Functionalized Naphthalimide for Highly Efficient Solution-Processed Multilevel Memory Devices. *Chem. - Asian J.* **2017**, *12* (12), 1374–1380.

[101] Gopikrishna, P.; Iyer, P. K. Monosubstituted Dibenzofulvene-Based Luminogens: Aggregation-Induced Emission Enhancement and Dual-State Emission. *J. Phys. Chem. C* **2016**, *120* (46), 26556–26568.

[102] Xia, T.; Wang, L.; Qu, Y.; Rui, Y.; Cao, J.; Hu, Y.; Yang, J.; Wua. J.; Xu, J. A Thermoresponsive Fluorescent Rotor Based on a Hinged Naphthalimide for a Viscometer and a Viscosity-Related Thermometer. *J. Mater. Chem. C* **2016**, *4*, 5696-5701.

[103] Chai, W.; Lin, R. Theoretical Investigations into Optical and Charge Transfer Properties Of Donor-Acceptor 1,8-Naphthalimide Derivatives as Possible Organic Light-Emitting Materials. *J. Mol. Struc.* **2016**, *1103*, 177-182.

[104] Zhang, Q.; He, J.; Li, H.; Li, N.; Xu, Q.; Chen, D.; Lu, J. A Novel Ternary Memory

Property Achieved through Rational Introduction of End-Capping Naphthalimide Acceptors. *J. Mater. Chem. C* **2017**, *5* (31), 7961–7968.

[105] Hendsbee, A. D.; Sun, J.-P.; Rutledge, L. R.; Hill, I. G.; Welch, G. C. Electron Deficient Diketopyrrolopyrrole Dyes for Organic Electronics: Synthesis by Direct Arylation, Optoelectronic Characterization, and Charge Carrier Mobility. *J. Mater. Chem. A* **2014**, *2* (12), 4198–4207.

[106] Li, Y.; Li, H.; He, J.; Xu, Q.; Li, N.; Chen, D.; Lu, J. Towards Highly-Efficient Phototriggered Data Storage by Utilizing a Diketopyrrolopyrrole-Based Photoelectronic Small Molecule. *Chem.- Asian. J.* **2016**, *11*(14), 2078-2084.

[107] McAfee, S. M.; Cann, J. R.; Josse, P.; Blanchard, P.; Cabanetos, C.; Welch, G. C. The Optimization of Direct Heteroarylation and Sonogashira Cross-Coupling Reactions as Efficient and Sustainable Synthetic Methods to Access π-Conjugated Materials with Near-Infrared Absorption. *ACS Sustainable Chem. Eng.* **2016**, *4* (6), 3504–3517.

[108] Xu, S. De; Fang, C. H.; Tian, G. X.; Chen, Y.; Dou, Y. H.; Kou, J. F.; Wu, X. H. Reduction of 4-Azidonaphthalimide with Different Phosphine Ligands and Exploration of Their Spectroscopic Properties. *J. Mol. Struct.* **2015**, *1102*, 197–202.

[109] Zhang, J.; Dumur, F.; Xiao, P.; Graff, B.; Bardelang, D.; Gigmes, D.; Fouassier, J. P.; Lalevée, J. Structure Design of Naphthalimide Derivatives: Toward Versatile Photoinitiators for Near-UV/Visible LEDs, 3D Printing, and Water-Soluble Photoinitiating Systems. *Macromolecules* **2015**, *48* (7), 2054–2063.

[110] Ivanov, I. P.; Dimitrova, M. B.; Tasheva, D. N.; Cheshmedzhieva, D. V; Lozanov, V. S.; Ilieva, S. V. Synthesis, Structural Analysis and Application of a Series of Solid-State Fluorochromes-Aryl Hydrazones of 4-Hydrazino-*N*-Hexyl-1,8-Naphthalimide. *Tetrahedron* **2013**, *69* (2), 712–721.

[111] Gudieka, D.; Lygaitis, R.; Mimaite, V.; Grazulevicius, J. V; Jankauskas, V.; Lapkowski, M.; Data, P. Hydrazones Containing Electron-Accepting and Electron-Donating Moieties. *Dyes Pigm.* **2011**, *91*, 13–19.

[112] Zhang, Y.; Zhu, W.; Wang, W.; Tian, H.; Su, J.; Wang, W. Synthesis and Nonlinear Optical Properties of Rod-Like Luminescent Materials Containing Schiff-Base and Naphthalimide Units. *J. Mater. Chem.* **2002**, *12*, 1294-1300.

[113] Dubey, R. K.; Inan, D.; Sengupta, S.; Sudhölter, E. J. R.; Grozema, F. C.; Jager, W. F. Tunable and Highly Efficient Light-Harvesting Antenna Systems Based on 1,7-Perylene-

3,4,9,10-Tetracarboxylic Acid Derivatives. *Chem. Sci.* **2016**, *7*, 3517-3532.

[114] Wang, H. Y.; Zhan, G. X. X.; Shi, J. J.; Chen, G.; Xu, X. P.; Ji, S. J. Synthesis, Spectroscopic Characteristic of Novel Fluorescent Dyes of Pyrazoline Compounds. *Spectrochim Acta A Mol Biomol Spectrosc*. **2012**, *93*, 343-347.

[115] Arkhipov, A. N.; Panchenko, P. A.; Fedorov, V.; Fedorova, O. A. Relationship between the Photochromic and Fluorescent Properties of 4-Styryl Derivatives of *N*-Butyl-1 , 8-Naphthalimide. *Mendeleev. Commun.* **2017**, *27* (1), 53–55.

[116] Panchenko, P. A.; Arkhipov, A. N.; Fedorov, O. A.; Fedorov, Y. V.; Marina A. Zakharko, M. A. Controlling Photophysics of Styrylnaphthalimides through TICT, Fluorescence And E,Z-Photoisomerization Interplay. *Phys. Chem. Chem. Phys*. **2017**, *19* (2), 1244 - 1256.

[117] Ren, W.; Zhuang, H.; Bao, Q.; Miao, S.; Li, H.; Lu, J.; Wang, L. Enhancing the Coplanarity of the Donor Moiety in a Donor-Acceptor Molecule to Improve the Efficiency of Switching Phenomenon for Flash Memory Devices. *Dyes Pigm.* **2014**, *100*, 127–134.

[118] Gudeika, D.; Lygaitis, R.; Mimait, V.; Grazulevicius, J. V.; Jankauskas, V.; Grigalevicius, S.; Miasojedovas, A.; Jursenas, S.; Sin, G. Structure Properties Relationship of Donor–Acceptor Derivatives of Triphenylamine and 1,8-Naphthalimide. *J. Phys. Chem. C* **2012**, *116*, 14811-14819.

[119] Gudeika, D.; Sini, G.; Jankauskas, V.; Sych, G.; Grazulevicius, J. V. Synthesis and Properties of the Derivatives of Triphenylamine and 1,8-Naphthalimide with the Olefinic Linkages between Chromophores. *RSC Adv.* **2016**, *6*, 2191-2201.

[120] Peebles, C.; Wight, C. D.; Iverson, B. L. Solutioni and Solid-State Photophysical and Stimuli-Responsive Behavior in Conjugated Monoalkoxynaphthalene–Naphthalimide Donor–Acceptor Dyads. *J. Mater. Chem. C* **2015**, *3*, 12156-12163.

[121] Kim, K.-W.; Kim, G.-H.; Park, C.-E.; Choi, J.-H. 1,8-Naphthalimide Derivatives Containing Ethynyl Linkage and Blue Light Emitting Properties. *Bull. Korean Chem. Soc.* **2017**, *38* (8), 956–959

[122] Gudeika, D.; Grazulevicius, J. V.; Volyniuk, D.; Juska, G.; Jankauskas, V.; Sini, G. Effect of Ethynyl Linkages on the Properties of the Derivatives of Triphenylamine and 1,8-Naphthalimide. *J. Phys. Chem. C* **2015**, *119* (51), 28335–28346.

[123] Liu, Y.; Wang, H. Y.; Chen, G.; Xu, X. P.; Ji, S. J. Synthesis and Properties of Novel "Ethyne-Linked" Compounds Containing Carbazole and 1, 8-Naphthalimide Groups. *Aust. J. Chem.* **2009**, *62* (8), 934–940.

References

[124] Cao, X.; Meng, L.; Li, Z.; Mao, Y.; Lan, H.; Chen, L.; Fan, Y.; Yi, T. Large Red-Shifted Fluorescent Emission via Intermolecular π-π Stacking in 4-Ethynyl-1,8-Naphthalimide-Based Supramolecular Assemblies. *Langmuir* **2014**, *30* (39), 11753–11760.

[125] Thompson, A. L.; Ahn, T. S.; Thomas, K. R. J.; Thayumanavan, S.; Martínez, T. J.; Bardeen, C. J. Using Meta Conjugation to Enhance Charge Separation versus Charge Recombination in Phenylacetylene Donor-Bridge-Acceptor Complexes. *J. Am. Chem. Soc.* **2005**, *127* (47), 16348–16349.

[126] Wang, G.; Miao, S.; Zhang, Q.; Liu, H.; Li,H.; Li, N.; Xu, Q.; Lu, J.; Wang, L. Effect of a π-spacer between a Donor and an Acceptor on Small Molecule-Based Data-Storage Device Performance. *Chem. Commun.* **2013**, *49*, 9470-9472.

[127] Maragani, R.; Bijesh, S.; Sharma, R.; Misra, R. C_s -Symmetric Donor-Acceptor Bis(thiazole)s: Synthesis and Photophysical, Electrochemical, and Computational Studies. *Asian J. Org. Chem.* **2017**, *6* (10), 1408–1414.

[128] Liu, S.; Li, F.; Wang, Y.; Li, X.; Zhu, C.; Cheng, Y. Circularly Polarized Luminescence of Chiral 1,8-Naphthalimide-Based Pyrene Fluorophore Induced via Supramolecular Self-Assembly. *J. Mater. Chem. C* **2017**, *5* (24), 6030–6036.

[129] Jin. R.; Ahmad, I. Theoretical Study on Photophysical Properties of Multifunctional Star-Shaped Molecules with 1,8-Naphthalimide Core for Organic Light-Emitting Diode and Organic Solar Cell Application. *Theor Chem Acc*. **2015**, *134*, 89.

[130] Jin. R. Rational Design of Star-Shaped Molecules with Benzene Core and Naphthalimides Derivatives End Groups as Organic Light-emitting Materials. *Org. Chem Curr Res*. **2014**, *4*, 134.

[131] Zhu, W.; Xu, Y.; Zhang, Y.; Shen, J.; Tian, H. Singlet Energy Transfer and Photoinduced Electron Transfer in Star-Shaped Naphthalimide Derivatives Based on Triphenylamine. *Bull. Chem. Soc. Jpn.* **2005**, *78* (7), 1362–1367.

[132] Jin, R. F.; Chang, Y. F. A Theoretical Study on Photophysical Properties of Triphenylamine-Cored Molecules with Naphthalimide Arms and Different π-Conjugated Bridges as Organic Solar Cell Materials. *Phys. Chem. Chem. Phys.* **2015**, *17* (3), 2094–2103.

[133] Wu, H-C.; Zhang, J.; Bo, Z.; Chen, W-C. Well-Defined Star-Shaped Donor–Acceptor Conjugated Molecules for Organic Resistive Memory Devices. *Chem. Commun.* **2015**, *51*, 14179-14182.

References

[134] Kolosov, D.; Adamovich, V.; Djurovich, P.; Thompson, M. E.; Adachi, C. 1,8-Naphthalimides in Phosphorescent Organic LEDs: The Interplay between Dopant, Exciplex, and Host Emission. *J. Am. Chem. Soc.* **2002**, *124* (33), 9945–9954.

[135] Zhang, W.; Xu, Y.; Hanif, M.; Zhang, S.; Zhou, J.; Hu, D.; Xie, Z.; Ma, Y. Enhancing Fluorescence of Naphthalimide Derivatives by Suppressing the Intersystem Crossing. *J. Phys. Chem. C* **2017**, *121*, 23218−23223.

[136] Triboni, E. R.; Fernandes, M. R.; Garcia, J. R.; Carreira, C.; Berlinck, R. G. S.; Filho, B.; Roman, L. S.; Reyes, Hümmelgen, I. A.; R.; Cremona, M. Naphthalimide-Derivative with Blue Electroluminescence for OLED Applications. *J. Taibah Uni. Sci.* **2015**, *9* (4), 579–585.

[137] Luo, Y.; Wang, Y.; Chen, S.; Wang, N.; Qi, Y.; Zhang, X.; Yang, M.; Huang, Y.; Li, M.; Yu, J. Facile Access to Twisted Intramolecular Charge-Transfer Fluorogens Bearing Highly Pretwisted Donor-Acceptor Systems Together with Readily Fine-Tuned Charge-Transfer Characters. *Small* **2017**, *13* (20), 1604113.

[138] Ulla, H.; Kiran, M. R.; Garudachari, B.; Ahipa, T. N.; Tarafder, K.; Adhikari, A. V.; Umesh, G.; Satyanarayan, M. N. Blue Emitting 1,8-Naphthalimides with Electron Transport Properties for Organic Light Emitting Diode Applications. *J. Mol. Struct.* **2017**, *1143*, 344–354.

[139] Li, J.; Qi, Y.; Zhao, D.; Li, M.; Lu, Z.; Yu, J. Pure White Organic Light-Emitting Devices with Excellent Color Stability Using a Non-Doped 4-Aryloxy-1,8-Naphthalimide Derivative. *J. Lumin.* **2017**, *192*, 463–469.

[140] Wang, X.; Zhou, J.; Zhao, J.; Lu, Z.; Yu, J. High Performance Fluorescent and Phosphorescent Organic Light-Emitting Diodes Based on a Charge-Transfer-Featured Host Material. *Org. Electron*. **2015**, *21*, 78-85.

[141] Gudieka, D.; Ivanauskaitea, A.; Lygaitisa, R.; Kosachb, V.; Volyniuka, D.; Butkutea, R.; Naumenkob, A. P.; Yashchukb, V.;. Grazulevicius, J. V. Charge-transporting Blue Emitters Having Donor and Acceptor Moieties. *J. Photochem. Photobiol. A* **2016**, *315*, 121–128.

[142] Gan, J.; Liang, Q.; Yuan, X.; Chen, K.; Tian, H. 1 , 8-Naphthalimides for Non-Doping OLEDs : The Tunable Emission Color from Blue , Green to Red. *J. Photochem. Photobiol. A* **2004**, *162*, 399–406.

[143] Luo, S.; Lin, J.; Zhou, J.; Wang, Y.; Liu, X.; Huang, Y.; Lu, Z.; Hu, C. Novel 1,8-

Naphthalimide Derivatives for Standard-Red Organic Light-Emitting Device Applications. *J. Mater. Chem. C* **2015**, *3*, 5259-5267.

[144] Zheng, X.; Peng, Q.; Lin, J.; Wang, Y.; Zhou, J.; Jiao, Y.; Bai, Y.; Huang, Y.; Li, F.; Liu, X.; Pu, X.; Lu, Z. Simultaneous Harvesting of Triplet Excitons In OLEDs by Both Guest and Host Materials with an Intramolecular Charge-Transfer Feature *via* Triplet–Triplet Annihilation. *J. Mater. Chem. C* **2015**, *3*, 6970-6978.

[145] Zhou, J.; Chen, P.; Wang, X.; Wang, Y.; Wang, Y.; Li, F.; Yang, M.; Huang, Y.; Yu, J.; Lu, Z. Charge-Transfer-Featured Materials-Promising Hosts for Fabrication of Efficient OLEDs through Triplet Harvesting via Triplet Fusion. *Chem. Commun.***2014**, *50* (57), 7586–7589.

[146] Shi, S.; Gao, F.; Sun, Z.; Zhan, Y.; Fahlman, M.; Ma, D. Effects of Side Groups on the Kinetics of Charge Carrier Recombination in Dye Molecule-Doped Multilayer Organic Light-Emitting Diodes. *J. Mater. Chem. C* **2015**, *3* (1), 46–50

[147] Arunchai, R.; Sudyoadsuk, T.; Prachumrak, N.; Namuangruk, S.; Promarak, V.; Sukwattanasinitt, M.; Rashatasakhon, P. Synthesis and Characterization of New Triphenylamino-1,8-Naphthalimides for Organic Light-Emitting Diode Applications. *New J. Chem.* **2015**, *39* (4), 2807–2814.

[148] Facchetti, A. Polymer Donor-Polymer Acceptor (All-Polymer) Solar Cells. *Mater. Today* **2013**, *16* (4), 123-132.

[149] Alam, M. M.; Jenekhe, S. A. Efficient Solar Cells from Layered Nanostructures of Donor and Acceptor Conjugated Polymers. *Chem. Mater.* **2004**, *16* (23), 4647–4656.

[150] Dang, M. T.; Hirsch, L.; Wantz, G.; Wuest, J. D. Controlling the Morphology and Performance of Bulk Heterojunctions in Solar Cells. Lessons Learned from the Benchmark poly(3-hexylthiophene):[6,6]-Phenyl- C_{61}-Butyric Acid Methyl Ester System. *Chem. Rev.* **2013**, *113* (5), 3734-3765.

[151] Nielsen, C. B.; Holliday, S.; Chen, H.-Y.; Cryer, S. J.; McCulloch, I. Non-Fullerene Electron Acceptors for Use in Organic Solar Cells. *Acc. Chem. Res.* **2015**, *48* (11), 2803-2812.

[152] Brunetti, F. G.; Kumar, R.; Wudl, F. Organic Electronics from Perylene to Organic Photovoltaics: Painting a Brief History with a Broad Brush. *J. Mater. Chem.* **2010**, *20* (15), 2934.

References

[153] Li, W.; Yao, H.; Zhang, H.; Li S.; Hou, J. Potential of Nonfullerene Small Molecules with High Photovoltaic Performance. *Chem.- Asian J*. **2017**, *12* (17), 2160-2171.

[154] Sonar, P.; Fong Lim, J. P.; Chan, K. L. Organic Non-Fullerene Acceptors for Organic Photovoltaics. *Energy Environ. Sci.* **2011**, *4* (5), 1558-1578.

[155] Eftaiha, A. F.; Sun, J.-P.; Hill, I. G.; Welch, G. C. Recent Advances of Non-Fullerene, Small Molecular Acceptors for Solution Processed Bulk Heterojunction Solar Cells. *J. Mater. Chem. A* **2014**, *2* (5), 1201-1213.

[156] Lin, Y.; Zhan, X. Non-Fullerene Acceptors for Organic Photovoltaics: An Emerging Horizon. *Mater. Horizons* **2014**, *1* (5), 470-488.

[157] Zhan, C.; Zhang, X.; Yao, J. New Advances in Non-Fullerene Acceptor Based Organic Solar Cells. *RSC Adv*. **2015**, *5* (113), 93002-93026.

[158] Liu, Z.; Wu, Y.; Zhang, Q.; Gao, X. Non-Fullerene Small Molecule Acceptors Based on Perylene Diimides. *J. Mater. Chem. A* **2016**, *4* (45), 17604-17622.

[159] Li, S.; Liu, W.; Li, C.-Z.; Shi, M.; Chen, H. Efficient Organic Solar Cells with Non-Fullerene Acceptors. *Small* **2017**, *13*, 1701120.

[160] Lin, Y.; Wang, J.; Zhang, Z.-G.; Bai, H.; Li, Y.; Zhu, D.; Zhan, X. An Electron Acceptor Challenging Fullerenes for Efficient Polymer Solar Cells. *Adv. Mater.* **2015**, *27* (7), 1170-1174.

[161] Liang, N.; Jiang, W.; Hou, J.; Wang, Z. New Developments in Non-Fullerene Small Molecule Acceptors for Polymer Solar Cells. *Mater. Chem. Front.* **2017**, *1* (7), 1291-1303.

[162] Sun, D.; Meng, D.; Cai, Y.; Fan, B.; Li, Y.; Jiang, W.; Huo, L.; Sun, Y.; Wang, Z. Non-Fullerene-Acceptor-Based Bulk-Heterojunction Organic Solar Cells with Efficiency over 7%. *J. Am. Chem. Soc.* **2015**, *137* (34), 11156-11162.

[163] Lu, R.-Q.; Zheng, Y.-Q.; Zhou, Y.-N.; Yan, X.-Y.; Lei, T.; Shi, K.; Zhou, Y.; Pei, J.; Zoppi, L.; Baldridge, K. K. Corannulene Derivatives as Non-Fullerene Acceptors in Solution-Processed Bulk Heterojunction Solar Cells. *J. Mater. Chem. A* **2014**, *2* (48), 20515–20519.

[164] He, Q.; Li, T.; Yan, C.; Liu, Y.; Wang, J.; Wang, M.; Lin, Y.; Zhan, X. Cracking Perylene Diimide Backbone for Fullerene-Free Polymer Solar Cells. *Dyes Pigm.* **2016**, *128*, 226–234.

References

[165] Zhang, X.; Zhang, J.; Lu, H.; Wu, J.; Li, G.; Li, C. A 1,8-naphthalimide Based Small Molecular Acceptor for Polymer Solar Cells with High Open Circuit Voltage. *J. Mater. Chem. C* **2015**, *3*, 6979–6985.

[166] Zhang, J.; Zhang, X.; Xiao, H.; Li, G.; Liu, Y.; Li, C.; Huang, H.; Chen, X.; Bo, Z. 1,8-Naphthalimide-Based Planar Small Molecular Acceptor for Organic Solar Cells. *ACS Appl. Mater. Interfaces*. **2016**, *8*, 5475-5483.

[167] Srivani, D.; Gupta, A.; La, D. D.; Bhosale, R. S.; Puyad, A. L.; Xiang, W.; Li, J.; Bhosale, S. V.; Bhosale, S. V. Small Molecular Non-Fullerene Acceptors Based on Naphthalenediimide and Benzoisoquinoline-Dione Functionalities for Efficient Bulk-Heterojunction Devices. *Dyes Pigm.* **2017**, *143*, 1–9.

[168] Dang, D.; Zhi, Y.; Wang, X.; Zhao, B.; Gao, C.; Meng, L. A1-A-A1 Type Small Molecules Terminated with Naphthalimide Building Blocks for Efficient Non-Fullerene Organic Solar Cells. *Dyes Pigm.* **2017**, *137*, 43–49.

[169] Chen, M.; Du, C.; Ren, X.; Yi, M.; Yi, J.; Chen, C.; Liu, F.; Li, M.; Ma, C.; Wang, H. Phthalimide and Naphthalimide end-Capped Diketopyrrolopyrrole for Organic Photovoltaic Applications. *Chin. J. Org. Chem.* **2017**, *35*, 1396-1404.

[170] McAfee, S. M.; Topple, J. M.; Sun, J.-P.; Hill, I. G.; Welch, G. C. The Structural Evolution of an Isoindigo-Based Non-Fullerene Acceptor for Use in Organic Photovoltaics. *RSC Adv.* **2015**, *5* (97), 80098–80109.

[171] Do, T. T.; Pham, H. D.; Manzhos, S.; Bell, J. M.; Sonar, P. Molecular Engineering Strategy for High Efficiency Fullerene-Free Organic Solar Cells Using Conjugated 1,8-Naphthalimide and Fluorenone Building Blocks. *ACS Appl. Mater. Interfaces* **2017**, *9* (20), 16967–16976.

[172] Bloking, J. T.; Han, X.; Higgs, A. T.; Kastrop, J. P.; Pandey, L.; Norton, J. E.; Risko, C.; Chen, C. E.; Brédas, J. L.; McGehee, M. D. Solution-Processed Organic Solar Cells with Power Conversion Efficiencies of 2.5% Using Benzothiadiazole/imide-Based Acceptors. *Chem. Mater.* **2011**, *23* (24), 5484–5490.

[173] Kwon, O. K.; Park, J.-H.; Park, S. K.; Park, S. Y. Soluble Dicyanodistyrylbenzene-Based Non-Fullerene Electron Acceptors with Optimized Aggregation Behavior for High-Efficiency Organic Solar Cells. *Adv. Energy Mater.* **2015**, *5*, 1400929.

[174] Min, J.; Kwon, O. K.; Cui, C.; Park, J.-H.; Wu, Y.; Park, S. Y.; Li, Y.; Brabec, C. J. High Performance All-Small-Molecule Solar Cells: Engineering the Nanomorphology via

Processing Additives. *J. Mater. Chem. A* **2016**, *4* (37), 14234–14240.

[175] Kwon, O. K.; Park, J.-H.; Kim, D. W.; Park, S. K.; Park, S. Y. An All-Small-Molecule Organic Solar Cell with High Efficiency Nonfullerene Acceptor. *Adv. Mater.* **2015**, *27*, 1951-1956.

[176] Kwon, O. K.; Uddin, M. A.; Park, J. H.; Park, S. K.; Nguyen, T. L.; Woo, H. Y.; Park, S. Y. A High Efficiency Nonfullerene Organic Solar Cell with Optimized Crystalline Organizations. *Adv. Mater.* **2016**, *28* (5), 910–916.

[177] Kwon, O. K.; Park, J. H.; Park, S. Y. An Efficient Nonfullerene Acceptor for All-Small-Molecule Solar Cells with Versatile Processability in Environmentally Benign Solvents. *Org. Electron.* **2016**, *30*, 105–111.

[178] Zhang, J. C.; Xiao, H. M.; Zhang, X. J.; Wu, Y.; Li, G. W.; Li, C. H.; Chen, X. B.; Ma, W.; Bo, Z. S. 1,8-Naphthalimide-Based Nonfullerene Acceptors for Wide Optical Band Gap Polymer Solar Cells with an Ultrathin Active Layer Thickness of 35 nm. *J. Mater. Chem. C* **2016**, *4* (24), 5656–5663.

[179] Zhang, J.; Zhang, X.; Li, G.; Xiao, H.; Li, W.; Xie, S.; Li, C.; Bo, Z. A Nonfullerene Acceptor for Wide Band Gap Polymer Based Organic Solar Cells. *Chem. Commun.* **2016**, *52*, 469-472.

[180] Gautam, P.; Sharma, R.; Misra, R.; Keshtov, M. L.; Kuklin, S. A.; Sharma, G. D. Donor–acceptor–acceptor (D–A–A) Type 1,8-Naphthalimides as Non-Fullerene Small Molecule Acceptors for Bulk Heterojunction Solar Cells. *Chem. Sci.* **2017**, *8* (3), 2017–2024.

[181] Gautam, P.; Misra, R.; Biswas, S.; Sharma, G. D. A D–π–A1–π–A2 Push–pull Small Molecule Donor for Solution Processed Bulk Heterojunction Organic Solar Cells. *Phys. Chem. Chem. Phys.* **2016**, *18* (20), 13918–13926.

[182] Chatterjee, S.; Ie, Y.; Karakawa, M.; Aso, Y. Naphtho[1,2-*c*:5,6-*c*′]bis[1,2,5]thiadiazole-Containing π-Conjugated Compound: Nonfullerene Electron Acceptor for Organic Photovoltaics. *Adv. Funct. Mater.* **2016**, *26* (8), 1161–1168.

[183] Zhang, J.; Li, G.; Kang, C.; Lu, H.; Zhao, X.; Li, C.; Li, W.; Bo, Z. Synthesis of Star-Shaped Small Molecules Carrying Peripheral 1,8-Naphthalimide Functional Groups and Their Applications in Organic Solar Cells. *Dyes Pigm.* **2015**, *115*, 181–189.

[184] Nazeeruddin, M. K.; Kay, A.; Rodicio, L.; Humphry-Baker, R.; Müller, E.; Liska, P.; Cevey, L.; Costa, E.; Shklover, V.; Spiccia, L.; Deacon, G. B.; Bignozzi, C. A.; Grätzel, M. Conversion of light to electricity by cis-X2bis(2,2'-bipyridyl-4,4'-

dicarboxylate)ruthenium(II) charge-transfer sensitizers (X = Cl-, Br-, I-, CN-, and SCN-) on nanocrystalline titanium dioxide electrodes. *J. Am. Chem. Soc.* **1993**, *115*, 6382-6390.

[185] Chen, C. Y.; Wu, S. J.; Wu, C. G.; Chen, J. G.; Ho, K. C. A Ruthenium Complex with Superhigh Light-Harvesting Capacity for Dye-Sensitized Solar Cells. *Angew. Chemie - Int. Ed.* **2006**, *45* (35), 5822-5825.

[186] Ooyama, Y.; Harima, Y. Photophysical and Electrochemical Properties and Molecular Structures of Organic Dyes for Dye-Sensitized Solar Cells. *Chem. Phys. Chem.* **2012**, *13*, 4032-4080.

[187] Kim, S.; Lee, J. K.; Kang, S. O.; Ko, J.; Yum, J. H.; Fantacci, S.; De Angelis, F.; Di Censo, D.; Nazeeruddin, K.; Grätzel, M. Molecular Engineering of Organic Sensitizers for Solar Cell Applications. *J. Am. Chem. Soc.* **2006**, *128* (51), 16701-16707.

[188] Mishra, A.; Fischer, M. K. R.; Bäuerle, P. Metal-free Organic Dyes for Dye-Sensitized Solar Cells, from Structure, Property Relationships to Design Rules. *Angew. Chem. Int. Ed.* **2009**, *48*, 2474-2499.

[189] Huang, X.; Fang, Y.; Li, X.; Xie, Y.; Zhu, W. Novel Dyes Based on Naphthalimide Moiety as Electron Acceptor for Efficient Dye-Sensitized Solar Cells. *Dyes Pigm.* **2011**, *90* (3), 297–303.

[190] Braña M. F.; Berlanga, J. M. C.; Roldan, C. M. DE patent 2, **1973**, *318*, 136, C.A.86 **1977**, *106*, 236.

[191] Braña M. F.; Ramos, A. Naphthalimides as Anti-Cancer Agents: Synthesis and Biological Activity. *Curr. Med. Chem. Anticancer Agents*, **2001**, *1* (3), 237-55.

[192] Braña, M. F.; Castellano, J. M.; Roldán, C. M.; Santos, A.; Vázquez, D.; Jiménez, A. Synthesis and Mode(s) of Action of a New Series of Imide Derivatives of 3-Nitro-1,8 Naphthalic Acid. *Cancer Chemother. Pharmacol.* **1980**, *4* (1), 61-66.

[193] Sami. S. M.; Dorr, R. T.; Alberts, D. S.; Remers, W. A. 2-substituted 1,2-dihydro-3H-dibenz[*de*,*h*]isoquinoline-1,3-diones. A New Class of Antitumor Agent. *J. Med. Chem.* **1993**, *36* (6), 765-770.

[194] Zee-Cheng R. K.; Cheng, C. C. *N*-(Aminoalkyl)imide Antineoplastic Agents. Synthesis and Biological Activity. *J. Med. Chem.* **1985**, *28* (9), 1216-1222.

[195] Braña M. F.; Castellano, J. M.; Morán, M.; Emling, F.; Kluge, M.; E. Schlick, E.; G. Klebe, G.; Walker, N. Synthesis, Structure and Antitumor Activity of New benz[d,e]isoquinoline-1,3-diones. *Arzneimittelforschung* **1995**, *45*, 1311-1318.

References

[196] Bousquet, P. F.; Brana, M. F.; Conlon, D.; Fitzgerald, K. M.; Perron, D.; Cocchiaro, C.; Miller, R.; Moran, M.; George, J.; Qian, X. D. Preclinical Evaluation of Lu-79553 - A Novel Bis-Naphthalimide with Potent Antitumor-Activity. *Cancer Res.* **1995**, *55* (5), 1176-1180.

[197] Xie, L.; Cui, J.; Qian, X.; Xu, Y.; Liu, J.; Xu, R. 5-Non-Amino Aromatic Substituted Naphthalimides as Potential Antitumor Agents: Synthesis via Suzuki Reaction, Antiproliferative Activity, and DNA-Binding Behavior. *Bioorg. Med. Chem.* **2011**, *19* (2), 961-967.

[198] Quaquebeke, E. V; Mahieu, T.; Dumont, P.; Dewelle, J.; Ribaucour, F.; Simon, G.; Sauvage, S.; Gaussin, J. F.; Tuti, J.; Yazidi, M. E. 2,2,2-Trichloro-*N*-({2-[2-(Dimethylamino)ethyl]-1,3-Dioxo-2,3-Dihydro-1H-Benzo[de]isoquinolin-5-yl}carbamoyl)acetamide (UNBS3157), a Novel Nonhematotoxic Naphthalimide Derivative with Potent Antitumor Activity. *J. Med. Chem.* **2007**, *50* (17), 4122-4134.

[199] Azab, A. S.; Alanazi, A. M.; Abdel-Aziz, N. I.; Al-Suwaidan, I. A.; El-Sayed, M. A. A.; El-Sherbeny, M. A.; Abdel-Aziz, A. A. M. Synthesis, Molecular Modeling Study, Preliminary Antibacterial, and Antitumor Evaluation of N-Substituted Naphthalimides and Their Structural Analogues. *Med. Chem. Res.* **2013**, *22* (5), 2360-2375.

[200] Fleming, C. L.; Ashton, T. D.; Nowell, C.; Devlin, M.; Natoli, A.; Schreuders, J.; Pfeffer, F. M. A Fluorescent Histone Deacetylase (HDAC) Inhibitor for Cellular Imaging. *Chem. Commun.* **2015**, *51* (37), 7827-7830.

[201] Un, H.-I.; Wu, S.; Huang, C,-B.; Zheng Xu, Z.; Xu, L. A Naphthalimide-Based Fluorescent Probe for Highly Selective Detection of Histidine in Aqueous Solution and its Application in In Vivo Imaging. *Chem. Commun*. **2015**, *51*, 3143-3146.

[202] Zhou, Y.; Yao, Y.-W.; Qi, Q.; Fang, Y.; Li, J.-Y.; Yao, C. A Click-Activated Fluorescent Probe for Selective Detection of Hydrazoic Acid and Its Application in Biological Imaging. *Chem. Commun.* **2013**, *49* (53), 5924-5926.

[203] Chen, Z.; Liang, X.; Zhang, H.; Xie, H.; Liu, J.; Xu, Y.; Zhu, W.; Wang, Y.; Wang, X.; Tan, S. A New Class of Naphthalimide-Based Antitumor Agents That Inhibit Topoisomerase II and Induce Lysosomal Membrane Permeabilization and Apoptosis. *J. Med. Chem.* **2010**, *53* (6), 2589-2600.

[204] Berry, S. N.; Soto-Cerrato, V.; Howe, E. N. W.; Clarke, H. J.; Mistry, I.; Tavassoli, A.; Chang, Y.-T.; Pérez-Tomás, R.; Gale, P. A. Fluorescent Transmembrane Anion

Transporters: Shedding Light on Anionophoric Activity in Cells. *Chem. Sci.* **2016**, *7* (8), 5069-5077.

[205] Wu, A.; Xu, Y.; Qian, X. Novel Naphthalimide-Amino Acid Conjugates with Flexible Leucine Moiety as Side Chain: Design, Synthesis and Potential Antitumor Activity. *Bioorg. Med. Chem.* **2009**, *17* (2), 592-599.

[206] Ott, I.; Xu, Y.; Liu, J.; Kokoschka, M.; Harlos, M.; Sheldrick, W. S.; Qian, X. Sulfur-Substituted Naphthalimides as Photoactivatable Anticancer Agents: DNA Interaction, Fluorescence Imaging, and Phototoxic Effects in Cultured Tumor Cells. *Bioorg.Med. Chem.* **2008**, *16* (15), 7107-7116.

[207] Li, X.; Lin, Y.; Wang, Q.; Yuan, Y.; Zhang, H.; Qian, X. The Novel Anti-Tumor Agents of 4-Triazol-1,8-Naphthalimides: Synthesis, Cytotoxicity, DNA Intercalation and Photocleavage. *Eur. J. Med. Chem.* **2011**, *46* (4), 1274-1279.

[208] Lu, Y.-T.; Chen, T.-L.; Chang, K.-S.; Chang, C.-M.; Wei, T.-Y.; Liu, J.-W.; Hsiao, C.-A.; Shih, T.-L. Synthesis of Novel C4-Benzazole Naphthalimide Derivatives with Potent Anti-Tumor Properties against Murine Melanoma. *Bioorg. Med. Chem.* **2017**, *25* (2), 789-794.

[209] Liu, Y.; Liu, Y.; Liu, W.; Liang, S. Two-Photon Fluorescent Probe Derived from Naphthalimide for Cysteine Detection and Imaging in Living Cells. *Spectrochim. Acta - Part A Mol. Biomol. Spectrosc.* **2015**, *137*, 509–515.

[210] Li, Y.; Wu, Y.; Chang, J.; Chen, M.; Liu, R.; Li, F. A Bioprobe Based on Aggregation Induced Emission (AIE) for Cell Membrane Tracking. *Chem. Commun.* **2013**, *49* (96), 11335-11337.

[211] Li, Y.; Liu, R.; Chang, J.; Huang, M.; Chang, H.; Miao, Y. SiO_2 Encapsulated Nanofluorophor: Photophysical Properties, Aggregation Induced Emission and its Application for Cell Mitochondria Imaging. *Dyes Pigm.* **2017**, *139*, 110-117.

[212] Zheng, X.; Zhu, W.; Liu, D.; Ai, H.; Huang, Y.; Lu, Z. Highly Selective Colorimetric/fluorometric Dual-Channel Fluoride Ion Probe, and Its Capability of Differentiating Cancer Cells. *ACS Appl. Mater. Interfaces* **2014**, *6* (11), 7996-8000.

[213] Lin, H.-H.; Chan, Y.-C.; Chen, J.-W.; Chang, C.-C. Aggregation-Induced Emission Enhancement Characteristics of Naphthalimide Derivatives and Their Applications in Cell Imaging. *J. Mater. Chem.* **2011**, *21* (9), 3170-3177.

[214] Dance, A. M.; Ralton, L.; Fuller, Z.; Milne, L.; Duthie, S.; Bestwick, C. S.; Lin, P. K. T. Synthesis and Biological Activities of Bisnaphthalimido Polyamines Derivatives:

Cytotoxicity, DNA Binding, DNA Damage and Drug Localization in Breast Cancer MCF 7 Cells. *Biochem. Pharmacol.* **2005**, *69* (1), 19–27.

[215] Rong, R.-X.; Sun, Q.; Ma, C.-L.; Chen, B.; Wang, W.-Y.; Wang, Z.-A.; Wang, K.-R.; Cao, Z.-R.; Li, X.-L. Development of Novel Bis-Naphthalimide Derivatives and Their Anticancer Properties. *Med. Chem. Commun.* **2016**, *7* (4), 679–685.

[216] Suzuki, K.; Nagasawa, H.; Uto, Y.; Sugimoto, Y.; Noguchi, K.; Wakida, M.; Wierzba, K.; Terada, T.; Asao, T.; Yamada, Y. Napthalimidobenzamide DB-51630: A Novel DNA Binding Agent Inducing p300 Gene Expression and Exerting a Potent Anti-Cancer Activity. *Bioorganic Med. Chem.* **2005**, *13* (12), 4014–4021.

[217] Chiang, C. K.; Fincher, C. R.; Park, Y. W.; Heeger, A. J.; Shirakawa, H.; Louis, E. J.; Gau, S. C.; MacDiarmid, A. G. Electrical Conductivity in Doped Polyacetylene. *Phys. Rev. Lett.* **1977**, *39* (17), 1098–1101.

[218] Kan, B.; Li, M.; Zhang, Q.; Liu, F.; Wan, X.; Wang, Y.; Ni, W.; Long, G.; Yang, X.; Feng, H. A Series of Simple Oligomer-like Small Molecules Based on Oligothiophenes for Solution-Processed Solar Cells with High Efficiency. *J. Am. Chem. Soc.* **2015**, *137* (11), 3886–3893.

[219] Mishra, A.; Bäuerle, P. Small Molecule Organic Semiconductors on the Move: Promises for Future Solar Energy Technology. *Angew. Chemie - Int. Ed.* **2012**, *51* (9), 2020–2067.

[220] Henson, Z. B.; Müllen, K.; Bazan, G. C. Design Strategies for Organic Semiconductors beyond the Molecular Formula. *Nat. Chem.* **2012**, *4*, 699-704.

[221] Li, W.; Wang, D.; Wang, S.; Ma, W.; Hedström, S.; James, D. I.; Xu, X.; Persson, P.; Fabiano, S.; Berggren, M. One-Step Synthesis of Precursor Oligomers for Organic Photovoltaics: A Comparative Study between Polymers and Small Molecules. *ACS Appl. Mater. Interfaces* **2015**, *7* (49), 27106–27114.

[222] Atwood, J. L.; Steed, J. W. *Organic Nanostructures*, Wiley: New York, 2008.

[223] Maggini, L.; Bonifazi, D. Hierarchised Luminescent Organic Architectures: Design, Synthesis, Self-Assembly, Self-Organisation and Functions. *Chem. Soc. Rev.* **2012**, *41* (1), 211–241.

[224] Zhao, Y. S.; Fu, H.; Hu, F.; Peng, A.; Yang, W.; Yao, J. Tunable Emission from Binary Organic One-Dimensional Nanomaterials: An Alternative Approach to White-Light Emission. *Adv. Mater.* **2008**, *20* (1), 79–83.

References

[225] Würthner, F. *Supramolecular Dye Chemistry, Topics in Current Chemistry*, Springer: Berlin, 2005.

[226] Xiao, D.; Xi, L.; Yang, W.; Fu, H.; Shuai, Z.; Fang, Y.; Yao, J. Size-Tunable Emission from 1,3-Diphenyl-5-(2-Anthryl)-2-Pyrazoline Nanoparticles. *J. Am. Chem. Soc.* **2003**, *125* (22), 6740–6745.

[227] Ye, Q.; Chi, C. Recent Highlights and Perspectives on Acene Based Molecules and Materials. *Chem. Mater.* **2014**, *26* (14), 4046–4056.

[228] Anthony, J. E.; Eaton, D. L.; Parkin, S. R. A Road Map to Stable, Soluble, Easily Crystallized Pentacene Derivatives. *Org. Lett.* **2002**, *4*, 15-18.

[229] Zhang, C.; Zhu, X. Thieno[3,4-*b*]thiophene-Based Novel Small-Molecule Optoelectronic Materials. *Acc. Chem. Res.* **2017**, *50*, 1342-1350.

[230] Chen, L.; Li, C.; Müllen, K. Beyond Perylene Diimides: Synthesis, Assembly and Function of Higher Rylene Chromophores. *J. Mater. Chem. C* **2014**, *2* (11), 1938–1956.

[231] Yan, Q.; Luo, Z.; Cai, K.; Ma, Y.; Zhao, D. Chemical Designs of Functional Photoactive Molecular Assemblies. *Chem. Soc. Rev.* **2014**, *43* (12), 4199–4221.

[232] Molla, M. R.; Ghosh, S. Aqueous Self-Assembly of Chromophore-Conjugated Amphiphiles. *Phys. Chem. Chem. Phys.* **2014**, *16* (48), 26672–26683.

[233] Das, A.; Ghosh, S. Supramolecular Assemblies by Charge-Transfer Interactions between Donor and Acceptor Chromophores. *Angew. Chemie - Int. Ed.* **2014**, *53* (8), 2038–2054.

[234] Bähring, S.; Martín-Gomis, L.; Olsen, G.; Nielsen, K. A.; Kim, D. S.; Duedal, T.; Sastre-Santos, Á.; Jeppesen, J. O.; Sessler, J. L. Design and Sensing Properties of a Self-Assembled Supramolecular Oligomer. *Chem. - Eur. J.* **2016**, *22* (6), 1958–1967.

[235] Das, A.; Ghosh, S. H-bonding directed programmed supramolecular assembly of naphthalene-diimide (NDI) derivatives. *Chem. Commun*. **2016**, *52*, 6860-6872.

[236] Céspedes-Guirao, F. J.; B. Ropero, A.; Font-Sanchis, E.; Nadal, Á.; Fernández-Lázaro, F.; Sastre-Santos, Á. A Water-Soluble Perylene Dye Functionalised with a 17β-Estradiol: A New Fluorescent Tool for Steroid Hormones. *Chem. Commun*. **2011**, *47* (29), 8307-8309.

[237] Yagai, S.; Kitamura, A. Recent Advances in Photoresponsive Supramolecular Self-Assemblies. *Chem. Soc. Rev.* **2008**, *37* (8), 1520.

[238] Kar, H.; Ghosh, S. J-aggregation of a Sulfur-Substituted Naphthalenediimide (NDI) with Remarkably Bright Fluorescence. *Chem. Commun*. **2016**, *52*, 8818-8821.

References

[239] Hoeben, F. J. M.; Jonkheijm, P.; Meijer, E. W.; Schenning, A. P. H. J. About Supramolecular Assemblies of π-Conjugated Systems. *Chem. Rev.* **2005**, *105* (4), 1491–1546.

[240] Poole, C. P. *Introduction to nanotechnology*. John Wiley & Sons: Hoboken, New Jersey, USA, 2003.

[241] Lehn, J.-M. *Supramolecular Chemistry: Concepts and Perspectives*, Wiley: New York, 1995.

[242] Zhao, Y. S. *Organic Nanophotonics: Fundamentals and Applications*. Wiley: New York, 2014.

[243] Zhang, C.; Zhao, Y. S.; Yao, J. Optical Waveguides at Micro/nanoscale Based on Functional Small Organic Molecules. *Phys. Chem. Chem. Phys.* **2011**, *13* (20), 9060.

[244] Zheng, H.; Li, Y.; Liu, H.; Yin, X.; Li, Y. Construction of Heterostructure Materials toward Functionality. *Chem. Soc. Rev.* **2011**, *40* (9), 4506.

[245] Kim, F. S.; Ren, G.; Jenekhe, S. A. One-Dimensional Nanostructures of π-Conjugated Molecular Systems: Assembly, Properties, and Applications from Photovoltaics, Sensors, and Nanophotonics to Nanoelectronics. *Chem. Mater.* **2011**, *23* (3), 682–732.

[246] Zhao, Y. S.; Fu, H. B.; Peng, A D.; Ma, Y.; Liao, Q.; Yao, J. N. Construction and Optoelectronic Properties of Organic One-Dimensional Nanostructures. *Acc. Chem. Res.* **2010**, *43* (3), 409–418.

[247] Huibiao Liu, H.; Jialiang Xu, J.; Yongjun Li, Y. Aggregate Nanostructures of Organic Molecular Materials. *Acc. Chem. Res.* **2010**, *43* (12), 1496–1508.

[248] Zang, L.; Che, Y.; Moore, J. F. One-Dimensional Self-Assembly of Planar π-Conjugated Molecules: Adaptable Building Blocks for Organic Nanodevices. *Acc. Chem. Res.* **2008**, *41*, 1596-1608.

[249] Li, Y.; Liu, T.; Liu, H.; Tian, M. Z.; Li, Y. Self-Assembly of Intramolecular Charge-Transfer Compounds into Functional Molecular Systems. *Acc. Chem. Res.* **2014**, *47* (4), 1186–1198.

[250] Li, R.; Hu, W.; Liu, Y.; Zhu, D. Micro- and Nanocrystals of Organic Semiconductors. *Acc. Chem. Res.* **2010**, *43* (4), 529–540.

[251] Reczek, J. J.; Villazor, K. R.; Lynch, V.; Swager, T. M.; Iverson, B. L. Tunable Columnar Mesophases Utilizing C2 Symmetric Aromatic Donor−Acceptor Complexes. *J. Am. Chem. Soc.* **2006**, *4*, 7560–7563.

References

[252] Sutton, C.; Risko, C.; Brédas, J.-L. Noncovalent Intermolecular Interactions in Organic Electronic Materials: Implications for the Molecular Packing vs Electronic Properties of Acenes. *Chem. Mater.* **2016**, *28* (1), 3–16.

[253] Mukherjee, S.; Thilagar, P. Insights into the AIEE of 1,8-Naphthalimides (NPIs): Inverse Effects of Intermolecular Interactions in Solution and Aggregates. *Chem. - Eur. J.* **2014**, *20* (26), 8012–8023.

[254] Palmer, L. C.; Stupp, S. I. Molecular Self-Assembly into One-Dimensional Nanostructures. *Acc. Chem. Res.* **2008**, *41* (12), 1674–1684.

[255] Grimsdale, A. C.; Müllen, K. The Chemistry of Organic Nanomaterials. *Angew. Chemie - Int. Ed.* **2005**, *44* (35), 5592–5629.

[256] Würthner, F. Perylene Bisimide Dyes as Versatile Building Blocks for Functional Supramolecular Architectures. *Chem. Commun.* **2004**, *14*, 1564–1579.

[257] Yao, W.; Yan, Y.; Xue, L.; Zhang, C.; Li, G.; Zheng, Q.; Zhao, Y. S.; Jiang, H.; Yao, J. Controlling the Structures and Photonic Properties of Organic Nanomaterials by Molecular Design. *Angew. Chemie - Int. Ed.* **2013**, *52* (33), 8713–8717.

[258] Ghodbane, A.; D'Altério, S.; Saffon, N.; McClenaghan, N. D.; Scarpantonio, L.; Jolinat, P.; Fery-Forgues, S. Facile Access to Highly Fluorescent Nanofibers and Microcrystals *via* Reprecipitation of 2-Phenyl-Benzoxazole Derivatives. *Langmuir* **2012**, *28* (1), 855–863.

[259] Chen, S.; Qin, Z.; Liu, T.; Wu, X.; Li, Y.; Liu, H.; Song, Y.; Li, Y. Aggregation-Induced Emission on Benzothiadiazole Dyads with Large Third-Order Optical Nonlinearity. *Phys. Chem. Chem. Phys.* **2013**, *15* (30), 12660-12666.

[260] Xu, J.; Semin, S.; Niedzialek, D.; Kouwer, P. H. J.; Fron, E.; Coutino, E.; Savoini, M.; Li, Y.; Hofkens, J.; Uji-I, H. Self-Assembled Organic Microfibers for Nonlinear Optics. *Adv. Mater.* **2013**, *25* (14), 2084–2089.

[261] Xu, J.; Zheng, H.; Liu, H.; Zhou, C.; Zhao, Y.; Li, Y.; Li, Y. Crystal Hierarchical Supramolecular Architectures from 1-D Precursor Single-Crystal Seeds. *J. Phys. Chem. C* **2010**, *114* (7), 2925–2931.

[262] Xu, J.; Wen, L.; Zhou, W.; Lv, J.; Guo, Y.; Zhu, M.; Liu, H.; Li, Y.; Jiang, L. Asymmetric and Symmetric Dipole-Dipole Interactions Drive Distinct Aggregation

and Emission Behavior of Intramolecular Charge-Transfer Molecules. *J. Phys. Chem. C* **2009**, *113* (15), 5924–5932.

[263] Xiao, J.; Xiao, X.; Zhao, Y.; Wu, B.; Liu, Z.; Zhang, X.; Wang, S.; Zhao, X.; Liu, L.; Jiang, L. Synthesis, Physical Properties and Self-Assembly Behavior of Azole-Fused Pyrene Derivatives. *Nanoscale* **2013**, *5* (12), 5420-5425.

[264] Li, J.; Li, P.; Wu, J.; Gao, J.; Xiong, W. W.; Zhang, G.; Zhao, Y.; Zhang, Q. [4 + 2]cycloaddition Reaction to Approach Diazatwistpentacenes: Synthesis, Structures, Physical Properties, and Self-Assembly. *J. Org. Chem.* **2014**, *79* (10), 4438–4445.

[265] Chandrasekhar, N.; Chandrasekar, R. Reversibly Shape-Shifting Organic Optical Waveguides: Formation of Organic Nanorings, Nanotubes, and Nanosheets. *Angew. Chemie - Int. Ed.* **2012**, *51* (15), 3556–3561.

[266] Sampath, S.; Boopathi, A. A.; Mandal, A. B. "Bottom-Up" Self-Assembly and "cold Crystallization" of Butterfly Shaped Tetrabenzofluorene Molecules. *Phys. Chem. Chem. Phys.* **2016**, *18* (31), 21251–21258.

[267] Wang, Y.; Fu, H.; Peng, A.; Zhao, Y.; Ma, J.; Ma, Y.; Yao, J. Distinct Nanostructures from Isomeric Molecules of Bis(iminopyrrole) Benzenes: Effects of Molecular Structures on Nanostructural Morphologies. *Chem. Commun.* **2007**, *16*, 1623-1625.

[268] Ajayaghosh, A.; George, S. J. First Phenylenevinylene Based Organogels: Self-Assembled Nanostructures via Cooperative Hydrogen Bonding and π-Stacking. *J. Am. Chem. Soc.* **2001**, *123*, 5148-5149.

[269] An, B. K.; Gierschner, J.; Park, S. Y. π-Conjugated Cyanostilbene Derivatives: A Unique Self-Assembly Motif for Molecular Nanostructures with Enhanced Emission and Transport. *Acc. Chem. Res.* **2012**, *45* (4), 544–554.

[270] Li, X.; Yan, T.; Bin, H.; Han, G.; Xue, L.; Liu, F.; Yi, Y.; Zhang, Z.-G.; Russell, T. P.; Li, Y. Insertion of Double Bond π-Bridges of A-D-A Acceptor for High Performance near-Infrared Polymer Solar Cells. *J. Mater. Chem. A* **2017**, *5*, 22588–22597.

[271] Sung, M. J.; Luzio, A.; Park, W. T.; Kim, R.; Gann, E.; Maddalena, F.; Pace, G.; Xu, Y.; Natali, D.; de Falco, C. High-Mobility Naphthalene Diimide and Selenophene-Vinylene-Selenophene-Based Conjugated Polymer: N-Channel Organic Field-Effect Transistors and Structure–Property Relationship. *Adv. Funct. Mater.* **2016**, *26* (27), 4984–4997.

[272] Lee, S.; Thomas, K. R. J.; S. Thayumanavan, S.; Bardeen, C. J. Dependence of the Two-

Photon Absorption Cross Section on the Conjugation of the Phenylacetylene Linker in Dipolar Donor-Bridge-Acceptor Chromophores. *J. Phys. Chem. A* **2005**, *109*, 9767-9774.

[273] Kivala, M.; Diederich, F. Acetylene-Derived Strong Organic Acceptors for Planar and Nonplanar Push-Pull Chromophores. *Acc. Chem. Res*. **2009**, *42*, 235-248.

[274] Katritzky, A. R.; Lan, X.; Yang, J. Z.; Denisko, O. V. Properties and Synthetic Utility of N-Substituted Benzotriazoles. *Chem. Rev.* **1998**, *98* (2), 409–548.

[275] Fagel, J. E.; Ewing, G. W. The Ultraviolet Absorption of Benzotriazole. *J. Am. Chem. Soc.* **1951**, *73* (9), 4360–4362.

[276] Borin, A. C.; Serrano-Andrés, L.; Ludwig, V.; Canuto, S. Theoretical Absorption and Emission Spectra of 1*H*- and 2*H*-Benzotriazole. *Phys. Chem. Chem. Phys.* **2003**, *5* (22), 5001.

[277] Keshtov, M. L.; Godovsky, D. Y.; Kuklin, S. A.; Lee, J.; Kim, J.; Lim, B.; Lee, H. K.; Biswas, S.; Koukaras, E. N.; Sharma, G. D. Design, Synthesis and Photophysical Properties of D1-A-D2-A-D1-Type Small Molecules Based on Fluorobenzotriazole Acceptor and Dithienosilole Core Donor for Solution Processed Organic Solar Cells. *Dyes Pigm.* **2016**, *132*, 387–397.

[278] Xiao, B.; Zhao, Y.; Tang, A.; Wang, H.; Yang, J.; Zhou, E. PTB7-Th Based Organic Solar Cell with a High V_{oc} of 1.05 V by Modulating the LUMO Energy Level of Benzotriazole-Containing Non-Fullerene Acceptor. *Sci. Bull.* **2017**, *62* (18), 1275–1282.

[279] Chen, Y.; Du, Z.; Chen, W.; Liu, Q.; Sun, L.; Sun, M.; Yang, R. Benzo[1,2-b:4,5-b'] dithiophene and Benzotriazole Based Small Molecule for Solution-Processed Organic Solar Cells. *Org. Electron.* **2014**, *15* (2), 405–413.

[280] Torres, I.; Díaz-Ortiz, A.; Sánchez, L.; Orduna, J.; Blesa, M. J.; Carrillo, J. R.; Prieto, P. Tunable Emission in Aggregated T-Shaped 2*H* -Benzo[d][1,2,3]triazoles with Waveguide Behaviour. *Dyes Pigm.* **2017**, *142*, 212–225.

[281] Torres, I.; Carrillo, J. R.; Díaz-Ortiz, A.; Martín, R.; Gómez, M. V.; Stegemann, L.; Strassert, C. A.; Orduna, J.; Buendía, J.; Greciano, E. E. Self-Assembly of T-Shape 2H-benzo[*d*][1,2,3]-Triazoles. Optical Waveguide and Photophysical Properties. *RSC Adv.* **2016**, *6* (43), 36544–36553.

[282] Thomas, K. R. J; Velusamy, M.; Lin, J. T.; Chuen, C. H.; Tao, Y. T. Chromophore-Labeled Quinoxaline Derivatives as Efficient Electroluminescent Materials. *Chem. Mater.* **2005**, *17* (7), 1860–1866.

References

[283] Tyagi, P.; Venkateswararao, A.; Thomas, K. R. J. Solution Processable Indoloquinoxaline Derivatives Containing Bulky Polyaromatic Hydrocarbons: Synthesis, Optical Spectra, and Electroluminescence. *J. Org. Chem.* **2011**, *76* (11), 4571–4581.

[284] Min, J.; Zhang, Z. G.; Zhang, S.; Li, Y. Conjugated Side-Chain-Isolated D-A Copolymers Based on benzo[1,2-b:4,5-B']dithiophene-Alt-Dithienylbenzotriazole: Synthesis and Photovoltaic Properties. *Chem. Mater.* **2012**, *24* (16), 3247–3254.

[285] Li, K.; Li, Z.; Feng, K.; Xu, X.; Wang, L.; Peng, Q. Development of Large Band-Gap Conjugated Copolymers for Efficient Regular Single and Tandem Organic Solar Cells. *J. Am. Chem. Soc.* **2013**, *135* (36), 13549–13557.

[286] Karakus, M.; Apaydn, D. H.; Yldz, D. E.; Toppare, L.; Cirpan, A. Benzotriazole and Benzothiadiazole Containing Conjugated Copolymers for Organic Solar Cell Applications. *Polym.* **2012**, *53* (6), 1198–1202.

[287] Suganya, S.; Kim, N.; Jeong, J. Y.; Park, J. S. Benzotriazole-Based Donor-Acceptor Type Low Band Gap Polymers with a Siloxane-Terminated Side-Chain for Electrochromic Applications. *Polym.* **2017**, *116*, 226–232.

[288] Kotowski, D.; Luzzati, S.; Bianchi, G.; Calabrese, A.; Pellegrino, A.; Po, R.; Schimperna, G.; Tacca, A. Double Acceptor D-A Copolymers Containing Benzotriazole and Benzothiadiazole Units: Chemical Tailoring towards Efficient Photovoltaic Properties. *J. Mater. Chem. A* **2013**, *1*, 10736–10744.

[289] Patel, D. G.; Feng, F.; Ohnishi, Y. Y.; Abboud, K. A.; Hirata, S.; Schanze, K. S.; Reynolds, J. R. It Takes More than an Imine: The Role of the Central Atom on the Electron-Accepting Ability of Benzotriazole and Benzothiadiazole Oligomers. *J. Am. Chem. Soc.* **2012**, *134* (5), 2599–2612.

[290] Min, J.; Zhang, Z.-G.; Zhang, S.; Zhang, M.; Zhang, J.; Li, Y. Synthesis and Photovoltaic Properties of Copolymers Based on 2,2-(1,5-Pentamethylene)-2H-Benzimidazole. *Macromolecules* **2011**, *44* (1–2), 7632-7638.

[291] Das, S.; Pati, P. B.; Zade, S. S. Cyclopenta[c]thiophene-Based D-A Conjugated Copolymers: Effect of Heteroatoms (S, Se, and N) of Benzazole Acceptors on the Properties of Polymers. *Macromolecules* **2012**, *45* (13), 5410–5417.

[292] Balan, A.; Baran, D.; Toppare, L. Benzotriazole Containing Conjugated Polymers for Multipurpose Organic Electronic Applications. *Polym. Chem.* **2011**, *2* (5), 1029.

[293] Wettach, H.; Pasker, F.; Ho, S. 2-Aryl-2 *H* -Benzotriazoles as Building Blocks for New

Low-Bandgap Poly(Arylene - Ethynylene). *Macromolecules* **2008**, 9513–9515.

[294] Balan, A.; Gunbas, G.; Durmus, A.; Toppare, L. Donor-Acceptor Polymer with Benzotriazole Moiety: Enhancing the Eleetrochromic Properties of the Donor Unit. *Chem. Mater.* **2008**, *20* (6), 7510–7513.

[295] Chen, S.; Chen, N.; Yan, Y. L.; Liu, T.; Yu, Y.; Li, Y.; Liu, H.; Zhao, Y. S.; Li, Y. Controlling Growth of Molecular Crystal Aggregates for Efficient Optical Waveguides. *Chem. Commun*. **2012**, *48* (72), 9011-9013.

[296] Zhao, Y. S.; Xu, J.; Peng, A.; Fu, H.; Ma, Y.; Jiang, L.; Yao, J. Optical Waveguide Based on Crystalline Organic Microtubes and Microrods. *Angew. Chemie - Int. Ed.* **2008**, *47* (38), 7301–7305.

[297] Wang, C.; Liu, Y.; Ji, Z.; Wang, E.; Li, R.; Jiang, H.; Tang, Q.; Li, H.; Hu, W. Cruciforms: Assembling Single Crystal Micro- and Nanostructures from One to Three Dimensions and Their Applications in Organic Field-Effect Transistors. *Chem. Mater*. **2009**, *21* (13), 2840–2845.

[298] Zhu, J.; Zhong, K.; Liang, Y.; Wang, Z.; Chen, T.; Jin, L. Y. Synthesis and Self-Assembly of Oligomers Containing Cruciform 9,10-Bis(arylethynyl)anthracene Unit: Formation of Supramolecular Nanostructures Based on Rod-Length-Dependent Organization. *Tetrahedron* **2014**, *70* (6), 1230-1235.

[299] Basak, S.; Nandi, N.; Baral, A.; Banerjee, A. Tailor-Made Design of J- or H-Aggregated Naphthalenediimide-Based Gels and Remarkable Fluorescence Turn On/off Behaviour Depending on Solvents. *Chem. Commun.* **2014**, *51* (4), 780–783.

[300] Kar, H.; Gehrig, D. W.; Laquai, F.; Ghosh, S. J-Aggregation, Its Impact on Excited State Dynamics and Unique Solvent Effects on Macroscopic Assembly of a Core-Substituted Naphthalenediimide. *Nanoscale* **2015**, *7*, 6729–6736.

[301] Balakrishnan, K.; Datar, A.; Oitker, R.; Chen, H.; Zuo, J.; Zang, L. Nanobelt Self-Assembly from an Organic *N*-Type Semiconductor: Propoxyethyl-PTCDI. *J. Am. Chem. Soc.* **2005**, *127* (30), 10496–10497.

[302] Balakrishnan, K.; Datar, A.; Naddo, T.; Huang, J.; Oitker, R.; Yen, M.; Zhao, J.; Zang, L. Effect of Side-Chain Substituents on Self-Assembly of Perylene Diimide Molecules: Morphology Control. *J. Am. Chem. Soc.* **2006**, *128* (22), 7390–7398.

References

[303] Datar, A.; Balakrishnan, K.; Zang, L. One-Dimensional Self-Assembly of a Water Soluble Perylene Diimide Molecule by pH Triggered Hydrogelation. *Chem. Commun*. **2013**, *49*, 6894−6896.

[304] Chen, S.; Wang, C.; Bunes, B. R.; Li, Y.; Wang, C.; Zang, L. Enhancement of Visible-Light-Driven Photocatalytic H_2 Evolution from Water over G-C3N4 through Combination with Perylene Diimide Aggregates. *Appl. Catal. A Gen.* **2015**, *498*, 63–68.

[305] Lambrecht, J.; Saragi, T. P. I.; Salbeck, J. Self-Assembled Organic Micro-/nanowires from an Air Stable N-Semiconducting Perylenediimide Derivative as Building Blocks for Organic Electronic Devices. *J. Mater. Chem.* **2011**, *21* (45), 18266-18270.

[306] Boobalan, G.; Imran, P. M.; Ramkumar, S. G.; Nagarajan, S. Fabrication of Luminescent Perylene Bisimide Nanorods. *J. Lumin*. **2014**, *146*, 387−393.

[307] Lambrecht, J.; Saragi, T. P. I.; Onken, K.; Salbeck, J. Ultralong Single Organic Semiconducting Nano/Microwires Based on Spiro-Substituted Perylenetetracarboxylic Diimide. *ACS Appl. Mater.Interfaces* **2011**, *3*, 1809−1812.

[308] Huang, Y. W.; Fu, L. N.; Zou, W. J.; Zhang, F. L.; Wei, Z. X. Ammonia Sensory Properties Based on Single-Crystalline Micro/ Nanostructures of Perylenediimide Derivatives: Core-Substituted Effect. *J. Phys. Chem. C* **2011**, *115*, 10399−10404.

[309] Zhao, Q. L.; Zhang, S.; Liu, Y.; Mei, J.; Chen, S. J.; Lu, P.; Qin, A. J.; Ma, Y. G.; Sun, J. Z.; Tang, B. Z. Tetraphenylethenyl-Modified Perylene Bisimide: Aggregation-Induced Red Emission, Electrochemical Properties and Ordered Microstructures. *J. Mater. Chem.* **2012**, *22*, 7387−7394.

[310] Shi, M. M.; Tung, V. C.; Nie, J. J.; Chen, H. Z.; Yang, Y. Bulky Rigid Substitutions: A Route to High Electron Mobility and High Solid-State Luminescence Efficiency of Perylene Diimide. *Org. Electron*. **2014**, *15*, 281−285.

[311] Yu, Y.; Li, Y.; Qin, Z.; Jiang, R.; Liu, H.; Li, Y. Designed Synthesis and Supramolecular Architectures of Furan-Substituted Perylene Diimide. *J. Colloid Interface Sci.* **2013**, *399*, 13–18.

[312] Li, Y.; Li, Y.; Li, J.; Li, C.; Liu, X.; Yuan, M.; Liu, H.; Wang, S. Synthesis, Characterization, and Self-Assembly of Nitrogen-Containing Heterocoronenetetracarboxylic Acid Diimide Analogues: Photocyclization of N-

Heterocycle-Substituted Perylene Bisimides. *Chem. - Eur. J.* **2006**, *12* (32), 8378–8385.

[313] Saini, A.; Thomas, K, R. J. Bis-Naphthalimides Bridged by Electron Acceptors: Optical and Self-assembly Characteristics. *RSC Adv.* **2016**, *6*, 71638–71651.

[314] Sonogashira, K.; Tohda, Y.; Hagihara, N. A convenient synthesis of acetylenes: catalytic substitutions of acetylenic hydrogen with bromoalkenes, iodoarenes and bromopyridines. *Tetrahedron Lett.* **1975**, *16*, 4467-4470.

[315] Rule H. G.; Thompson, S. B. Bromo- and Nitro-derivatives of Naphthalic Acid. *J. Chem. Soc.* **1937**, 1764-1767.

[316] Zhang, X.; Han, J. Bin; Li, P. F.; Ji, X.; Zhang, Z. Improved, Highly Efficient, and Green Synthesis of Bromofluorenones and Nitrofluorenones in Water. *Synth. Commun.* **2009**, *39* (21), 3804–3815.

[317] Pilgram, K.; Zupan, M.; Skiles, R. Bromination of 2,1,3-benzothiadiazoles. *J. Hetero. Chem.* **1970**, *7*, 629-633.

[318] Unver, E. K.; Tarkuc, S.; Udum, Y. A.; Tanyeli, C.; Toppare, L. Effect of Conjugated Core Building Block Dibenzo[a,c]phenazine Unit on π-Conjugated Electrochromic Polymers: Red-Shifted Absorption. *J. Polym. Sci. Part A Polym. Chem.* **2010**, *48* (8), 1714–1720.

[319] Thomas, K. R. J.; Tyagi, P. Synthesis, Spectra, and Theoretical Investigations of the Triarylamines Based on 6*H* -indolo[2,3- *b*]Quinoxaline. *J. Org. Chem.* **2010**, *75* (23), 8100–8111.

[320] Estrada L. A.; Neckers, D. C. Synthesis and Photophysics of Dibenz[*a,c*]phenazine Derivatives. *Org. Lett.* **2011**, *13*, 3304-3307.

[321] Thomas, K. R. J.; Kapoor, N.; Bolisetty, M. N. K. P.; Jou, J.-H.; Chen, Y.-L.; Jou, Y.-C. Pyrene-Fluorene Hybrids Containing Acetylene Linkage as Color-Tunable Emitting Materials for Organic Light-Emitting Diodes. *J. Org. Chem.* **2012**, *77*, 3921-3932.

[322] Lakowicz, J. R. *Principles of Fluorescence Spectroscopy*, 3rd Edition, Springer Science + Business Media: New York, 2006.

[323] Jelley, E. E. Spectral Absorption and Fluorescence of Dyes in the Molecular State. *Nature* **1936**, *138*, 1009-1010.

[324] Scheibe, G. Über die Veränderlichkeit der Absorptionsspektren in Lösungen und die Nebenvalenzen als ihre Ursache. *Angew. Chem.* **1937**, *50*, 212-219.

References

[325] Mukherjee S.; Thilagar, P. Fine-tuning Solid-State Luminescence in NPIs (1,8-Naphthalimides): Impact of the Molecular Environment and Cumulative Interactions. *Phys. Chem. Chem. Phys.* **2014**, *16*, 20866-20877.

[326] Reger, D. L.; Debreczeni, A.; Horger, J. J.; Smith, M. D. Structures of Bifunctional Molecules Containing Two Very Different Supramolecular Synthons: Carboxylic Acid and Strong π-π Stacking 1,8-Naphthalimide Ring. *Cryst. Growth Des.* **2011**, *11*, 4068-4079.

[327] Krasovitskii, B. M.; Bolotin, B. M. *Organic Luminescent Materials*. VCH: Weinheim, Germany, 2002.

[328] Silinsh, E. A. *Organic Molecular Crystals*. Springer-Verlag: Berlin, 1980.

[329] Birks, J. B. *Photophysics of Aromatic Molecules*. Wiley: London, 1970.

[330] Reichardt, C. Solvatochromic Dyes as Solvent Polarity Indicators. *Chem. Rev.* **1994**, *94* (8), 2319–2358.

[331] Sillen A.; Engelborghs, Y. The Correct Use of "Average" Fluorescence Parameters. *Photochem. Photobiol.* **1998**, *67*, 475.

[332] Spano, F. C. Analysis of the UV/Vis and CD Spectral Line Shapes of Carotenoid Assemblies: Spectral Signatures of Chiral *H*-aggregates. *J. Am. Chem. Soc.* **2009**, *131*, 4267-4278.

[333] Würthner, F.; Kaiser T. E.; Saha-Müller C. R. *J*-aggregates: From Serendipitous Discovery to Supramolecular Engineering of Functional Dye Materials. *Angew. Chem., Int. Ed.* **2011**, *50*, 3376-3410.

[334] Kobayashi, T. *J-Aggregates*, World Scientific: Singapore, 1996.

[335] Ventura, B.; Bertocco, A.; Braga, D.; Catalano, L.; D'Agostino, S.; Grepioni, F.; Taddei, P. Luminescence Properties of 1,8-Naphthalimide Derivatives in Solution, in Their Crystals, and in Co-Crystals: Toward Room-Temperature Phosphorescence from Organic Materials. *J. Phys. Chem. C* **2014**, *118* (32), 18646–18658.

[336] Babu, S. S.; Prasanth, S.; Ajayaghosh, A. Self-Assembled Gelators for Organic Electronics. *Angew. Chem. Int. Ed.* **2012**, *51*, 1766–1776.

[337] Terech, P.; Weiss, R. G. Low Molecular Mass Gelators of Organic Liquids and the Properties of Their Gels. *Chem. Rev.* **1997**, *97* (8), 3133–3160.

[338] Mandal, A. K.; Sreejith, S.; He, T.; Maji, S. K.; Wang, X. J.; Ong, S. L.; Joseph, J.; Sun, H.; Zhao, Y. Three-Photon-Excited Luminescence from Unsymmetrical

Cyanostilbene Aggregates: Morphology Tuning and Targeted Bioimaging. *ACS Nano* **2015**, *9* (5), 4796–4805.

[339] Zhao, Y. S.; Fu, H.; Hu, F.; Peng, A. D.; Yao, J. Multicolor Emission from Ordered Assemblies of Organic ID Nanomaterials. *Adv. Mater.* **2007**, *19* (21), 3554–3558.

[340] Frisch, M. J.; Trucks, G. W.; Schlegel, H. B.; Scuseria, G. E.; Robb, M. A.; Cheeseman, J. R.; Scalmani, G.; Barone, V.; Mennucci, B.; Petersson, G. A.; Nakatsuji, H.; Caricato, M.; Li, X.; Hratchian, H. P.; Izmaylov, A. F.; Bloino, J.; Zheng, G.; Sonnenberg, J. L.; Hada, M.; Ehara, M.; Toyota, K.; Fukuda, R.; Hasegawa, J.; Ishida, M.; Nakajima, T.; Honda, Y.; Kitao, O.; Nakai, H.; Vreven, T.; Montgomery, J. A., Jr.; Peralta, J. E.; Ogliaro, F.; Bearpark, M.; Heyd, J. J.; Brothers, E.; Kudin, K. N.; Staroverov, V. N.; Kobayashi, R.; Normand, J.; Raghavachari, K.; Rendell, A.; Burant, J. C.; Iyengar, S. S.; Tomasi, J.; Cossi, M.; Rega, N.; Millam, N. J.; Klene, M.; Knox, J. E.; Cross, J. B.; Bakken, V.; Adamo, C.; Jaramillo, J.; Gomperts, R.; Stratmann, R. E.; Yazyev, O.; Austin, A. J.; Cammi, R.; Pomelli, C.; Ochterski, J. W.; Martin, R. L.; Morokuma, K.; Zakrzewski, V. G.; Voth, G. A.; Salvador, P.; Dannenberg, J. J.; Dapprich, S.; Daniels, A D Farkas,Foresman, J. B.; Ortiz, J. V.; Cioslowski, J.; Fox, D. J. Gaussian 09, revision A.02; Gaussian, Inc.: Wallingford, CT, 2009.

[341] Lee, C.; Yang, W.; Parr, R. G. Development of the Colle-Salvetti Correlation-Energy Formula into a Functional of the Electron Density. *Phys. Rev. B* **1988**, *37*, 785-789.

[342] Zhao, Y.; Truhlar, D. G. The M06 Suite of Density Functionals for Main Group Thermochemistry, Thermochemical Kinetics, Noncovalent Interactions, Excited States, And Transition Elements: Two New Functionals and Systematic Testing of Four M06-Class Functionals and 12 Other Functionals. *Theor. Chem. Acc.* **2008**, *120*, 215-241.

[343] Beaujuge, P. M.; Fréchet, J. M. J. Molecular Design and Ordering Effects in π-Functional Materials for Transistor and Solar Cell Applications. *J. Am. Chem. Soc.* **2011**, *133*, 20009-20029.

[344] Liu, J.; Ma, J.; Zhang, K.; Ravat, P; Machata, P.; Avdoshenko, S.; Hennersdorf, F.; Komber, H.; Pisula, W.; Weigand, J. J.; Popov, A. A.; Berger, R.; Müllen, K.; Feng, X. π-Extended and Curved Antiaromatic Polycyclic Hydrocarbons. *J. Am. Chem. Soc.* **2017**, *139*, 7513-7521.

[345] Clar, E.; Schoental, R. *Polycyclic Hydrocarbons*. Springer: Berlin, 1964; Vol. 2.

References

[346] Swartz, C. R.; Parkin, S. R.; Bullock, J. E.; Anthony, J. E.; Mayer, A. C.; Malliaras, G. G. Synthesis and Characterization of Electron-Deficient Pentacenes. *Org. Lett.* **2005**, *7*, 3163-3166.

[347] Li, X-J.; M. L.;Lu, H-Y.; Chen, C-F._A dinaphtho[8,1,2-*cde*:2′,1′,8′-*uva*]pentacene Derivative and Analogues: Synthesis, Structures, Photophysical and Electrochemical Properties. *Org. Biomol. Chem.* **2015**, *13*, 7628-7632.

[348] Figueira-Duarte, T. M.; Müllen, K. Pyrene-Based Materials for Organic Electronics. *Chem. Rev.* **2011**, *111*, 7260-7314.

[349] Ballestas-Barrrientos, A. R.; Woodward, A. W.; Moreshead, W. V.; Bondar, M. V.; Belfield, K. D. Synthesis and Linear and Nonlinear Photophysical Characterization of Two Symmetrical Pyrene-terminated Squaraine Derivatives. *J. Phys. Chem. C* **2016**, *120*, 7829-7838.

[350] Kumar, D.; Thomas, K. R. J.; Lin, C-C.; Jwo-Huei Jou, J-H. Pyrenoimidazole-Based Deep-Blue-Emitting Materials: Optical, Electrochemical, and Electroluminescent Characteristics. *Chem.-Asian J.* **2013**, *8*, 2111-2124.

[351] Zhao, K.; Liu, T.; Wang, G.; Chang, X.; Xue, D.; Belfield, K. D.; Fang, Y. A Butterfly-Shaped Pyrene Derivative of Cholesterol and its uses as a Fluorescent Probe. *J. Phys. Chem. B* **2013**, *117*, 5659-5667.

[352] Oh, J-W.; Lee, Y. O.; Kim, T. H.; Ko, K. C.; Lee, J. Y.; Kim, H.; Kim, J. S. Enhancement of Electrogenerated Chemiluminescence and Radical Stability by Peripheral Multidonors on Alkynylpyrene Derivatives. *Angew. Chem. Int. Ed.* **2009**, *48*, 2522-2524.

[353] Mallesham,G.; Swetha, C.; Niveditha, S.; Mohanty, M. E.; Babu, N. J.; Kumar, A.; Bhanuprakash, K.; Rao, V. J. Phosphine Oxide Functionalized Pyrenes as Efficient Blue Light Emitting Multifunctional Materials for Organic Light Emitting Diodes. *J. Mater. Chem. C*, **2015**, *3*, 1208–1224.

[354] Kim, H. M.; Lee, Y. O.; Lim, C. S.; Kim, J. S.; Cho, B. R. Two-Photon Absorption Properties of Alkynyl-Conjugated Pyrene Derivatives. *J. Org. Chem.* **2008**, *73*, 5127-5130.

[355] Venkataramana, G.; Sankararaman, S. Synthesis and Spectroscopic Investigation of Aggregation through Cooperative π−π and C−H-O Interactions in a Novel Pyrene Octaaldehyde Derivative. *Org. Lett.* **2006**, *8*, 2739-2742.

[356] Oh, H. Y.; Lee, C.; Lee, S. Efficient Blue Organic Light-Emitting Diodes Using Newly-Developed Pyrene-Based Electron Transport Materials. *Org. Electron.* **2009**, *10*, 163-169.

References

[357] Sung, J.; Kim, P.; Lee, Y. O.; Kim, J. S.; Kim, D. Characterization of Ultrafast Intramolecular Charge Transfer Dynamics in Pyrenyl Derivatives: Systematic Change of the Number of Peripheral *N*,*N*-Dimethyaniline Substituents. *J. Phys. Chem. Lett.* **2011**, *2*, 818–823.

[358] Konidena, R. K.; Thomas, K. R. J.; Singh, M.; Jou, J.-H. Thienylphenothiazine Integrated Pyrenes: An Account on the Influence of Substitution Pattern on Optical and Electroluminescent Properties**.** *J. Mater. Chem. C* **2016**, *4*, 4246-4258.

[359] Feng, X.; Tomiyasu, H.; Hu, J-Y.; Wei, X.; Redshaw, C.; Elsegood, M. R. J.; Horsburgh, L.; Teat, S. J.; Yamato, T. Regioselective Substitution at the 1,3- and 6,8-Positions of Pyrene for the Construction of Small Dipolar Molecules. *J. Org. Chem*. **2015**, *80*, 10973-10978.

[360] Niko, Y.; Kawauchi, S.; Otsu, S.; Tokumaru, K.; Konishi, G.-I. Fluorescence Enhancement of Pyrene Chromophores Induced by Alkyl Groups through σ−π Conjugation: Systematic Synthesis of Primary, Secondary, and Tertiary Alkylated Pyrenes at the 1, 3, 6, and 8 Positions and Their Photophysical Properties. *J. Org. Chem*. **2013**, *78*, 3196-3207.

[361] Niko, Y.; Sasaki, S.; Narushima, K.; Sharma, D. K.; Vacha, M.; Konishi, G.-I. 1-, 3-, 6- and 8-Tetrasubstituted Asymmetric Pyrene Derivatives with Electron Donors and Acceptors: High Photostability and Regioisomer-Specific Photophysical Properties. *J. Org. Chem*. **2015**, *80*, 10794-10805.

[362] Sonar, P.; Soh, M. S.; Cheng, Y. H.; Henssler, J. T.; Sellinger, A. 1,3,6,8-Tetrasubstituted Pyrenes: Solution-Processable Materials for Application in Organic Electronics. *Org. Lett*. **2010**, *12*, 3292−3295.

[363] Moorthy, J. N.; Natarajan, P.; Venkatakrishnan, P.; Huang, D.-F.; Chow, T. J. Steric Inhibition of π-Stacking: 1,3,6,8-Tetraarylpyrenes as Efficient Blue Emitters in Organic Light Emitting Diodes (OLEDs). *Org. Lett*. **2007**, *9*, 5215−5218.

[364] Seifert, S.; Shoyama, K.; Schmidt, D.; and Würthner, F. An Electron-Poor C64 Nanographene by Palladium-Catalyzed Cascade C-C Bond Formation: One-Pot Synthesis and Single-Crystal Structure Analysis. *Angew. Chem. Int. Ed.* **2016**, *55*, 6390-6395.

[365] Ji, S.; Yang, J.; Yang, Q.; Liu, S.; Chen, M.; Zhao, J. Tuning the Intramolecular Charge Transfer of Alkynylpyrenes: Effect on Photophysical Properties and Its Application in Design of OFF-ON Fluorescent Thiol Probes. *J. Org. Chem.* **2009**, *74*, 4855-4865.

References

[366] Yang, S.-W.; Elangovan, A.; Hwang, K.-C.; Ho, T. I. Electronic Polarization Reversal and Excited State Intramolecular Charge Transfer in Donor/Acceptor Ethynylpyrenes. *J. Phys. Chem. B* **2005**, *109*, 16628-16635.

[367] Venkataramana, G.; Sankararaman, S. Synthesis, Absorption, and Fluorescence-Emission Properties of 1,3,6,8-Tetraethynylpyrene and Its Derivatives. *Eur. J. Org. Chem.* **2005**, 4162–4166.

[368] Gama. P. E.; Corrêa, R. J.;.Garden, S. J. Synthesis, characterization and photophysical study of ethynyl pyrene derivatives as promising materials for organic optoelectronics. *J. Lumin.* **2015**, *161*, 37-46.

[369] Fujimoto, K.; Shimizu, H.; Furusyo, M.; Akiyama, S.; Ishida, M.; Furukawa, U.; Toshiaki Yokoo, T.; Masahiko Inouye, M. Photophysical properties of 1,3,6,8 tetrakis(arylethynyl)pyrenes with donor or acceptor substituents: their fluorescence solvatochromism and lightfastness. *Tetrahedron* **2009**, *65*, 9357-9361.

[370] Chidirala, S.; Ulla, H.; Valaboju, A.; Kiran, M. R.; Mohanty, M. E.; Satyanarayan, M. N.; G. Umesh, G.; Bhanuprakash, K.; and Rao, V. J. Pyrene−Oxadiazoles for Organic Light-Emitting Diodes: Triplet to Singlet Energy Transfer and Role of Hole-Injection/Hole-Blocking Materials. *J. Org. Chem*. **2016**, *81*, 603-614

[371] Zhao, Z.; Xu, X.; Jiang, Z.; Lu, P.; Yu, G.; Liu, Y. Oligo(2,7-fluorene ethynylene)s with Pyrene Moieties: Synthesis, Characterization, Photoluminescence, and Electroluminescence. *J. Org. Chem.* **2007**, *72*, 8345-8353.

[372] Grimshaw, J.; Grimshaw, J. T. Characterisation of 1,6- and 1,8-dibromopyrenes. *J. Chem. Soc. Perkin Trans. 1* **1972**, 1622-1623

[373] Vollmann, H.; Becker, M.; Correll, H. S. Beiträge zur Kenntnis des Pyrens und seiner Derivate. *Justus Liebigs Ann. Chem.* **1937**, *531*, 1-159.

[374] Clar, E. *Polycyclic hydrocarbons ;* Acad. Press: New York, NY, 1964, *1*.

[375] Yoshinaga, T.; Hiratsuka, H.; Tanizaki, Y. Electronic Absorption Spectra of Pyrene and Hydropyrenes. *Bull. Chem. Soc. Jpn.*, **1977**, *50*, 3096-3102.

[376] Lippert, E. Z. Dipolmoment und Elektronenstruktur von angeregten Molekülen. *Naturforsch*. **1955**, *10A*, 541-545.

[377] Mataga, N.; Kaifu, Y.; Koizumi, M. Solvent Effects upon Fluorescence Spectra and the Dipole moments of Excited Molecules. *Bull. Chem. Soc. Jpn*. **1956**, *29*, 465-470.

[378] He, G. S.; Tan, L. S.; Zheng, Q.; Prasad, P. N. Multiphoton Absorbing Materials:

Molecular Designs, Characterizations, and Applications. *Chem. Rev.* **2008**, *108* (4), 1245–1330.

[379] Zassowski, P.; Ledwon, P.; Kurowska, A.; Herman, A. P.; Lapkowski, M.; Cherpak, V.; Hotra, Z.; Turyk, P.; Ivaniuk, K.; Stakhira, P. 1,3,5-Triazine and Carbazole Derivatives for OLED Applications. *Dyes Pigm.* **2018**, *149*, 804–811.

[380] Leriche, P.; Piron, F.; Ripaud, E.; Frère, P.; Allain, M.; Roncali, J. Star-Shaped Triazine-Thiophene Conjugated Systems. *Tetrahedron Lett.* **2009**, *50* (40), 5673–5676.

[381] Liu, T.; Bondar, M. V.; Belfield, K. D.; Anderson, D.; Masunov, A. E.; Hagan, D. J.; Van Stryland, E. W. Linear Photophysics and Femtosecond Nonlinear Spectroscopy of a Star-shaped Squaraine Derivative with Efficient Two-photon Absorption. *J. Phys. Chem. C* **2016**, *120*, 11099-11110.

[382] Kukhta, N. A.; Volyniuk, D.; Peciulyte, L.; Ostrauskaite, J.; Juska, G.; Grazulevicius, J. V. Structure-Property Relationships of Star-Shaped Blue-Emitting Charge-Transporting 1,3,5-Triphenylbenzene Derivatives. *Dyes Pigm.* **2015**, *117*, 122–132.

[383] Khan, Q. U.; Lu, J.; Guo, J.; Tian, G.; Qi, S.; Wu, D. Synthesis of Linear, V-Shaped and Star-Shaped Asymmetrical Perylene Diimides Bearing Triphenylamine Moiety for Resistive Memory Application. *Dyes Pigm.* **2018**, *149*, 193–200.

[384] Hrobárik, P.; Hrobáriková, V.; Sigmundov, I.; Zahradnìk, P.; Fakis, M.; Polyzos, I.; Persephonis, P. Benzothiazoles with Tunable Electron-Withdrawing Strength and Reverse Polarity: A Route to Triphenylamine-Based Chromophores with Enhanced Two-Photon Absorption. *J. Org. Chem.* **2011**, *76* (21), 8726–8736.

[385] Kukhta, N. A.; Volyniuk, D.; Grazulevicius, J. V.; Juska, G. Effect of the Nature of the Core on the Properties of the Star-Shaped Compounds Containing Bicarbazolyl Moieties. *J. Phys. Chem. C* **2016**, *120* (2), 1208–1217.

[386] Kang, M. S.; Sung, S. Do; Choi, I. T.; Kim, H.; Hong, M.; Kim, J.; Lee, W. I.; Kim, H. K. Novel Carbazole-Based Hole-Transporting Materials with Star-Shaped Chemical Structures for Perovskite-Sensitized Solar Cells. *ACS Appl. Mater. Interfaces* **2015**, *7* (40), 22213–22217.

[387] Paek, S.; Choi, H.; Sim, J.; Song, K.; Lee, J. K.; Ko, J. Efficient Organic Solar Cells with Star-Shaped Small Molecules Comprising of Planar Donating Core and Accepting Edges. *J. Phys. Chem. C* **2014**, *118* (47), 27193–27200.

[388] Ren, S.; Zeng, D.; Zhong, H.; Wang, Y.; Qian, S.; Fang, Q. Convergent Synthesis and

Multifunctional Properties. *J. Phys. Chem. B* **2010**, *114*, 10374–10383.

[389] Diring, S.; Puntoriero, F.; Nastasi, F.; Campagna, S.; Ziessel, R. Star-Shaped Multichromophoric Arrays from Bodipy Dyes Grafted on Truxene Core. *J. Am. Chem. Soc.* **2009**, *131* (17), 6108–6110.

[390] Beltrán, E.; Garzoni, M.; Feringán, B.; Vancheri, A.; Barberá, J.; Serrano, J. L.; Pavan, G. M.; Giménez, R.; Sierra, T. Self-Organization of Star-Shaped Columnar Liquid Crystals with a Coaxial Nanophase Segregation Revealed by a Combined Experimental and Simulation Approach. *Chem. Commun.* **2015**, *51* (10), 1811–1814.

[391] Katan, C.; Terenziani, F.; Le Droumaguet, C.; Mongin, O.; Werts, M. H. V.; Tretiak, S.; Blanchard-Desce, M. Effects of (Multi)branching of Dipolar Chromophores on Photophysical Properties and Two-Photon Absorption. *J. Phys. Chem. A* **2005**, *109*, 3024-3037.

[392] Beltrán, E.; Serrano, L.; Sierra, T.; Gime, R. Tris(Triazolyl) Triazine via Click-Chemistry : A C3 Electron-Deficient Core with Liquid Crystalline and Luminescent Properties. *Org. Let.* **2010**, *7*, 1404–1407.

[393] Maragani, R.; Jadhav, T.; Mobin, S. M.; Misra, R. C3 Symmetric Ferrocenyl Triazines: Synthesis, Structure, and Properties. *RSC Adv.* **2013**, *3* (9), 2889-2892.

[394] Kim, M.; Jeon, S. K.; Hwang, S. H.; Lee, J. Y. Stable Blue Thermally Activated Delayed Fluorescent Organic Light-Emitting Diodes with Three Times Longer Lifetime than Phosphorescent Organic Light-Emitting Diodes. *Adv. Mater.* **2015**, *27* (15), 2515–2520.

[395] Oh, C. S.; Kang, Y. J.; Jeon, S. K.; Lee, J. Y. High Efficiency Exciplex Emitters Using Donor-Acceptor Type Acceptor Material. *J. Phys. Chem. C* **2015**, *119* (39), 22618–22624.

[396] Kim, M.; Jeon, S. K.; Hwang, S. H.; Lee, S. S.; Yu, E.; Lee, J. Y. Correlation of Molecular Structure with Photophysical Properties and Device Performances of Thermally Activated Delayed Fluorescent Emitters. *J. Phys. Chem. C* **2016**, *120* (5), 2485–2493.

[397] Lee, D. R.; Kim, M.; Jeon, S. K.; Hwang, S. H.; Lee, C. W.; Lee, J. Y. Design Strategy for 25% External Quantum Efficiency in Green and Blue Thermally Activated Delayed Fluorescent Devices. *Adv. Mater.* **2015**, *27* (39), 5861–5867.

[398] Hisamatsu, Y.; Aihara, H. Diverse Dimerization of Molecular Tweezers with a 2,4,6-Triphenyl-1,3,5-Triazine Spacer in the Solid State. *Chem. Commun.* **2010**, *46* (27), 4902–4904.

References

[399] Wagner, D.; Hoffmann, S. T.; Schrögel, P.; Heinemeyer, U.; Münster, I. Köhler, A.; Strohriegl, P. Novel Host Materials for Blue Phosphorescent OLEDs. *Chem. Mater*. **2013**, *25*, 3758-3765.

[400] Chen, H.-F.; Yang, S.-J.; Tsai, Z.-H.; Hung, W.-Y.; Wang, T.-C.; Wong, K.-T. 1,3,5-Triazine Derivatives as New Electron Transport–type Host Materials for Highly Efficient Green Phosphorescent OLEDs. *J. Mater. Chem.* **2009**, *19* (43), 8112-8118.

[401] Huang, B.; Jiang, W.; Tang, J.; Ban, X.; Zhu, R.; Xu, H.; Yang, W.; Sun, Y. A Novel, Bipolar Host Based on Triazine for Efficient Solution-Processed Single-Layer Green Phosphorescent Organic Light-emitting Diodes. *Dyes Pigm.* **2014**, *101*, 9-14.

[402] Ma, J.; Zhao, J.; Yang, P.; Huang, D.; Zhang, C.; Li, Q. New Excited State Intramolecular Proton Transfer (ESIPT) Dyes Based on Naphthalimide and Observation of Long-Lived Triplet Excited States. *Chem. Commun.* **2012**, *48* (78), 9720-9722.

[403] Lee, S.; Thomas, K. R. J.; Thayumanavan, S.; Bardeen, C. J. Dependence of the Two-Photon Absorption Cross Section on the Conjugation of the Phenylacetylene Linker in Dipolar Donor-Bridge-Acceptor Chromophores. *J. Phys. Chem. A* **2005**, *109*, 9767-9774.

[404] Yang, J.; Wang, X.; Xu, L. Studies on the Synthesis and Spectral Properties of Novel 4-Benzofuranyl-1,8-Naphthalimide Derivatives. *Dyes Pigm.* **2005**, *67* (1), 27–33.

[405] Zhang, Q.; Zhuang, H.; He, J.; Xia, S.; Li, H.; Li, N.; Xu, Q.; Lu, J. Improved Ternary Memory Performance of Donor–acceptor Structured Molecules through Cyano Substitution. *J. Mater. Chem. C* **2015**, *3* (26), 6778–6785.

[406] Zhang, L.; Zou, L.; Xiao, J.; Zhou, P.; Zhong, C.; Chen, X.; Qin, J.; Mariz, I. F. A.; Maçôas, E. Symmetrical and Unsymmetrical Multibranched D–π–A Molecules Based on 1,3,5-Triazine Unit: Synthesis and Photophysical Properties. *J. Mater. Chem.* **2012**, *22* (33), 16781-16790.

[407] Matulaitis, T.; Kostiv, N.; Grazulevicius, J. V.; Peciulyte, L.; Simokaitiene, J.; Jankauskas, V.; Luszczynska, B.; Ulanski, J. Synthesis and Properties of Bipolar Derivatives of 1,3,5-Triazine and Carbazole. *Dyes Pigm.* **2016**, *127*, 45–58.

[408] Tanaka, H.; Shizu, K.; Nakanotani, H.; Adachi, C. Twisted Intramolecular Charge Transfer State for Long-Wavelength Thermally Activated Delayed Fluorescence. *Chem. Mater.* **2013**, *25*, 3766−3771.

References

[409] Jia, J.; Zhu, L.; Wei, Y.; Wu, Z.; Xu, H.; Ding, D.; Chen, R.; Ma, D.; Huang, W. Triazine-Phosphine Oxide Electron Transporter for Ultralow-Voltage-Driven Sky Blue PHOLEDs. *J. Mater. Chem. C* **2015**, *3* (19), 4890–4902.

[410] Pang, J.; Tao, Y.; Freiberg, S.; Yang, X-P.; D'Iorio, M.; Wang, S. Syntheses, structures, and electroluminescence of new blue luminescent star-shaped compounds based on 1,3,5-triazine and 1,3,5-trisubstituted benzene. *J. Mater. Chem.* **2002**, *12*, 206–212.

[411] Aihara, H.; Tanaka, T.; Satou, M.; Yamakawa, T. Synthesis and Electroluminescence of New Organic Emitters Based on a π-Conjugated 1,3,5-Triazine Core. *Trans. Mater. Res. Soc. Jpn.* **2010**, *35* (3), 675–680.

[412] Ranganathan, A.; Heisen, B. C.; Dix, I.; Meyer, F. A Triazine-Based Three-Directional Rigid-Rod Tecton Forms a Novel 1D Channel Structure. *Chem. Commun*. **2007**, 3637–3639.

[413] Zhang, Z.; Liu, R.; Zhu, X.; Li, Y.; Chang, J.; Zhu, H.; Ma, L.; Lv, W.; Guo, J. Synthesis and Luminescent Properties of Star-Burst D-π-A Compounds Based on 1,3,5-Triazine Core and Carbazole End-Capped Phenylene Ethynylene Arms. *J. Lumin.* **2014**, *156*, 130–136.

[414] Zou, L.; Liu, Z.; Yan, X.; Liu, Y.; Fu, Y.; Liu, J.; Huang, Z.; Chen, X.; Qin, J. Star-Shaped D-π-A Molecules Containing a 2,4,6-Tri(thiophen-2-Yl)-1,3,5- Triazine Unit: Synthesis and Two-Photon Absorption Properties. *Eur. J. Org. Chem.* **2009**, 32, 5587–5593.

[415] Yasuda, T.; Shimizu, T.; Liu, F.; Ungar, G.; Kato, T. Electro-Functional Octupolar Pi-Conjugated Columnar Liquid Crystals. *J. Am. Chem. Soc.* **2011**, *133* (34), 13437–13444.

[416] Guo, H.; Li, Q.; Ma, L.; Zhao, J. Fluorene as π-Conjugation Linker in N^N Pt(ii) Bisacetylide Complexes and Their Applications for Triplet–triplet Annihilation Based Upconversion. *J. Mater. Chem.* **2012**, *22* (31), 15757-15768.

[417] Lee, M. H.; Kim, J. Y.; Han, J. H.; Bhuniya, S.; Sessler, J. L.; Kang, C.; Kim, J. S. Direct Fluorescence Monitoring of the Delivery and Cellular Uptake of a Cancer-Targeted RGD Peptide-Appended Naphthalimide Theragnostic Prodrug. *J. Am. Chem. Soc.* **2012**, *134*, 12668-12674.

[418] Capodilupo, A. L.; Vergaro, V.; Fabiano, E.; Giorgi, M. D.; Baldassarre, F.; Cardone, A.; Maggiore, A.; Maiorano, V.; Sanvitto, D.; Gigli, G.; Ciccarella, G. Design and Synthesis of Fluorenone-Based Dyes: Two-Photon Excited Fluorescent Probes for Imaging of Lysosomes and Mitochondria in Living Cells. *J. Mater. Chem. B* **2015**, *3*, 3315-3323.

References

[419] Singh, R. S.; Gupta, R. K.; Paitandi, R. P.; Dubey, M.; Sharma, G.; Koch, B.; Pandey, S. Morphological Tuning *via* Structural Modulations in AIE Luminogens with the Minimum Number of Possible Variables and their Use in Live Cell Imaging. *Chem. Commun.* **2015**, *51*, 9125-9128.

[420] Kumar, M.; Kumar, N.; Bhalla, V. A Naphthalimide Based Chemosensor for Zn^{2+}, Pyrophosphate and H_2O_2: Sequential Logic Operations at the Molecular Level. C*hem. Commun.* **2013**, *49*, 877- 879.

[421] Dong, B.; Song, X.; Wang, C.; Kong, X.; Tang, Y.; Lin, W. Dual Site-Controlled and Lysosome-Targeted Intramolecular Charge Transfer-Photoinduced Electron Transfer-Fluorescence Resonance Energy Transfer Fluorescent Probe for Monitoring pH Changes in Living Cells. *Anal. Chem.* **2016**, *88*, 4085-4091.

[422] Wang, S.; Zeng, P.J.; Liu, Y.Q.; Yu, G.; Sun, X. B.; Niu, H. B.; Zhu, D. B. Luminescent properties of a novel naphthalimide-fluorene molecule. *Synth. Met.* **2005**, *150*, 33-38.

[423] Zhu, W.; Hu, M.; Yao, R.; Tian, H. A Novel Family of Twisted Molecular Luminescent Materials Containing Carbazole Unit for Single-Layer Organic Electroluminescent Devices. *J. Photochem. Photobiol. A.* **2003**, *154*, 169-177.

[424] Saini, A.; Thomas, K. R. J.; Sachdev, A.; Gopinath, P. Photophysics, Electrochemistry, Morphology, and Bioimaging Applications of New 1,8-Naphthalimide Derivatives Containing Different Chromophores. *Chem. - Asian J.* **2017**, *12* (19), 2612–2622.

[425] Stille, J. K. Palladium-katalysierte Kupplungsreaktionen Organischer Elektrophile mit Organozinn-Verbindungen. *Angew. Chem., Int. Ed.* **1986**, *98*, 504-519.

[426] Tomkeviciene, A.; Grazulevicius, J. V.; Volyniuk, D.; Jankauskasb, V.; Sini, G. Structure–Properties Relationship of Carbazole and Fluorene Hybrid Trimers: Experimental and Theoretical Approaches. *Phys. Chem. Chem. Phys.* **2014**, *16*, 13932-13942.

[427] Naga, N.; Tagaya, N.; Noda, H.; Imai, T.; Tomoda, H. Synthesis and Properties of Fluorene or Carbazole-Based Alternating Copolymers Containing Si And Vinylene Units in the Main Chain. *J. Polym. Sci., Part A: Polym. Chem.* **2008**, *46*, 4513-4521.

Supplementary Information

(*^{1}H and ^{13}C NMR spectra of unpublished compounds*)

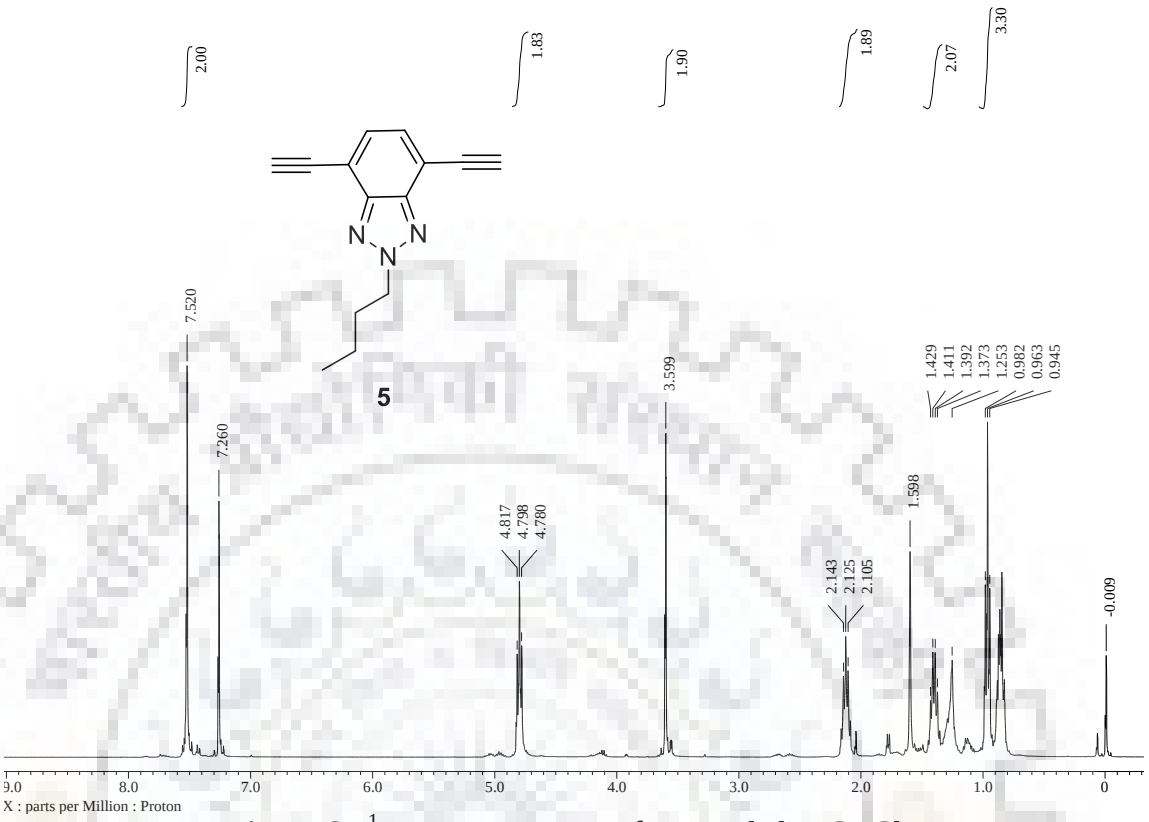

Figure S1 ^{1}H NMR spectrum of **5** recorded in $CDCl_3$.

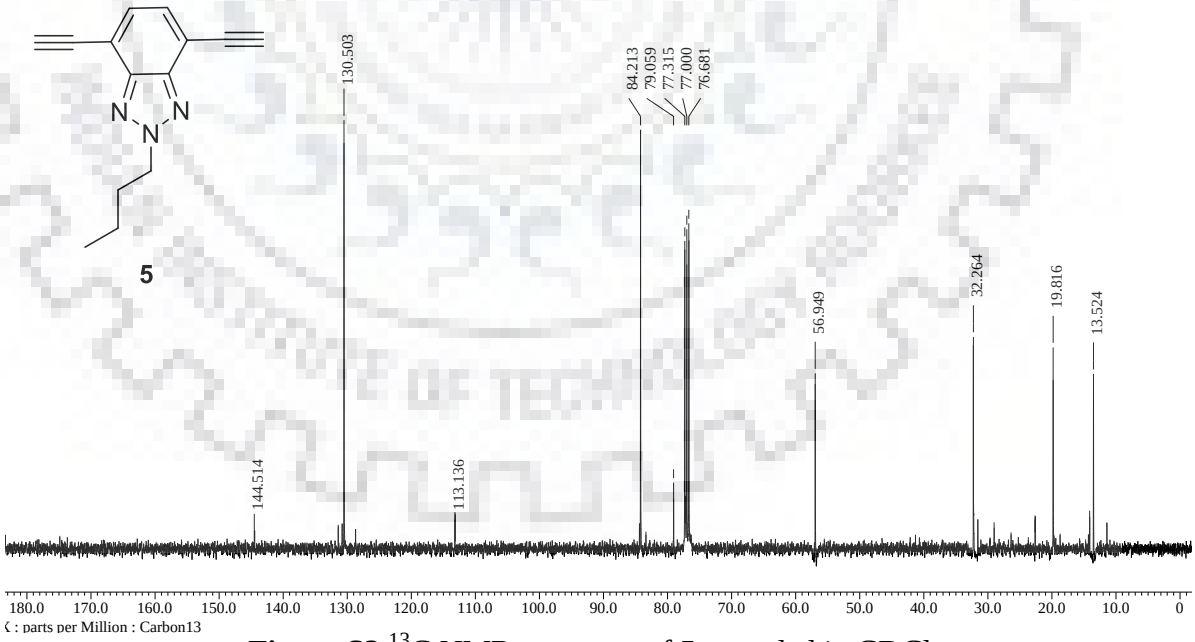

Figure S2 ^{13}C NMR spectrum of **5** recorded in $CDCl_3$.

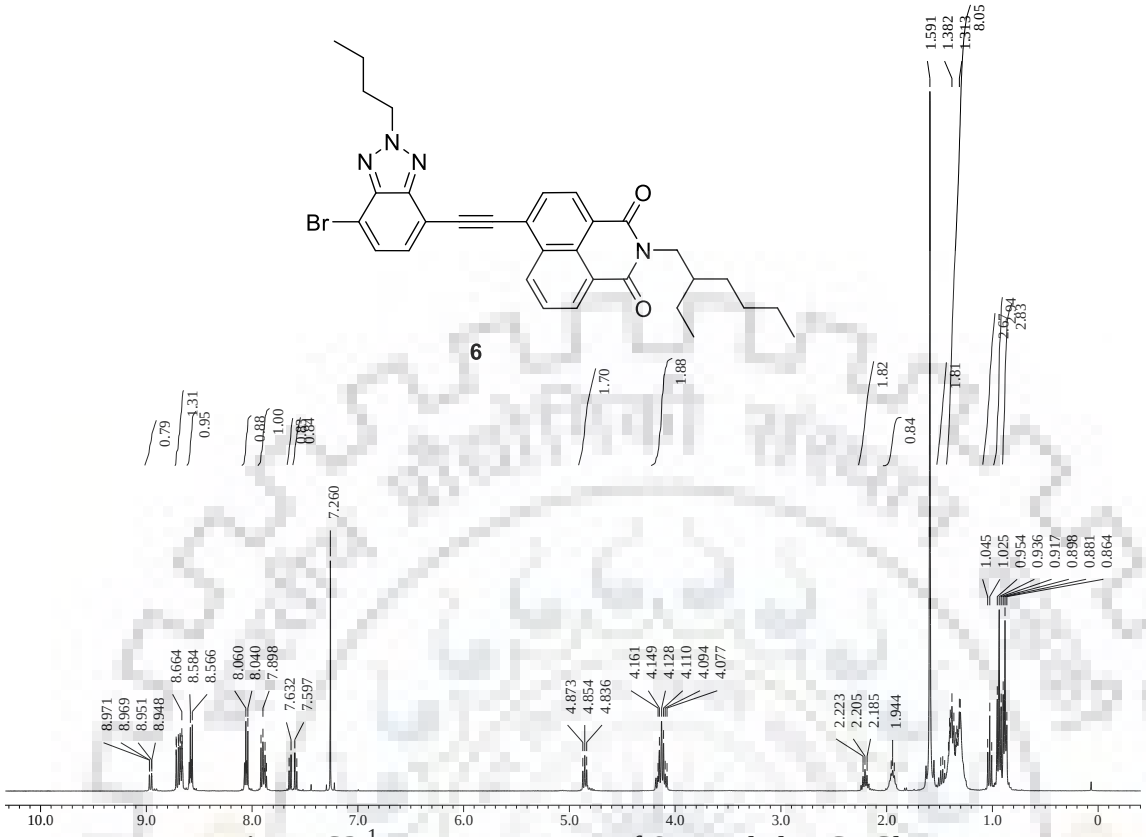

Figure S3 ^{1}H NMR spectrum of **6** recorded in $CDCl_3$.

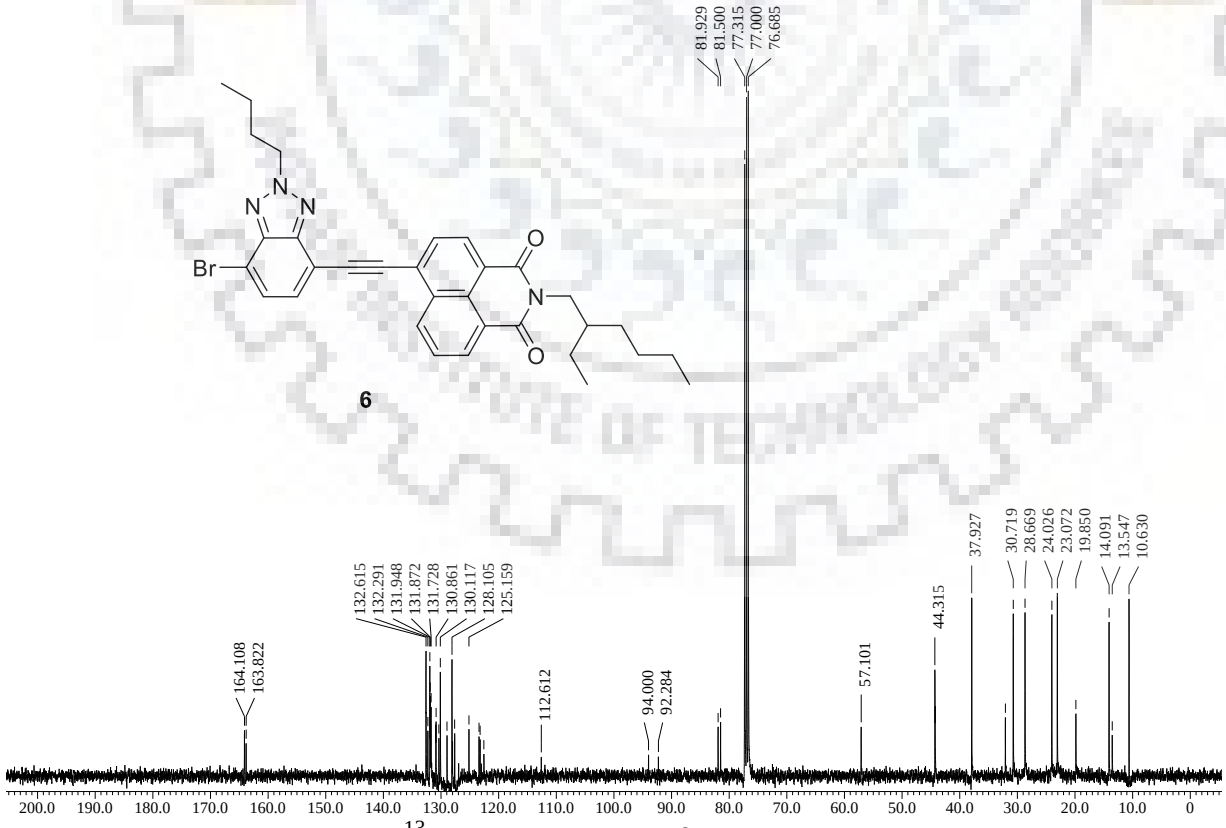

Figure S4 ^{13}C NMR spectrum of **6** recorded in $CDCl_3$.

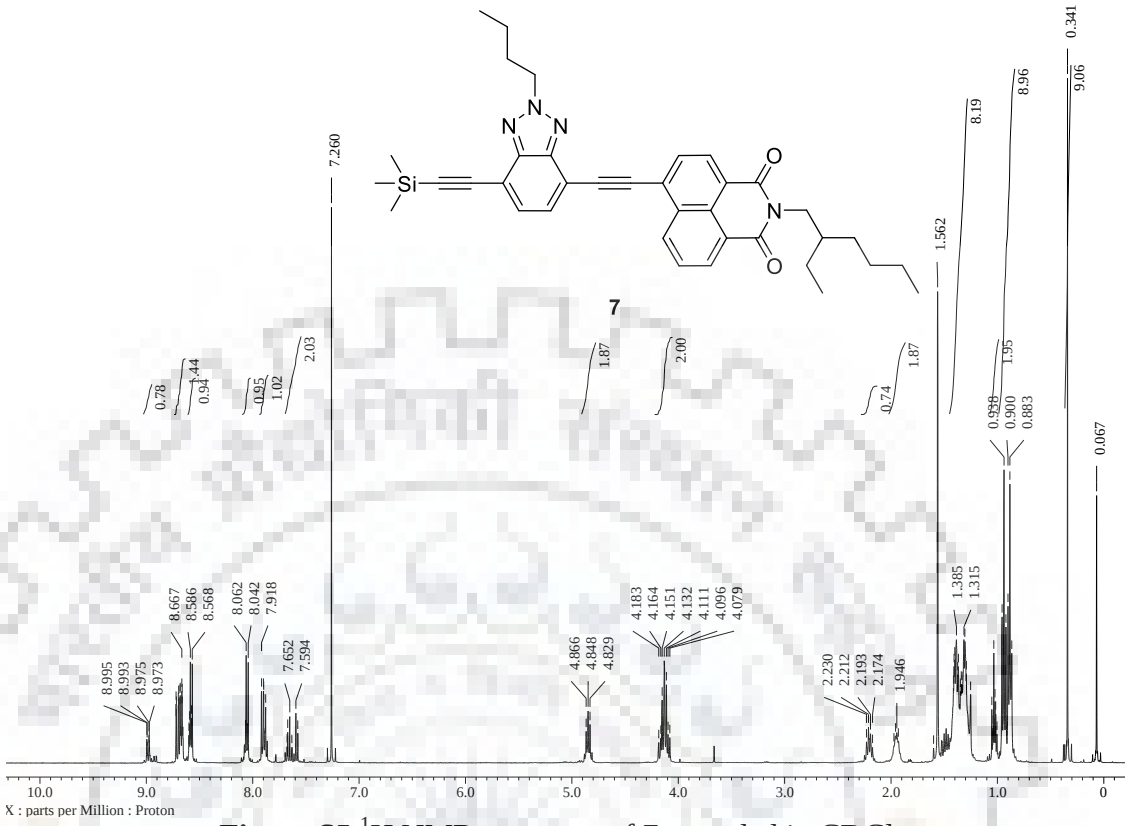

Figure S5 ^{1}H NMR spectrum of **7** recorded in $CDCl_3$.

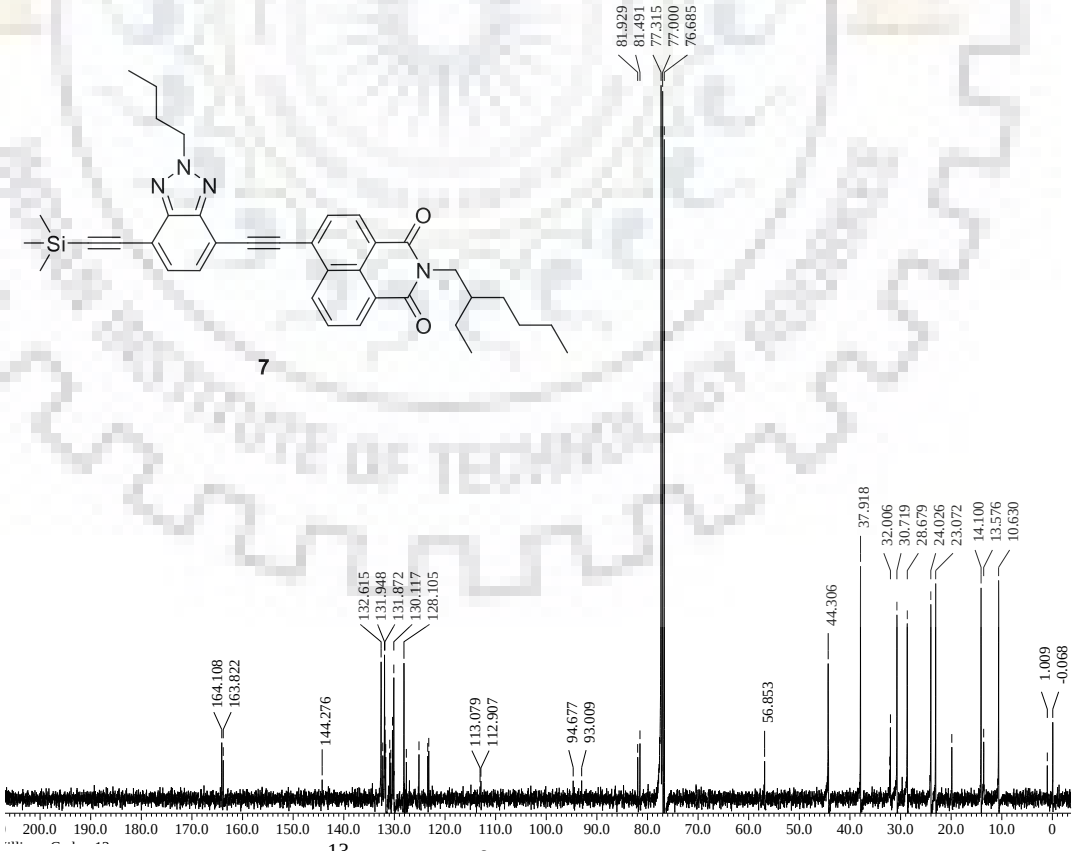

Figure S6 ^{13}C NMR of spectrum **7** recorded in $CDCl_3$.

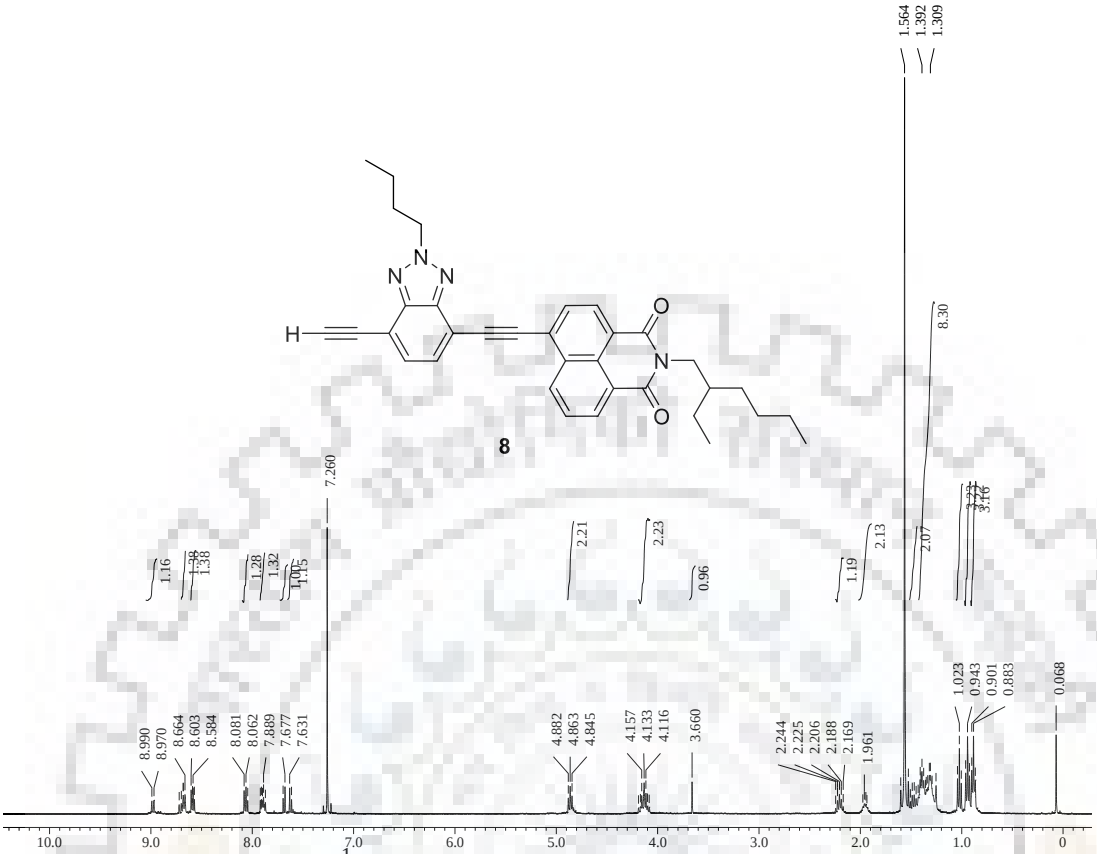

Figure S7 ^{1}H NMR spectrum of **8** recorded in $CDCl_3$.

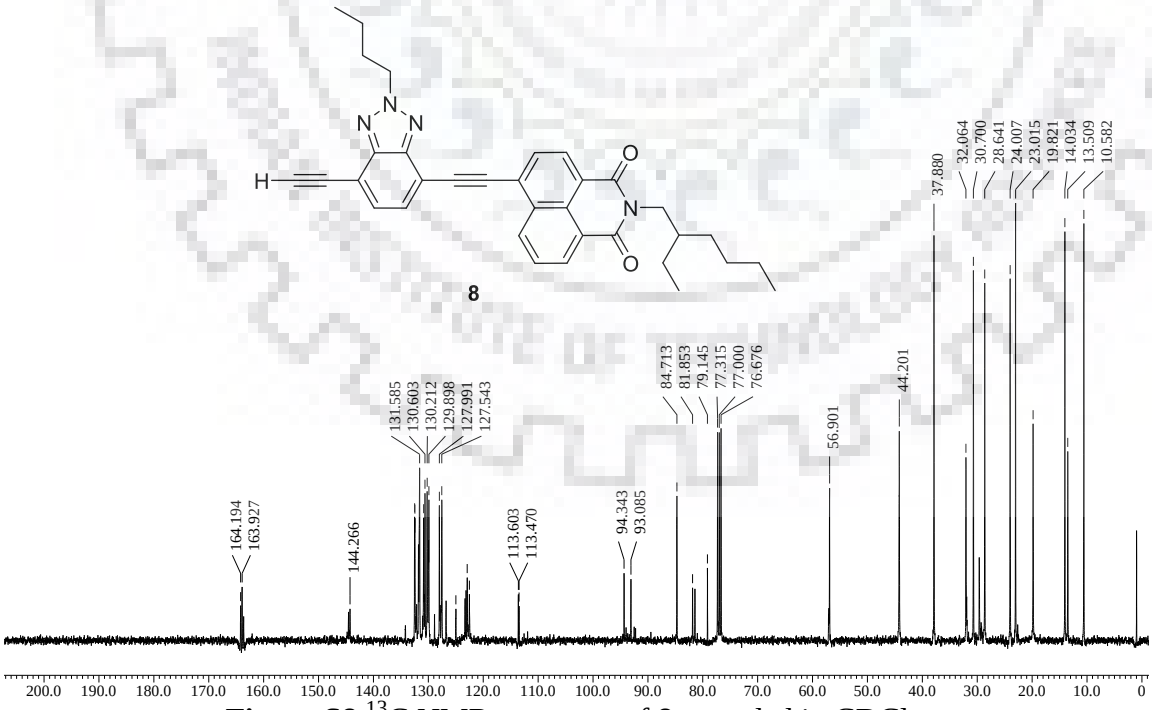

Figure S8 ^{13}C NMR spectrum of **8** recorded in $CDCl_3$.

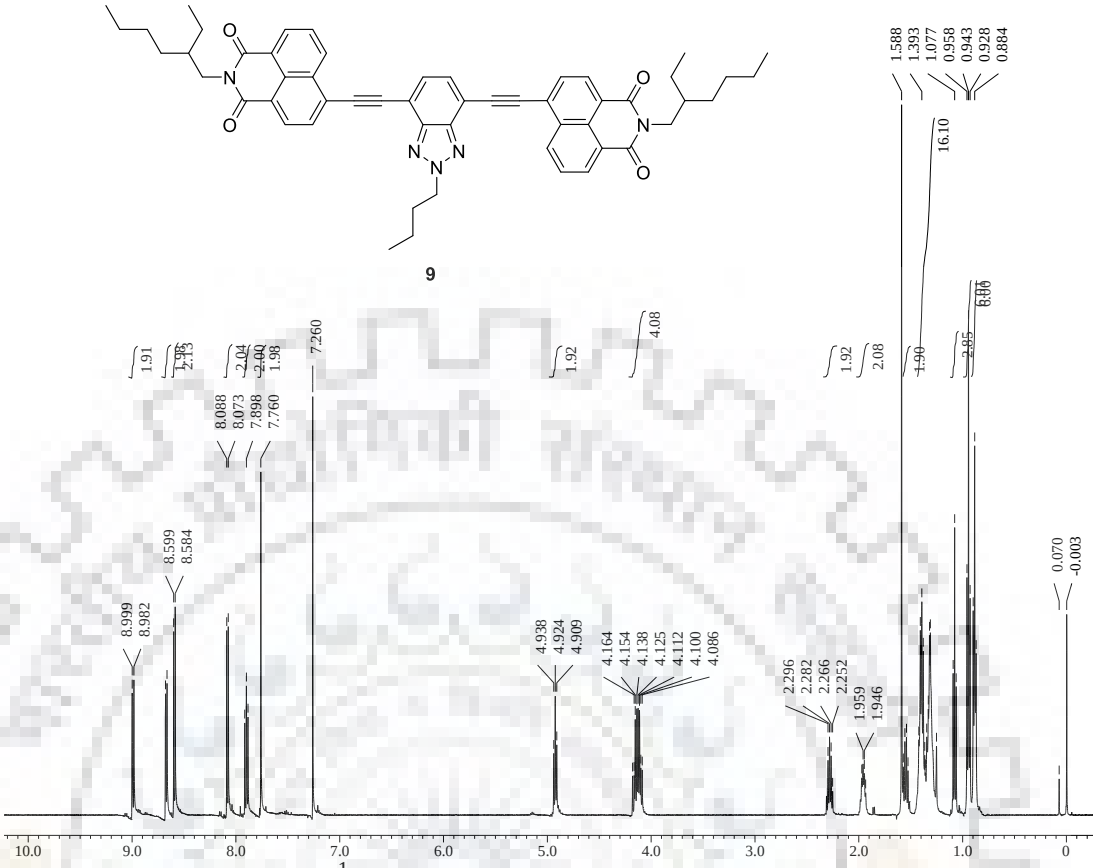

Figure S9[1]H NMR spectrum of **9** recorded in $CDCl_3$.

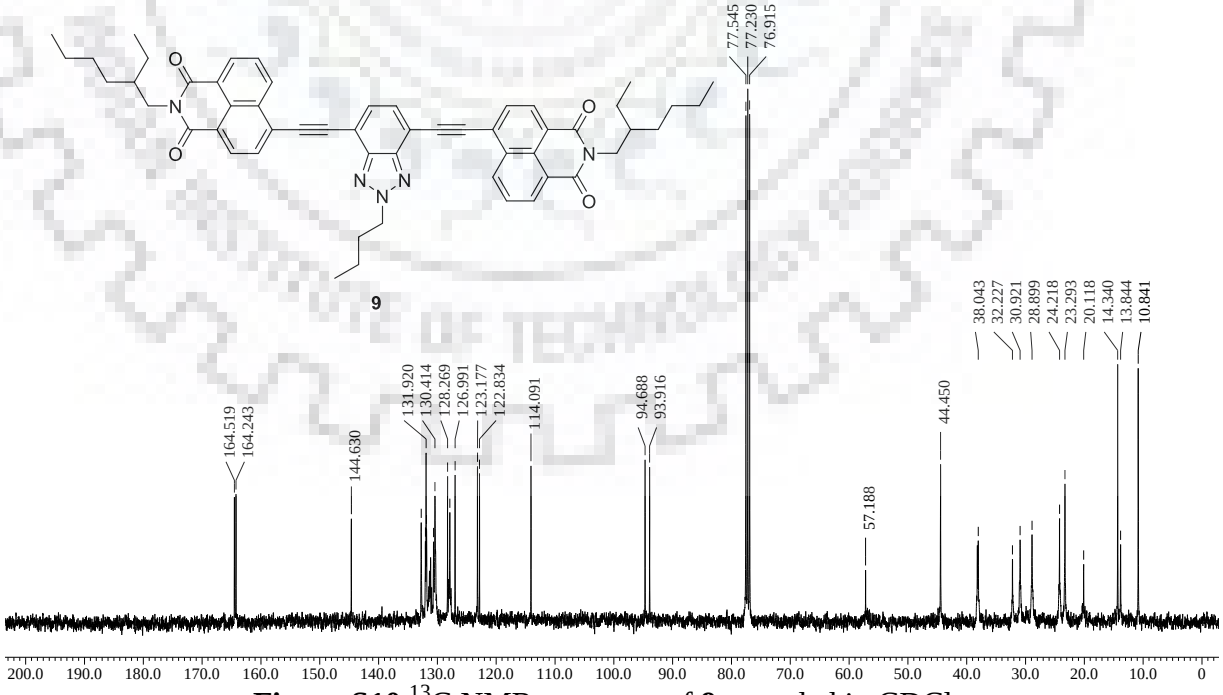

Figure S10 [13]C NMR spectrum of **9** recorded in $CDCl_3$.

Figure S11 ^{1}H NMR spectrum of **10** recorded in $CDCl_3$.

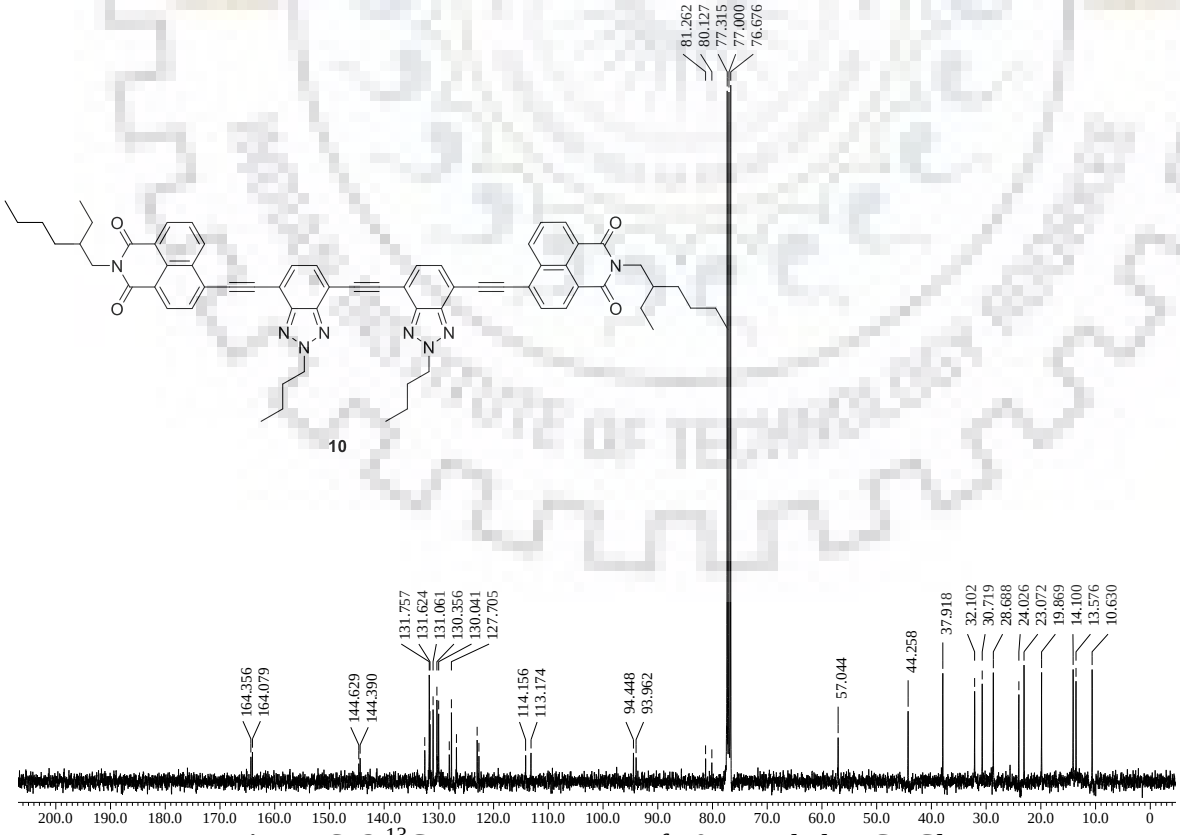

Figure S12 ^{13}C NMR spectrum of **10** recorded in $CDCl_3$**.**

Figure S13 ^{13}H NMR spectrum of **11** recorded in $CDCl_3$.

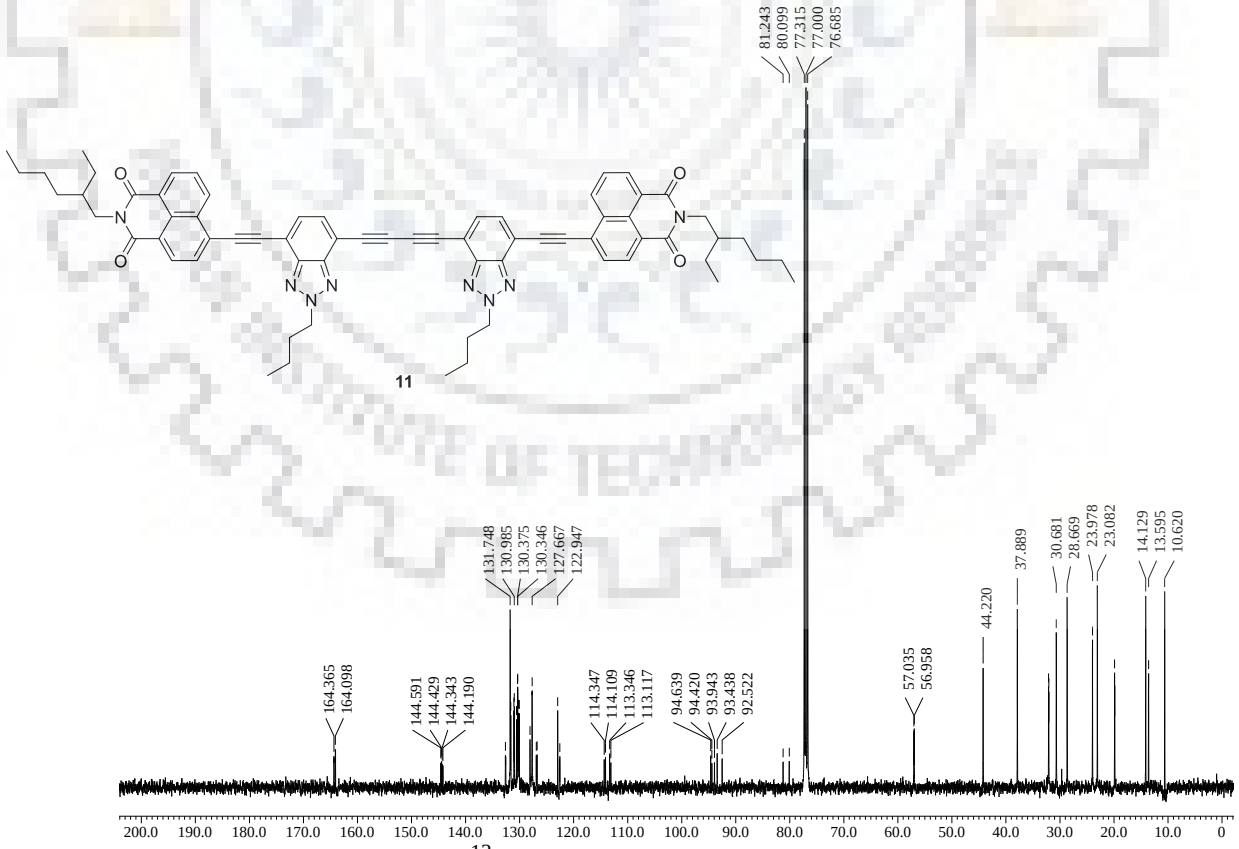

Figure S14 ^{13}C NMR spectrum of **11** recorded in $CDCl_3$

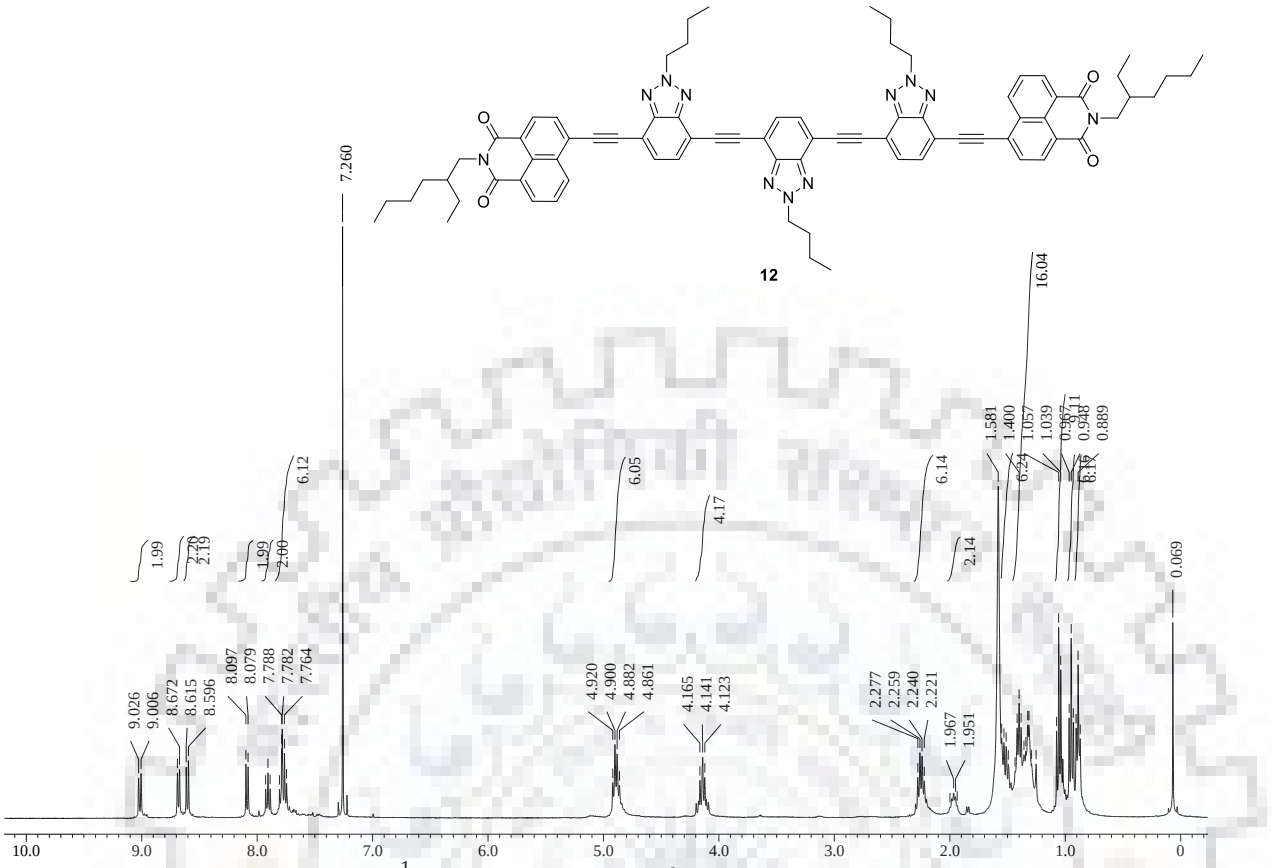

Figure S15 ^{1}H NMR spectrum of **12** recorded in $CDCl_3$.

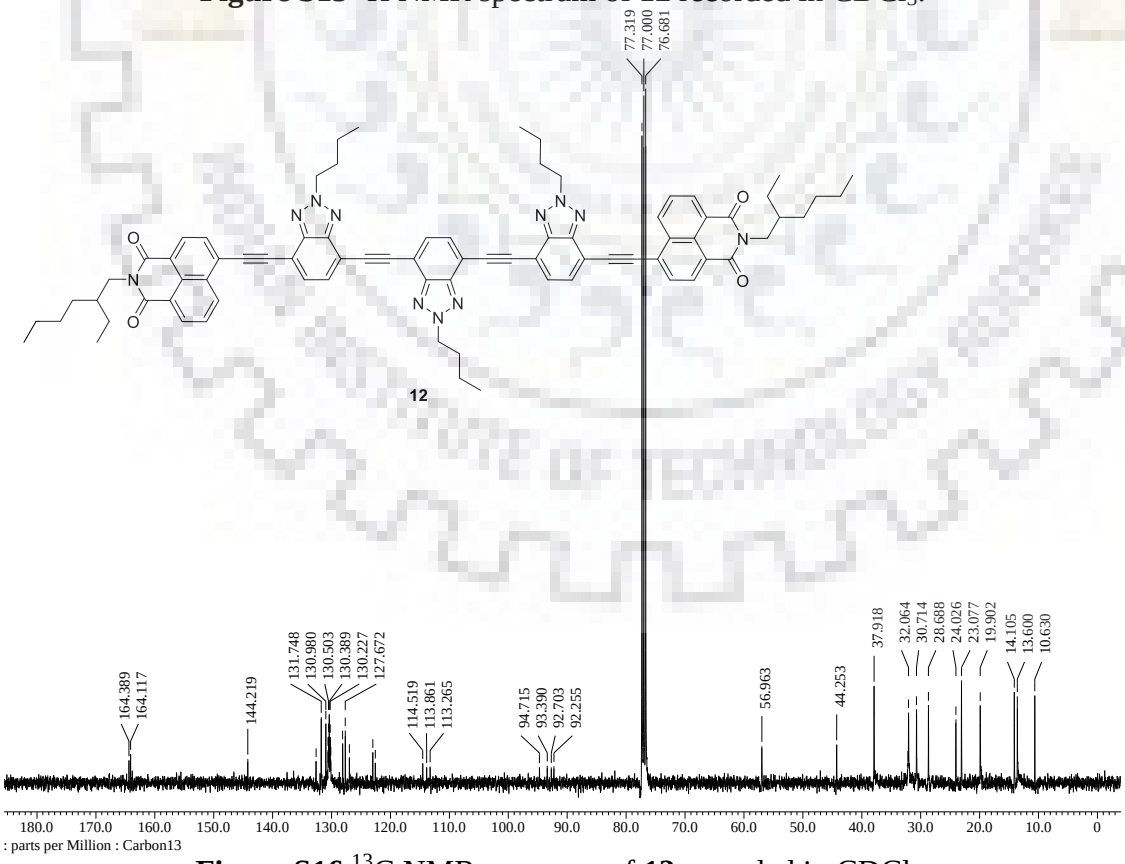

Figure S16 ^{13}C NMR spectrum of **12** recorded in $CDCl_3$.

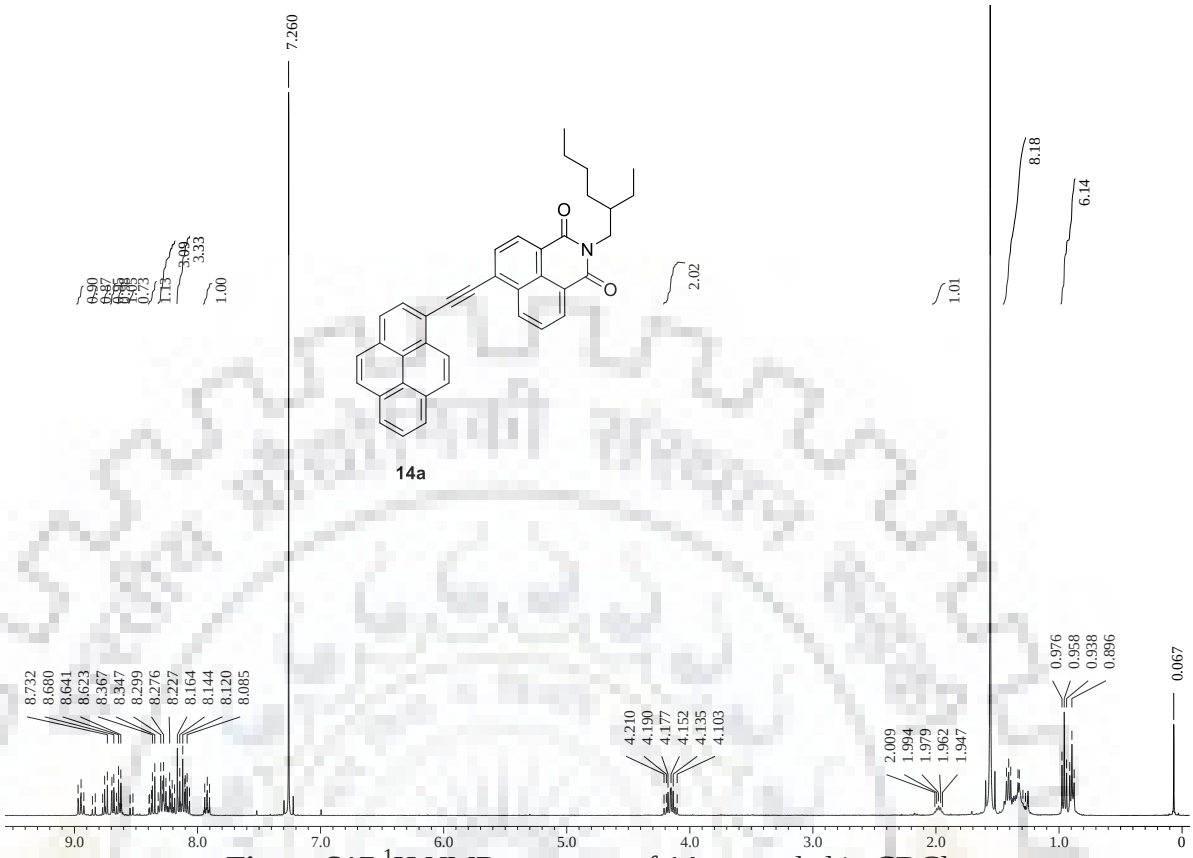

Figure S17 ^{1}H NMR spectrum of **14a** recorded in $CDCl_3$.

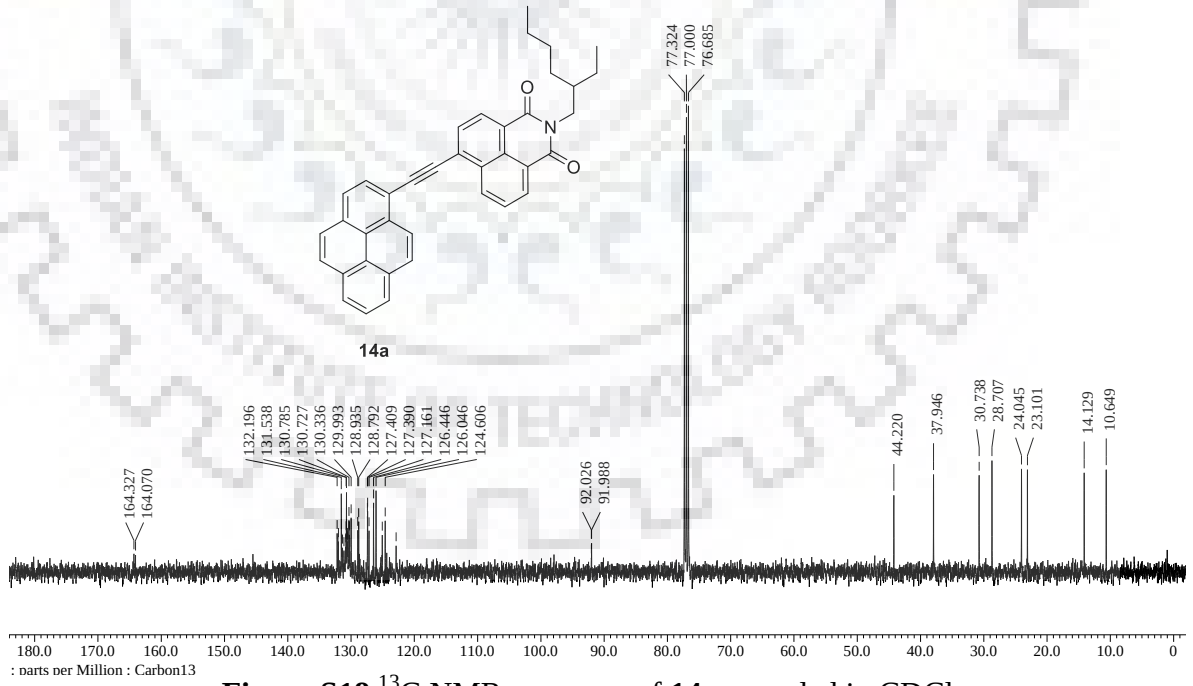

Figure S18 ^{13}C NMR spectrum of **14a** recorded in $CDCl_3$.

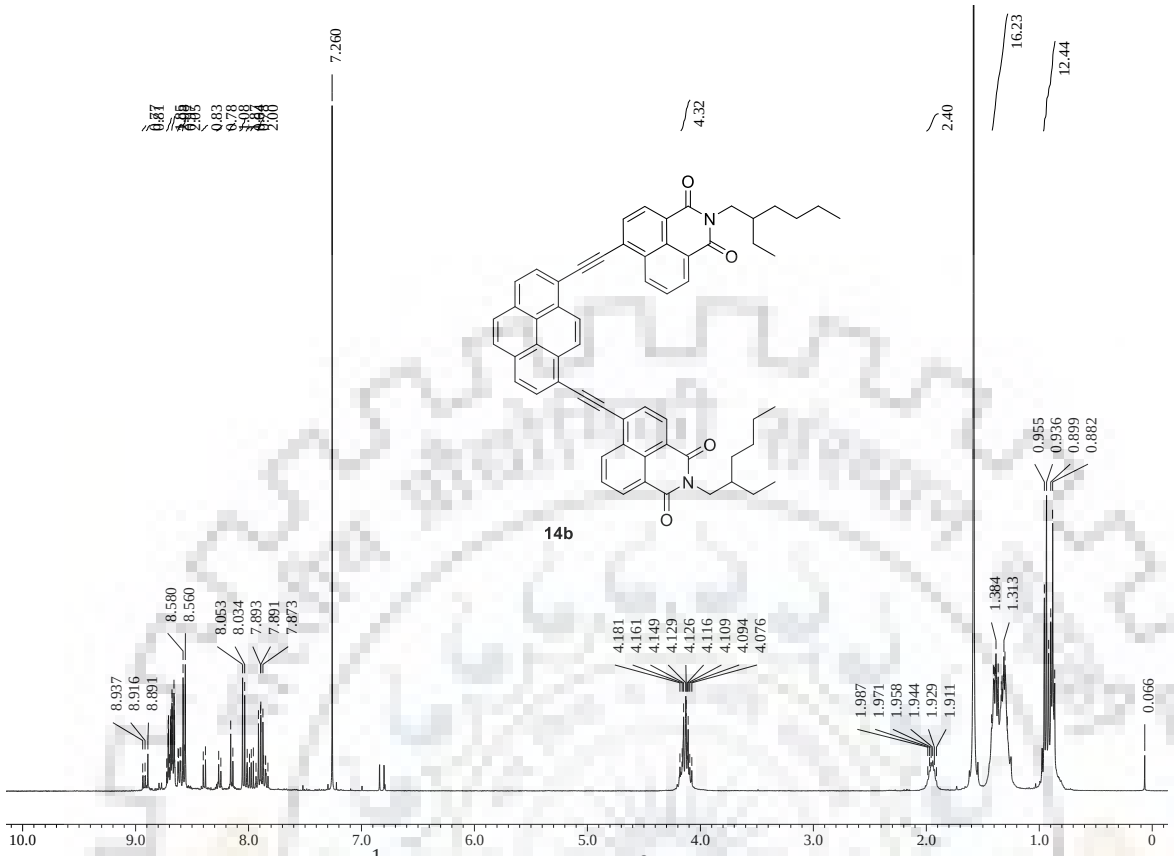

Figure S19 ^{1}H NMR spectrum of **14b** recorded in $CDCl_3$.

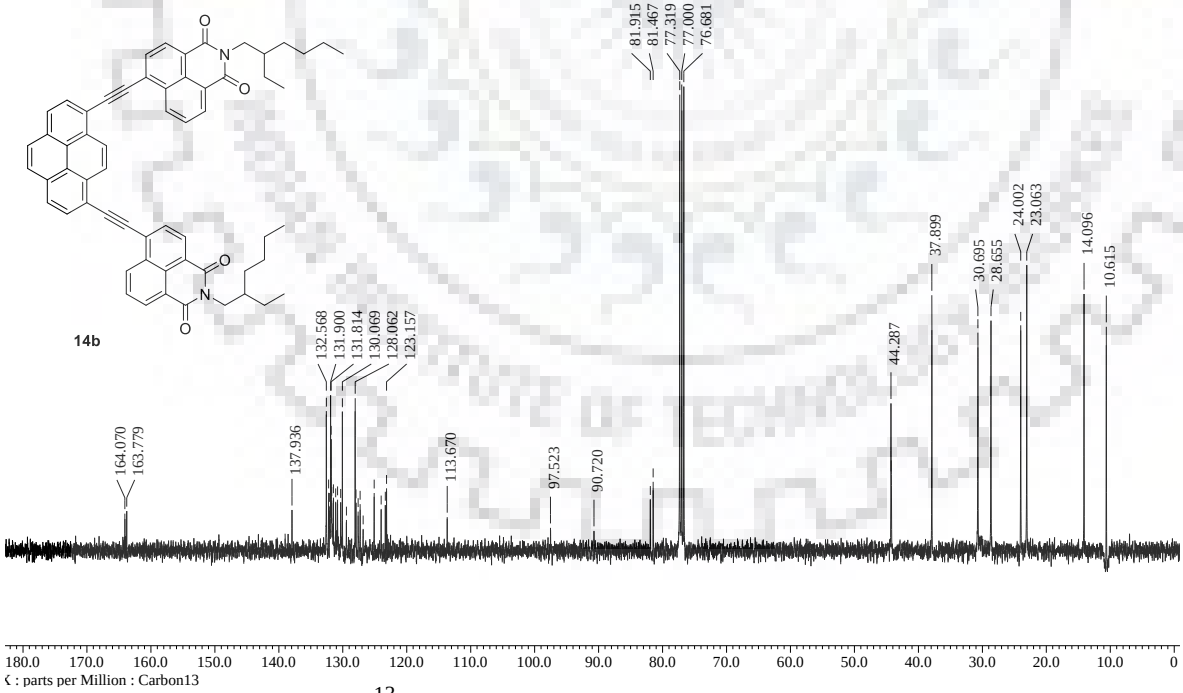

Figure S20 ^{13}C NMR spectrum of **14b** recorded in $CDCl_3$.

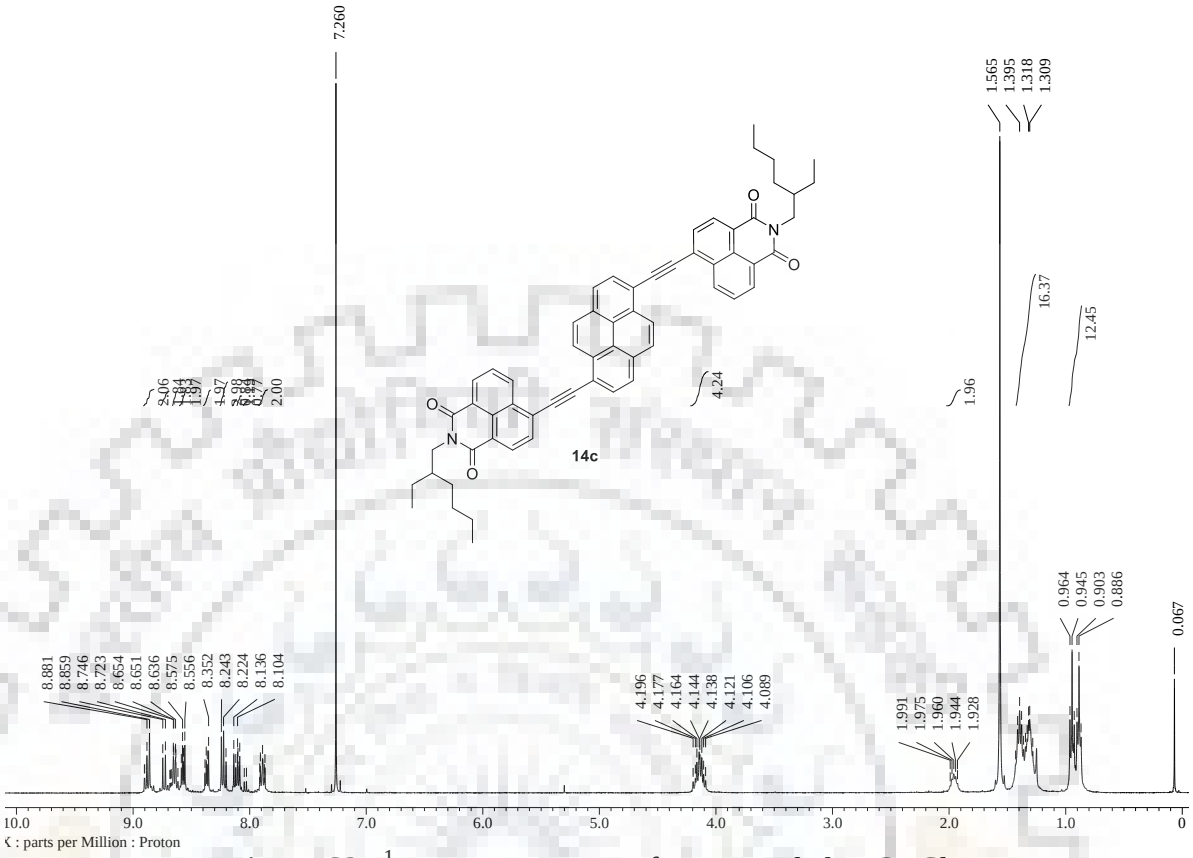

Figure S21 ^{1}H NMR spectrum of **14c** recorded in $CDCl_3$.

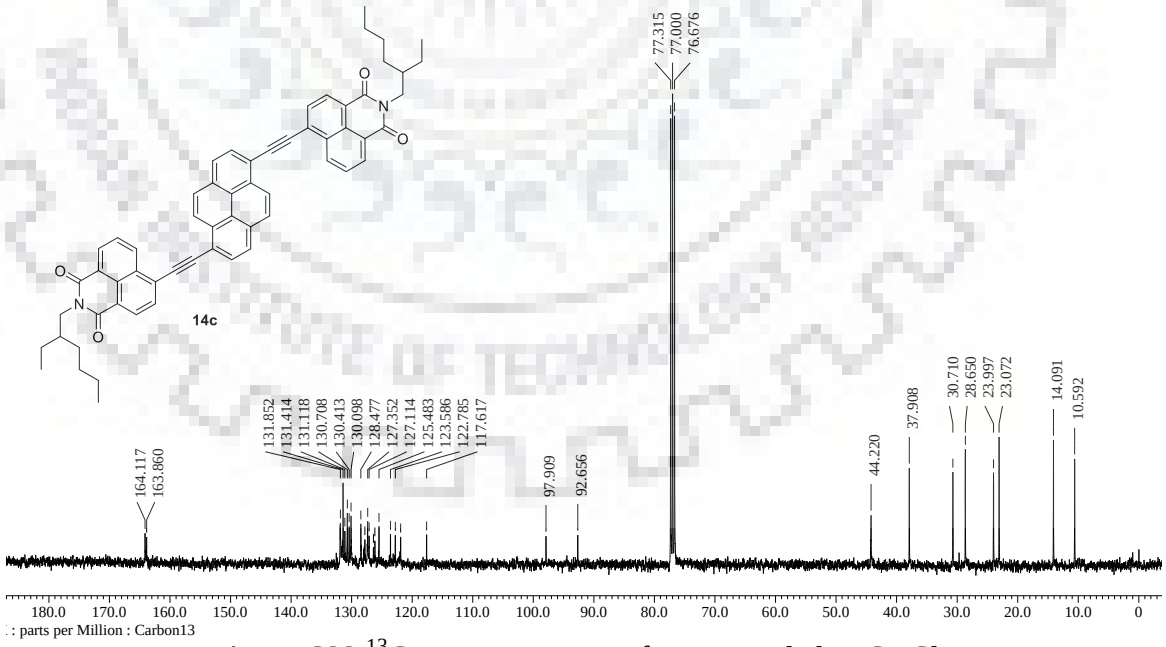

Figure S22 ^{13}C NMR spectrum of **14c** recorded in $CDCl_3$.

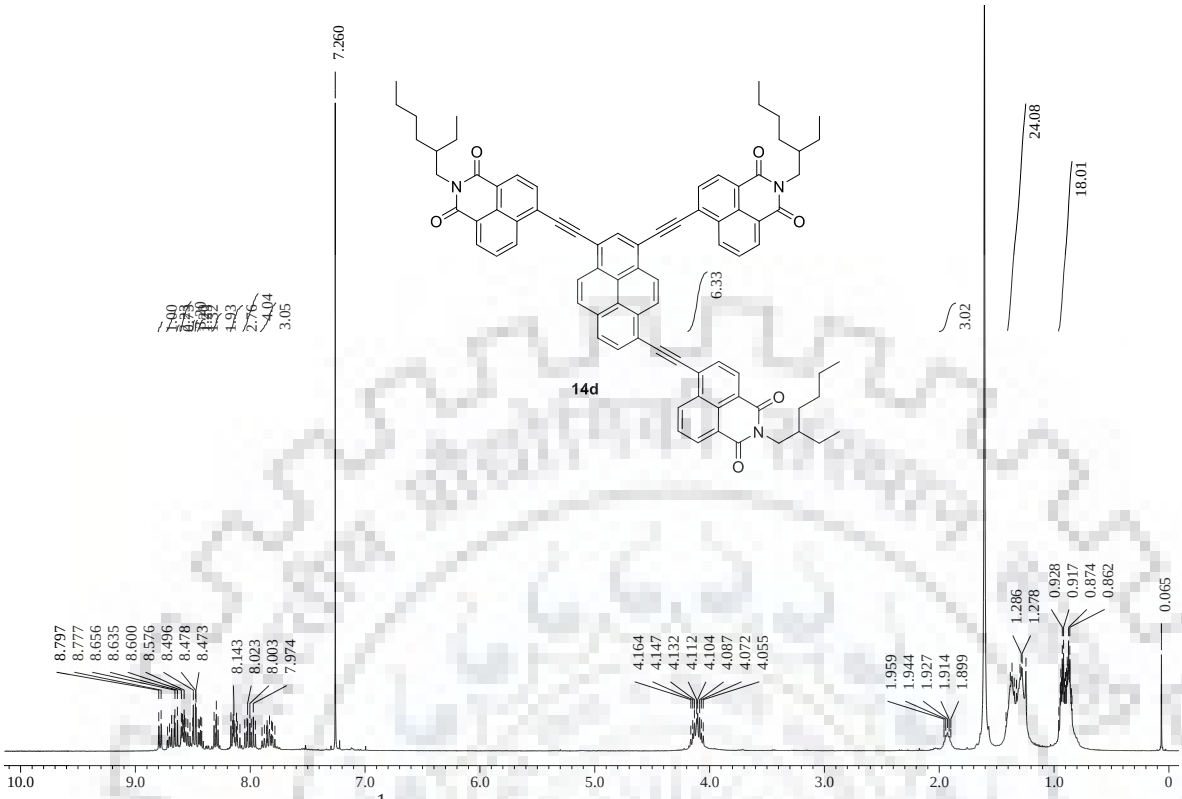

Figure S23 ^{1}H NMR spectrum of **14d** recorded in $CDCl_3$.

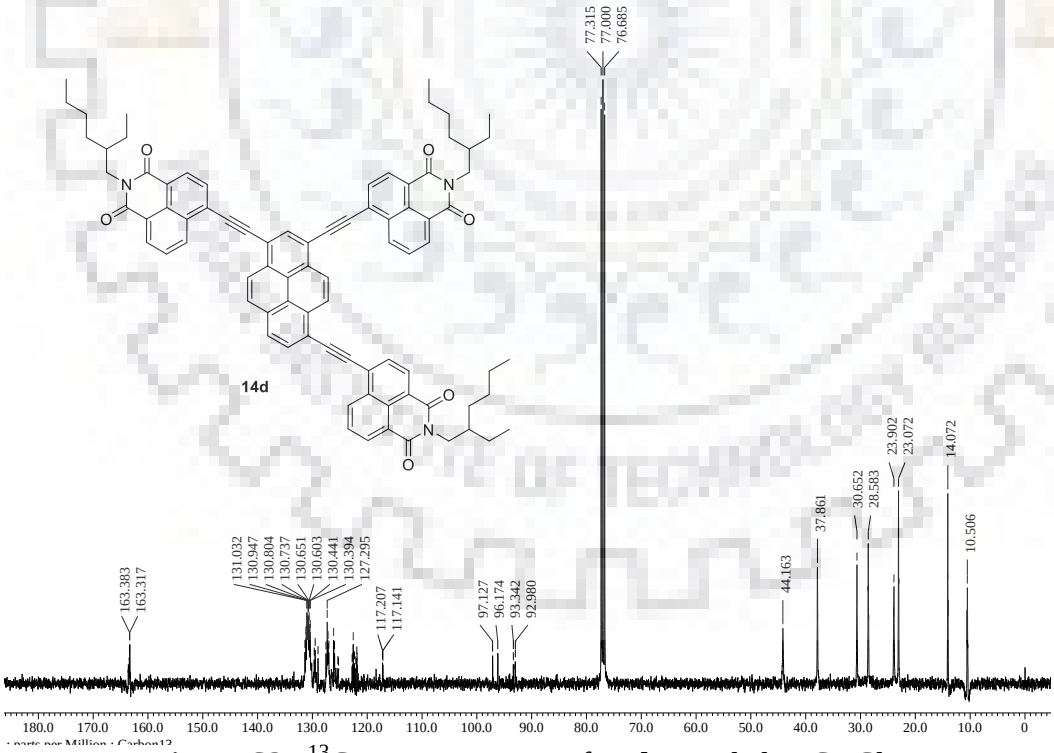

Figure S24 ^{13}C NMR spectrum of **14d** recorded in $CDCl_3$.

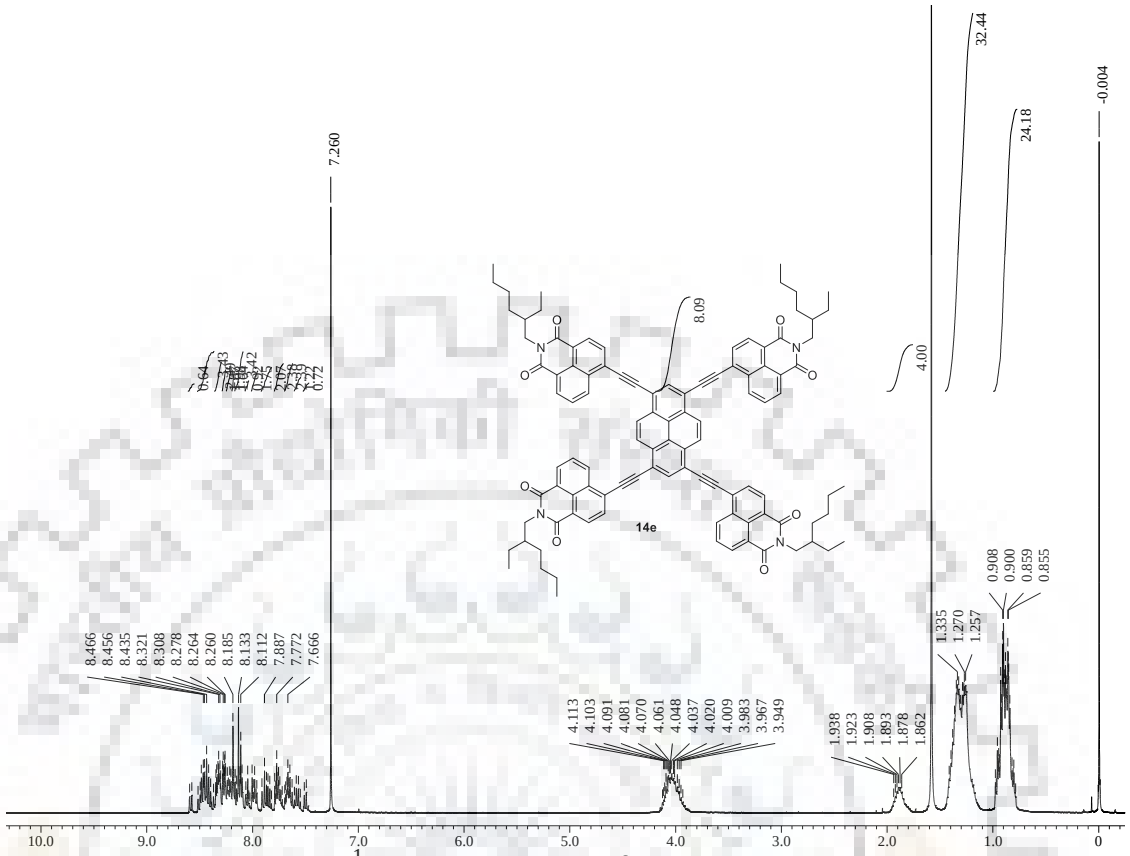

Figure S25 ^{1}H NMR spectrum of **14e** recorded in $CDCl_3$.

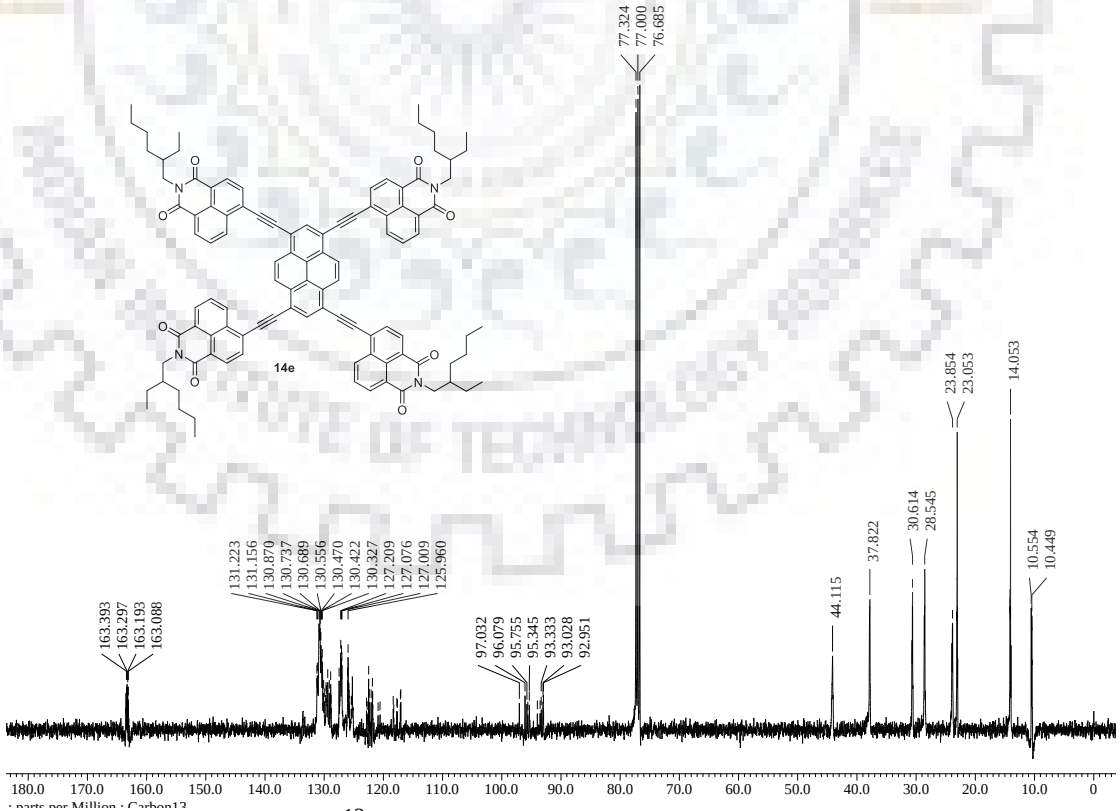

Figure S26 ^{13}C NMR spectrum of **14e** recorded in $CDCl_3$.

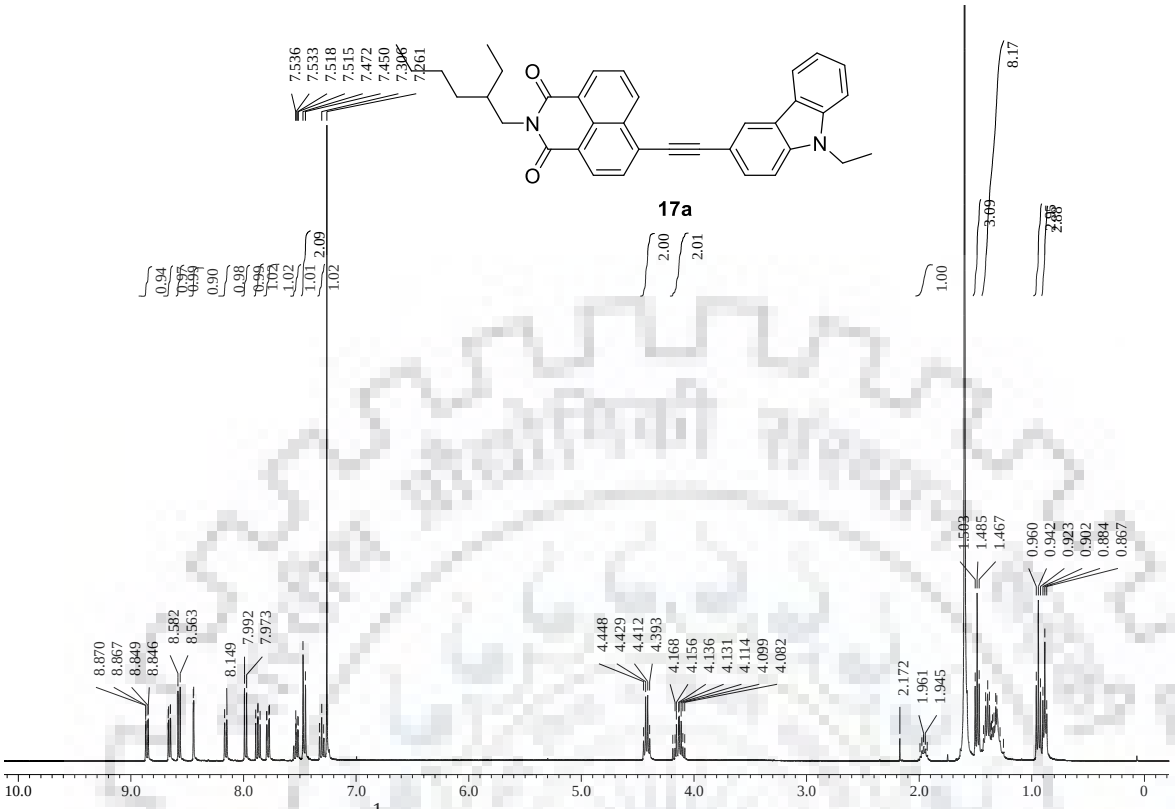

Figure S27 ^{1}H NMR spectrum of **17a** recorded in $CDCl_3$.

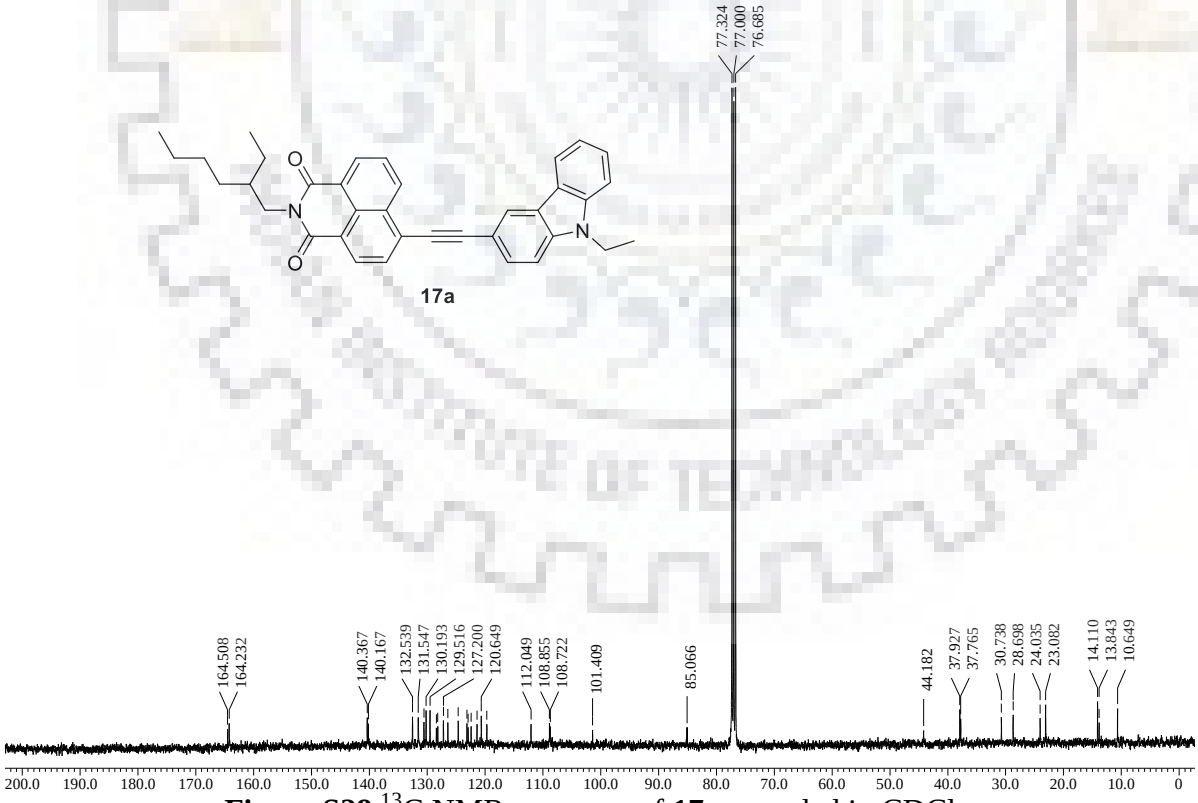

Figure S28 ^{13}C NMR spectrum of **17a** recorded in $CDCl_3$.

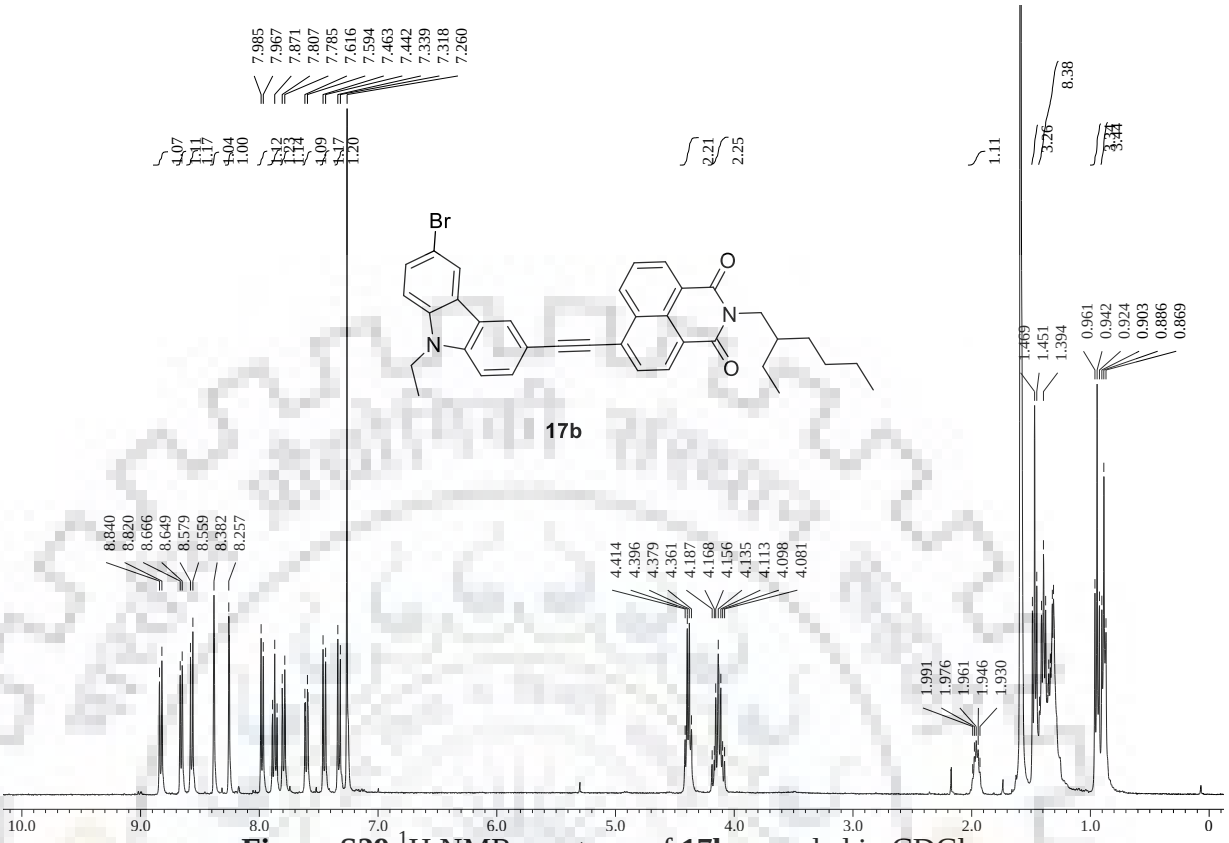

Figure S29 ^{1}H NMR spectrum of **17b** recorded in $CDCl_3$.

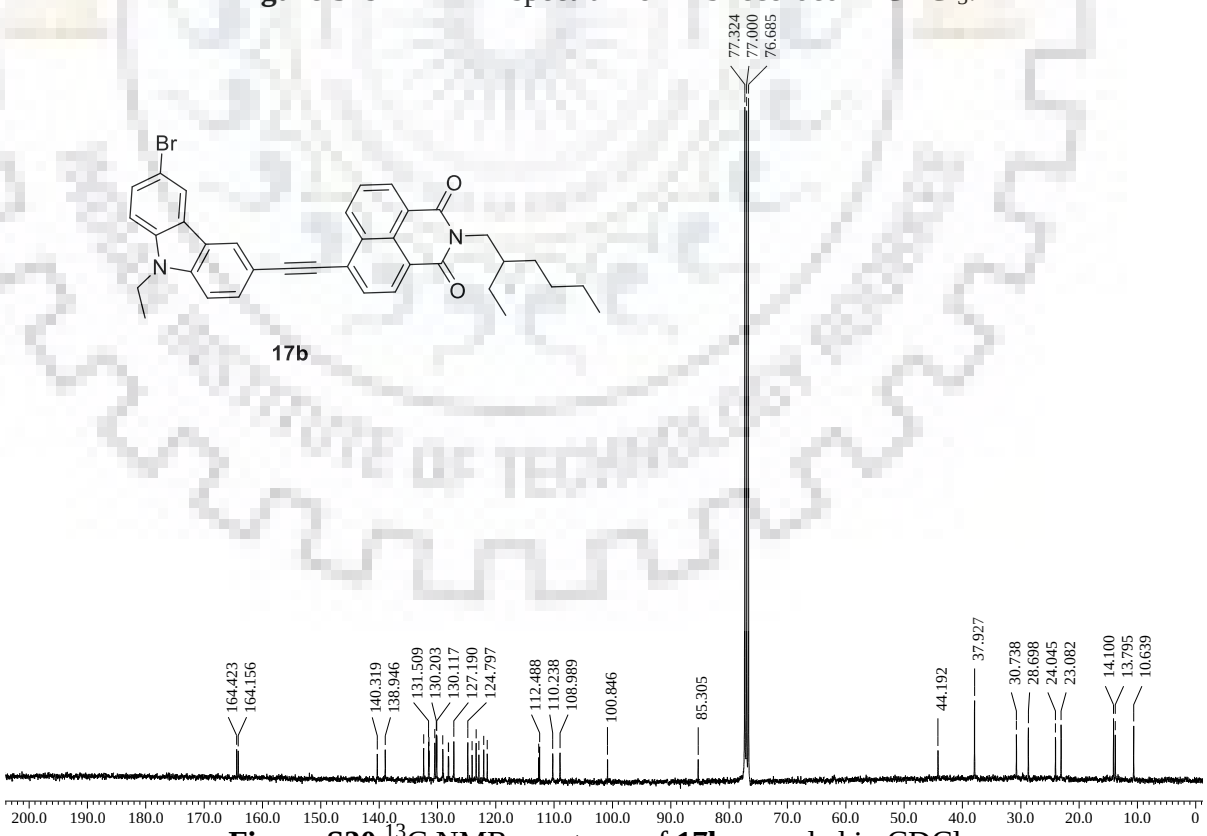

Figure S30 ^{13}C NMR spectrum of **17b** recorded in $CDCl_3$.

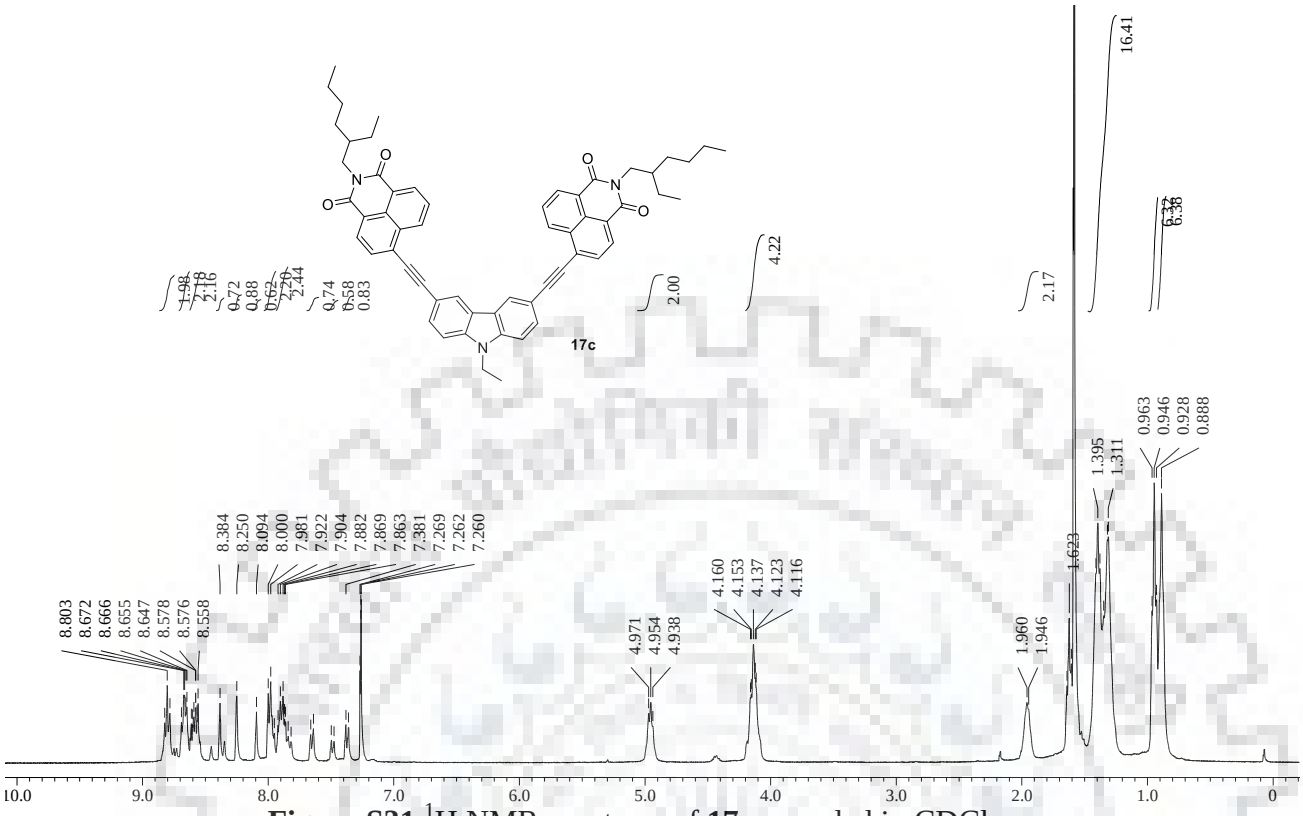

Figure S31 ^{1}H NMR spectrum of **17c** recorded in $CDCl_3$.

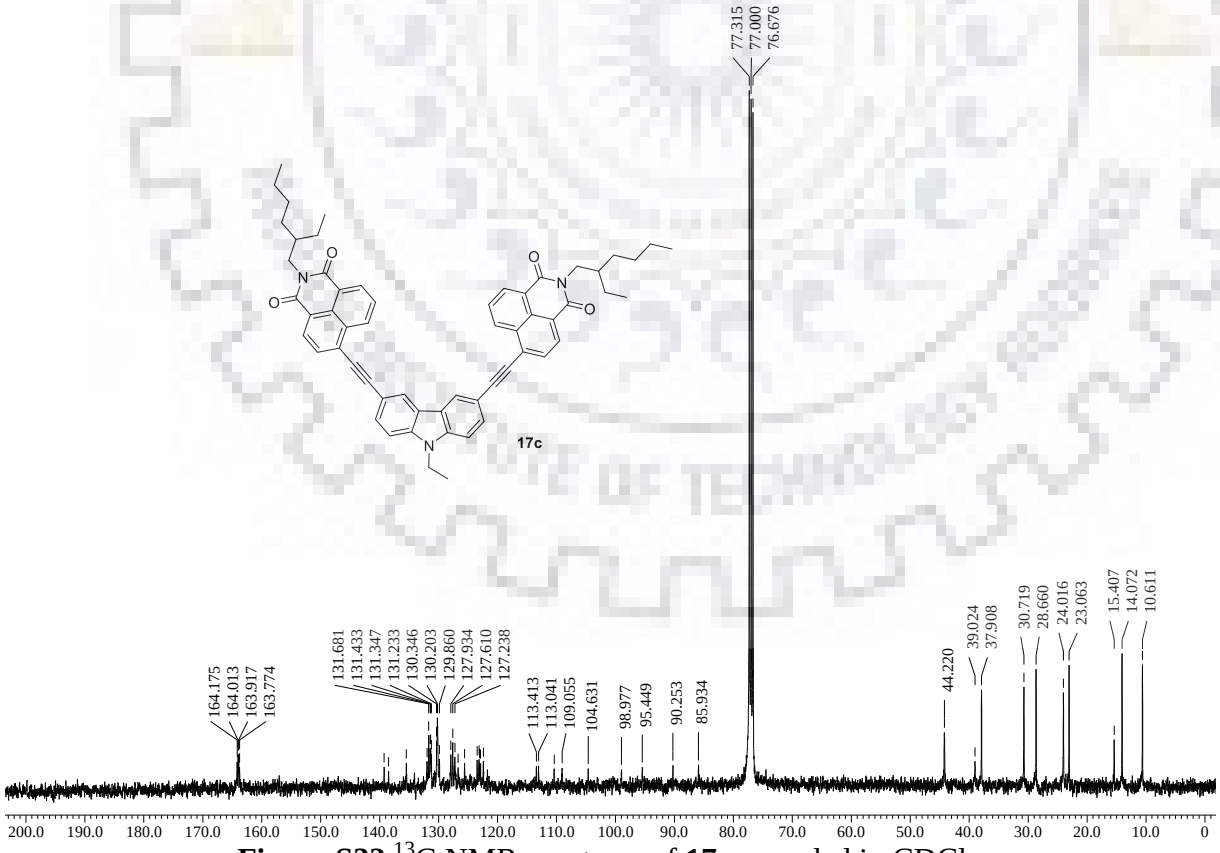

Figure S32 ^{13}C NMR spectrum of **17c** recorded in $CDCl_3$.

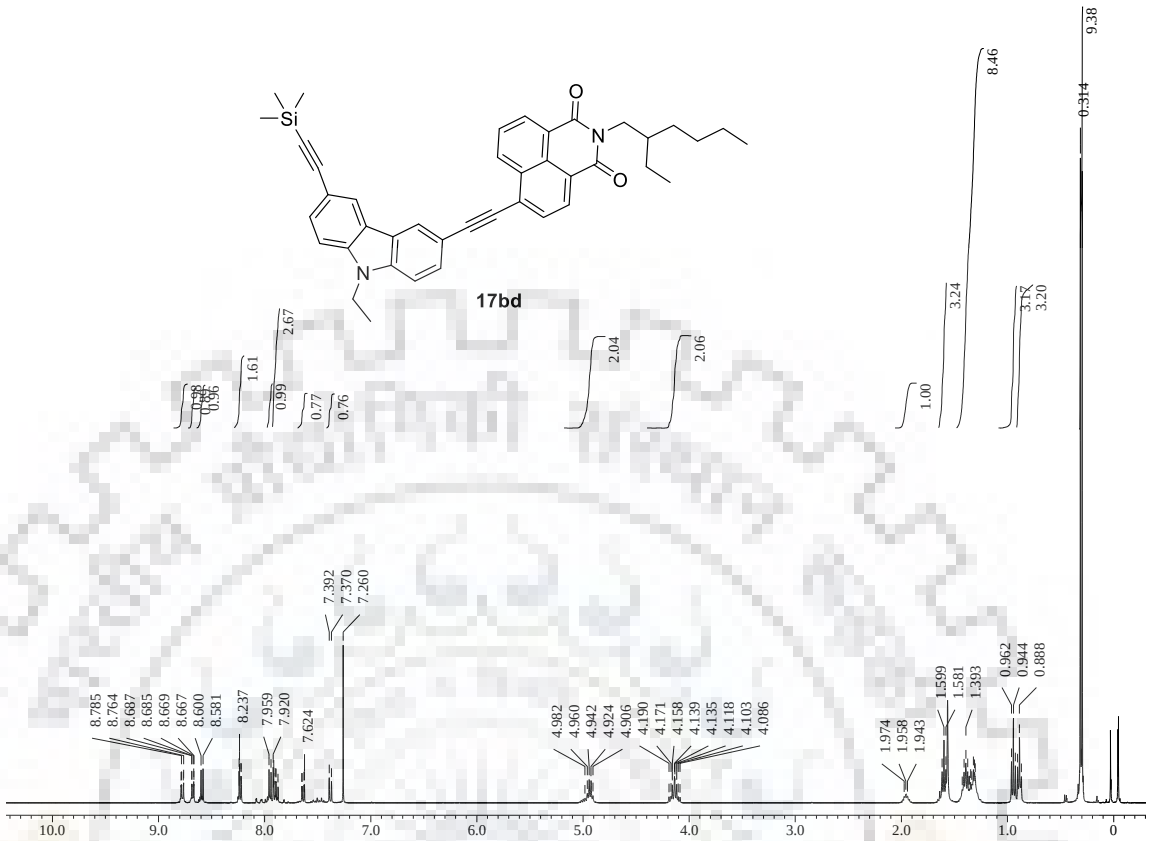

Figure S33 ^{1}H NMR spectrum of **17bd** recorded in $CDCl_3$.

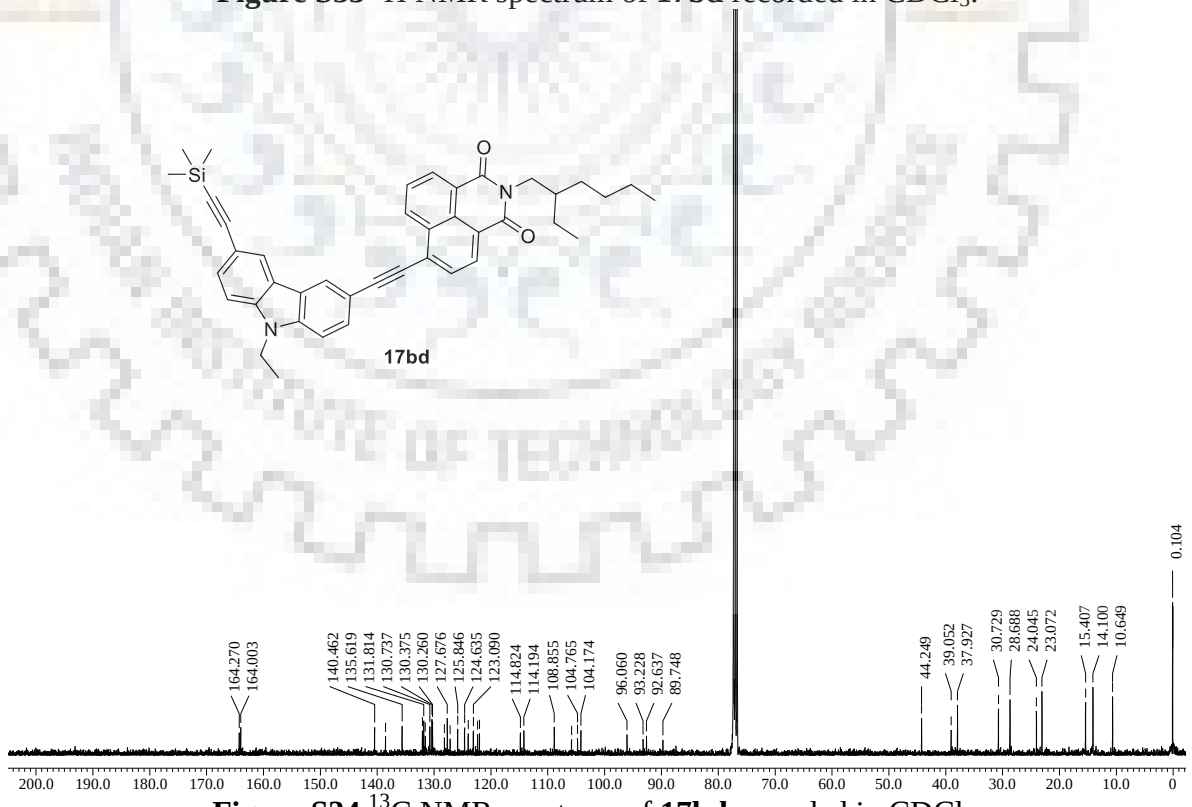

Figure S34 ^{13}C NMR spectrum of **17bd** recorded in $CDCl_3$.

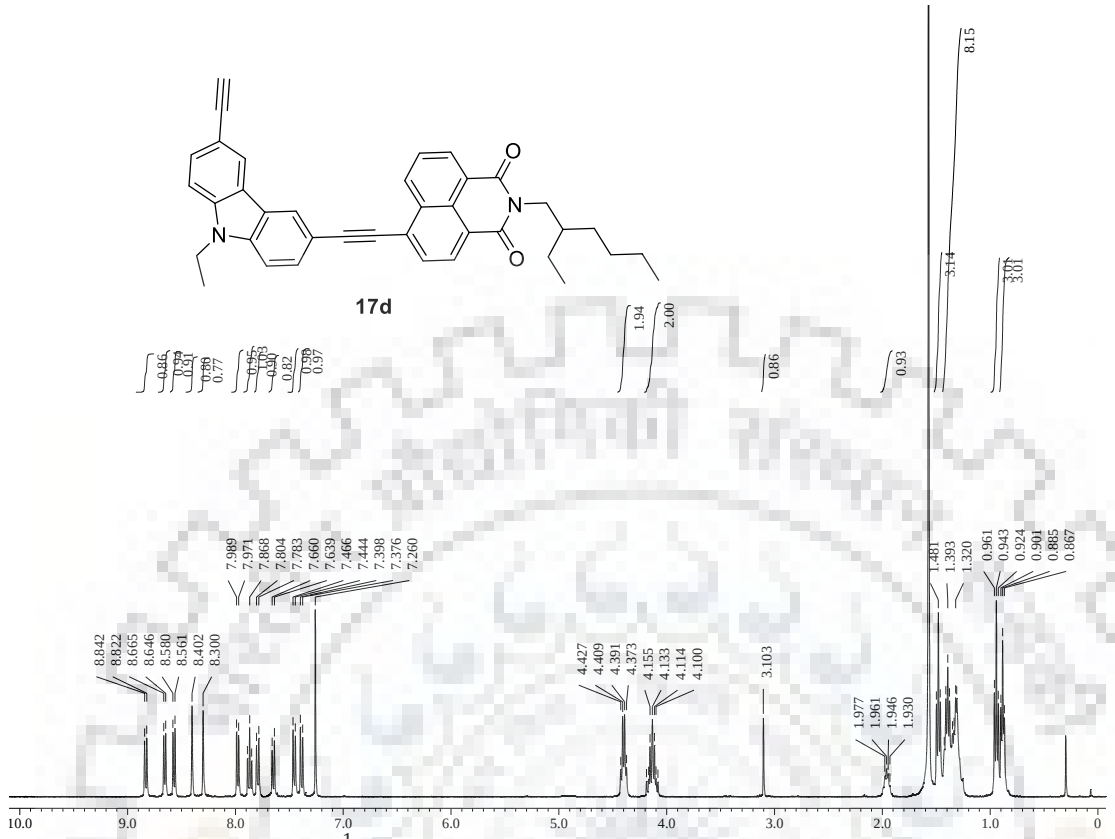

Figure S35 ^{1}H NMR spectrum of **17d** recorded in $CDCl_3$.

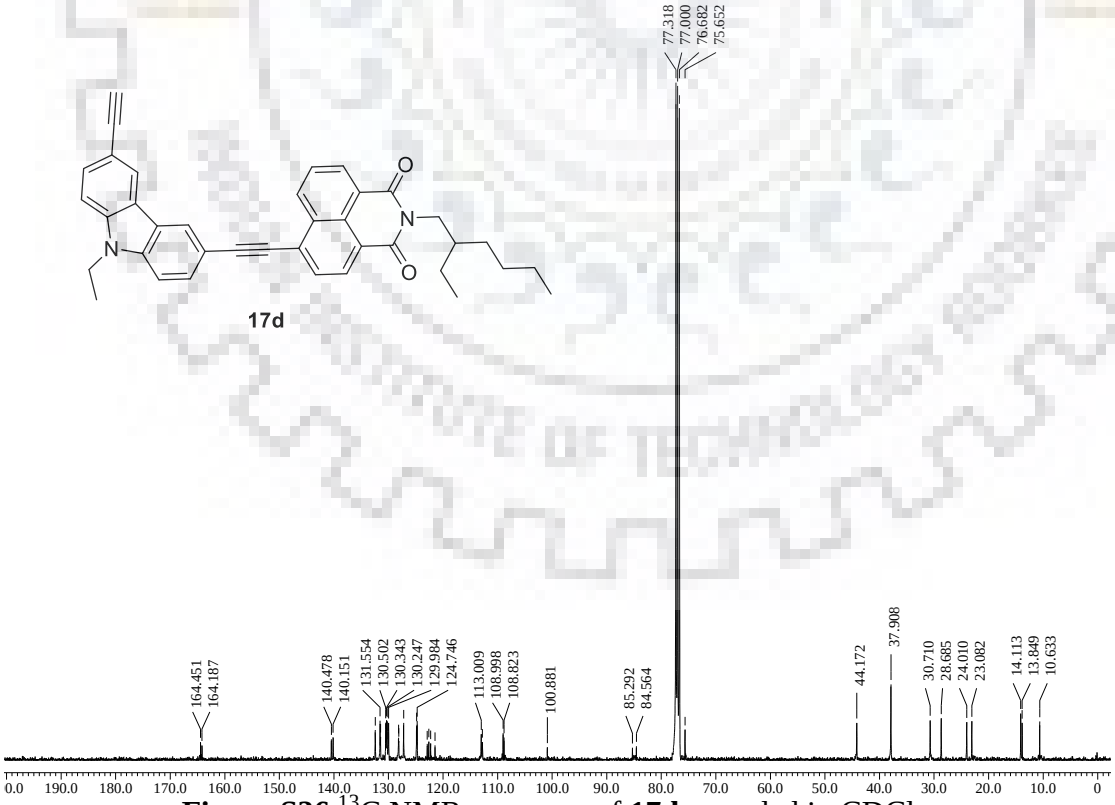

Figure S36 ^{13}C NMR spectrum of **17d** recorded in $CDCl_3$.

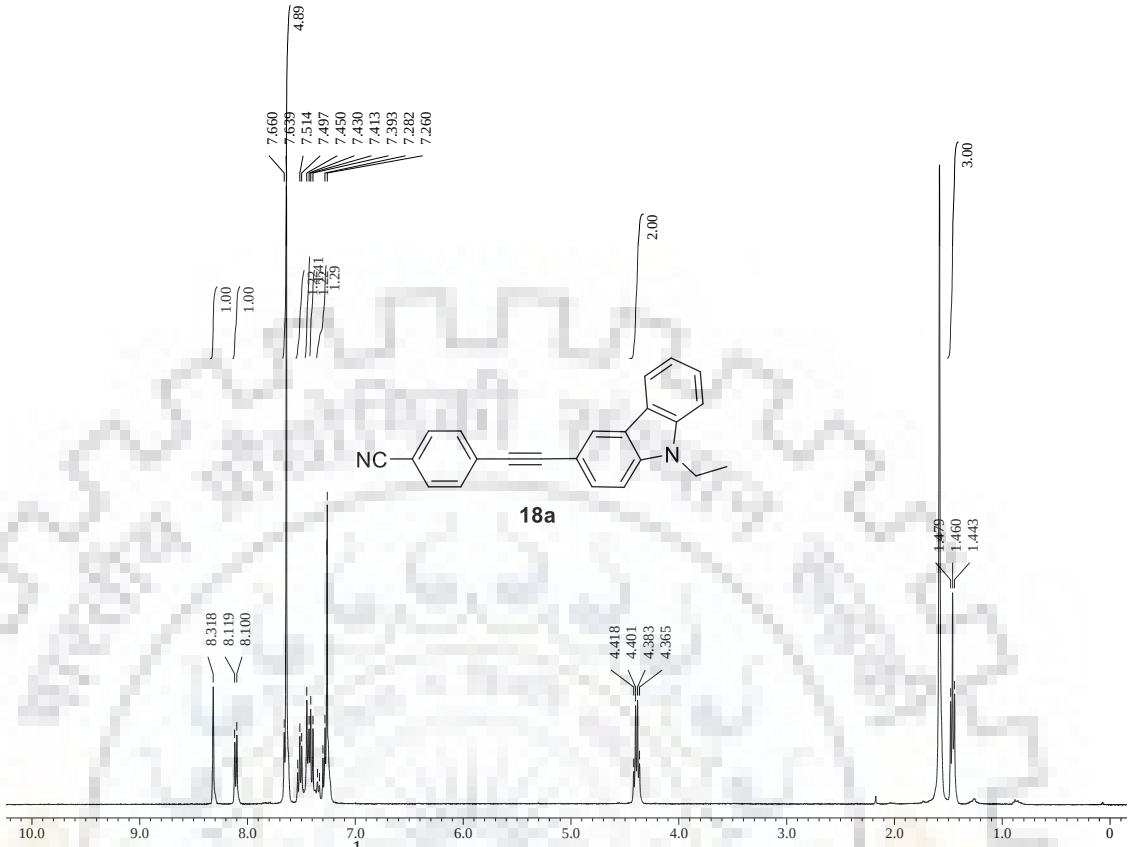

Figure S37 ^{1}H NMR spectrum of **18a** recorded in $CDCl_3$.

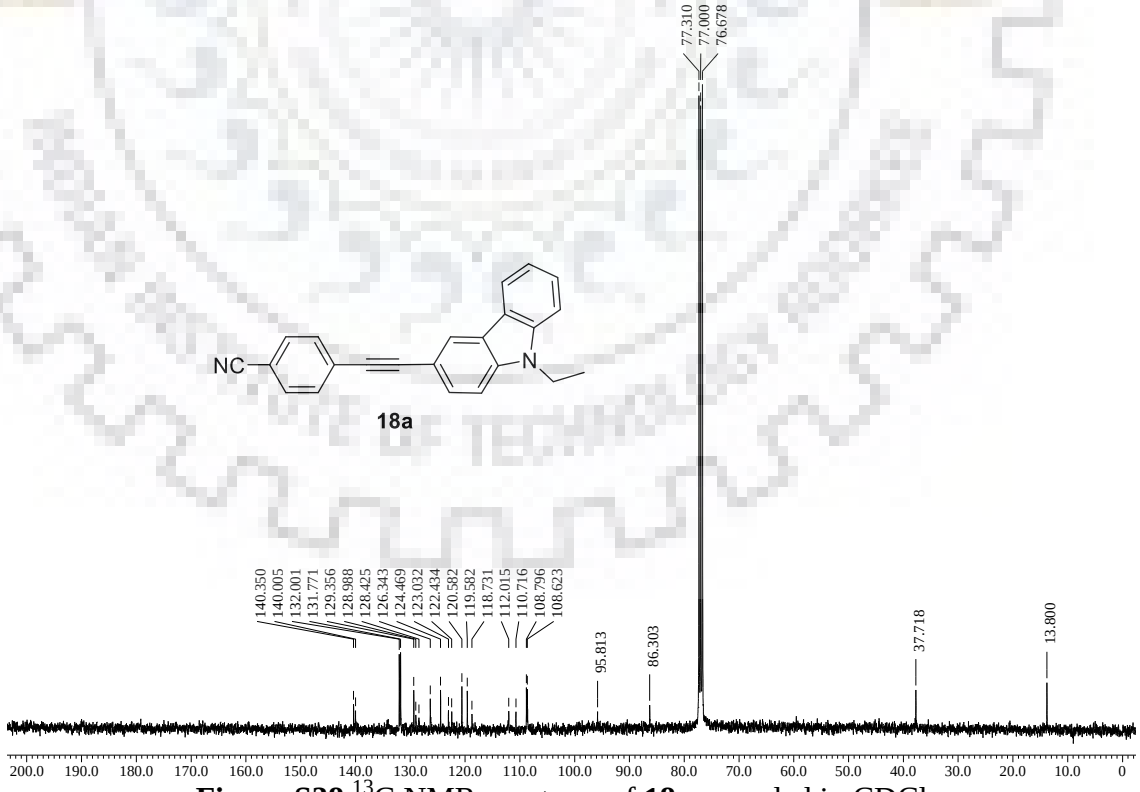

Figure S38 ^{13}C NMR spectrum of **18a** recorded in $CDCl_3$.

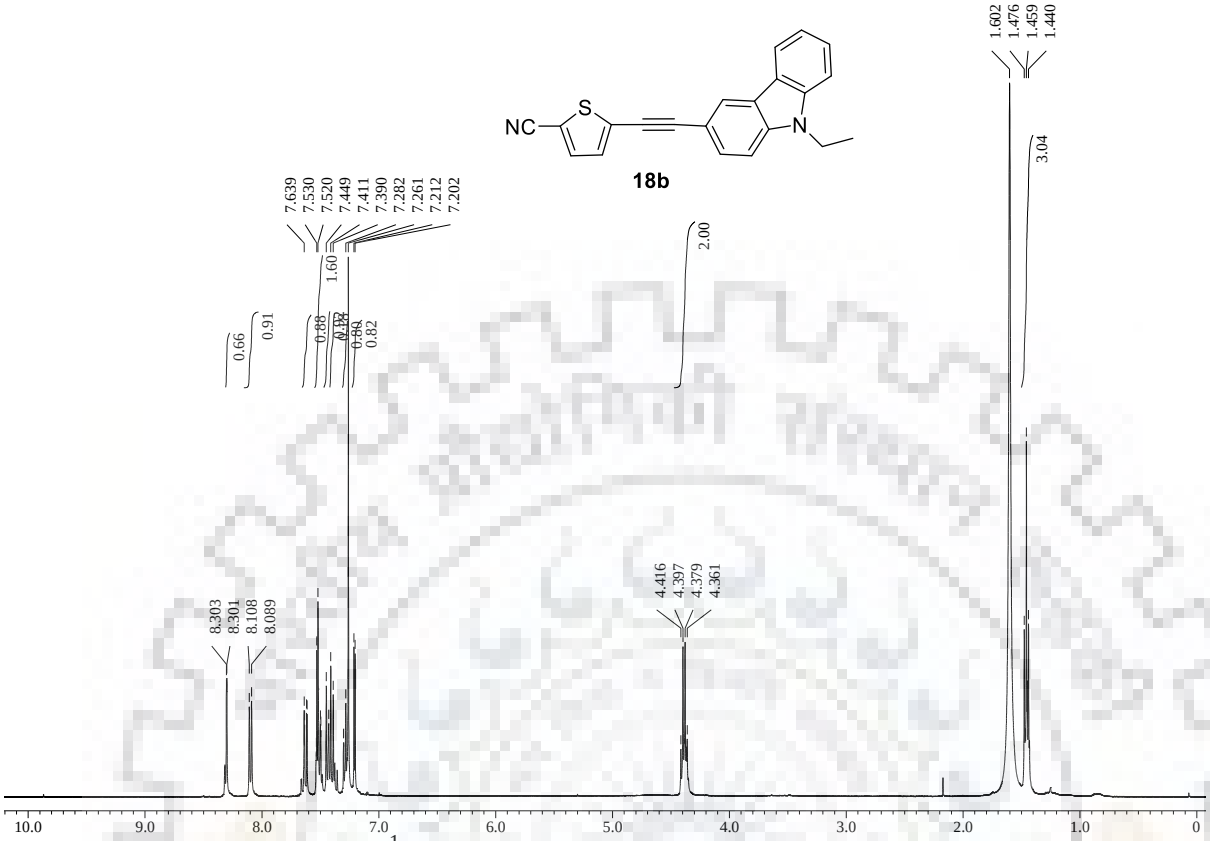

Figure S39 ^{1}H NMR spectrum of **18b** recorded in $CDCl_3$.

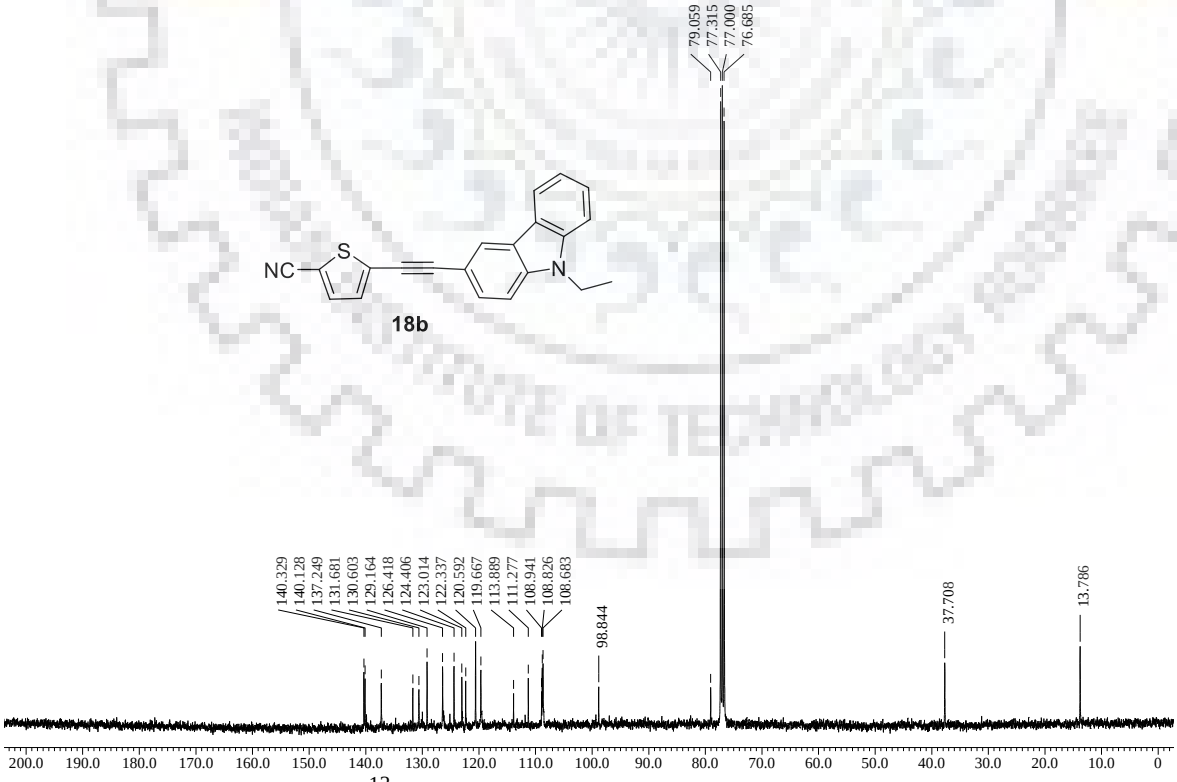

Figure S40 ^{13}C NMR spectrum of **18b** recorded in $CDCl_3$.

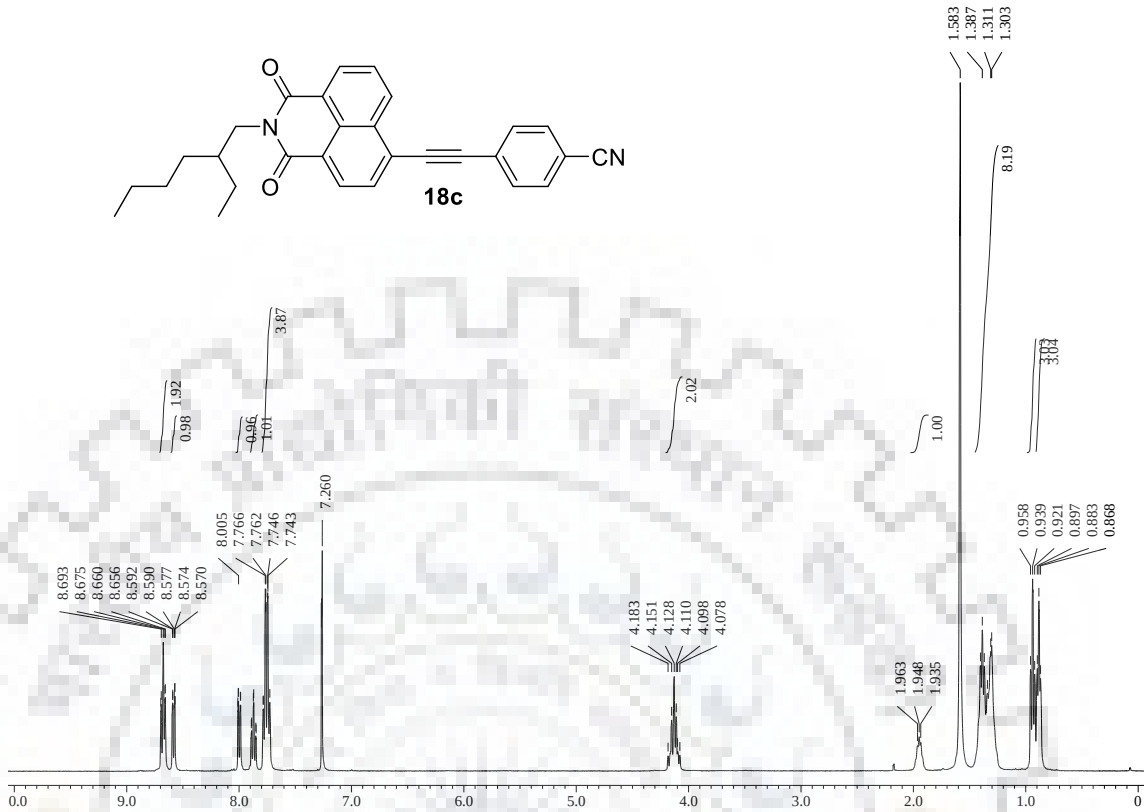

Figure S41 ^{1}H NMR spectrum of **18c** recorded in $CDCl_3$.

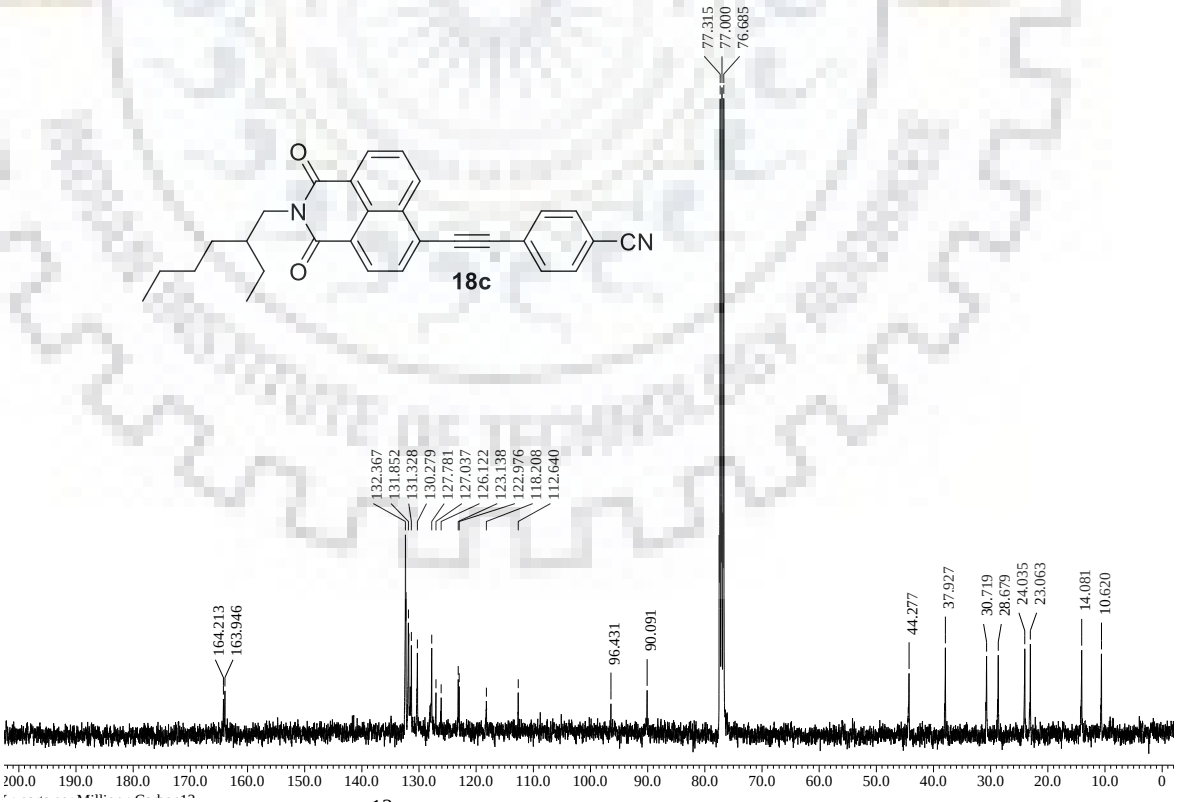

Figure S42 ^{13}C NMR spectrum of **18c** recorded in $CDCl_3$.

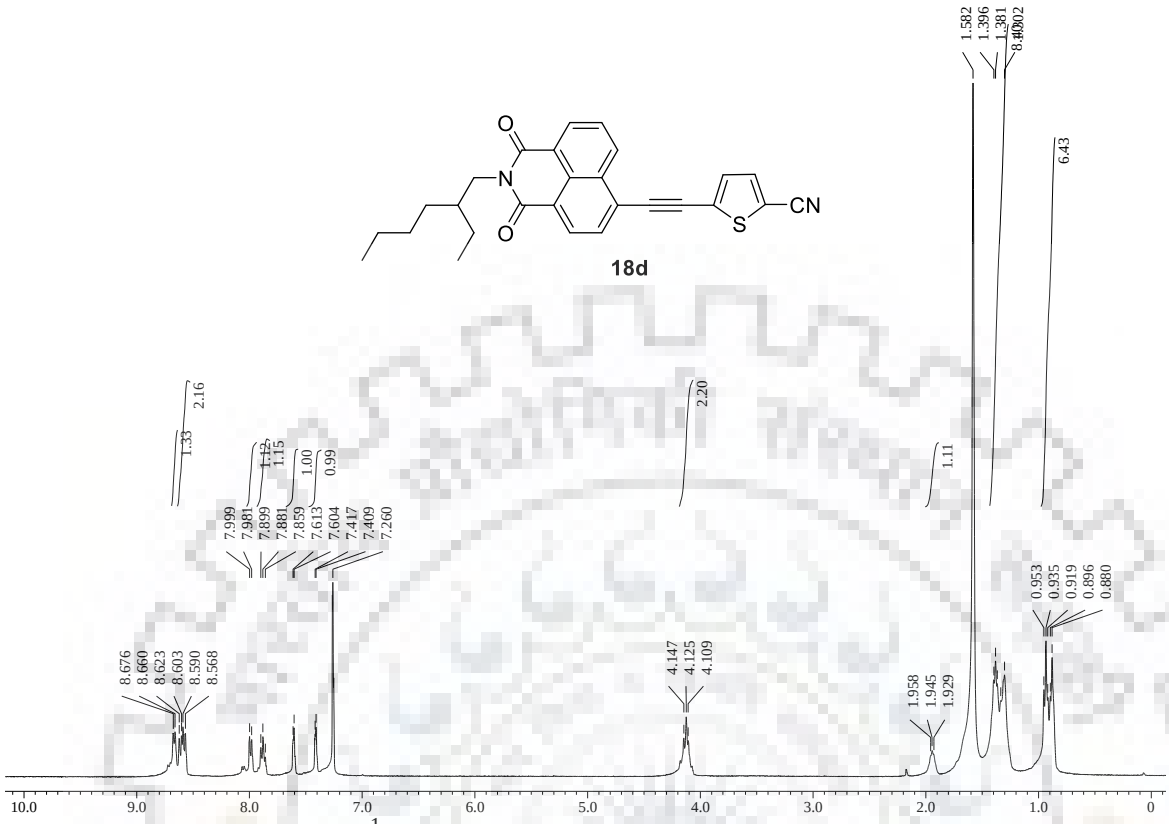

Figure S43 ^{1}H NMR spectrum of **18d** recorded in $CDCl_3$.

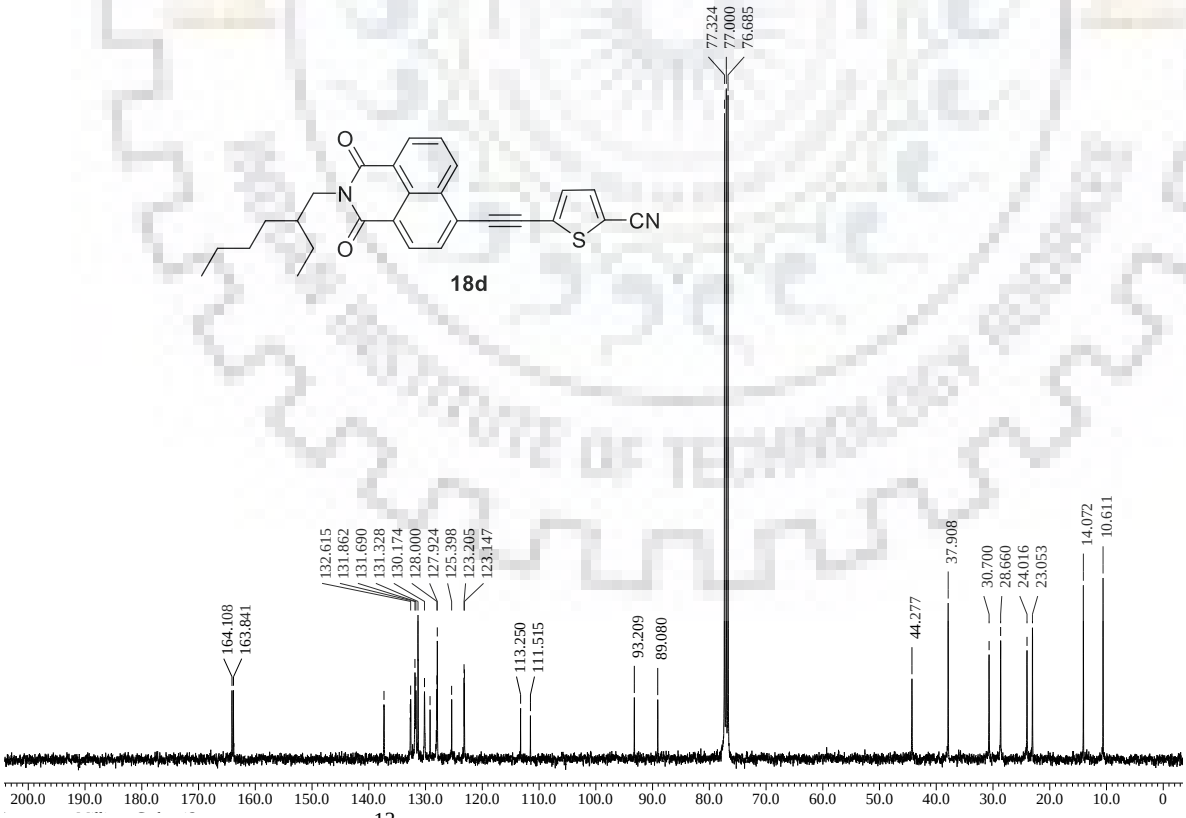

Figure S44 ^{13}C NMR spectrum of **18d** recorded in $CDCl_3$.

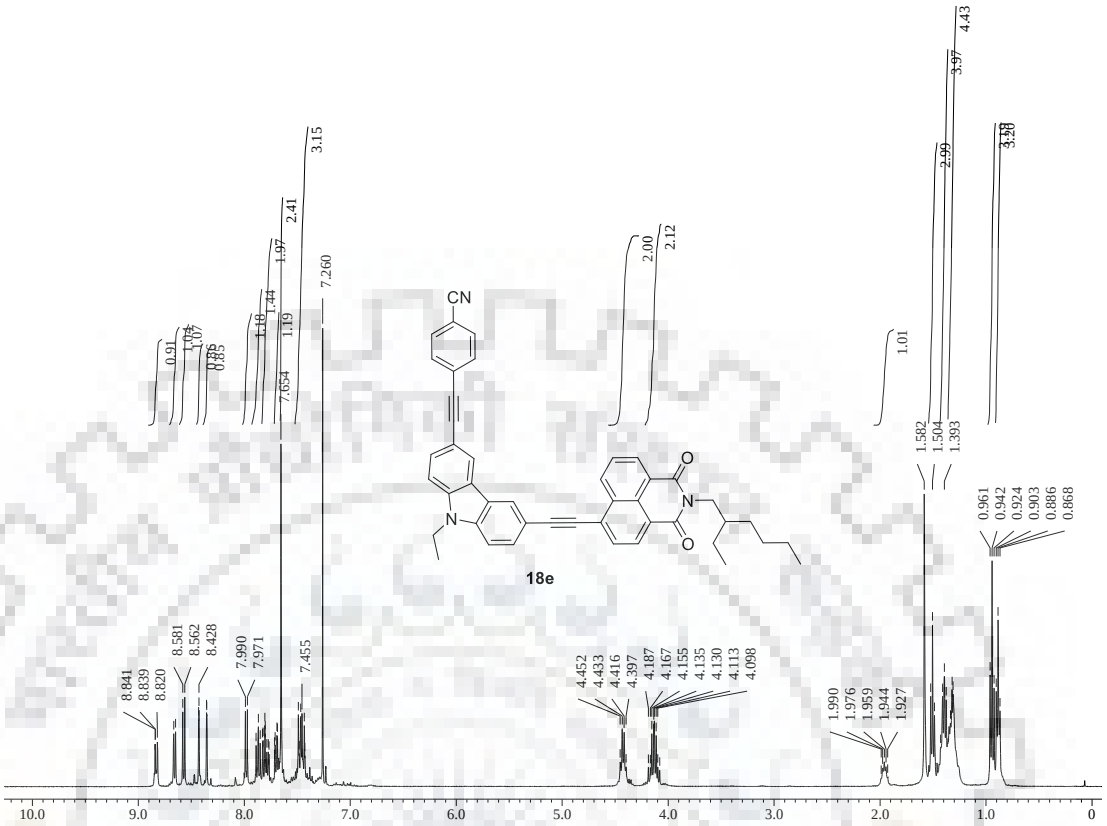

Figure S45 ^{1}H NMR spectrum of **18e** recorded in $CDCl_3$.

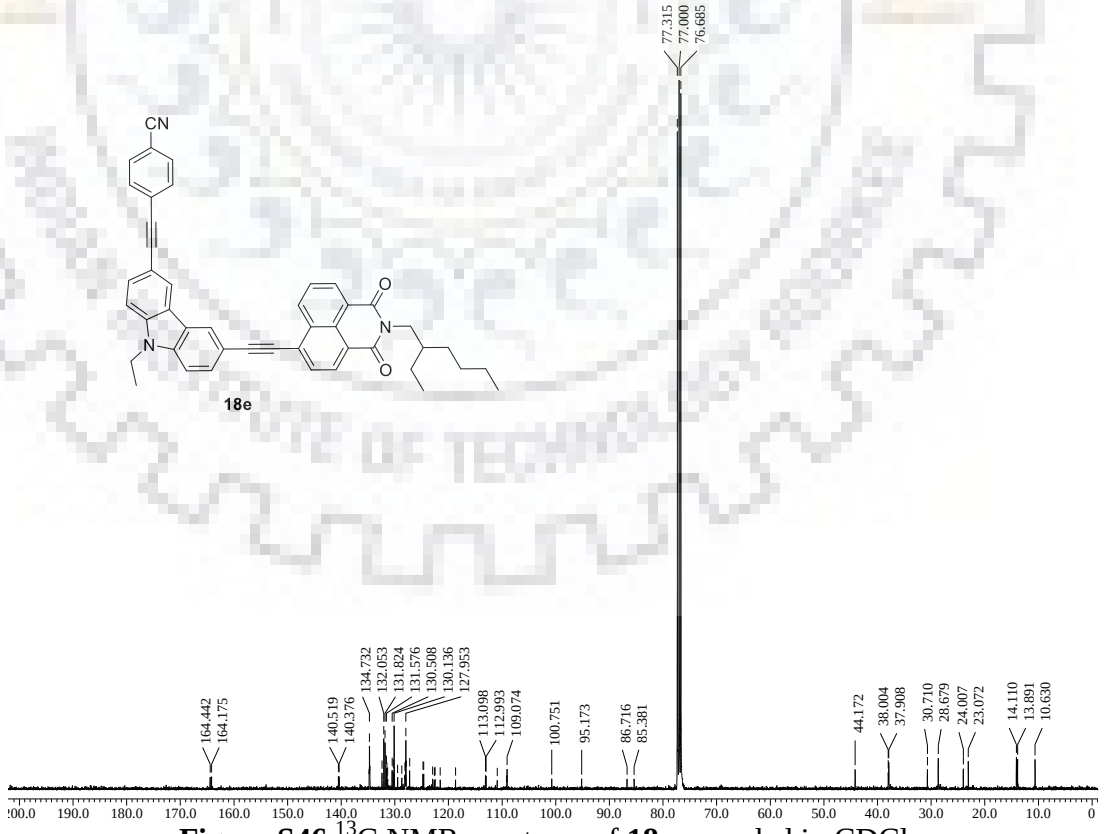

Figure S46 ^{13}C NMR spectrum of **18e** recorded in $CDCl_3$.

Figure S47 ^{1}H NMR spectrum of **18f** recorded in $CDCl_3$.

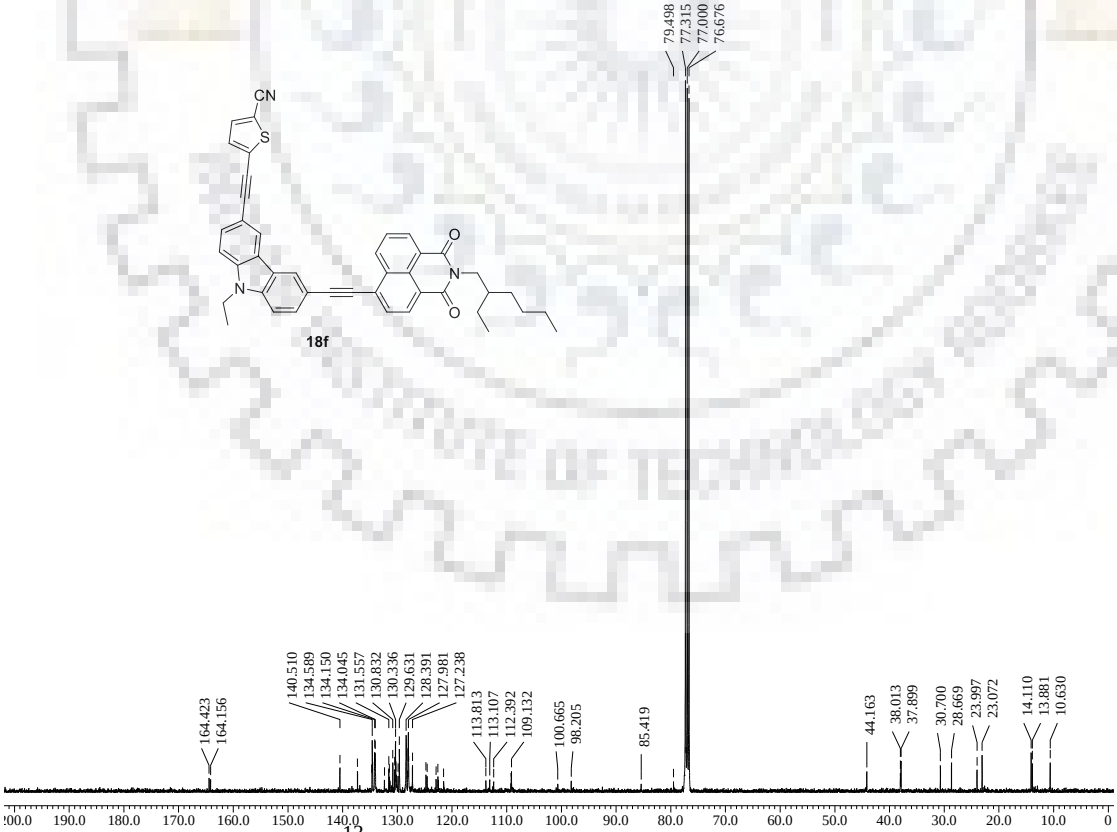

Figure S48 ^{13}C NMR spectrum of **18f** recorded in $CDCl_3$.

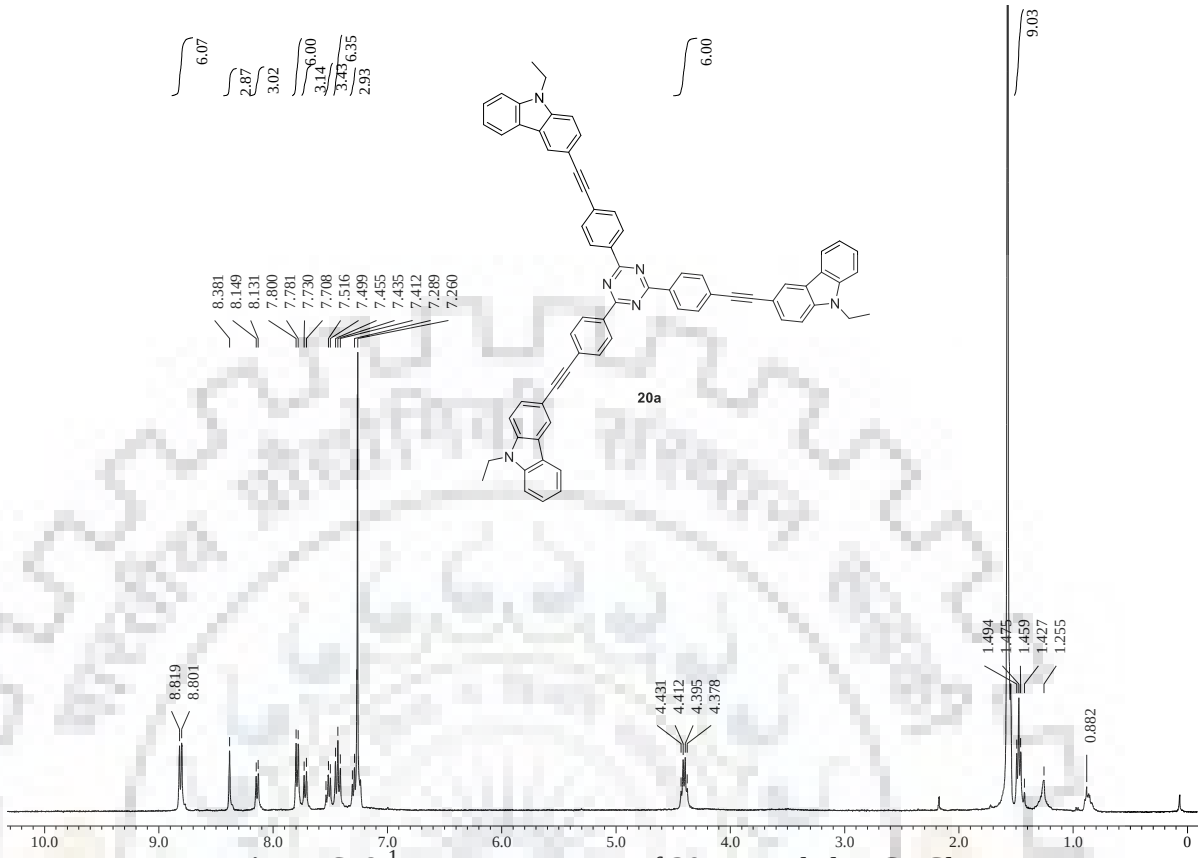

Figure S49 ^{1}H NMR spectrum of **20a** recorded in $CDCl_3$.

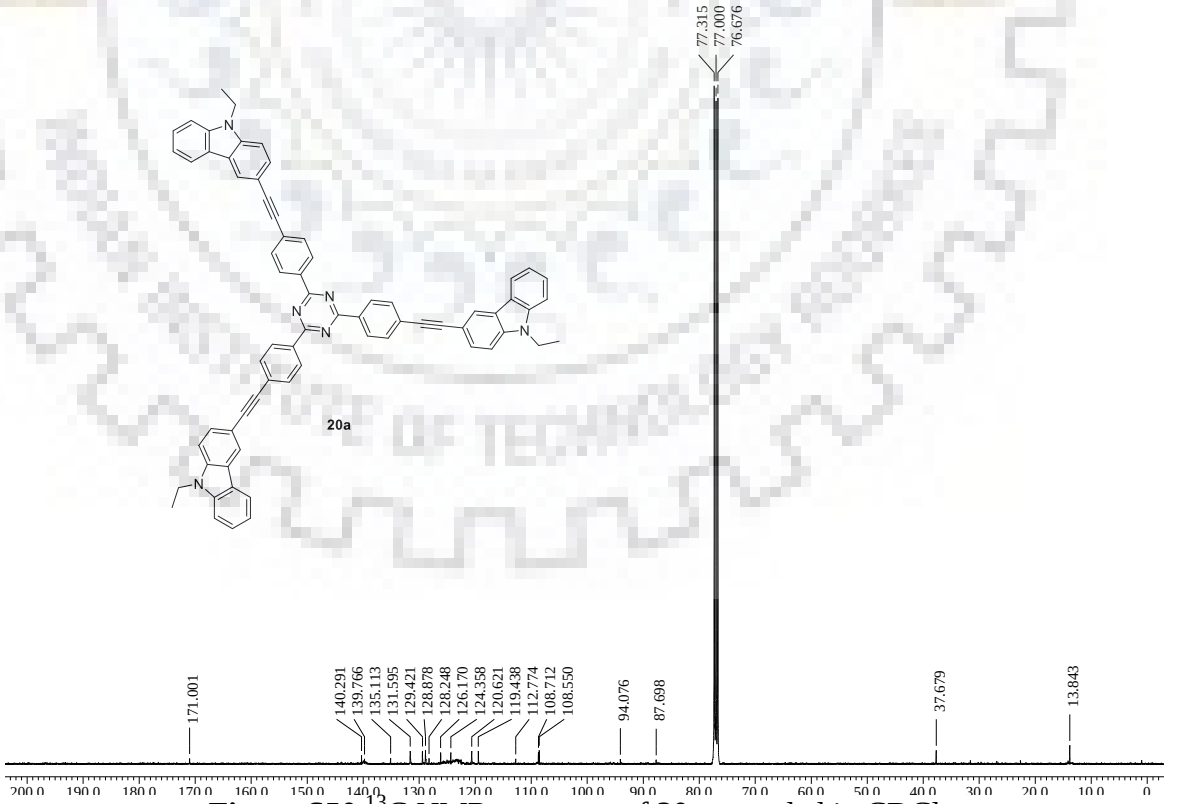

Figure S50 ^{13}C NMR spectrum of **20a** recorded in $CDCl_3$.

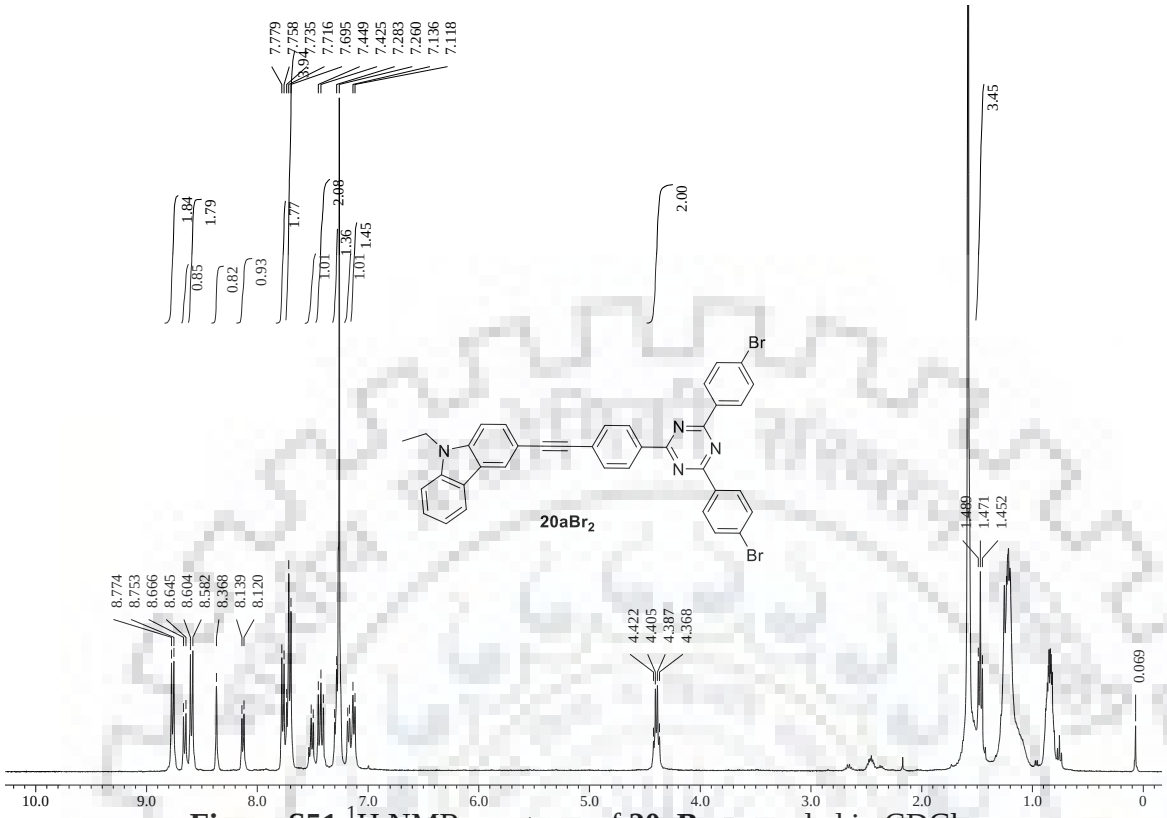

Figure S51 ^{1}H NMR spectrum of **20aBr$_2$** recorded in $CDCl_3$.

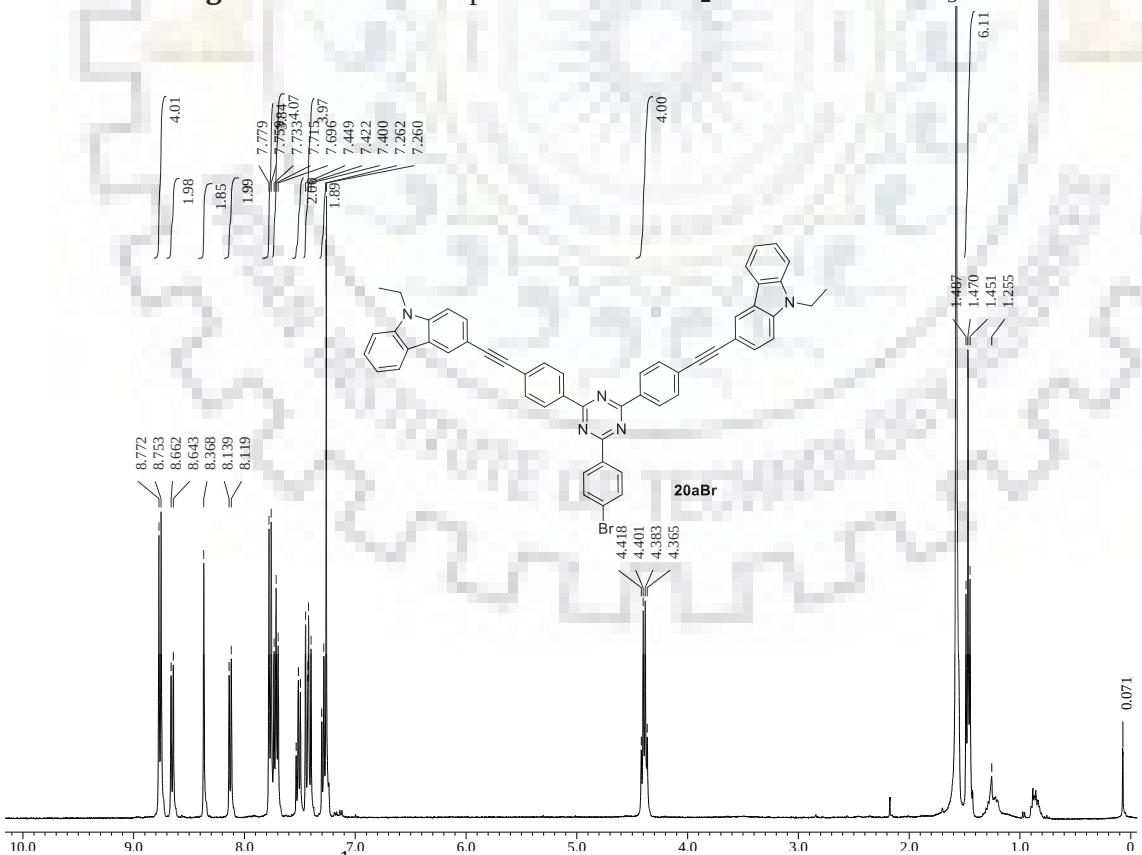

Figure S52 ^{1}H NMR spectrum of **20aBr** recorded in $CDCl_3$.

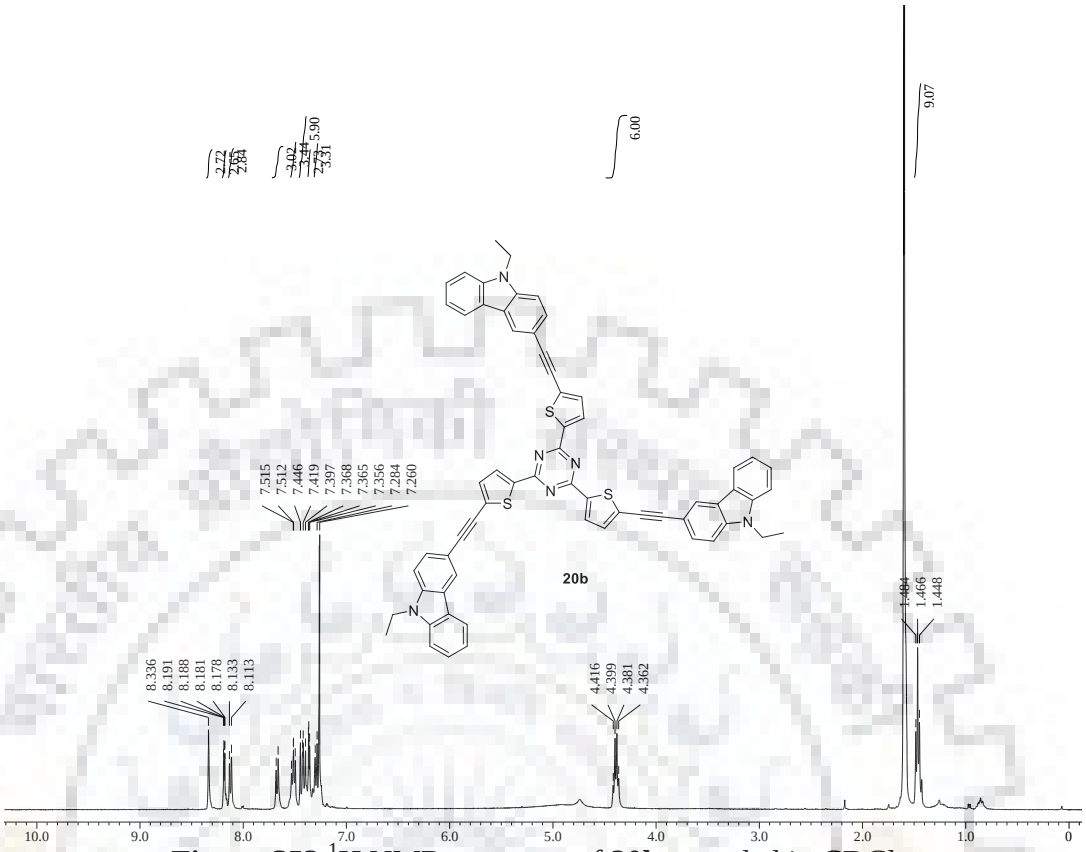

Figure S53 ^{1}H NMR spectrum of **20b** recorded in $CDCl_3$.

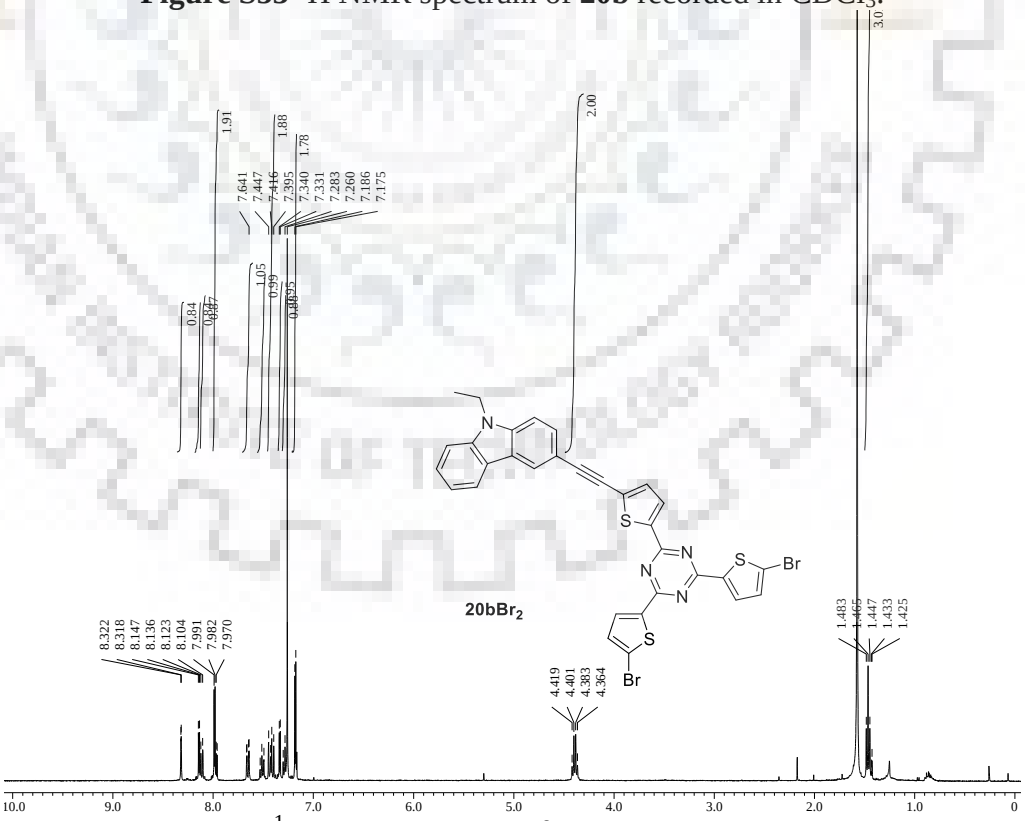

Figure S54 ^{1}H NMR spectrum of **20bBr$_2$** recorded in $CDCl_3$.

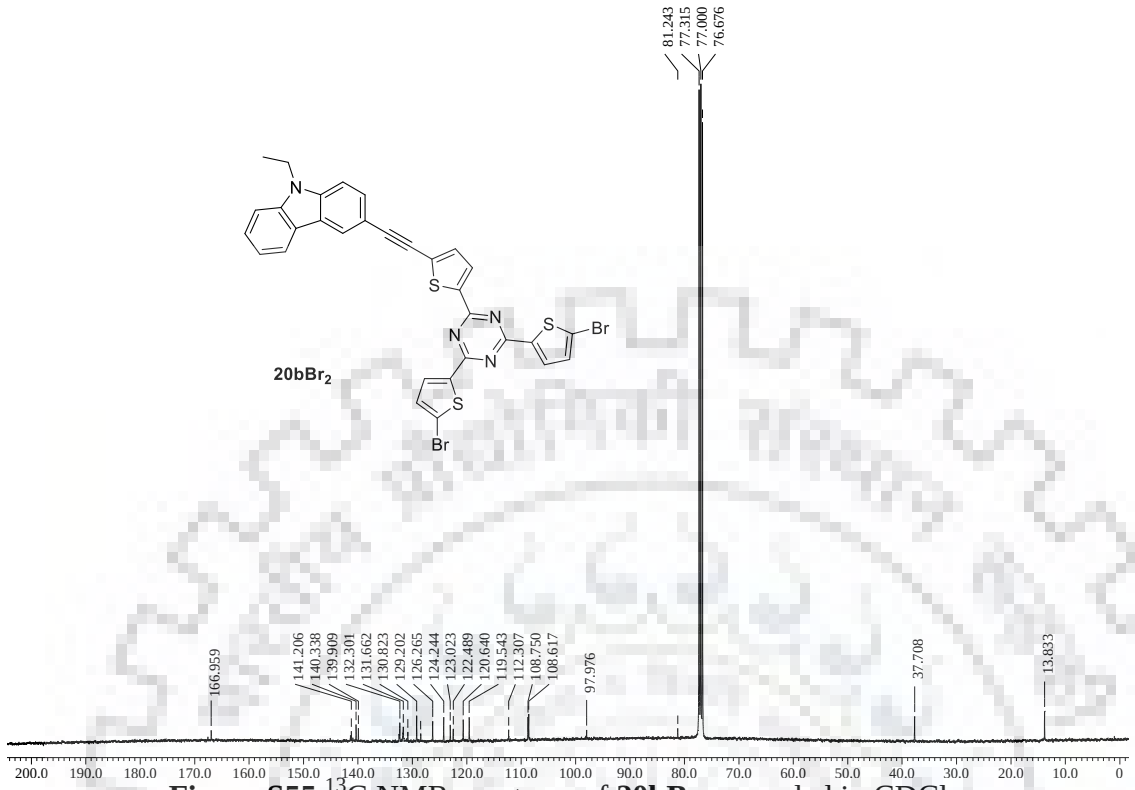

Figure S55 ^{13}C NMR spectrum of **20bBr$_2$** recorded in $CDCl_3$.

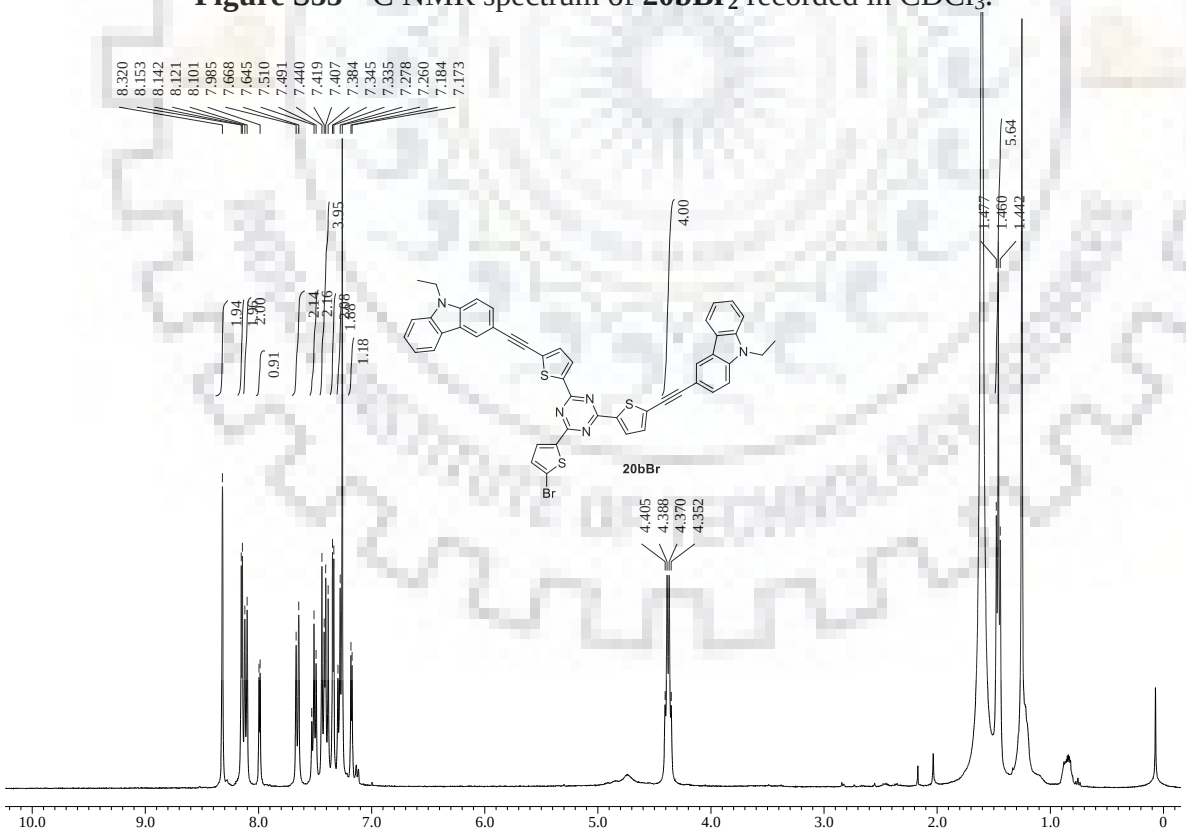

Figure S56 ^{1}H NMR spectrum of **20aBr** recorded in $CDCl_3$.

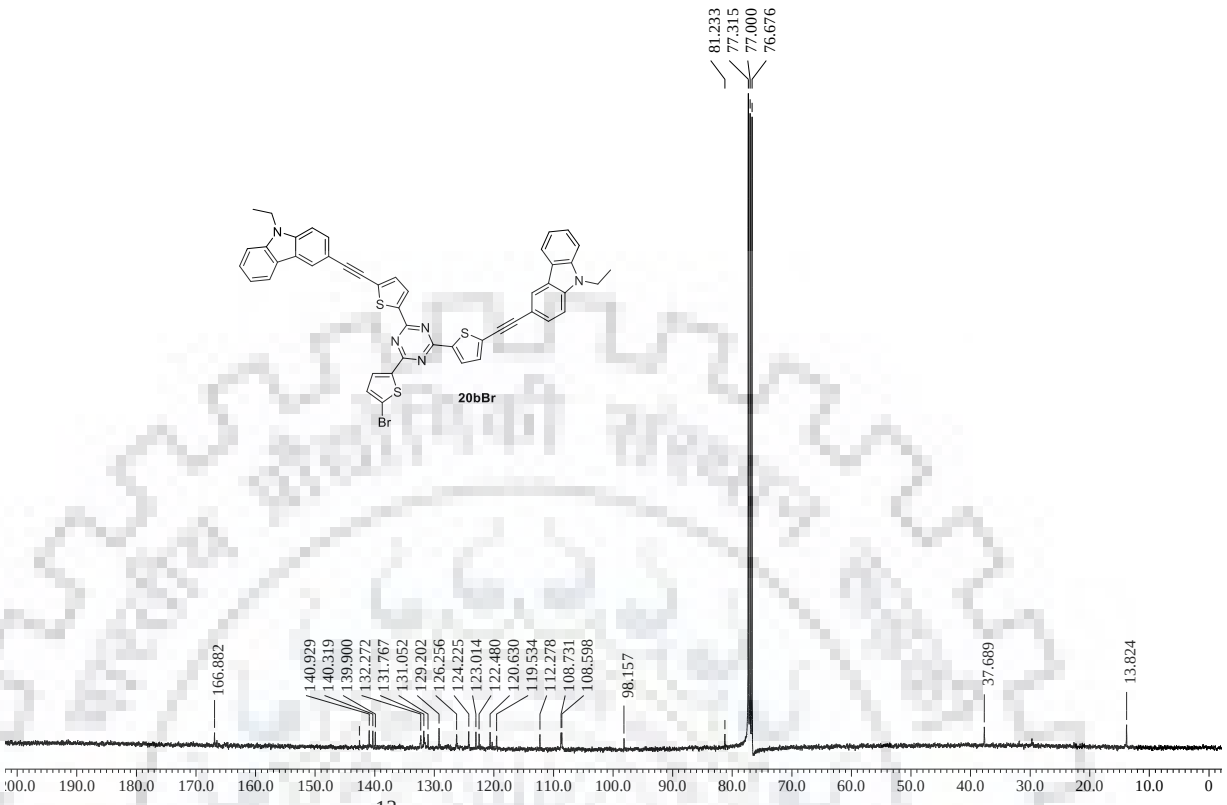

Figure S57 ^{13}C NMR spectrum of **20bBr** recorded in $CDCl_3$.

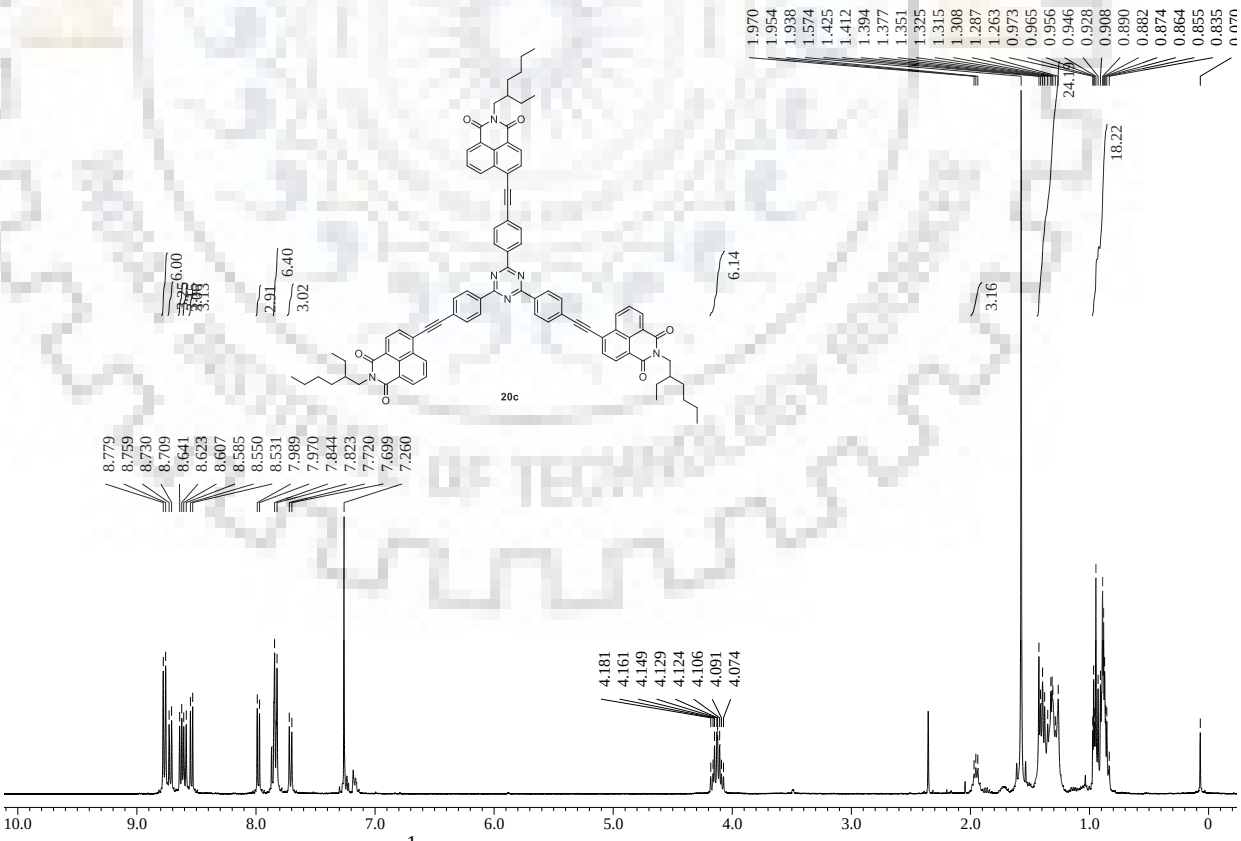

Figure S58 ^{1}H NMR spectrum of **20c** recorded in $CDCl_3$.

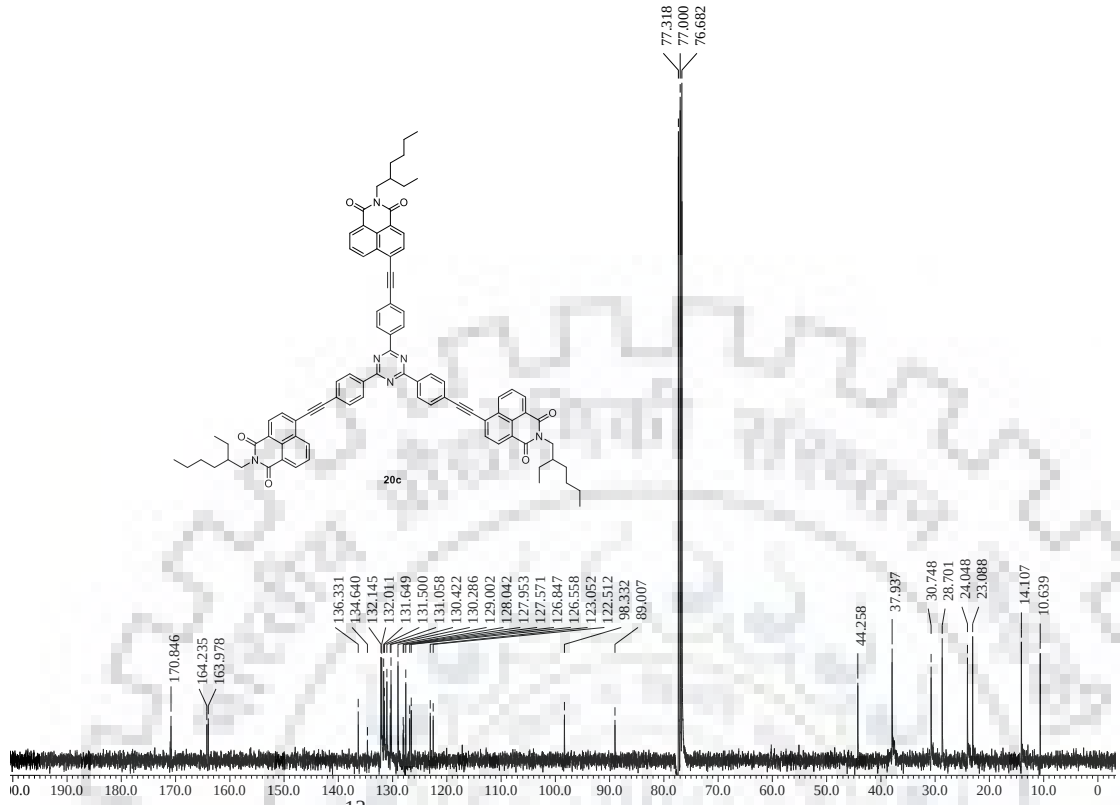

Figure S59 ^{13}C NMR spectrum of **20c** recorded in $CDCl_3$.

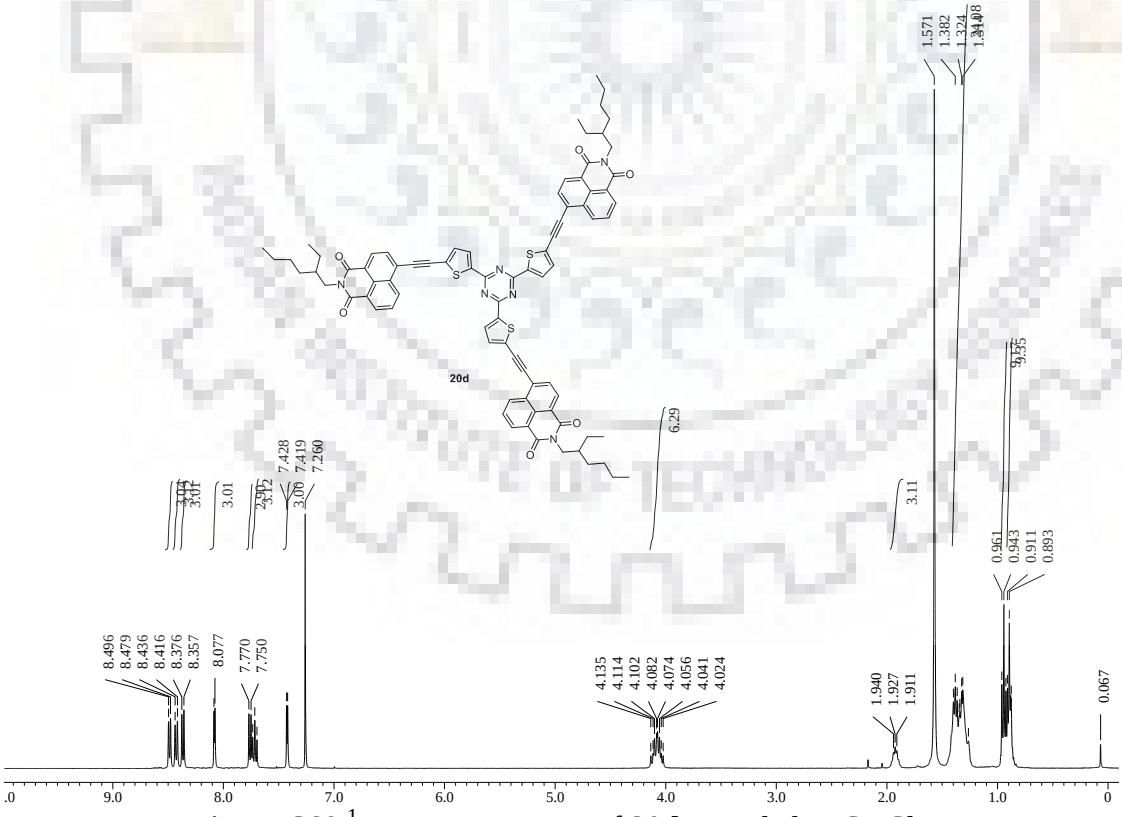

Figure S60 ^{1}H NMR spectrum of **20d** recorded in $CDCl_3$.

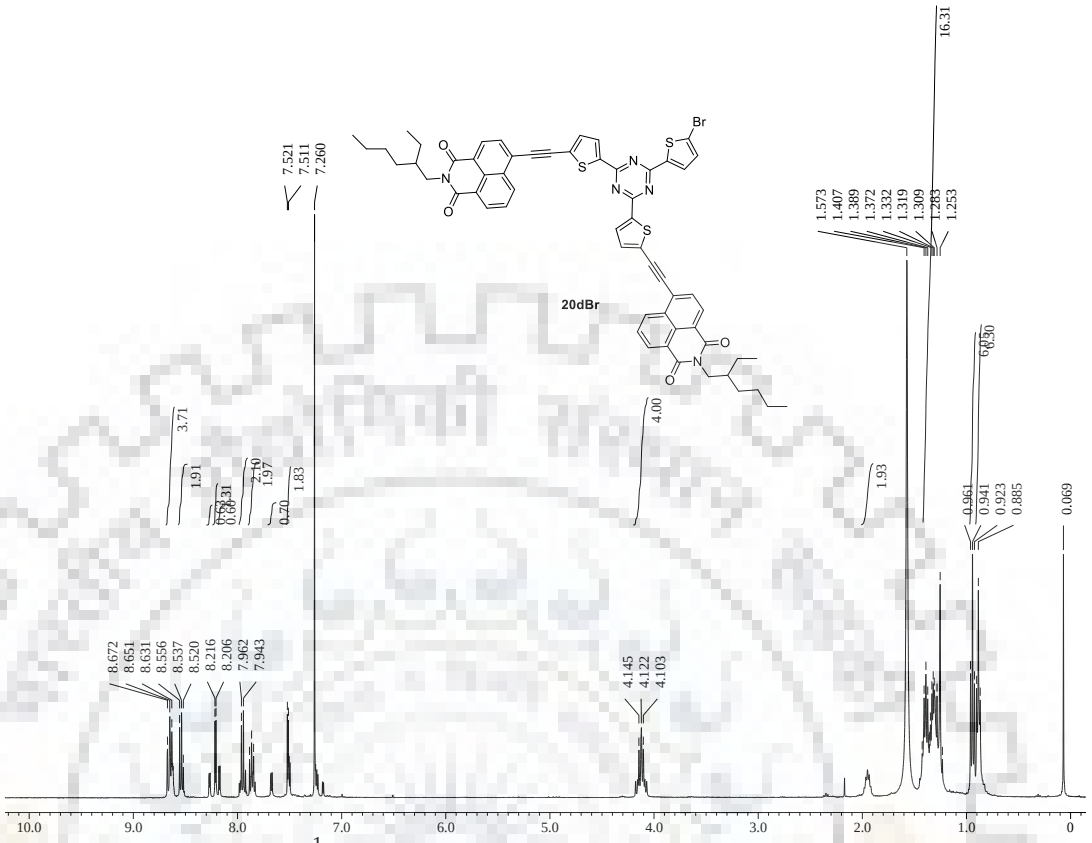

Figure S61 ^{1}H NMR spectrum of **20dBr** recorded in $CDCl_3$.

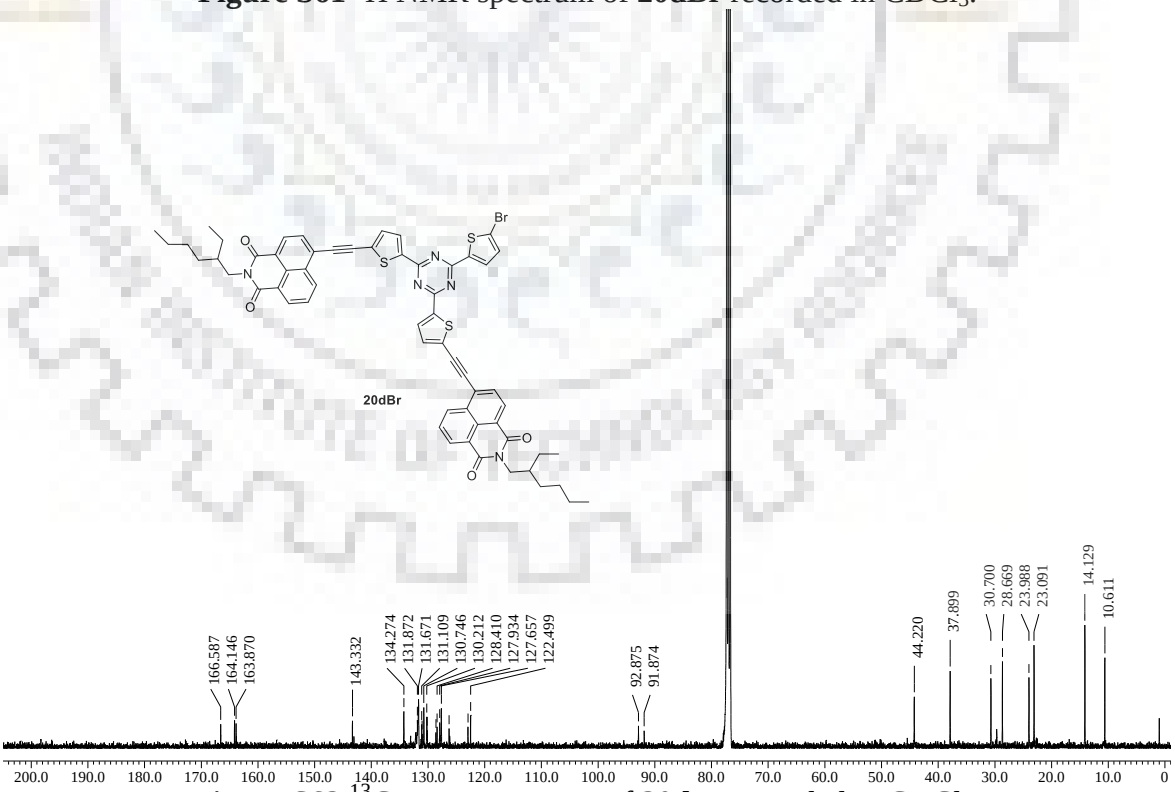

Figure S62 ^{13}C NMR spectrum of **20dBr** recorded in $CDCl_3$.